Advanced

by MicroVention

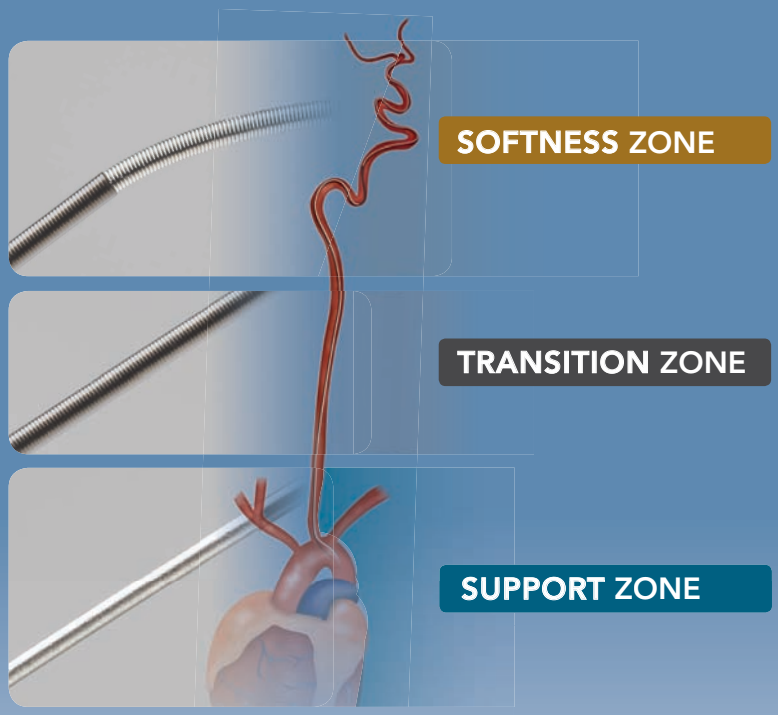

V-Trak® Advanced Coil System

ENHANCED CONTROL TO MAXIMIZE COIL PERFORMANCE

The **V-Trak® Advanced Coil System**, the next generation to power the performance of our most technically advanced line of coils. Offering the optimal combination of support and flexibility.

microvention.com

CE 0297

Versatility

by MicroVention

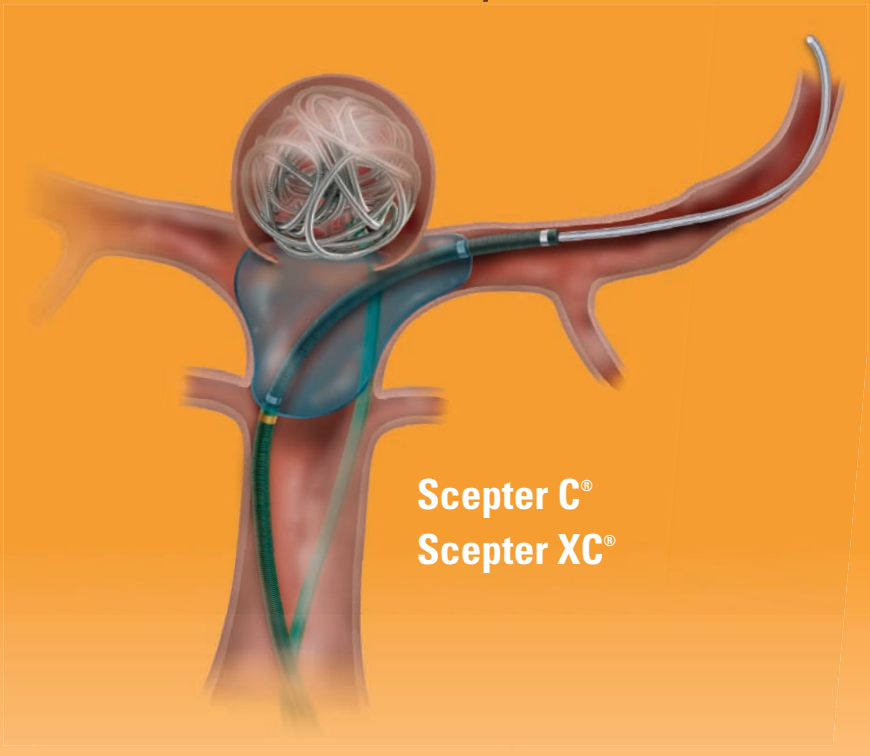

Scepter
Occlusion Balloon Catheter

REDEFINING DELIVERABILITY, VERSATILITY AND CONTROL

MicroVention has developed two occlusion balloon catheters. **Scepter C®** compliant balloon is designed for reliable vessel occlusion yet conforms to vessel anatomy. **Scepter XC®** x-tra compliant balloon conforms to extremely complex anatomies where neck coverage is more challenging.

• *Used with* Headway Microcatheter

For more information or a product demonstration, contact your local MicroVention representative:

MicroVention® TERUMO

MicroVention, Inc.
Worldwide Headquarters PH +1.714.247.8000
1311 Valencia Avenue
Tustin, CA 92780 USA
MicroVention UK Limited PH +44 (0) 191 258 6777
MicroVention Europe, S.A.R.L. PH +33 (1) 39 21 77 46
MicroVention Deutschland GmbH PH +49 211 210 798-0

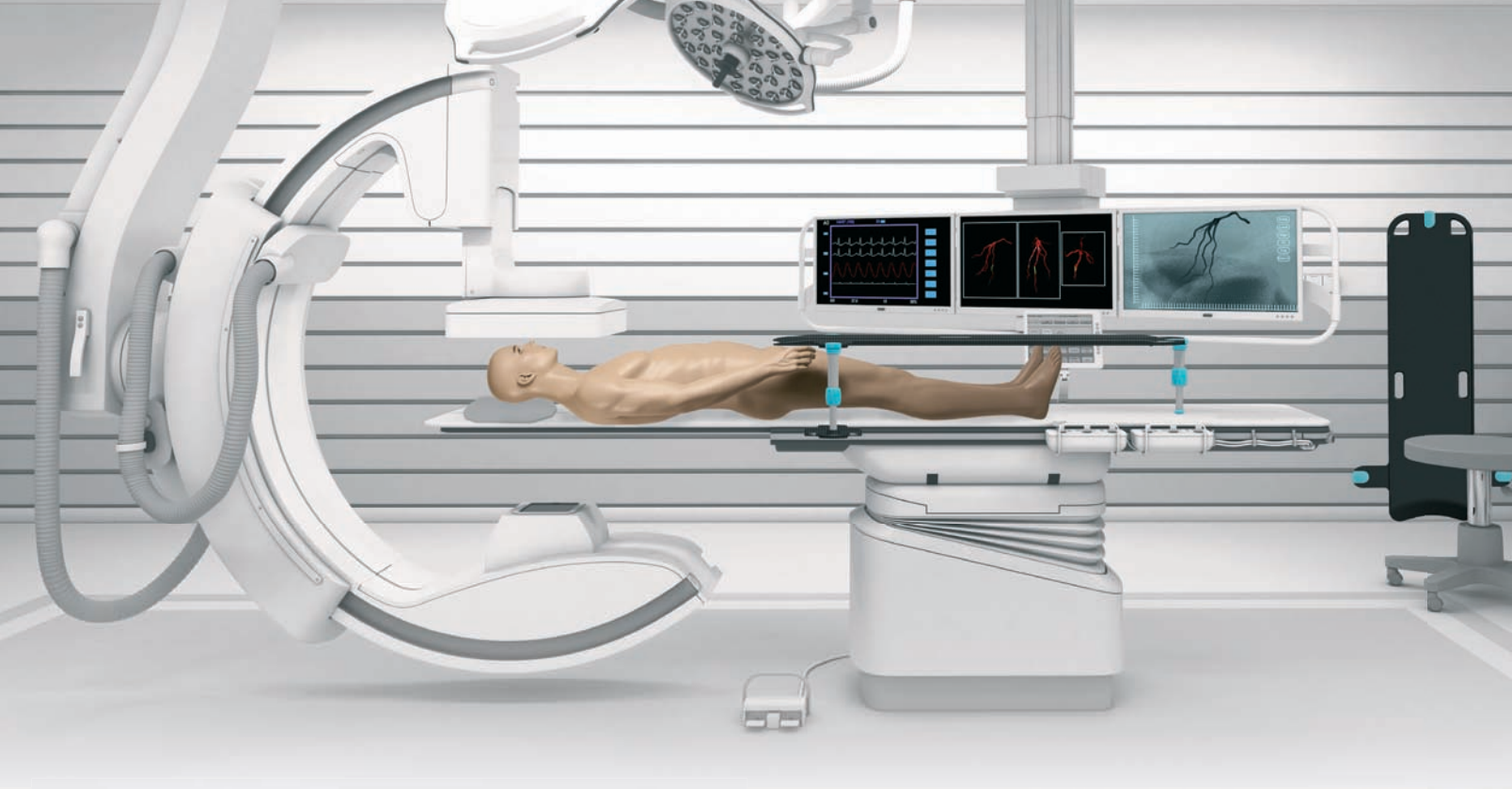

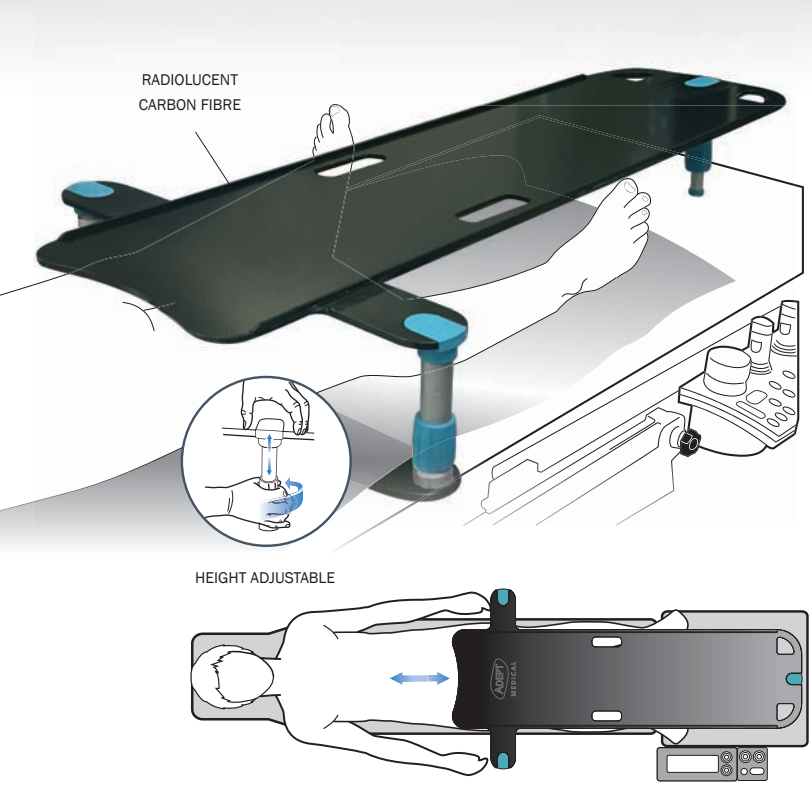

ADEPT
MEDICAL

A TABLE DESIGNED SPECIALLY FOR NEURO INTERVENTIONS VIA FEMORAL ACCESS

Designed in conjunction with a leading Neuroradiologist, the femoral table is an effective solution for all femoral access procedures. It offers clinical benefits to the current practice of laying procedural equipment over the draped patient's legs. The height adjustable radiolucent work surface facilitates stable catheter/guide wire manipulation and provides a surface for syringes, bowls and other equipment. For more details and instructional video please visit

www.adeptmedical.com/neuro

FITS ANY BED

EASY POSITIONING

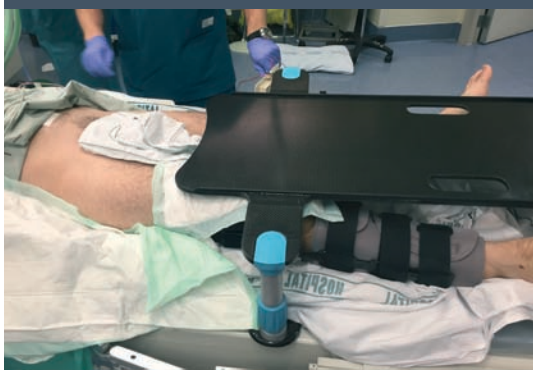

FLAT WORK SURFACE

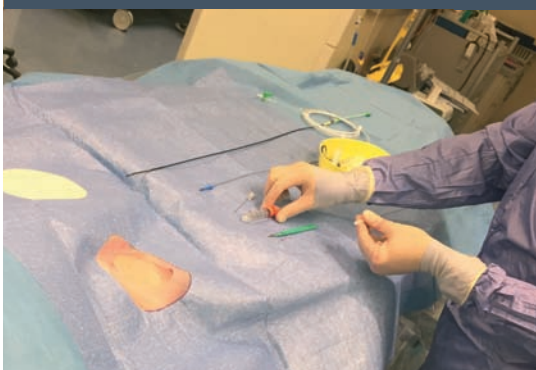

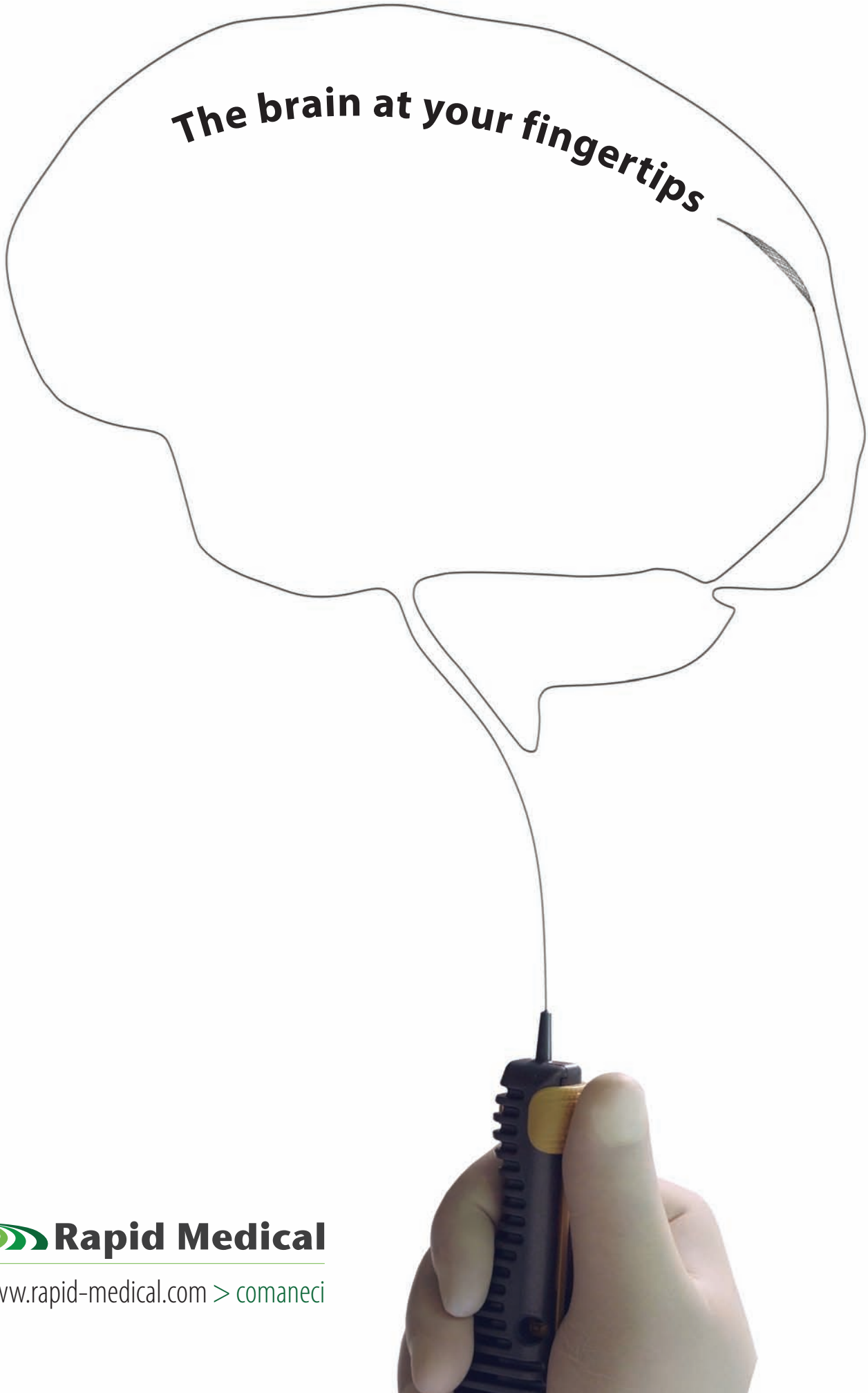

Smooth and Stable

Whether you are framing, filling or finishing, Target Detachable Coils deliver consistently smooth deployment and exceptional microcatheter stability. Focused on design, Target Coils feature a host of advantages to ensure the high-powered performance you demand.

For more information, please visit www.strykerneurovascular.com/Target or contact your local Stryker Neurovascular sales representative.

stryker® Neurovascular

Stroke: *Our Only Focus. Our Ongoing Promise.*

AJNR

CALL FOR AJNR EDITORIAL FELLOWSHIP CANDIDATES

ASNR and AJNR are pleased once again to join efforts with other imaging-related journals that have training programs on editorial aspects of publishing for trainees or junior staff (3–5 years after training), including Radiology (Olmsted fellowship), AJR (Figley and Rogers fellowships), JACR (Bruce J. Hillman fellowship), and Radiologia.

2016 Candidate Information and Requirements

GOALS

- Increase interest in "editorial" and publication-related activities in younger individuals.
- Increase understanding and participation in the AJNR review process.
- Incorporate into AJNR's Editorial Board younger individuals who have previous experience in the review and publication process.
- Fill a specific need in neuroradiology not offered by other similar fellowships.
- Increase the relationship between "new" generation of neuroradiologists and more established individuals.
- Increase visibility of AJNR among younger neuroradiologists.

ACTIVITIES OF THE FELLOWSHIP

- Serve as Editorial Fellow for one year. This individual will be listed on the masthead as such.
- Review at least one manuscript per month for 12 months. Evaluate all review articles submitted to AJNR.
- Access to our electronic manuscript review system will be granted so that the candidate can learn how these systems work.
- Be involved in the final decision of selected manuscripts together with the Editor-in-Chief.
- Participate in all monthly Senior Editor telephone conference calls.
- Participate in all meetings of the Editors and Publications Committee during the annual meetings of ASNR and RSNA as per candidate's availability. The Foundation of the ASNR will provide $2000 funding for this activity.
- Evaluate progress and adjust program to specific needs in annual meeting or telephone conference with the Editor-in-Chief.
- Write at least one editorial for AJNR.
- Embark on an editorial scientific or bibliometric project that will lead to the submission of an article to AJNR or another appropriate journal as determined by the Editor-in-Chief. This project will be presented by the Editorial Fellow at the ASNR annual meeting.
- Serve as liaison between AJNR and ASNR's Young Professionals Network and the 3 YPs appointed to AJNR as special consultants. Participate in meetings and telephone calls with this group. Design one electronic survey/year polling the group regarding readership attitudes and wishes.
- Recruit trainees as reviewers as determined by the Editor-in-Chief.
- Participate in Web improvement projects.
- Invite Guest Editors for AJNR's News Digest to cover a variety of timely topics.

QUALIFICATIONS

- Be a fellow in neuroradiology from North America, including Canada (this may be extended to include other countries).
- Be a junior faculty neuroradiology member (< 3 years) in either an academic or private environment.
- Be an "in-training" or member of ASNR in any other category.

APPLICATION

- Include a short letter of intent with statement of goals and desired research project. CV must be included.
- Include a letter of recommendation from the Division Chief or fellowship program director. A statement of protected time to perform the functions outlined is desirable.
- Applications will be evaluated by AJNR's Senior Editors and the Chair of the Publications Committee prior to the ASNR meeting. The name of the selected individual will be announced at the meeting.
- Applications should be received by March 4, 2016 and sent to Ms. Karen Halm, AJNR Managing Editor, electronically at khalm@asnr.org.

ASNR 2016
Washington, DC
ASFNR • ASHNR • ASPNR • ASSR • SNIS
THE FOUNDATION OF THE ASNR

THE FOUNDATION OF THE ASNR SYMPOSIUM 2016: EMERGENCY NEURORADIOLOGY MAY 21-22

ASNR 54TH ANNUAL MEETING MAY 23-26

THE FOUNDATION OF THE ASNR SYMPOSIUM 2016: EMERGENCY NEURORADIOLOGY

The Symposium 2016 will be held from May 21-22 and will feature world-renowned speakers providing a comprehensive review of Emergency Neuroradiology and neuroimaging issues in critical care. Neuroimaging has become an indispensable tool for triage and management of both adults and children in emergency settings. Efficient and appropriate use of CT and MRI are critical to the urgent management of brain, spine, head & neck, and neurovascular emergencies, all of which will be highlighted by expert faculty. Best practices for traumatic and non-traumatic emergencies will be discussed, including methods to ensure optimal workflow, image post-processing, PACS integration, telemedicine, safety, and quality. Challenges and solutions for providing 24/7 coverage will be presented and debated.

ASNR 54TH ANNUAL MEETING: The meeting will be held from May 23-26 with an estimated 1,700 physicians and medical professionals worldwide who are interested in the latest products and services to deliver the highest quality care in the realm of Neuroradiology and allied professions. The Annual Meeting will provide informative updates on general Neuroradiology and showcase specialty programming from the ASFNR, ASHNR, ASPNR, ASSR, and SNIS. The heart of the meeting will be the invited lectures, original presentations, scientific posters and educational exhibits.

Howard A. Rowley, MD, ASNR 2016 Program Chair/President-Elect
Programming developed in cooperation with …

American Society of Functional Neuroradiology (ASFNR)
Christopher G. Filippi, MD

American Society of Head and Neck Radiology (ASHNR)
Lindell R. Gentry, MD

American Society of Pediatric Neuroradiology (ASPNR)
Erin Simon Schwartz, MD

American Society of Spine Radiology (ASSR)
Gregory J. Lawler, MD

Society of NeuroInterventional Surgery (SNIS)
Charles J. Prestigiacomo, MD

American Society of Neuroradiology (ASNR) Committee Programming:
Health Policy Committee
Robert M. Barr, MD, FACR

Computer Science and Informatics (CSI) Committee
John L. Go, MD, FACR

Research Scientists Committee
Dikoma C. Shungu, PhD

ASNR 54TH ANNUAL MEETING
c/o American Society of Neuroradiology
800 Enterprise Drive, Suite 205
Oak Brook, Illinois 60523-4216
Phone: 630-574-0220
Fax: 630 574-0661
www.asnr.org/2016

SCAN NOW TO VISIT OUR WEBSITE

SAVE THE DATE… MAY 21-26, 2016
WASHINGTON MARRIOTT WARDMAN PARK • WASHINGTON, DC

PHYSICIANS BOOST THE ECONOMY.

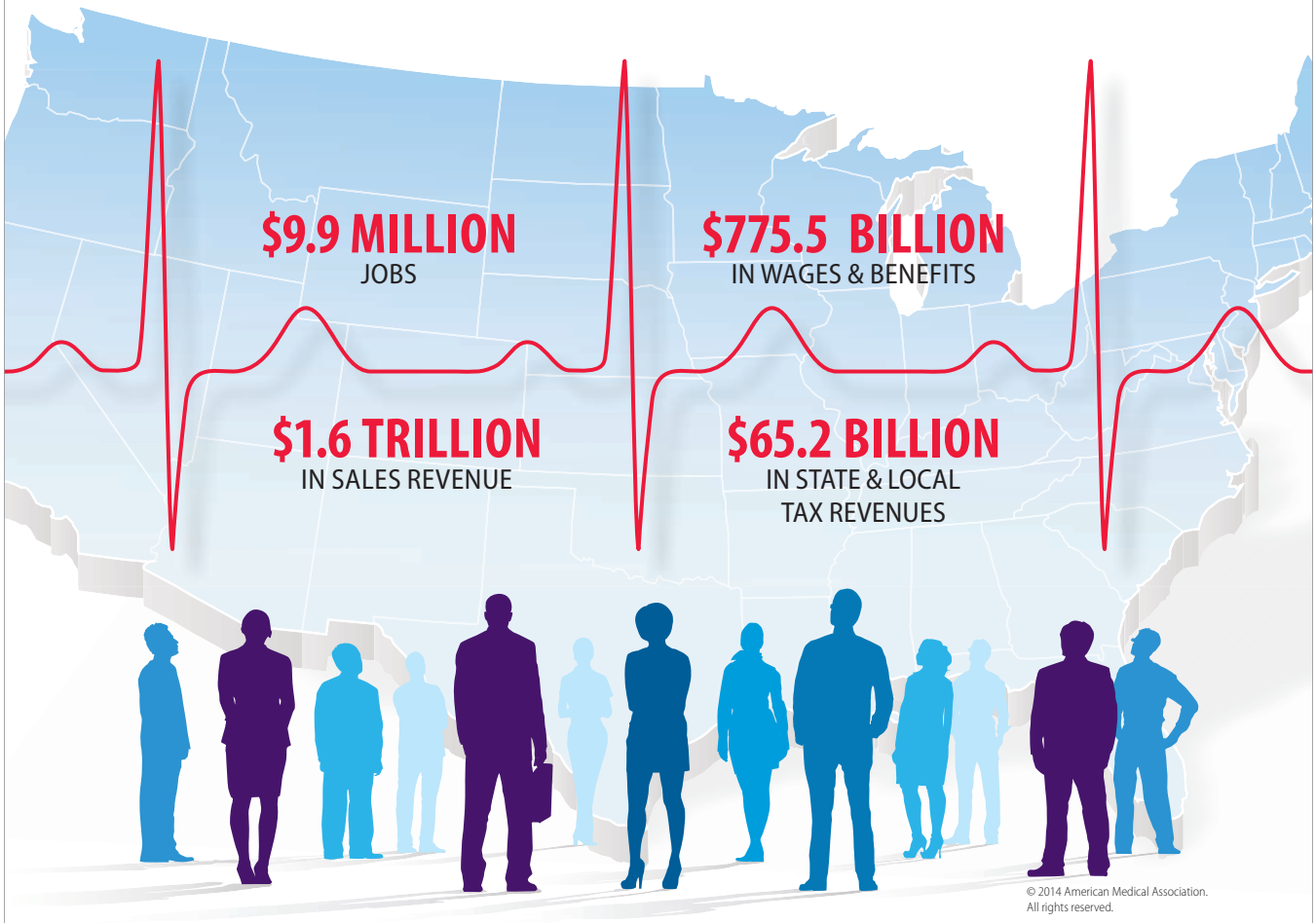

See the effects across the nation.

The American Medical Association 2014 Economic Impact Study shows how much physicians add to the economic health of our nation.

Check the effect physicians have on the U.S. economy by viewing the entire national report from the AMA Advocacy Resource Center at **ama-assn.org/go/eis**.

AMA
AMERICAN MEDICAL ASSOCIATION

Please activate your 2015 AMA membership by calling (800) 262-3211 or visit ama-assn.org/go/join.

The American Society of Emergency Radiology

2016 Postgraduate Course in Emergency and Trauma Radiology

September 14 – 17, 2016
Hyatt Regency San Francisco
San Francisco, California

For more information visit:
www.erad.org

Target® Detachable Coil

See package insert for complete indications, contraindications, warnings and instructions for use.

INTENDED USE / INDICATIONS FOR USE
Target Detachable Coils are intended to endovascularly obstruct or occlude blood flow in vascular abnormalities of the neurovascular and peripheral vessels.
Target Detachable Coils are indicated for endovascular embolization of:
- Intracranial aneurysms
- Other neurovascular abnormalities such as arteriovenous malformations and arteriovenous fistulae
- Arterial and venous embolizations in the peripheral vasculature

CONTRAINDICATIONS
None known.

POTENTIAL ADVERSE EVENTS
Potential complications include, but are not limited to: allergic reaction, aneurysm perforation and rupture, arrhythmia, death, edema, embolus, headache, hemorrhage, infection, ischemia, neurological/intracranial sequelae, post-embolization syndrome (fever, increased white blood cell count, discomfort), TIA/stroke, vasospasm, vessel occlusion or closure, vessel perforation, dissection, trauma or damage, vessel rupture, vessel thrombosis. Other procedural complications including but not limited to: anesthetic and contrast media risks, hypotension, hypertension, access site complications.

WARNINGS
- Contents supplied STERILE using an ethylene oxide (EO) process. Do not use if sterile barrier is damaged. If damage is found, call your Stryker Neurovascular representative.
- For single use only. Do not reuse, reprocess or resterilize. Reuse, reprocessing or resterilization may compromise the structural integrity of the device and/or lead to device failure which, in turn, may result in patient injury, illness or death. Reuse, reprocessing or resterilization may also create a risk of contamination of the device and/or cause patient infection or cross-infection, including, but not limited to, the transmission of infectious disease(s) from one patient to another. Contamination of the device may lead to injury, illness or death of the patient.
- After use, dispose of product and packaging in accordance with hospital, administrative and/or local government policy.
- **This device should only be used by physicians who have received appropriate training in interventional neuroradiology or interventional radiology and preclinical training on the use of this device as established by Stryker Neurovascular.**
- Patients with hypersensitivity to 316LVM stainless steel may suffer an allergic reaction to this implant.
- MR temperature testing was not conducted in peripheral vasculature, arteriovenous malformations or fistulae models.
- The safety and performance characteristics of the Target Detachable Coil System (Target Detachable Coils, InZone Detachment Systems, delivery systems and accessories) have not been demonstrated with other manufacturer's devices (whether coils, coil delivery devices, coil detachment systems, catheters, guidewires, and/or other accessories). Due to the potential incompatibility of non Stryker Neurovascular devices with the Target Detachable Coil System, the use of other manufacturer's device(s) with the Target Detachable Coil System is not recommended.
- To reduce risk of coil migration, the diameter of the first and second coil should never be less than the width of the ostium.
- In order to achieve optimal performance of the Target Detachable Coil System and to reduce the risk of thromboembolic complications, it is critical that a continuous infusion of appropriate flush solution be maintained between a) the femoral sheath and guiding catheter, b) the 2-tip microcatheter and guiding catheters, and c) the 2-tip microcatheter and Stryker Neurovascular guidewire and delivery wire. Continuous flush also reduces the potential for thrombus formation on, and crystallization of infusate around, the detachment zone of the Target Detachable Coil.
- Do not use the product after the "Use By" date specified on the package.
- Reuse of the flush port/dispenser coil or use with any coil other than the original coil may result in contamination of, or damage to, the coil.
- Utilization of damaged coils may affect coil delivery to, and stability inside, the vessel or aneurysm, possibly resulting in coil migration and/or stretching.
- The fluoro-saver marker is designed for use with a Rotating Hemostatic Valve (RHV). If used without an RHV, the distal end of the coil may be beyond the alignment marker when the fluoro-saver marker reaches the microcatheter hub.
- If the fluoro-saver marker is not visible, do not advance the coil without fluoroscopy.
- Do not rotate delivery wire during or after delivery of the coil. Rotating the Target Detachable Coil delivery wire may result in a stretched coil or premature detachment of the coil from the delivery wire, which could result in coil migration.
- Verify there is no coil loop protrusion into the parent vessel after coil placement and prior to coil detachment. Coil loop protrusion after coil placement may result in thromboembolic events if the coil is detached.
- Verify there is no movement of the coil after coil placement and prior to coil detachment. Movement of the coil after coil placement may indicate that the coil could migrate once it is detached.
- Failure to properly close the RHV compression fitting over the delivery wire before attaching the InZone® Detachment System could result in coil movement, aneurysm rupture or vessel perforation.
- Verify repeatedly that the distal shaft of the catheter is not under stress before detaching the Target Detachable Coil. Axial compression or tension forces could be stored in the 2-tip microcatheter causing the tip to move during coil delivery. Microcatheter tip movement could cause the aneurysm or vessel to rupture.
- Advancing the delivery wire beyond the microcatheter tip once the coil has been detached involves risk of aneurysm or vessel perforation.
- The long term effect of this product on extravascular tissues has not been established so care should be taken to retain this device in the intravascular space.

Damaged delivery wires may cause detachment failures, vessel injury or unpredictable distal tip response during coil deployment. If a delivery wire is damaged at any point during the procedure, do not attempt to straighten or otherwise repair it. Do not proceed with deployment or detachment. Remove the entire coil and replace with undamaged product.

- After use, dispose of product and packaging in accordance with hospital, administrative and/or local government policy.

CAUTIONS / PRECAUTIONS
- Federal Law (USA) restricts this device to sale by or on the order of a physician.
- Besides the number of InZone Detachment System units needed to complete the case, there must be an extra InZone Detachment System unit as back up.
- Removing the delivery wire without grasping the introducer sheath and delivery wire together may result in the detachable coil sliding out of the introducer sheath.
- Failure to remove the introducer sheath after inserting the delivery wire into the RHV of the microcatheter will interrupt normal infusion of flush solution and allow back flow of blood into the microcatheter.
- Some low level overhead light near or adjacent to the patient is required to visualize the fluoro-saver marker; monitor light alone will not allow sufficient visualization of the fluoro-saver marker.
- Advance and retract the Target Detachable Coil carefully and smoothly without excessive force. If unusual friction is noticed, slowly withdraw the Target Detachable Coil and examine for damage. If damage is present, remove and use a new Target Detachable Coil. If friction or resistance is still noted, carefully remove the Target Detachable Coil and microcatheter and examine the microcatheter for damage.
- If it is necessary to reposition the Target Detachable Coil, verify under fluoroscopy that the coil moves with a one-to-one motion. If the coil does not move with a one-to-one motion or movement is difficult, the coil may have stretched and could possibly migrate or break. Gently remove both the coil and microcatheter and replace with new devices.
- Increased detachment times may occur when:
  - Other embolic agents are present.
  - Delivery wire and microcatheter markers are not properly aligned.
  - Thrombus is present on the coil detachment zone.
- Do not use detachment systems other than the InZone Detachment System.
- Increased detachment times may occur when delivery wire and microcatheter markers are not properly aligned.
- Do not use detachment systems other than the InZone Detachment System.

Stryker Neurovascular
47900 Bayside Parkway
Fremont, CA 94538-6515

stryker.com/neurovascular

Date of Release: FEB/2014

EX_EN_US

NV00006677.AA

Trevo® XP ProVue Retrievers

See package insert for complete indications, complications, warnings, and instructions for use.

INDICATIONS FOR USE
The Trevo Retriever is intended to restore blood flow in the neurovasculature by removing thrombus in patients experiencing ischemic stroke within 8 hours of symptom onset. Patients who are ineligible for intravenous tissue plasminogen activator (IV t-PA) or who fail IV t-PA therapy are candidates for treatment.

COMPLICATIONS
Procedures requiring percutaneous catheter introduction should not be attempted by physicians unfamiliar with possible complications which may occur during or after the procedure. Possible complications include, but are not limited to, the following: air embolism; hematoma or hemorrhage at puncture site; infection; distal embolization; pain/headache; vessel spasm, thrombosis, dissection, or perforation; emboli; acute occlusion; ischemia; intracranial hemorrhage; false aneurysm formation; neurological deficits including stroke; and death.

COMPATIBILITY
3x20 mm retrievers are compatible with Trevo® Pro 14 Microcatheters (REF 90231) and Trevo® Pro 18 Microcatheters (REF 90238). 4x20 mm retrievers are compatible with Trevo® Pro 18 Microcatheters (REF 90238). Compatibility of the Retriever with other microcatheters has not been established. Performance of the Retriever device may be impacted if a different microcatheter is used. The Merci® Balloon Guide Catheters are recommended for use during thrombus removal procedures. Retrievers are compatible with the Abbott Vascular DOC® Guide Wire Extension (REF 22260).

WARNINGS
- Contents supplied STERILE, using an ethylene oxide (EO) process. Nonpyrogenic.
- To reduce risk of vessel damage, adhere to the following recommendations:
  - Take care to appropriately size Retriever to vessel diameter at intended site of deployment.
  - Do not perform more than six (6) retrieval attempts in same vessel using Retriever devices.
  - Maintain Retriever position in vessel when removing or exchanging Microcatheter.
- To reduce risk of kinking/fracture, adhere to the following recommendations:
  - Immediately after unsheathing Retriever, position Microcatheter tip marker just proximal to shaped section. Maintain Microcatheter tip marker just proximal to shaped section of Retriever during manipulation and withdrawal.
  - Do not rotate or torque Retriever.
  - Use caution when passing Retriever through stented arteries.
- Do not resterilize and reuse. Structural integrity and/or function may be impaired by reuse or cleaning.
- The Retriever is a delicate instrument and should be handled carefully. Before use and when possible during procedure, inspect device carefully for damage. Do not use a device that shows signs of damage. Damage may prevent device from functioning and may cause complications.
- Do not advance or withdraw Retriever against resistance or significant vasospasm. Moving or torquing device against resistance or significant vasospasm may result in damage to vessel or device. Assess cause of resistance using fluoroscopy and if needed resheath the device to withdraw.
- If Retriever is difficult to withdraw from the vessel, do not torque Retriever. Advance Microcatheter distally, gently pull Retriever back into Microcatheter, and remove Retriever and Microcatheter as a unit. If undue resistance is met when withdrawing the Retriever into the Microcatheter, consider extending the Retriever using the Abbott Vascular DOC guidewire extension (REF 22260) so that the Microcatheter can be exchanged for a larger diameter catheter such as a DAC® catheter. Gently withdraw the Retriever into the larger diameter catheter.
- Administer anti-coagulation and anti-platelet medications per standard institutional guidelines.

PRECAUTIONS
- Prescription only – device restricted to use by or on order of a physician.
- Store in cool, dry, dark place.
- Do not use open or damaged packages.
- Use by "Use By" date.
- Exposure to temperatures above 54°C (130°F) may damage device and accessories. Do not autoclave.
- Do not expose Retriever to solvents.
- Use Retriever in conjunction with fluoroscopic visualization and proper anti-coagulation agents.
- To prevent thrombus formation and contrast media crystal formation, maintain a constant infusion of appropriate flush solution between guide catheter and Microcatheter and between Microcatheter and Retriever or guidewire.
- Do not attach a torque device to the shaped proximal end of DOC® Compatible Retriever. Damage may occur, preventing ability to attach DOC® Guide Wire Extension.

Concentric Medical
301 East Evelyn
Mountain View, CA 94041

EC REP

EMERGO Europe
Molenstraat 15
2513 BH, The Hague
The Netherlands

Stryker Neurovascular
47900 Bayside Parkway
Fremont, CA 94538-6515

stryker.com/neurovascular
stryker.com/emea/neurovascular

Date of Release: JUN/2014

EX_EN_GL

CE 0459

NV00009028.AA

66%

of Patients in MR CLEAN Were Treated with a Trevo® Stent Retriever

stryker® Neurovascular

Trevo®

PROVUE RETRIEVER

MR CLEAN[1]

First clinical evidence for intra-arterial treatment with stent retrievers

- **Largest** of the randomized AIS trials[2], with over 500 patients enrolled
- The Trevo Retriever was the **#1** device used in the **MR CLEAN** Trial

[1] O.A. Berkhemer et al. A Randomized Trial for Intra-arterial Treatment for Acute Ischemic Stroke. *N Eng J Med* December 2014.
[2] MR CLEAN is the largest AIS Trial in which stent retrievers were used.
http://www.mrclean-trial.org/

Stroke: *Our Only Focus. Our Ongoing Promise.*

COILING OPTIMIZED

NOW AVAILABLE

BARRICADE COMPLEX
FINISHING COIL

- Extremely soft profile of The Barricade Finishing coil now in a complex shape
- Excellent microcatheter stability for confident coil placement
- Available in a size range of 1mm-5mm

BARRICADE™ COIL SYSTEM

MADE IN AMERICA

The Barricade Coil System is intended for the endovascular embolization of intracranial aneurysms and other neurovascular abnormalities such as arteriovenous malformations and arteriovenous fistulae. The System is also intended for vascular occlusion of blood vessels within the neurovascular system to permanently obstruct blood flow to an aneurysm or other vascular malformation and for arterial and venous embolizations in the peripheral vasculature. Refer to the instructions for use for complete product information.

18 TECHNOLOGY DRIVE #169, IRVINE CA 92618
p: 949.788.1443 | f: 949.788.1444

WWW.BLOCKADEMEDICAL.COM

MKTG-031 Rev. A

BLOCKADE MEDICAL

AJNR

AMERICAN JOURNAL OF NEURORADIOLOGY

JANUARY 2016
VOLUME 37
NUMBER 1
WWW.AJNR.ORG

THE JOURNAL OF DIAGNOSTIC AND INTERVENTIONAL NEURORADIOLOGY

Cryoablation for spine tumors

Minimizing radiation exposure in pediatric head trauma

MR-based estimation of *IDH1* status in glioblastoma

Official Journal ASNR • ASFNR • ASHNR • ASPNR • ASSR

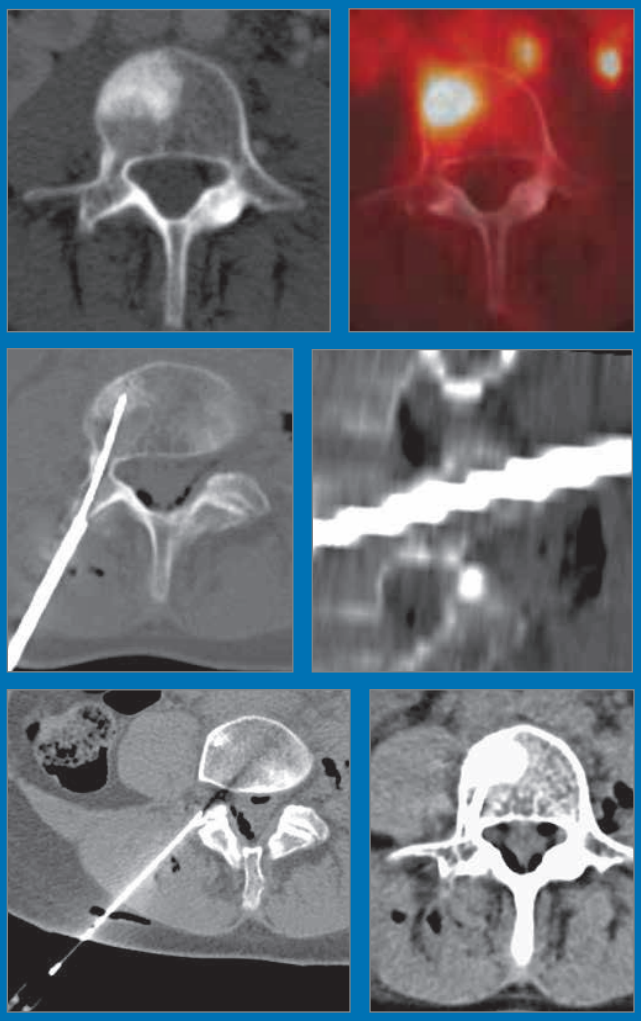

AJNR

AMERICAN JOURNAL OF NEURORADIOLOGY

JANUARY 2016
VOLUME 37
NUMBER 1
WWW.AJNR.ORG

Publication Preview at www.ajnr.org features articles released in advance of print. Visit www.ajnrblog.org to comment on AJNR content and chat with colleagues and AJNR's News Digest at http://ajnrdigest.org to read the stories behind the latest research in neuroimaging.

ONLINE FEATURES

LETTERS

BOOK REVIEWS *R.M. Quencer, Section Editor*

Please visit www.ajnrblog.org to read and comment on Book Reviews.

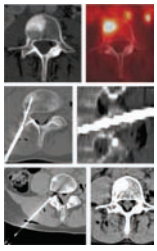

Treatment of a patient with lung cancer metastasis with 17-gauge cryoprobe via right transpedicular approach, with carbon dioxide injected into the epidural space as a thermal insulator.

Indicates Editor's Choices selection

Indicates Fellows' Journal Club selection

Indicates open access to non-subscribers at www.ajnr.org

Indicates article with supplemental on-line table

Indicates article with supplemental on-line photo

Indicates article with supplemental on-line video

Evidence-Based Medicine Level 1

Evidence-Based Medicine Level 2

AJNR

AMERICAN JOURNAL OF NEURORADIOLOGY

Publication Preview at www.ajnr.org features articles released in advance of print. Visit www.ajnrblog.org to comment on AJNR content and chat with colleagues and AJNR's News Digest at http://ajnrdigest.org to read the stories behind the latest research in neuroimaging.

JANUARY 2016 • VOLUME 37 • NUMBER 1 • WWW.AJNR.ORG

AJNR (Am J Neuroradiol ISSN 0195–6108) is a journal published monthly, owned and published by the American Society of Neuroradiology (ASNR), 800 Enterprise Drive, Suite 205, Oak Brook, IL 60523. Annual dues for the ASNR include $170.00 for journal subscription. The journal is printed by Cadmus Journal Services, 5457 Twin Knolls Road, Suite 200, Columbia, MD 21045; Periodicals postage paid at Oak Brook, IL and additional mailing offices. Printed in the U.S.A. POSTMASTER: Please send address changes to American Journal of Neuroradiology, P.O. Box 3000, Denville, NJ 07834, U.S.A. Subscription rates: nonmember $380 ($450 foreign) print and online, $305 online only; institutions $440 ($510 foreign) print and basic online, $875 ($940 foreign) print and extended online, $365 online only (basic), extended online $790; single copies are $35 each ($40 foreign). Indexed by PubMed/Medline, BIOSIS Previews, Current Contents (Clinical Medicine and Life Sciences), EMBASE, Google Scholar, HighWire Press, Q-Sensei, RefSeek, Science Citation Index, and SCI Expanded.

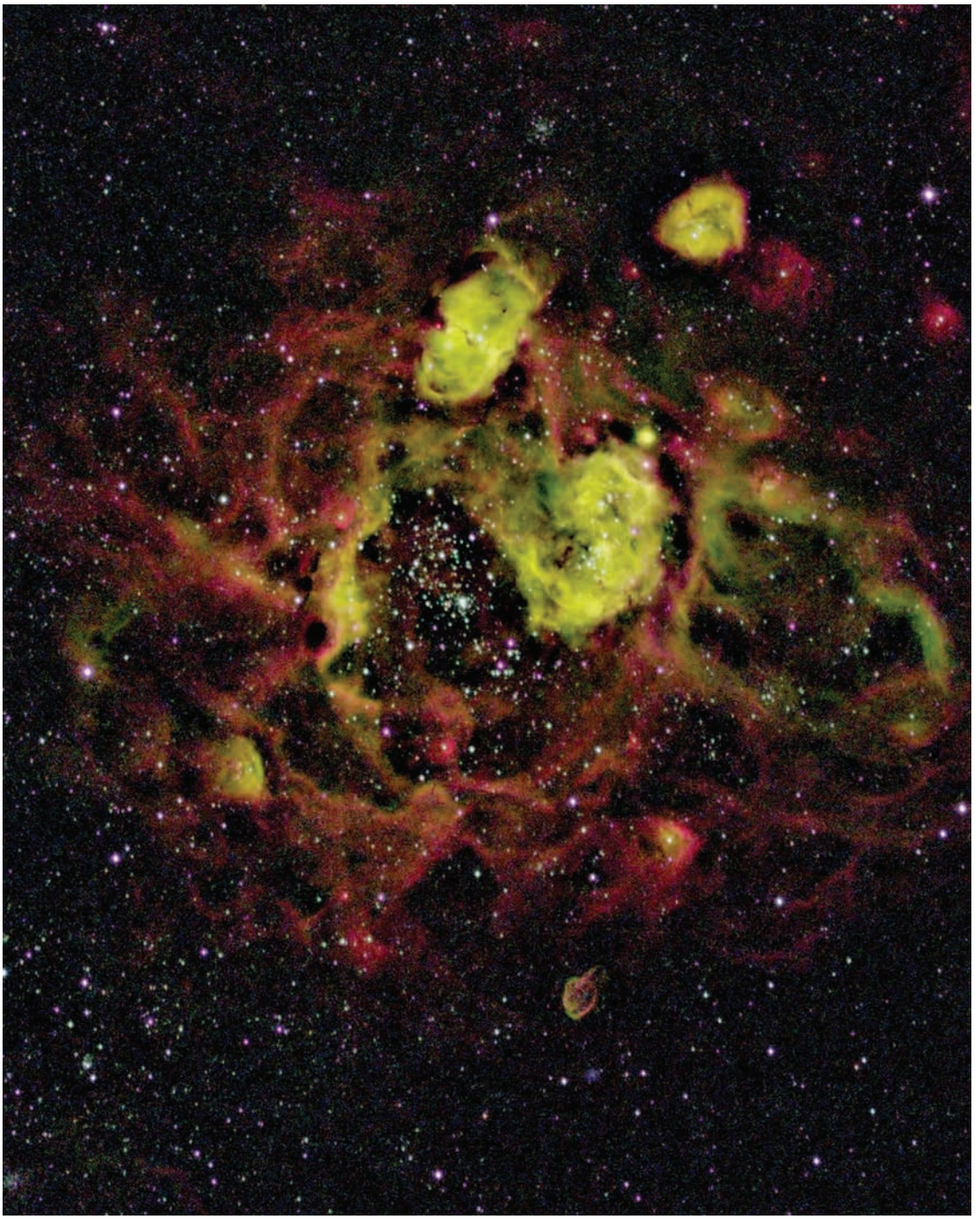

This is a false-color view of the so-called Bean Nebula in the Large Magellanic Cloud in the southern hemisphere. The N11 nebula complex contains a mixture of gaseous nebulae and open clusters. NGC1763 (also -69 and -73) provides the name for the group. This image was obtained as a series of 300-second filtered exposures in H-alpha, OIII, and SII and acquired on a Planewave 510-mm CDK telescope from Australia. The image was processed in Pixinsight and Photoshop with red = H-alpha, green = OIII, and blue = SII. Total imaging time was 1h, 45min. Data were acquired in January 2015.

Jeffrey S. Ross, Mayo Clinic, Phoenix, Arizona

Carotid Near-Occlusion: A Comprehensive Review, Part 1—Definition, Terminology, and Diagnosis

E. Johansson and A.J. Fox

ABSTRACT

SUMMARY: Carotid near-occlusion is distal ICA luminal collapse beyond a tight stenosis, where the distal lumen should not be used for calculating percentage stenosis. Near-occlusion with full ICA collapse is well-known, with a threadlike lumen. However, near-occlusion without collapse is often subtle and can be overlooked as a usual severe stenosis. More than 10 different terms have been used to describe near-occlusion, sometimes causing confusion. This systematic review presents what is known about carotid near-occlusion. In this first part, the foci are definition, terminology, and diagnosis.

ABBREVIATION: ECA = external carotid artery

Carotid near-occlusion is distal luminal collapse of the internal carotid artery beyond a tight stenosis.[1] Various terms have been used to describe near-occlusion, which can mislead students or those doing literature searches: near-occlusion[1-44] (or "near total occlusion"[45-51]), pseudo-occlusion,[1-20,43,45,47,48,50-70] string sign,[1-5,7,9-13,16,18-20,22,24,26,30,40,42,43,45,47-50,52,56,60-62,65,66,68-74] slim sign,[1,2,4,6,9-20,28,31,45,47-51,55,59,60,62,64,68,69,71,72,75] critical stenosis,[50,70] small or narrow distal internal carotid artery (with variations),[1,11,28,36,39-42] preocclusive stenosis,[5,46,50,62,64,67] subtotal stenosis,[67,76,77] subtotal occlusion,[1,9,40,72] functional occlusion,[40] subocclusion,[50] hypoplasia,[11,12,18,45] 99% stenosis,[66] hairline residual lumen,[20,43] and incomplete occlusion.[1]

Calculating percentage stenosis for carotid near-occlusion is fallacious, and near-occlusion assessment is advised before measuring for percentage stenosis.[1,2,32,34] Near-occlusion with full collapse is well-recognized as a threadlike distal lumen. However, partial distal collapse is subtle—near-occlusion without full collapse is sometimes overlooked as stenosis. Carotid near-occlusion was described in 1970 as the carotid slim sign, a severe collapse, and today as near-occlusion with full collapse (Figs 1–5).[75] The near-occlusion definition was widened to recognize partial collapse (near-occlusion without full collapse) (Figs 1–5).[1,2]

The aim of this review was to present the definition, terminology, diagnosis, prognosis, treatment, and pathophysiology of carotid near-occlusion; highlight areas of confusion; and highlight areas in need of future improvement. In this first part, the foci are definition, terminology, and diagnosis.

Articles

A PubMed search was performed in December 2014 with the terms "carotid near-occlusion," "carotid pseudo-occlusion," "carotid string sign," "carotid slim sign," "carotid critical stenosis," "small distal carotid artery," "narrow distal carotid artery," "carotid preocclusive stenosis," "carotid pre occlusive stenosis," "carotid subtotal stenosis," "carotid sub total stenosis," "carotid subtotal occlusion," "carotid sub total occlusion," "carotid functional occlusion," "carotid sub-occlusion," "carotid hypoplasia," "carotid incomplete occlusion," and "carotid hairline," without search restrictions. This yielded 1076 articles. Title review selected 115 articles of greatest interest. Excluded were articles not in English ($n = 14$) and those with inaccessible abstracts or full articles ($n = 4$). Excluded were 26 articles with ≤5 cases ($n = 8$), not carotid near-occlusion ($n = 16$), in a non-peer-reviewed journal ($n = 1$), and not analyzing humans ($n = 1$). Seventy-one articles were audited. All reference lists were examined, rendering an additional 17 articles. Two key articles[1,22] were deemed likely to be cited; we examined all articles that had cited these articles by using the Web of Science data base, yielding 3 additional articles. In total, 91 articles were reviewed.

Received February 28, 2015; accepted after revision April 8.

From the Department of Pharmacology and Clinical Neuroscience (E.J.), Umeå University, Umeå, Sweden; and Department of Neuroradiology (A.J.F.), Sunnybrook Heath Sciences Centre, University of Toronto, Toronto, Ontario, Canada.

This study was funded by the Swedish Stroke Foundation, the Northern Swedish Stroke Fund, the Foundation for Neuroscientific research at Umeå University Hospital, the County of Västerbotten, and the medical faculty of Umeå University.

Please address correspondence to Elias Johansson, MD, Department of Neurology, Institution of Pharmacology and Clinical Neuroscience, Umeå University, 901 82 Umeå, Sweden; e-mail: elias.johansson@umu.se

Indicates open access to non-subscribers at www.ajnr.org

http://dx.doi.org/10.3174/ajnr.A4432

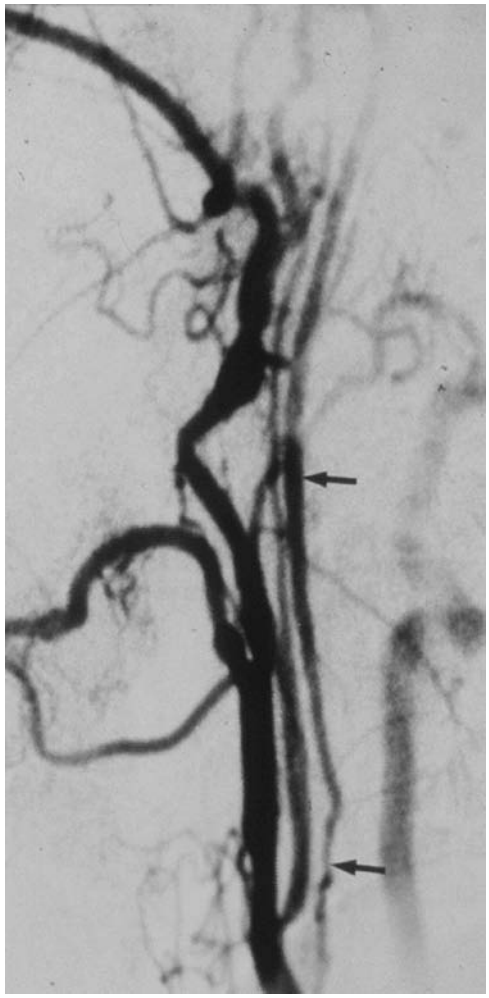

FIG 1. A case with near-occlusion with full collapse, reprinted with permission from Fox et al.[1] Lateral common carotid angiogram shows the thin, threadlike, collapsed lumen (*arrows*) of the ICA above a prominent ICA stenosis at the bulb (not shown).

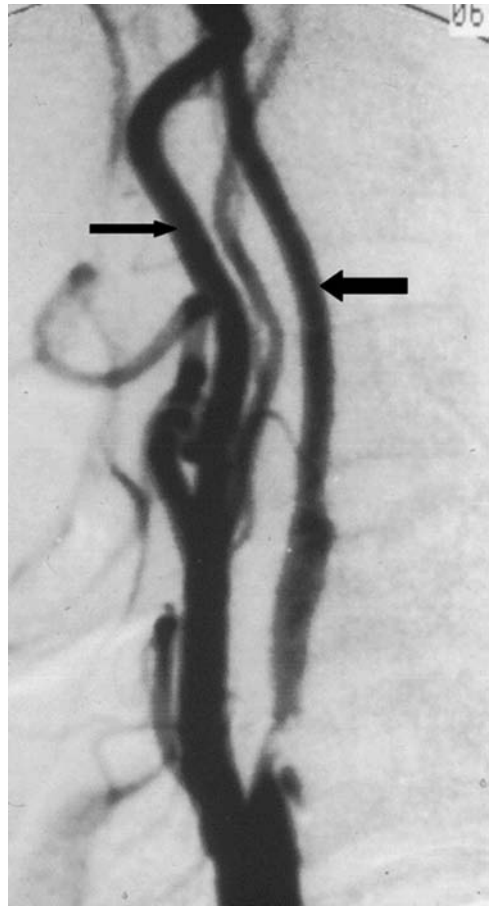

FIG 2. A case with near-occlusion without full collapse, reprinted with permission from Fox et al.[1] Lateral carotid angiogram shows a reduced ICA lumen distal to the stenosis (*larger arrow*); the diameter is slightly less than the ECA diameter (*smaller arrow*). The distal ICA lumen is normal-appearing (not threadlike).

Definition of Near-Occlusion

A carotid near-occlusion is a very tight atherosclerotic stenosis in which the artery beyond the stenosis is collapsed.[1] The remaining patency differs from that in total occlusions and is separate from that in conventional carotid stenoses because of this collapse.[1] Near-occlusion can be with and without full collapse: Near-occlusion with full collapse shows pronounced distal collapse with a threadlike lumen.[1,21] Near-occlusion without full collapse shows a less pronounced distal collapse with a more normal-appearing distal artery.[1,21]

Previous Definition of Near-Occlusion. To the best of our knowledge, near-occlusion and its synonym terms are limited in publications to "near-occlusion with full collapse" between 1970 and 1997, with only 1 exception (presented below).[1,2] Before 1997, partial near-occlusion was largely unrecognized, and such cases were likely considered usual stenoses. In 1997, NASCET collaborators redefined near-occlusion, including less complete collapse, more subtle than that previously known,[2] effectively presuming that ICAs beyond severe stenosis would progressively decrease from their normal caliber to fully collapsed as a critical degree is reached rather than experiencing sudden collapse. Near-occlusions were then subdivided into those with or without pronounced collapse, also called near-occlusion with and without the "string sign" (here called "near-occlusion with and without full collapse").[2]

Terminology

First Descriptions Found in our Article Search. A collapsed ICA on cervical angiography was described by Riishede and Ethelberg[78] in 1953, caused by raised intracranial pressure in brain death. A case of possible near-occlusion was described as "teilweisem verschluss" (roughly "partial closure") in German by Mumenthaler et al[79] in 1961, though without special attention to distal collapse compared with conventional stenosis or occlusion. Lippman et al[75] clearly described distal collapse from atherosclerosis in 1970.

Slim Sign. Lippman et al[75] also called distal collapse the "poststenotic carotid slim sign" (later simply "slim sign") and "spurious hypoplasia" (false hypoplasia).[75] Several subsequent authors inappropriately dropped "spurious" when referencing this article ("hypoplasia" instead of "false hypoplasia").[11,12,18,45] Radiographs published by Lippman et al today fit near-occlusion with full collapse. However, the "slim sign" has not been used

as the main term in any near-occlusion article after that of Lippman et al; it has been used as a synonym of the main term.[1,2,4,6,9-20,28,31,45,47-51,55,59,60,62,64,68,69,71,72]

Pseudo-Occlusion. The term "pseudo-occlusion" was used for cases with raised intracranial pressure by Newton and Couch in 1960.[80] In 1978, Macpherson[54] suggested pseudo-occlusions as possibly caused by "thrombosis or embolus." In 1980, Sekhar et al[51] suggested "atheromatous pseudo-occlusion" to separate atherosclerotic causes from similar findings caused by raised intracranial pressure, intracranial occlusion, dissection, and hypoplasia. Images from Sekhar et al can be called "near-occlusion with full collapse." "Pseudo-occlusion" has been used for the appearance of a collapsed artery,[1-9,11,13-20,45-48,56-62,65-70] but also quite literally when diagnosis changed from occlusion to patent after re-review (not necessarily with distal collapse.[10,12,55,63,64,81]

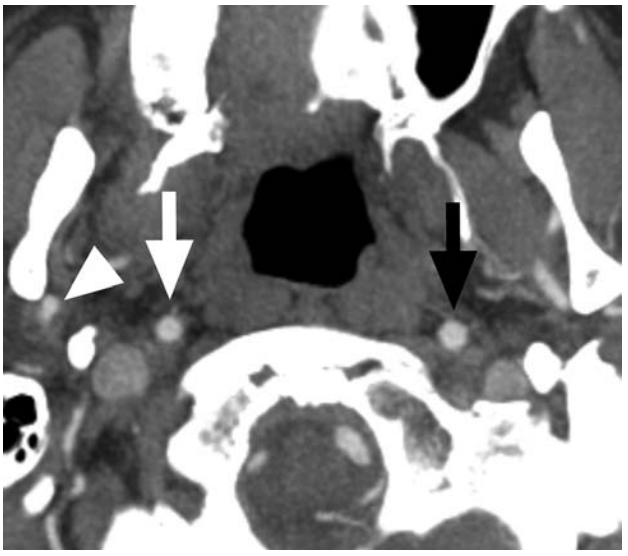

FIG 3. A case with a conventional carotid stenosis and no distal collapse. Axial CTA at the level of the distal extracranial ICA. The distal ICA (*white arrow*) is similar to, though slightly smaller than, the contralateral ICA (*black arrow*) and is wider than the right ECA (*arrowhead*).

String Sign. The "string sign" was first used for distal ICA collapse in spontaneous dissection as coined by Ojemann et al in 1972.[82] In 1980, Mehigan and Olcott[71] used the "string sign" term to describe the appearance of a distal artery collapse and presented several cases with different causes: dissection, postradiation carotid disease, and various forms of atherosclerosis or thrombosis. Since then, "string sign" has often described near-occlusion with full collapse (excluding nonatherosclerotic causes). Those who recognized near-occlusion as with and without full collapse have often used with and without the "string sign" to describe this.[2,7,22,24,26]

Near-Occlusion. "Nearly occluded" was used by Gabrielsen et al[31] in 1981 to describe a tight carotid stenoses with distal collapse. They noted that the reduced caliber usually (not always) was severe, though they featured a case of near-occlusion without full collapse; this is the first instance we found in our article search. However, Gabrielsen et al did not suggest that "near-occlusion" should mean something other than "slim sign."

Narrowing of the Internal Carotid Artery (ICA/Common Carotid Artery Ratio). Not recognizing narrowing of the distal artery as near-occlusion was not considered problematic for the European Carotid Surgery Trial because it calculated stenosis degree by measuring the diameter at maximal stenosis compared with the unseen original ICA bulb diameter (European Carotid Surgery Trial grading system).[36] As a secondary analysis, the authors identified patients with a collapsed distal artery by examining a ratio between the distal ICA and common carotid artery (ICA/common carotid artery ratio)[42] (different from their grading of stenosis by using the common carotid artery method[83]). The collaborators examined neck sides with <50% European Carotid Surgery Trial–type stenosis (similar to <30% NASCET-type stenosis[83]) and derived a threshold of <0.42 for ICA narrowing (mean ± 2 SDs).[42]

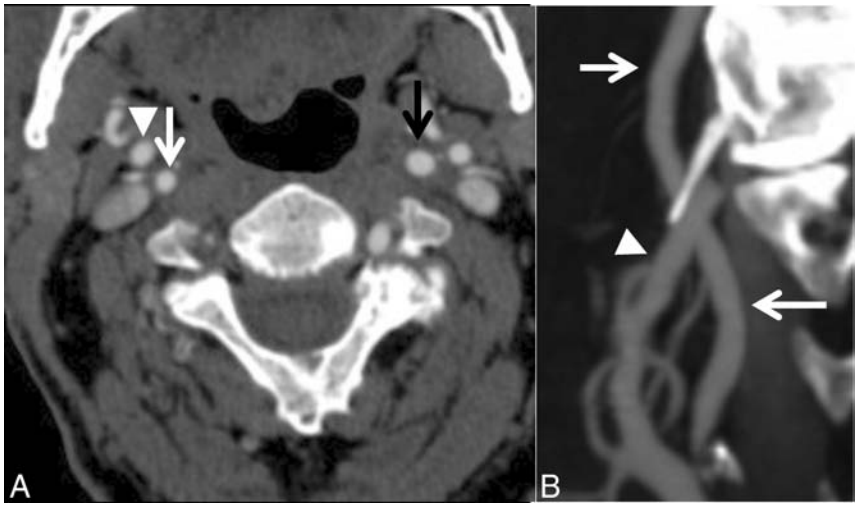

FIG 4. A case with near-occlusion without full collapse. *A*, Axial CTA at the level of the distal extracranial ICA. *B*, Sagittal reformat of *A*. The distal right ICA (*white arrow*) is narrower than the contralateral ICA (*black arrow*) and similar to the right ECA (*arrowhead*) but otherwise is normal-appearing (not threadlike).

Recommendation. Regardless of which term one chooses, it is important to recognize that near-occlusions with and without full collapse exist. We recommend the term "near-occlusion" because it was used in large clinical trials to describe atherosclerotic stenosis with a distal collapse.[1,2,32] We suggest not using "pseudo-occlusion" or "string sign" because of their use for other entities. "Slim sign" was used to describe near-occlusions with full collapse, but not for near-occlusion without full collapse; the use of "slim sign" might cause confusion. Therefore, when we discussed the terminology to use in a recent article,[21] near-occlusion with and without full collapse was introduced and we recommended it for consistent use henceforth.

Diagnosis

Near-occlusion with full collapse above a prominent ICA bulb stenosis is easy enough to recognize. However, occlusion can be misdiagnosed with suboptimal imaging and interpretation (Table 1). An ICA occlusion definition requires identification of the ascending pharyngeal artery as a tiny artery ascending adjacent to the expected course of the unseen ICA, but with typical branches just below the skull base. Collapsed near-occlusion smoothly continues into the carotid canal of the temporal bone; the ascending pharyngeal artery is a second nearby vessel. True ICA hypoplasia or long distal ICA tapering of dissection does not show a prominent ICA bulb stenosis. Quality interpretation separates atherosclerosis from high intracranial pressure and postradiation carotid disease. It is also important to consider distal stenoses/occlusions by assessing the main cervical and intracranial arteries for the rare ICA hypoplasia, which shows a tiny bony carotid canal.

Near-occlusion without full collapse can be mistaken for conventional stenosis if one does not constantly search for subtle distal collapse. The NASCET collaborators recognized that if a collapsed distal ICA is used for percentage caluculation, the stenosis will be underrated. The NASCET method uses the normal distal ICA for percentage[1,84] and requires near-occlusion assessment first. If you do not seek it, you will not find it.

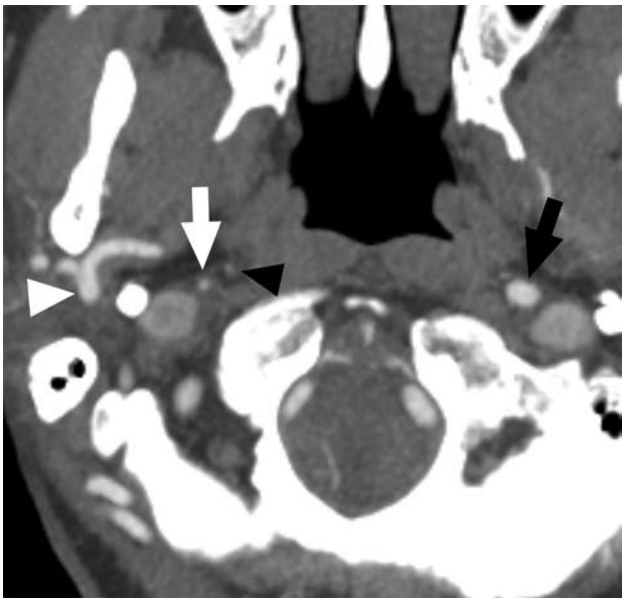

FIG 5. A case with near-occlusion with full collapse. Axial CTA at the level of the distal extracranial ICA. The distal right ICA (*white arrow*) is clearly collapsed with a threadlike appearance, clearly narrower than the contralateral ICA (*black arrow*) and the right ECA (*white arrowhead*). The *black arrowhead* points to the left ascending pharyngeal artery, ensuring that this is not an ICA occlusion.

One should also not overcall near-occlusion without full collapse. The relative small size of a distal ICA with a larger contralateral ICA can be an anatomic variation. Other causes of asymmetry exist: intracranial occlusion/stenosis and variance of ICA size depending on circle of Willis variations, such as a fetal posterior cerebral artery or a single ICA supplying both anterior cerebral arteries. Artery diameter can fluctuate slightly: It is important to apply the best diagnostic judgment for reasons of variance. In case of contralateral disease, emphasis should shift toward the comparison of the distal ICA and ipsilateral external carotid artery (ECA).[22] Consistent diagnostic judgment is needed regarding true distal collapse as reduced: Diagnostic criteria presented below are aids for that. NASCET suggested early on not to calculate percentage stenosis if near-occlusion could be interpreted,[84] yet it seems that not all who assess percentage stenosis look for subtle near-occlusion.[34]

Sometimes a nearly occluded stenosis is associated with intraluminal thrombus,[85] a near-occlusion variant. Because the prognosis likely differs, it is reasonable that the presence of a thrombus be mentioned specifically in both clinical and scientific articles.

Most articles on near-occlusion were based on conventional angiography, so we present diagnostic issues based on that technique, with some added aspects of other modalities. Diagnostic studies of near-occlusion need interpretation with caution because there can be misdiagnoses of near-occlusion as occlusion due inadequate angiography findings if a long-enough delay was not allowed, further adding skepticism to occlusion diagnosed with screening tests. The use of conventional angiography is no guarantee of a criterion standard study.

Separating Near-Occlusion from Occlusion. Some suggested "occlusions" are indeed patent, needing angiography time to detect delayed contrast through a severely collapsed artery.[23] Contrast remaining through the venous phase has been reported.[23] The ascending pharyngeal artery should be seen as a tiny artery separate from and running parallel to an occluded or nearly occluded ICA. The ascending pharyngeal artery can be overlooked

Table 1: Mimics of near-occlusion on conventional angiography and CTA

Cause	Mimic	Way to Separate/Reason for Mimic
Similar appearance, but not atherosclerosis	Dissection	Cervical ICA lesion without severe bulb stenosis, possibly patient history
	High ICP	Patient history, likely no focal stenosis
	Postradiation disease	Patient history, possibly no focal stenosis
	Hypoplasia	No prominent bulb stenosis, narrow bony canal
Imaging protocol	NrOc mistaken for occlusion	Delayed images reveal patent lumen
Interpretation	Occlusion mistaken for NrOc	Ascending pharyngeal artery mistaken for ICA
	Stenosis mistaken for NrOc	Larger opposite ICA from anatomic variations: opposite ICA supplies fetal PCA and/or both ACAs
	NrOc mistaken for stenosis	Partially collapsed NrOc overlooked as a normal lumen when it is not threadlike
	Intracranial disease mistaken for NrOc	Exclude distal disease as cause for the collapse

Note:—PCA indicates posterior cerebral artery; ICP, intracranial pressure; NrOc, near-occlusion; ACA, anterior cerebral artery.

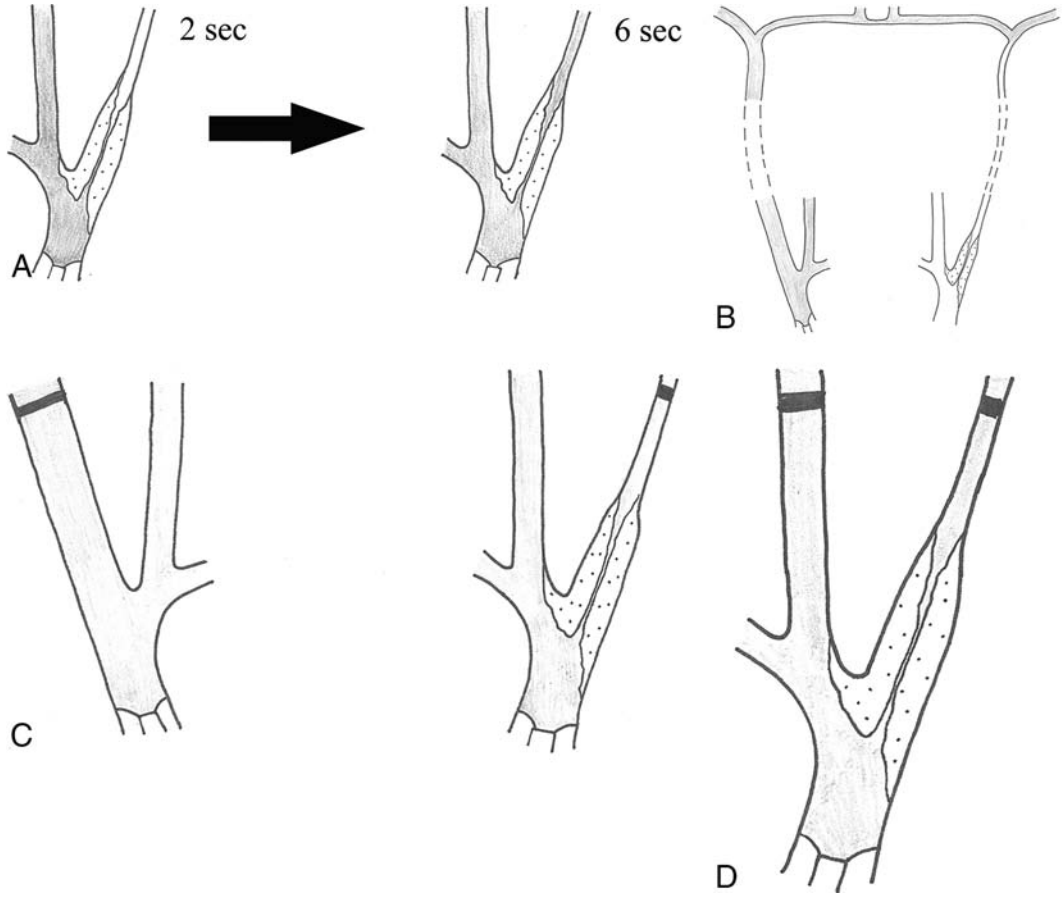

FIG 6. Schematic drawing of the 4 criteria for near-occlusion on conventional angiography. Delayed filling (*A*), evidence of intracranial collaterals when the contralateral side is examined (*B*), ipsilateral distal ICA less than the contralateral distal ICA (*C*), and ipsilateral distal ICA equal to or less than the ipsilateral ECA (*D*). In all figures, the contrast is gray.

as a collapsed ICA in cases of ICA occlusion ("pseudostring sign"[11]).

Separating Near-Occlusion from Conventional Stenosis. NASCET used descriptive criteria to distinguish near-occlusion (with and without full collapse) from conventional stenosis: 1) delayed filling, 2) intracranial collaterals, 3) ipsilateral distal ICA less than the contralateral distal ICA, and 4) ipsilateral distal ICA equal to or less than the ipsilateral ECA (the ICA normally is substantially larger than the ECA) (Fig 6). Two of the 4 criteria were required for diagnosis.[1] Separating near-occlusion is justifiable from its observed lower stroke risk compared with severe stenosis, and the potential fallacious calculation of percentage stenosis if not recognized, yielding incorrect percentages as low as 50%–60%, potentially managed differently.[1]

Separating Near-Occlusion with Full Collapse from Near-Occlusion without Full Collapse. Near-occlusion can be fully collapsed or without full collapse. The current diagnostic criterion for near-occlusion with full collapse is a "threadlike" distal lumen (with variations).[1] The transition between near-occlusion with and without full collapse is not distinct. Even so, 90% agreement was reported in a small study ($n = 21$) between blinded reviewers separating near-occlusions with and without full collapse by using descriptive criteria alone.[21] Fully collapsed near-occlusion shows striking ICA collapse and can be overlooked as complete occlusion if images or interpretation are suboptimal. All cases of presumed occlusion need delayed study to seek a late, slow-flowing collapsed lumen. With CTA, ICA occlusion diagnosis may be incorrect without a delayed CTA phase or a routine postcontrast head CT for possible ICA filling-in at the skull base or carotid canal to identify near-occlusion. The incidence of delayed studies with CTA changing the diagnosis from occlusion to near-occlusion is not well-known; certainly near-occlusions with full collapse are seen with CTA, even without delayed studies.[70]

Diagnosis with Sonography. There are several mimics of near-occlusion for sonography (Table 2). Sonography aspires to distinguish near-occlusion and occlusion by the presence or absence of flow. Accuracy depends on the sonographic methodology with more accurate distinctions by using Color Doppler with pulsed wave velocity measurements and Power Doppler than the outdated continuous wave technique.[8,17,23,45,67,69] Color Doppler with pulsed wave velocity measurements has been reported as separating near-occlusion from occlusion with good accuracy.[8,17,23,45,67] Presumably, the small error rate includes very slow and collapsed near-occlusion cases with nondetectable flow. Perhaps the commonly used additional method, power Doppler, may better detect slow flow, but only 2 small studies analyzed this.[5,17] Adding transoral sonography to also assess distal artery patency at the level of the pharynx

Table 2: Ultrasound-specific mimics of near-occlusion

Cause	Mimic	Reason for Mimic
Imaging protocol	NrOc mistaken for occlusion	Small low-flow channel not visualized
Interpretation	NrOc mistaken for intracranial disease	Low flow with systolic spikes could be either
	NrOc mistaken for no stenosis	Normal velocities with tight stenosis on B-mode
Limitation of ultrasound	NrOc mistaken for stenosis	NrOc without full collapse has high flow velocities

Note:—NrOc indicates near-occlusion.

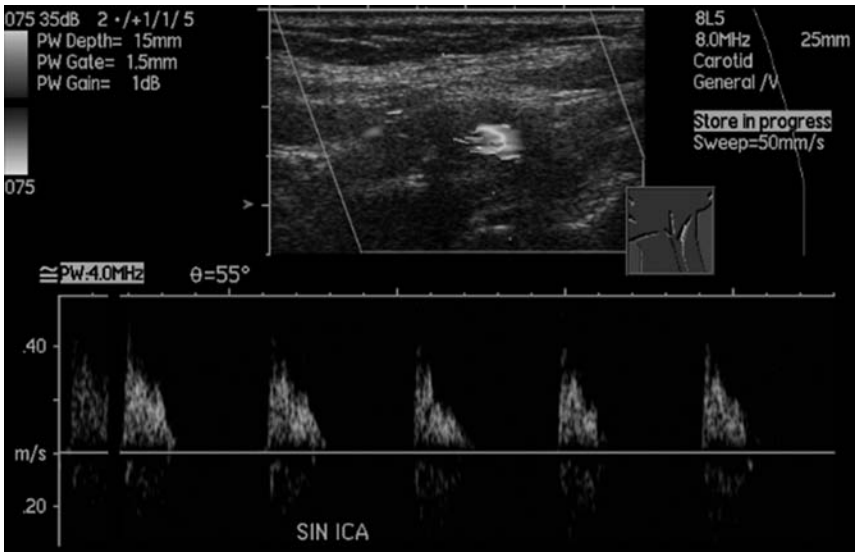

FIG 7. Sonographic findings of near-occlusion with full collapse. It is difficult to discern the narrow flow channel despite the low-flow setting and very low-flow velocities with systolic spikes without diastolic flow. CTA confirmed the diagnosis with a patent fully collapsed distal ICA (not shown).

shows promising initial findings.[8] Contrast-enhanced sonography might also increase the accuracy, but this has not been evaluated.

Near-occlusion with full collapse can be seen on sonography with very low flow velocity. The typical recognized sonography appearance is a very tight stenosis with a minimal flow channel, slow flow velocities, and a grossly pathologic flow profile (Fig 7). This finding is 71% (42/59) sensitive[5,45,67] and 98.8% (932/943) specific[45,67] for near-occlusion with full collapse. Dampened, pseudovenous flow with low pulsatility is highly specific as published in Mansour et al,[45] with only 1 false-positive with distal occlusion. A flow profile with systolic triangular spikes and no diastolic flow can be either distal occlusion or stenosis[5,18,45,47] or near-occlusion with full collapse[12,18,67,76]; the sonography report should reflect this uncertainty. Systolic spikes with reversed diastolic flow have been reported in a small series.[8] False-negatives were either mistaken occlusions or mistaken conventional stenosis with high flow velocity. Rarely, an important pitfall is when velocity drops to the range of normal flow; a peak systolic velocity of 140 cm/s was presented by Bowman et al.[18] As such, the appearance with 2D B-mode of a very tight stenosis and "normal" flow velocities does not add up, requiring suspicion of near-occlusion. However, if the stenosis appearance on B-mode is ignored, the near-occlusion can be mistakenly reported as "no significant stenosis."

Near-occlusions without full collapse seems indistinguishable from conventional stenosis because both have high flow velocities.[5,21] However, near-occlusion without full collapse has only been analyzed for peak systolic velocity in 2 studies totalling 30 patients,[5,21] and one of these studies did not clearly define near-occlusion without full collapse.[5] Thus, more than peak systolic velocity is needed to distinguish near-occlusion without full collapse from conventional stenoses.

Thus, when very tight stenosis with low flow is detected, it is often near-occlusion with full collapse, though possibly distal disease. Angiographic confirmation (with CTA including delayed images) is reasonable. A finding of a suggested >70% carotid stenosis with velocity on sonography can be >70% stenosis or a near-occlusion. Thus, virtually all near-occlusions without full collapse and some near-occlusions with full collapse can be overlooked if sonography is used alone.

Diagnosis with CTA. CTA diagnostic accuracy to separate near-occlusion from occlusion has been moderately studied. In 2 studies, 30/30 near-occlusions and 33/33 occlusions were correctly identified.[33,37] Separating near-occlusions (mostly partial near-occlusion) from conventional stenosis has been less analyzed. In 1 study, 4/4 near-occlusion (at least 1 was without full collapse) and 22/22 30%–99% stenoses were correctly distinguished.[33] Further studies that include delayed imaging are needed.

With a consistent expert observer as the criterion standard, Bartlett et al[22] presented CTA-specific diameter-measurement criteria for separating near-occlusion (with and without full collapse) from conventional stenoses: 1) stenosis diameter of ≤1.3 mm, 2) ipsilateral distal ICA diameter of ≤3.5 mm, 3) ipsilateral distal ICA/contralateral distal ICA ratio of ≤0.87, and 4) ipsilateral distal ICA/ipsilateral ECA of ≤1.27. These criteria were not compared with those of conventional angiography.

MRA Diagnosis. MRA literature for near-occlusion is limited. To diagnose near-occlusion versus occlusion, TOF MRA is limited because slow-flow signal likely is below the visibility threshold; 2D TOF may be superior to 3D TOF.[5,17] Approximately 75% (14/19) of all near-occlusions show a flow gap on 2D TOF.[5] A flow gap seems similarly common for near-occlusion both with full collapse and without full collapse, though that study did not clearly separate the near-occlusion types.[5] Segmental flow gaps suggest vessel patency because occlusions are more likely to show full-length signal absence.[5] While it was suggested that the clinical

usefulness of TOF MRA is limited because distal occlusions can present with flow gaps,[5] it is uncertain that these were truly distal occlusions. No study sought to separate near-occlusions from conventional stenosis. Contrast-enhanced MRA for near-occlusion is scarcely studied.[5]

Alternative Diagnostic Criteria. After publication of the 2005 NASCET/European Carotid Surgery Trial near-occlusion criteria with conventional angiography in 2005,[1] modifications were suggested. A numeric ipsilateral distal ICA/contralateral distal ICA ratio of <0.5 was sought from one report,[28] and <0.2,[35] from another. With CTA criteria for near-occlusion, a side-to-side ratio of only ≤0.87 suggested near-occlusion (with and without full collapse), though the authors concluded that an overall interpretation be used rather than measurements because of the variability of disease and anatomic variants to diagnose partial near-occlusion.[22] However, the ≤0.87 ratio was derived from diagnostic analyses,[22] whereas the other 2 ratios were presented without reference to how they were derived.[28,35] It seems that these measured criteria transfer the diagnosis of near-occlusion from a skilled interpretation to synthesized numbers applied without the same skill.

The minimal diameter of maximal stenosis on CTA is an alternative way to grade stenoses, replacing percentage calculations to avoid measuring the distal artery.[86] This would remove inconsistencies and ambiguities of creating percentage stenosis. If that method is used, the presence or absence of near-occlusions may still need to be assessed to list near-occlusions separately.

Recommendation

CTA is suggested for current near-occlusion diagnosis. CTA is very accurate in separating near-occlusion from occlusion with delayed imaging, and criteria exist to separate near-occlusion (with and without full collapse) from conventional stenoses. The usual technical concerns with CTA, contrast and radiation, apply. In comparison with conventional angiography, the criteria can be more specific with absolute measurements, with no procedural stroke risk.

The diagnosis of complete ICA occlusion needs delayed imaging to exclude the slowly filling distal ICA of near-occlusion with full collapse. That can be a routine postcontrast head CT after CTA (which also evaluates enhancing brain lesions and delayed collateral pial arteries not shown on initial "snapshot" CTA) or multiphased CTA. While enhanced MRA could show some slow distal ICAs, with acquisition longer than that in the subsecond scan of CTA at each level, MRA, however, has inherent lower spatial resolution.

For sonography, emphasis has often been on the separation of near-occlusion and occlusion; possibly this can be further improved with power Doppler and/or contrast enhancement. More important, it is impossible to separate near-occlusion without full collapse from conventional stenoses with sonography. This lack of sensitivity is a relatively recent finding (from 2014[21]), and many recommendations for diagnostic work-up predated this finding. Recommendations for the diagnostic work-up should be revised accordingly. It seems appropriate to always perform CTA in addition because near-occlusions can be missed with sonography, and those that are detected might be caused by distal occlusion or stenosis.

MRA with 2D TOF or contrast enhancement can separate some near-occlusions from occlusion, but not all. It is uncertain whether MRA can consistently separate near-occlusion from conventional stenosis.

Confusion and Need for Further Improvement

Please refer to Part 2 of this review for the confusion and need for further improvement regarding the definition, terminology, and diagnosis of near-occlusion.

Disclosures: Elias Johansson—*RELATED*: *Grant*: several non-profit organizations,* *Comments*: standard research grants, listed in the footnotes; none had any influence over the work; conforms to "no disclosures." Allan J. Fox—*UNRELATED*: *Expert Testimony*: medical malpractice cases, none related to the topic of this article. *Money paid to the institution.

REFERENCES

1. Fox AJ, Eliasziw M, Rothwell PM, et al. **Identification, prognosis, and management of patients with carotid artery near occlusion.** *AJNR Am J Neuroradiol* 2005;26:2086–94 Medline
2. Morgenstern LB, Fox AJ, Sharpe BL, et al. **The risks and benefits of carotid endarterectomy in patients with near occlusion of the carotid artery: North American Symptomatic Carotid Endarterectomy Trial (NASCET) Group.** *Neurology* 1997;48:911–15 CrossRef Medline
3. Son S, Choi DS, Kim SK, et al. **Carotid artery stenting in patients with near occlusion: a single-center experience and comparison with recent studies.** *Clin Neurol Neurosurg* 2013;115:1976–81 CrossRef Medline
4. Sakamoto S, Kiura Y, Kajihara Y, et al. **Carotid artery stenting using the proximal or dual protection method for near occlusion of the cervical internal carotid artery.** *Neurosurg Rev* 2013;36:551–57; discussion 557–48 CrossRef Medline
5. El-Saden SM, Grant EG, Hathout GM, et al. **Imaging of the internal carotid artery: the dilemma of total versus near total occlusion.** *Radiology* 2001;221:301–08 CrossRef Medline
6. Martin MA, Marotta TR. **Vasa vasorum: another cause of the carotid string sign.** *AJNR Am J Neuroradiol* 1999;20:259–62 Medline
7. Gil-Peralta A, González A, González-Marcos JR, et al. **Internal carotid artery stenting in patients with symptomatic atheromatous pseudo-occlusion.** *Cerebrovasc Dis* 2004;17(suppl 1):105–12 CrossRef Medline
8. Fujimoto S, Toyoda K, Kishikawa K, et al. **Accuracy of conventional plus transoral carotid ultrasonography in distinguishing pseudo-occlusion from total occlusion of the internal carotid artery.** *Cerebrovasc Dis* 2006;22:170–76 CrossRef Medline
9. Ogata T, Yasaka M, Kanazawa Y, et al. **Outcomes associated with carotid pseudo-occlusion.** *Cerebrovasc Dis* 2011;31:494–98 CrossRef Medline
10. Kniemeyer HW, Aulich A, Schlachetzki F, et al. **Pseudo- and segmental occlusion of the internal carotid artery: a new classification, surgical treatment and results.** *Eur J Vasc Endovasc Surg* 1996;12:310–20 CrossRef Medline
11. Archie JP. **Carotid endarterectomy when the distal internal carotid artery is small or poorly visualized.** *J Vasc Surg* 1994;19:23–30; discussion 30–31 CrossRef Medline
12. Ascher E, Markevich N, Hingorani A, et al. **Pseudo-occlusions of the internal carotid artery: a rationale for treatment on the basis of a modified carotid duplex scan protocol.** *J Vasc Surg* 2002;35:340–45 CrossRef Medline
13. Nikas DN, Ghany MA, Stabile E, et al. **Carotid artery stenting with proximal cerebral protection for patients with angiographic appearance of string sign.** *JACC Cardiovasc Interv* 2010;3:298–304 CrossRef Medline

14. Ringelstein EB, Berg-Dammer E, Zeumer H. **The so-called atheromatous pseudoocclusion of internal carotid artery: a diagnostic and therapeutical challenge.** *Neuroradiology* 1983;25:147–55 CrossRef Medline
15. Terada T, Tsuura M, Matsumoto H, et al. **Endovascular treatment for pseudo-occlusion of the internal carotid artery.** *Neurosurgery* 2006;59:301–09; discussion 301–09 CrossRef Medline
16. O'Leary DH, Mattle H, Potter JE. **Atheromatous pseudo-occlusion of the internal carotid artery.** *Stroke* 1989;20:1168–73 CrossRef Medline
17. Fürst G, Saleh A, Wenserski F, et al. **Reliability and validity of noninvasive imaging of internal carotid artery pseudo-occlusion.** *Stroke* 1999;30:1444–49 CrossRef Medline
18. Bowman JN, Olin JW, Teodorescu VJ, et al. **Carotid artery pseudo-occlusion: does end-diastolic velocity suggest need for treatment?** *Vasc Endovascular Surg* 2009;43:374–78 CrossRef Medline
19. Dimakakos PB. **Carotid internal pseudo-occlusion: what should we do?** *Vasc Surg* 1999;33:123–24 CrossRef
20. Hirata Y, Sakata N, Inoue T, et al. **Histopathological features with angiographic correlates of internal carotid artery pseudo-occlusion: impact of plaque compositions—clinical article.** *J Neurosurg* 2011;115:350–58 CrossRef Medline
21. Johansson E, Öhman K, Wester P. **Carotid near-occlusion with full collapse might cause a high risk of stroke.** *J Int Med* 2015;277:615–23 CrossRef Medline
22. Bartlett ES, Walters TD, Symons SP, et al. **Diagnosing carotid stenosis near-occlusion by using CT angiography.** *AJNR Am J Neuroradiol* 2006;27:632–37 Medline
23. Lee DH, Gao FQ, Rankin RN, et al. **Duplex and color Doppler flow sonography of occlusion and near occlusion of the carotid artery.** *AJNR Am J Neuroradiol* 1996;17:1267–74 Medline
24. Gonzalez A, Gil-Peralta A, Mayol A, et al. **Internal carotid artery stenting in patients with near occlusion: 30-day and long-term outcome.** *AJNR Am J Neuroradiol* 2011;32:252–58 CrossRef Medline
25. Paciaroni M, Caso V, Cardaioli G, et al. **Is ultrasound examination sufficient in the evaluation of patients with internal carotid artery severe stenosis or occlusion?** *Cerebrovasc Dis* 2003;15:173–76 CrossRef Medline
26. Choi BS, Park JW, Shin JE, et al. **Outcome evaluation of carotid stenting in high-risk patients with symptomatic carotid near occlusion.** *Interv Neuroradiol* 2010;16:309–16 Medline
27. Saba L, Mallarini G. **Comparison between quantification methods of carotid artery stenosis and computed tomographic angiography.** *J Comput Assist Tomogr* 2010;34:421–30 CrossRef Medline
28. Oka F, Ishihara H, Kato S, et al. **Cerebral hemodynamic benefits after carotid artery stenting in patients with near occlusion.** *J Vasc Surg* 2013;58:1512–17 CrossRef Medline
29. Ruiz-Salmerón RJ, Gamero MA, Carrascosa C, et al. **Carotid artery stenting: clinical and procedural implications for near-occlusion stenosis** [Article in English, Spanish]. *Neurologia* 2013;28:535–42 CrossRef Medline
30. Edgell RC, Yavagal DR, Agner C, et al. **Recanalization of a symptomatic extracranial internal carotid artery near occlusion with proximal and distal protection: technical case report.** *Neurosurgery* 2007; 61:E174 CrossRef Medline
31. Gabrielsen TO, Seeger JF, Knake JE, et al. **The nearly occluded internal carotid artery: a diagnostic trap.** *Radiology* 1981;138:611–18 CrossRef Medline
32. Fox AJ. **How to measure carotid stenosis.** *Radiology* 1993;186: 316–18 CrossRef Medline
33. Leclerc X, Godefroy O, Lucas C, et al. **Internal carotid arterial stenosis: CT angiography with volume rendering.** *Radiology* 1999; 210:673–82 CrossRef Medline
34. Fox AJ, Symons SP, Aviv RI, et al. **Falsely claiming use of NASCET percentage stenosis method.** *Radiology* 2009;253:574–75; author reply 575 CrossRef Medline
35. Anzidei M, Napoli A, Marincola BC, et al. **Gadofosveset-enhanced MR angiography of carotid arteries: does steady-state imaging improve accuracy of first-pass imaging? Comparison with selective digital subtraction angiography.** *Radiology* 2009;251:457–66 CrossRef Medline
36. Rothwell PM, Gutnikov SA, Warlow CP. **Reanalysis of the final results of the European Carotid Surgery Trial.** *Stroke* 2003;34:514–23 CrossRef Medline
37. Chen C, Lee TH, Hsu HL, et al. **Multi-slice CT angiography in diagnosing total versus near occlusions of the internal carotid artery: comparison with catheter angiography.** *Stroke* 2004;35:83–85 Medline
38. Fox AJ, Symons SP, Aviv RI, et al. **Should modeling methodology suppress anatomic excellence?** *Stroke* 2009;40:3411–12 CrossRef Medline
39. Dix JE, McNulty BJ, Kalimes DF. **Frequency and significance of a small distal ICA in carotid stenosis.** *AJNR Am J Neuroradiol* 1998;19: 1215–18 Medline
40. Yadav JS. **Functional occlusions of the carotid artery (string signs): to treat or not to treat?** *JACC Cardiovasc Interv* 2010;3:305–06 CrossRef Medline
41. Henderson R, Eliasziw M, Fox AJ, et al. **Angiographically defined collateral circulation and risk of stroke in patients with severe carotid artery stenosis: North American Symptomatic Carotid Endarterectomy Trial (NASCET) Group.** *Stroke* 2000;31:128–32 CrossRef Medline
42. Rothwell PM, Warlow CP; On behalf of the European Carotid Surgery Trialists' Collaborative Group. **Low risk of ischemic stroke in patients with reduced internal carotid artery lumen diameter distal to severe symptomatic carotid stenosis: cerebral protection due to low poststenotic flow?** *Stroke* 2000;31:622–30 CrossRef Medline
43. Lev MH, Romero JM, Goodman DN, et al. **Total occlusion versus hairline residual lumen of the internal carotid arteries: accuracy of single section helical CT angiography.** *AJNR Am J Neuroradiol* 2003; 24:1123–29 Medline
44. Koutsoumpelis A, Kouvelos G, Peroulis M, et al. **Surgical and endovascular intervention on internal carotid artery near occlusion.** *Int Angiol* 2015;34:172–81 Medline
45. Mansour MA, Mattos MA, Hood DB, et al. **Detection of total occlusion, string sign, and preocclusive stenosis of the internal carotid artery by color-flow duplex scanning.** *Am J Surg* 1995;170:154–58 CrossRef Medline
46. Radak DJ, Tanaskovic S, Ilijevski NS, et al. **Eversion carotid endarterectomy versus best medical treatment in symptomatic patients with near total internal carotid occlusion: a prospective nonrandomized trial.** *Ann Vasc Surg* 2010;24:185–89 CrossRef Medline
47. Samson RH, Showalter DP, Yunis JP, et al. **Color flow scan diagnosis of the carotid string sign may prevent unnecessary surgery.** *Cardiovasc Surg* 1999;7:236–41 CrossRef Medline
48. Spacek M1, Martinkovicova L, Zimolova P, et al. **Mid-term outcomes of carotid artery stenting in patients with angiographic string sign.** *Catheter Cardiovasc Interv* 2012;79:174–79 CrossRef Medline
49. Androulakis AE, Labropoulos N, Allan R, et al. **The role of common carotid artery end-diastolic velocity in near total or total internal carotid artery occlusion.** *Eur J Vasc Endovasc Surg* 1996;11:140–47 CrossRef Medline
50. Giannoukas AD, Labropoulos N, Smith FC, et al. **Management of the near total internal carotid artery occlusion.** *Eur J Vasc Endovasc Surg* 2005;29:250–55 CrossRef Medline
51. Sekhar LN, Heros RC, Lotz PR, et al. **Atheromatous pseudo-occlusion of the internal carotid artery.** *J Neurosurg* 1980;52:782–89 CrossRef Medline
52. Greiner C, Wassmann H, Palkovic S, et al. **Revascularization procedures in internal carotid artery pseudo-occlusion.** *Acta Neurochir (Wien)* 2004;146:237–43 CrossRef Medline
53. Momjian-Mayor I, Burkhard P, Murith N, et al. **Diagnosis of and treatment for symptomatic carotid stenosis: an updated review.** *Acta Neurol Scand* 2012;126:293–305 CrossRef Medline
54. Macpherson P. **Pseudo-occlusion of the internal carotid artery.** *Br J Radiol* 1978;51:5–10 CrossRef Medline

55. Regina G, Testini M, Fullone M, et al. **Pseudo-occlusion of the internal carotid artery: report of 15 cases and review of the literature.** *Int Angiol* 1997;16:147–50 Medline
56. Pulli R, Frosini P, Gatti M, et al. **Internal carotid pseudo-occlusion: early and late results.** *J Cardiovasc Surg (Torino)* 1997;38:15–20 Medline
57. Heros RC, Sekhar LN. **Diagnostic and therapeutic alternatives in patients with symptomatic "carotid occlusion" referred for extracranial-intracranial bypass surgery.** *J Neurosurg* 1981;54:790–96 CrossRef Medline
58. Berman SS, Bernhard VM, Erly WK, et al. **Critical carotid artery stenosis: diagnosis, timing of surgery and outcome.** *J Vasc Surg* 1994;20:499–508; discussion 508–10 CrossRef Medline
59. Yonas H, Meyer J. **Extreme pseudo-occlusion of the internal carotid artery.** *Neurosurgery* 1982;11:681–86 CrossRef Medline
60. Romero JM, Lev MH, Chan ST, et al. **US of neurovascular occlusive disease: interpretive pearls and pitfalls.** *Radiographics* 2002;22:1165–76 CrossRef Medline
61. Remonda L, Heid O, Schroth G. **Carotid artery stenosis, occlusion, and pseudo-occlusion: first-pass, gadolinium-enhanced, three-dimensional MR angiography—preliminary study.** *Radiology* 1998;209:95–102 CrossRef Medline
62. Berman SS, Devine JJ, Erodes LS, et al. **Distinguishing carotid artery pseudo-occlusion with color-flow Doppler.** *Stroke* 1995;26:434–38 CrossRef Medline
63. Sitzer M, Fürst G, Fischer H, et al. **Between-method correlation in quantifying internal carotid stenosis.** *Stroke* 1993;24:1513–18 CrossRef Medline
64. Ammar AD, Turrentine MW, Farha SJ. **The importance of arteriographic interpretation in occlusion or pseudo-occlusion of the carotid artery.** *Surg Gyn Obst* 1988;167:119–23 Medline
65. Barker CM, Gomez J, Grotta JC, et al. **Feasibility of carotid artery stenting in patients with angiographic string sign.** *Catheter Cardiovasc Interv* 2010;75:1104–09 CrossRef Medline
66. Bazan HA. **Carotid string sign is not necessarily a functional occlusion: admit, anticoagulate, and revascularize urgently.** *Catheter Cardiovasc Interv* 2010;75:1110 CrossRef Medline
67. Hetzel A, Eckenweber B, Trummer B, et al. **Colour-coded duplex sonography of preocclusive carotid stenoses.** *Eur J Ultrasound* 1998;8:183–91 CrossRef Medline
68. Kashyap VS, Clair DG. **Carotid string sign.** *J Vasc Surg* 2006;43:401 CrossRef Medline
69. Fredericks RK,ThomasTD, Lefkowitz DS, et al. **Implications of the angiographic string sign in carotid atherosclerosis.** *Stroke* 1990;21:476–79 CrossRef Medline
70. Bennett DL, Hamberg LM, Wang B, et al. **Diagnostic yield of delayed phase imaging in CT angiography of the head and neck: a retrospective study.** *PLoS One* 2014;9:e99020 CrossRef Medline
71. Mehigan JT, Olcott C 4th. **The carotid "string" sign. Differential diagnosis and management.** *Am J Surg* 1980;140:137–43 CrossRef Medline
72. Labropoulos N, Androulakis A, Allan R, et al. **The value of colour flow imaging in the detection of subtotal and total internal carotid artery occlusion.** *Vasc Endovasc Surg* 1997;31:7757–59 CrossRef
73. Gross K, Wang H. **The string sign.** *J Vasc Nurs* 2000;18:72 CrossRef Medline
74. Pappas JN. **The angiographic string sign.** *Radiology* 2002;222:237–38 CrossRef Medline
75. Lippman HH, Sundt TM Jr, Holman CB. **The poststenotic carotid slim sign: spurious internal carotid hypolasia.** *Mayo Clin Proc* 1970;45:762–67 Medline
76. Görtler M, Niethammer R, Widder B. **Differentiating subtotal carotid artery stenoses from occlusions by colour-coded duplex sonography.** *J Neurol* 1994;241:301–05 CrossRef Medline
77. Szabo K, Kern R, Gass A, et al. **Acute stroke patterns in patients with internal carotid artery disease: a diffusion-weighted magnetic resonance imaging study.** *Stroke* 2001;32:1323–29 CrossRef Medline
78. Riishede J, Ethelberg S. **Angiographic changes in sudden and severe herniation of the brain stem through the tentorial incisure: report of five cases.** *AMA Arch Neural Psychiatry* 1953;70:399–409 CrossRef Medline
79. Mumenthaler VM, Wellauer J, Schamaun M. **"Apoplexie" bei vollständigen und unvollständigen Carotisverschlüssen.** *Helv Med Acta* 1961;28:705–40, continued 808–30
80. Newton TH, Couch RSC. **Possible errors in the arteriographic diagnosis of internal carotid artery occlusion.** *Radiology* 1960;75:766–73 CrossRef Medline
81. Marquering HA, Nederkoorn PJ, Beenen LF, et al. **Carotid pseudo-occlusion on CTA in patients with acute ischemic stroke: a concerning observation.** *Clin Neurol Neurosurg* 2013;115:1591–94 CrossRef Medline
82. Ojemann RG, Fisher CM, Rich JC. **Spontaneous dissecting aneurysm of the internal carotid artery.** *Stroke* 1972;3:434–40 CrossRef Medline
83. Rothwell PM, Gibson RJ, Slattery J, et al. **Equivalence of measurements of carotid stenosis: a comparison of three methods on 1001 angiograms—European Carotid Surgery Trialists' Collaborative Group.** *Stroke* 1994;25:2435–39 CrossRef Medline
84. Bartlett ES, Walters TD, Symons SP, et al. **Quantification of carotid stenosis on CT angiography.** *AJNR Am J Neuroradiol* 2006;27:13–19 Medline
85. Buchan A, Gates P, Pelz D, et al. **Intraluminal thrombus in the cerebral circulation: implications for surgical management.** *Stroke* 1988;19:681–87 CrossRef Medline
86. North American Symptomatic Carotid Endarterectomy Trial (NASCET) Steering Committee. **North American Symptomatic Carotid Endarterectomy Trial: methods, patient characteristics, and progress.** *Stroke* 1991;22:711–20 CrossRef Medline

Minimizing Radiation Exposure in Evaluation of Pediatric Head Trauma: Use of Rapid MR Imaging

H. Mehta, J. Acharya, A.L. Mohan, M.E. Tobias, L. LeCompte, and D. Jeevan

ABSTRACT

BACKGROUND AND PURPOSE: With >473,000 annual emergency department visits for children with traumatic brain injuries in the United States, the risk of ionizing radiation exposure during CT examinations is a real concern. The purpose of this study was to assess the validity of rapid MR imaging to replace CT in the follow-up imaging of patients with head trauma.

MATERIALS AND METHODS: A retrospective review of 103 pediatric patients who underwent initial head CT and subsequent follow-up rapid MR imaging between January 2010 and July 2013 was performed. Patients had minor head injuries (Glasgow Coma Scale, >13) that required imaging. Initial head CT was performed, with follow-up rapid MR imaging completed within 48 hours. A board-certified neuroradiologist, blinded to patient information and scan parameters, then independently interpreted the randomized cases.

RESULTS: There was almost perfect agreement in the ability to detect extra-axial hemorrhage on rapid MR imaging and CT ($\kappa = 0.84$, $P < .001$). Evaluation of hemorrhagic contusion/intraparenchymal hemorrhage demonstrated a moderate level of agreement between MR imaging and CT ($\kappa = 0.61$, $P < .001$). The ability of MR imaging to detect a skull fracture also showed a substantial level of agreement with CT ($\kappa = 0.71$, $P < .001$). Detection of diffuse axonal injury demonstrated a slight level of agreement between MR imaging and CT ($\kappa = 0.154$, $P = .04$). However, the overall predictive agreement for the detection of an axonal injury was 91%.

CONCLUSIONS: Rapid MR imaging is a valid technique for detecting traumatic cranial injuries and an adequate examination for follow-up imaging in lieu of repeat CT.

ABBREVIATION: rMRI = rapid MR imaging

Head trauma continues to be a leading cause of death and disability in children in the United States.[1] Every year, >473,000 visits to the emergency department are related to brain injury,[2] most resulting from minor injuries or falls. Although most head injuries are classified as mild, approximately 10%–15% of children sustain a severe one. The incidence of intracranial injury following minor head trauma is unknown; however, with increasing public awareness of traumatic brain injury and concussion, there has been a rise in research of minor head injuries. Methods of diagnosis,[3,4] hospital admission criteria,[5,6] and return-to-play criteria[7,8] are a few of the active areas of research.

Children with head trauma, at risk for intracranial injury, should be initially imaged with CT[9] because it remains the criterion standard technique for the evaluation of head trauma.[10] Although the incidence of injuries requiring neurosurgical intervention in children with minor head injuries is low, the use of CT for evaluation has been increasing. The use of CT increased from 13% to 22% from 1995 to 2003, with a peak of 29% in 2000.[11] The decision to obtain neuroimaging for children with minor head trauma must balance the importance of identifying head injuries with the risks of CT. There is growing awareness in the medical community and public of increased cancer risk caused by ionizing radiation.[12] Brenner et al[13] estimated that 170 additional fatal cancers will develop due to head CT examinations performed in children younger than 15 years of age in the United States in a single year. In addition, some children may require sedation to obtain an adequate CT examination, which can be associated with as high as a 20.1% chance of an adverse event.[14]

MR imaging is an alternative technique that avoids ionizing radiation exposure altogether and produces high-quality images. A study with conventional sequences requires long acquisition times and is susceptible to motion artifacts. The need for sedation increases the risk to the patient, lengthens the time needed to

Received March 31, 2015; accepted after revision May 20.

From the Departments of Radiology (H.M., J.A., L.L.) and Neurosurgery (A.L.M., M.E.T., D.J.), New York Medical College, Valhalla, New York.

Please address correspondence to Hasit Mehta, MD, New York Medical College, Department of Radiology, 100 Woods Rd, Valhalla, NY 10595; e-mail: MehtaH@wcmc.com

http://dx.doi.org/10.3174/ajnr.A4464

acquire patient images, and further increases the cost of standard MR imaging.[14,15]

Modified MR imaging protocols with reduced acquisition times have been used successfully in non-neurosurgical patients,[16,17] and rapid MR imaging (rMRI) or "quick-brain" MR imaging protocols have become an accepted technique to evaluate and follow patients with hydrocephalus.[18-20] Missios et al[21] investigated the use of rMRI in patients without hydrocephalus and concluded that it was an adequate neuroimaging tool for evaluation and follow-up. The use of rMRI protocols in evaluating pediatric patients with minor head injuries remains to be validated.

As far as we are aware, a systematic search of current literature did not yield a previous study examining the validity of rMRI in the imaging of pediatric patients with head trauma. The purpose of our study was to demonstrate the efficacy of replacing ionizing CT imaging with nonionizing rMRI for follow-up of patients with minor head trauma.

MATERIALS AND METHODS

Our institutional review board approved this study, with a waiver of informed consent. All CT and MR imaging examinations were performed as a standard of care; the results were retrospectively reviewed. The study protocol complied with the Health Insurance Portability and Accountability Act.

Patient Group

Patients evaluated at Westchester Medical Center, a level 1 pediatric trauma center, between January 2010 and July 3013 were screened for eligibility; inclusion criteria were patients presenting with minor head injury (Glasgow Coma Scale, >13) who were evaluated with rMRI performed within 48 hours following an initial CT. Patients were selected for CT on the basis of regional emergency department criteria for imaging, and rMRI was completed at our institution regardless of CT findings.

Imaging Protocol

CT studies performed at our institution used a Brilliance 64–detector row CT scanner (Philips Healthcare, Best, the Netherlands); images were acquired helically and reconstructed into a contiguous 3-mm axial dataset acquired from the base of the skull to the vertex. Images obtained at an outside institution were uploaded to our system as per our protocol for interpretation of outside imaging studies. Images obtained from outside institutions used their own protocol for image acquisition; minimum imaging requirements for outside studies included datasets acquired from the base of the skull to the vertex with contiguous axial images of ≤5 mm.

rMRI examinations were performed by using 1.5T (Achieva 1.5T; Philips Healthcare) and 3T (Achieva 3T X; Philips Healthcare) scanners. rMRI sequences included the following: axial single-shot T2 fast-field echo EPI: 5-second scanning time; TR, 2000 ms; TE, 25 ms; axial single-shot diffusion-weighted imaging: 35-second scanning time; TR, 3000 ms; TE, 65 ms; axial single-shot FLAIR: 45-second scanning time; TR, 12,000 ms; TI, 2850 ms; TE, 135 ms; axial T2 fast-field echo: 35-second scanning time; TR, 550 ms; TE, 15 ms; coronal T2 turbo spin-echo: 35-second scanning time; TR, 3500 ms; TE, 80 ms. Axial T2 turbo spin-echo (30-second scanning time; TR, 3000 ms; TE, 80 ms) may be performed if desired by the radiologist or MR imaging technologist, with a total scanning time of 2.5–3 minutes (Fig 1: rMRI sequences obtained).

Image Interpretation

CT and rMRI studies that met the inclusion criteria were randomized, then independently and retrospectively evaluated by a board-certified radiologist, with added board certification in neuroradiology, on a digital PACS workstation. The studies were retrospectively reviewed during a 3-month period from October 2013 to January 2014. The reader was blinded to patient-identifying information and imaging parameters. Furthermore, all CT and rMRI studies were reviewed independent of one another.

During interpretation, the radiologist evaluated the presence or absence of the following findings: extra-axial hemorrhage (subdural, epidural, or subarachnoid hemorrhage), hemorrhagic contusion/intraparenchymal hemorrhage, calvarial fracture, and/or diffuse axonal injury. The radiologist was also asked to comment on the presence of motion degradation.

Statistical Evaluation

We performed statistical evaluation of the data by using commercially available statistical software (SPSS; IBM, Armonk, New York). Cohen κ statistics[22] were performed to determine whether there was agreement between the 2 imaging modalities as to the presence or absence of extra-axial hemorrhage, hemorrhagic contusion/intraparenchymal hemorrhage, fracture, and/or diffuse axonal injury. Positive and negative percentage agreement and overall percentage agreement of the findings on CT and rMRI were also analyzed.

RESULTS

A total of 103 pediatric patients presenting with minor head trauma (presenting Glasgow Coma Scale, >13) underwent rMRI following initial CT as per regional head trauma injury criteria. Two patients were excluded because the rMRI was performed following surgical intervention for intracranial hemorrhage. The mean age of the 101 subjects was 6 years (range, 0–19 years); there were 57 males (55%) and 46 females (45%). The most common mechanism of injury was a fall. rMRI was performed within 48 hours of arrival at our institution and CT imaging; the average time between initial CT and follow-up rMRI was 19 hours. No patient received anesthesia for the study.

On review of the imaging, 24 patients had some degree of motion degradation on rMRI compared with only 7 patients on CT. Only 4 patients had evidence of motion degradation on both CT and rMRI. The degree of motion artifacts on the examinations was mild to moderate and not enough to require exclusion from the study because the studies were deemed diagnostic. Overall, the correlation of traumatic findings between initial CT and rMRI was $\kappa = 0.73$ ($P < .001$; 95% CI, 0.88–0.94). This indicates a substantial agreement in findings between imaging modalities (Table 1). An overall percentage agreement of 92%, positive percentage accuracy of 91%, and negative predictive accuracy of 94% further demonstrated this agreement.

When one looks at subtypes of injuries, the ability to detect

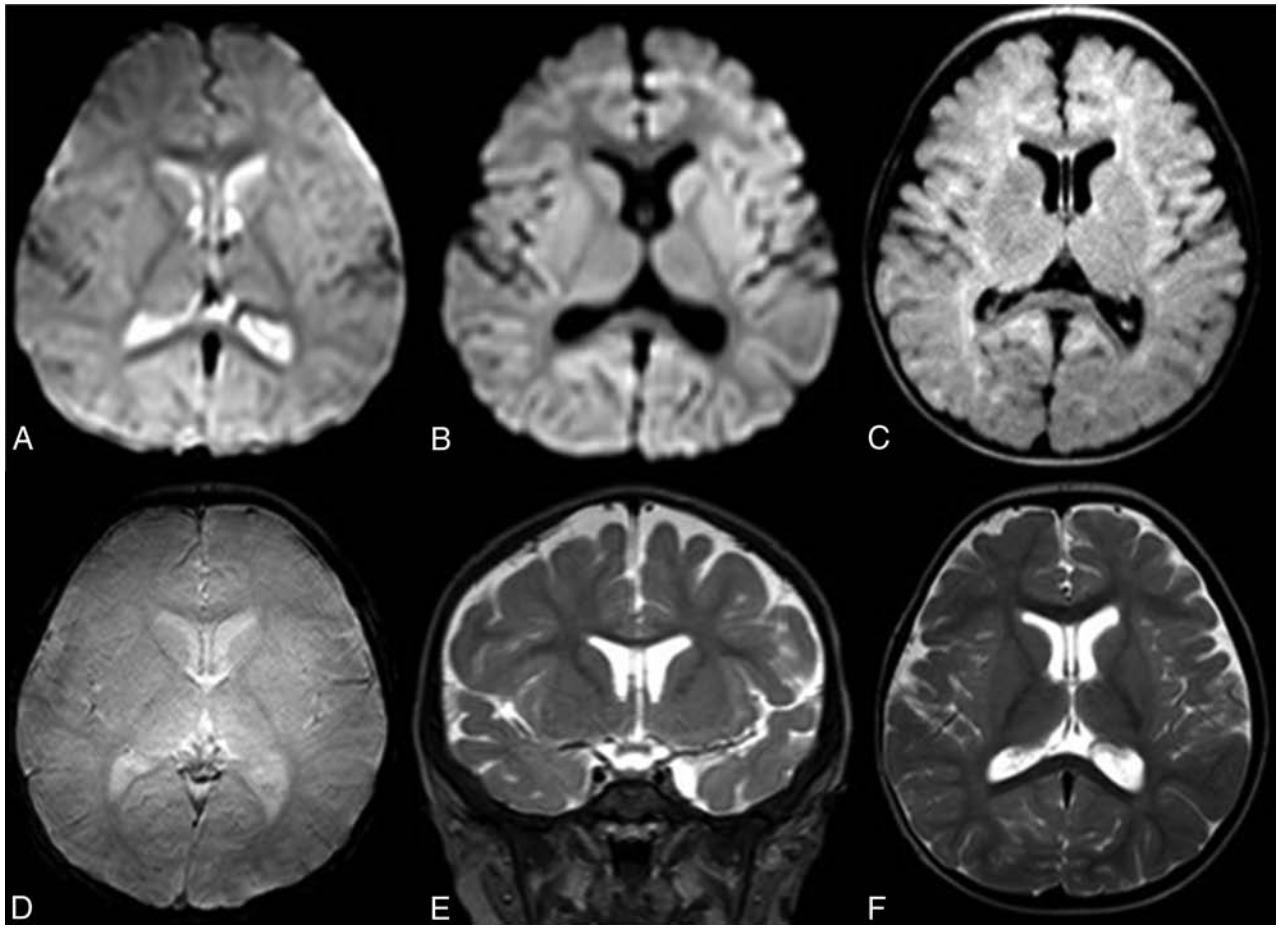

FIG 1. Sample images from a routine rMRI examination. Axial single-shot T2 fast-field echo echo-planar (*A*), axial single-shot diffusion-weighted (*B*), axial single-shot FLAIR (*C*), axial T2 fast-field echo (T2*) (*D*), coronal T2 TSE (*E*), and axial T2 TSE (*F*) images.

Table 1: Presence of a positive image finding following minor head injury[a]

Positive Scan Findings	CT		
	Negative	Positive	Total
rMRI			
Negative	22	10	32
Positive	1	68	69
Total	23	78	101

[a] κ measure of agreement, 0.728; $P < .001$; standard error, 0.075; overall percentage agreement, 92%; positive percentage agreement, 91%; negative percentage agreement, 94%.

Table 2: Presence of extra-axial hemorrhage following minor head injury[a]

Extra-Axial Hemorrhage	CT		
	Negative	Positive	Total
rMRI			
Negative	44	5	49
Positive	3	49	52
Total	47	54	101

[a] κ measure of agreement, 0.841; $P < 0.001$; standard error, 0.054; overall percentage agreement, 92%; positive percentage agreement, 91%; negative percentage agreement, 94%.

Table 3: Presence of a contusion/intraparenchymal hemorrhage following minor head injury[a]

Contusion	CT		
	Negative	Positive	Total
rMRI			
Negative	74	1	75
Positive	12	14	26
Total	86	15	101

[a] κ measure of agreement, 0.609; $P < .001$; standard error, 0.095; overall percentage agreement, 87%; positive percentage agreement, 93%; negative percentage agreement, 86%.

extra-axial hemorrhage (epidural, subdural, subarachnoid hemorrhage) on CT and rMRI was comparable, with a $\kappa = 0.84$ ($P < .001$; 95% CI, 0.74–0.95). With an overall percentage agreement of 92% and a positive percentage agreement of 91% and a negative percentage agreement of 94%, the ability to detect extra-axial hemorrhage on rMRI was almost in perfect agreement with findings on CT (Table 2).

Although there was substantial agreement between rMRI and CT on the presence of hemorrhagic contusion/intraparenchymal hemorrhage (Table 3), the correlation was not as great as that for the presence of extra-axial hemorrhage, with $\kappa = 0.61$ ($P < .001$; 95% CI, 0.42–0.80). However, when we looked at the results, there was a high positive predictive agreement of findings on rMRI (93%), with a high overall percentage agreement (87%). The negative percentage agreement was also high at 86%. It appears that rMRI detects more contusive changes than initially seen on CT and may be more sensitive in detecting intraparenchymal blood.

A similar finding was noted when looking at the presence of diffuse axonal injury (Table 4). There was only slight agreement for the presence of axonal injury between rMRI and CT with $\kappa = 0.15$ ($P = .04$; 95% CI, −0.15–0.45). However, the overall percentage agreement was 91%, and the negative percentage agreement was 92%. The positive percentage agreement was only 50%, with 8 cases in which rMRI-suspected axonal injury was not seen on CT. The relatively low positive percentage agreement may be secondary to increased sensitivity to this injury type with the use of rMRI, especially because only a single case had a description of positive axonal injury seen on CT that was not seen on rMRI.

Even though it was predicted that CT would be more reliable in detecting skull fractures compared with rMRI, this reliability was not demonstrated (Table 5). The reliability of rMRI to detect skull fractures was found to be $\kappa = 0.71$ ($P < .001$; 95% CI, 0.56–0.84), indicating substantial agreement. The overall percentage agreement was 85%, with a negative percentage agreement of 94% and a positive percentage agreement of 78%. In 12 cases, rMRI failed to detect a skull fracture seen on CT. None of these cases necessitated neurosurgical intervention.

Table 4: Presence of diffuse axonal injury following minor head injury[a]

Diffuse Axonal Injury	CT		
	Negative	Positive	Total
rMRI			
Negative	91	1	92
Positive	8	1	9
Total	99	2	101

[a] κ measure of agreement, 0.154; $P = .039$; standard error, 0.153; overall percentage agreement, 91%; positive percentage agreement, 50%; negative percentage agreement, 92%.

Table 5: Presence of a skull fracture following minor head injury[a]

Skull Fracture	CT		
	Negative	Positive	Total
rMRI			
Negative	44	12	56
Positive	3	42	45
Total	47	54	101

[a] κ measure of agreement, 0.705; $P < .001$; standard error, 0.069; overall percentage agreement, 85%; positive percentage agreement, 78%; negative percentage agreement, 94%.

DISCUSSION

The results of this study demonstrate that rMRI can detect traumatic injuries with a similar sensitivity and specificity compared with CT in the setting of minor head injuries. This finding was particularly true in the detection of extra-axial hemorrhage and intraparenchymal contusion (Fig 2; extra-axial hemorrhage). In the case of intraparenchymal hemorrhage, only a single patient had a positive finding that was not detected on rMRI. Conversely, however, 12 patients had contusive changes identified on rMRI, which were not seen on CT. This finding may simply be a reflection of the ability of the rMRI sequences to detect the presence of blood with increased sensitivity (Fig 3; left temporal lobe contusion not seen on CT but visualized on follow-up rMRI). We found that the T2 fast-field echo EPI sequence was most useful in appreciating acute blood products due to the susceptibility effects from deoxyhemoglobin. The coronal T2 TSE was also particularly useful for detecting smaller convexity blood products and traumatic brain injury at the inferior frontal lobes.

While it had been previously thought that rMRI would be insensitive for detecting skull fracture,[23] our study did not reflect that supposition. Of the 101 patients, only 12 had a skull fracture found on CT that was not identified on rMRI. However, as with other clinical studies, none of these skull fractures required surgical intervention (Fig 4; fracture, CT and rMRI).[24] The fractures not identified on rMRI typically were nondepressed skull fractures. Although these fractures were not identified on rMRI when the reader was blinded to the initial CT, when they were retrospectively reviewed with the initial head CT, most fractures were identified as in the case shown in Fig 4*F*, -*G*.

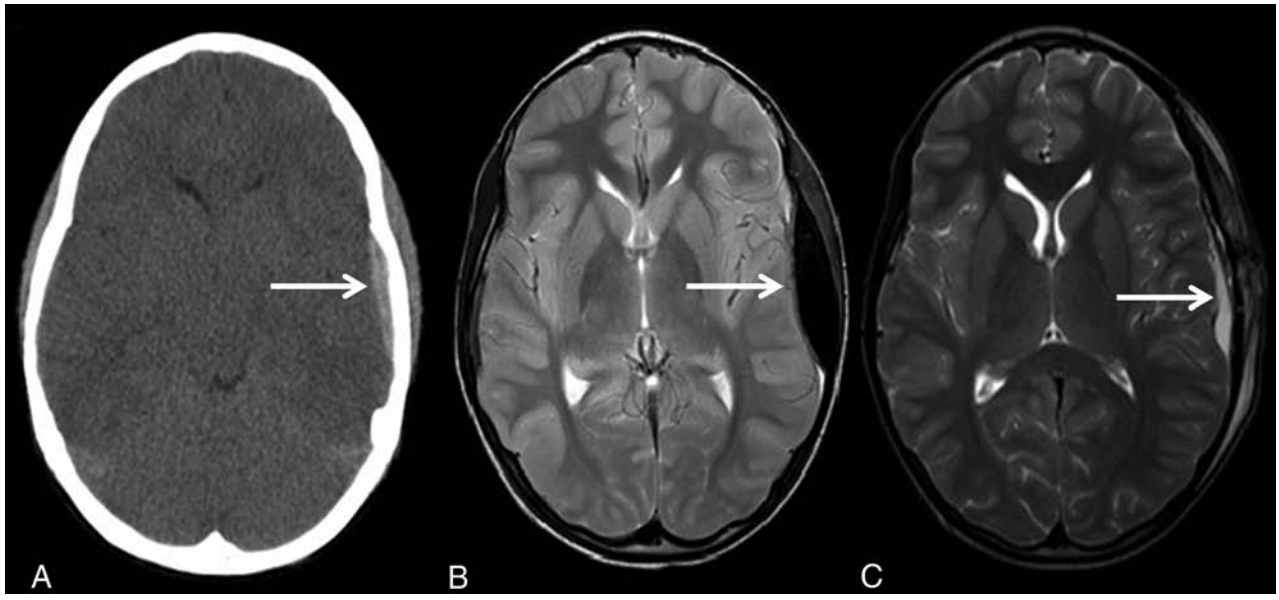

FIG 2. An 8-year-old child who fell from a bike. Initial noncontrast head CT shows a left epidural hemorrhage (*A*). Follow-up rMRI axial T2 TSE shows interval-increased size of the left epidural hemorrhage (*B*). Follow-up rMRI axial T2 TSE shows interval craniotomy and evacuation of the left epidural hemorrhage (*C*).

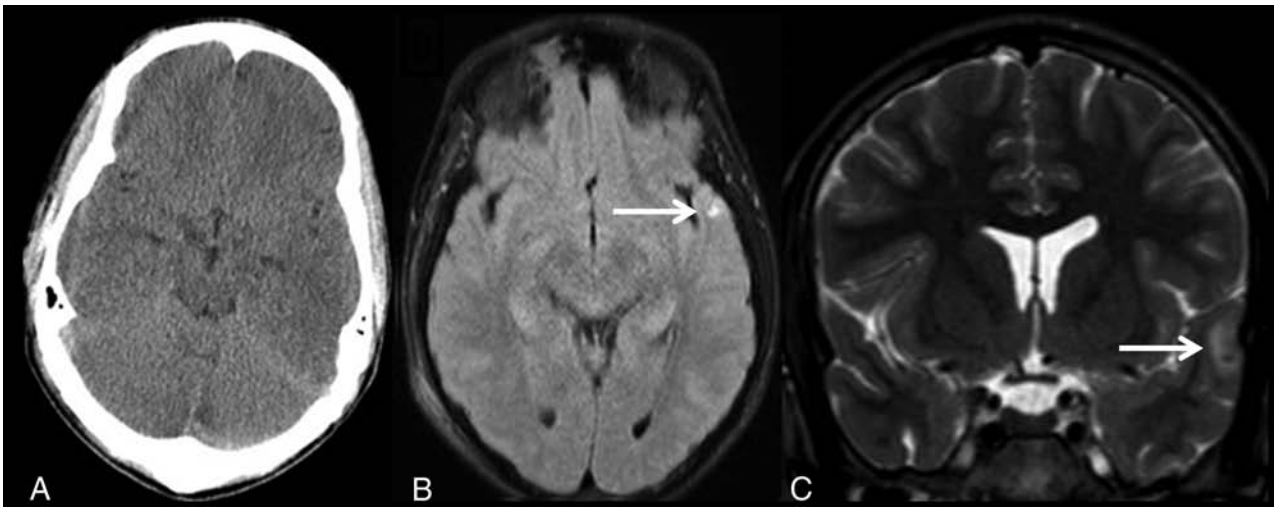

FIG 3. A 16-year-old pedestrian struck by an automobile. Negative noncontrast CT of the head (*A*), axial single-shot FLAIR (*B*), and coronal T2 TSE (*C*) demonstrate a small left temporal lobe contusion.

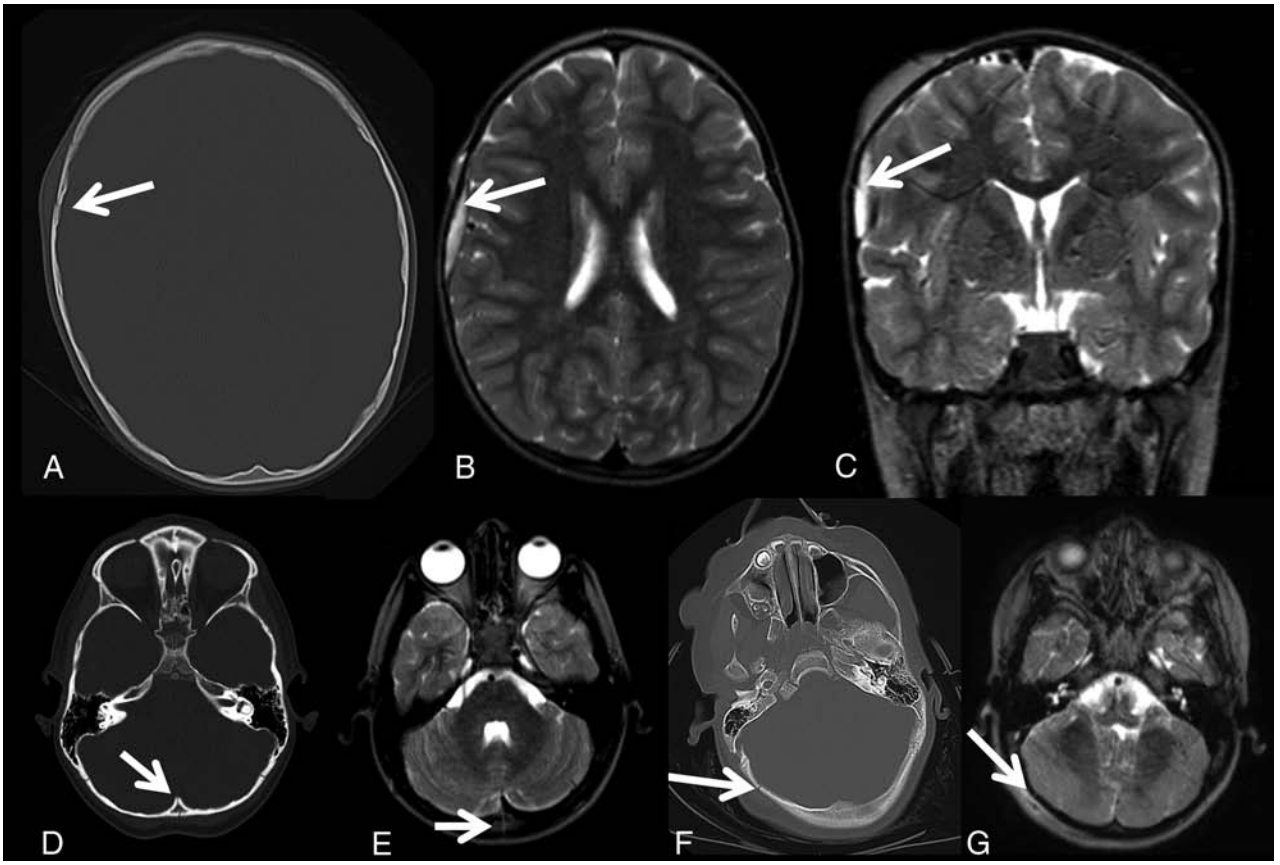

FIG 4. Axial noncontrast head CT (*A*) demonstrates a right frontal bone fracture. On the same patient, a right frontal extra-axial hemorrhage with fracture is present on the axial T2 TSE (*B*) and coronal T2 TSE (*C*). Axial noncontrast head CT (*D*) shows an occipital fracture with a corresponding fracture seen on the axial T2 TSE sequence (*E*). Axial noncontrast head CT (*F*) shows the right occipital fracture. The fracture was not identified prospectively on rMRI; however, it can be identified retrospectively on rMRI (*G*) when read in conjunction with the initial head CT.

In the detection of diffuse axonal injury/shear injuries, there was a very clear difference between rMRI and CT. Although a significant correlation and a high negative percentage agreement were found, there was a comparatively low positive percentage agreement, with 8 cases having a positive rMRI interpretation compared with CT. This finding as in the case of detection of contusive injuries, may simply reflect the higher sensitivity of MR imaging to these injuries, as previously demonstrated in other studies.[25-29] The time delay between initial CT and follow-up rMRI could also result in increased conspicuity of axonal injury due to interval blossoming. Additionally, DWI and FLAIR imaging may be more sensitive for the detection of diffuse axonal in-

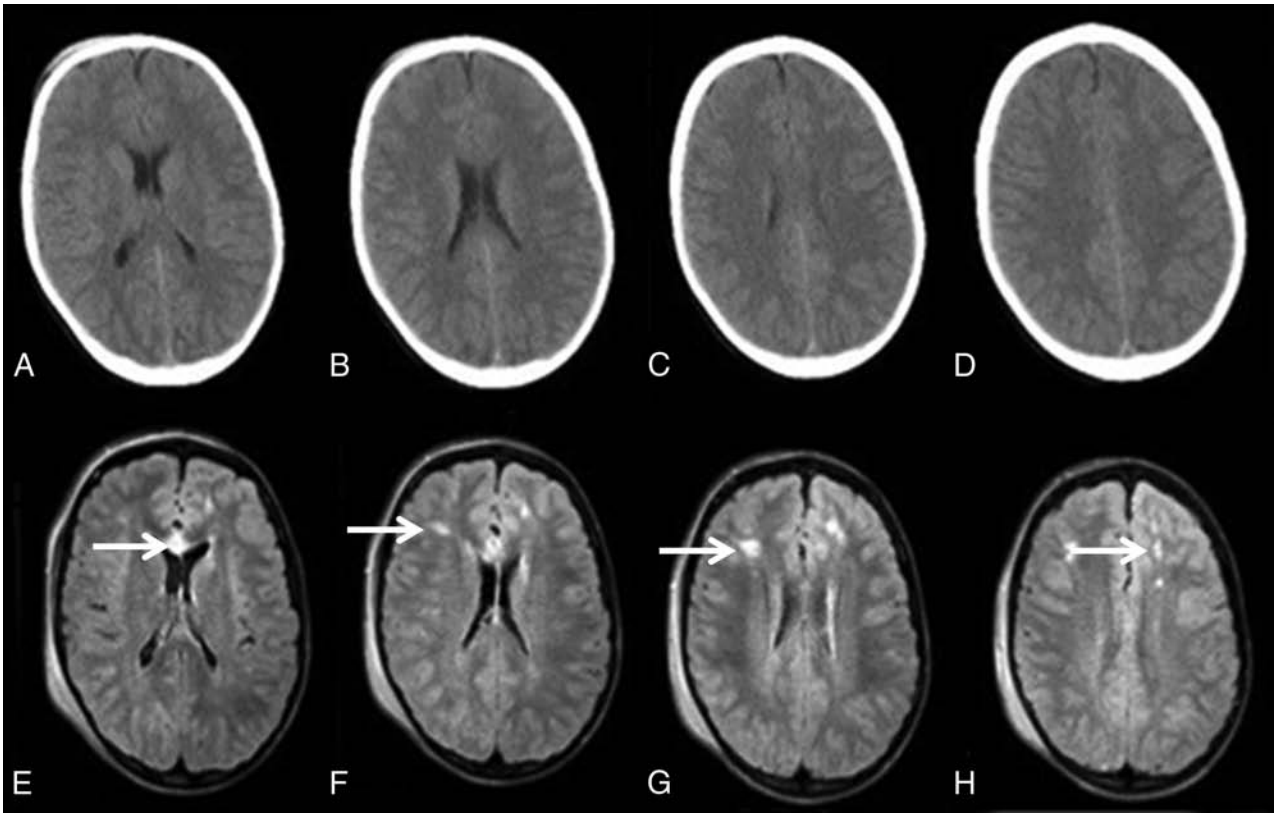

FIG 5. A 15-year-old adolescent involved in an all-terrain vehicle rollover. Axial noncontrast head CT images *(A–D)* demonstrate no abnormal finding. The axial single-shot FLAIR images (*E–H*) demonstrate multiple foci of abnormal signal in the frontal white matter and genu of the corpus callosum, compatible with diffuse axonal injury.

jury and parenchymal contusion compared with CT. An example of the increased sensitivity of FLAIR imaging to detect diffuse axonal injury is demonstrated in the case example shown in Fig 5, in which a pediatric patient with a minor head injury demonstrated multiple FLAIR signal changes not detected on CT (Fig 5; axonal injury, CT and rMRI).

Most reports have focused on the use of rMRI in the evaluation of hydrocephalus; however, other disorders may also be successfully imaged with this technology. CT has increasingly become part of the routine algorithm in the setting of trauma, particularly given its speed of acquisition. In this population, rMRI has been primarily used for follow-up imaging,[21] even though the sensitivity and specificity of rMRI for various findings that influence the medical and surgical management of cranial trauma have yet to be firmly established. Previous studies that have looked at the use of MR imaging in patients with trauma have focused on prognostication[30] and, as such, have included full-sequence studies, often completed several weeks after the injury. A strength of our study is the short duration between the 2 modalities, with an average time between the acquisition of CT and rMRI of 19 hours, with the longest duration <48 hours.

Only one other study has attempted to validate the use of rapid-sequence MR imaging techniques as an alternative to CT in select patients with traumatic brain injury.[23] However, this study was limited to 30 patients, often with worse presenting levels of injury, in whom the authors admit that an MR imaging may have been performed to allow prognostication or to find injuries not seen on CT that could explain the severity of neurologic injury. However, similar to our findings, MR imaging seemed to detect intracranial injuries with similar accuracy compared with CT and had a higher accuracy in detecting diffuse axonal injuries.

No consensus exists on the clinical relevance of focal posttraumatic findings on neuroimaging studies in minor head trauma; most studies have demonstrated a correlation between intracranial hemorrhage on admission head CT with acute and long-term neuropsychiatric deficits.[31-33] The disadvantages of CT, including degradation of image quality due to beam-hardening effects and displacement of the CT signal near metal objects, bone, calcifications, and high concentrations of contrast, limit the accurate assessment of brain injury. Furthermore, CT examinations performed within 3 hours of trauma may not show mature intracranial damage, thus underestimating the extent of injury.[34] Full-sequence MR imaging at both 1.5T and 3T has shown a higher sensitivity for focal, small traumatic intracranial lesions and diffuse axonal injury. More recently, these injuries have been shown to improve outcome prediction following minor head injury.[35] In a similar manner, higher sensitivity to detect these injuries in rMRI studies may allow better outcome prediction.

rMRI brain imaging allows acquisition times around 2–3 minutes, which obviates sedation or anesthesia in the pediatric patient. Motion degradation is of obvious concern when obtaining full-sequence MR imaging: In rMRI sequences in our series, 24 patients had some degree of motion artifacts on their imaging studies, compared with only 7 such cases on CT. However, despite this finding, imaging quality was adequate to reach the high level of percentage agreement seen in our study. The fastest rMRI se-

quence, the single-shot T2 fast-field echo EPI acquired in <5 seconds, is almost never degraded by motion artifacts.

Decreasing the peak voltage and effective milliampere-second settings, using iterative reconstruction algorithms, and limiting the imaging area can reduce the radiation dose of a single CT examination. However, avoiding ionizing radiation altogether in the pediatric population is ideal. Many institutions across the United States have an rMRI protocol in place to image patients with shunted hydrocephalus. However, this technology is likely underused. The lack of emergency access to MR imaging facilities, lack of staffing during nights and weekends, and the inability to obtain reimbursement from third-party payers are some of the common reasons given for its underuse.[20] Despite these obstacles, we have demonstrated that images can be obtained in a timely manner, and no patient had a missed lesion requiring emergency intervention. This finding is similar to that in a previous study in which 64 patients with minor head injury underwent initial evaluation with rMRI and had no clinically significant missed lesion.[21] In our study, approximately 85% of head CTs were performed between 6 AM and 10 PM, when an in-house MR imaging technician is available. Thus, on the basis of this study of validity, a significant dose reduction in ionizing radiation could be achieved.

Our study has limitations. Initial CT scans of many patients were performed at an outside facility, with variable imaging techniques. One of the outside CTs, limited by motion artifacts, had no evidence of hemorrhage; however, hemorrhage was present on the subsequent rMRI performed at our institution. The time interval between imaging modalities may have also allowed evolution and increased conspicuity of contusions and shear injuries and an increased amount of bias. However, compared with other series, the time interval between modalities was significantly shorter.

Although only a history of trauma was provided to the interpreter in our study, the reader could assume that the studies included within the criteria had a high probability of positive findings given that a follow-up rMRI examination was indeed performed. However, for researching the validity of rMRI as an imaging technique, our institutional policy was to image all patients presenting primarily to our institution with minor head injuries with both CT and rMRI regardless of CT findings, assuming the patient met the criteria for imaging. This policy was not necessarily followed for those individuals transferred from regional institutions, who were transferred because of a positive CT finding. The radiologist interpreting the rMRI was blinded to images and the final report of the corresponding initial CT. However, in actual clinical practice, the initial CT scans are used for direct comparison during interpretation of rMRI. The availability of a comparison CT may further improve the diagnostic yield of the rMRI examination in actual clinical workflow.

CONCLUSIONS

rMRI is an adequate imaging technique for the follow-up of pediatric patients with minor head trauma. The use of rMRI could significantly reduce radiation exposure in the pediatric population.

REFERENCES

1. Luerssen TG, Klauber MR, Marshall LF. **Outcome from head injury related to patient's age: a longitudinal prospective study of adult and pediatric head injury.** *J Neurosurg* 1988;68:409–16 CrossRef Medline
2. Rutland-Brown W, Langlois JA, Thomas KE, et al. **Incidence of traumatic brain injury in the United States, 2003.** *J Head Trauma Rehabil* 2006;21:544–48 CrossRef Medline
3. Colvin JD, Thurm C, Pate BM, et al. **Diagnosis and acute management of patients with concussion at children's hospitals.** *Arch Dis Child* 2013;98:934–38 CrossRef Medline
4. Morrison J, Mâsse B, Ouellet P, et al. **Four-film X-ray series is more sensitive than 2-film for diagnosis of skull fractures in children.** *Pediatr Emerg Care* 2013;29:1189–93 CrossRef Medline
5. Af Geijerstam JL, Britton M, Marke LA. **Mild head injury: observation or computed tomography? Economic aspects by literature review and decision analysis.** *Emerg Med J* 2004;21:54–58 CrossRef Medline
6. Stein SC, Burnett MG, Glick HA. **Indications for CT scanning in mild traumatic brain injury: a cost-effectiveness study.** *J Trauma* 2006;61:558–66 CrossRef Medline
7. Sarsfield MJ, Morley EJ, Callahan JM, et al. **Evaluation of emergency medicine discharge instructions in pediatric head injury.** *Pediatr Emerg Care* 2013;29:884–87 CrossRef Medline
8. Schnadower D, Vazquez H, Lee J, et al. **Controversies in the evaluation and management of minor blunt head trauma in children.** *Curr Opin Pediatr* 2007;19:258–64 CrossRef Medline
9. Schutzman SA, Greenes DS. **Pediatric minor head trauma.** *Ann Emerg Med* 2001;37:65–74 CrossRef Medline
10. Toyama Y, Kobayashi T, Nishiyama Y, et al. **CT for acute stage of closed head injury.** *Radiat Med* 2005;23:309–16 Medline
11. Blackwell CD, Gorelick M, Holmes JF, et al. **Pediatric head trauma: changes in use of computed tomography in emergency departments in the United States over time.** *Ann Emerg Med* 2007;49:320–24 CrossRef Medline
12. Klig JE. **Issues of computerized tomography scans in children and implications for emergency care.** *Curr Opin Pediatr* 2006;18:231–33 CrossRef Medline
13. Brenner D, Elliston C, Hall E, et al. **Estimated risks of radiation-induced fatal cancer from pediatric CT.** *AJR Am J Roentgenol* 2001;176:289–96 CrossRef Medline
14. Malviya S, Voepel-Lewis T, Eldevik OP, et al. **Sedation and general anaesthesia in children undergoing MRI and CT: adverse events and outcomes.** *Br J Anaesth* 2000;84:743–48 CrossRef Medline
15. Coté CJ, Karl HW, Notterman DA, et al. **Adverse sedation events in pediatrics: analysis of medications used for sedation.** *Pediatrics* 2000;106:633–44 CrossRef Medline
16. Partovi S, Fram EK, Karis JP. **Fast spin echo MR imaging.** *Neuroimaging Clin N Am* 1999;9:553–76 Medline
17. Ikeda K, Hokuto I, Mori K, et al. **Intrauterine MRI with single-shot fast-spin echo imaging showed different signal intensities in hypoplastic lungs.** *J Perinat Med* 2000;28:151–54 Medline
18. Ashley WW Jr, McKinstry RC, Leonard JR, et al. **Use of rapid-sequence magnetic resonance imaging for evaluation of hydrocephalus in children.** *J Neurosurg* 2005;103(2 suppl):124–30 CrossRef Medline
19. O'Neill BR, Pruthi S, Bains H, et al. **Rapid sequence magnetic resonance imaging in the assessment of children with hydrocephalus.** *World Neurosurg* 2013;80:e307–312 CrossRef Medline
20. Thompson EM, Baird LC, Selden NR. **Results of a North American survey of rapid-sequence MRI utilization to evaluate cerebral ventricles in children.** *J Neurosurg Pediatr* 2014;13:636–40 CrossRef Medline
21. Missios S, Quebada PB, Forero JA, et al. **Quick-brain magnetic resonance imaging for nonhydrocephalus indications.** *J Neurosurg Pediatr* 2008;2:438–44 CrossRef Medline
22. Landis JR, Koch GG. **The measurement of observer agreement for categorical data.** *Biometrics* 1977;33:159–74 CrossRef Medline

23. Roguski M, Morel B, Sweeney M, et al. **Magnetic resonance imaging as an alternative to computed tomography in select patients with traumatic brain injury: a retrospective comparison.** *J Neurosurg Pediatr* 2015;15:529–34 CrossRef Medline
24. Hennelly KE, Mannix R, Nigrovic LE, et al. **Pediatric traumatic brain injury and radiation risks: a clinical decision analysis.** *J Pediatr* 2013;162:392–97 CrossRef Medline
25. Lee H, Wintermark M, Gean AD, et al. **Focal lesions in acute mild traumatic brain injury and neurocognitive outcome: CT versus 3T MRI.** *J Neurotrauma* 2008;25:1049–56 CrossRef Medline
26. Gentry LR, Godersky JC, Thompson B, et al. **Prospective comparative study of intermediate-field MR and CT in the evaluation of closed head trauma.** *AJR Am J Roentgenol* 1988;150:673–82 CrossRef Medline
27. Jenkins A, Teasdale G, Hadley MD, et al. **Brain lesions detected by magnetic resonance imaging in mild and severe head injuries.** *Lancet* 1986;2:445–46 Medline
28. Mittl RL, Grossman RI, Hiehle JF, et al. **Prevalence of MR evidence of diffuse axonal injury in patients with mild head injury and normal head CT findings.** *AJNR Am J Neuroradiol* 1994;15:1583–89 Medline
29. Orrison WW, Gentry LR, Stimac GK, et al. **Blinded comparison of cranial CT and MR in closed head injury evaluation.** *AJNR Am J Neuroradiol* 1994;15:351–56 Medline
30. Yuh EL, Mukherjee P, Lingsma HF, et al; TRACK-TBI Investigators. **Magnetic resonance imaging improves 3-month outcome prediction in mild traumatic brain injury.** *Ann Neurol* 2013;73:224–35 CrossRef Medline
31. Smith-Bindman R, Lipson J, Marcus R, et al. **Radiation dose associated with common computed tomography examinations and the associated lifetime attributable risk of cancer.** *Arch Intern Med* 2009; 169:2078–86 CrossRef Medline
32. Linton OW, Mettler FA Jr; National Council on Radiation Protection and Measurements. **National conference on dose reduction in CT, with an emphasis on pediatric patients.** *AJR Am J Roentgenol* 2003; 181:321–29 CrossRef Medline
33. White KS. **Invited article: helical/spiral CT scanning—a pediatric radiology perspective.** *Pediatr Radiol* 1996;26:5–14 CrossRef Medline
34. Kashluba S, Hanks RA, Casey JE, et al. **Neuropsychologic and functional outcome after complicated mild traumatic brain injury.** *Arch Phys Med Rehabil* 2008;89:904–11 CrossRef Medline
35. Sadowski-Cron C, Schneider J, Senn P, et al. **Patients with mild traumatic brain injury: immediate and long-term outcome compared to intra-cranial injuries on CT scan.** *Brain Inj* 2006;20:1131–37 CrossRef Medline

A New Aneurysm Occlusion Classification after the Impact of Flow Modification

H.S. Cekirge and I. Saatci

ABSTRACT

SUMMARY: A new classification is proposed for cerebral aneurysms treated with any endovascular technique, for example, coiling with or without adjunctive devices, flow diversion, intrasaccular flow modifiers, or any combination of the above. Raymond-Roy Occlusion Classification is expanded with novel subgroups such as class 1 represents complete occlusion and is subdivided if a branch is integrated to, or originated from, the aneurysm sac; class 2 represents neck filling; class 3 represents incomplete occlusion with aneurysm filling as in the previous classification; and class 4 describes the immediate postoperative status after extra- or intrasaccular flow modification treatment. A new concept, "stable remodeling," is included as class 5, which represents filling in the neck region that stays unchanged or reduced, as shown with at least 2 consecutive control angiographies, at least 6 months apart, for not <1 year, or the remodeled appearance of a dilated and/or tortuous vessel in continuation with the parent artery without sac filling.

ABBREVIATION: FM = flow modifier

Although endovascular cerebral aneurysm treatment has already been established,[1,2] there is still controversy in regard to the possibility of not always providing complete occlusion or showing recanalization. However, it has also been shown that only a small group of incomplete occlusions or aneurysm remnants have clinical relevance.[3,4] However, the Cerebral Aneurysm Rerupture After Treatment study[5] reported that the degree of aneurysm occlusion after treatment was strongly associated with risk of rerupture. Aneurysm re-treatment may or may not carry a higher risk than the stable incomplete occlusion or recanalization.[6,7] Unfortunately, the relevant information mostly originates from coiled aneurysms and, therefore, may not be generalized to the entire population of cerebral aneurysms, particularly those aneurysms treated with new devices that modify flow from inside or outside of the aneurysm sac.

Flow modifiers (FMs) (dedicated extrasaccular flow diverters, multiple stent-in-stent applications, and intrasaccular flow disrupters) have been introduced as a new concept for treatment of cerebral aneurysms; FMs cause, over time, curative reconstruction of the aneurysm neck. The reconstruction after extrasaccular FMs (ie, flow diverters) starts immediately after the construct is in place and then evolves over a period of weeks to months.[8] Intrasaccular FMs (ie, flow disrupters) may result in instantaneous occlusion after placement or may require some time for final effect.[9] The delay in aneurysm occlusion with FMs occurs consistently if the flow through the sac continues due to flow demand through a branch coming off or integrated into the sac. Hence, in most cases, the initial result immediately after treatment does not represent the ultimate goal, and reconstruction proceeds after surgery over time.[8,9] Overall, it is evident that evolution of aneurysm management necessitates development of unified terminology to describe both initial and delayed procedural efficacies, regardless of treatment technique.

In the literature, there have been several classifications published to describe the appearance of aneurysm and/or remnant filling. The Raymond-Roy Occlusion Classification, also known as the Montreal scale[10] has been the most widely used, and it classifies the results after aneurysm coiling, which can be applied immediately after the treatment as well as during the follow-up.[10,11] In the literature, there exist some articles about the implications on future management of aneurysm and/or neck remnants that state class 3 aneurysm remnants, according to Raymond-Roy Occlusion Classification, are more likely to be retreated than class 2 neck remnants, which are most often followed up.[12,13]

Received March 9, 2015; accepted after revision June 8.

From the Department of Radiology (H.S.C), Bayindir Hospital, Ankara, Turkey; and Department of Radiology (I.S.), Yüksek Ihtisas University, Koru Hospital, Ankara, Turkey.

Please address correspondence to Isil Saatci, MD, Incek Bulvari Havuzlubag Evleri No: 11, Incek, Golbasi, Ankara, 06830, Turkey; e-mail: isaatci@gmail.com

Indicates open access to non-subscribers at www.ajnr.org

Indicates article with supplemental on-line photo.

http://dx.doi.org/10.3174/ajnr.A4489

Classification of angiographic results after endovascular treatment with any technique

Classification
Class 1: Complete occlusion of the aneurysm sac. When there is a branch integrated with the aneurysm sac, ie, coming off the aneurysm, at any point of the sac, further analysis is carried out with subgroups
1A: Complete occlusion with the full patency of the integrated branch
1B: Complete occlusion with the branch reduced in caliber
1C: Complete occlusion with no antegrade filling of the branch
Class 2: Neck filling
Class 3: Incomplete occlusion with aneurysm filling
Class 4: Aneurysm filling. This class is reserved for an immediate postoperative result based on end-of-treatment DSA; after extra- and/or intrasaccular flow modification treatment
4A: With contrast stagnation—contrast stagnation is referred to when there happens to be any change in the duration of the contrast stay within the aneurysm sac after treatment
4B: Without contrast stagnation
Class 5: Stable remodeling with flow modification. Filling in the neck region, which stays unchanged or reduced; to be included in this group, there have to be at least 2 consecutive control angiographies, by definition, at least 6 months apart, and expanding for a period of not <1 year; exceptionally, 1 control angiography could be sufficient for definition of class 5, only in selected cases of contrast filling the branch coming off the sac, with an appearance of a different vessel course than the original, eg, tortuous or dilated, given that it is in continuation with the parent artery with no sac filling

The introduction of extrasaccular flow diverters created a need for different classifications, not only to describe the initial results but also to anticipate the outcome, including the risk of infrequent but severe complications of postoperative rupture.[14-16] However, these classifications are exclusively for the extrasaccular FMs, and, yet, none has gained common acceptance.

Subsequently, with the use of intrasaccular FMs, the control angiographic findings become even more controversial. Lubicz et al[17] described 4 patterns in the follow-up of intrasaccular FM treatment, namely, complete occlusion, filling of the proximal recess of the device, neck remnant, and aneurysm remnant. Based on their follow-up experience, the investigators suggested a different definition, that is, "adequate occlusion," which includes the first 3 patterns.

So far in the literature, none of the classifications address the entire spectrum of current endovascular aneurysm treatment, irrespective to treatment technique. To solve this problem of ambiguity and to exclude the need for the use of different classifications for different modalities, we propose a new classification system, by expanding on the widely used Raymond-Roy Occlusion Classification scale, that describes results with current and evolving treatment techniques.

MATERIALS AND METHODS

The proposed classification is presented in the Table, and the schematic drawing (Fig 1) highlights the newly added class 1 A, B, and C as well as class 5 in different case settings. Class 1 calls for complete occlusion of an aneurysm when a branch is not directly involved, and the subgroups of class 1—A, B, C—are to be used when a branch is originating directly from a sidewall aneurysm (Figs 2 and 3) or filling from a bifurcation aneurysm (Fig 4). To assign class 5 (Figs 4*B* and 5–7; On-line Figs 1 and 2), at least 2 angiographic controls, at least 6 months apart, and expanding for a period of not <1 year are required to demonstrate the stability. DSA is the criterion standard at the moment, although CTA may serve the purpose for the aneurysms treated with FMs. However, with the evolving technology, noninvasive angiographic imaging may replace this in the future. The remodeling concept[18] was first defined in a more restricted concept that referred to 1 as "infundibulum like" enlargement of the branch coming off the aneurysm sac after the shrinkage of the aneurysm after flow diverter treatment (Fig 5) and 2, as a tortuous course of the branch (which is coming off the aneurysm sac) at its proximal segment after flow diverter treatment of the sac and the sac not filling (Figs 4 and 7).[19] These 2 situations, in which the branch that originates from

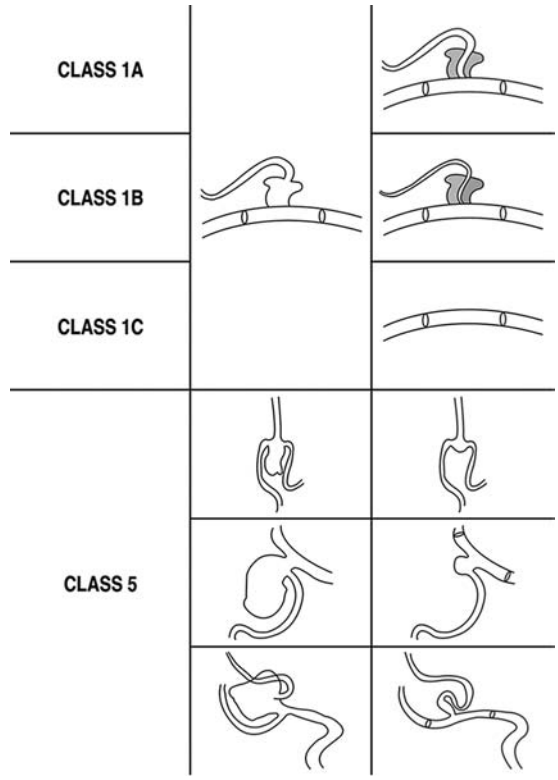

FIG 1. Schematic drawing of class 1 subgroups and class 5 in different case settings. The last column shows the control angiographic appearance. The first example of class 5 represents the control result after intrasaccular FM placement, given that the control appearance remains unchanged, as required. The second and third examples of class 5 represent the remodeling after extrasaccular flow diverter treatment.

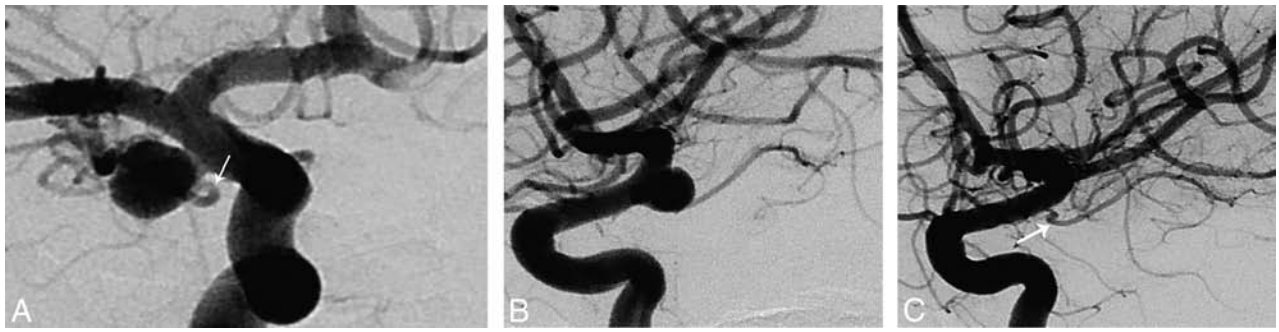

FIG 2. Class 1A. *A* and *B*, Preoperative images show the ICA aneurysm in which the anterior choroidal artery (*arrow*) is originating from the aneurysm at the neck. *C*, Six-month control angiography after single Pipeline device (Covidien, Irvine, California) placement demonstrates total occlusion of the aneurysm with the anterior choroidal artery preserved (*arrow*). Reprinted from Saatci et al.[18]

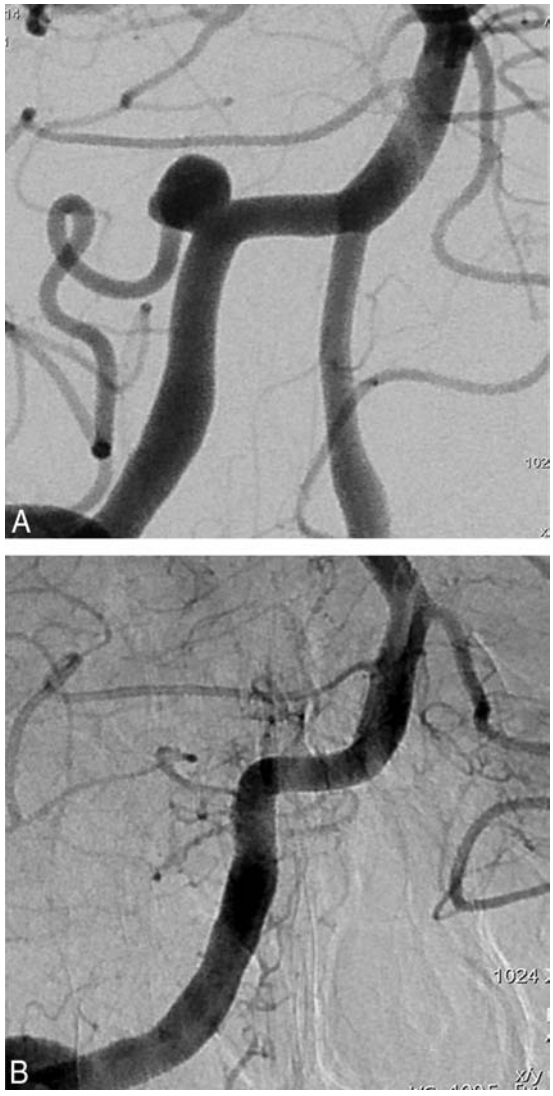

FIG 3. Class 1C. *A*, Preoperative angiography shows right vertebral artery aneurysm with the posterior inferior cerebellar artery originating from the sac. *B*, Single Pipeline device was placed, and a 6-month control angiography demonstrates complete occlusion of the aneurysm sac, along with the posterior inferior cerebellar artery. The patient was asymptomatic.

the aneurysm sac is in continuation with the parent artery with no filling of the sac any more, are the only exceptions for which we do not require a second angiography to grade as class 5 occlusion (On-line Fig 1 for class 5 after intrasaccular FM). In the other situations, remodeling is called for after confirmation of the stability (as described above) when 3, the bifurcation appears enlarged after the intrasaccular FM obliterates the sac, which stays stable in the controls (Fig 6), and 4, when there is an unchanged focal bulging at the neck region (On-line Fig 2). Therefore, in such cases, the first control result would be classified as class 2 (neck remnant) by definition; then, after confirmation of stability, it can be changed to class 5 (Fig 6 and On-line Fig 2).

DISCUSSION

The healing process or so-called reconstruction of the vessel wall at the aneurysm neck after FM and/or flow diverter treatment is different from that after endosaccular coiling,[18,20-22] and aneurysms may behave differently when treated with flow modification treatments versus endosaccular coiling.[23,24] Therefore, the previous classifications, particularly Raymond-Roy Occlusion Classification, described for coiled aneurysms could not address the results of flow modification treatments. Several new classifications[14,17] have been introduced. In these previous classifications for extrasaccular flow diverter treatment, flow stagnation is defined as a determining feature.[14-16] However, the flow stagnation does not necessarily have a direct implication regarding the future or final treatment result. That is, flow stagnation within the aneurysm may or may not result in total occlusion of the aneurysm sac. On the contrary, an aneurysm that shows no or little, if any, postoperative contrast stagnation may end up in complete occlusion in the follow-up. Yet, the presumed importance of the contrast stagnation is whether or not it has any predictive value in regard to postoperative rupture of the index (treated) aneurysm. This is a controversial issue, with no proven data to date. Our classification system does not emphasize the degree of contrast filling (eg, the pattern, timing) immediately after the FM treatment, not only for these reasons but also because it may be relatively subjective or may vary in regard to technical parameters, such as contrast injection power, acquisition parameters, and so forth. Contrast stagnation is referred to in the immediate postoperative DSA findings (class 4) after FM treatment to differentiate that grade from the aneurysm filling after aneurysm packing (class 3).

In some grading scales previously described exclusively for use after flow diverter treatment,[15,16] parent artery size is taken into

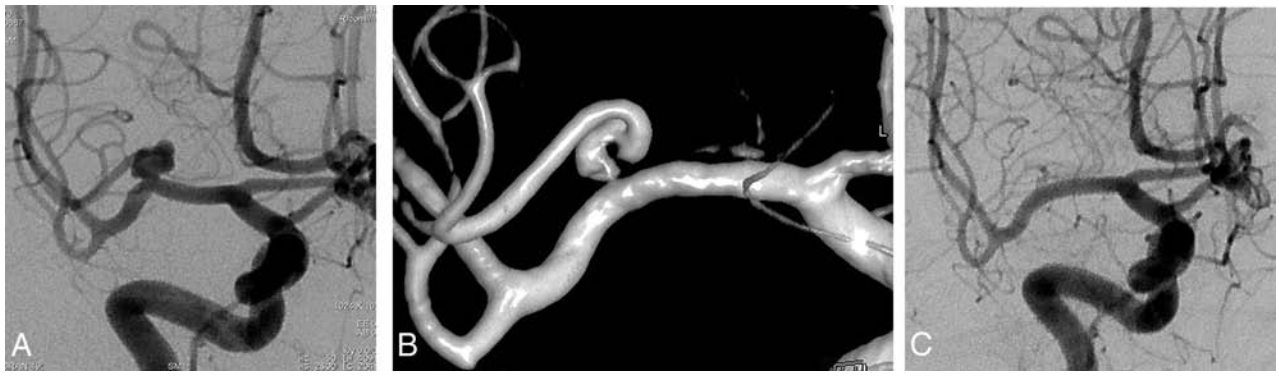

FIG 4. Class 5 evolving into class 1B eventually. *A*, Preoperative angiography shows right MCA aneurysm with a branch coming off from the sac. *B*, A 3D image from a 6-month control angiography after treatment with single Pipeline device shows remodeling of the flow with a tortuous appearance of the branch proximally at its direct continuation with the parent artery, and no sac filling. This appearance is referred to as class 5. *C*, An 18-month control angiography shows complete occlusion of the aneurysm with the originating branch in reduced caliber, that is, class 1B. Reprinted from Yavuz et al.[19]

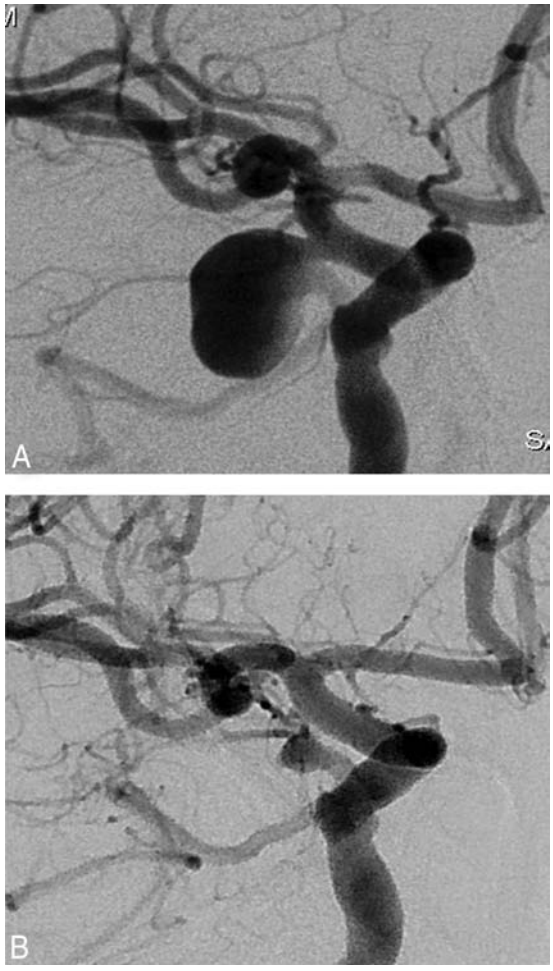

FIG 5. Class 5. *A*, Right internal carotid angiogram shows a posterior communicating artery aneurysm (the ipsilateral P1 is aplastic, not shown). *B*, A 2-year angiography after a single Pipeline device placement shows that the aneurysm sac is not filling and the origin of the posterior communicating artery is remodeled. Reprinted from Saatci et al.[18]

consideration. Parent artery occlusion may occur, at least in some cases, related to the inefficiency of antiaggregating medication, but, the rate of in-stent stenosis is reported to be not any higher than that of conventional stents[18,22] and in-stent stenosis is not a part of this classification.

The patency of the branch that originates from, or is integrated to, the aneurysm is assessed in this classification, which has not been included in previous classifications. The flow demand through the relevant branch is important in its patency after the treatment.[18-20] Although the aneurysm is getting occluded, the branch originating from the aneurysm may remain the same, reduce in caliber, or may not be filling antegrade. This classification can apply to the results of flow diverter treatment not only in sidewall aneurysms but also in bifurcation aneurysms[19]; the series of exclusive MCA bifurcation aneurysms treated with flow diverter placement demonstrated 84% of class 1 occlusions with a variety of occlusion patterns, including branch occlusion in 12%. Another 8% showed class 5 occlusion. In addition, transition between classes is also possible (Fig 4) in the group of aneurysms with integrated branches, whether located at the side wall or the bifurcation.

This classification is also well grounded for the intrasaccular FM treatments in that it takes not only the involving branches into consideration but also the interval change in regard to stability. With these features, this classification is differentiated from the classification for intrasaccular FMs previously described.[17]

Another advantage of this proposed classification is that it can be applied by single angiographic images, in several planes, and does not necessitate seeing the entire series of the angiographic run to evaluate the flow pattern within the aneurysm. Therefore, objective findings on the angiographic image are enough for classification, with no further subjective interpretation. However, rotational angiography may be a requisite, particularly in the definition of class 5 in some cases.

CONCLUSIONS

With preventing rupture as the ultimate goal of cerebral aneurysm treatment, if the treatment serves this purpose and the aneurysm is secured, then the treatment can be called "successful" and the angiographic appearance of the vascular reconstruction can be considered irrelevant. Long-term stability of remodeling is to be determined and not free of concern until that time. How-

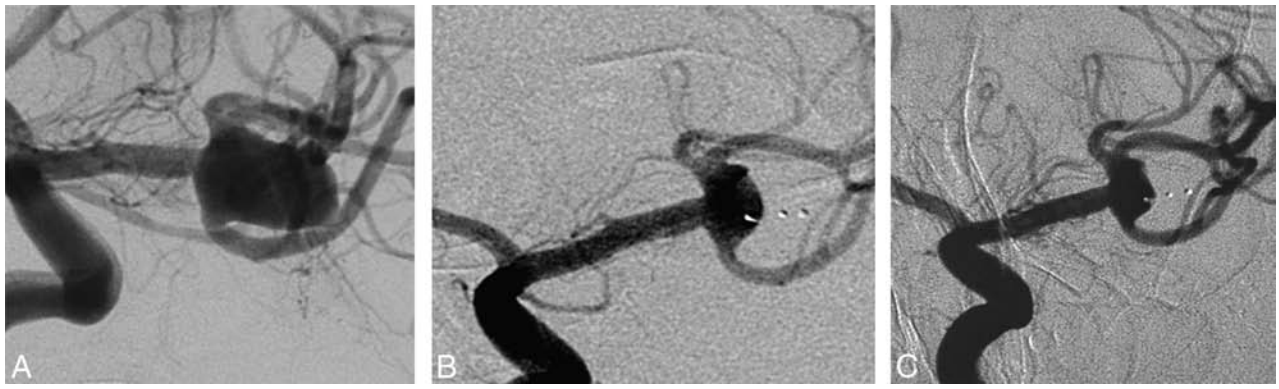

FIG 6. Class 5. *A*, Preoperative angiography shows a large left MCA aneurysm at the trifurcation, with the branches incorporated in the sac. *B*, Six months after the treatment with a WEB device (Sequent Medical, Aliso Viejo, California), control angiography shows neck filling at the trifurcation, with the branches patent, and this result is classified as class 2. *C*, An 18-month control angiography shows an unchanged appearance of the MCA trifurcation, and this result is classified as class 5, with the apparently "stable" remodeling.

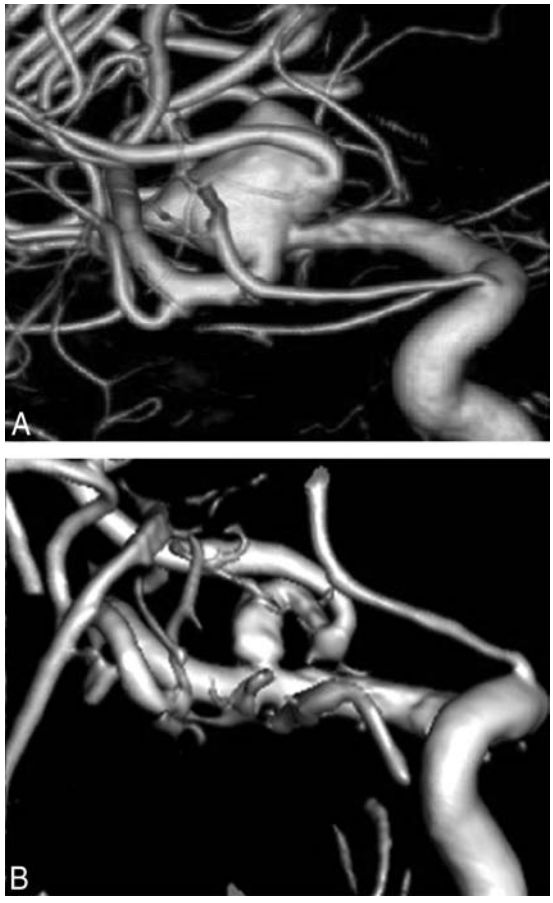

FIG 7. Class 5. *A*, Preoperative angiography shows a large, irregular shaped, right MCA bifurcation aneurysm with both bifurcation branches coming off the sac. A Pipeline device was placed, extending from the inferior trunk to the M1 in addition to a WEB device within the sac. *B*, A 6-month control angiography shows a patent inferior trunk, a tortuous origin of the superior trunk, no sac filling; this result is referred to as class 5.

ever, in complex aneurysms where "perfect" anatomic results may not be possible or at least have increased risks, then, "remodeling" may be acceptable, given that it is stable. This classification not only addresses the new concept of remodeling that emerged after the use of extra- and intrasaccular flow modifications but also covers the entire spectrum of result possibilities with any current technique.

We acknowledge that this classification should be validated in regard to the interobserver agreement to test its reproducibility. In addition, we also plan to extract a random sample of credible size among our entire aneurysm population to review the stability in long-term follow-up (eg, 5 years) to investigate the outcome of "designated" classes. This classification may then be ready to establish a clinical algorithm for follow-up, including the risk of bleeding after endovascular treatment.

Disclosures: H. Saruhan Cekirge—*UNRELATED*: *Consultancy*: Covidien/Medtronic, MicroVention, Sequent. Isil Saatci—*UNRELATED*: *Consultancy*: Covidien, Medtronic.

REFERENCES

1. Molyneux A, Kerr R, Stratton I, et al; International Subarachnoid Aneurysm Trial (ISAT) Collaborative Group. **International Subarachnoid Aneurysm Trial (ISAT) of neurosurgical clipping versus endovascular coiling in 2143 patients with ruptured intracranial aneurysms: a randomised trial.** *Lancet* 2002;360:1267–74 CrossRef Medline
2. McDougall CG, Spetzler RF, Zabramski JM, et al. **The Barrow Ruptured Aneurysm Trial.** *J Neurosurg* 2012;116:135–44 CrossRef Medline
3. Campi A, Ramzi N, Molyneux AJ, et al. **Retreatment of ruptured cerebral aneurysms in patients randomized by coiling or clipping in the International Subarachnoid Aneurysm Trial (ISAT).** *Stroke* 2007;38:1538–44 CrossRef Medline
4. Molyneux AJ, Birks J, Clarke A, et al. **The durability of endovascular coiling versus neurosurgical clipping of ruptured cerebral aneurysms: 18 year follow-up of the UK cohort of the International Subarachnoid Aneurysm Trial (ISAT).** *Lancet* 2015;385:691–97 CrossRef Medline
5. Johnston SC, Dowd CF, Higashida RT, et al; CARAT Investigators. **Predictors of rehemorrhage after treatment of ruptured intracranial aneurysms: the Cerebral Aneurysm Rerupture After Treatment (CARAT) study.** *Stroke* 2008;39:120–25 CrossRef Medline
6. Molyneux AJ, Kerr RS, Birks J, et al; ISAT Collaborators. **Risk of recurrent subarachnoid haemorrhage, death, or dependence and standardised mortality ratios after clipping or coiling of an intracranial aneurysm in the International Subarachnoid Aneurysm Trial (ISAT): long-term follow-up.** *Lancet Neurol* 2009;8:427–33 CrossRef Medline
7. Crobeddu E, Lanzino G, Kallmes DF, et al. **Review of 2 decades of aneurysm-recurrence literature, part 2: managing recurrence after**

endovascular coiling. *AJNR Am J Neuroradiol* 2013;34:481–85 CrossRef Medline
8. Fiorella D, Lylyk P, Szikora I, et al. **Curative cerebrovascular reconstruction with the Pipeline embolization device: the emergence of definitive endovascular therapy for intracranial aneurysms.** *J Neurointerv Surg* 2009;1:56–65 CrossRef Medline
9. Ding YH, Lewis DA, Kadirvel R, et al. **The Woven EndoBridge: a new aneurysm occlusion device.** *AJNR Am J Neuroradiol* 2011;32:607–11 CrossRef Medline
10. Roy D, Milot G, Raymond J. **Endovascular treatment of unruptured aneurysms.** *Stroke* 2001;32:1998–2004 CrossRef Medline
11. Raymond J, Guilbert F, Weill A, et al. **Long-term angiographic recurrences after selective endovascular treatment of aneurysms with detachable coils.** *Stroke* 2003;34:1398–403 CrossRef Medline
12. Mascitelli JR, Moyle H, Oermann EK, et al. **An update to the Raymond-Roy Occlusion Classification of intracranial aneurysms treated with coil embolization.** *J Neurointerv Surg* 2015;7:496–502 CrossRef Medline
13. Mascitelli JR, Oermann EK, De Leacy RA, et al. **Angiographic outcome of intracranial aneurysms with neck remnant following coil embolization.** *J Neurointerv Surg* 2015;7:484–89 CrossRef Medline
14. O'Kelly CJ, Krings T, Fiorella D, et al. **A novel grading scale for the angiographic assessment of intracranial aneurysms treated using flow diverting stents.** *Interv Neuroradiol* 2010;16:133–37 CrossRef Medline
15. Kamran M, Yarnold J, Grunwald IQ, et al. **Assessment of angiographic outcomes after flow diversion treatment of intracranial aneurysms: a new grading schema.** *Neuroradiology* 2011;53:501–08 CrossRef Medline
16. Grunwald IQ, Kamran M, Corkill RA, et al. **Simple measurement of aneurysm residual after treatment: the SMART scale for evaluation of intracranial aneurysms treated with flow diverters.** *Acta Neurochir (Wien)* 2012;154:21–26; discussion 26 CrossRef Medline
17. Lubicz B, Klisch J, Gauvrit JY, et al. **WEB-DL endovascular treatment of wide-neck bifurcation aneurysms: short- and midterm results in a European study.** *AJNR Am J Neuroradiol* 2014;35:432–38 CrossRef Medline
18. Saatci I, Yavuz K, Ozer C, et al. **Treatment of intracranial aneurysms using the Pipeline flow-diverter embolization device: a single-center experience with long-term follow-up results.** *AJNR Am J Neuroradiol* 2012;33:1436–46 CrossRef Medline
19. Yavuz K, Geyik S, Saatci I, et al. **Endovascular treatment of middle cerebral artery aneurysms with flow modification with the use of the Pipeline embolization device.** *AJNR Am J Neuroradiol* 2014;35:529–35 CrossRef Medline
20. Dai D, Ding YH, Kadirvel R, et al. **Patency of branches after coverage with multiple telescoping flow-diverter devices: an in vivo study in rabbits.** *AJNR Am J Neuroradiol* 2012;33:171–74 CrossRef Medline
21. Pierot L, Liebig T, Sychra V, et al. **Intrasaccular flow-disruption treatment of intracranial aneurysms: preliminary results of a multicenter clinical study.** *AJNR Am J Neuroradiol* 2012;33:1232–38 CrossRef Medline
22. Becske T, Kallmes DF, Saatci I, et al. **Pipeline for uncoilable or failed aneurysms: results from a multicenter clinical trial.** *Radiology* 2013;267:858–68 CrossRef Medline
23. Kadirvel R, Ding YH, Dai D, et al. **Cellular mechanisms of aneurysm occlusion after treatment with a flow diverter.** *Radiology* 2014;270:394–99 CrossRef Medline
24. Dai D, Ding YH, Rezek I, et al. **Characterizing patterns of endothelialization following coil embolization: a whole-mount, dual immunostaining approach.** *J Neurointerv Surg* 2015 Feb 2. [Epub ahead of print] CrossRef Medline

Social Media and Scientific Meetings: An Analysis of Twitter Use at the Annual Meeting of the American Society of Neuroradiology

A. Radmanesh and A.L. Kotsenas

Given the enormous potential and easy access by using mobile devices, social media are being increasingly used during radiology and other medical specialty meetings (Figure).[1-5] Social media use during scientific meetings allows attendees to post commentaries on sessions, questions about conference logistics, calls for casual meetings ("tweet-ups"), or even tips for a good dinner. It also allows meeting organizers to make announcements and nonattendees to participate in the conference virtually.

Twitter users can embed metadata "tags" in their posts to make them searchable by using hashtags, a word or acronym preceded by the # character. Given the 140-character limit for each tweet, brief or abbreviated hashtags are usually favored. Many specialty meeting organizers now publish a meeting-specific hashtag such as #ASNR14 used at the 52nd annual meeting of the American Society of Neuroradiology (ASNR).

In many professional meetings currently, hallways and foyers are equipped with large screens displaying all meeting-related tweets posted from inside or outside the venue. These make it easy for attendees to have a glance at the latest posts during scheduled breaks or as they walk from one session to another. In large meetings where many tweets are posted, each session may be assigned a specific hashtag so that people can follow the streams related to their session of interest and post questions to presenters and moderators. Users can also "reply" to others' posts to start a conversation on the topic. People who share interests can "follow" each other's posts, arrange to meet in person, and stay in touch even after the conference is over. Sometimes, these professional connections last for years.

Recognizing the current pattern of social media use in our subspecialty society can guide planning for future societal meetings to take advantage of the existing potentials. In this article, we will analyze Twitter use during the 2014 annual meeting of the American Society of Neuroradiology (May 17–22, 2014, Montréal, Quebec, Canada).

From the Department of Radiology and Biomedical Imaging (A.R.), University of California, San Francisco, San Francisco, California; and Department of Radiology (A.L.K.), Mayo Clinic, Rochester, Minnesota.

Please address correspondence to Alireza Radmanesh, MD, Neuroradiology Section, UCSF, 505 Parnassus Ave, L-352, San Francisco, CA 94143; e-mail: Alireza.Radmanesh@ucsf.edu; @AliRadmanMD

http://dx.doi.org/10.3174/ajnr.A4168

We reviewed all Twitter posts (Twitter.com, San Francisco, California) that included the meeting hashtag #ASNR14 and were posted from May 7, 2014 (the date the hashtag was registered with Symplur) to May 22, 2014 (midnight following the final day of the conference). The transcripts of the tweets were obtained from Symplur (Symplur, Upland, California; Symplur.com), a health care social media analytics organization.

The number of participants (microbloggers) and the number of tweets posted by each were recorded. On the basis of the information on Twitter account profiles, the microbloggers were categorized into radiologists, nonradiologist physicians/postdoctoral researchers, radiology technologists, nurses, vendors, social media professionals, journals, imaging societies, and the host city. The content of each tweet was categorized into commentary on meeting sessions, questions directed to presenters/moderators, meeting-related announcements, questions about meeting logistics, commentary about the use of social media for health care/meeting-related purposes, arranging tweet-ups, status updates, journal promotions, vendor marketing promotions, and not otherwise categorized. We analyzed the original tweets and those that were reposted by other users as "retweets" or "favorites." For our analysis, retweets and favorites were grouped together. The language in which tweets were posted was also recorded. Analysis was performed by using the statistical tools of Excel (Microsoft, Redmond, Washington).

Fifty-four microbloggers posted 410 tweets with the #ASNR14 hashtag during May 7–22, 2014. The breakdown of the microbloggers can be seen in Table 1. Of 410 total tweets, 238 tweets (68%) were original posts, and the rest were retweets or favorites. The posted tweets resulted in 415,102 total views or impressions. Nine tweets (2.2%) were posted in Spanish. A few posts contained phrases in French, the official language of the host city, but none were posted predominantly using that language. The remainder of the tweets were posted in English.

A mean of 8 tweets per participant was generated (range, 1–119; SD, 19; median, 2). The top 3 tweeters, all neuroradiologists, generated 223 (54.4% of all) tweets.

The most common tweet content was related to commentary on sessions, which encompassed 202 (49% of all) tweets. Social tweets, including those related to the use of social media, arranging tweet-ups, and participant status updates accounted for 176

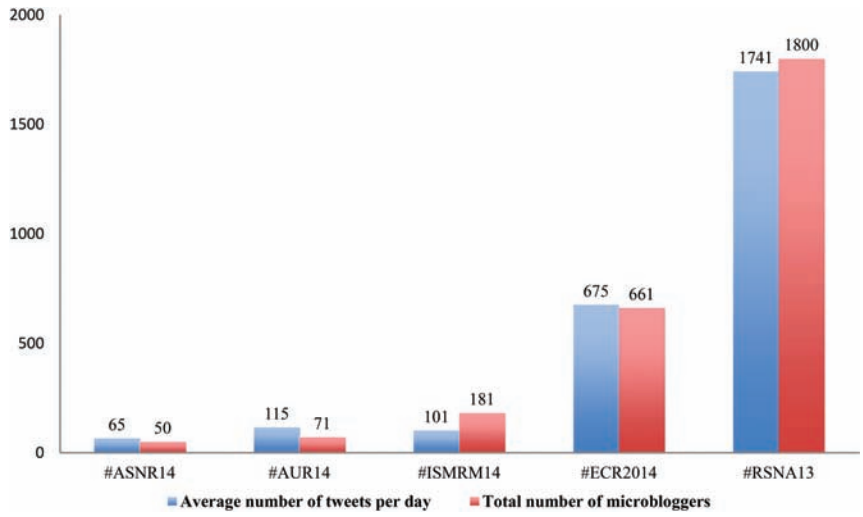

FIG. Average number of tweets per day and total number of microbloggers for the duration of conferences at some most recent societal conferences in radiology. The difference in the number of tweets or microbloggers among different radiology societal meetings is at least in part related to the difference in the number of attendees. Of note, some of the tweets related to each meeting were posted by microbloggers who were not attending the venue. ASNR14 indicates American Society of Neuroradiology, May 17–22, 2014, Montréal, Quebec, Canada; AUR14, Association of University Radiologists, April 1–4, 2014, Baltimore, Maryland; ISMRM14, International Society for Magnetic Resonance in Medicine, May 10–16, 2014, Milan, Italy; ECR2014, European Congress of Radiology, March 6–10, 2014, Vienna, Austria; RSNA13, Radiological Society of North America, November 30–December 5, 2013, Chicago, Illinois. Data were obtained from Symplur.com.

Table 1: Analysis of microbloggers posting tweets with #ASNR14 hashtag during May 7–22, 2014

Microblogger Category	No. (% of All Microbloggers)
Radiologist	20 (37.0%)
Vendors	11 (20.1%)
Radiology/imaging departments	7 (13%)
Other physicians/postdoctoral researchers	5 (9.3%)
Social media professionals	4 (7.4%)
Radiology journals	3 (5.6%)
Technologists	1 (1.9%)
Nurses	1 (1.9%)
Host city	1 (1.9%)
Unidentifiable	1 (1.9%)
Total	54

Table 2: Analysis of content for tweets with #ASNR14 hashtag posted during May 7–22, 2014

Content Category	Total No. (% of Total Tweets)	Original Posts (% of Total Original Tweets)	Reposts (% of Original Posts in That Category)
Commentary on sessions	202 (49%)	124 (60.5%)	78 (38.6%)
Social posts	176 (42.9%)	92 (44%)	84 (47.7%)
Use of social media	76 (18.5%)	33 (16.1%)	43 (56.6%)
Tweet-up arrangement	61 (14.8%)	33 (16.1%)	28 (45.9%)
Participant status update	39 (9.5%)	26 (12.7%)	13 (33.3%)
Journal promotion	10 (2,4%)	5 (2,4%)	5 (50%)
Vendor marketing	9 (2.2%)	8 (3.9%)	1 (11.1%)
Meeting announcement	6 (1.5%)	3 (1.5%)	3 (50%)
Meeting logistics	1 (<1%)	1 (<1%)	0
Others	6 (1.5%)	5 (2.4%)	1 (16.7%)
Total	410 (100%)	238 (58%)	172 (42%)

(42.9% of all) tweets. See Table 2 for a complete breakdown of tweet content. No questions were posted to the presenters or moderators.

The session that generated the greatest number of tweets was "The Foundation of the ASNR Special Session on Traumatic Brain Injury: Is DTI Ready for Prime Time?" (44 tweets accounting for 21.8% of the tweets related to session content) followed by Dr Stanely Prusiner's keynote address "A Unifying Role for Prions in Neurodegenerative Diseases" (13 tweets accounting for 6.4% of the tweets related to session content).

Social tweets were most likely to be retweeted (84 of 176 tweets in that category, 47.7%), followed by tweets related to session content (78 of 202 tweets in that category, 49.2%). Vendor marketing tweets were least likely to be retweeted (1 of 9 tweets, 11.1%).

Our analysis shows that Twitter use by radiologists at the annual meeting of the ASNR is still in its infancy. Given that there were only 20 radiologist microbloggers using the hashtag #ASNR14, it is clear that the neuroradiology community has not yet fully embraced the use of social media for this purpose. This lack of participation likely contributes to the paucity of content related to meeting logistics and questions directed to meeting organizers. This scenario may be because of insufficient knowledge of the potentials for professional use of social media at medical conferences and scientific meetings. Although the @ASNRStaff Twitter handle has indeed been inactive, organizers of the ASNR meeting have attempted to promote Twitter use at each of the prior two meetings by building a Twitter feature into the meeting Guidebook mobile application.

To our knowledge, our analysis is the first to look at specific meeting-related tweet content for a radiology meeting. Most of the posts at the annual meeting were related to session content. Of particular interest was the debate session on the use of diffusion tensor imaging for traumatic brain injury, which prompted comments by many postdoctoral researchers and members of the neuroimaging community who virtually participated in the discussion. Not surprisingly, this was followed by social content relating to the use of social media for meeting-related purposes, planning tweet-ups with other users, and alerting followers to the current "status" of the user or his or her presence at the meeting. Vendor marketing content made up a distinct minority of posts and was least likely to be retweeted or marked as favorite by microbloggers.

Although some have argued that live-tweeting lectures is a form of "neoliberalism" and is more an attempt at personal branding than at scholarship,[6] "live-tweeting encouraged" has become the default mode for many scientific meetings. Presenters are encouraged to share their Twitter handles with the audience during opening remarks so that the handle can be used to quote, paraphrase, or discuss the work. Some meeting organizers have established optional inclusion of Twitter handles on attendee identification badges.

Social media channels open up convention floors to members and scholars from around the world who have been unable to physically attend, while rendering attendees' academic accomplishments more visible to the public.[7] In a study of social media participation at an international emergency medicine conference, more than 60% of individuals posting tweets were not physically present at the meeting.[3] During the 2014 ASNR meeting, approximately 50% of radiologists posting with the #ASNR14 hashtag attended the meeting virtually.[8]

Some attendees have found live-tweeting to be a great way to take notes and remain focused on what is being presented,[9] while others may find it a source of distraction. As more and more conferences adopt a parallel-session format, social media users can virtually attend more than one session at the same time by reading the posts from other sessions, either as they come in or—if distraction is a concern—later by searching the posts or reviewing a transcript created by an enabler such as Symplur.

During the 2014 meeting of the International Society for Magnetic Resonance in Medicine (#ISMRM14), audience members were given the opportunity to pose their questions to the presenters and moderators by using session-specific hashtags, and moderators were instructed to monitor the session-specific feeds for questions and comments (C.P. Hess, MD, PhD, personal e-mail communication, July 18, 2014). This option can be explored at future ASNR meetings.

Social media platforms are considered public domains. Some presenters or panelists may feel uncomfortable about having their findings mentioned on social media before having them published as a journal article. In such cases, presenters or panelists are strongly encouraged to make an announcement to that effect to the audience at the beginning of the presentation. In the near future, organizers of scientific meetings may ask presenters to reveal their wishes in regard to social media coverage at the time of submission or final acceptance of their abstracts, similar to the existing policy in regard to photography during poster sessions. It is considered professional etiquette to respect the presenter's wishes on data sharing.

In summary, tweeting during scientific meetings promotes discussion on topics of interest among those who attend either in person or virtually. It provides a way to find out about upcoming or ongoing popular sessions and helps expand professional networks through connecting with people whom we otherwise might not meet.

REFERENCES

1. Hawkins CM, Duszak R, Rawson JV. **Social media in radiology: early trends in Twitter microblogging at radiology's largest international meeting.** *J Am Coll Radiol* 2014;11:387–90
2. Wilkinson SE, Basto MY, Perovic G, et al. **The social media revolution is changing the conference experience: analytics and trends from eight international meetings.** *BJU Int* 2015;115:839–46
3. Neill A, Cronin JJ, Brannigan D, et al. **The impact of social media on a major international emergency medicine conference.** *Emerg Med J* 2014;31:401–04
4. Logghe H, Maa J, Schwartz J. **Twitter usage at Clinical Congress rises markedly over two years.** *Bull Am Coll Surg* 2013;98:22–24
5. McKendrick DR, Cumming GP, Lee AJ. **Increased use of Twitter at a medical conference: a report and a review of the educational opportunities.** *J Med Internet Res* 2012;14:e176
6. Kolowich S. The academic twitterazzi. *Technology*. October 2, 2012. https://www.insidehighered.com/news/2012/10/02/scholars-debate-etiquette-live-tweeting-academic-conferences. Accessed September 15, 2014
7. Fitzgerald RT, Radmanesh A. **Social media and research visibility.** *AJNR Am J Neuroradiol* 2015;36:637
8. Radmanesh A, Fitzgerald RT. **Social media and the neuroradiologist: a brief introduction.** *AJNR Am J Neuroradiol* 2015;36:30–31
9. Croxall B. Ten tips for tweeting at conferences. *The Chronicle of Higher Education*. January 6, 2014. http://chronicle.com/blogs/profhacker/ten-tips-for-tweeting-at-conferences/54281. Accessed September 14, 2014

Differentiating Tumor Progression from Pseudoprogression in Patients with Glioblastomas Using Diffusion Tensor Imaging and Dynamic Susceptibility Contrast MRI

S. Wang, M. Martinez-Lage, Y. Sakai, S. Chawla, S.G. Kim, M. Alonso-Basanta, R.A. Lustig, S. Brem, S. Mohan, R.L. Wolf, A. Desai, and H. Poptani

ABSTRACT

BACKGROUND AND PURPOSE: Early assessment of treatment response is critical in patients with glioblastomas. A combination of DTI and DSC perfusion imaging parameters was evaluated to distinguish glioblastomas with true progression from mixed response and pseudoprogression.

MATERIALS AND METHODS: Forty-one patients with glioblastomas exhibiting enhancing lesions within 6 months after completion of chemoradiation therapy were retrospectively studied. All patients underwent surgery after MR imaging and were histologically classified as having true progression (>75% tumor), mixed response (25%–75% tumor), or pseudoprogression (<25% tumor). Mean diffusivity, fractional anisotropy, linear anisotropy coefficient, planar anisotropy coefficient, spheric anisotropy coefficient, and maximum relative cerebral blood volume values were measured from the enhancing tissue. A multivariate logistic regression analysis was used to determine the best model for classification of true progression from mixed response or pseudoprogression.

RESULTS: Significantly elevated maximum relative cerebral blood volume, fractional anisotropy, linear anisotropy coefficient, and planar anisotropy coefficient and decreased spheric anisotropy coefficient were observed in true progression compared with pseudoprogression ($P < .05$). There were also significant differences in maximum relative cerebral blood volume, fractional anisotropy, planar anisotropy coefficient, and spheric anisotropy coefficient measurements between mixed response and true progression groups. The best model to distinguish true progression from non–true progression (pseudoprogression and mixed) consisted of fractional anisotropy, linear anisotropy coefficient, and maximum relative cerebral blood volume, resulting in an area under the curve of 0.905. This model also differentiated true progression from mixed response with an area under the curve of 0.901. A combination of fractional anisotropy and maximum relative cerebral blood volume differentiated pseudoprogression from nonpseudoprogression (true progression and mixed) with an area under the curve of 0.807.

CONCLUSIONS: DTI and DSC perfusion imaging can improve accuracy in assessing treatment response and may aid in individualized treatment of patients with glioblastomas.

ABBREVIATIONS: AUC = area under the curve; CL = linear anisotropy coefficient; CP = planar anisotropy coefficient; CS = spheric anisotropy coefficient; FA = fractional anisotropy; LRM = logistic regression model; max = maximum; MD = mean diffusivity; PsP = pseudoprogression; rCBV = relative cerebral blood volume; TP = true progression

The current standard of care for newly diagnosed glioblastomas is surgical resection and concurrent temozolomide radiation therapy, followed by at least 6 months of adjuvant temozolomide. Treatment outcome is generally monitored by using standard clinical MR imaging based on accepted guidelines such as the updated Response Assessment in Neuro-Oncology criteria.[1,2] However, the appearance of enhancing lesions on MR imaging within the first 6 months after completion of chemoradiation therapy poses a challenge because it can reflect true progression (TP) or treatment-related changes known as pseudoprogression (PsP). PsP occurs in approximately a third of all patients with glioblastoma,[3] in which lesions often decrease in size or stabilize without further treatment, resulting in a longer survival. Accurate identifica-

Received March 10, 2015; accepted after revision June 2.

From the Departments of Radiology (S.W., Y.S., S.M., R.L.W., H.P.), Division of Neuroradiology, Pathology and Laboratory Medicine (M.M.-L.), Radiation Oncology (M.A.-B., R.A.L.,), Neurosurgery (S.B.), and Hematology-Oncology (A.D.), Hospital of the University of Pennsylvania, Philadelphia, Pennsylvania; and Department of Radiology (S.C., S.G.K.), Center for Biomedical Imaging, New York University School of Medicine, New York, New York.

Current affiliation for H.P.: Department of Cellular and Molecular Physiology, University of Liverpool, UK.

This work was supported by National Institutes of Health grant 1R21CA170284.

Please address correspondence to Harish Poptani, PhD, Department of Cellular and Molecular Physiology, University of Liverpool, 2/012 Nuffield Wing, Sherrington Building, Crown St, Liverpool L69 3BX, UK; e-mail: Harish.Poptani@liverpool.ac.uk

Indicates open access to non-subscribers at www.ajnr.org

Indicates article with supplemental on-line photo.

http://dx.doi.org/10.3174/ajnr.A4474

tion of PsP and TP is critical because patients with TP may require a change in therapeutic strategy while those with PsP may not. While published reports have attempted to differentiate PsP from TP,[4-7] these studies did not account for the common finding of a mixture of treatment-related changes and recurrent tumor. Management of these partial responders may be challenging, with short-interval imaging studies often required to determine clinical course. If identified early, these patients may benefit from novel therapeutics.

Mean diffusivity (MD), measured from diffusion imaging, has been used to diagnose and monitor treatment response in brain tumors.[8,9] Both mean and minimum MD values have been used in differentiating PsP from TP.[4-6,10] However, due to the heterogeneity of treatment response, MD may have a limited role because reduced diffusion could represent not only highly cellular tumor areas but also inflammatory processes.[9] DTI is increasingly being used in the characterization of glioblastomas[9,11]; anisotropy measures, including fractional anisotropy (FA), linear anisotropy (CL), planar anisotropy (CP), and spheric anisotropy (CS), have been used to differentiate glioblastomas from metastasis[11-13] and primary cerebral lymphomas.[12,14] However, only 1 study has used DTI for differentiation of PsP and TP.[15]

Relative cerebral blood volume (rCBV) obtained from DSC perfusion imaging has been widely used for tumor grading,[16] distinguishing recurrent tumor from radiation necrosis,[17] and differentiating PsP from TP.[18,19] Some studies have suggested that median rCBV and histogram analysis of rCBV can help differentiate PsP from TP.[18,20-22] However, rCBV has not been used to identify a mixed or partial response.

The clinical management of patients with recurrent glioblastoma is rapidly changing because several alternative therapeutic options are being investigated, including bevacizumab,[23] tumor treating fields,[24] and immunotherapy.[25] Increased incidence of PsP poses a dilemma for the treating physicians because determining the optimal therapeutic approach relies on a definitive diagnosis of TP, PsP, or mixed response. We hypothesize that DTI and DSC parameters have added value in making this differentiation and thus evaluated them for differentiating these 3 categories of treatment response.

MATERIALS AND METHODS

Patients

This study was approved by the institutional review board and was compliant with the Health Insurance Portability and Accountability Act. MR imaging data from 41 patients with glioblastomas (14 women/27 men; 55.71 ± 11.83 years of age; age range, 23–80 years), who had initially undergone gross total resection of the tumor followed by standard radiation therapy and temozolomide chemotherapy and exhibited new enhancing lesions on follow-up MR imaging within 6 months after completion of radiation therapy, were retrieved from the University of Pennsylvania data base from May 2011 to May 2014 and retrospectively analyzed. All patients underwent repeat surgery within 2 weeks after the MR imaging study in which the new enhancing lesions were first observed.

MR Imaging Data Acquisition

MR imaging studies were performed on a Tim Trio 3T whole-body scanner (Siemens, Erlangen, Germany) by using a 12-channel phased array head coil. Routine sequences included axial T1-weighted 3D MPRAGE (TR/TE/TI = 1760/3.1/950 ms, 192 × 256 matrix size, 1-mm section thickness) and axial FLAIR (TR/TE/TI = 9420/141/2500 ms, 3-mm section thickness). DTI data were acquired by using a single-shot spin-echo EPI sequence with parallel imaging by using generalized autocalibrating partially parallel acquisition and an acceleration factor of 2. Diffusion weighting was applied in 30 isotropically distributed directions by using a b-value of 1000 s/mm^2, with a total acquisition time of 8 minutes. For DSC imaging, a bolus of gadobenate dimeglumine (MultiHance; Bracco Diagnostics, Princeton, New Jersey) was injected with a preloading dose of 0.07 mmol/kg, which was used to reduce the effect of contrast agent leakage on CBV measurements.[26] DSC imaging was performed by using a gradient-echo echo-planar imaging sequence during a second 0.07-mmol/kg bolus of contrast agent (TR/TE = 2000/45 ms, FOV = 22 × 22 cm^2, resolution = 1.72 × 1.72 × 3 mm^3, 20 sections, 45 measurements with at least 10 image volumes before bolus arrival, acquisition time = 1 minute 38 seconds). The injection rate was 5 mL/s for all patients and was immediately followed by a bolus injection of saline (total of 20 mL at the same rate). Postcontrast T1-weighted 3D MPRAGE images were acquired after completion of the DSC sequence.

Image Processing

The diffusion tensor datasets were coregistered to the b=0 s/mm^2 images by using a 3D affine transformation estimated by maximizing the mutual information between the images.[13] The corrected raw images were combined to estimate the DTI parametric maps by using in-house software (IDL; ITT Visual Information Solutions, Boulder, Colorado). Pixel-wise MD, FA, CL, CP, and CS maps were computed by using the methods described earlier.[11,12] Leakage-corrected CBV maps using the γ variate function were generated by using NordicICE software (NordicNeuroLab, Bergen, Norway).

The DTI, CBV maps, and FLAIR images were coregistered to contrast-enhanced T1-weighted images. The CBV maps were normalized to the contralateral normal white matter to generate rCBV. A semiautomatic segmentation approach was used to generate a mask from the enhancing region by using the methods described earlier.[11-13] The median DTI metrics and rCBV values from the enhancing region were measured. In addition, the lower 10th percentile MD values were measured from the enhancing region and reported as minimum MD.[27] The top 90th percentile rCBV values were measured from the enhancing region and reported as $rCBV_{max}$.[12] Data analysis tools, including DTI computing, image coregistration, and segmentation, were implemented by using IDL routines. The total time for postprocessing was approximately 2 hours.

Histologic Analysis

Pathologic samples were originally cut, mounted, and stained with hematoxylin-eosin by standard methods. Immunohistochemistry for Ki-67 (mouse monoclonal, MIB-1, IR62661; Dako, Carpinteria, California) and p53 (mouse monoclonal, 1:60; DO-7, M7001; Dako) was performed by using a Bond III automated system (Leica Biosystems, Buffalo Grove, Illinois). The entirety of submitted material for each case was examined by a board-certified neuropathologist (M.M.-L.) who was blinded to the results of the MR imaging studies. The slides were examined to determine the relative degree of recurrent glioma and treatment-related changes. The percentage of geo-

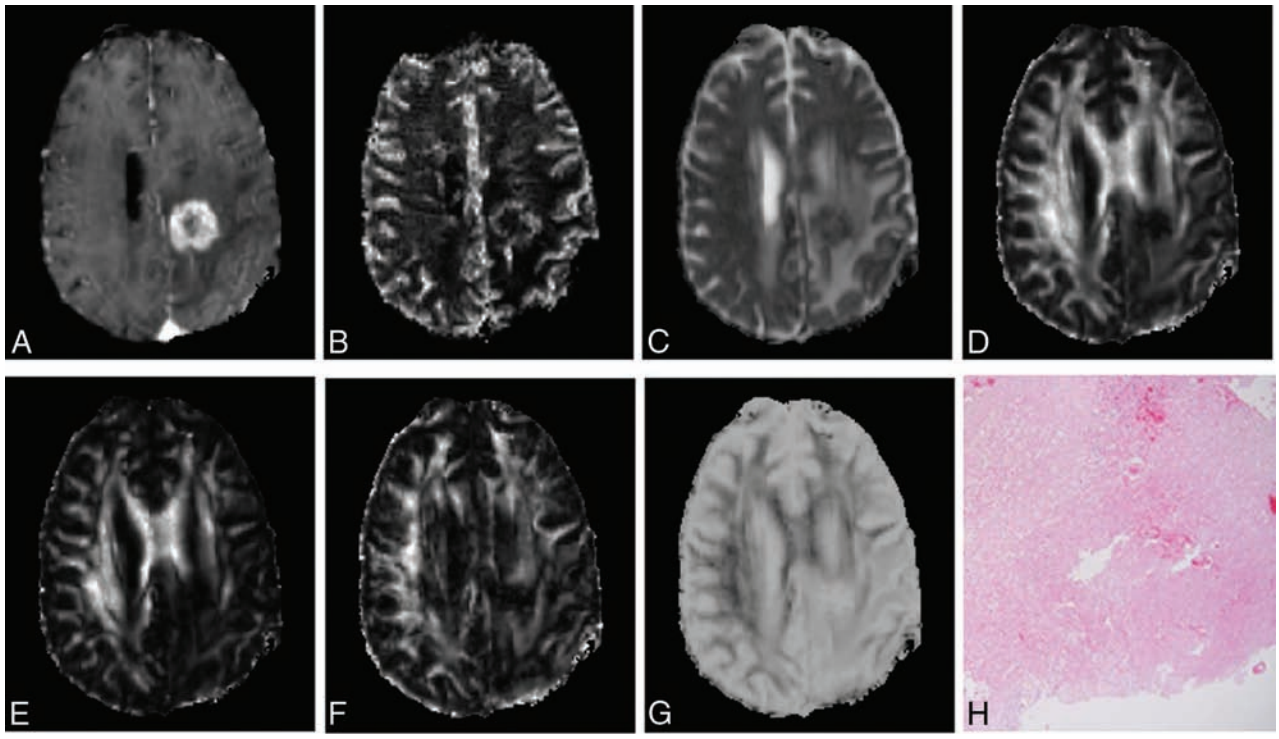

FIG 1. Axial MR images of a 44-year-old man with PsP. Contrast-enhanced T1-weighted image (*A*) shows a new enhancing lesion in the left parietal lobe. CBV map (*B*) shows moderately increased CBV from the lesion. MD (*C*) looks similar to the normal white matter. Decreased FA (*D*), CL (*E*), and CP (*F*) and increased CS (*G*) are observed from the enhancing part compared with normal white matter. Photomicrograph of a histologic section (*H*, hematoxylin-eosin stain, 50× magnification) reveals most of the tissue with treatment-related changes, including extensive geographic necrosis and vascular fibrinoid necrosis (90%).

graphic tissue necrosis across the specimen was assessed in an initial approach, excluding normal or quasinormal brain parenchyma. Histologic features associated with treatment, including vascular necrosis, hyalinization, hemosiderin, lymphocyte and macrophage infiltrates, gliosis, fibrosis, and dystrophic calcification, were also documented. Tumor-specific characteristics within the specimen, including neoplastic high cellularity, the presence of pseudopalisading necrosis, endothelial cell proliferation, and increased mitotic activity were additionally used to either increase or decrease the weightage for the presence of overall malignant features. The patients were grouped in 3 categories: <25% malignant features, PsP (8 patients; 3 women/5 men; 48.5 ± 12.72 years of age); 25%–75% malignant features, mixed tumor with treatment response (12 patients; 5 women/7 men; 58.25 ± 7.47 years of age); and >75% malignant features, TP (21 patients; 6 women/15 men; 57.0 ± 12.9 years of age). Strong and diffuse nuclear staining for p53 was used as supportive evidence of the presence of tumor, but the lack of staining did not reject the presence of recurrent glioma. We calculated the proliferative index with Ki-67 for each case as a percentage of positive tumor cells, avoiding areas of inflammatory infiltrates.

Statistical Analysis

A Mann-Whitney *U* test was used to compare the difference in the median MD, FA, CL, CP, CS, and rCBV values and minimum MD and $rCBV_{max}$ among PsP, mixed, and TP groups. Bonferroni correction was used to adjust for multiple comparisons, and a *P* value < .05 was considered significant. A multivariate logistic regression model (LRM) was used to determine the best classification model, and a leave-one-out cross-validation approach was applied to estimate the accuracy of the LRM. Areas under the receiver operating characteristic curves (AUCs) were computed by using the selected parameters and the LRM output. A cutoff value for each parameter was determined by maximizing the sum of sensitivity and specificity. All statistical analyses were conducted by using PASW Statistics, Version 18 (IBM, Armonk, New York).

RESULTS

Representative MR images and histologic photomicrographs from patients with PsP, mixed, and TP features are shown in Figs 1–3, respectively. MD maps demonstrate variable degrees of diffusivity from the enhancing parts of the tumor. Anisotropy and rCBV maps also show variability. However, quantitative analysis revealed significantly higher median FA, CL, and CP values and higher rCBV in patients with TP compared with PsP and mixed response (Fig 4).

A pair-wise comparison of DTI and DSC parameters from enhancing tissue is shown in Fig 4. While median MD values did not show significant differences between groups ($P > .05$), significantly higher $rCBV_{max}$ (4.75 versus 2.90, $P = .007$), FA (0.14 versus 0.11, $P = .008$), CL (0.05 versus 0.04, $P = .04$), and CP (0.08 versus 0.06, $P = .002$), and decreased CS (0.87 versus 0.90, $P = .004$) were observed in TP compared with PsP. There were also significant differences between mixed and TP groups in $rCBV_{max}$ (4.75 versus 3.31, $P = .02$), FA (0.14 versus 0.11, $P = .01$), CP (0.08 versus 0.06, $P = .001$), and CS (0.87 versus 0.89, $P = .02$) measurements. None of the parameters demonstrated a significant difference between PsP and mixed response. Of all the parameters, CP and CS showed a significant difference between PsP

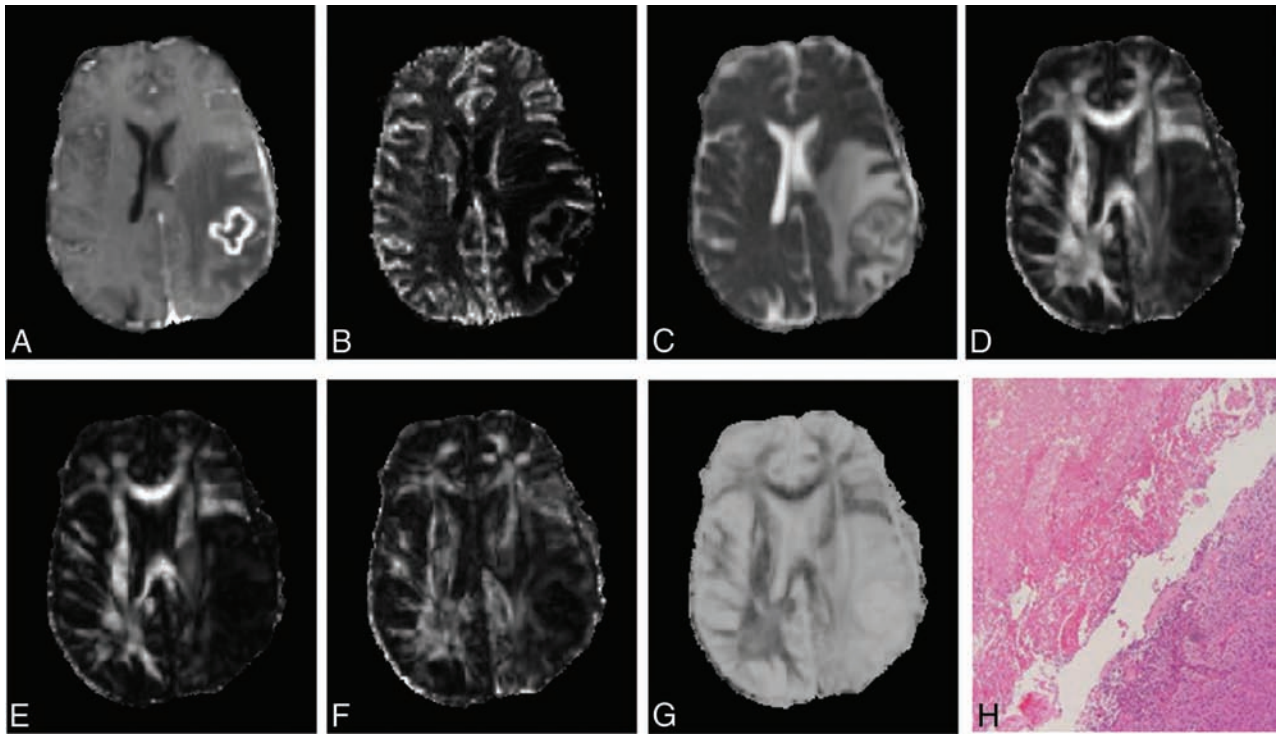

FIG 2. Axial images from the brain of a 59-year-old woman with mixed features of response, including areas of treatment-related changes and TP. Contrast-enhanced T1-weighted image (*A*) shows a new enhancing lesion in the left parietal lobe. The lesion shows slightly elevated perfusion on the CBV map (*B*) and lower MD (*C*). Lower FA (*D*), CL (*E*), CP (*F*), and higher CS (*G*) values from the enhancing part are noticed relative to the normal white matter. The imaging appearance looks similar to that of PsP (Fig 1). Photomicrograph of a histologic section (*H*, hematoxylin-eosin stain, 50× magnification) has similar amounts of treatment-related changes (50%) and viable tumor (50%).

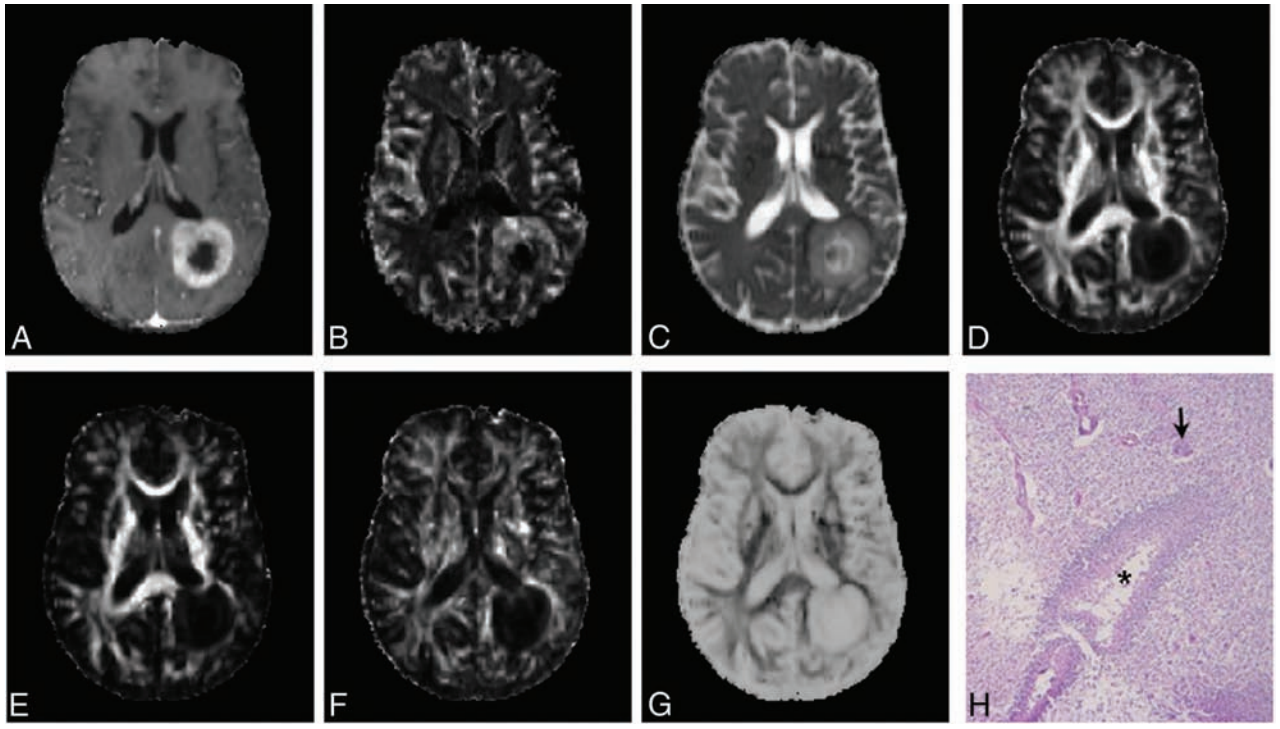

FIG 3. Axial brain images from a 54-year-old man showing TP. Contrast-enhanced T1-weighted image (*A*) shows a ring-enhancing lesion in the left parietal lobe. High rCBV (*B*) and increased MD (*C*) are observed from the lesion. The enhancing part of the lesion demonstrates decreased FA (*D*), CL (*E*), and CP (*F*) and increased CS (*G*). Findings in a photomicrograph of a histologic section (*H*, hematoxylin-eosin stain, 50× magnification) are similar to the patient's de novo glioblastoma, with areas of high tumor cellularity, pseudopalisading necrosis (*asterisks*), and endothelial proliferation (*arrow*) and increased mitotic activity.

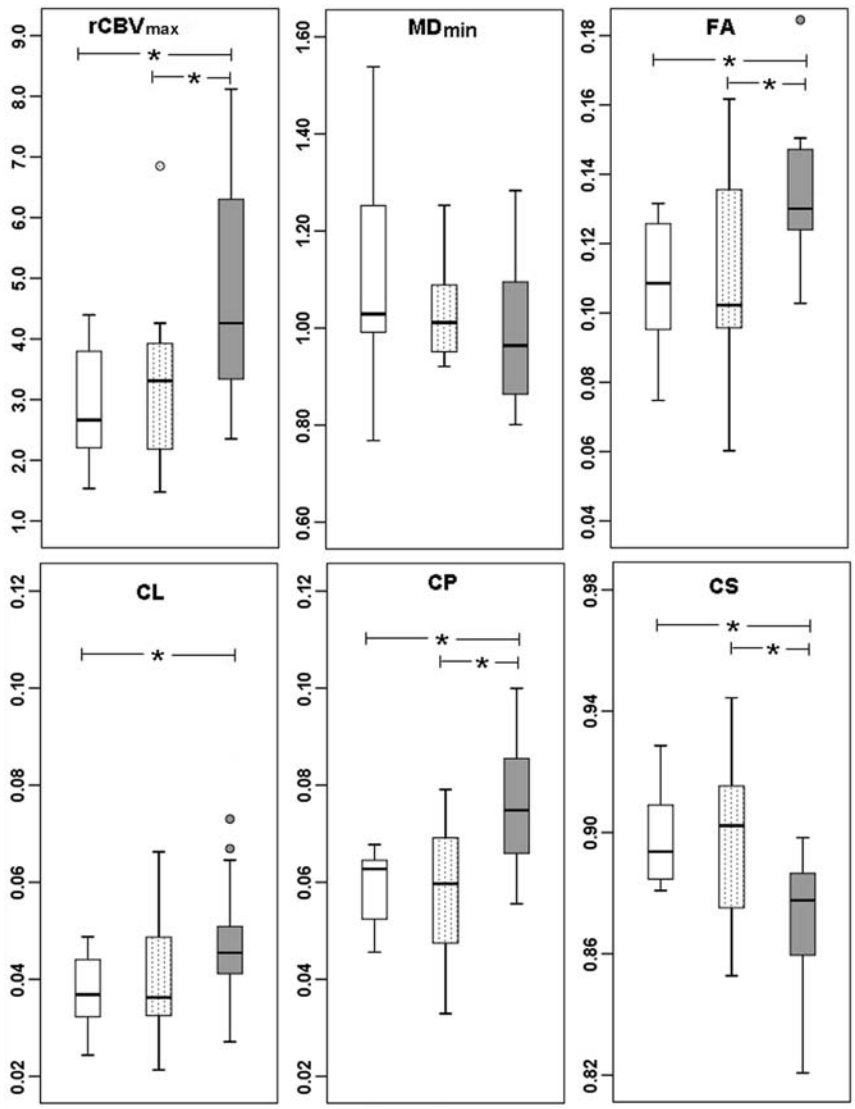

FIG 4. Boxplots of diffusion (minimum MD, FA, CL, CP, and CS) and perfusion (maximum rCBV) characteristics for patients with posttreatment glioblastomas in TP (gray), PsP (white), and mixed tumor (*dotted*). The *solid line* inside each box represents the median value, while the edges represent the 25th and 75th percentiles. The *straight line* (bars) on each box indicates the range of data distribution. *Circles* represent outliers (values >1.5 box length from the 75th/25th percentiles). The *asterisk* indicates a significant difference ($P < .05$) for group comparison.

and TP, and CP showed a significant difference between mixed and TP after Bonferroni correction ($P < .006$).

Discrimination of TP versus PsP and Mixed Response

The discrimination analysis was first performed to distinguish TP from PsP and mixed response. CP was the single best predictor for classification (AUC = 0.84), followed by FA and $rCBV_{max}$ (AUC = 0.78, Table). The imaging parameters were then used for a multivariate logistic regression analysis with backward stepwise selection, which indicated that the best classification of TP from non-TPs, including PsP and mixed, was achieved with 3 parameters, FA, CL, and $rCBV_{max}$, as follows:

$$f(FA, CL, rCBV_{max}) = \frac{1}{1 + \exp[-(\beta_0 + \beta_1 FA + \beta_2 CL + \beta_3 rCBV_{max})]},$$

where $\beta_0 = -16.17$, $\beta_1 = 194.01$, $\beta_2 = -285.65$, and $\beta_3 = 1.21$. Figure 5*A* shows the receiver operating characteristic curves for the best LRM and selected parameters. The cutoff value for the LRM was 0.55 with a sensitivity = 76%, specificity = 95%, and AUC = 0.905 (Table). Leave-one-out cross-validation analysis revealed that 78% of cases were correctly classified by using the LRM. Although CP was the single best predictor, it was not selected by the statistical model for highest sensitivity. Using forward stepwise selection, the best model included CP and $rCBV_{max}$, resulting in an AUC of 0.89, similar to the model FA, CL, and $rCBV_{max}$. In addition, there was a high correlation ($r = 0.84$) between FA and CP (On-line Figure), suggesting that the results from either model were similar.

Discrimination of PsP versus TP and Mixed Response

The single best predictor for classification was CP (AUC = 0.74), followed by $rCBV_{max}$ (AUC = 0.73) and FA (AUC = 0.70, Table). The best LRM for classification of PsP from non-PsPs, including TP and mixed response, was achieved with 2 parameters, FA and $rCBV_{max}$, as follows:

$$f(FA, rCBV_{max}) = \frac{1}{1 + \exp[-(\beta_0 + \beta_1 FA + \beta_2 rCBV_{max})]},$$

where $\beta_0 = -3.59$, $\beta_1 = 23.52$, and $\beta_2 = 0.62$. Figure 5*B* shows the receiver operating characteristic curves for the best LRM and selected parameters. The cutoff value for the LRM was 0.77 with sensitivity = 79%, specificity = 75%, and AUC = 0.807 (Table). Leave-one-out cross-validation analysis revealed that 63.4% of cases were correctly classified by using the LRM.

Discrimination between TP and Mixed Response

A subanalysis was performed to differentiate TP from mixed response so that the patients with mixed response could be closely monitored with short-interval imaging scans or enrolled in novel therapeutic trials. CP was again the single best predictor for classification (AUC = 0.83), followed by FA (AUC = 0.76) and $rCBV_{max}$ (AUC = 0.74, Table). The LRM for classification of TP from mixed response was achieved with 3 parameters, including FA, CL, and $rCBV_{max}$, as follows:

$$f(FA, CL, rCBV_{max}) = \frac{1}{1 + \exp[-(\beta_0 + \beta_1 FA + \beta_2 CL + \beta_3 rCBV_{max})]},$$

Sensitivity, specificity, and cutoff values of best models for classification[a]

Model	Sensitivity	Specificity	Cutoff Values	AUC	95% CI
TP vs PsP + mixed					
CP	0.71	0.90	0.07	0.84	0.72–0.96
FA	0.71	0.75	0.13	0.78	0.64–0.93
CL	0.71	0.75	0.04	0.72	0.56–0.88
$rCBV_{max}$	0.62	0.80	4.06	0.77	0.63–0.92
FA + CL + $rCBV_{max}$	0.76	0.95	0.55	0.90	0.81–1.00
PsP vs TP + mixed					
CP	0.57	1.00	0.07	0.74	0.59–0.89
FA	0.40	1.00	0.13	0.70	0.52–0.87
$rCBV_{max}$	0.82	0.63	2.77	0.73	0.54–0.91
FA + $rCBV_{max}$	0.79	0.75	0.77	0.81	0.66–0.95
TP vs mixed					
CP	0.71	0.83	0.07	0.83	0.69–0.97
FA	0.71	0.75	0.13	0.76	0.56–0.95
CL	0.71	0.75	0.04	0.69	0.49–0.90
$rCBV_{max}$	0.62	0.83	4.06	0.74	0.57–0.92
FA + CL + $rCBV_{max}$	0.76	1.00	0.65	0.90	0.78–1.00
PsP vs mixed					
MD_{min}	0.50	0.88	0.98	0.62	0.34–0.89

Note:—MD_{min} indicates minimum MD.
[a] The unit for MD is $\times 10^{-3} mm^2/s$.

where $\beta_0 = -15.43$, $\beta_1 = 202.14$, $\beta_2 = -313.99$, and $\beta_3 = 1.20$. Figure 5*C* shows the receiver operating characteristic curves for the best LRM and selected parameters. The cutoff value for the LRM was 0.65 with sensitivity = 76%, specificity = 100%, and AUC = 0.901 (Table). Leave-one-out cross-validation analysis revealed that 72.7% of cases were correctly classified by using the LRM.

Discrimination of PsP from Mixed Response

A final analysis to differentiate patients with PsP from those with mixed response showed a significant overlap between the 2 groups, with only MD having some predictive value with an AUC = 0.62 followed by $rCBV_{max}$ (AUC = 0.57).

DISCUSSION

The heterogeneity and variability in response did not allow differentiating TP from PsP simply by visual inspection of the parametric maps. However, a quantitative analysis of DTI parameters and $rCBV_{max}$ from the enhancing regions of the lesion demonstrated better assessment of treatment response in patients with glioblastomas. Such a categorization is clinically feasible because the postprocessing time was only approximately 2 hours, indicating that our proposed analytic approach may aid in individualized treatment management and better clinical decision-making.

Identification of TP

Early identification of TP could prevent further delays in repeat surgery or enrollment in alternative clinical trials. The LRM analysis indicated that the best model to distinguish TP from PsP or mixed responses was based on FA, CL, and $rCBV_{max}$. Higher anisotropy values have been reported in glioblastomas compared with brain metastases and primary cerebral lymphomas.[11-13] High FA in glioblastomas is probably related to the orientation of overproduced extracellular matrix.[11,28] Glioblastoma tumor cells produce large amounts of tumor-specific extracellular matrix components, which can serve as a substrate for adhesion and subsequent migration of the tumor cells through the enlarged extracellular space,[28] which may explain the elevated anisotropy observed in patients with TP. However, a previous study reported no difference in anisotropy measures between PsP and TP.[15] Potential reasons for this discrepancy may be because we divided the patients on the basis of the histologic features as opposed to grouping on the basis of follow-up imaging used in the previous study.[15] In addition, we assessed 3 categories, including mixed response, instead of just separating PsP and TP.

DSC imaging can be helpful in differentiating tumor recurrence from radiation necrosis.[17,29] Recent studies have also used DSC imaging[18,19,21] to detect TP from PsP. Kong et al[18] reported that a mean rCBV value of 1.47 had 81.5% sensitivity and 77.8% specificity in differentiating PsP from TP, while Kim et al[20] reported a histogram analysis of rCBV, in which a peak height position of 1.7 showed 90.2% sensitivity and 91.1% specificity for differentiating tumor recurrence from treatment changes. In comparison, we used $rCBV_{max}$ and observed that a threshold $rCBV_{max}$ value of 4.06 led to a sensitivity of 62% and specificity of 80% in differentiating TP from PsP and mixed tumors.

Identification of PsP

Accurate identification of PsP is critical for patient management because unnecessary repeat surgery/biopsy can be avoided in these patients and they can continue on an effective temozolomide regimen with standard imaging follow-up of 3–6 months, thereby reducing patient care costs. Logistic regression analysis showed that the best model to differentiate PsP from TP and mixed response included FA and $rCBV_{max}$.

Pseudoprogression is predominantly a subacute treatment-related reaction. Pathologically, it corresponds to gliosis and radiation-induced reactive changes including disruption of the BBB, inflammation, increased permeability, and edema. These changes cause increased enhancement on MR imaging and can mimic TP.[9] Several studies have reported that PsP exhibits higher MD values from the enhancing region than TP, partly due to the extent of cellular death and vascular changes in PsP.[4,6] Minimum MD values have been reported to be prognostic of outcomes in gliomas.[30] Chu et al[5] reported that the fifth percentile of the cumulative MD histogram was the most promising parameter in the differentiation of TP and PsP. Although we found a similar trend for minimum MD, calculated from the 10th percentile of the MD value, it did not reach statistical significance. There are a limited number of studies regarding the role of FA in the evaluation of treatment response.[15,31] Xu et al[31] reported a low FA ratio in radiation necrosis compared with recurrent tumor. rCBV measurements have also been used in identifying PsP.[9,32] The inflammation/necrotic processes involved in PsP result in lower rCBV values,[9,32] and our results confirm this hypothesis. In addition, our study showed that a combination of FA and $rCBV_{max}$ can help in identifying PsP from TP or mixed response.

Identification of Mixed Response

On a practical level, posttreatment new enhancing lesions usually contain a mixture of viable neoplasm and treatment-induced changes, and a more accurate assessment of the relative contribution of each entity can guide clinical decision-making. However,

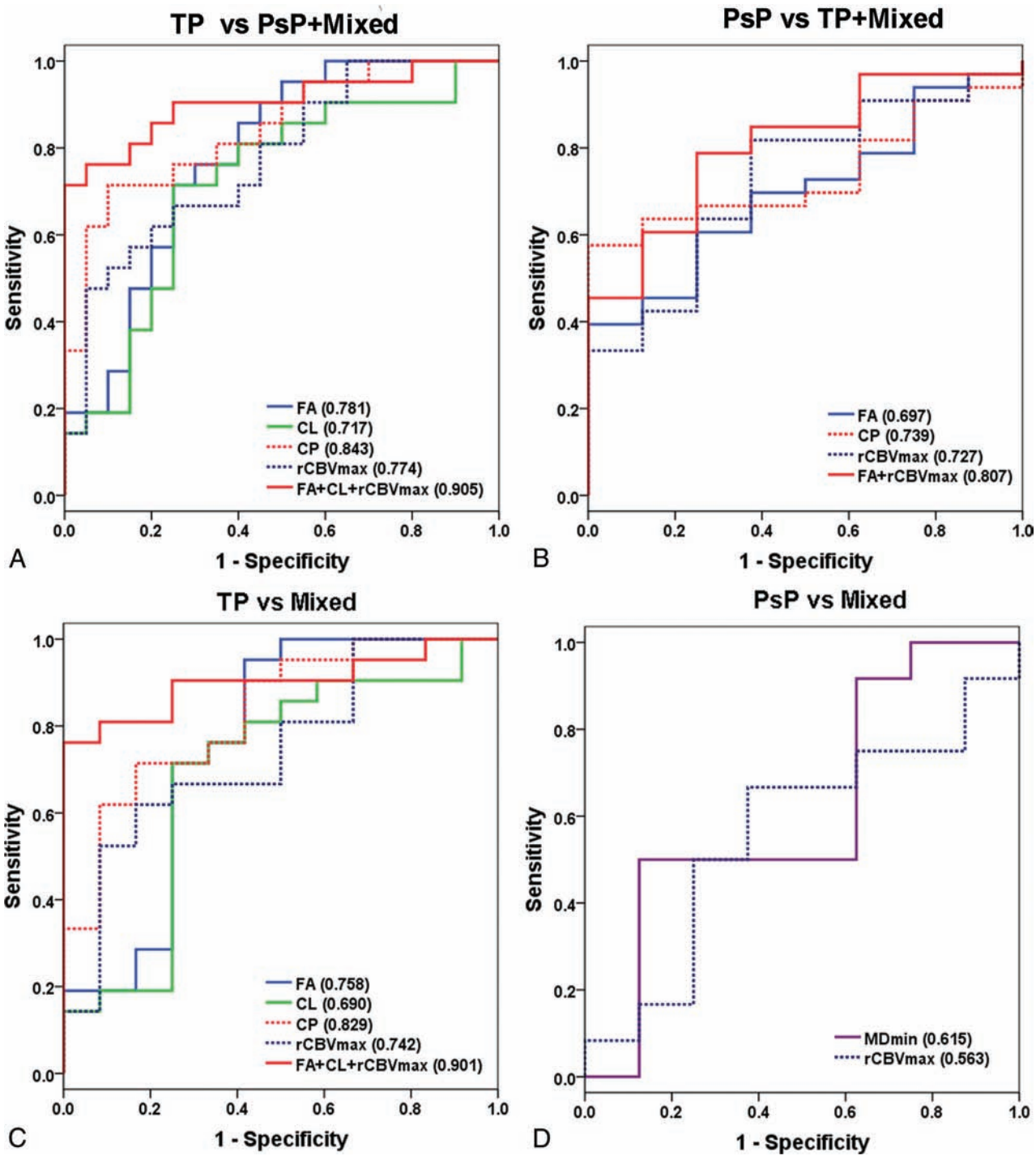

FIG 5. Receiver operating characteristic curves of the imaging parameters for identifying different groups. The numbers in the parentheses show AUC values. The logistic regression model of FA, CL, and $rCBV_{max}$ from the enhancing part of the tumor was the best predictor for differentiation of TP from non-TP, including PsP and mixed response with an AUC = 0.905 (*A*). This model can also distinguish TP from mixed tumor with an AUC = 0.901 (*C*). A combination of FA and $rCBV_{max}$ differentiates PsP from non-PsP (TP and mixed) with an AUC of 0.807 (*B*). There is a significant overlap between the PsP and the mixed group, and only MD is shown to have some predictive value with an AUC = 0.615 (*D*).

most previous studies have attempted to only differentiate between PsP and TP.[4,6,15,19] DTI and DSC imaging findings between viable neoplasm and treatment-induced changes are variable and difficult to synthesize on routine visual inspection. We believe the quantitative analysis of imaging parameters[8,33] should yield a better estimate of each component. Our findings indicate that DTI and perfusion may have a complementary predictive value for the evaluation of treatment response and demonstrate that a combination of FA, CL and $rCBV_{max}$ can differentiate mixed response from TP with high sensitivity. Although similar trends were observed between PsP and mixed response, DTI and DSC parameters had relatively modest utility in distin-

guishing mixed response from PsP. Because dynamic contrast-enhanced MR imaging is increasingly being used to assess brain tumors, we believe future studies including quantitative dynamic contrast-enhanced–based parameters may further enhance the sensitivity of our method in differentiating PsP from mixed response.

While these results are promising, the study has some limitations, including a retrospective analysis design and a relatively smaller sample size. In addition, image-guided biopsy may be necessary to evaluate the pathophysiologic basis of higher CP and FA in TP. A clinical follow-up study by using progression-free or overall analysis as end points for determination of PsP and TP at the time of initial MR imaging is desirable because not all patients will undergo repeat surgery for confirmation of imaging findings.

CONCLUSIONS

Our study shows that a combination of DTI and DSC perfusion parameters can help in the evaluation of treatment response in glioblastomas and may aid in the optimal management of these patients.

ACKNOWLEDGMENTS

We acknowledge Tianyu Yin for assistance in data analysis; Dr Ruyun Jin, Medical Data Research Center, Providence Health & Services, Portland, Oregon, for statistical analysis; and research coordinators Lisa Desiderio, Katelyn Reilly, and Krista Huff.

Disclosures: Maria Martinez-Lage—*RELATED*: National Institutes of Health (Principal Investigator: Harish Poptani).* Suyash Mohan—*RELATED*: *Grant*: National Institutes of Health (R21 grant).* Ronald L. Wolf—*RELATED*: *Grant*: National Institutes of Health,* *Comments*: 5-R21-CA-170284–02 direct/indirect support. I get a small amount of salary support under this grant (<$10,000); previous Principal Investigator H. Poptani, but now I am the Principal Investigator on behalf of the University of Pennsylvania. Arati Desai—*RELATED*: *Grant*: National Institutes of Health (R21).* Harish Poptani—*RELATED*: *Grant*: National Institutes of Health*; *UNRELATED*: *Consultancy*: American College of Radiology Image Metrix, *Comments*: consulting for MRS study trials; *Grants/Grants Pending*: National Institutes of Health.* *Money paid to the institution.

REFERENCES

1. Macdonald DR, Cascino TL, Schold SC Jr, et al. **Response criteria for phase II studies of supratentorial malignant glioma.** *J Clin Oncol* 1990;8:1277–80 Medline
2. Wen PY, Macdonald DR, Reardon DA, et al. **Updated response assessment criteria for high-grade gliomas: response assessment in neuro-oncology working group.** *J Clin Oncol* 2010;28:1963–72 CrossRef Medline
3. Topkan E, Topuk S, Oymak E, et al. **Pseudoprogression in patients with glioblastoma multiforme after concurrent radiotherapy and temozolomide.** *Am J Clin Oncol* 2012;35:284–89 CrossRef Medline
4. Cha J, Kim ST, Kim HJ, et al. **Differentiation of tumor progression from pseudoprogression in patients with posttreatment glioblastoma using multiparametric histogram analysis.** *AJNR Am J Neuroradiol* 2014;35:1309–17 CrossRef Medline
5. Chu HH, Choi SH, Ryoo I, et al. **Differentiation of true progression from pseudoprogression in glioblastoma treated with radiation therapy and concomitant temozolomide: comparison study of standard and high-b-value diffusion-weighted imaging.** *Radiology* 2013;269:831–40 CrossRef Medline
6. Lee WJ, Choi SH, Park CK, et al. **Diffusion-weighted MR imaging for the differentiation of true progression from pseudoprogression following concomitant radiotherapy with temozolomide in patients with newly diagnosed high-grade gliomas.** *Acad Radiol* 2012;19:1353–61 CrossRef Medline
7. Suh CH, Kim HS, Choi YJ, et al. **Prediction of pseudoprogression in patients with glioblastomas using the initial and final area under the curves ratio derived from dynamic contrast-enhanced T1-weighted perfusion MR imaging.** *AJNR Am J Neuroradiol* 2013;34:2278–86 CrossRef Medline
8. Hamstra DA, Chenevert TL, Moffat BA, et al. **Evaluation of the functional diffusion map as an early biomarker of time-to-progression and overall survival in high-grade glioma.** *Proc Natl Acad Sci U S A* 2005;102:16759–64 CrossRef Medline
9. Hygino da Cruz LC Jr, Rodriguez I, Domingues RC, et al. **Pseudoprogression and pseudoresponse: imaging challenges in the assessment of posttreatment glioma.** *AJNR Am J Neuroradiol* 2011;32:1978–85 CrossRef Medline
10. Hu X, Wong KK, Young GS, et al. **Support vector machine multiparametric MRI identification of pseudoprogression from tumor recurrence in patients with resected glioblastoma.** *J Magn Reson Imaging* 2011;33:296–305 CrossRef Medline
11. Wang S, Kim SJ, Poptani H, et al. **Diagnostic utility of diffusion tensor imaging in differentiating glioblastomas from brain metastases.** *AJNR Am J Neuroradiol* 2014;35:928–34 CrossRef Medline
12. Wang S, Kim S, Chawla S, et al. **Differentiation between glioblastomas, solitary brain metastases, and primary cerebral lymphomas using diffusion tensor and dynamic susceptibility contrast-enhanced MR imaging.** *AJNR Am J Neuroradiol* 2011;32:507–14 CrossRef Medline
13. Wang S, Kim S, Chawla S, et al. **Differentiation between glioblastomas and solitary brain metastases using diffusion tensor imaging.** *Neuroimage* 2009;44:653–60 CrossRef Medline
14. Toh CH, Castillo M, Wong AM, et al. **Primary cerebral lymphoma and glioblastoma multiforme: differences in diffusion characteristics evaluated with diffusion tensor imaging.** *AJNR Am J Neuroradiol* 2008;29:471–75 CrossRef Medline
15. Agarwal A, Kumar S, Narang J, et al. **Morphologic MRI features, diffusion tensor imaging and radiation dosimetric analysis to differentiate pseudo-progression from early tumor progression.** *J Neurooncol* 2013;112:413–20 CrossRef Medline
16. Lacerda S, Law M. **Magnetic resonance perfusion and permeability imaging in brain tumors.** *Neuroimaging Clin N Am* 2009;19:527–57 CrossRef Medline
17. Gasparetto EL, Pawlak MA, Patel SH, et al. **Posttreatment recurrence of malignant brain neoplasm: accuracy of relative cerebral blood volume fraction in discriminating low from high malignant histologic volume fraction.** *Radiology* 2009;250:887–96 CrossRef Medline
18. Kong DS, Kim ST, Kim EH, et al. **Diagnostic dilemma of pseudoprogression in the treatment of newly diagnosed glioblastomas: the role of assessing relative cerebral blood flow volume and oxygen-6-methylguanine-DNA methyltransferase promoter methylation status.** *AJNR Am J Neuroradiol* 2011;32:382–87 CrossRef Medline
19. Tsien C, Galbán CJ, Chenevert TL, et al. **Parametric response map as an imaging biomarker to distinguish progression from pseudoprogression in high-grade glioma.** *J Clin Oncol* 2010;28:2293–99 CrossRef Medline
20. Kim HS, Kim JH, Kim SH, et al. **Posttreatment high-grade glioma: usefulness of peak height position with semiquantitative MR perfusion histogram analysis in an entire contrast-enhanced lesion for predicting volume fraction of recurrence.** *Radiology* 2010;256:906–15 CrossRef Medline
21. Baek HJ, Kim HS, Kim N, et al. **Percent change of perfusion skewness and kurtosis: a potential imaging biomarker for early treatment response in patients with newly diagnosed glioblastomas.** *Radiology* 2012;264:834–43 CrossRef Medline
22. Mangla R, Singh G, Ziegelitz D, et al. **Changes in relative cerebral blood volume 1 month after radiation-temozolomide therapy can help predict overall survival in patients with glioblastoma.** *Radiology* 2010;256:575–84 CrossRef Medline
23. Chowdhary S, Chamberlain M. **Bevacizumab for the treatment of**

glioblastoma. *Expert Rev Neurother* 2013;13:937–49 CrossRef Medline
24. **Tumor treating fields therapy for recurrent glioblastoma.** *Manag Care* 2012;21:43–44 Medline
25. Finocchiaro G, Pellegatta S. **Perspectives for immunotherapy in glioblastoma treatment.** *Curr Opin Oncol* 2014;26:608–14 CrossRef Medline
26. Boxerman JL, Prah DE, Paulson ES, et al. **The role of preload and leakage correction in gadolinium-based cerebral blood volume estimation determined by comparison with MION as a criterion standard.** *AJNR Am J Neuroradiol* 2012;33:1081–87 CrossRef Medline
27. Kim DY, Kim HS, Goh MJ, et al. **Utility of intravoxel incoherent motion MR imaging for distinguishing recurrent metastatic tumor from treatment effect following gamma knife radiosurgery: initial experience.** *AJNR Am J Neuroradiol* 2014;35:2082–90 CrossRef Medline
28. Zamecnik J. **The extracellular space and matrix of gliomas.** *Acta Neuropathol* 2005;110:435–42 CrossRef Medline
29. Barajas RF Jr, Chang JS, Segal MR, et al. **Differentiation of recurrent glioblastoma multiforme from radiation necrosis after external beam radiation therapy with dynamic susceptibility-weighted contrast-enhanced perfusion MR imaging.** *Radiology* 2009;253:486–96 CrossRef Medline
30. Pope WB, Lai A, Mehta R, et al. **Apparent diffusion coefficient histogram analysis stratifies progression-free survival in newly diagnosed bevacizumab-treated glioblastoma.** *AJNR Am J Neuroradiol* 2011;32:882–89 CrossRef Medline
31. Xu JL, Li YL, Lian JM, et al. **Distinction between postoperative recurrent glioma and radiation injury using MR diffusion tensor imaging.** *Neuroradiology* 2010;52:1193–99 CrossRef Medline
32. Jahangiri A, Aghi MK. **Pseudoprogression and treatment effect.** *Neurosurg Clin N Am* 2012;23:277–87, viii-ix CrossRef Medline
33. Aquino D, Di Stefano AL, Scotti A, et al. **Parametric response maps of perfusion MRI may identify recurrent glioblastomas responsive to bevacizumab and irinotecan.** *PLoS One* 2014;9:e90535 CrossRef Medline

Texture Feature Ratios from Relative CBV Maps of Perfusion MRI Are Associated with Patient Survival in Glioblastoma

J. Lee, R. Jain, K. Khalil, B. Griffith, R. Bosca, G. Rao, and A. Rao

ABSTRACT

BACKGROUND AND PURPOSE: Texture analysis has been applied to medical images to assist in tumor tissue classification and characterization. In this study, we obtained textural features from parametric (relative CBV) maps of dynamic susceptibility contrast-enhanced MR images in glioblastoma and assessed their relationship with patient survival.

MATERIALS AND METHODS: MR perfusion data of 24 patients with glioblastoma from The Cancer Genome Atlas were analyzed in this study. One- and 2D texture feature ratios and kinetic textural features based on relative CBV values in the contrast-enhancing and nonenhancing lesions of the tumor were obtained. Receiver operating characteristic, Kaplan-Meier, and multivariate Cox proportional hazards regression analyses were used to assess the relationship between texture feature ratios and overall survival.

RESULTS: Several feature ratios are capable of stratifying survival in a statistically significant manner. These feature ratios correspond to homogeneity ($P = .008$, based on the log-rank test), angular second moment ($P = .003$), inverse difference moment ($P = .013$), and entropy ($P = .008$). Multivariate Cox proportional hazards regression analysis showed that homogeneity, angular second moment, inverse difference moment, and entropy from the contrast-enhancing lesion were significantly associated with overall survival. For the nonenhancing lesion, skewness and variance ratios of relative CBV texture were associated with overall survival in a statistically significant manner. For the kinetic texture analysis, the Haralick correlation feature showed a *P* value close to .05.

CONCLUSIONS: Our study revealed that texture feature ratios from contrast-enhancing and nonenhancing lesions and kinetic texture analysis obtained from perfusion parametric maps provide useful information for predicting survival in patients with glioblastoma.

ABBREVIATIONS: ASM = angular second moment; CEL = contrast-enhancing lesion; GBM = glioblastoma multiforme; GLCM = gray-level co-occurrence matrix; IDM = inverse difference moment; LoG = Laplacian of Gaussian; NEL = nonenhancing lesion; rCBV = relative CBV; ROC = receiver operating characteristic

Glioblastoma multiforme (GBM) is one of the most common and aggressive types of malignant brain tumors. The prognosis for patients with GBM remains very poor with median survival rates between 12 and 15 months.[1,2] Several computer-based analyses, including image texture analysis, have been proposed to improve the diagnostic performance of imaging-derived measurements in cancer studies including GBM.[3] Image texture analysis measures the local characteristic pattern of image intensity and has been applied to different image-processing domains, such as texture classification and texture segmentation, to identify distinct textural regions in an image.[4] In recent studies, texture analysis has been applied to medical images to assist in tumor tissue classification and characterization. One study of PET and CT showed that the features for tumor heterogeneity extracted from the normalized gray-level co-occurrence matrix (GLCM) could represent an independent prognostic predictor in patients.[5] Another texture study in PET/CT suggested that regional and local characterization of the PET tracer heterogeneity in tumors is more powerful than global measurements currently used in clinical practice.[6] Also, a textural feature study in non-small cell lung cancer showed that baseline fluorine 18 fluorodeoxyglucose (^{18}F-FDG) PET scan uptake values are associated with nonresponse to chemoradiotherapy.[7] Recently, a novel method defined, as tex-

Received March 31, 2015; accepted after revision May 26.

From the Departments of Bioinformatics and Computational Biology (J.L., A.R.) and Neurosurgery (G.R.), The University of Texas MD Anderson Cancer Center, Houston, Texas; Department of Radiology (R.J.), New York University School of Medicine, Langone Medical Center, New York, New York; Department of Radiology (K.K., B.G.), Henry Ford Hospital, Detroit, Michigan; and Department of Medical Physics (R.B.), University of Wisconsin, Madison, Wisconsin.

This work was supported by the National Cancer Institute Cancer Center Support Grant NCI P30 CA016672, a Career Development Award from the Brain Tumor SPORE P50CA127001-07 (to A.R.), and start-up funding from MD Anderson Cancer Center to support J.L.'s research.

Please address correspondence to Arvind Rao, PhD, Department of Bioinformatics and Computational Biology, The University of Texas MD Anderson Cancer Center, 1515 Holcombe Blvd, Unit 1410, Houston, TX 77030; e-mail: aruppore@mdanderson.org

Indicates open access to non-subscribers at www.ajnr.org

http://dx.doi.org/10.3174/ajnr.A4534

Table 1: Patient demographics

Age at First Diagnosis (yr) (range) (mean)	Overall Survival (mo) (range) (mean)	Disease-Free Survival (mo) (range) (mean)	Sex	Overall Status
40∼77 60.0	3.4∼56.9 19.5	2.6∼46.9 10.8	17 Males, 7 females	22 Deceased, 2 living

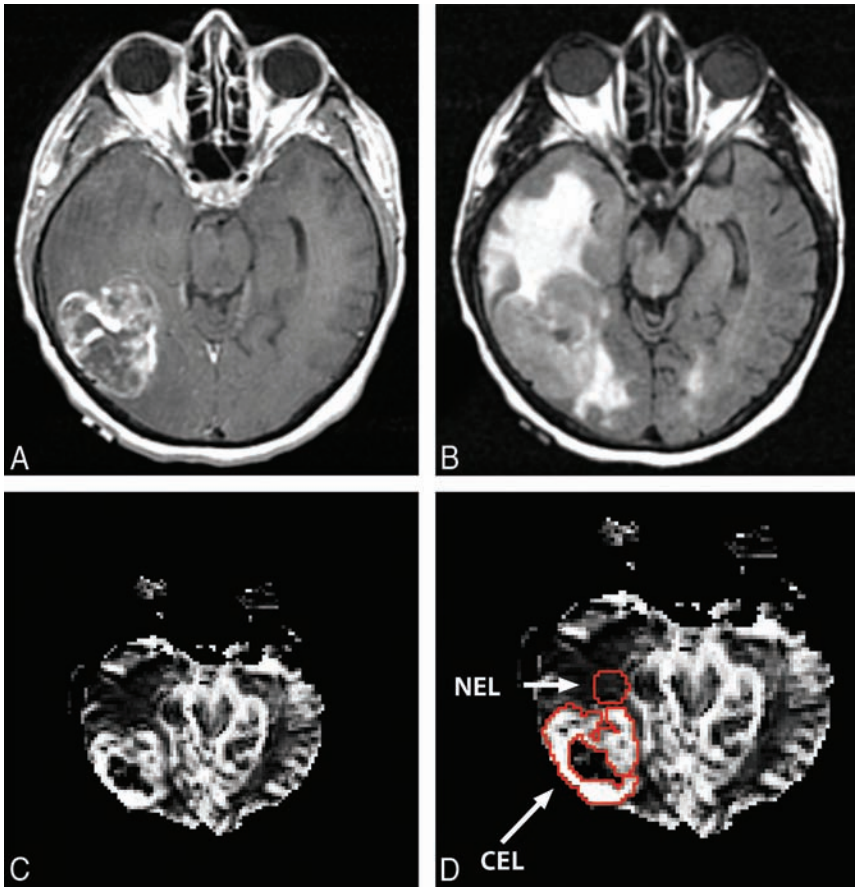

FIG 1. *A*, T1 postcontrast image. *B*, T2 FLAIR image. *C*, rCBV map of the brain in a female patient. *D*, The CEL and NEL ROIs on the rCBV map.

tural kinetics, was studied with breast dynamic contrast-enhanced MR imaging by Agner et al.[8] This method attempted to capture spatiotemporal changes in breast lesion texture for classifying malignant and benign lesions.

In this work, we investigated tumor-derived texture feature ratios from relative CBV (rCBV) values (derived from dynamic contrast-enhanced MR imaging) of 2 different tumor regions: the contrast-enhancing lesion (CEL) region and the nonenhancing lesion (NEL) region. We extracted first-order statistics, such as homogeneity, mean, SD, skewness, and kurtosis from the intensity histogram, as well as Haralick texture features obtained from the intensity GLCM.[9] Subsequently, ratios of these texture features between Laplacian-of-Gaussian (LoG) filtered and unfiltered versions of the rCBV map were also derived. Basically, the Laplacian-of-Gaussian filters are useful for detecting edges in images, and the feature ratio can give us quantitative relations of features between filtered and unfiltered versions of the rCBV map, which would provide an effective normalization to minimize the effects of any potential variations in MR images from different patients.[10] In addition, we obtained textural kinetic features of brain tumor dynamic susceptibility contrast MR imaging data within these CEL/NEL ROIs. The purpose of this study was to determine the association of these DSC-MR imaging textural feature ratios with the overall survival status of GBM.

MATERIALS AND METHODS

Data

We identified 24 patients with GMB from The Cancer Genome Atlas based on the availability of companion perfusion DSC-MR imaging data in The Cancer Imaging Archive. One of the patients had tumors in both the left occipital region and left frontal region. These 2 tumors are treated distinctly. Previously, these data were assessed for genomic relationships with rCBV values.[11] In this study, we performed 1D and 2D texture analysis and kinetic texture analysis of rCBV values within CEL and NEL regions for survival prediction. The clinical data were obtained from the cBioPortal for Cancer Genomics (http://www.cbioportal.org) (Table 1). In addition, a survival class variable was created by dichotomizing the overall survival value at 12 months based on the typical median survival time (∼15 months) in GBM.[2,12]

Relative cerebral blood volume values were calculated from ROIs within the CEL, the NEL, and the normal-appearing white matter, respectively, on the basis of rCBV maps obtained previously.[11] The methods for this processing are explained in more detail in Jain et al.[11] The rCBV intensities for the CEL and NEL were normalized with the mean value of the rCBV intensities for the unaffected normal-appearing white matter region.[13] The ROIs of the CEL, NEL, and normal-appearing white matter were segmented by experts manually after coregistering rCBV parametric maps with T1 postcontrast and T2 FLAIR images, respectively. The NEL ROIs were placed adjacent to the CEL margin in the white matter within the FLAIR signal-abnormality region. Figure 1 shows an example of an rCBV map from the tumor in a female patient.

Image Texture Feature Ratio Computation

Textural feature ratios were computed from the normalized rCBV data in 2 steps. First, we applied a Laplacian-of-Gaussian Equation 1, $\nabla^2 G$, LoG filter to a normalized rCBV ROI to obtain filtered images.

Table 2: Spearman rank correlation and associated *P* values from the following feature ratios for the CEL region

	Homogeneity	ASM	IDM	Entropy
Homogeneity	–	0.83 (<.001)	0.99 (<.001)	−0.84 (<.001)
ASM	0.83 (<.001)	–	0.84 (<.001)	−0.94 (<.001)
IDM	0.99 (<.001)	0.84 (<.001)	–	−0.85 (<.001)
Entropy	−0.84 (<.001)	−0.94 (<.001)	−0.85 (<.001)	–

Note:—– indicates not applicable.

Table 3: The rank correlation and *P* values within the NEL region

	Skewness	Variance	Sum Average	Sum Variance
Skewness	–	−0.47 (.022)	−0.51 (.010)	−0.52 (.008)
Variance	−0.47 (.022)	–	0.94 (<.001)	0.95 (<.001)
Sum average	−0.51 (.010)	0.94 (<.001)	–	0.99 (<.001)
Sum variance	−0.52 (.008)	0.95 (<.001)	0.99 (<.001)	–

Note:—– indicates not applicable.

Table 4: Range in texture feature ratios with and without LoG filtration for CEL

	Homogeneity	ASM	IDM	Entropy
LoG/unfiltered	1.08 ± 0.18	1.11 ± 0.74	1.10 ± 0.24	1.02 ± 0.18

[a] Data are means.

Table 5: Range in texture feature ratios with and without LoG filtration for NEL

	Skewness	Variance	Sum Average	Sum Variance
LoG/unfiltered	3.57 ± 11.83	2.30 ± 3.77	1.37 ± 0.83	2.84 ± 5.50

[a] Data are means.

Table 6: Areas under ROC curves (for prediction of 12-month survival status) from the CEL and NEL texture feature ratios[a]

	AUC	95% CI	*P* Value
CEL			
Homogeneity	0.826	0.542–0.986	.003
ASM	0.757	0.500–0.951	.019
IDM	0.806	0.562–0.972	.006
Entropy	0.799	0.556–0.972	.007
NEL			
Skewness	0.799	0.549–0.944	.007
Variance	0.715	0.465–0.896	.042
Sum average	0.715	0.465–0.889	.042
Sum variance	0.708	0.438–0.847	.048

Note:—AUC indicates area under the curve.
[a] Only features with statistically significant AUCs are shown.

$$1)\qquad \nabla^2 G(x,y) = \frac{-1}{\pi\sigma^4}\left(1 - \frac{x^2+y^2}{2\sigma^2}\right)e^{-(x^2+y^2)/2\sigma^2},$$

where σ corresponds to the SD of the LoG filter (here we use a medium level of coarseness, $\sigma = 1.8$).[10,14] The filter size chosen is 11×11, which was determined from the SD value. The LoG filter derives edge-like features from the local-intensity variations in images. Gray-level co-occurrence matrices were derived from both unfiltered and filtered images. Next, 1D and 2D textural features were computed from the GLCMs of the unfiltered and filtered images.[14] Finally, ratios of filtered texture descriptors to the unfiltered texture descriptors were calculated to yield texture feature ratios.

1D and 2D Texture Features

Image gray-level heterogeneity was quantified by using first-order statistics such as mean, SD, skewness, and kurtosis of the pixel-intensity distribution. Skewness and kurtosis are measures of the asymmetry and peakedness of the distribution, respectively. For the 2D texture features, to quantify the spatial distribution of the pixel values (rCBV values) within the ROI, we derived the GLCMs from the unfiltered and filtered images. The GLCM measures the probability of the occurrence of a specific gray-level value pair as a function of distance and direction. We used 8 gray levels, commonly used in these types of studies[15] with 1 pixel offset to compute the GLCMs from the filtered and original images. We then computed 13 different second-order Haralick statistical measures from the GLCMs.[16] The detailed equations for the second-order texture features are described in the Appendix.

Kinetic Texture

For the kinetic texture analysis, the gadolinium concentration time-series of the DSC perfusion data in both CEL and NEL regions were extracted by using an open-source software package: Quantitative Utility for Assessing TreatmenT RespOnse (https://github.com/rjbosca/QUATTRO).[17] Each ROI voxel from the dynamic perfusion dataset was normalized by the corresponding mean normal-appearing white matter intensity, and all 18 features discussed above were calculated for each time point in the DSC series. Thus, we have 18 kinetic texture features for each perfusion dataset. Each time-series texture feature was then fitted to a third-order polynomial model (Equation 2) to yield 4 coefficients (b_0, b_1, b_2, b_3).

$$2)\qquad f(t) = b_0 + b_1 t + b_2 t^2 + b_3 t^3.$$

This 4D coefficient vector was then projected to 1D by using metric multidimensional scaling.[16]

Statistical Analysis

Eighteen texture feature ratios were obtained and compared between the overall survival groups (>12 or ≤12 months). The predictive accuracy of the CEL and NEL texture feature ratios for survival status was assessed by using the receiver operating characteristic (ROC) curve.

Correlations between 18 texture feature ratios and 18 kinetic texture features with *P* values were assessed via the Spearman rank correlation, which is a nonparametric measure of statistical dependence between 2 variables. Statistical significance was defined as a P value $< .05$. The Kruskal-Wallis test, a nonparametric method for testing the equality of population medians among groups, was used to determine whether the median feature value differed significantly between survival groups. Texture feature ratios were assessed with Kaplan-Meier and ROC analyses to measure their associations with overall survival. Each feature ratio was dichotomized on the basis of an optimum cutoff value derived from ROC analysis. Survival difference between the groups was assessed via a log-rank test. Multivariate Cox proportional hazards regression analysis was performed to assess the texture feature ratios as predictors, independent of volume, age, and Karnof-

sky Performance Status, for overall survival.[18] In this study, MATLAB Version 8.0 (MathWorks, Natick, Massachusetts) and R software (R Project for Statistical Computing, http://www.r-project.org) were used for statistical analyses.

RESULTS

The texture features with and without Laplacian-of-Gaussian filtration were obtained, and the ratios between the Laplacian-of-Gaussian filtered and unfiltered features were calculated for the CEL and NEL regions, respectively. For the CEL, there were strong positive correlations between homogeneity and inverse difference moment (IDM) ($r = 0.99$, $P < .001$), and there were strong negative correlations between angular second moment (ASM) and entropy ($r = -0.94$, $P < .001$). For the NEL, there were strong positive correlations between the variance and sum average ($r = 0.94$, $P < .001$) and between the variance and sum variance ($r = 0.95$, $P < .001$) and between the sum average and sum variance ($r = 0.99$, $P < .001$). The summaries of the Spearman rank correlations and *P* values for the CEL and NEL are listed in Tables 2 and 3. Information about the 4 most significant feature ratios, such as homogeneity, ASM, IDM, and entropy for the CEL and skewness, variance, sum average, and sum variance for the NEL, are listed in Tables 4 and 5.

The areas under the ROC curve for each significant predictor of 12-month survival status (survival class) and corresponding *P* values were assessed and are summarized in Table 6. The areas under the curve for the CEL-derived feature ratios were 0.83 for homogeneity, 0.76 for ASM, 0.81 for IDM, and 0.80 for entropy. The areas under the curve for the NEL-derived feature ratios were 0.80 for skewness, 0.72 for variance, 0.72 for sum average, and 0.71 for sum variance. There was also a significant difference between survival classes for homogeneity ($P = .008$), ASM ($P = .036$), IDM ($P = .013$), and entropy ($P = .015$) from the CEL. However, no significant difference was found for the NEL-derived texture feature ratios (Tables 7 and 8).

Kaplan-Meier survival curves for groups induced by the ROC-optimized cutoffs for the CEL-derived homogeneity, ASM, IDM, and entropy feature ratios were significantly different ($P < .05$) (Fig 2). The optimal cutoff points were 1.118 ($P = .008$) for homogeneity, 0.971 ($P = .003$) for ASM, 1.085 ($P = .013$) for IDM, and 1.00 ($P = .008$) for entropy. The median survival (in months) for each of the groups induced by the cutoff is listed in Table 9 for the CEL. Multivariate Cox proportional hazards regression analysis (including clinical variables such as volume, age, Karnofsky Performance Status) showed that CEL-derived homogeneity, ASM, IDM, and entropy feature ratios had *P* values of .004, .012, .006, and .001, respectively, indicating that these feature ratios were independent predictors of overall survival. For the NEL, only skewness and variance feature ratios had *P* values $< .05$ (Table 10). From the kinetic texture analysis, only the Haralick correlation feature showed a *P* value close to .05. All

Table 7: Kruskal-Wallis test for the CEL texture feature ratios (across survival classes)

	Homogeneity	ASM	IDM	Entropy
P value	.008	.036	.013	.015

Table 8: Kruskal-Wallis test for the NEL texture feature ratios (across survival classes)

	Skewness	Variance	Sum Average	Sum Variance
P value	.13	.19	.26	.21

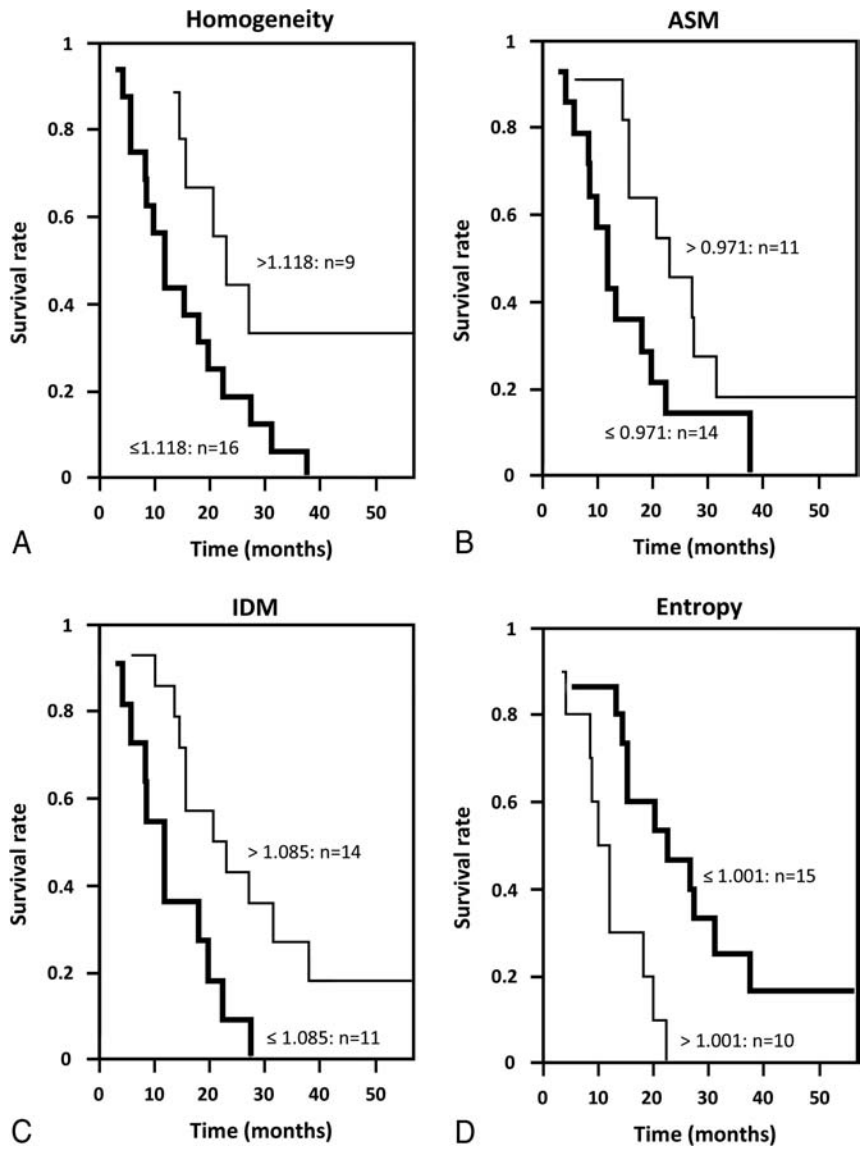

FIG 2. Kaplan-Meier survival curves from ROC-induced cutoffs for CEL-derived feature ratios: homogeneity (*A*), ASM (*B*), IDM (*C*), and entropy (*D*).

Table 9: Kaplan-Meier analysis based on ROCs for the CEL texture feature ratios (only significant features are shown)

		Median (mo) (No. of Cases)		
	Threshold	Above Threshold	Below Threshold	*P* Value
Homogeneity	1.118	23 (9)	12 (16)	.008
ASM	0.971	23 (11)	12 (14)	.003
IDM	1.085	22 (14)	12 (11)	.013
Entropy	1.001	11 (10)	23 (15)	.008

Table 10: Multivariate Cox proportional hazards regression analysis (in a model that includes volume, age, KPS) for the CEL- and NEL-derived rCBV texture feature ratios

		95% Confidential		
	Hazard Ratio	Interval		*P* Value
CEL				
Homogeneity	0.019	0.001	0.272	.004
ASM	0.121	0.023	0.632	.012
IDM	0.068	0.010	0.457	.006
Entropy	96.895	7.179	1307.8	<.001
NEL				
Skewness	0.79	0.638	0.977	.029
Variance	1.507	1.011	2.245	.044
Sum average	2.203	0.996	5.024	.060
Sum variance	1.207	0.929	1.568	.159

Note:—KPS indicates Karnofsky Performance Status.

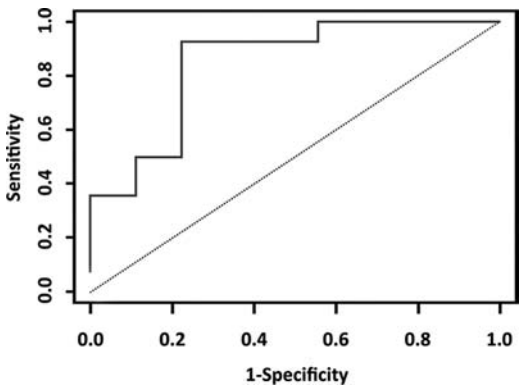

FIG 3. ROC curve for prediction of survival status based on correlation features from kinetic texture analysis. The area under the curve value was 0.849 and the 2.5% and 97.5% confidence intervals for the Mann-Whitney statistic were 0.667 and 0.952.

Table 11: AUC for the correlation feature from kinetic texture analysis

			Confidence Interval	
	AUC	*P* Value	2.5%	97.5%
Mann-Whitney	0.849	.003	0.667	0.952

Note:—AUC indicates area under the curve.

other features were not statistically significant ($P > .1$). Figure 3 shows the ROC curve for the kinetic Haralick correlation feature, with an area under the curve of 0.849 and a *P* value of .003 (Table 11).

DISCUSSION

Several studies have shown that the hemodynamic parameter rCBV from DSC-MR imaging is an important prognostic imaging biomarker that provides useful prognostic information in patients with GBM.[11,19] Boxerman et al[13] have shown that the rCBV measurement is significantly correlated with GBM grade and can be used to predict time to progression and clinical outcome. Jain et al[20] showed that increased maximum rCBV in CEL is associated with an increased risk of death and that high rCBV in NEL and wild-type epidermal growth factor receptor mutation are associated with poor survival. In our study, we applied texture analysis to the normalized hemodynamic parameter rCBV values from the ROIs of the CEL and NEL in the rCBV map to investigate the association of the perfusion MR imaging–derived image textural feature ratios with overall survival in GBM.

Laplacian-of-Gaussian filter is a precalculated filter obtained from combining the Gaussian and Laplacian filters and is useful for detecting edges in images.[10] The texture feature ratios in our study represent the quantitative relationship of features between the Laplacian-of-Gaussian filtered images and the unfiltered images.[14] In a preliminary study, these feature ratios demonstrated lower dependence on scanner type compared with the original features. The purpose of the use of feature ratios (aside from following previous literature, such as Ganeshan et al[21]) is to minimize the effects of any potential systematic variations in MR images from various patients across different scanning or acquisition protocols. With these texture feature ratios, statistically significant differences were found for CEL-derived homogeneity, ASM, IDM, and entropy feature ratios between survival classes that dichotomized survival at 12 months. This finding implies that these feature ratios are associated with overall survival rates of GBM.

First-order statistics such as SD, skewness, and kurtosis describe the probability distributions of the pixel intensities; and second-order statistics, such as Haralick features, describe the spatial relationship between pairs of pixels. Tumor-derived pixel-based heterogeneity can be measured by using first- and second-order statistics. Many researchers have sought to determine whether such heterogeneity is associated with malignancy.[22] Several studies of ^{18}F-FDG PET/CT have suggested that tumor heterogeneity might provide better prognostic information, tissue characterization, and tumor segmentation.[23]

Our results from the Kruskal-Wallis test indicate that the texture feature ratios for homogeneity ($P = .008$), ASM ($P = .036$), IDM ($P = .013$), and entropy ($P = .015$) from the CEL had a strong correlation with the survival group, suggesting that these texture feature ratios are associated with overall survival and could provide additional prognostic information. In addition, the results of kinetic texture analysis showed that the correlation feature from kinetic texture analysis had a high predictive (area under the curve) value (0.85). Conversely, the texture feature ratios for the NEL exhibited no significant correlation with overall survival.

There were several limitations in our study. First, this was a retrospective study performed on a publicly available patient subset, consisting of data acquired on multiple MR imaging systems with varying protocols. A study that evaluates the robustness of these feature ratios for the survival prediction task across scanning protocols, scanner resolutions, and a larger sample size is essential to establishing their predictive value. A large-sample-size study will also enable the application of appropriate multiple testing corrections to identify reliably predictive features (there is no cor-

rection for multiple testing in the current study because of its exploratory nature). In addition, variable treatment regimens with surgery, radiation, and chemotherapy may have a confounding effect on the survival rates of patients. A separate dataset with uniformity of treatment regimens is the next step to validating the predictive value of these feature ratios. Furthermore, incorporating molecular markers like *IDH* mutation status or molecular subtype can be useful to assess the additional predictive value of imaging-based measurements to existing molecular markers. The inclusion of other modalities or contrasts such as T1 postcontrast or FLAIR MR imaging is a great area for future work as well.

Previous studies have suggested that textural features can be used in several areas of image analysis, such as segmentation, classification, and prediction of tissue abnormality. In this study, we found that several feature ratios obtained from the rCBV map, in addition to kinetic textures, provided useful information for predicting the 12-month survival status from the CEL and NEL regions of patients with GBM.

CONCLUSIONS

The methods developed in this work are sufficiently general and might be applicable to other disease processes and sites where perfusion MR imaging is used for assessment of disease or treatment response. Our study presents the results of an exploratory study demonstrating the relationship of texture feature ratios (from 1D and 2D texture features and kinetic texture features) with survival in patients with GBM. These findings suggest that texture feature ratios from perfusion MR imaging data are promising as a clinical prognostic tool.

APPENDIX

We provide detailed equations for 2D texture features such as 13 Haralick texture features and homogeneity features in equations A1 to A14.

The angular second moment measures the homogeneity of an image. A more homogeneous image has fewer gray levels with higher pixel elements of the GLCM and sum of square values:

A1) $$f_1 = \sum_{i=1}^{N_g} \sum_{j=1}^{N_g} p(i,j)^2,$$

where N_g is the number of gray levels present in an image and $p(i, j)$ corresponds to the $(i, j)^{th}$ element of the GLCM.

Contrast measures the luminance (differences in gray-level intensity values) present in an image:

A2) $$f_2 = \sum_{k=0}^{N_g-1} k^2 \left(\sum_{i=1}^{N_g} \sum_{j=1}^{N_g} p(i,j) \right), \; k = |i - j|.$$

Correlation measures the gray-level linear dependence of pixels at specified positions:

A3) $$f_3 = \frac{1}{\sigma_x \sigma_y} \sum_{i=1}^{N_g} \sum_{j=1}^{N_g} (ij) p(i,j) - \mu_x \mu_y$$

Variance differentially weighs the gray levels that significantly deviate from the mean value of $p(i, j)$:

A4) $$f_4 = \sum_{i=1}^{N_g} \sum_{j=1}^{N_g} (i - \mu)^2 \, p(i,j).$$

The local homogeneity or inverse difference moment enhances local homogeneous regions by reducing the weight of inhomogeneous regions where $i \neq j$:

A5) $$f_5 = \sum_{i=1}^{N_g} \sum_{j=1}^{N_g} \frac{1}{1 + (i - j)^2} \, p(i,j).$$

The sum and difference histograms form the principal axes of the second-order probability attenuation function. The sum average (A6) and variance (A7) quantify the mean and extent of the sum histogram, respectively. The sum entropy (A8) and difference entropy (A11) measure the homogeneity of the sum and difference histograms, respectively.

Sum average:

A6) $$f_6 = \sum_{k=0}^{2N_g-2} k \times p_{x+y}(k),$$

Sum variance:

A7) $$f_7 = \sum_{k=0}^{2N_g-2} (k - f_8)^2 \, p_{x+y}(k).$$

Sum entropy:

A8) $$f_8 = -\sum_{k=0}^{2N_g-2} p_{x+y}(k) \log(P_{x+y}(k)).$$

Entropy quantifies the homogeneity of the image, suggesting that homogeneous regions have lower entropy values:

A9) $$f_9 = -\sum_{i=1}^{N_g} \sum_{j=1}^{N_g} p(i,j) \log(p(i,j)).$$

Difference variance:

A10) $$f_{10} = \sum_{k=0}^{N_g-1} \left[\left(k - \sum_{l=0}^{N_g-1} l \times P_{|x-y|}(k) \right)^2 \right] p_{|x+y|}.$$

Difference entropy:

A11) $$f_{11} = -\sum_{k=0}^{N_g-1} p_{|x-y|}(k) \log(P_{|x-y|}(k)).$$

Information measure of correlation I and II:

A12) $$f_{12} = \frac{\left(f_9 + \sum_{i=1}^{N_g} \sum_{j=1}^{N_g} P_{(i,j)} \log[p_{(i)} p_{(j)}] \right)}{\sum_{g=1}^{N_g} p_{(g)} \log[p_{(g)}]},$$

A13)

$$f_{13} = \sqrt{1 - \exp\left[-2 \left| -\sum_{i=1}^{N_g} \sum_{j=1}^{N_g} p_{(i)} p_{(j)} \log[p_{(i)} p_{(j)}] - f_9 \right| \right]}.$$

In addition to the Haralick texture features, we added a homogeneity feature that measures the closeness of the distribution of elements in the GLCM to the GLCM diagonal.

A14) $$f_{14} = \sum_{i=1}^{N_g} \sum_{j=1}^{N_g} \frac{1}{1+(i-j)} p(i,j).$$

The definitions for $p_{x+y}(k)$ and $p_{|x+y|}(k)$ are given in Equations A15 and A16, respectively:

A15) $$p_{x+y}(k) = \sum_{i=1}^{N_g} \sum_{j=1}^{N_g} p(i,j),\ k = i + j,$$

A16) $$p_{|x-y|}(k) = \sum_{i=1}^{N_g} \sum_{j=1}^{N_g} p(i,j),\ k = |i - j|.$$

ACKNOWLEDGMENTS

We thank Ms Markeda Wade for scientific editing.

Disclosures: Joonsang Lee—*RELATED*: *Grant*: National Cancer Institute (P30 CA016672). Arvind Rao—*UNRELATED*: *Board Membership*: GTCBio, *Comments*: Scientific Advisory Board (no compensation).

REFERENCES

1. Johnson DR, O'Neill BP. **Glioblastoma survival in the United States before and during the temozolomide era.** *J Neurooncol* 2012;107:359–64 CrossRef Medline
2. Mazurowski MA, Desjardins A, Malof JM. **Imaging descriptors improve the predictive power of survival models for glioblastoma patients.** *Neuro Oncol* 2013;15:1389–94 CrossRef Medline
3. Chen W, Giger ML, Bick U, et al. **Automatic identification and classification of characteristic kinetic curves of breast lesions on DCE-MRI.** *Med Phys* 2006;33:2878–87 CrossRef Medline
4. Liu X, Wang D. **Image and texture segmentation using local spectral histograms.** *IEEE Trans Image Process* 2006;15:3066–77 CrossRef Medline
5. Cheng NM, Fang YH, Chang JT, et al. **Textural features of pretreatment 18F-FDG PET/CT images: prognostic significance in patients with advanced T-stage oropharyngeal squamous cell carcinoma.** *J Nucl Med* 2013;54:1703–09 CrossRef Medline
6. Tixier F, Le Rest CC, Hatt M, et al. **Intratumor heterogeneity characterized by textural features on baseline 18F-FDG PET images predicts response to concomitant radiochemotherapy in esophageal cancer.** *J Nucl Med* 2011;52:369–78 CrossRef Medline
7. Cook GJ, Yip C, Siddique M, et al. **Are pretreatment 18F-FDG PET tumor textural features in non-small cell lung cancer associated with response and survival after chemoradiotherapy?** *J Nucl Med* 2013;54:19–26 CrossRef Medline
8. Agner SC, Soman S, Libfeld E, et al. **Textural kinetics: a novel dynamic contrast-enhanced (DCE)-MRI feature for breast lesion classification.** *J Digit Imaging* 2011;24:446–63 CrossRef Medline
9. Haralick RM, Shanmugam K, Dinstein IH. **Textural features for image classification.** *IEEE Systems, Man, and Cybernetics Society* 1973;SMC-3:610–21 CrossRef
10. Ganeshan B, Miles KA, Young RC, et al. **Texture analysis in noncontrast enhanced CT: Impact of malignancy on texture in apparently disease-free areas of the liver.** *Eur J Radiol* 2009;70:101–10 CrossRef Medline
11. Jain R, Poisson L, Narang J, et al. **Genomic mapping and survival prediction in glioblastoma: molecular subclassification strengthened by hemodynamic imaging biomarkers.** *Radiology* 2013;267:212–20 CrossRef Medline
12. Affronti ML, Heery CR, Herndon JE, et al. **Overall survival of newly diagnosed glioblastoma patients receiving carmustine wafers followed by radiation and concurrent temozolomide plus rotational multiagent chemotherapy.** *Cancer* 2009;115:3501–11 CrossRef Medline
13. Boxerman JL, Schmainda KM, Weisskoff RM. **Relative cerebral blood volume maps corrected for contrast agent extravasation significantly correlate with glioma tumor grade, whereas uncorrected maps do not.** *AJNR Am J Neuroradiol* 2006;27:859–67 Medline
14. Ng F, Ganeshan B, Kozarski R, et al. **Assessment of primary colorectal cancer heterogeneity by using whole-tumor texture analysis: contrast-enhanced CT texture as a biomarker of 5-year survival.** *Radiology* 2013;266:177–84 CrossRef Medline
15. Renzetti F, Zortea L. **Use of a gray level co-occurrence matrix to characterize duplex stainless steel phases microstructure.** *F&IS* 2011;16:43–51 CrossRef
16. Borg I, Groenen PJ. *Modern Multidimensional Scaling: Theory and Applications.* Berlin: Springer-Verlag; 2005
17. Bosca R, Johnson V, Jackson E. **SU-E-QI-18: QUATTRO: an open-source software package for quantitative imaging applications in assessing treatment response.** *Med Phys* 2014;41:380–81 CrossRef
18. Zinn PO, Sathyan P, Mahajan B, et al. **A novel volume-age-KPS (VAK) glioblastoma classification identifies a prognostic cognate microRNA-gene signature.** *PLoS One* 2012;7:e41522 CrossRef Medline
19. Law M, Young RJ, Babb JS, et al. **Gliomas: predicting time to progression or survival with cerebral blood volume measurements at dynamic susceptibility-weighted contrast-enhanced perfusion MR imaging.** *Radiology* 2008;247:490–98 CrossRef Medline
20. Jain R, Poisson LM, Gutman D, et al. **Outcome prediction in patients with glioblastoma by using imaging, clinical, and genomic biomarkers: focus on the nonenhancing component of the tumor.** *Radiology* 2014;272:484–93 CrossRef Medline
21. Ganeshan B, Panayiotou E, Burnand K, et al. **Tumour heterogeneity in non-small cell lung carcinoma assessed by CT texture analysis: a potential marker of survival.** *Eur Radiol* 2012;22:796–802 CrossRef Medline
22. Bedard PL, Hansen AR, Ratain MJ, Siu LL. **Tumour heterogeneity in the clinic.** *Nature* 2013;501:355–64 CrossRef Medline
23. Yu H, Caldwell C, Mah K, et al. **Automated radiation targeting in head-and-neck cancer using region-based texture analysis of PET and CT images.** *Int J Radiat Oncol Biol Phys* 2009;75:618–25 CrossRef Medline

Diagnostic and Prognostic Value of ^{11}C-Methionine PET for Nonenhancing Gliomas

K. Takano, M. Kinoshita, H. Arita, Y. Okita, Y. Chiba, N. Kagawa, Y. Fujimoto, H. Kishima, Y. Kanemura, M. Nonaka, S. Nakajima, E. Shimosegawa, J. Hatazawa, N. Hashimoto, and T. Yoshimine

ABSTRACT

BACKGROUND AND PURPOSE: Noninvasive radiologic evaluation of glioma can facilitate correct diagnosis and detection of malignant transformation. Although positron-emission tomography is considered valuable in the care of patients with gliomas, ^{18}F-fluorodeoxyglucose and ^{11}C-methionine have reportedly shown ambiguous results in terms of grading and prognostication. The present study compared the diagnostic and prognostic capabilities of diffusion tensor imaging, FDG, and ^{11}C-methionine PET in nonenhancing gliomas.

MATERIALS AND METHODS: Thirty-five consecutive newly diagnosed, histologically confirmed nonenhancing gliomas that underwent both FDG and ^{11}C-methionine PET were retrospectively investigated (23 grade II and 12 grade III gliomas). Apparent diffusion coefficient, fractional anisotropy, and tumor-to-normal tissue ratios of both FDG and ^{11}C-methionine PET were compared between grade II and III gliomas. Prognostic values of these parameters were also tested by using progression-free survival.

RESULTS: Grade III gliomas showed significantly higher average tumor-to-normal tissue and maximum tumor-to-normal tissue than grade II gliomas in ^{11}C-methionine ($P = .013$, $P = .0017$, respectively), but not in FDG-PET imaging. There was no significant difference in average ADC, minimum ADC, average fractional anisotropy, and maximum fractional anisotropy. ^{11}C-methionine PET maximum tumor-to-normal tissue ratio of 2.0 was most suitable for detecting grade III gliomas among nonenhancing gliomas (sensitivity, 83.3%; specificity, 73.9%). Among patients not receiving any adjuvant therapy, median progression-free survival was 64.2 ± 7.2 months in patients with maximum tumor-to-normal tissue ratio of <2.0 for ^{11}C-methionine PET and 18.6 ± 6.9 months in patients with maximum tumor-to-normal tissue ratio of >2.0 ($P = .0044$).

CONCLUSIONS: ^{11}C-methionine PET holds promise for World Health Organization grading and could offer a prognostic imaging biomarker for nonenhancing gliomas.

ABBREVIATIONS: MET = ^{11}C-methionine; PFS = progression-free survival; T/N = tumor-to-normal tissue; T/N_{ave} = average tumor-to-normal tissue; T/N_{max} = maximum tumor-to-normal tissue

Gliomas are categorized from grade I to IV according to the World Health Organization classification, which is based on histopathologic findings.[1] Although molecular and genetic information is gaining importance,[2] therapeutic strategy is still heavily based on World Health Organization grading. Biopsy is occasionally chosen instead of surgical resection due to various factors such as tumor location, and the heterogeneous features of the tumor often complicate accurate diagnosis, leading to undergrading of the tumor.[3,4]

MR imaging is one of the noninvasive methods for tumor grading and is now considered the criterion standard imaging procedure for glioma.[5] Although contrast enhancement of the tumor is regarded as a hallmark of high-grade glioma, anaplastic tumors and even glioblastoma can lack contrast enhancement. Previous reports have shown that 32%–42% of nonenhancing gliomas are high-grade. In other words, as many as 92%–100% of

Received March 2, 2015; accepted after revision May 7.

From the Department of Neurosurgery (K.T., M.K.), Osaka Medical Center for Cancer and Cardiovascular Diseases, Osaka, Japan; Departments of Neurosurgery (K.T., M.K., H.A., Y.C., N.K., H.K., N.H., T.Y.) and Nuclear Medicine and Tracer Kinetics (E.S., J.H.), Osaka University Graduate School of Medicine, Osaka, Japan; Department of Neurosurgery (Y.O., Y.K., M.N., S.N.) and Division of Regenerative Medicine (Y.K.), Institute for Clinical Research, Osaka National Hospital, National Hospital Organization, Osaka, Japan; Department of Neurosurgery (Y.C.), Kansai Rosai Hospital, Itami, Japan; Department of Neurosurgery (Y.F.), Osaka Neurological Institute, Osaka, Japan; and Department of Neurosurgery (M.N.), Kansai Medical University, Osaka, Japan.

This investigation was supported by the Aichi Cancer Research Foundation, the SENSIN Medical Research Foundation, the Life Science Foundation of Japan, the Japanese Foundation for Multidisciplinary Treatment of Cancer, and Japan Society for the Promotion of Science KAKENHI (25462256).

Please address correspondence to Manabu Kinoshita, MD, PhD, Department of Neurosurgery, Osaka Medical Center for Cancer and Cardiovascular Diseases, 1-3-3 Nakamichi, Higashinari-ku, Osaka 537-8511, Japan; e-mail: m-kinoshita@nsurg.med.osaka-u.ac.jp

Indicates open access to non-subscribers at www.ajnr.org
Indicates article with supplemental on-line tables.
Indicates article with supplemental on-line photo.
http://dx.doi.org/10.3174/ajnr.A4460

nonenhancing gliomas are grade II or III gliomas.[6–11] As a result, nonenhancing glioma contains various tumor grades ranging from grade II to IV. In the context of nonenhancing tumor, accurate preoperative diagnosis may change the initial management of the tumor, and if grade III is suspected, a more aggressive surgical resection, rather than biopsy, may be pursued. This treatment strategy poses a challenge to physicians to achieve a correct preoperative diagnosis and leads to a need for additional imaging modalities to visualize tumor characteristics. Although previous investigations have attempted to solve this problem by using various advanced MR imaging techniques such as diffusion tensor imaging, perfusion-weighted imaging, and MR spectroscopy,[6,7,9,12] the clinical significance of these methods remains controversial. In this context, positron-emission tomography is considered a promising imaging technique supplementing MR imaging in the care of patients with gliomas. Past investigations, however, have analyzed mixtures of both high- and low-grade gliomas for their analyses, leading to inconclusive results in terms of its usefulness in clinical practice. The most important question to be answered is the clinical impact of PET on nonenhancing gliomas, in which tumor grading is difficult using conventional MR imaging alone. Hence, the current investigation was conducted to test the hypothesis that PET could be useful for both radiologic tumor grading and prognostication of nonenhancing gliomas. More specifically, our aim was to test the hypothesis that ^{11}C-methionine (MET) PET not only has greater specificity and positive predictive power than ^{18}F-fluorodeoxyglucose-PET for determination of grade in nonenhancing gliomas but also predicts progression-free survival in newly diagnosed nonenhancing gliomas receiving standard therapy. The results obtained from PET were further compared with apparent diffusion coefficient obtained by DTI.

MATERIALS AND METHODS

Patients

Thirty-five patients with newly diagnosed, histologically confirmed nonenhancing supratentorial gliomas were retrospectively collected (18 men, 17 women; mean age, 39.9 ± 15.8 years; World Health Organization grade II, $n = 23$; grade III, $n = 12$). Four of the 23 grade II gliomas and 3 of the 12 grade III gliomas showed oligodendrocytic components. Histologic grading was performed according to the World Health Organization criteria after partial (<95% tumor removal) or total (≥95% tumor removal) resection of the lesion or stereotactic biopsy (total resection, $n = 11$; partial resection, $n = 21$; stereotactic biopsy, $n = 3$). Three patients with grade II gliomas and all patients with grade III gliomas received adjuvant therapy postoperatively, such as radiation therapy alone, radiation therapy with chemotherapy, or chemotherapy alone. Both FDG and MET PET were performed preoperatively except in 1 case, in which PET was performed 69 days after stereotactic biopsy. The mean duration of follow-up was 29.6 ± 18.1 months. "Tumor progression" was defined as either distinct enlargement of high-intensity lesions on T2 or fluid-attenuated inversion recovery imaging or the appearance of a contrast-enhancing lesion. "Progression-free survival" was defined as the duration between surgery and tumor progression. Detailed characteristics of patients are given in On-line Table 1. Use of clinical data was approved for research purposes by the local institutional review board.

PET Methods

PET studies were performed by using an Eminence-G (Shimadzu, Kyoto, Japan). Synthesis of MET was performed according to the method described by Berger et al,[13] and MET was injected intravenously at a dose of 3 MBq/kg. Tracer accumulation was recorded for 12 minutes in 59 or 99 transaxial sections over the entire brain. Summed activity from 20 to 32 minutes after tracer injection was used for image reconstruction. For FDG-PET, after a 10-minute transmission scan, an amount of FDG determined in proportion to weight was injected intravenously (3.7 MBq/kg). Tracer accumulation was recorded in 3D mode for 12 minutes in 59 or 99 transaxial sections from the entire brain. Total activity from 45 to 57 minutes after tracer injection was used for image reconstruction. Both images were stored in 256 × 256 × 59 or 99 anisotropic voxels, with each voxel being 1 × 1 × 2.6 mm. The mean interval between preceding PET and an operation was 60.4 ± 68.8 days (range, −69 to 347 days).

MR Imaging

All patients were studied by using either a 1.5T or 3T MR imaging scanner within a week before the operation. T1-weighted imaging with gadolinium enhancement was used to select patients with nonenhancing gliomas. T2-weighted or FLAIR images were acquired in all cases for delineation of tumors. Diffusion tensor imaging was performed in all except 4 patients (21 with grade II glioma and 10 with grade III glioma) by using a 3T MR imaging scanner (Signa; GE Healthcare, Milwaukee, Wisconsin). Images were acquired by using a single-shot echo-planar imaging technique with TE = 80 and TR = 10,000. Diffusion gradient encoding in 25 directions with b=2000 s/mm^2 and an additional measurement without the diffusion gradient (b=0 s/mm^2) were performed.[14] A parallel imaging technique was used to record data with a 128 × 128 spatial resolution for a 260 × 260 mm FOV. Fifty sections were obtained, with a section thickness of 3 mm and no intersection gap. Apparent diffusion coefficient was processed by using the Diffusion Toolkit (TrackVis; http://www.trackvis.org/dtk/).

Image Fusion and Analysis

After all images had been obtained, PET images, ADC, and FA maps were all registered to T2 or FLAIR images by using VINCI image analysis software (http://www.nf.mpg.de/vinci/). Correct coregistration of images was visually confirmed. After image registration was complete, all image sets were converted to anisotropic images (256 × 256 × 59 or 99, 1 × 1 × 2.6 mm), enabling further analysis. For PET images, the standard uptake value of the contralateral tumor-unaffected gray matter in the axial plane at the level of the thalamus was averaged, and the derived value was used to normalize standard uptake value in a voxelwise manner, enabling reconstruction of tumor-to-normal tissue (T/N) ratio images. All datasets were exported to in-house software written in Matlab 7.14 (MathWorks, Natick, Massachusetts) for further analysis. High-intensity lesions delineated in T2 or FLAIR images

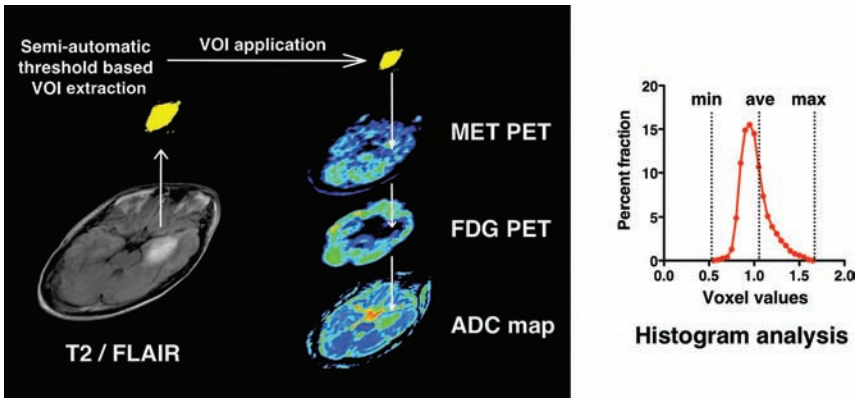

FIG 1. Schematic overview of the image-analysis process. High-intensity lesions on T2/FLAIR imaging were semiautomatically segmented in 3D by an image-intensity threshold. The segmented voxels of interest were applied to registered PET images and ADC fractional anisotropy maps, followed by calculation of the average and maximum or minimal values of each parameter within the VOI.

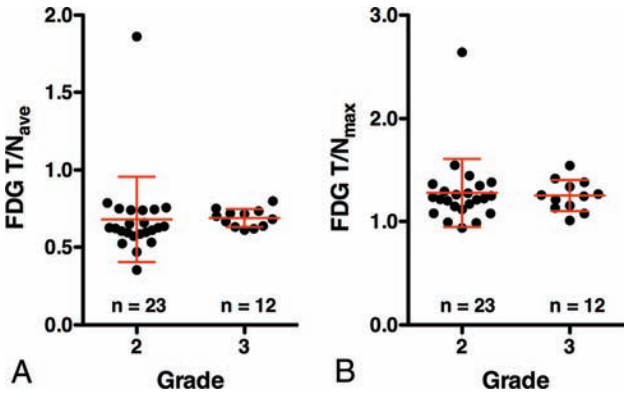

FIG 2. T/N_{ave} (*A*) and T/N_{max} (*B*) of FDG-PET in patients with grade II and III gliomas. No significant difference was seen between grade II and III gliomas ($P = .11$ and 0.72, respectively).

Table 1: Various imaging modalities and tumor grade

Imaging Parameters	Grade II	Grade III	*P* Value
T/N_{ave} of FDG	0.68 ± 0.28	0.69 ± 0.06	.11
T/N_{max} of FDG	1.28 ± 0.33	1.25 ± 0.15	.72
T/N_{ave} of MET	1.12 ± 0.18	1.31 ± 0.21	.013[a]
T/N_{max} of MET	1.91 ± 0.62	2.69 ± 0.66	.0017[a]
ADC_{ave} ($\times 10^{-3}mm^2/s$)	1.09 ± 0.25	0.92 ± 0.22	.13
ADC_{min} ($\times 10^{-3}mm^2/s$)	0.18 ± 0.26	0.18 ± 0.23	.82

Note:—ADC_{ave} indicates average ADC; ADC_{min}, minimum ADC.
[a] $P < .05$.

were semiautomatically segmented in 3D by image-intensity threshold as voxels of interest. Average tumor-to-normal tissue (T/N_{ave}) and maximum tumor-to-normal tissue values (T/N_{max}) of FDG and MET PET, average ADC, and minimum ADC within the VOI were calculated (Fig 1 and On-line Fig 1). In particular, the same VOIs were applied to all 4 images. All values are reported as mean ± SD.

Statistical Analysis

Statistical analysis was performed by using JMP Version 10 software (SAS Institute, Cary, North Carolina). A threshold level of .05 was established for statistical significance. The Mann-Whitney *U* test was used for group comparisons. Receiver operating characteristic analysis was performed to compare the performance of each imaging parameter in distinguishing grade III from grade II gliomas. The duration of progression-free survival (PFS; reported as median ± standard error) was analyzed by Kaplan-Meier curves, and log-rank testing was performed to determine the statistical significance of any observed differences in PFS between groups. Overall survival was not analyzed because most patients have not yet reached this end point.

RESULTS

FDG Uptake is Not Statistically Different between Grade II and III Nonenhancing Gliomas

The T/N_{ave} of FDG-PET for grade II and III gliomas was 0.68 ± 0.28 and 0.69 ± 0.06, and T/N_{max} was 1.28 ± 0.33 and 1.25 ± 0.15, respectively (Fig 2 and Table 1). These differences were not significant ($P = .11$ and $P = .72$, respectively). Receiver operating characteristic analysis showed that the T/N_{ave} of FDG-PET performed best at a cutoff value of 0.61, with an area under the curve of 0.67 for discriminating grade III from grade II gliomas (Table 2).

MET Uptake Was Statistically Significantly Higher in Grade III Nonenhancing Gliomas Than in Grade II Nonenhancing Gliomas

The T/N_{ave} of MET PET for grade II and III gliomas was 1.12 ± 0.18 and 1.31 ± 0.21, and T/N_{max} was 1.91 ± 0.62 and 2.69 ± 0.66, respectively (Fig 3 and Table 1). Grade III gliomas showed significantly higher MET T/N_{ave} and T/N_{max} than grade II gliomas ($P = .013$, $P = .0017$, respectively). Receiver operating characteristic analysis showed that the T/N_{max} of MET PET performed best at a cutoff value of 2.0, with an area under the curve of 0.83 for discriminating grade III from grade II gliomas (Fig 4 and Table 2).

ADC Did Not Show a Statistically Significant Difference between Grade II and III Nonenhancing Gliomas

Average ADCs for grade II and III gliomas were 1.09 ± 0.25 and 0.92 ± 0.22, and minimum ADCs were 0.18 ± 0.26 and 0.18 ± 0.23, respectively (Table 1). These differences were not statistically significant ($P = .13$ and $P = .82$, respectively). Receiver operating characteristic analysis based on ADC further supported these findings (Table 2).

MET PET Is Prognostic for PFS in Nonenhancing Gliomas

The median PFS for patients with grade II gliomas was 64.2 ± 6.0 months (95% CI, 20.6–64.2 months), while the median PFS for patients with grade III glioma was 36.3 ± 4.9 months (95% CI, 4.5 months not available). No difference in PFS was evident between grade II and III gliomas ($P = .32$) (Fig 5*A*).

On the other hand, median PFS was 64.2 ± 6.3 months (95% CI, 34.0–64.2 months) for patients with T/N_{max} of <2.0 for MET PET ($n = 19$) and 18.8 ± 4.0 months (95% CI, 7.4–37.0 months)

Table 2: ROC analysis to discriminate tumor grade

Imaging Parameters	No.	Cutoff Value	AUC	Sensitivity	Specificity	PPV	NPV	Accuracy
T/N_{ave} of FDG	35	0.611	0.67	1.000	0.435	0.480	1.000	0.629
T/N_{max} of FDG	35	1.54	0.46	1.000	0.087	0.364	1.000	0.400
T/N_{ave} of MET	35	1.10	0.76	1.000	0.565	0.545	1.000	0.714
T/N_{max} of MET	35	2.01	0.83	0.833	0.739	0.625	0.895	0.771
ADC_{ave} ($\times 10^{-3}mm^2/s$)	31	0.928	0.67	0.600	0.714	0.500	0.789	0.677
ADC_{min} ($\times 10^{-3}mm^2/s$)	31	0.057	0.47	0.500	0.667	0.417	0.737	0.613

Note:—AUC indicates area under the curve; PPV, positive predictive value; NPV, negative predictive value; ROC, receiver operating characteristic.

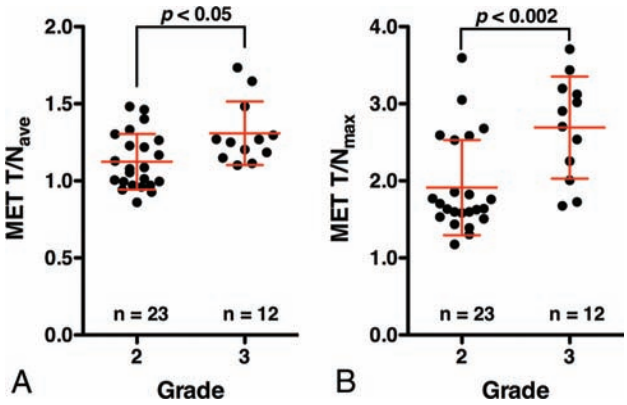

FIG 3. T/N_{ave} (*A*) and T/N_{max} (*B*) of MET PET in patients with grade II and III gliomas. Grade III gliomas show significantly higher T/N_{ave} and T/N_{max} than grade II gliomas ($P = .013$, $P = .0017$, respectively).

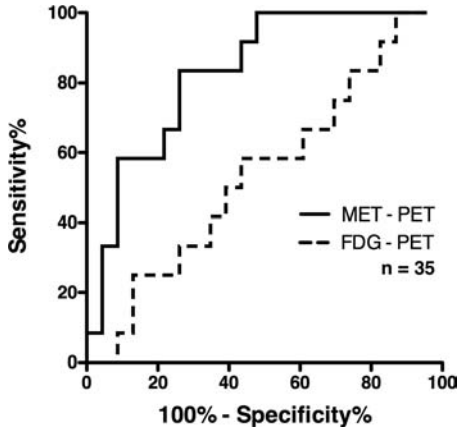

FIG 4. Receiver operating characteristic analysis of MET PET and FDG-PET T/N_{max} was used for discriminating grade III from grade II gliomas. The area under the curve was 0.83, and the sensitivity and specificity were 83.3% and 73.9% at a cutoff T/N_{max} of 2.0 for MET PET. FDG-PET was unable to discriminate grade III glioma from grade II.

for patients with T/N_{max} of >2.0 ($n = 16$). There was a statistically significant difference for the PFS between these groups ($P = .006$) (Fig 5*B*).

Because some patients underwent adjuvant therapy, which could affect PFS, such as radiation therapy alone, radiation therapy with chemotherapy, or chemotherapy alone, further analysis was performed for patients who did not receive any adjuvant therapy ($n = 20$, all grade II gliomas). Median PFS was 64.2 ± 7.2 months (95% CI, 34.0–64.2 months) for patients with T/N_{max} of <2.0 for MET PET ($n = 15$) and 18.6 ± 6.9 months (95% CI, 7.4–37.0 months) for patients with T/N_{max} of >2.0 ($n = 5$). This difference was statistically significant ($P = .0044$) (Fig 5*C*). On the other hand, MET PET was not prognostic among patients who received adjuvant therapy ($P = .37$). The above findings were confirmed even when PFS was calculated as the duration between PET examination and tumor progression (On-line Fig 2). Finally, MET PET was prognostic among patients with grade II gliomas but not among patients with grade III gliomas ($P = .016$ and $P = .22$, respectively). Detailed data are shown in On-line Table 2.

DISCUSSION

The utility of FDG-PET in glioma was reported in 1982 by Di Chiro et al,[15] followed by many reports confirming that FDG-PET is indeed useful for detection, grading, and prognostication for gliomas.[8,16-23] On the other hand, MET PET was first reported in 1983 by Bergström et al[24] as a useful imaging technique to delineate glioma. Because MET PET has a low normal cortical uptake and high uptake in gliomas, this method has been considered superior to FDG-PET for delineation of the lesion.[25-27]

However, reports on grading and prognostication of gliomas by MET PET have been conflicting. Some reports have claimed that FDG-PET is better for grading and prognostication than MET PET,[26,28-30] while others have claimed otherwise.[27,31-33] In theory, accumulation of MET is influenced not only by specific carrier-mediated uptake but also by passive diffusion in areas with a disrupted blood-brain barrier,[34-36] while background normal cortical uptake of the tracer markedly interferes with accumulation of FDG in brain tumors. One possible reason for the above-mentioned controversy could be the patient populations analyzed in those studies, in which both enhancing and nonenhancing tumors were analyzed together.[26-33] Moreover, from a clinical point of view, because contrast enhancement is one of the hallmarks of high-grade tumor, the most important clinical question to be answered would be the tumor grade in nonenhancing tumors, in which tumor grading is difficult by using conventional MR imaging alone.

When analysis was restricted to nonenhancing glioma by using a semiautomatic T2/FLAIR-based VOI segmentation, the presented results clearly proved the superb performance of MET PET for tumor grading (Figs 2–4 and Tables 1 and 2). Receiver operating characteristic analysis further revealed that T/N_{max} of MET PET was most efficient in extracting grade III gliomas among nonenhancing gliomas, with an area under the curve of 0.83 (Fig 4 and Table 2). These findings imply that MET PET could be a valuable noninvasive radiologic tool for making significant clinical judgments for nonenhancing gliomas because preoperative identification of grade III gliomas would justify clinicians putting those patients into radical treatment rather than biopsy or observation of the tumor. The considerable overlap of MET T/N between grade II and III gliomas (Fig 3), however, mandates cautious interpretation of MET PET to supplement conventional MR

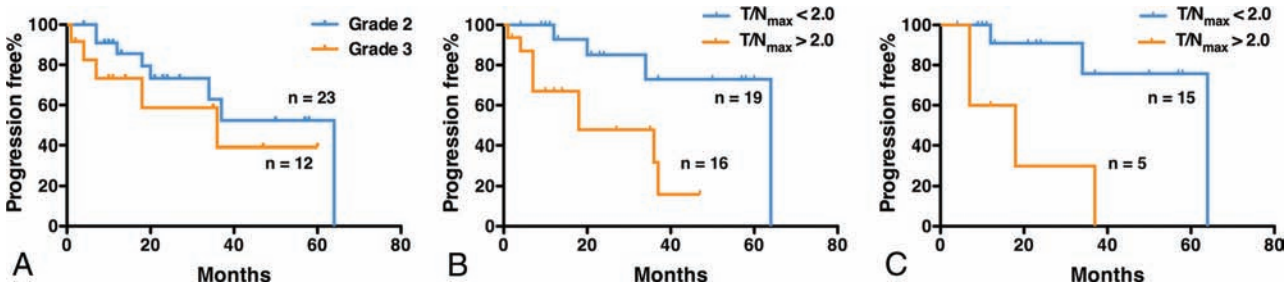

FIG 5. Progression-free survival analysis by tumor grade and MET PET results. Progression-free survival is shown in Kaplan-Meier curves according to tumor grade (*A*). Patients with T/N_{max} of <2.0 showed prolonged progression-free survival compared with those with T/N_{max} of >2.0 (*B*, $P = .006$). This was also true when the analysis was restricted to patients who received no adjuvant therapy (*C*, $P = .004$).

imaging for grading of nonenhancing gliomas. On the other hand, FDG-PET was not useful in this respect (Figs 2–4 and Tables 1 and 2).

Similar to FDG-PET, ADC obtained from DTI was also incompetent to distinguish both grade II and III nonenhancing gliomas (Tables 1 and 2). Because glioma grading by using DTI can be heavily affected by the method used for VOI or ROI design,[7,9,37,38] it could be that T2/FLAIR-based semiautomatic MR imaging intensity-based VOI segmentation was not sensitive for this purpose. Further investigation is indeed necessary to clarify the impact of the method used for VOI segmentation on analysis of both PET and MR imaging.

Finally, no significant difference in PFS was seen between grade II and III gliomas in our cohort. In the Long-Term Efficacy of Early versus Delayed Radiotherapy for Low-Grade Astrocytoma and Oligodendroglioma in Adults trial, a randomized controlled trial comparing early-versus-delayed radiation therapy for low-grade gliomas, median PFS was 5.3 years in the early radiation therapy group and 3.4 years in the delayed group.[39] Among grade III gliomas, on the other hand, median PFS was reported as 7.6–36 months for patients treated by radiation therapy and chemotherapy and 13–18 months for patients treated by using radiation therapy alone.[40-45] Considering that all except 3 patients with grade II gliomas were followed postoperatively with careful observation alone and that all except 1 patient with a grade III glioma were treated by using both radiation therapy and chemotherapy, PFS of our cohort for grade II and III gliomas seems to be in range with past studies. Early intervention by adjuvant therapy against grade III gliomas could have prolonged PFS of patients with grade III gliomas to a similar level of grade II gliomas. More important, MET PET was prognostic of PFS not only in all patients with nonenhancing gliomas but also in patients without adjuvant therapy; this outcome makes MET PET a potential prognostic imaging biomarker for nonenhancing gliomas.

Limitations of our study should also be noted. The present study compared radiologic with pathologic tumor grading under the assumption that correct pathologic diagnosis was obtained. Because there was only 1 patient in this cohort who was diagnosed as having grade II glioma by biopsy, it is highly unlikely that tissue-sampling error has occurred in our analysis. Possible pathologic undergrading, however, should always be considered, even if the tumor has been largely resected. Another limitation is in PFS analysis. Many potentially confounding factors influence PFS, such as age, extent of removal, histopathologic subtype, and molecular prognostic biomarkers, as well as adjuvant therapy. Because it has become clear that grade II and grade III gliomas exhibit different clinical courses according to their molecular subtypes,[46,47] future studies should incorporate this information when conducting survival analysis on the basis of radiologic findings. Finally, prognostic values of imaging parameters should be analyzed not only with PFS but also with overall survival, which requires further future investigation.

CONCLUSIONS

MET PET holds promise as a noninvasive World Health Organization grading technique and prognostic imaging biomarker, offering valuable information in determining treatment strategy for nonenhancing gliomas, while FDG-PET or ADC offer little diagnostic and prognostic value.

Disclosures: Manbu Kinoshita—*RELATED*: *Grant*: Aichi Cancer Research Foundation, SENSIN Medical Research Foundation,* Life Science Foundation of Japan,* Japanese Foundation for Multidisciplinary Treatment of Cancer and Japan Society for the Promotion of Science KAKENHI (25462256).* Koji Takano—*UNRELATED*: *Grants/Grants Pending*: KAKENHI grant No. 26670642. Haruhiko Kishima—*UNRELATED*: *Grants/Grants Pending*: Grants-in-Aid for Scientific Research (T 26462207) from the Ministry of Education, Culture, Sports, Science and Technology of Japan. Yonehiro Kanemura—*UNRELATED*: *Grants/Grants Pending*: Kaneka Corp, Japan,* *Comments*: This is a research grant for stem cell technology. The author declares no conflicts of interest associated with this article; *Patents (planned, pending, or issued)*: Kaneka Corp, Japan,* *Comments*: This is a patent for stem cell technology. The author declares no conflicts of interest associated with this article. *Money paid to the institution.

REFERENCES

1. Louis DN, Ohgaki H, Wiestler OD, et al. **The 2007 WHO classification of tumours of the central nervous system.** *Acta Neuropathol* 2007;114:97–109 CrossRef Medline
2. Marumoto T, Saya H. **Molecular biology of glioma.** *Adv Exp Med Biol* 2012;746:2–11 CrossRef Medline
3. Shapiro JR, Yung WK, Shapiro WR. **Isolation, karyotype, and clonal growth of heterogeneous subpopulations of human malignant gliomas.** *Cancer Res* 1981;41:2349–59 Medline
4. Lasocki A, Tsui A, Tacey MA, et al. **MRI grading versus histology: predicting survival of World Health Organization grade II-IV astrocytomas.** *AJNR Am J Neuroradiol* 2015;36:77–83 CrossRef Medline
5. Chen W, Silverman DH. **Advances in evaluation of primary brain tumors.** *Semin Nucl Med* 2008;38:240–50 CrossRef Medline
6. Batra A, Tripathi RP, Singh AK. **Perfusion magnetic resonance imaging and magnetic resonance spectroscopy of cerebral gliomas showing imperceptible contrast enhancement on conventional magnetic resonance imaging.** *Australas Radiol* 2004;48:324–32 CrossRef Medline

7. Fan GG, Deng QL, Wu ZH, et al. **Usefulness of diffusion/perfusion-weighted MRI in patients with non-enhancing supratentorial brain gliomas: a valuable tool to predict tumour grading?** *Br J Radiol* 2006; 79:652–58 CrossRef Medline
8. Barker FG 2nd, Chang SM, Valk PE, et al. **18-Fluorodeoxyglucose uptake and survival of patients with suspected recurrent malignant glioma.** *Cancer* 1997;79:115–26 Medline
9. Liu X, Tian W, Kolar B, et al. **MR diffusion tensor and perfusion-weighted imaging in preoperative grading of supratentorial nonenhancing gliomas.** *Neuro Oncol* 2011;13:447–55 CrossRef Medline
10. Scott JN, Brasher PM, Sevick RJ, et al. **How often are nonenhancing supratentorial gliomas malignant? A population study.** *Neurology* 2002;59:947–49 CrossRef Medline
11. Ginsberg LE, Fuller GN, Hashmi M, et al. **The significance of lack of MR contrast enhancement of supratentorial brain tumors in adults: histopathological evaluation of a series.** *Surg Neurol* 1998;49: 436–40 CrossRef Medline
12. Maia AC Jr, Malheiros SM, da Rocha AJ, et al. **MR cerebral blood volume maps correlated with vascular endothelial growth factor expression and tumor grade in nonenhancing gliomas.** *AJNR Am J Neuroradiol* 2005;26:777–83 Medline
13. Berger G, Maziere M, Knipper R, et al. **Automated synthesis of 11C-labelled radiopharmaceuticals: imipramine, chlorpromazine, nicotine and methionine.** *Int J Appl Radiat Isot* 1979;30:393–99 CrossRef Medline
14. Yoshiura T, Mihara F, Tanaka A, et al. **High b value diffusion-weighted imaging is more sensitive to white matter degeneration in Alzheimer's disease.** *Neuroimage* 2003;20:413–19 CrossRef Medline
15. Di Chiro G, DeLaPaz RL, Brooks RA, et al. **Glucose utilization of cerebral gliomas measured by [18F] fluorodeoxyglucose and positron emission tomography.** *Neurology* 1982;32:1323–29 CrossRef Medline
16. Ishikawa M, Kikuchi H, Miyatake S, et al. **Glucose consumption in recurrent gliomas.** *Neurosurgery* 1993;33:28–33 CrossRef Medline
17. De Witte O, Levivier M, Violon P, et al. **Prognostic value positron emission tomography with [18F]fluoro-2-deoxy-D-glucose in the low-grade glioma.** *Neurosurgery* 1996;39:470–76; discussion 476–77 CrossRef Medline
18. Patronas NJ, Di Chiro G, Kufta C, et al. **Prediction of survival in glioma patients by means of positron emission tomography.** *J Neurosurg* 1985;62:816–22 CrossRef Medline
19. Alavi JB, Alavi A, Chawluk J, et al. **Positron emission tomography in patients with glioma: a predictor of prognosis.** *Cancer* 1988;62: 1074–78 Medline
20. Goldman S, Levivier M, Pirotte B, et al. **Regional glucose metabolism and histopathology of gliomas: a study based on positron emission tomography-guided stereotactic biopsy.** *Cancer* 1996;78:1098–106 Medline
21. Pirotte B, Goldman S, Bidaut LM, et al. **Use of positron emission tomography (PET) in stereotactic conditions for brain biopsy.** *Acta Neurochir (Wien)* 1995;134:79–82 CrossRef Medline
22. Ishizu K, Nishizawa S, Yonekura Y, et al. **Effects of hyperglycemia on FDG uptake in human brain and glioma.** *J Nucl Med* 1994;35: 1104–09 Medline
23. Padma MV, Said S, Jacobs M, et al. **Prediction of pathology and survival by FDG PET in gliomas.** *J Neurooncol* 2003;64:227–37 CrossRef Medline
24. Bergström M, Collins VP, Ehrin E, et al. **Discrepancies in brain tumor extent as shown by computed tomography and positron emission tomography using [68Ga]EDTA, [11C]glucose, and [11C]methionine.** *J Comput Assist Tomogr* 1983;7:1062–66 CrossRef Medline
25. Kato T, Shinoda J, Nakayama N, et al. **Metabolic assessment of gliomas using 11C-methionine, [18F] fluorodeoxyglucose, and 11C-choline positron-emission tomography.** *AJNR Am J Neuroradiol* 2008;29:1176–82 CrossRef Medline
26. Borbély K, Nyáry I, Tóth M, et al. **Optimization of semi-quantification in metabolic PET studies with 18F-fluorodeoxyglucose and 11C-methionine in the determination of malignancy of gliomas.** *J Neurol Sci* 2006;246:85–94 CrossRef Medline
27. Voges J, Herholz K, Hölzer T, et al. **11C-methionine and 18F-2-fluorodeoxyglucose positron emission tomography: a tool for diagnosis of cerebral glioma and monitoring after brachytherapy with 125I seeds.** *Stereotact Funct Neurosurg* 1997;69(1–4 pt 2):129–35 Medline
28. Ogawa T, Inugami A, Hatazawa J, et al. **Clinical positron emission tomography for brain tumors: comparison of fludeoxyglucose F 18 and L-methyl-11C-methionine.** *AJNR Am J Neuroradiol* 1996;17: 345–53 Medline
29. Singhal T, Narayanan TK, Jain V, et al. **11C-L-methionine positron emission tomography in the clinical management of cerebral gliomas.** *Mol Imaging Biol* 2008;10:1–18 CrossRef Medline
30. Utriainen M, Metsähonkala L, Salmi TT, et al. **Metabolic characterization of childhood brain tumors: comparison of 18F-fluorodeoxyglucose and 11C-methionine positron emission tomography.** *Cancer* 2002;95:1376–86 CrossRef Medline
31. Derlon JM, Chapon F, Noël MH, et al. **Non-invasive grading of oligodendrogliomas: correlation between in vivo metabolic pattern and histopathology.** *Eur J Nucl Med* 2000;27:778–87 CrossRef Medline
32. Kaschten B, Stevenaert A, Sadzot B, et al. **Preoperative evaluation of 54 gliomas by PET with fluorine-18-fluorodeoxyglucose and/or carbon-11-methionine.** *J Nucl Med* 1998;39:778–85 Medline
33. Singhal T, Narayanan TK, Jacobs MP, et al. **11C-methionine PET for grading and prognostication in gliomas: a comparison study with 18F-FDG PET and contrast enhancement on MRI.** *J Nucl Med* 2012; 53:1709–15 CrossRef Medline
34. Bergström M, Lundqvist H, Ericson K, et al. **Comparison of the accumulation kinetics of L-(methyl-11C)-methionine and D-(methyl-11C)-methionine in brain tumors studied with positron emission tomography.** *Acta Radiol* 1987;28:225–29 CrossRef Medline
35. Roelcke U, Radü E, Ametamey S, et al. **Association of rubidium and C-methionine uptake in brain tumors measured by positron emission tomography.** *J Neurooncol* 1996;27:163–71 Medline
36. Jager PL, Vaalburg W, Pruim J, et al. **Radiolabeled amino acids: basic aspects and clinical applications in oncology.** *J Nucl Med* 2001;42: 432–45 Medline
37. Kinoshita M, Hashimoto N, Goto T, et al. **Fractional anisotropy and tumor cell density of the tumor core show positive correlation in diffusion tensor magnetic resonance imaging of malignant brain tumors.** *Neuroimage* 2008;43:29–35 CrossRef Medline
38. LaViolette PS, Mickevicius NJ, Cochran EJ, et al. **Precise ex vivo histological validation of heightened cellularity and diffusion-restricted necrosis in regions of dark apparent diffusion coefficient in 7 cases of high-grade glioma.** *Neuro Oncol* 2014;16:1599–606 CrossRef Medline
39. van den Bent MJ, Afra D, de Witte O, et al. **Long-term efficacy of early versus delayed radiotherapy for low-grade astrocytoma and oligodendroglioma in adults: the EORTC 22845 randomised trial.** *Lancet* 2005;366:985–90 CrossRef Medline
40. Intergroup Radiation Therapy Oncology Group Trial 9402, Cairncross G, Berkey B, Shaw E, et al. **Phase III trial of chemotherapy plus radiotherapy compared with radiotherapy alone for pure and mixed anaplastic oligodendroglioma: Intergroup Radiation Therapy Oncology Group Trial 9402**. *J Clin Oncol* 2006;24:2707–14 CrossRef Medline
41. Gilbert MR, Friedman HS, Kuttesch JF, et al. **A phase II study of temozolomide in patients with newly diagnosed supratentorial malignant glioma before radiation therapy.** *Neuro Oncol* 2002;4: 261–67 CrossRef Medline
42. Shibui S, Narita Y, Mizusawa J, et al. **Randomized trial of chemoradiotherapy and adjuvant chemotherapy with nimustine (ACNU) versus nimustine plus procarbazine for newly diagnosed anaplastic astrocytoma and glioblastoma (JCOG0305).** *Cancer Chemother Pharmacol* 2013;71:511–21 CrossRef Medline
43. Brandes AA, Nicolardi L, Tosoni A, et al. **Survival following adjuvant**

PCV or temozolomide for anaplastic astrocytoma. *Neuro Oncol* 2006;8:253–60 CrossRef Medline
44. van den Bent MJ, Carpentier AF, Brandes AA, et al. **Adjuvant procarbazine, lomustine, and vincristine improves progression-free survival but not overall survival in newly diagnosed anaplastic oligodendrogliomas and oligoastrocytomas: a randomized European Organisation for Research and Treatment of Cancer phase III trial.** *J Clin Oncol* 2006;24:2715–22 CrossRef Medline
45. Wick W, Hartmann C, Engel C, et al. **NOA-04 randomized phase III trial of sequential radiochemotherapy of anaplastic glioma with procarbazine, lomustine, and vincristine or temozolomide.** *J Clin Oncol* 2009;27:5874–80 CrossRef Medline
46. Cairncross G, Wang M, Shaw E, et al. **Phase III trial of chemoradiotherapy for anaplastic oligodendroglioma: long-term results of RTOG 9402.** *J Clin Oncol* 2013;31:337–43 CrossRef Medline
47. Suzuki H, Aoki K, Chiba K, et al. **Mutational landscape and clonal architecture in grade II and III gliomas.** *Nat Genet* 2015;47:458–68 CrossRef Medline

Comparison of the Effect of Vessel Size Imaging and Cerebral Blood Volume Derived from Perfusion MR Imaging on Glioma Grading

H.-Y. Kang, H.-L. Xiao, J.-H. Chen, Y. Tan, X. Chen, T. Xie, J.-Q. Fang, S. Wang, Y. Yang, and W.-G. Zhang

ABSTRACT

BACKGROUND AND PURPOSE: Vascular proliferation is a major criterion for grading gliomas on the basis of histology. Relative cerebral blood volume can provide pathophysiologic information about glioma grading. Vessel size imaging, in some animals, can be used to estimate the microvascular caliber of a glioma, but its clinical use remains unclear. Herein, we aimed to compare the predictive power of relative cerebral blood volume and vessel size imaging in glioma grading, with grading based on histology.

MATERIALS AND METHODS: Seventy patients with glioma participated in the study; 30 patients underwent MR perfusion imaging with a spin-echo sequence and vessel size imaging with a gradient-echo and spin-echo sequence successively at 24-hour intervals before surgery. We analyzed the vessel size imaging values and relative cerebral blood volume of differently graded gliomas. The microvessel parameters were histologically evaluated and compared with those on MR imaging. The cutoff values of vessel size imaging and relative cerebral blood volume obtained from receiver operating characteristic curve analyses were used to predict glioma grading in another 40 patients.

RESULTS: Vessel size imaging values and relative cerebral blood volume were both increased in high-grade gliomas compared with low-grade gliomas ($P < .01$). Moreover, vessel size imaging values had higher specificity and sensitivity in differentiating high-grade from low-grade gliomas compared with relative cerebral blood volume. In addition, a significant correlation was observed between vessel size imaging values and microvessel diameters ($r > 0.8$, $P < .05$) and between relative cerebral blood volume and microvessel area ($r = 0.6579$, $P < .05$). Most important, the use of vessel size imaging cutoff values to predict glioma grading was more accurate (100%) than use of relative cerebral blood volume (85%) values.

CONCLUSIONS: Vessel size imaging can provide more accurate information on glioma grading and may serve as an effective biomarker for the prognosis of patients with gliomas.

ABBREVIATIONS: HGG = high-grade glioma; LGG = low-grade glioma; max = maximum; MVA = microvessel area; MVD = microvessel density; rCBV = relative cerebral blood volume; SE = spin-echo; VSI = vessel size imaging

Gliomas with different grades have different clinical behaviors that determine treatment planning and patient prognosis in clinical practice.[1,2] Biopsy or examination of tumor tissues from surgical resection specimens is the only method available to establish the final diagnosis of tumor grading in cases of malignancy; however, this procedure is invasive.[3] With regard to gliomas, tumor heterogeneity limits the ability of biopsies to accurately grade glioma tumors.

Functional MR imaging can provide quantitative or semiquantitative hemodynamic parameters, thereby allowing preoperative evaluation of the status of tumor angiogenesis, an important index in evaluating the grade of tumors and patient prognosis.[4] CBV maps, derived from MR imaging during the application of first-pass bolus-tracking analysis, provide complementary information in the diagnosis of tumor grade and the extent of malignancy. Several authors have found that maximal relative cerebral blood volume (rCBV) correlates with glioma grading.[5-7] However, studies have shown that there were no significant differences in rCBV values between grade II and III glio-

Received March 17, 2015; accepted after revision May 14.

From Departments of Radiology (H.-Y.K., J.-H.C., H.-L.X., Y.T., X.C., T.X., J.-q.F., W.-G.Z.) and Pathology (H.-L.X.), and State Key Laboratory of Trauma, Burns and Combined Injury (W.-G.Z.), Institute of Surgery Research, Daping Hospital, Third Military Medical University, Chongqing, China; and Departments of Radiology (S.W.) and Medicine (Y.Y.), Perelman School of Medicine, University of Pennsylvania, Philadelphia, Pennsylvania.

This study was supported by grants from Natural Science Foundation of China (No. 81271626), Natural Science Foundation Project of Chongqing (cstc2012jjB10028), and the Scientific Foundation of the Institute of Surgery Research, Daping Hospital, Third Military Medical University (No. 2014YLC03).

Please address correspondence to Wei-Guo Zhang, MD, Institute of Surgery Research, Daping Hospital, Third Military Medical University, Chongqing, 400042, China; e-mail: wgzhang01@163.com

Indicates open access to non-subscribers at www.ajnr.org
Indicates article with supplemental on-line table and appendix.
Indicates article with supplemental on-line photo.
http://dx.doi.org/10.3174/ajnr.A4477

mas[8] or between grade III and IV gliomas.[9] Moreover, a growing body of research has demonstrated the limited predictive power of rCBV to grade oligodendrogliomas, which tend to have high rCBVs regardless of glioma grade. Furthermore, oligodendrogliomas exhibit greater microvascular proliferation than astrocytomas[8,10-12]; thus, rCBV may not be an ideal diagnostic tool for oligodendroglioma.[8,13,14] Therefore, it is essential to explore an effective index for glioma grading that is independent of blood volume.

Vessel size imaging (VSI), which is obtained from the ratio of gradient-echo and spin-echo (SE) relaxation rate changes ($\triangle R2^*/\triangle R2$) induced by intravascular superparamagnetic contrast agents, provides information on the average vessel size under certain conditions, such as the concentration of contrast agent, the main magnetic field, and TE.[15] Recently, an increasing number of articles have reported that VSI can reflect the microvascular structures of tumors in animal models and strongly correlates with brain tumor grade.[16,17] For example, Kiselev et al[18] reported that VSI increased the information value on brain histopathology obtained during dynamic perfusion measurements and that the mean vessel size correlated with the tumor type. Lemasson et al indicated that VSI in MR imaging estimates was closest to histology and provided complementary information on characterizing angiogenesis beyond fractioned blood volume in the rat brain tumor model.[4] Although several studies have indicated that VSI had a high accuracy rate for the diagnosis of the degree of tumor malignancy in animal models, the predictive power of VSI in human gliomas remains largely unknown.[16,18,19] To our knowledge, the comparison of VSI and rCBV in human glioma grading has not been addressed previously.

We designed this prospective study, in which the sensitivities and specificities of rCBV and VSI in distinguishing low-grade glioma (LGG) from high-grade glioma (HGG) were compared, and the final diagnosis of the grades of gliomas and the measurement of microvessel parameters were performed histologically on the basis of surgical resection specimens. The optimal cutoff values of rCBV and VSI were used to evaluate their diagnostic accuracy rates for predicting glioma grading.

MATERIALS AND METHODS

Patients and Samples

We selected patients with suspected primary gliomas followed by undergoing prospective perfusion-weighted imaging between March 2013 and August 2014. Then, tumors were diagnosed and classified according to World Health Organization 2007 criteria as confirmed by surgery. Among the selected patients, at least 30 had undergone both SE-perfusion and VSI at 24- to 48-hour intervals; these patients were assigned to group 1, from which the optimal cutoff value of VSI and rCBV to distinguish HGG from LGG would be generated, respectively. Once the optimal cutoff values were obtained, we needed to evaluate their diagnostic accuracy rates in the grading of gliomas. Thus, we designed protocols for the enrollment of, at minimum, 40 patients with suspected primary gliomas, followed by those who underwent SE-perfusion (20 patients), assigned to group 2, or VSI (20 patients), assigned to group 3 (On-line Table 1). In our next step, we used the optimal cutoff values of rCBV and VSI to predict the glioma grading of patients in groups 2 and 3, prospectively. Finally, diagnostic accuracy was calculated by comparing calculated values with pathologic results.

The inclusion criteria were the following: 1) MR imaging examination before the histologic examination; 2) no therapy before the MR imaging examination; 3) gliomas confirmed histologically; and 4) patients in group 1, whose clinical symptoms occurred in lesser degrees, able to undergo both SE perfusion and VSI and agreeing to undergo perfusion twice. The exclusion criteria were the following: 1) patients older than 80 years of age; 2) gliomas with grade I and histologic results showing no gliomas or rare gliomas; 3) in group 1, patients not having enough time (>24 hours) to have both SE perfusion and VSI before undergoing their operation; 4) contraindications to MR imaging; and 5) patients having false teeth, which would result in poor image quality. The study was approved by the local ethics committee at our institution, and all patients completed a written consent form.

MR Imaging

A 3T scanner (Magnetom Verio; Siemens, Erlangen, Germany) was used to acquire conventional MR imaging and DWI (details shown in the On-line Appendix) and spin-echo echo-planar perfusion scans. VSI was performed by using a 1.5T imager (Sigma HDx; GE Healthcare, Milwaukee, Wisconsin). The location line for all axial MR imaging was the central intercommissural (anterior/posterior commissure) line as previously described[13,20] or parallel to this line.

Dynamic susceptibility contrast-enhanced perfusion MR imaging was performed by using the SE-EPI technique during administration of Gd-DTPA (Magnevist; Bayer HealthCare Pharmaceuticals, Wayne, New Jersey). The imaging parameters were as follows: TR/TE, 1500/30 ms; flip angle, 90°; matrix size, 128 × 128; NEX, 1.0; FOV, 23 × 23 cm. We selected 20 sections for perfusion imaging, in accordance with the T2-weighted imaging; at each section, 60 images were obtained. After 8 acquisitions, a bolus of gadobutrol (0.2 mmol per kilogram of body weight) was injected at a rate of 3 mL/s, immediately followed by a 20-mL bolus of saline at the same rate.

MR imaging data for VSI were acquired followed by intravenous injection of Gd-DTPA by using a gradient-echo and spin-echo sequence, with the following acquisition parameters: TR, 1500 ms; TE (gradient echo), 30 ms; TE (SE), 100 ms; flip angle, 90°; matrix size, 64 × 64; NEX, 1; FOV, 24 × 24 cm. Seven sections were selected across the tumor, with 120 images obtained at each section. In addition, VSI was obtained during injection of a bolus of 0.2 mmol/kg body weight of gadopentetate dimeglumine contrast agent at a rate of 3.5 mL/s with a time delay of 18 seconds, followed by a 20-mL bolus of saline.

VSI Measurements

The VSI images were analyzed by using an Advantage Workstation (Version 4.9; GE Healthcare) equipped with a dedicated software package (VSI; GE Healthcare). Using wide-bound or whole-observed brain as the input function and the generation of contrast-enhancement time–signal intensity curves for the input function, we calculated $\triangle R2^*/\triangle R2$ according to the decay curve.

On the basis of the known observation that $\triangle R2^*/\triangle R2$ is a function of vessel size,[21] VSI can be computed from this ratio according to the equation[4,19]: $VSI = 0.425(ADC/\gamma\triangle \times B0)^{1/2} \times (\Delta R2^*/\Delta R2)^{3/2}$, where *ADC* is the diffusion coefficient, by using 0.8 μm^2/ms as analog data[18]; γ is the gyromagnetic ratio, the gyromagnetic ratio of hydrogen proton being 42.58 MHz/T; $\Delta\gamma$ is the change values in magnetization rate; and *B0* is the stationary field, 1.5T. The software (VSI) generated color-coded VSI images, the threshold of which was adjusted to 0–80 μm or 0–120 μm.

The preoperative and postoperative MR images were compared to outline the extent of surgery to increase the consistency between the regions of MR imaging and pathology measurements. A hand-drawn ROI of constant size (56 mm^2) corresponding to the greatest visualized regions of perfusion was achieved by repeatedly moving the region in adjacent parts at least 5 times until the highest value was determined. We obtained approximately 10 values from at least 3 regions of the different cross-sectional images, while avoiding the vessels and necrotic tissue, recording the mean and maximal (max) values of all data as the VSI_{mean} and VSI_{max} values for each patient. Measurements were performed by 2 neuroradiologists (H.-Y.K. and J.-Q.F, with 7 and 6 years of experience, respectively). Each observer, who was blinded to the histopathologic diagnosis, conducted each measurement twice and independently.

rCBV Measurements

The original SE images were processed with a commercial software package (SyngoMMWP VE36A; Siemens) and were used to generate color-coded CBV maps.[3,22,23] The enhanced T1-weighted images were used as a guide for the location of the tumors to avoid the large vessels and necrotic tissue. The highest CBV values were obtained, and the $rCBV_{max}$ normalization to the contralateral unaffected white matter CBV value was based on previously published methods.[1,23,24] Measurements were performed by 2 neuroradiologists (H.-Y.K. and J.-Q.F). Each ROI was independently checked for accuracy by another observer, and any changes were made by joint agreement. The size of the ROIs was kept constant (radius = 2.6 mm). All analyses were performed without knowledge of tissue analyses.

Immunohistology Analysis

Each paraffin block from the 30 patients of group 1 was processed into a 4-μm-thick section, with 2–6 paraffin sections produced per patient. To measure the diameter of microvessels, microvessel area (MVA), and microvessel density (MVD) for grades II, III, or IV gliomas, we performed a histologic evaluation by immunohistochemistry for the CD34 antigen, which identified vascular endothelial cells as previously described.[3,25] The reagent PV-6000-G Polymer Detection System for Immuno-Histologic Staining was bought from Beijing Zhong Shan-Golden Bridge Biologic Technology Company (Beijing, China). All tissue sections were digitized by using a fluorescence microscope (BX41; Olympus, Rungis, France) and the CellSens Standard software (http://www.scientific-computing.com/press-releases/product_details.php?product_id=809).

We examined entire sections at ×40 magnification, covering an area of 1.308 × 1.757 mm/field, to identify "hot spot" regions of microvascular diameter, MVA, and MVD, from which 5–10 hot spots were selected for imaging.[26] By definition, the smallest countable blood vessels were used to estimate microvessel parameters.[27] Microvascular diameter and MVA were measured at ×200 magnification, and MVD, at ×100 magnification.[28] Quantitative microvascular analysis was performed by using Image-Pro Plus 5.0 software (http://www.mediacy.com/index.aspx?page=IPP), the microvessel diameter and MVA were determined by using the feret (min) and area (polygon) function,[3] but the vessels with thick walls and lumens >72 μm were excluded.[27] To minimize bias in the correlation between MR imaging and the histologic estimates, we analyzed the average diameter of all microvessels, MVD, and total area of all hot spot regions of each tissue section, and we compared sections from each patient to identify the highest values. Two experienced neuropathologists (H.-L.X and S.-G.F., with >10 years of experience) were blinded to the MR imaging results and completed the histologic measurements.

Statistical Analysis

Statistical analyses were performed by using commercially available software (SPSS, Version 19.0; IBM, Armonk, New York) to compare the MR imaging and pathologic data of different grades of glioma from patient group 1. Due to part of the data not being well-represented by a normal distribution, the results have been expressed as mean ± SD or median ± quartile range. The Kruskal-Wallis H test was used to evaluate differences in the VSI_{mean} values, microvascular diameter, MVA, and MVD in patients with glioma of different grades, and the Nemenyi method of the multiple comparison was performed. Multiple comparisons between groups were corrected by using the Bonferroni method. The ANOVA and the Least Significant Difference test were used to analyze differences in VSI_{max} and $rCBV_{max}$ values in patients with glioma of different grades. P values $< .05$ were statistically significant. Pearson correlation analysis was used to evaluate the relationship among VSI values, $rCBV_{max}$ values, microvascular diameter, MVA, and MVD. Receiver operating characteristic curves were used to assess the specificity and sensitivity of the VSI_{max}, VSI_{mean}, and $rCBV_{max}$ values in distinguishing LGG from HGG. Interrater reliability between the 2 independent VSI observers and the two measurements of interobserver was assessed by using an intraclass correlation coefficient.

RESULTS

Patient Population

Overall, 70 of 117 patients participated in our study. Thirty patients (15 women and 15 men; median age, 42 years; age range, 18–79 years) met the inclusion criteria of group 1, in which there were 9 low-grade (3 diffuse astrocytomas, grade II; 5 oligodendrogliomas, grade II; 1 oligoastrocytoma, grade II) and 21 HGGs. Among the high-grade tumors, 8 were diagnosed as grade III (3 anaplastic oligodendrogliomas, 2 anaplastic oligoastrocytomas, 3 anaplastic astrocytomas), and 13, as grade IV. In addition, we enrolled 20 patients into groups 2 and 3, respectively (On-line Table 1).

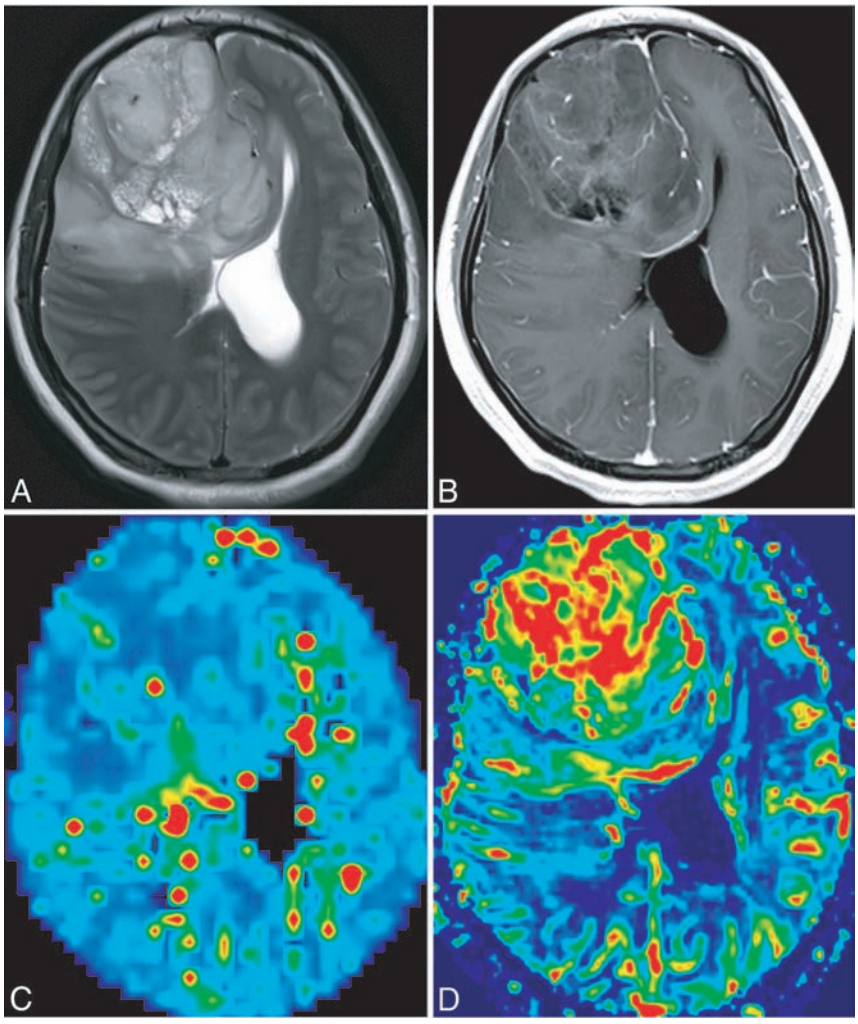

FIG 1. A 25-year-old woman with an oligodendroglioma (World Health Organization grade II). *A*, Axial T2-weighted MR imaging demonstrates a right frontal and temporal lobe lesion with mass effect, a small amount of edema, and signal-intensity heterogeneity. *B*, Contrast-enhanced T1-weighted imaging demonstrates mild enhancement. *C*, The VSI map shows homogeneous low VSI values and is represented in blue-green. *D*, CBV map demonstrates clearly elevated perfusion in the tumor parenchyma.

Characteristics of VSI and rCBV in Gliomas with Different Grades

Based on the reference standard, there was excellent intraobserver and interobserver agreement for VSI_{mean} (intraclass correlation coefficient > 0.879) and VSI_{max} (intraclass correlation coefficient > 0.809).[1] The final step was a calculation of the mean values generated from the 4 measurements made by the 2 independent observers. The VSI color map of grade II gliomas is represented in blue-green, denoting low VSI values (VSI_{mean} and VSI_{max} values, 42.96 ± 26.43 μm and 79.10 ± 29.17 μm, respectively); however, the CBV maps of the 2 cases of grade II oligodendrogliomas are represented in red (Fig 1). The VSI and CBV colors maps of grade III and IV gliomas were inhomogeneous and are represented in red, denoting high VSI_{mean} values (glioma grade III, 130.89 ± 54.74 μm, and glioblastoma, 154.72 ± 13.64 μm), VSI_{max} values (glioma grade III, 187.44 ± 43.63 μm, and glioblastoma, 212.26 ± 19.69 μm), and rCBV (glioma grade III, 9.15 ± 5.11, and glioblastoma, 10.78 ± 3.66). Although the high perfusion region of CBV partially overlapped that of VSI, the highest perfusion region did not match entirely (Fig 2).

Role of VSI and rCBV in Grading Gliomas and Receiver Operating Characteristic Analysis

We found that the VSI_{mean} and VSI_{max} values and rCBV of grade III or IV gliomas were significantly higher than those of grade II gliomas ($P < .01$), whereas no significant differences were found in rCBV and the VSI_{mean} and VSI_{max} values between gliomas with grades III and IV (On-line Fig 1*A–C*). To further explore the role of VSI values and rCBV in distinguishing LGG (grade II) from HGG (grade III and IV), we analyzed the sensitivity and specificity of the VSI_{mean} and VSI_{max} values and rCBV by using receiver operating characteristic analysis. At the optimal cutoff VSI_{mean} values of 99.93 μm with the value of sensitivity + specificity-1 considered maximal, the sensitivity and specificity were both 100%. When the VSI_{max} values were at the optimal cutoff of 138.3 μm, the sensitivity and specificity were 95.24% and 100%, and the AUC value was 0.9947 (On-line Fig 1*D*, -*E*). However, rCBV values at an optimal cutoff of 5.73, with just 85.71% sensitivity and 88.89% specificity, differentiated grade II gliomas from grade III or IV gliomas (On-line Fig 1*F*).

Histopathologic Characteristics

From the 30 subjects we enrolled, we collected a total of 75 paraffin blocks, which were used for both histopathologic diagnosis and microvascular quantification. The results revealed that the microvascular diameters and MVA of grade II gliomas were smaller (9.74 ± 6.17 μm and 3365.00 ± 3287.34 μm^2) than those of grade III gliomas (23.93 ± 9.90 μm and $18{,}236.00 \pm 7543.25$ μm^2) and grade IV gliomas (40.48 ± 18.30 μm and $18{,}196.00 \pm 7534.50$ μm^2). The microvessel diameter and MVA of grade III and IV gliomas were significantly higher than those in grade II gliomas ($P < .01$). The MVD values of grade IV gliomas were significantly higher than those of grade II gliomas ($P < .01$); however, no significant differences were observed between grade II and III gliomas or grade III and IV gliomas (On-line Fig 2). Furthermore, the microvascular diameters of several grade II oligodendrogliomas were generally smaller than those of diffuse astrocytomas. However, the MVD and MVA of grade II oligodendrogliomas were larger than those of astrocytomas (data not shown).

Correlation between MR Imaging and Microvessel Parameters in Gliomas

Correlations between MVA and VSI_{mean} values, MVA and VSI_{max} values, MVA and rCBV, microvessel diameter and VSI_{mean} values, microvessel diameter and VSI_{max} values, and microvessel di-

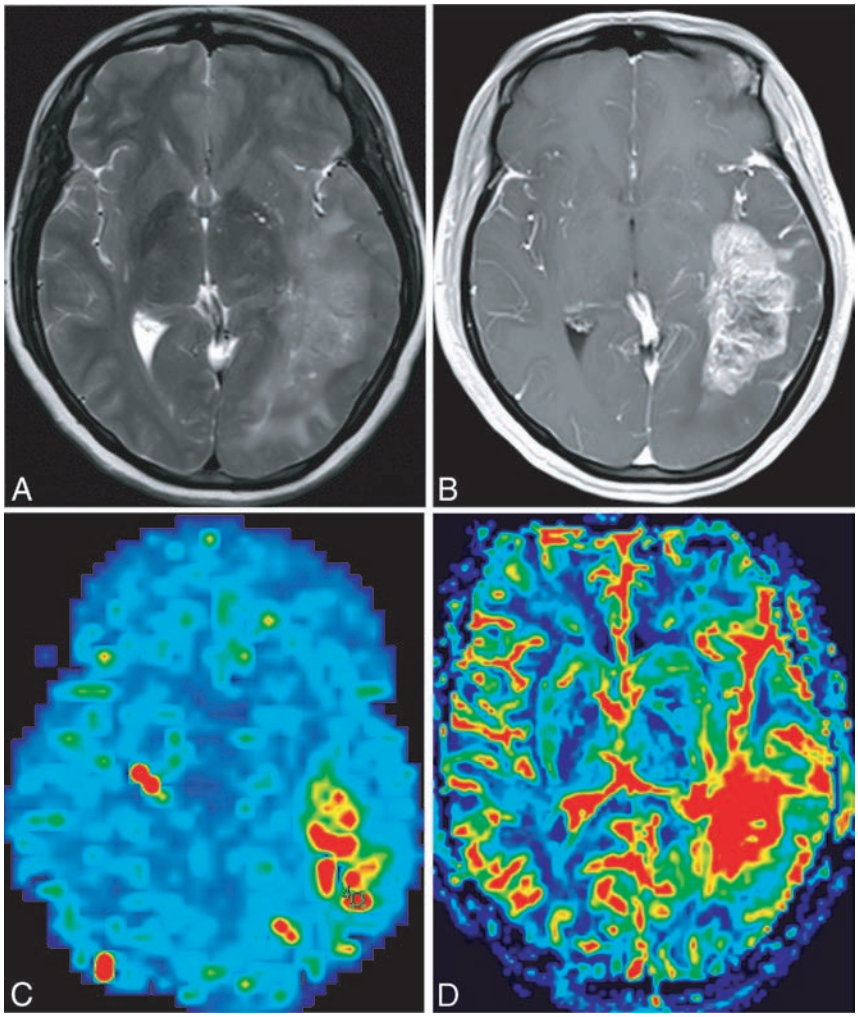

FIG 2. A 42-year-old woman with glioblastoma (World Health Organization grade IV). *A*, Axial T2-weighted MR imaging reveals a left temporal and occipital lobe lesion with mass effect, a moderate amount of edema, and homogeneous signal intensity. *B*, Contrast-enhanced T1-weighted imaging reveals marked enhancement. *C*, VSI map shows high VSI values. *D*, CBV map reveals the elevated perfusion more extensively. The highest perfusion region of CBV does not match entirely that of VSI.

ameter and rCBV were all statistically significant ($P < .01$). Comparing MR imaging and microvessel parameters, we observed the strongest correlation between VSI_{max} values and microvascular diameter ($r = 0.831$), followed by VSI_{mean} values and microvascular diameter ($r = 0.824$). Moreover, no clear correlation could be identified between rCBV and MVD or between MVD and VSI values (On-line Fig 3).

VSI and rCBV Values as Predictive Factors for Glioma Grading

The results revealed that the VSI_{mean} values in 14 patients were higher than the cutoff value (99.93 μm), whereas those in 6 patients were lower. The rCBV values in 13 patients were higher than the cutoff value (5.73), whereas those in 7 patients were lower. Compared with diagnosis by histology (On-line Table 1), as expected, the prediction of VSI for glioma grade had a 100% accuracy, whereas the accuracy of rCBV was 85%, in which 2 low-grade oligodendrogliomas had rCBV values higher than the cutoff value and 1 anaplastic astrocytoma was lower than the cutoff value (Fig 3).

DISCUSSION

In this study, we evaluated the sensitivities and specificities of rCBV and VSI in distinguishing LGGs from HGGs, and we obtained the optimal cutoff values of rCBV and VSI for glioma grading. We found that VSI had a higher accuracy rate in predicting glioma grading compared with rCBV. In addition, we measured microvascular diameter, MVD, and MVA by using CD34 to stain vascular endothelial cells. We found that microvascular diameters and MVA were strongly correlated with the glioma grade compared with MVD.

Histopathologically, endothelial proliferation is an important factor in determining the grades of gliomas.[28] In recent years, several studies have indicated that tumor grades were strongly correlated with microvessel caliber and MVA, but MVD revealed a poor association with tumor grades.[25] Consistent with this evidence, our results confirm that microvascular diameters and MVA could differentiate LGGs from HGGs, but MVD only distinguished grade II from grade IV gliomas. These findings suggest that microvessel structure has better efficacy in the grading of gliomas. Furthermore, the comparisons among rCBV, VSI, and histologic results were performed together in the same patients, and the results showed that VSI had better efficacy in reflecting the histologic features of glioma microvessels.

Although an increasing number of articles have shown that rCBV has a high accuracy rate in predicting glioma grades,[3,29] oligodendrogliomas were shown to have preferentially high rCBV values regardless of glioma grade.[6] In our study, we misdiagnosed 2 cases of low-grade oligodendrogliomas by using the rCBV cutoff value, suggesting that rCBV has limitations in the grading of gliomas. Most interesting, we found that the VSI_{mean} cutoff value had 100% accuracy in differentiating LGG and HGG, suggesting that VSI can be used to predict the oligodendroglioma grade. In addition, we found that grade II oligodendrogliomas had shorter microvessel diameters and higher MVD compared with diffuse astrocytomas, possibly resulting in high rCBV arising from oligodendrogliomas.

VSI was considered to noninvasively describe the pathologic changes of vessels in quantitative terms.[17] In recent years, for VSI investigation, a large number of studies mainly focused on animal models. For example, Troprès et al[17] found that VSI positively

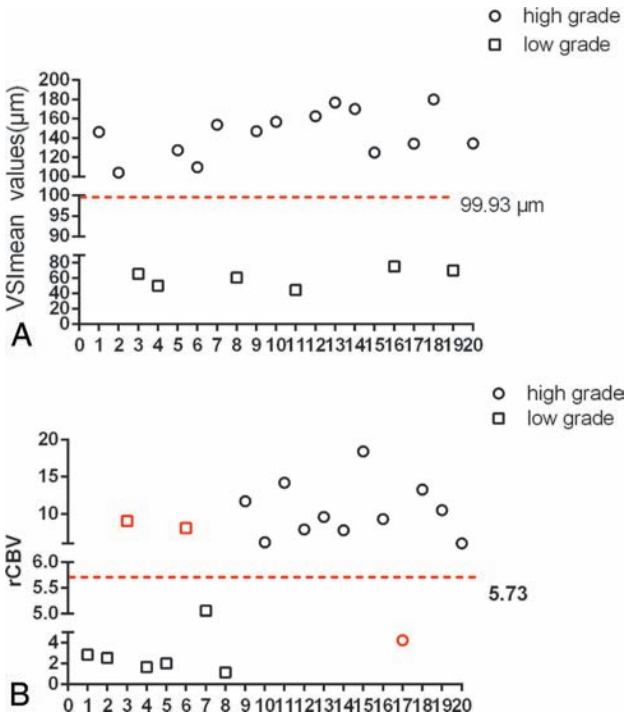

FIG 3. VSI and rCBV values in predicting the grade of gliomas. *A*, The VSI_{mean} values show no overlap between HGG and LGG and provide 100% accuracy in predicting the glioma grade. *B*, The glioma grade could not be exactly identified on the basis of the cutoff values of rCBV. Black indicates the cases correctly identified, and red denotes the cases incorrectly identified.

correlated with the pathologic diagnosis, a Spearman coefficient of 0.74. Lemasson et al reported that MR imaging and histologic estimates of VSI correlated well and may be used to characterize angiogenesis in vivo beyond CBV, as determined in 27 rats with intracranial gliomas.[4] Recently, Emblem et al[16] indicated that vessel architectural imaging had the potential to identify patients who might benefit from certain therapies. However, the application of VSI in human glioma grading remains unclear. In our study, we showed that the VSI values were positively correlated with the histologic results, with a correlation coefficient of >0.80, and VSI had a high accuracy rate in predicting glioma grades. In addition, we found that VSI_{mean} values had higher AUC, sensitivity, and specificity for glioma diagnosis than VSI_{max} values; this outcome may have been the result of the following 2 points: 1) VSI_{mean} values better reflect the status of whole tumors; and 2) the signal-to-noise ratio of VSI is poor, resulting in a higher rate of errors in the measurement of VSI_{max} values.

Our study had limitations. First, the number of the glioma samples, especially grade II and III gliomas, was modest. Second, robust VSI estimates should be obtained from patients at 3T or higher magnetic fields by using the DSC approach.[30] Third, we used the "hot-spot" method, which cannot ensure the consistency between MR imaging regions and pathology measurements. Fourth, the time and space resolution of VSI was not as good as that of CBV; the signal-to-noise ratio of VSI images required enhancing to demonstrate regions of scattered perfusion in the cerebral tissue or lateral cerebral ventricles. Fifth, the lack of a unified approach to performing VSI measurement may result in unstable VSI cutoff values. In future studies, we will search for more objective and effective methods for VSI measurement.

CONCLUSIONS

In this study, we compared VSI, rCBV, and histologic results in grading gliomas and showed that VSI has greater accuracy at predicting glioma grading than rCBV, suggesting that VSI may serve as an effective tool for the diagnosis of patients with gliomas and for guiding the clinical therapeutic strategy.

ACKNOWLEDGMENTS

We thank He Wang, Jing Ning, and Hui Lin for their technical assistance, and San-Gao Fang for the contribution to pathology measurement in this study.

Disclosures: Hou-Yi Kang, Jin-Hua Chen, Yong Tan, Tian Xie, Wei-Guo Zhang—*RELATED*: *Grant*: Natural Science Foundation of China (No. 81271626) and Chongqing (No. cstc2012jjB10028), and the Scientific Foundation of Institute of Surgery Research, Daping Hospital, Third Military Medical University (NO. 2014YLC03).* Xiao Chen—*RELATED*: *Grant*: National Natural Science Foundation of China (grant No. 81271626).* *Money paid to the institution.

REFERENCES

1. Caulo M, Panara V, Tortora D, et al. **Data-driven grading of brain gliomas: a multiparametric MR imaging study.** *Radiology* 2014;272:494–503 CrossRef Medline
2. Haegler K, Wiesmann M, Böhm C, et al. **New similarity search based glioma grading.** *Neuroradiology* 2012;54:829–37 CrossRef Medline
3. Hu LS, Eschbacher JM, Dueck AC, et al. **Correlations between perfusion MR imaging cerebral blood volume, microvessel quantification, and clinical outcome using stereotactic analysis in recurrent high-grade glioma.** *AJNR Am J Neuroradiol* 2012;33:69–76 CrossRef Medline
4. Lemasson B, Valable S, Farion R, et al. **In vivo imaging of vessel diameter, size, and density: a comparative study between MRI and histology.** *Magn Reson Med* 2013;69:18–26 CrossRef Medline
5. Knopp EA, Cha S, Johnson G, et al. **Glial neoplasms: dynamic contrast-enhanced T2*-weighted MR imaging.** *Radiology* 1999;211:791–98 CrossRef Medline
6. Spampinato MV, Smith JK, Kwock L, et al. **Cerebral blood volume measurements and proton MR spectroscopy in grading of oligodendroglial tumors.** *AJR Am J Roentgenol* 2007;188:204–12 CrossRef Medline
7. Law M, Yang S, Babb JS, et al. **Comparison of cerebral blood volume and vascular permeability from dynamic susceptibility contrast-enhanced perfusion MR imaging with glioma grade.** *AJNR Am J Neuroradiol* 2004;25:746–55 Medline
8. Hilario A, Ramos A, Perez-Nuñez A, et al. **The added value of apparent diffusion coefficient to cerebral blood volume in the preoperative grading of diffuse gliomas.** *AJNR Am J Neuroradiol* 2012;33:701–07 CrossRef Medline
9. Hakyemez B, Erdogan C, Ercan I, et al. **High-grade and low-grade gliomas: differentiation by using perfusion MR imaging.** *Clin Radiol* 2005;60:493–502 CrossRef Medline
10. Khalid L, Carone M, Dumrongpisutikul N, et al. **Imaging characteristics of oligodendrogliomas that predict grade.** *AJNR Am J Neuroradiol* 2012;33:852–57 CrossRef Medline
11. Bian W, Khayal IS, Lupo JM, et al. **Multiparametric characterization of grade 2 glioma subtypes using magnetic resonance spectroscopic, perfusion, and diffusion imaging.** *Transl Oncol* 2009;2:271–80 CrossRef Medline
12. Guillevin R, Menuel C, Abud L, et al. **Proton MR spectroscopy in predicting the increase of perfusion MR imaging for WHO grade II gliomas.** *J Magn Reson Imaging* 2012;35:543–50 CrossRef Medline
13. Lin Y, Dawant BM. **Automatic detection of the anterior and poste-**

rior commissures on MRI scans using regression forests. *Conf Proc IEEE Eng Med Biol Soc* 2014;2014:1505–08 CrossRef Medline
14. Roy B, Gupta RK, Maudsley AA, et al. **Utility of multiparametric 3-T MRI for glioma characterization.** *Neuroradiology* 2013;55:603–13 CrossRef Medline
15. Boxerman JL, Hamberg LM, Rosen BR, et al. **MR contrast due to intravascular magnetic susceptibility perturbations.** *Magn Reson Med* 1995;34:555–66 CrossRef Medline
16. Emblem KE, Mouridsen K, Bjornerud A, et al. **Vessel architectural imaging identifies cancer patient responders to anti-angiogenic therapy.** *Nat Med* 2013;19:1178–83 CrossRef Medline
17. Troprès I, Lamalle L, Péoc'h M, et al. **In vivo assessment of tumoral angiogenesis.** *Magn Reson Med* 2004;51:533–41 CrossRef Medline
18. Kiselev VG, Strecker R, Ziyeh S, et al. **Vessel size imaging in humans.** *Magn Reson Med* 2005;53:553–63 CrossRef Medline
19. Hsu YY, Yang WS, Lim KE, et al. **Vessel size imaging using dual contrast agent injections.** *J Magn Reson Imaging* 2009;30:1078–84 CrossRef Medline
20. Choi SH, Chi JG, Kim YB, et al. **Anterior commissure–posterior commissure revisited.** *Korean J Radiol* 2013;14:653–61 CrossRef Medline
21. Jerome NP, Hekmatyar SK, Kauppinen RA. **Blood oxygenation level dependent, blood volume, and blood flow responses to carbogen and hypoxic hypoxia in 9L rat gliomas as measured by MRI.** *J Magn Reson Imaging* 2014;39:110–19 CrossRef Medline
22. Hu LS, Baxter LC, Pinnaduwage DS, et al. **Optimized preload leakage-correction methods to improve the diagnostic accuracy of dynamic susceptibility-weighted contrast-enhanced perfusion MR imaging in posttreatment gliomas.** *AJNR Am J Neuroradiol* 2010;31:40–48 CrossRef Medline
23. Paulson ES, Schmainda KM. **Comparison of dynamic susceptibility-weighted contrast-enhanced MR methods: recommendations for measuring relative cerebral blood volume in brain tumors.** *Radiology* 2008;249:601–13 CrossRef Medline
24. Emblem KE, Nedregaard B, Nome T, et al. **Glioma grading by using histogram analysis of blood volume heterogeneity from MR-derived cerebral blood volume maps.** *Radiology* 2008;247:808–17 CrossRef Medline
25. Deb P, Boruah D, Dutta V. **Morphometric study of microvessels in primary CNS tumors and its correlation with tumor types and grade.** *Microvasc Res* 2012;84:34–43 CrossRef Medline
26. Korkolopoulou P, Patsouris E, Konstantinidou AE, et al. **Hypoxia-inducible factor 1alpha/vascular endothelial growth factor axis in astrocytomas: associations with microvessel morphometry, proliferation and prognosis.** *Neuropathol Appl Neurobiol* 2004;30:267–78 CrossRef Medline
27. Sharma S, Sharma MC, Sarkar C. **Morphology of angiogenesis in human cancer: a conceptual overview, histoprognostic perspective and significance of neoangiogenesis.** *Histopathology* 2005;46:481–89 CrossRef Medline
28. Daumas-Duport C, Scheithauer B, O'Fallon J, et al. **Grading of astrocytomas: a simple and reproducible method.** *Cancer* 1988;62:2152–65 Medline
29. Lemasson B, Chenevert TL, Lawrence TS, et al. **Impact of perfusion map analysis on early survival prediction accuracy in glioma patients.** *Transl Oncol* 2013;6:766–74 CrossRef Medline
30. Pannetier N, Lemasson B, Christen T, et al. **Vessel size index measurements in a rat model of glioma: comparison of the dynamic (Gd) and steady-state (iron-oxide) susceptibility contrast MRI approaches.** *NMR Biomed* 2012;25:218–26 CrossRef Medline

MR Imaging–Based Analysis of Glioblastoma Multiforme: Estimation of *IDH1* Mutation Status

K. Yamashita, A. Hiwatashi, O. Togao, K. Kikuchi, R. Hatae, K. Yoshimoto, M. Mizoguchi, S.O. Suzuki, T. Yoshiura, and H. Honda

ABSTRACT

BACKGROUND AND PURPOSE: Glioblastoma multiforme is highly aggressive and the most common type of primary malignant brain tumor in adults. Imaging biomarkers may provide prognostic information for patients with this condition. Patients with glioma with *isocitrate dehydrogenase 1* (*IDH1*) mutations have a better clinical outcome than those without such mutations. Our purpose was to investigate whether the *IDH1* mutation status in glioblastoma multiforme can be predicted by using MR imaging.

MATERIALS AND METHODS: We retrospectively studied 55 patients with glioblastoma multiforme with wild type *IDH1* and 11 patients with mutant *IDH1*. Absolute tumor blood flow and relative tumor blood flow within the enhancing portion of each tumor were measured by using arterial spin-labeling data. In addition, the maximum necrosis area, the percentage of cross-sectional necrosis area inside the enhancing lesions, and the minimum and mean apparent diffusion coefficients were obtained from contrast-enhanced T1-weighted images and diffusion-weighted imaging data. Each of the 6 parameters was compared between patients with wild type *IDH1* and mutant *IDH1* by using the Mann-Whitney *U* test. The performance in discriminating between the 2 entities was evaluated by using receiver operating characteristic analysis.

RESULTS: Absolute tumor blood flow, relative tumor blood flow, necrosis area, and percentage of cross-sectional necrosis area inside the enhancing lesion were significantly higher in patients with wild type *IDH1* than in those with mutant *IDH1* ($P < .05$ each). In contrast, no significant difference was found in the $ADC_{minimum}$ and ADC_{mean}. The area under the curve for absolute tumor blood flow, relative tumor blood flow, percentage of cross-sectional necrosis area inside the enhancing lesion, and necrosis area were 0.850, 0.873, 0.739, and 0.772, respectively.

CONCLUSIONS: Tumor blood flow and necrosis area calculated from MR imaging are useful for predicting the *IDH1* mutation status.

ABBREVIATIONS: ASL = arterial spin-labeling; aTBF = absolute tumor blood flow; AUC = area under the curve; GBM = glioblastoma multiforme; *IDH1* = *isocitrate dehydrogenase 1*; *IDH1m* = mutant *IDH1*; *IDH1w* = wild type *IDH1*; *MGMT* = *O^6-methylguanine-DNA methyltransferase*; %NEC = percentage of cross-sectional necrosis area inside the enhancing lesion; NEC_{area} = necrosis area; rTBF = relative tumor blood flow; TBF = tumor blood flow

Glioblastoma multiforme (GBM) is highly aggressive and the most common type of primary malignant brain tumor in adults. The characteristic histologic appearance of GBM includes hypercellularity, nuclear polymorphism, high mitotic activity, prominent microvascular proliferation, and/or necrosis. MR imaging is the main noninvasive technique for diagnosing GBM. Conventional MR imaging techniques including pre- and postcontrast T1WI show precise anatomic localization and/or centrally nonenhancing regions, which are typically related histologically to necrotic areas. Diehn et al[1] provided evidence that the amount of necrosis correlated with outcome in patients with GBM. In addition, correlations were recently identified between the prognosis of patients with GBM and several functional imaging parameters, including ADC derived from DWI, tumor blood volume calculated from DSC, and tumor blood flow (TBF) calculated from arterial spin-labeling (ASL) perfusion MR imaging.[2-7] ASL is a recently developed MR perfusion imaging technique that has advantages of being noninvasive, not requiring an extrinsic tracer, and allowing reliable absolute quantification, which is not affected by a disrupted blood-brain barrier.[8] ASL is increasingly

Received March 19, 2015; accepted after revision May 22.

From the Departments of Clinical Radiology (K.Yamashita, A.H., O.T., K.K., T.Y., H.H.), Neurosurgery (R.H., K.Yoshimoto., M.M.), and Neuropathology (S.O.S.), Graduate School of Medical Sciences, Kyushu University, Fukuoka, Japan; and Department of Radiology (T.Y.), Kagoshima University Graduate School of Medical and Dental Sciences, Kagoshima, Japan.

This work was supported by Japan Society for the Promotion of Science KAKENHI (grant No. 26461828).

Please address correspondence to Akio Hiwatashi, MD, PhD, Department of Clinical Radiology, Graduate School of Medical Sciences, Kyushu University, 3-1-1 Maidashi, Higashi-ku, Fukuoka 812-8582, Japan; e-mail: hiwatasi@radiol.med.kyushu-u.ac.jp

Indicates open access to non-subscribers at www.ajnr.org

http://dx.doi.org/10.3174/ajnr.A4491

recognized as a noninvasive method for quantitative CBF measurement for assessing stroke, neurodegenerative diseases, and brain tumors.[8-14] ADC measurement is a widely used method. Good correlations have been reported between ADC and tumor cellularity, and its utility for application in glioma grading has been addressed in many studies.[15-19]

GBMs are classified into primary and secondary GBMs. Primary GBMs develop rapidly de novo, without clinical or histologic evidence of a less malignant precursor lesion.[20] In contrast, secondary GBMs develop by progressing from a low-grade diffuse astrocytoma or anaplastic astrocytoma.[20] These GBM subtypes are usually indistinguishable histologically. However, genetic evidence suggests that mutations in *isocitrate dehydrogenase (IDH1)* can be used to identify most secondary GBMs. The *IDH1* mutation status is an independent prognostic factor in patients with gliomas.[21-23] In previous reports, patients with gliomas with *IDH1* mutations had a better clinical outcome (median overall survival = 2.0–3.8 years) than those without such mutations (median overall survival = 0.8–1.1 years).[24,25] In addition, a specific compound impairs the growth of mutant *IDH1* but not wild type *IDH1* glioma cells.[26] These approaches may offer new possibilities for targeted therapy. The status of *O^6-methylguanine-DNA methyltransferase* (*MGMT*) promotor methylation is also an important factor for the prognosis of patients with GBM. Patients with GBM with *MGMT* promotor methylation are more responsive to temozolomide therapy and have better clinical outcome than those without it.[27-29] Therefore, the detection of *IDH1* mutations and *MGMT* promotor methylation is of great importance for patients with GBM. Carrillo et al[29] suggested that patients with mutant *IDH1* have low vascular endothelial growth factor levels, which are associated with contrast enhancement. These findings led to the hypothesis that measurement of tumor vascularity and the necrosis area would be helpful to differentiate *IDH1* mutation status.

Our purpose was to investigate whether the *IDH1* mutation and *MGMT* methylation status in GBM can be predicted by using MR imaging.

MATERIALS AND METHODS

This study was approved by the institutional review board of Kyushu University Hospital. Informed consent for study participation was waived due to the retrospective nature of this study.

MR imaging data of consecutive patients between May 2007 and August 2013 were obtained and retrospectively analyzed. Considering the effect of perfusion parameters, we excluded enrolled patients who received bevacizumab. Consequently, we examined data for 55 patients with GBM (54 primary and 1 recurrent) with wild type *IDH1* (*IDH1w*: mean age, 54.8 ± 18.6 years; range, 5–83 years) and 11 patients with GBM (5 primary and 6 recurrent) with mutant *IDH1* (*IDH1m*: mean age, 39.9 ± 11.8 years; range, 26–62 years). Among them, ASL was performed in 61.8% (34/55) of patients with *IDH1w* and 81.8% (9/11) of those with *IDH1m*. DWI was performed in 98.1% (54/55) of those with *IDH1w* and 100% (11/11) of those with *IDH1m*, and conventional MR imaging was performed in 100% (55/55) of those with *IDH1w* and 100% (11/11) of those with *IDH1m*. All primary and recurrent GBMs were histopathologically diagnosed by board-certified neuropathologists. The average interval between MR imaging and the operation was 7.1 days (range, 0–15 days).

MR Imaging

All images were obtained by using a 3T MR imaging unit (Achieva 3T TX; Philips Healthcare, Best, the Netherlands) and an 8-channel head array receiving coil for sensitivity encoding parallel imaging.

ASL

ASL was performed by using quantitative signal targeting with alternating radiofrequency labeling of the arterial region, a pulsed ASL technique developed by Petersen et al.[30] The details of the sequence have been described elsewhere.[7] Our quantitative signal targeting with alternating radiofrequency labeling of the arterial region protocol consisted of 84 dynamic or 42 pairs of labeled and nonlabeled image acquisitions. Of these, 24 pairs were acquired with crusher gradients (velocity-encoding threshold = 4 cm/s) and 12 pairs were acquired without crushers. These 36 pairs were acquired at a flip angle of 35°. An additional 6 pairs were acquired at a lower flip angle (11.7°) without crushers to estimate the actual flip angle that might vary across the brain due to inhomogeneity of B1. Other imaging parameters were as follows: labeling slab thickness = 150 mm, gap between the labeling and imaging slabs = 15 mm, sensitivity encoding factor = 2.5, TR/TE = 4000/ 22 ms, sampling interval = 300 ms, sampling time points = 13, FOV = 240 mm, matrix size = 64 × 64, imaging time = 5 minutes 52 seconds. Seven 6-mm-thick transverse sections (gap = 2 mm) were placed to cover the tumor.

DWI

DWI was performed by using a single-shot spin-echo echo-planar sequence with the following parameters: TR/TE = 3421/62 ms, 90° flip angle, NEX = 1, 22 transverse sections, sensitivity encoding factor = 2.5, section thickness/gap = 5/1 mm, FOV = 230 mm, 126 × 160 matrix, imaging time = 44.5 seconds. Diffusion sensitizing gradients were applied sequentially in the x, y, and z directions with b factors of 0 and 1000 s/mm^2.

Conventional MR Imaging

Postcontrast transverse T1-weighted spin-echo images (TR/TE = 400/10 ms, flip angle = 75°, NEX = 1, 22 sections, section thickness/gap = 5/1 mm, FOV = 230 mm, 256 × 173 matrix, imaging time = 2 minutes 43 seconds) were obtained. A standard dose (0.1 mmol/kg body weight) of a gadolinium-based contrast agent, gadopentate dimeglumine (Magnevist; Bayer HealthCare Pharmaceuticals, Wayne, New Jersey), gadoteridol (ProHance; Bracco Diagnostics, Princeton, New Jersey), or gadodiamide (Omniscan; GE Healthcare, Piscataway, New Jersey) was injected intravenously. Precontrast T1-weighted spin-echo, T2-weighted turbo spin-echo, and fluid-attenuated inversion recovery images were also obtained.

Detection of IDH1 Mutations and MGMT Promotor Methylation in Glioblastoma Tissues

GBM samples were obtained from each patient during the operation at our hospital. A portion of the tumor tissue was snap-

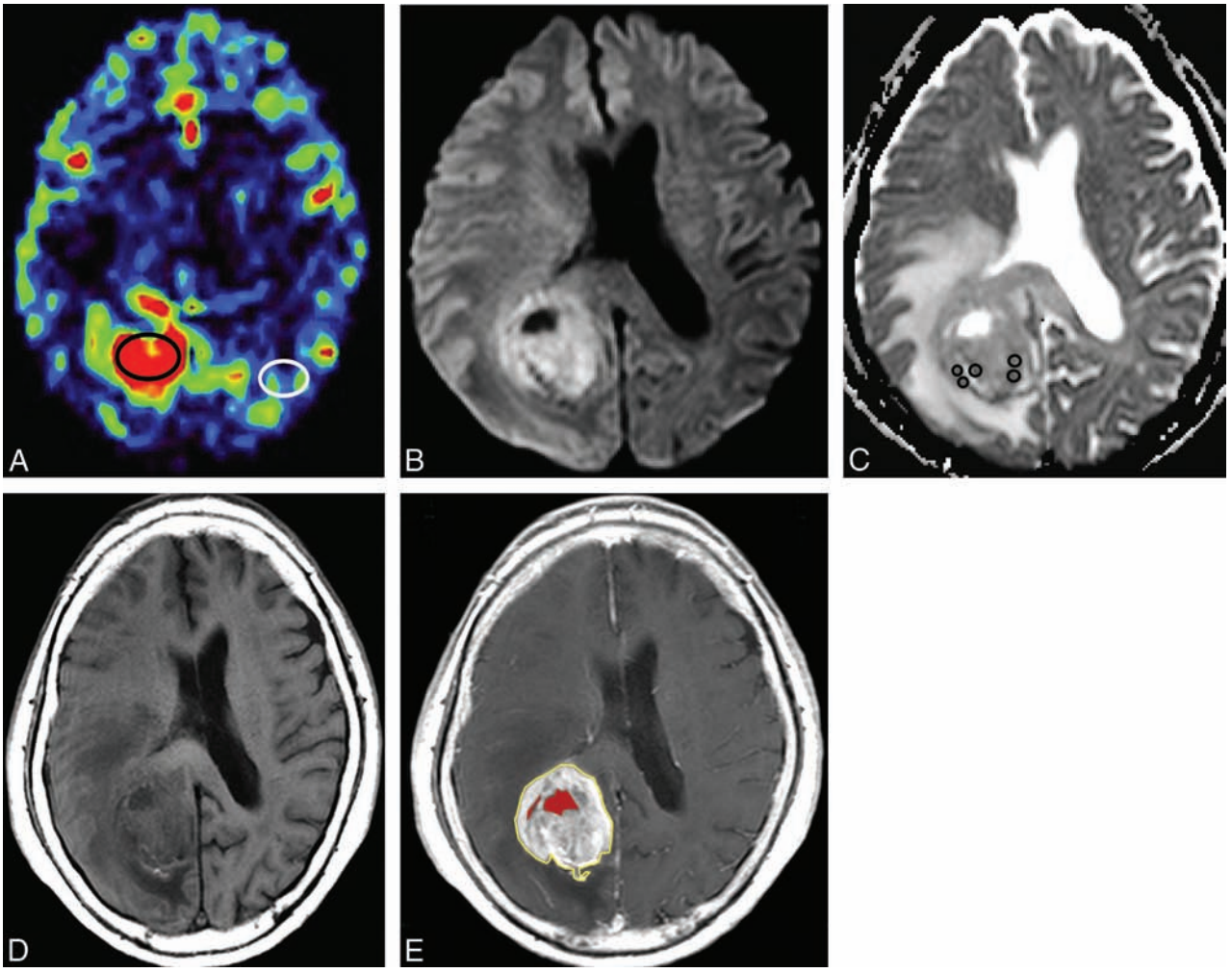

FIG 1. Images showing an example of determination of the TBF (*A*), ADC (*B* and *C*), and necrosis area (*D* and *E*). To determine absolute tumor blood flow, we placed the ROI in the enhancing lesion (*A*, *black circle*). Relative TBF was obtained by normalizing the aTBF by a blood flow measurement from the reference region (*white circle*). For ADC measurements, circular ROIs (*C*, *black circles*) were placed on ADC maps within the area that corresponded to the enhancing area on postcontrast T1WI, and the mean ADC value was obtained for each ROI. The lowest mean ADC value within all ROIs was determined as the minimum ADC. Regions with relatively low ADC were targeted. *D* and *E*, The largest cross-sectional necrosis area (red) and the percentage of the nonenhancing area inside the largest cross-sectional enhancing lesion were identified by manually outlining both the inside (red) and outside (yellow) enhancing contour to determine the NEC_{area}. The enhancing area was carefully determined with reference to both pre- and postcontrast T1WI.

frozen in liquid nitrogen and stored at −80°C. Tumor DNA was isolated from the frozen blocks by using a QIAamp DNA Blood Mini Kit (QIAGEN, Tokyo, Japan). A 129-bp fragment spanning the catalytic domain of *IDH1* including codon 132 was amplified by using the sense primer IDH1f 5′-CGGTCTTCAGAGAAGC-CATT-3′ and the antisense primer IDH1r 5′-GCAAAATC-ACATTATTGCCAAC-3′, as described previously.[31,32] Sequences were determined by using an ABI 3100 Genetic Analyzer (Applied Biosystems, Foster City, California).

DNA methylation status of the *MGMT* promotor was determined by bisulfite modification and subsequent methylation-specific polymerase chain reactions. Methylation-specific polymerase chain reactions were performed by using the primers previously reported by Esteller et al[33] and 50-ng bisulfite-modified tumor DNA, in addition to both methylated and unmethylated control samples (CpGenome Universal Methylated and Unmethylated DNA; EMD Millipore, Billerica, Massachusetts). The polymerase chain reaction conditions included 35 cycles of 30 seconds each at 95°C, 60°C, and 72°C. The polymerase chain reaction products were electrophoresed on 3% agarose gels. The method has been described in detail before.[34]

Image Analysis

The ASL data were analyzed on a desktop computer (Let's note, Panasonic Corporation, Osaka, Japan). Maps of CBF were obtained by using dedicated software running on Interactive Data Language (Research Systems, Boulder, Colorado), which was developed and provided by Petersen et al (National Neuroscience Institute, Singapore). Measurement of blood flow was performed by using ROI analysis by 2 independent neuroradiologists (K. Yamashita and O.T.), who were blinded to the clinical and pathologic information. A free software package (MRIcro, http://www.mccauslandcenter.sc.edu/mricro/mricro/mricro.html) was used to draw ROIs on the CBF maps. For each tumor, mean absolute (aTBF) and relative tumor blood flow (rTBF) were measured in each ROI (Fig 1*A*).[35-38] Interrater agreement was evaluated by the

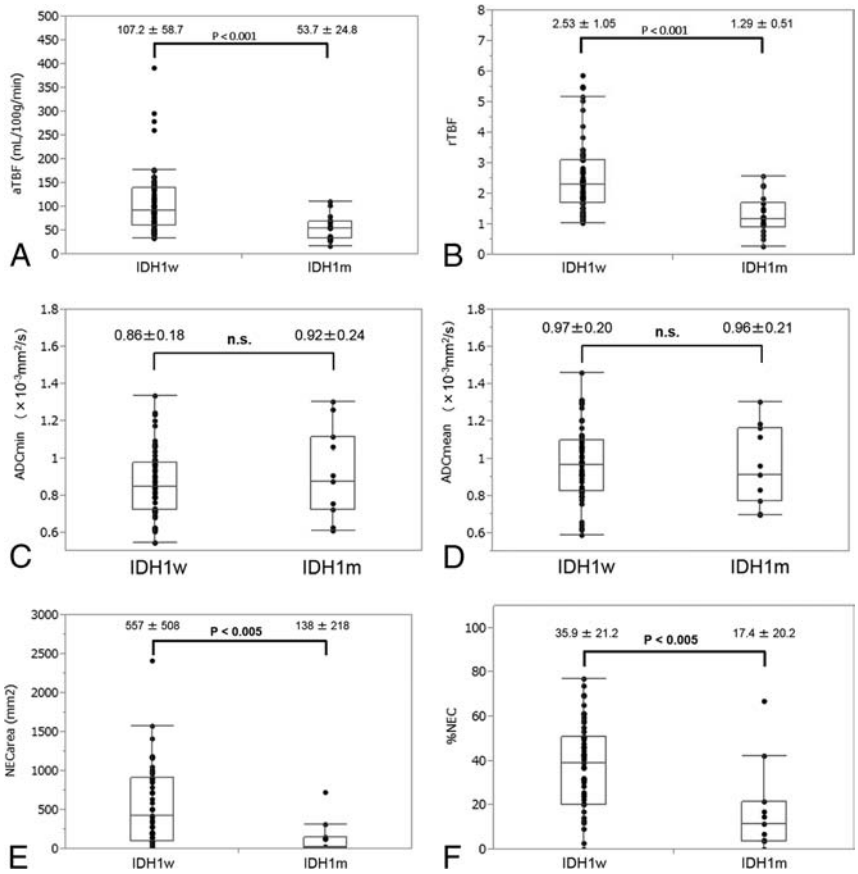

FIG 2. Plots of aTBF (*A*), rTBF (*B*), $ADC_{minimum}$ (*C*), ADC_{mean} (*D*), NEC_{area} (*E*), and %NEC (*F*) in patients with *IDH1w* and *IDH1m*. The aTBF, rTBF, NEC_{area}, and %NEC were significantly higher in patients with *IDH1w* compared with those with *IDH1m* ($P < .05$ each). In contrast, no significant difference was found in the $ADC_{minimum}$ and ADC_{mean}.

Bland-Altman analysis, the intraclass correlation coefficient, and the Spearman rank correlation coefficient.

Maps of ADC were calculated by using the following formula: $\ln(S/S_0) = -b \times ADC$, where S_0 and S are the signal intensities when the b values are 0 and 1000 s/mm^2, respectively, and b itself is 1000 s/mm^2. For ADC measurements, 1 author (K. Yamashita performed the ROI analysis by using a PACS system. Four or more circular ROIs (area, ≥10 mm^2) were placed on ADC maps within the area that corresponded to the enhancing area on postcontrast T1WI, and the mean ADC value was obtained for each ROI (Fig 1*B*, -*C*).[4,19,39] Regions with relatively low ADC were targeted, whereas blood vessels, calcifications, necrosis, and hemorrhages were strictly avoided for ROI placement. The lowest and the average mean ADC values within all ROIs were determined as the minimum ADC and the mean ADC.

In addition, the largest cross-sectional necrosis area (NEC_{area}) and the percentage of nonenhancing area inside the largest cross-sectional enhancing lesion (%NEC) were identified by manually outlining both the inside and outside enhancing contour to determine the necrosis area. The enhancing area was carefully determined with reference to both pre- and postcontrast T1WI (Fig 1*D*, -*E*). These determinations were performed by 1 author (K. Yamashita), followed by visual inspection by another neuroradiologist (O.T.). When multifocal lesions were noted, the maximum enhancing lesion was targeted.

Each of the 6 parameters (aTBF, rTBF, $ADC_{minimum}$, ADC_{mean}, NEC_{area}, and %NEC) was compared between patients with *IDH1w* and *IDH1m* and between patients with a methylated *MGMT* promoter and those with an unmethylated *MGMT* promoter by using the Student t test. A P value $< .05$ was statistically significant. The performance in discriminating between patients with *IDH1w* and *IDH1m* was evaluated by using receiver operating characteristic analysis. Area under the curve (AUC) values for the discrimination were calculated for parameters that were statistically significant. Multivariate logistic regression analysis was performed to evaluate the combination of the parameters. AUC values were compared with each other by using a nonparametric approach.[40] All statistical analyses were performed by using JMP 11 Pro software (SAS Institute, Cary, North Carolina).

RESULTS

aTBF, rTBF, NEC_{area}, and %NEC were significantly higher in patients with *IDH1w* (mean aTBF = 107.2 ± 58.7 mL/100 g/min, mean rTBF = 2.53 ± 1.05, mean NEC_{area} = 557 ± 508 mm^2, and mean %NEC = 35.9% ± 21.2%) than in those with *IDHm* (mean aTBF = 53.7 ± 24.8 mL/100 g/min, mean rTBF = 1.29 ± 0.51, mean NEC_{area} = 138 ± 218 mm^2, and mean %NEC = 17.4% ± 20.2%) ($P < .05$ each, Fig 2). In contrast, no significant differences were found in $ADC_{minimum}$ ($ADC_{minimum}$ = 0.86 ± 0.18 × 10^{-3}mm^2/s; range, 0.54–1.33 × 10^{-3}mm^2/s in *IDH1w*, 0.92 ± 0.24 × 10^{-3}mm^2/s; range, 0.61–1.30 × 10^{-3}mm^2/s in *IDH1m*) and ADC_{mean} (ADC_{mean} = 0.97 ± 0.20 × 10^{-3}mm^2/s; range, 0.59–1.46 × 10^{-3}mm^2/s in *IDH1w*, 0.96 ± 0.21 × 10^{-3}mm^2/s; range, 0.69–1.30 × 10^{-3}mm^2/s in *IDH1m*) ($P > .05$ each).

No significant differences were observed in any parameters between patients with a methylated *MGMT* promoter and those with an unmethylated *MGMT* promoter (Table).

The optimal cutoff value was 70.0 mL/100 g/min for aTBF with 76.5% sensitivity, 88.9% specificity, and 79.1% accuracy. For rTBF, the optimal cutoff value was 1.55 with 88.2% sensitivity, 77.8% specificity, and 86.0% accuracy. For %NEC, the optimal cutoff value was 22.5 with 72.7% sensitivity, 81.8% specificity, and 74.2% accuracy. For NEC_{area}, the optimal cutoff value was 151 mm^2 with 72.7% sensitivity, 81.8% specificity, and 74.2% accuracy. The AUCs for aTBF, rTBF, %NEC, and NEC_{area} were 0.850, 0.873, 0.739, and 0.772, respectively (Fig 3). No significant difference in AUC values was found among aTBF, rTBF, %NEC, and NEC_{area}. The combination of the 4 parameters increased the diagnostic performance (AUC = 0.915). The AUC value was sig-

Comparison between 6 parameters and *MGMT* methylation status

	Methylated	Unmethylated	*P* Value
aTBF (mL/100 g/min)	100.4 ± 1.13 ($n = 19$)	99.4 ± 55.4 ($n = 15$)	.96
rTBF	2.54 ± 1.31 ($n = 19$)	2.35 ± 0.81 ($n = 15$)	.62
$ADC_{minimum}$ ($\times 10^3 mm^2/s$)	0.88 ± 0.19 ($n = 24$)	0.84 ± 0.20 ($n = 21$)	.57
ADC_{mean} ($\times 10^3 mm^2/s$)	0.97 ± 0.19 ($n = 24$)	0.96 ± 0.21 ($n = 21$)	.92
NEC_{area} (mm^2)	503 ± 424 ($n = 25$)	621 ± 430 ($n = 21$)	.36
%NEC	37.3 ± 21.1 ($n = 25$)	38.6 ± 22.7 ($n = 21$)	.85

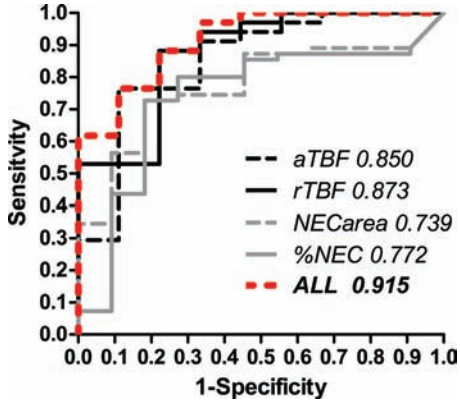

FIG 3. Receiver operating characteristic curves for discrimination between patients with *IDH1w* and those with *IDH1m* with the parameters aTBF, rTBF, NEC_{area}, and %NEC. The AUC was significantly higher with the combination of all parameters than with NEC_{area} or %NEC alone ($P < .05$).

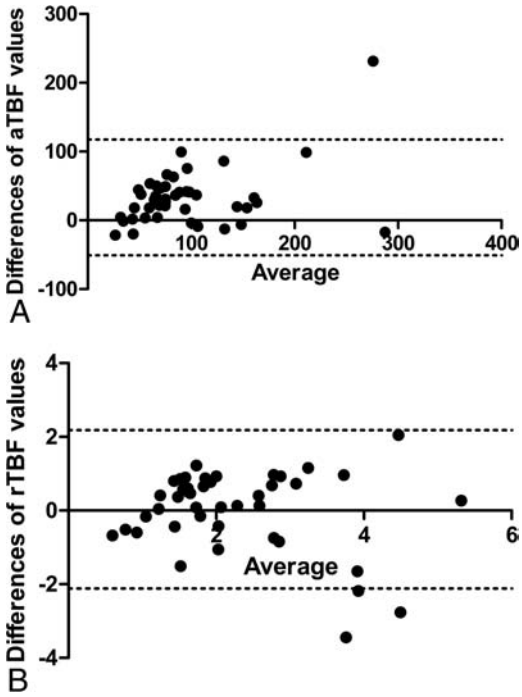

FIG 4. Bland-Altman plots showing the interobserver variability of the differences versus average of aTBF (*A*) and rTBF (*B*) values. *Dashed lines* represent the 95% limits of agreement.

nificantly higher with the combination of all parameters than with NEC_{area} or %NEC alone ($P < .05$).

Bland-Altman analysis resulted in a mean bias of 33.4 with 95% limits of agreement in differences versus the average of the aTBF values, which ranged from −50.7 to 117.6, and 0.03 with 95% limits of agreement in differences versus the average of the rTBF values, which ranged from −2.12 to 2.18 (Fig 4). The intraclass correlation coefficient was 0.861 (95% confidence interval, 0.743–0.925) for aTBF and 0.745 (95% confidence interval, 0.530–0.862) for rTBF, which indicated a high correlation. For the Spearman rank correlation coefficient, good correlation was shown for both aTBF ($\rho = 0.774$, $P < .01$) and rTBF ($\rho = 0.709$, $P < .01$) for the values between the 2 neuroradiologists.

Figures 5 and 6 show representative cases of *IDH1w* and *IDH1m*, respectively.

DISCUSSION

Our study demonstrated that both aTBF and rTBF were significantly higher in patients with *IDH1w* than in those with *IDH1m*. Microvascular proliferation is induced by the vascular endothelial growth factor, which shows markedly higher expression in primary than secondary GBMs.[41] Diehn et al[1] suggested that vascular endothelial growth factor production is associated with angiogenesis and contrast enhancement. The relationship between vascular endothelial growth factor and *IDH1* remains uncertain. However, these results suggested that a correlation may exist between tumor vascularity and *IDH1* mutation status. In addition, a previous study by using ASL showed that high TBF in GBM is associated with poor overall survival.[42] ASL measurements may provide additional prognostic information.

In this study, both NEC_{area} and %NEC were significantly higher in patients with *IDH1w* than in those with *IDH1m*. In GBM, hypoxia-mediated activation of the coagulation system causes intravascular thrombosis, which further increases intratumoral hypoxia and leads to abnormal endothelial cell proliferation and tumor necrosis.[43] Previous studies demonstrated that large areas of ischemic and/or pseudopalisading necrosis are more frequent in primary than in secondary GBMs,[44] and in patients with *IDH1w* than in those with *IDH1m*.[25] Carlson et al[45] indicated that necrosis is associated with higher levels of vascular endothelial growth factor. Our results are in line with these previous reports.

We found that both TBF and the necrosis area in patients with *IDH1w* were significantly higher than in those with *IDH1m*. The AUC value was significantly higher with the combination of all 4 parameters (aTBF, rTBF, NEC_{area}, and %NEC) than with NEC_{area} or %NEC alone. This is the first report to compare the performance of ASL, DWI, and gadolinium T1WI for predicting the *IDH1* mutation status in GBM, to our knowledge. Our results suggested that the combination of TBF derived from ASL and measurement of the necrosis area may be a surrogate marker for predicting the *IDH1* mutation status. Noninvasive estimates of tumor vascularity (aTBF, rTBF) and necrosis (NEC_{area}, %NEC) may be useful for evaluating the prognosis of patients with GBM and their *IDH1* mutation status. Patients with *IDH1w* and *IDH1m* follow different clinical courses, and GBMs with these mutations are considered to be 2 distinct disease entities.[46] TBF and tumor necrosis area measurements play supportive roles as predictors of

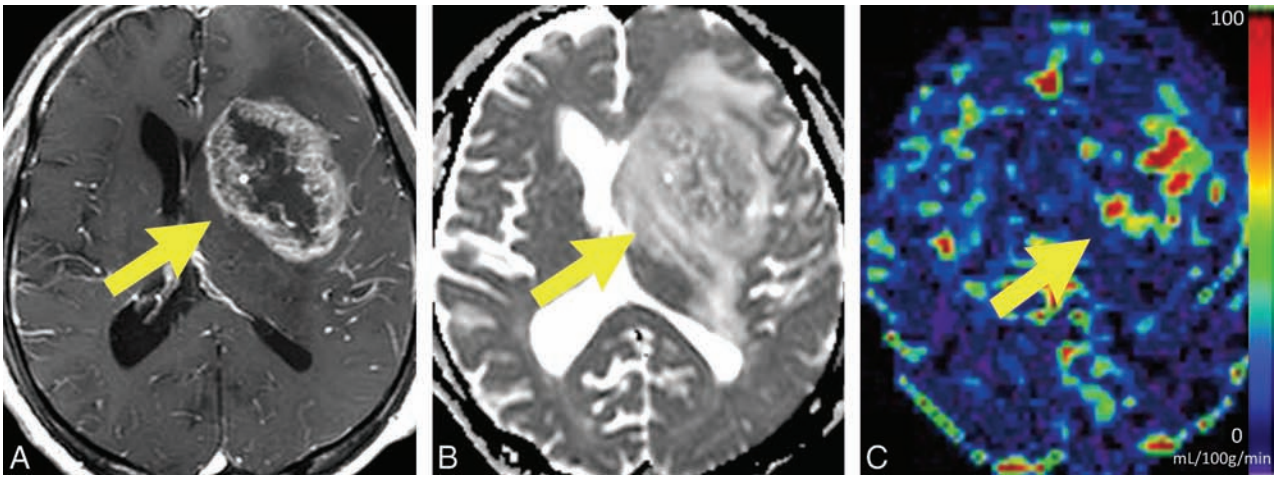

FIG 5. Contrast-enhanced T1WI (*A*), ADC map derived from DWI (*B*), and TBF map derived from ASL (*C*) of a 73-year-old woman with *IDH1w*. High aTBF (96.2 mL/100 g/min) and rTBF (2.78) were demonstrated in the enhancing tumor. The tumor also showed a high NEC_{area} (518 mm^2) and %NEC (44.2).

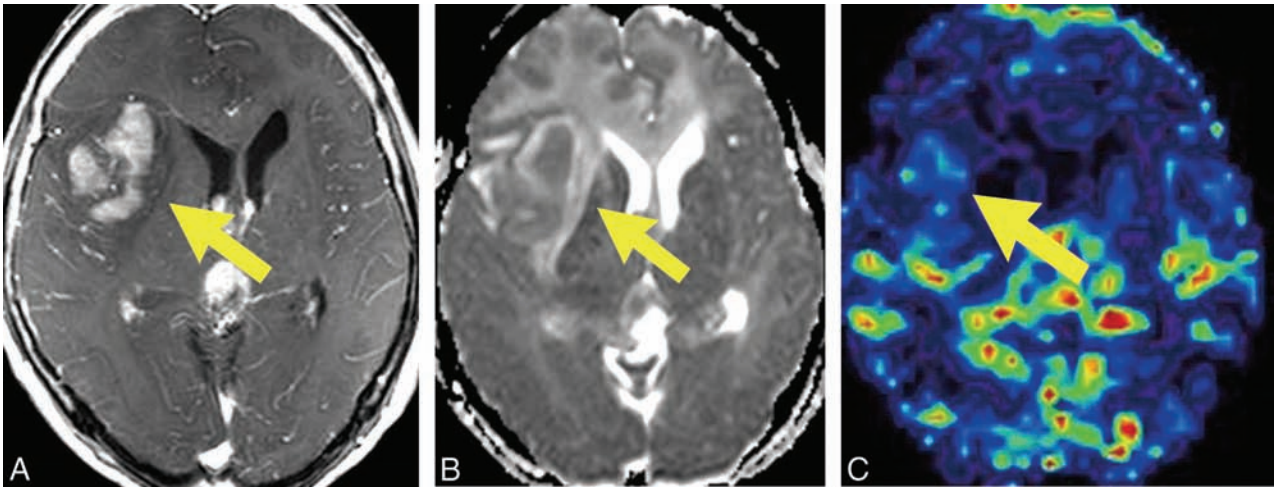

FIG 6. Contrast-enhanced T1WI (*A*), ADC map derived from DWI (*B*), and TBF map derived from ASL (*C*) of a 62-year-old woman with *IDH1m*. ASL perfusion demonstrated a relatively low aTBF (31.6 mL/100 g/min) and rTBF (1.05) in the enhancing tumor. The tumor also showed a low NEC_{area} (30 mm^2) and %NEC (4.14).

the response to current treatment and tumor aggressiveness. These measurements may provide important information for selecting more or less intensive treatment.

With ADC measurement, no significant difference was found between patients with *IDH1w* and those with *IDH1m* in our study. Lee et al[47] showed that the mean ADC value in patients with *IDH1m* was significantly higher than that in those with *IDH1w*. This difference may be attributed to patient selection. The *IDH1m* group had a significantly higher proportion of anaplastic astrocytoma than the *IDH1w* group in their study. In our study, only patients with GBM were included. Lazovic et al[48] found no significant differences in ADC in nonnecrotic tumor regions between patients with *IDH1w* and those with *IDH1m*. On the basis of a radiologic-pathologic correlation study, no significant correlation between the Ki-67 labeling index and minimum ADC was noted for the GBM group.[19] Our results are consistent with those in the literature.

IDH1m and *MGMT* promotor methylation are related to a better clinical prognosis.[21-23,27-29] A selective inhibitor of mutant *IDH1* has been proved to delay glioma growth.[26] Patients with GBM with *MGMT* promotor methylation are more sensitive to temozolomide therapy and are associated with a favorable outcome.[27-29] Noninvasive prediction of *IDH1* mutation and *MGMT* promotor methylation could contribute to the development of treatment strategies such as further targeted therapy. No significant differences were observed in any parameters derived from MR imaging between patients with a methylated *MGMT* promoter and those with an unmethylated *MGMT* promoter. Carrillo et al[29] indicated that the methylation status does not correlate with any imaging features (size, enhancement, noncontrast enhancing tumor, necrosis, edema, cysts, and location). The group of patients with an unmethylated *MGMT* promoter showed a significant difference in mean rCBV between pseudoprogression and real progression, though the group with a methylated *MGMT* promoter showed no significant difference in another study.[49] These results suggest that predicting *MGMT* promoter methylation status from MR imaging may be challenging.[29]

Our study has some limitations. First, as mentioned earlier, not all patients were studied with all 3 imaging modalities (ASL, DWI, and postcontrast T1WI). Some recurrent cases of *IDH1w* and *IDH1m* were included in our study. The tumor sample was not acquired stereotactically before resection. However, a 3D MR image overlay navigation system and 5-aminolevulinic acid fluorescence-guided surgery were used to avoid necrotic or nonenhancing tumor regions when obtaining the GBM sample. Finally, automated MR imaging volumetric quantification of tumor necrosis was not applied because we believe that both pre- and postcontrast T1WI are required to correctly determine the enhancing area.

CONCLUSIONS

Our results suggested that TBF calculated from ASL and tumor necrosis area derived from conventional MR imaging are useful for predicting the *IDH1* mutation status.

Disclosures: Koji Yamashita—*RELATED*: *Grant*: Japan Society for the Promotion of Science (Japanese grant) KAKENHI 26461828.* Akio Hiwatashi—*UNRELATED*: *Grants/Grants Pending*: Japan Society for the Promotion of Science KAKENHI for MRI. *Money paid to the institution.

REFERENCES

1. Diehn M, Nardini C, Wang DS, et al. **Identification of noninvasive imaging surrogates for brain tumor gene-expression modules.** *Proc Natl Acad Sci U S A* 2008;105:5213–18 CrossRef Medline
2. Henson JW, Gaviani P, Gonzalez RG. **MRI in treatment of adult gliomas.** *Lancet Oncol* 2005;6:167–75 CrossRef Medline
3. Hakyemez B, Erdogan C, Bolca N, et al. **Evaluation of different cerebral mass lesions by perfusion-weighted MR imaging.** *J Magn Reson Imaging* 2006;24:817–24 CrossRef Medline
4. Calli C, Kitis O, Yunten N, et al. **Perfusion and diffusion MR imaging in enhancing malignant cerebral tumors.** *Eur J Radiol* 2006;58:394–403 CrossRef Medline
5. Yamasaki F, Kurisu K, Satoh K, et al. **Apparent diffusion coefficient of human brain tumors at MR imaging.** *Radiology* 2005;235:985–91 CrossRef Medline
6. Weber MA, Zoubaa S, Schlieter M, et al. **Diagnostic performance of spectroscopic and perfusion MRI for distinction of brain tumors.** *Neurology* 2006;66:1899–906 CrossRef Medline
7. Yamashita K, Yoshiura T, Hiwatashi A, et al. **Differentiating primary CNS lymphoma from glioblastoma multiforme: assessment using arterial spin labeling, diffusion-weighted imaging, and ^{18}F-fluorodeoxyglucose positron emission tomography.** *Neuroradiology* 2013;55:135–43 CrossRef Medline
8. Warmuth C, Gunther M, Zimmer C. **Quantification of blood flow in brain tumors: comparison of arterial spin labeling and dynamic susceptibility-weighted contrast-enhanced MR imaging.** *Radiology* 2003;228:523–32 CrossRef Medline
9. Alsop DC, Detre JA, Grossman M. **Assessment of cerebral blood flow in Alzheimer's disease by spin-labeled magnetic resonance imaging.** *Ann Neurol* 2000;47:93–100 CrossRef Medline
10. Chalela JA, Alsop DC, Gonzalez-Atavales JB, et al. **Magnetic resonance perfusion imaging in acute ischemic stroke using continuous arterial spin labeling.** *Stroke* 2000;31:680–87 CrossRef Medline
11. Detre JA, Alsop DC, Vives LR, et al. **Noninvasive MRI evaluation of cerebral blood flow in cerebrovascular disease.** *Neurology* 1998;50:633–41 CrossRef Medline
12. Noguchi T, Yoshiura T, Hiwatashi A, et al. **Perfusion imaging of brain tumors using arterial spin-labeling: correlation with histopathologic vascular density.** *AJNR Am J Neuroradiol* 2008;29:688–93 CrossRef Medline
13. Yoshiura T, Hiwatashi A, Noguchi T, et al. **Arterial spin labelling at 3-T MR imaging for detection of individuals with Alzheimer's disease.** *Eur Radiol* 2009;19:2819–25 CrossRef Medline
14. Tourdias T, Rodrigo S, Oppenheim C, et al. **Pulsed arterial spin labeling applications in brain tumors: practical review.** *J Neuroradiol* 2008;35:79–89 CrossRef Medline
15. Kim HS, Kim SY. **A prospective study on the added value of pulsed arterial spin-labeling and apparent diffusion coefficients in the grading of gliomas.** *AJNR Am J Neuroradiol* 2007;28:1693–99 CrossRef Medline
16. Kono K, Inoue Y, Nakayama K, et al. **The role of diffusion-weighted imaging in patients with brain tumors.** *AJNR Am J Neuroradiol* 2001;22:1081–88 Medline
17. Provenzale JM, Mukundan S, Barboriak DP. **Diffusion-weighted and perfusion MR imaging for brain tumor characterization and assessment of treatment response.** *Radiology* 2006;239:632–49 CrossRef Medline
18. Tien RD, Felsberg GJ, Friedman H, et al. **MR imaging of high-grade cerebral gliomas: value of diffusion-weighted echoplanar pulse sequences.** *AJR Am J Roentgenol* 1994;162:671–77 CrossRef Medline
19. Higano S, Yun X, Kumabe T, et al. **Malignant astrocytic tumors: clinical importance of apparent diffusion coefficient in prediction of grade and prognosis.** *Radiology* 2006;241:839–46 CrossRef Medline
20. Ohgaki H, Kleihues P. **Genetic pathways to primary and secondary glioblastoma.** *Am J Pathol* 2007;170:1445–53 CrossRef Medline
21. Ichimura K, Pearson DM, Kocialkowski S, et al. **IDH1 mutations are present in the majority of common adult gliomas but rare in primary glioblastomas.** *Neuro Oncol* 2009;11:341–47 CrossRef Medline
22. Myung JK, Cho HJ, Park CK, et al. **IDH1 mutation of gliomas with long-term survival analysis.** *Oncol Rep* 2012;28:1639–44 Medline
23. Ducray F, Marie Y, Sanson M. **IDH1 and IDH2 mutations in gliomas.** *N Engl J Med* 2009;360:2248–49; author reply 2249 Medline
24. Parsons DW, Jones S, Zhang X, et al. **An integrated genomic analysis of human glioblastoma multiforme.** *Science* 2008;321:1807–12 CrossRef Medline
25. Nobusawa S, Watanabe T, Kleihues P, et al. **IDH1 mutations as molecular signature and predictive factor of secondary glioblastomas.** *Clin Cancer Res* 2009;15:6002–07 CrossRef Medline
26. Rohle D, Popovici-Muller J, Palaskas N, et al. **An inhibitor of mutant IDH1 delays growth and promotes differentiation of glioma cells.** *Science* 2013;340:626–30 CrossRef Medline
27. Kreth S, Thon N, Eigenbrod S, et al. **O-methylguanine-DNA methyltransferase (MGMT) mRNA expression predicts outcome in malignant glioma independent of MGMT promoter methylation.** *PLoS One* 2011;6:e17156 CrossRef Medline
28. Hegi ME, Liu L, Herman JG, et al. **Correlation of O6-methylguanine methyltransferase (MGMT) promoter methylation with clinical outcomes in glioblastoma and clinical strategies to modulate MGMT activity.** *J Clin Oncol* 2008;26:4189–99 CrossRef Medline
29. Carrillo JA, Lai A, Nghiemphu PL, et al. **Relationship between tumor enhancement, edema, IDH1 mutational status, MGMT promoter methylation, and survival in glioblastoma.** *AJNR Am J Neuroradiol* 2012;33:1349–55 CrossRef Medline
30. Petersen ET, Lim T, Golay X. **Model-free arterial spin labeling quantification approach for perfusion MRI.** *Magn Reson Med* 2006;55:219–32 CrossRef Medline
31. Ma X, Yoshimoto K, Guan Y, et al. **Associations between microRNA expression and mesenchymal marker gene expression in glioblastoma.** *Neuro Oncol* 2012;14:1153–62 CrossRef Medline
32. Fuller GN, Hess KR, Rhee CH, et al. **Molecular classification of human diffuse gliomas by multidimensional scaling analysis of gene expression profiles parallels morphology-based classification, correlates with survival, and reveals clinically-relevant novel glioma subsets.** *Brain Pathol* 2002;12:108–16 CrossRef Medline
33. Esteller M, Garcia-Foncillas J, Andion E, et al. **Inactivation of the DNA-repair gene MGMT and the clinical response of gliomas to alkylating agents.** *N Engl J Med* 2000;343:1350–54 CrossRef Medline
34. Araki Y, Mizoguchi M, Yoshimoto K, et al. **Quantitative digital as-**

sessment of MGMT immunohistochemical expression in glioblastoma tissue. *Brain Tumor Pathol* 2011;28:25–31 CrossRef Medline
35. Yamashita K, Yoshiura T, Hiwatashi A, et al. **Arterial spin labeling of hemangioblastoma: differentiation from metastatic brain tumors based on quantitative blood flow measurement.** *Neuroradiology* 2012;54:809–13 CrossRef Medline
36. Lehmann P, Monet P, de Marco G, et al. **A comparative study of perfusion measurement in brain tumours at 3 Tesla MR: arterial spin labeling versus dynamic susceptibility contrast-enhanced MRI.** *Eur Neurol* 2010;64:21–26 CrossRef Medline
37. Löbel U, Sedlacik J, Reddick WE, et al. **Quantitative diffusion-weighted and dynamic susceptibility-weighted contrast-enhanced perfusion MR imaging analysis of T2 hypointense lesion components in pediatric diffuse intrinsic pontine glioma.** *AJNR Am J Neuroradiol* 2011;32:315–22 CrossRef Medline
38. Loeber RT, Sherwood AR, Renshaw PF, et al. **Differences in cerebellar blood volume in schizophrenia and bipolar disorder.** *Schizophr Res* 1999;37:81–89 CrossRef Medline
39. Sugahara T, Korogi Y, Kochi M, et al. **Usefulness of diffusion-weighted MRI with echo-planar technique in the evaluation of cellularity in gliomas.** *J Magn Reson Imaging* 1999;9:53–60 Medline
40. DeLong ER, DeLong DM, Clarke-Pearson DL. **Comparing the areas under two or more correlated receiver operating characteristic curves: a nonparametric approach.** *Biometrics* 1988;44:837–45 CrossRef Medline
41. Godard S, Getz G, Delorenzi M, et al. **Classification of human astrocytic gliomas on the basis of gene expression: a correlated group of genes with angiogenic activity emerges as a strong predictor of subtypes.** *Cancer Res* 2003;63:6613–25 Medline
42. Farace P, Amelio D, Ricciardi GK, et al. **Early MRI changes in glioblastoma in the period between surgery and adjuvant therapy.** *J Neurooncol* 2013;111:177–85 CrossRef Medline
43. Ohgaki H, Kleihues P. **The definition of primary and secondary glioblastoma.** *Clin Cancer Res* 2013;19:764–72 CrossRef Medline
44. Homma T, Fukushima T, Vaccarella S, et al. **Correlation among pathology, genotype, and patient outcomes in glioblastoma.** *J Neuropathol Exp Neurol* 2006;65:846–54 CrossRef Medline
45. Carlson MR, Pope WB, Horvath S, et al. **Relationship between survival and edema in malignant gliomas: role of vascular endothelial growth factor and neuronal pentraxin 2.** *Clin Cancer Res* 2007;13:2592–98 CrossRef Medline
46. Lai A, Kharbanda S, Pope WB, et al. **Evidence for sequenced molecular evolution of IDH1 mutant glioblastoma from a distinct cell of origin.** *J Clin Oncol* 2011;29:4482–90 CrossRef Medline
47. Lee S, Choi SH, Ryoo I, et al. **Evaluation of the microenvironmental heterogeneity in high-grade gliomas with IDH1/2 gene mutation using histogram analysis of diffusion-weighted imaging and dynamic-susceptibility contrast perfusion imaging.** *J Neurooncol* 2015;121:141–50 CrossRef Medline
48. Lazovic J, Soto H, Piccioni D, et al. **Detection of 2-hydroxyglutaric acid in vivo by proton magnetic resonance spectroscopy in U87 glioma cells overexpressing isocitrate dehydrogenase-1 mutation.** *Neuro Oncol* 2012;14:1465–72 CrossRef Medline
49. Kong DS, Kim ST, Kim EH, et al. **Diagnostic dilemma of pseudoprogression in the treatment of newly diagnosed glioblastomas: the role of assessing relative cerebral blood flow volume and oxygen-6-methylguanine-DNA methyltransferase promoter methylation status.** *AJNR Am J Neuroradiol* 2011;32:382–87 CrossRef Medline

Improved Brain Tumor Classification by Sodium MR Imaging: Prediction of *IDH* Mutation Status and Tumor Progression

A. Biller, S. Badde, A. Nagel, J.-O. Neumann, W. Wick, A. Hertenstein, M. Bendszus, F. Sahm, N. Benkhedah, and J. Kleesiek

ABSTRACT

BACKGROUND AND PURPOSE: MR imaging in neuro-oncology is challenging due to inherent ambiguities in proton signal behavior. Sodium-MR imaging may substantially contribute to the characterization of tumors because it reflects the functional status of the sodium-potassium pump and sodium channels.

MATERIALS AND METHODS: Sodium-MR imaging data of patients with treatment-naïve glioma WHO grades I–IV ($n = 34$; mean age, 51.29 ± 17.77 years) were acquired by using a 7T MR system. For acquisition of sodium-MR images, we applied density-adapted 3D radial projection reconstruction pulse sequences. Proton-MR imaging data were acquired by using a 3T whole-body system.

RESULTS: We demonstrated that the initial sodium signal of a treatment-naïve brain tumor is a significant predictor of *isocitrate dehydrogenase (IDH)* mutation status ($P < .001$). Moreover, independent of this correlation, the Cox proportional hazards model confirmed the sodium signal of treatment-naïve brain tumors as a predictor of progression ($P = .003$). Compared with the molecular signature of *IDH* mutation status, information criteria of model comparison revealed that the sodium signal is even superior to *IDH* in progression prediction. In addition, sodium-MR imaging provides a new approach to noninvasive tumor classification. The sodium signal of contrast-enhancing tumor portions facilitates differentiation among most glioma types ($P < .001$).

CONCLUSIONS: The information of sodium-MR imaging may help to classify neoplasias at an early stage, to reduce invasive tissue characterization such as stereotactic biopsy specimens, and overall to promote improved and individualized patient management in neuro-oncology by novel imaging signatures of brain tumors.

ABBREVIATIONS: AA = anaplastic astrocytoma; CE = contrast-enhancing; GB = glioblastoma; GG = ganglioglioma; *IDH* = *isocitrate dehydrogenase*; NaR = relaxation-weighted sodium signal; NaT = total sodium signal; PA = pilocytic astrocytoma; PFS = progression-free survival; PH = proportional hazard; WHO = World Health Organization

Gliomas are the most common type of primary brain tumor.[1] They are classified on the basis of MR imaging, histopathologic, and clinical criteria. However, MR imaging in neuro-oncology is challenging due to inherent ambiguities in proton (^{1}H) signal behavior. Contrast-enhancing (CE) tumor portions in T1WI do not necessarily represent a malignant tumor.[2] For example, gangliogliomas (GGs) and pilocytic astrocytomas (PAs), both low-grade gliomas, demonstrate vivid contrast enhancement.[3] In turn, tissue that appears normal without contrast enhancement or physiologic T2 signal may be tumorous tissue.[4,5] The evolving method of sodium (Na) MR imaging may substantially contribute to the characterization of tumors by neuro-oncologic imaging because it reflects the functional status of the sodium-potassium pump and Na channels. It allows 2 signals to be determined, which reflect the total amount of tissue Na (NaT)[6,7] as well as the amount of ions with short relaxation times (NaR).[7,8] The NaR signal is dependent on the microstructural

Received March 25, 2015; accepted after revision June 9.

From the Departments of Neuroradiology (A.B., M.B., J.K.), Neurosurgery (J.-O.N.), Neuro-Oncology (W.W., A.H.), and Neuropathology (F.S.), and Multidimensional Image Processing Group (J.K.), HCI/IWR, University of Heidelberg, Heidelberg, Germany; Departments of Radiology (A.B., J.K.) and Medical Physics in Radiology (A.N., N.B.), German Cancer Research Centre (DKFZ), Heidelberg, Germany; and Department of Biological Psychology and Neuropsychology (S.B.), University of Hamburg, Hamburg, Germany.

A. Biller and A. Nagel were supported by an educational grant from the National Centre of Tumour Diseases Heidelberg (NCT IFP V/3). J. Kleesiek was supported by a postdoctoral fellowship from the Medical Faculty of the University of Heidelberg.

Paper previously presented at: Annual Meeting of the American Society of Neuroradiology and the Foundation of the ASNR Symposium, May 17–22, 2014; Montreal, Quebec, Canada.

Please address correspondence to Armin Biller, MD, Department of Neuroradiology, University of Heidelberg, Im Neuenheimer Feld 400, 69120 Heidelberg, Germany; e-mail: armin.biller@med.uni-heidelberg.de

Indicates open access to non-subscribers at www.ajnr.org

Indicates article with supplemental on-line appendix and tables.

Indicates article with supplemental on-line photos.

http://dx.doi.org/10.3174/ajnr.A4493

environment, and, mainly, intracellular Na ions contribute to it. It correlates with the Ki-67 proliferation index of tumor cells.[7] To evaluate the implications of Na-MR imaging for neuro-oncologic patient management, we analyzed Na-MR imaging data of treatment-naïve gliomas in correlation with progression-free survival (PFS) and tumor classification. We propose that the Na signal ratio NaR:NaT is a predictor for PFS and show that NaR:NaT is superior even to the prognostic information of the *isocitrate dehydrogenase (IDH)* mutational status. In contrast to the genetic characterization of *IDH*, Na-MR imaging is noninvasive and no contrast medium is needed. Moreover, Na-MR imaging yields highly relevant information that promotes tumor classification. Overall, our observations underline that Na-MR imaging is a valuable noninvasive tool for prognostic and diagnostic assessment in neuro-oncology.

MATERIALS AND METHODS

Ethics Statement

The study was approved by the local medical ethics committee (Faculty of Clinical Medicine, University of Heidelberg), and all the participants gave written informed consent before enrollment. The procedures that followed were in accordance with the Declaration of Helsinki.

Patient Cohort

Inclusion criteria were 1) the suspected diagnosis of a glioma, 2) in patients >18 years, and 3) without neurologic or psychiatric illness or head trauma in their history; furthermore, 4) neoplasias had to be treatment naïve, that is, no chemotherapy, radiation or surgery was performed. We measured 34 patients whose ^{1}H-MR imaging was suggestive of a glioma by using Na-MR imaging. Epidemiologic data and tumor characteristics are presented in On-line Table 1. Diagnoses of our patient population included PA, astrocytoma World Health Organization (WHO) grade II, anaplastic astrocytoma (AA), glioblastoma (GB), oligodendroglioma WHO grade II, anaplastic oligodendroglioma, anaplastic ependymoma, and gliomatosis cerebri. In addition, histopathologic analyses diagnosed 2 cerebral metastases (breast and prostate cancer), which mimicked GB on ^{1}H-MR images.

Histopathologic Analysis

Tissue was evaluated according to the current WHO classification.[1] Ki-67 index and *IDH* status were evaluated as described previously by Sahm et al.[9,10]

MR Imaging

Na-MR imaging was performed by using a 7T whole-body MR system (Magnetom 7T; Siemens, Erlangen, Germany) by using a double-resonant (^{1}H/^{23}Na) quadrature birdcage coil with an inner coil diameter of 26 cm (Rapid Biomed, Rimpar, Germany). All Na-MR images were based on a 3D attenuation-adapted projection reconstruction technique (see On-line Table 2 for details).[11] ^{1}H-MR data were acquired by using a 3T whole-body system (Tim Trio 3T; Siemens) with T2-TSE, T2-FLAIR, native and contrast-enhanced T1–3D ultrafast gradient sequences.

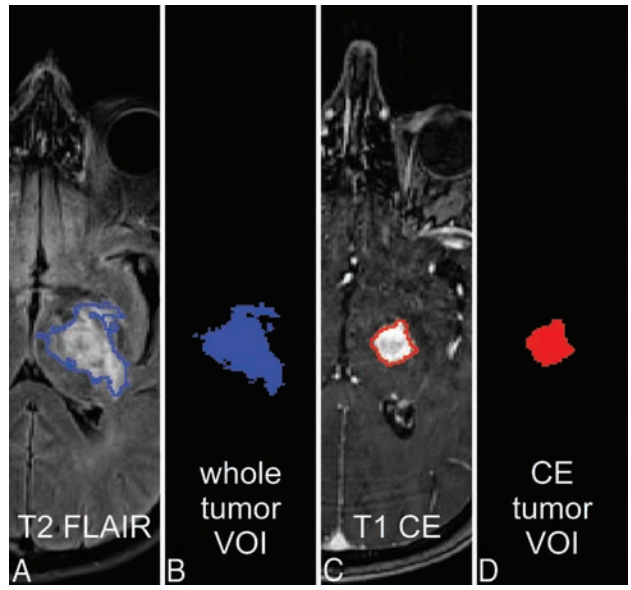

FIG 1. Tumor masking. The T2 signal of tumor and perifocal edema is shown on an exemplary T2-FLAIR image (*A*) of a patient with GG (ID no. 2, On-line Table 1); it is the basis of the whole tumor VOI (*A* and *B*, blue). CE tumor portions (*C*) define the CE tumor VOI (*C* and *D*, red). All tumor VOIs were created by using ilastik (see Materials and Methods; Image Processing; and On-line Appendix, Methods).

Image Processing

Na image reconstruction was performed off-line; Na and anatomic ^{1}H data were coregistered into the individual standard space (for details see On-line Appendix, Methods). We defined the tumor volumes of interest by their global T2 signal alterations (whole tumor VOI) and, where applicable, by their T1 signal of CE portions (CE tumor VOI) (Fig 1). In addition, we segmented healthy gray and white matter, CSF, and vessels. Segmentation was performed by using the Interactive Learning and Segmentation Toolkit (ilastik)[12] (see On-line Appendix, Methods). Data were normalized to CSF as multimodally defined by the ilastik segmentation. We integrated the information from the NaR and the NaT signal into a single quantity (arbitrary units), the NaR:NaT signal ratio, which can be understood as normalizing the NaR signal with NaT. For an illustration of this quantity, we plotted the average NaR:NaT distributions of healthy gray matter, white matter, CSF, and GB (On-line Fig 1). The NaR and NaT signal behavior in both low-grade glioma and high-grade glioma is exemplarily shown in On-line Fig 2.

Statistical Analysis

Statistical analysis was performed by using R statistical computing software (version 3.0.3; http://www.r-project.org/).[13]

Prediction of IDH Mutation Status from NaR:NaT

A logistic regression model was fitted to evaluate the predictive value of NaR:NaT for *IDH* mutation status. Based on the resulting receiver operating characteristic curve, an NaR:NaT threshold was determined, which simultaneously optimized sensitivity and specificity of the prediction (On-line Fig 3).

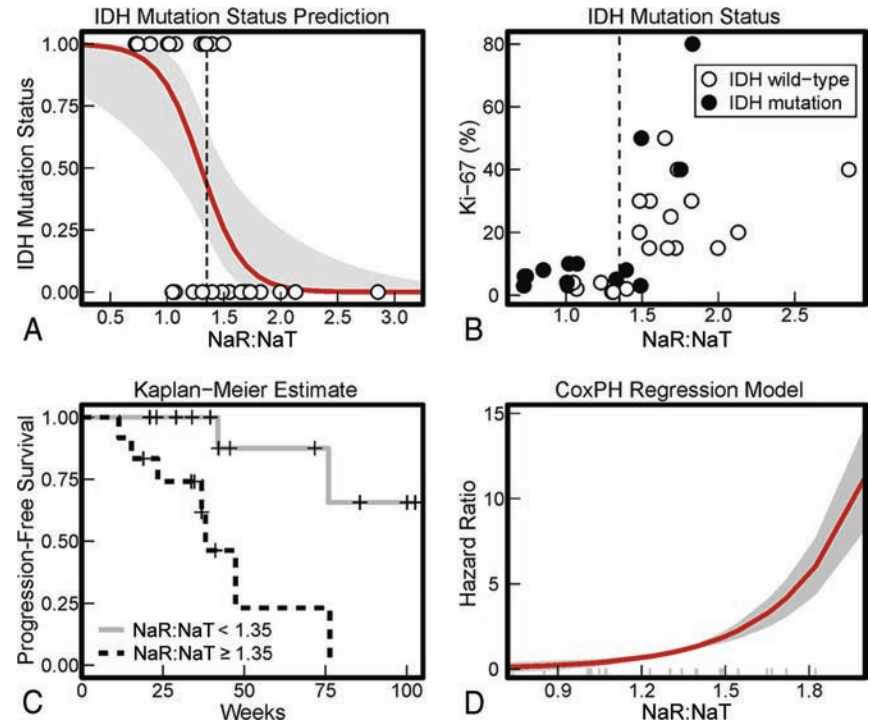

FIG 2. *A*, Prediction of *IDH* mutation status from NaR:NaT. Each circular marker indicates 1 tumor's mean NaR:NaT value and its *IDH* mutation status. These values were entered into a logistic regression model, and the resulting probabilities of *IDH* wild type based on NaR:NaT are depicted in red (the gray area shows the 95% CI of the predictions). *B*, *IDH* mutation status. With a combined optimization of sensitivity and specificity, the logistic regression model yielded an NaR:NaT threshold of 1.35 (Fig 2*A* and On-line Fig 3; area under the curve = 0.87). *IDH* mutations were found in 71% of tumors with an NaR:NaT below threshold and in 18% of tumors with an NaR:NaT above threshold. *C*, Kaplan-Meier estimates of PFS. The estimated percentage of progression-free patients is shown in dependence on time. Patients were divided into 2 groups, having an NaR:NaT value either below or above 1.35. The threshold of 1.35 was derived based on the prediction of *IDH* mutation status from NaR:NaT (Fig 2*A*). *D*, The Cox PH regression model for NaT:NaR. Predicted hazard ratios in dependence on NaR:NaT mean values from the whole tumor VOI are shown. *Long gray marks* indicate single patient values. A positive hazard ratio indicates an increase in hazard rate that can be attributed to an increase in NaT:NaR. Practically, it describes the relative risk at the instantaneous moment, which is assumed to be constant across time.

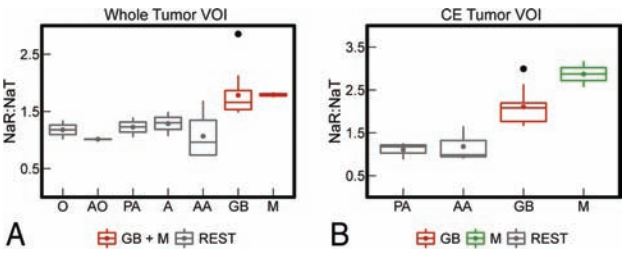

FIG 3. NaR:NaT values of different tumor classes. The boxplots visualize the mean NaR:NaT of the whole tumor VOI (*A*) and the CE tumor VOI (*B*) for different tumor classes. Because of the low sample size, gliomatosis cerebri ($n = 1$), anaplastic ependymoma ($n = 1$), and anaplastic oligodendroglioma ($n = 1$) are not depicted. For NaR:NaT of the whole tumor VOI, GB could be separated from all other gliomas (REST) but not from metastasis. NaR:NaT of the CE tumor VOI enabled all (CE) gliomas to be separated from each other except for PA versus AA (REST). Moreover, GB can be differentiated from metastasis. The box extends from the lower to upper quartile values of the data; *lines* represent the median; and *colored filled circles* depict the modal. Vertical axes indicate the range of the data; flier points are shown as *black filled circles*. O indicates oligodendroglioma; AO, anaplastic oligodendroglioma; AE, anaplastic ependymoma; GC, gliomatosis cerebri; A, astrocytoma; M, metastasis.

PFS Hazards Based on NaR:NaT

Based on the NaR:NaT threshold obtained via the *IDH* mutation status, we computed the Kaplan-Meier estimate of the resulting 2 groups. Further, to estimate the predictive properties of NaR:NaT for PFS, a Cox proportional hazard (PH) model was fitted to the right-censored survival data of the patient cohort (On-line Fig 4). The goodness of fit of this model was compared with a Cox PH model with *IDH* mutation status as a predictor (On-line Fig 5). Due to the relationship between the magnitude of NaR:NaT and *IDH* mutation status (as shown with the logistic regression), separate models, rather than a combined model, were fitted and compared based on the Akaike information criterion. To be able to compare both models, the models were constructed by using only data in which *IDH* mutation status was available.

NaR:NaT Differences among Tumor Classes

By using analysis of variance NaR:NaT from 1) whole tumor VOIs were compared among PA, astrocytoma, AA, GB, oligodendroglioma WHO grade II, anaplastic oligodendroglioma, and metastasis; and NaR:NaT from 2) CE tumor VOIs were compared among PA, AA, GB, and metastasis. Anaplastic ependymoma and gliomatosis cerebri were excluded from whole tumor VOI analysis because each group contained only a single patient. Similarly, CE tumor VOI analysis was restricted to tumors with a group size of at least 2. Post hoc analysis of significant effects was conducted with pair-wise *t* tests, corrected for multiple comparisons after Benjamini-Hochberg. All analyses used the mean NaR:NaT values of the VOI.

To determine the predictive discriminability of GB and metastasis from the remaining histopathologic classes (REST) based on NaR:NaT, we computed a logistic regression model for the whole tumor VOI and evaluated the receiver operating characteristic curve (On-line Fig 6). Next, to discriminate GB from metastasis and from PA plus AA, 2 logistic regressions were calculated for NaR:NaT values from CE VOI.

RESULTS

Prediction of IDH *Mutation from NaR:NaT*

Analysis of a logistic regression model revealed that NaR:NaT of the whole tumor VOI is a significant predictor of *IDH* mutation status ($\chi^2[1] = 14.47$, $P < .001$) (Fig 2*A*). With an increase in NaR:NaT by 0.1, the odds ratio of an *IDH* mutation grows by 21.7 ($\beta_0 = 7.00$, SE

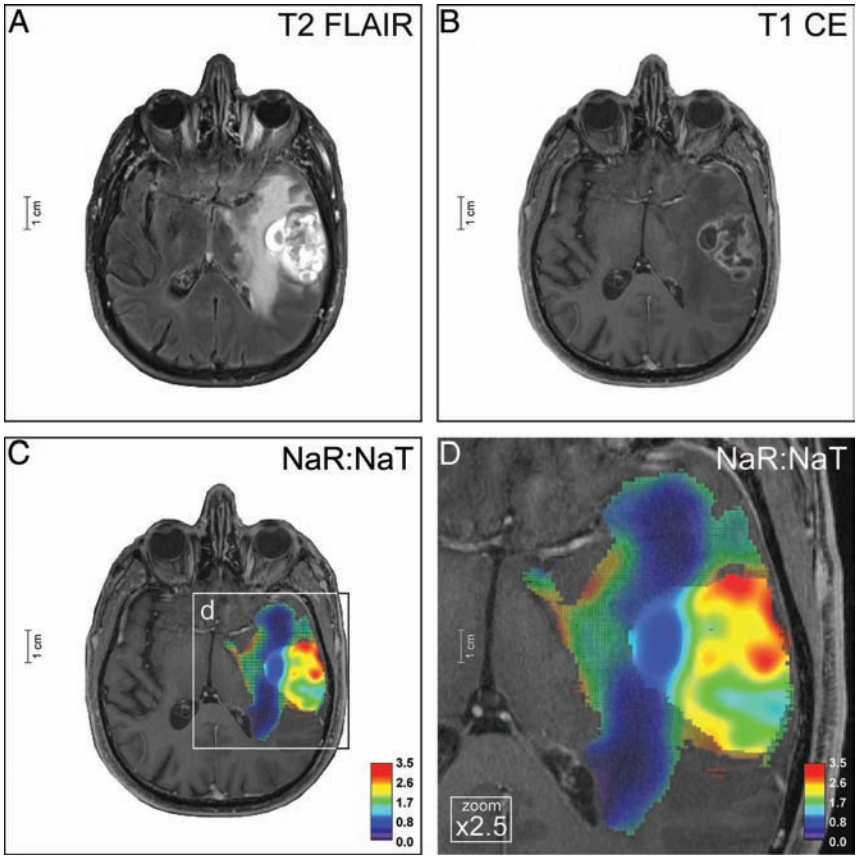

FIG 4. Ganglioglioma. The neoplasia of a 49-year-old patient (ID no. 2, On-line Table 1) affects the left thalamus, pallidum, and putamen, and is characterized by a largely homogeneous elevated T2-FLAIR signal (*A*) and somewhat rim-like contrast enhancement (*B*). Based on ^{1}H-MR imaging, differential diagnostic considerations included low-grade tumors such as GG and PA but also malignant neoplasias such as GB and cerebral metastasis. Na-MR imaging reveals a mean NaR:NaT of 1.39 (whole tumor VOI) and 1.26 (CE tumor VOI) (*C* and *D*) compatible with a low-grade tumor (Fig 3*A*, -*B*; On-line Fig 2*E*, -*F*; On-line Table 1). Thus, the differential diagnoses of GB and M could be ruled out. This result was confirmed by histopathology (On-line Fig 8). Na images are overlaid on T1-weighted postcontrast images; *color mesh grid*: whole tumor VOI, *solid color*: CE tumor VOI.

$[\beta_0] = 2.67$; $\beta_{\mathrm{NaR:NaT}} = -5.38$, SE $[\beta_{\mathrm{NaR:NaT}}] = 1.96$). With a combined optimization of sensitivity and specificity, the model yielded an NaR:NaT threshold of 1.35 (On-line Fig 3; area under the curve = 0.87), which corresponds to an odds ratio of *IDH* mutation of 0.57. *IDH* mutations were found in 71% of tumors with an NaR:NaT below threshold and in 18% of tumors with an NaR:NaT above threshold (Fig 2*B*).

Progression-Free Survival

Kaplan-Meier Estimates Based on NaR:NaT. To use the prognostic information of the *IDH* mutation status, we used the NaR:NaT threshold of 1.35 to separate tumors into a group below threshold (mean, 1.05) and a group above threshold (mean, 1.72 [95% CI, 0.47–0.86]). Based on the NaR:NaT signal threshold of 1.35, the Kaplan-Meier estimates revealed differences in the time from MR measurement to the time of disease progression (PFS) ($\chi^2[1] = 8.2$, $P = .004$). Tumors below the threshold demonstrated a substantially longer PFS than those above the threshold (Fig 2*C*).

Cox Proportional Hazard PFS Based on NaR:NaT. Analysis of a Cox PH model confirmed that NaR:NaT was a significant predictor of PFS ($\chi^2[1] = 8.77$, $P = .003$; for an analysis of the residuals see On-line Fig 4). An increase in NaR:NaT by 0.1 is associated with an increase in progression hazard rate of 340% ($\beta_{\mathrm{NaR:NaT}} = 3.53$, SE $[\beta_{\mathrm{NaR:NaT}}] = 1.34$) (Fig 2*D*). The 95% CI of the logarithmic hazard ratio $\beta_{\mathrm{NaR:NaT}}$, 2.50–271.70, indicated that, for different patient cohorts, the associated increases in hazard will, though a mild overestimation is principally possible, most probably lead to a considerable underestimation of progression rate.

In addition, the hazard ratio, that is, the change of hazard rate, of *IDH* mutation and wild type was estimated by using a Cox PH model (On-line Fig 5). Hazard rates were reliably predicted by *IDH* mutation status ($\chi^2[1] = 7.76$, $P = .005$). The hazard of progression is 9.9 times larger in the wild-type group than in the mutation group ($\beta_{IDH} = 2.30$, SE $[\beta_{IDH}] = 0.10$). A comparison of both Cox PH models revealed that NaR:NaT is a better predictor of PFS (Akaike information criterion$_{\mathrm{NaR:NaT}}$ = 36.48 < Akaike information criterion$_{IDH}$ = 37.49) than the *IDH* mutational status.

Tumor Classification

When examining NaR:NaT data of the whole tumor VOI, an ANOVA with Benjamini-Hochberg corrected *P* values of post hoc pair-wise *t* tests revealed that all brain tumors enrolled showed significantly lower NaR:NaT compared with GB and M ($F[6,25] = 5.03$, $P = .002$; no violation of homogeneity of variances assumption (Levene test $F[6,25] = 0.76$, $P = .605$); Fig 3*A* and On-line Table 3). An ANOVA on NaR:NaT from the CE tumor VOI (Fig 3*B*) revealed a significant NaR:NaT difference between GB, metastasis, and PA plus AA ($F[3,14] = 11.84$, $P < .001$; no violation of homogeneity of variances assumption [Levene test $F\{3,14\} = 0.45$, $P = .718$]; see On-line Table 4 for Benjamini-Hochberg corrected pair-wise *t* tests). A significant difference in NaR:NaT between PA and AA did not emerge. To examine the prediction quality of these significant differences in mean NaR:NaT, logistic regression models were established. The first logistic regression confirmed that NaR:NaT mean values from the whole tumor VOI are a significant predictor for the binary classification of GB plus metastasis versus REST ($\chi^2[1] = 28.96$, $P < .001$). With an increase in NaR:NaT of 0.001, the odds ratio of a tumor being either GB or metastasis grows by 968.77 ($\beta_0 = -20.44$, SE$[\beta_0] = 8.79$; $\beta_{\mathrm{NaR:NaT}} = 13.78$, SE$[\beta_{\mathrm{NaR:NaT}}] = 5.90$). At an NaR:NaT threshold of 1.50, a specificity of 94% and a sensitivity of 86% are achieved, whereas the corresponding area under the curve is 96% (On-line Fig 6). Further logistic regression models confirmed that NaR:NaT mean values from the CE tumor VOI are significant

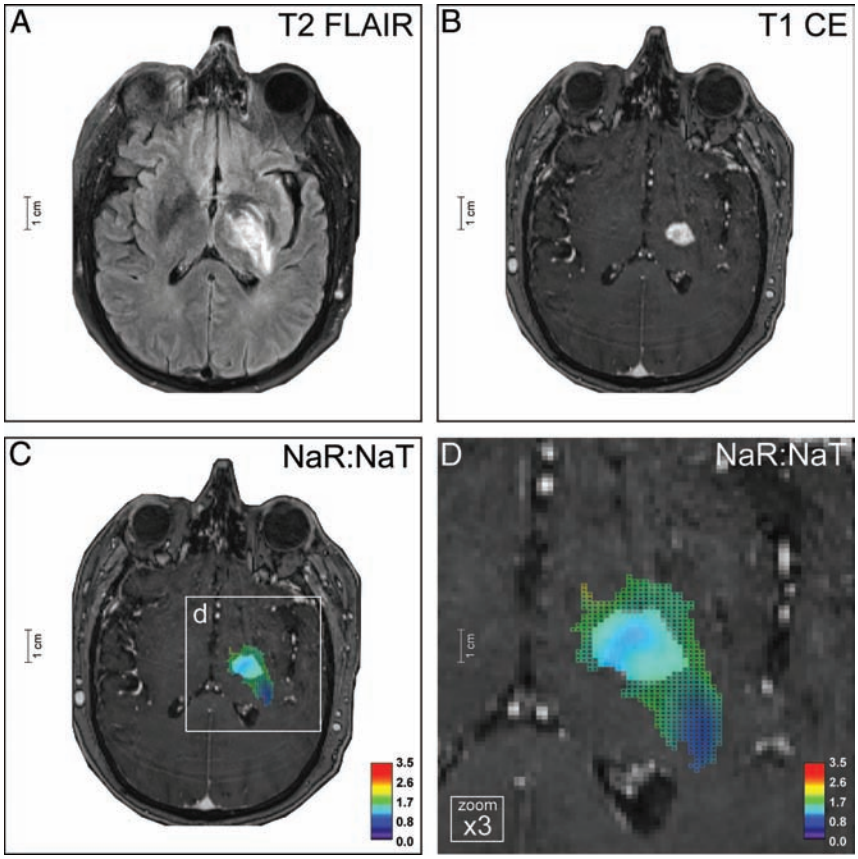

FIG 5. Glioblastoma. The left-temporal tumor of a 71-year-old male patient (ID no. 21, On-line Table 1) shows inhomogeneous central and large homogeneous perifocal T2-FLAIR hyperintensities (*A*). There is a rim-like contrast enhancement of the central tumor portion, as seen on T2-FLAIR (*A*) and T1-weighted images (*B*). Na-MR imaging demonstrates a mean NaR:NaT of 1.65 (whole tumor VOI) and 2.02 (CE tumor VOI) (*C* and *D*) compatible with GB (Fig 3*A*, -*B*; On-line Fig 2*G*, -*H*; On-line Table 1). The diagnosis was histopathologically proved (On-line Fig 8). Na-MR images are overlaid onto T1-weighted postcontrast images; *color mesh grid*: whole tumor VOI, *solid color*: CE tumor VOI.

predictors for the classification of GB versus AA plus PA ($\chi^2[1] = 4.20$, $P = .050$) and for the classification of GB versus metastasis ($\chi^2[1] = 4.28$, $P = .039$).

DISCUSSION

The current study identifies NaR:NaT as a noninvasive predictor of PFS. Furthermore, we observed a strong relationship between NaR:NaT and *IDH* mutation status. An NaR:NaT threshold is provided for the prediction of *IDH* mutation status by logistic regression. Model comparison showed that NaR:NaT was even better at predicting PFS than the genetic analyses of *IDH* based on MR imaging data. Moreover, NaR:NaT reflects relevant tissue characteristics that provide valuable information for improved tumor classification.

Gliomas are classified on the basis of MR imaging, histopathologic, and clinical criteria. In addition, molecular abnormalities in gliomas such as *IDH* mutations, *O6-methylguanine methyltransferase* promoter methylation status,[14,15] or 1p/19q co-deletions have moved into the focus of scientific interest. They are increasingly considered as supportive markers to assist diagnosis and patient management.[16] The *IDH* mutational status of a glioma is a strong prognostic marker of outcome.[17-19] Patients with WHO grades II–IV gliomas with *IDH* mutation have a better overall survival and PFS than those with wild-type *IDH*.[16,20-23] Here, we found that NaR:NaT is a significant predictor of *IDH* mutations. Based on this prediction, the logistic regression model established a threshold that made patient stratification possible. The frequency of *IDH* mutations in the group above and below this threshold was in accordance with the literature data for high- and low-grade tumors,[24,25] respectively, underlining that the threshold is not only sensible in theory but also when used in physiologic context. Kaplan-Meier estimates demonstrated a significantly longer PFS in patients with NaR:NaT below threshold. The established association does not necessarily imply causality. Still, Cox PH fits independently confirmed that both NaR:NaT and *IDH* were predictors of PFS. Moreover, model comparison based on the Akaike information criterion revealed that NaR:NaT is even superior to *IDH* in predicting PFS. Our observations are compatible with a genomic analysis of GB that revealed mutations in Na channel genes.[26] These mutations were associated with shorter survival compared with tumors with wild-type Na channels.[27] Interestingly, none of the tumors with *IDH* gene mutation had a Na channel gene mutation. The potential of NaR:NaT to predict *IDH* mutation status, as well as PFS, grants access to information that is usually restricted to genetic analyses. Hence, it extends the scope of Na-MR imaging from mere diagnosis to both diagnosis and prognosis.

Contrast-enhanced routine ^{1}H-MR imaging contributes to glioma classification through anatomic information and indication of areas with blood-brain barrier disruption. However, due to the limited specificity of T2- and T1-weighted imaging,[3,4] a nonenhancing glioma, is not always low grade (eg, AA), and a CE glioma is not necessarily malignant (eg, PA/GG). As a consequence, often only histopathologic analysis of tumor specimens provides the diagnosis. Na-MR imaging, however, yields significant information in unraveling this diagnostic dilemma. The pathophysiologic correlate is a strong relation between NaR:NaT and the tumor proliferation index Ki-67 (On-line Fig 7) on the one hand and the significant role of Na channels in tumor cell division and migration[27-31] on the other hand. NaR:NaT of the CE tumor VOI enabled differentiation of all CE tumors in our patient population except for PA versus AA. Moreover, cerebral metastases, which were initially accidentally considered to be a high-grade glioma based on ^{1}H-MR images and thus included in our study, were cor-

rectly attributed to a separate class by NaR:NaT (Fig 3*B*). To translate these findings into clinical application, we present a 49-year-old patient (ID no. 2, On-line Table 1) with a supratentorial tumor of the left thalamus, internal capsule, and pallidum. The neoplasia revealed elevated T2 signals and bulky contrast enhancement with central T1 signal reduction. Based on ^{1}H-MR imaging (Fig 4*A, -B*), the spectrum of differential diagnoses includes PA/GG, GB, and metastasis, and thus no reliable tumor classification could be provided. However, Na-MR imaging yielded additional information for tumor classification. NaR:NaT indicated the diagnosis of PA/GG (Fig 3 and Fig 4*C, -D*) and discarded the differential diagnoses of GB and M (On-line Table 1). This finding is contrasted to a case of GB in a 71-year-old patient (ID no. 21; Fig 5) which demonstrated NaR:NaT values that are indicative of GB and exclude the diagnosis of PA/GG (and metastasis) (Fig 3). Our classifications were confirmed by the histopathologic examination of the biopsy specimens (On-line Fig 8).

This exemplary clinical application underlines that the Na signal yielded significant prognostic and diagnostic information on PFS and tumor classification that will be able to guide clinical decision making in neuro-oncology in the future. Advanced physiologic ^{1}H-MR imaging techniques such as perfusion-weighted imaging, diffusion-weighted imaging, and spectroscopy (^{1}H-MR spectroscopy) provide relevant information for tumor characterization as well. For example, tumor grade is associated with relative cerebral blood volume[32-34]; volume transfer coefficient[35-38]; apparent diffusion coefficient[39,40]; and cerebral metabolite ratios, for example, the choline to *N*-acetylaspartate[33] and the choline to creatine ratios.[33,41] Also, relative cerebral blood volume,[34,42-48] volume transfer coefficient,[35,49] apparent diffusion coefficient,[50-52] and metabolite ratios, for example, the choline to *N*-acetylaspartate ratio,[53] aid prediction of PFS. Moreover, ^{1}H-MR spectroscopy of 2-hydroxyglutarate enables the detection of *IDH* mutations.[54] Future studies are needed to integrate the specific contribution of advanced ^{1}H-MR imaging and X-nuclei-MR imaging techniques, respectively, to tumor grading as well as prediction of *IDH* mutation status and PFS.

Na-MR imaging struggles to differentiate CE PA/GG from AA. This is mainly due to the large standard deviation of NaR:NaT in AA. One cause for the large standard deviation in the Na signal ratios may be the limited spatial resolution. Larger voxel sizes intrinsically smooth local signal differences to a certain extent. Another cause of this variability in NaR:NaT may be the substantial overlap in tumor cell proliferation between astrocytoma (WHO grade II), AA (WHO grade III), and GB (WHO grade IV).[1] This means that AA, which recently developed from astrocytoma, would exhibit lower NaR:NaT than AA in malignant transformation to GB. The proposed relationship between NaR:NaT and the developmental state of the tumor is supported by the strong correlation between NaR:NaT and the tumor proliferation index Ki-67 (On-line Appendix, Results; On-line Fig 7). Analysis of our data indeed indicate that NaR:NaT of AA may reflect the state of malignant transformation and that NaR:NaT as well as corresponding Ki-67 may range from values compatible with low-grade gliomas (eg, ID no. 9, On-line Table 1) to those of high-grade gliomas (eg, ID no. 10, On-line Table 1). If that is true, then future analyses of the same dataset with updated data on outcome will indicate a correlation between NaR:NaT data and the time to malignant transformation.

A future challenge in Na-MR imaging is improvement of the spatial resolution, which would, for example, enable a more-precise characterization and might allow for defining subclones of varying malignancies in high-grade tumors.[55] Besides the application of high magnetic field strengths, an increased spatial resolution can be achieved by using iterative image reconstruction techniques or multichannel receiver coils. One approach incorporates a priori information from ^{1}H-MR imaging into the image reconstruction of Na-MR data. Thereby, intensity variations in the Na image are promoted at the position of known tissue boundaries, which translate into an improved spatial resolution and enable quantification with higher accuracy.[56]

One limitation of this study is the low sample size, which was partly due to the inclusion criteria. Patients with a brain tumor had to be treatment naïve and be in a medical condition that permitted an additional MR imaging for scientific purposes. Clinical studies with larger patient populations are needed to prospectively test our prediction models and to analyze the interdependencies of the measures NaR:NaT and *IDH* as well as the effect of influencing parameters such as radiation or chemotherapy, a task that is beyond the scope of this pilot study.

CONCLUSIONS

Na-MR imaging allows for PFS prediction, which we showed is superior even to the *IDH* mutation status and improves the accuracy of brain tumor classification. Hence, Na-MR imaging is a promising candidate for noninvasive outcome prediction and tumor diagnosis, which may help to classify neoplasias at an early stage, to reduce invasive tissue characterization such as stereotactic biopsy specimens, and, overall, to promote improved patient management in neuro-oncology.

Disclosures: Armin Biller—*RELATED*: *Grant*: National Centre for Tumour Diseases.* Jan-Oliver Neumann—*RELATED*: *Grant*: National Centre of Tumour Diseases Heidelberg (NCT IFP V/3).* Wolfgang Wick—*UNRELATED*: *Board Membership*: Roche, Celldex; *Grants/Grants Pending*: Roche,* Boehringer Ingelheim*; *Patents (planned, pending or issued)*: IDH antibody.* Martin Bendszus—*UNRELATED*: *Board Membership*: Data Safety Monitoring Board for Vascular Dynamics; *Consultancy*: Codman, Guerbet, Roche; *Grants/Grants Pending*: German Research Foundation,* Hopp Foundation,* Novartis,* Guerbet,* Siemens,* Codman*; *Payment for Lectures (including service on Speakers Bureaus)*: Roche, Novartis, Guerbet, Codman. Felix Sahm—*UNRELATED*: *Grants/Grants Pending*: German Cancer Aid,* *Comments*: Exome-sequencing of meningioma; *Patents (planned, pending or issued)*: Detection of antigen presentation in-situ (patent pending).* *Money paid to the institution.

REFERENCES

1. Louis DN, Ohgaki H, Wiestler OD, et al. **The 2007 WHO classification of tumours of the central nervous system.** *Acta Neuropathol* 2007;114:97–109 CrossRef Medline
2. Cha S. **Neuroimaging in neuro-oncology.** *Neurotherapeutics* 2009;6:465–77 CrossRef Medline
3. White ML, Zhang Y, Kirby P, et al. **Can tumor contrast enhancement be used as a criterion for differentiating tumor grades of oligodendrogliomas?** *AJNR Am J Neuroradiol* 2005;26:784–90 Medline
4. Scott JN, Brasher PM, Sevick RJ, et al. **How often are nonenhancing**

supratentorial gliomas malignant? A population study. *Neurology* 2002;59:947–49 CrossRef Medline
5. Price SJ, Gillard JH. **Imaging biomarkers of brain tumour margin and tumour invasion.** *Br J Radiol* 2011;84 Spec No 2:S159–67 CrossRef Medline
6. Boada FE, LaVerde G, Jungreis C, et al. **Loss of cell ion homeostasis and cell viability in the brain: what sodium MRI can tell us.** *Curr Topics Dev Biol* 2005;70:77–101 CrossRef Medline
7. Nagel AM, Bock M, Hartmann C, et al. **The potential of relaxation-weighted sodium magnetic resonance imaging as demonstrated on brain tumors.** *Invest Radiol* 2011;46:539–47 CrossRef Medline
8. Stobbe R, Beaulieu C. **In vivo sodium magnetic resonance imaging of the human brain using soft inversion recovery fluid attenuation.** *Magn Reson Med* 2005;54:1305–10 CrossRef Medline
9. Sahm F, Capper D, Preusser M, et al. **BRAFV600E mutant protein is expressed in cells of variable maturation in Langerhans cell histiocytosis.** *Blood* 2012;120:e28–34 CrossRef Medline
10. Sahm F, Koelsche C, Meyer J, et al. **CIC and FUBP1 mutations in oligodendrogliomas, oligoastrocytomas and astrocytomas.** *Acta Neuropathol* 2012;123:853–60 CrossRef Medline
11. Nagel AM, Laun FB, Weber MA, et al. **Sodium MRI using a density-adapted 3D radial acquisition technique.** *Magn Reson Med* 2009;62:1565–73 CrossRef Medline
12. Sommer C, Straehle C, Koethe U, et al. **ilastik: Interactive Learning and Segmentation Toolkit.** In: *Proceedings of the 8th IEEE International Symposium on Biomedical Imaging*, Chicago, Illinois. March 30–April 2, 2011:230–33 CrossRef
13. R Core Team. **R: A Language and Environment for Statistical Computing.** Vienna: R Foundation for Statistical Computing, 2014
14. Wick W, Weller M, van den Bent M, et al. **MGMT testing: the challenges for biomarker-based glioma treatment.** *Nat Rev Neurol* 2014;10:372–85 CrossRef Medline
15. Weller M, van den Bent M, Hopkins K, et al. **EANO guideline for the diagnosis and treatment of anaplastic gliomas and glioblastoma.** *Lancet Oncol* 2014;15:e395–403 CrossRef Medline
16. Weiler M, Wick W. **Molecular predictors of outcome in low-grade glioma.** *Curr Opin Neurol* 2012;25:767–73 CrossRef Medline
17. Sanson M, Marie Y, Paris S, et al. **Isocitrate dehydrogenase 1 codon 132 mutation is an important prognostic biomarker in gliomas.** *J Clin Oncol* 2009;27:4150–54 CrossRef Medline
18. van den Bent MJ, Dubbink HJ, Marie Y, et al. **IDH1 and IDH2 mutations are prognostic but not predictive for outcome in anaplastic oligodendroglial tumors: a report of the European Organization for Research and Treatment of Cancer Brain Tumor Group.** *Clin Cancer Res* 2010;16:1597–604 CrossRef Medline
19. Weller M, Felsberg J, Hartmann C, et al. **Molecular predictors of progression-free and overall survival in patients with newly diagnosed glioblastoma: a prospective translational study of the German Glioma Network.** *J Clin Oncol* 2009;27:5743–50 CrossRef Medline
20. Yan H, Parsons DW, Jin G, et al. **IDH1 and IDH2 mutations in gliomas.** *N Engl J Med* 2009;360:765–73 CrossRef Medline
21. Sun H, Yin L, Li S, et al. **Prognostic significance of IDH mutation in adult low-grade gliomas: a meta-analysis.** *J Neurooncol* 2013;113:277–84 CrossRef Medline
22. Hartmann C, Hentschel B, Wick W, et al. **Patients with IDH1 wild type anaplastic astrocytomas exhibit worse prognosis than IDH1-mutated glioblastomas, and IDH1 mutation status accounts for the unfavorable prognostic effect of higher age: implications for classification of gliomas.** *Acta Neuropathol* 2010;120:707–18 CrossRef Medline
23. Wick W, Hartmann C, Engel C, et al. **NOA-04 randomized phase III trial of sequential radiochemotherapy of anaplastic glioma with procarbazine, lomustine, and vincristine or temozolomide.** *J Clin Oncol* 2009;27:5874–80 CrossRef Medline
24. Kloosterhof NK, Bralten LB, Dubbink HJ, et al. **Isocitrate dehydrogenase-1 mutations: a fundamentally new understanding of diffuse glioma?** *Lancet Oncol* 2011;12:83–91 CrossRef Medline
25. Balss J, Meyer J, Mueller W, et al. **Analysis of the IDH1 codon 132 mutation in brain tumors.** *Acta Neuropathol* 2008;116:597–602 CrossRef Medline
26. Parsons DW, Jones S, Zhang X, et al. **An integrated genomic analysis of human glioblastoma multiforme.** *Science* 2008;321:1807–12 CrossRef Medline
27. Joshi AD, Parsons DW, Velculescu VE, et al. **Sodium ion channel mutations in glioblastoma patients correlate with shorter survival.** *Mol Cancer* 2011;10:17 CrossRef Medline
28. Cuddapah VA, Sontheimer H. **Ion channels and transporters [corrected] in cancer. 2. Ion channels and the control of cancer cell migration.** *Am J Physiol Cell Physiol* 2011;301:C541–49 CrossRef Medline
29. Kunzelmann K. **Ion channels and cancer.** *J Membrane Biol* 2005;205:159–73 CrossRef Medline
30. Rooj AK, McNicholas CM, Bartoszewski R, et al. **Glioma-specific cation conductance regulates migration and cell cycle progression.** *J Biol Chem* 2012;287:4053–65 CrossRef Medline
31. Spector M, O'Neal S, Racker E. **Phosphorylation of the beta subunit of Na+K+-ATPase in Ehrlich ascites tumor by a membrane-bound protein kinase.** *J Biol Chem* 1980;255:8370–73 Medline
32. Bulakbasi N, Kocaoglu M, Farzaliyev A, et al. **Assessment of diagnostic accuracy of perfusion MR imaging in primary and metastatic solitary malignant brain tumors.** *AJNR Am J Neuroradiol* 2005;26:2187–99 Medline
33. Law M, Yang S, Wang H, et al. **Glioma grading: sensitivity, specificity, and predictive values of perfusion MR imaging and proton MR spectroscopic imaging compared with conventional MR imaging.** *AJNR Am J Neuroradiol* 2003;24:1989–98 Medline
34. Lev MH, Ozsunar Y, Henson JW, et al. **Glial tumor grading and outcome prediction using dynamic spin-echo MR susceptibility mapping compared with conventional contrast-enhanced MR: confounding effect of elevated rCBV of oligodendrogliomas [corrected].** *AJNR Am J Neuroradiol* 2004;25:214–21 Medline
35. Mills SJ, Patankar TA, Haroon HA, et al. **Do cerebral blood volume and contrast transfer coefficient predict prognosis in human glioma?** *AJNR Am J Neuroradiol* 2006;27:853–58 Medline
36. Nguyen TB, Cron GO, Mercier JF, et al. **Diagnostic accuracy of dynamic contrast-enhanced MR imaging using a phase-derived vascular input function in the preoperative grading of gliomas.** *AJNR Am J Neuroradiol* 2012;33:1539–45 CrossRef Medline
37. Roberts HC, Roberts TP, Brasch RC, et al. **Quantitative measurement of microvascular permeability in human brain tumors achieved using dynamic contrast-enhanced MR imaging: correlation with histologic grade.** *AJNR Am J Neuroradiol* 2000;21:891–99 Medline
38. Zhang N, Zhang L, Qiu B, et al. **Correlation of volume transfer coefficient Ktrans with histopathologic grades of gliomas.** *J Magn Reson Imag* 2012;36:355–63 CrossRef Medline
39. Hilario A, Sepulveda JM, Perez-Nuez A, et al. **A prognostic model based on preoperative MRI predicts overall survival in patients with diffuse gliomas.** *AJNR Am J Neuroradiol* 2014;35:1096–102 CrossRef Medline
40. Kono K, Inoue Y, Nakayama K, et al. **The role of diffusion-weighted imaging in patients with brain tumors.** *AJNR Am J Neuroradiol* 2001;22:1081–88 Medline
41. Fountas KN, Kapsalaki EZ, Vogel RL, et al. **Noninvasive histologic grading of solid astrocytomas using proton magnetic resonance spectroscopy.** *Stereotact Funct Neurosurg* 2004;82:90–7 CrossRef Medline
42. Bisdas S, Kirkpatrick M, Giglio P, et al. **Cerebral blood volume measurements by perfusion-weighted MR imaging in gliomas: ready for prime time in predicting short-term outcome and recurrent disease?** *AJNR Am J Neuroradiol* 2009;30:681–88 CrossRef Medline
43. Hirai T, Murakami R, Nakamura H, et al. **Prognostic value of perfusion MR imaging of high-grade astrocytomas: long-term follow-up study.** *AJNR Am J Neuroradiol* 2008;29:1505–10 CrossRef Medline
44. Law M, Oh S, Babb JS, et al. **Low-grade gliomas: dynamic suscepti-**

bility-weighted contrast-enhanced perfusion MR imaging—prediction of patient clinical response. *Radiology* 2006;238:658–67 CrossRef Medline

45. Law M, Young RJ, Babb JS, et al. **Gliomas: predicting time to progression or survival with cerebral blood volume measurements at dynamic susceptibility-weighted contrast-enhanced perfusion MR imaging.** *Radiology* 2008;247:490–98 CrossRef Medline
46. Spampinato MV, Schiarelli C, Cianfoni A, et al. **Correlation between cerebral blood volume measurements by perfusion-weighted magnetic resonance imaging and two-year progression-free survival in gliomas.** *Neuroradiol J* 2013;26:385–95 CrossRef Medline
47. Tzika AA, Astrakas LG, Zarifi MK, et al. **Spectroscopic and perfusion magnetic resonance imaging predictors of progression in pediatric brain tumors.** *Cancer* 2004;100:1246–56 CrossRef Medline
48. Jain R, Poisson LM, Gutman D, et al. **Outcome prediction in patients with glioblastoma by using imaging, clinical, and genomic biomarkers: focus on the nonenhancing component of the tumor.** *Radiology* 2014;272:484–93 CrossRef Medline
49. Cao Y, Nagesh V, Hamstra D, et al. **The extent and severity of vascular leakage as evidence of tumor aggressiveness in high-grade gliomas.** *Cancer Res* 2006;66:8912–17 CrossRef Medline
50. Ellingson BM, Malkin MG, Rand SD, et al. **Volumetric analysis of functional diffusion maps is a predictive imaging biomarker for cytotoxic and anti-angiogenic treatments in malignant gliomas.** *J Neurooncol* 2011;102:95–103 CrossRef Medline
51. Barajas RF Jr, Rubenstein JL, Chang JS, et al. **Diffusion-weighted MR imaging derived apparent diffusion coefficient is predictive of clinical outcome in primary central nervous system lymphoma.** *AJNR Am J Neuroradiol* 2010;31:60–66 CrossRef Medline
52. Valles FE, Perez-Valles CL, Regalado S, et al. **Combined diffusion and perfusion MR imaging as biomarkers of prognosis in immunocompetent patients with primary central nervous system lymphoma.** *AJNR Am J Neuroradiol* 2013;34:35–40 CrossRef Medline
53. Li Y, Lupo JM, Parvataneni R, et al. **Survival analysis in patients with newly diagnosed glioblastoma using pre- and postradiotherapy MR spectroscopic imaging.** *Neuro Oncol* 2013;15:607–17 CrossRef Medline
54. Andronesi OC, Rapalino O, Gerstner E, et al. **Detection of oncogenic IDH1 mutations using magnetic resonance spectroscopy of 2-hydroxyglutarate.** *J Clin Invest* 2013;123:3659–63 CrossRef Medline
55. Park CC, Hartmann C, Folkerth R, et al. **Systemic metastasis in glioblastoma may represent the emergence of neoplastic subclones.** *J Neuropathol Exp Neurol* 2000;59:1044–50 Medline
56. Gnahm C, Behl NGR, Biller A, et al. **Anatomically Weighted 2nd Order Total Variation Reconstruction of 23Na MRI Using 1H Prior Information.** In: *Proceedings of the 22nd ISMRM Scientific Meeting*, Milan, Italy. May 10–16, 2014

The Combined Performance of ADC, CSF CXC Chemokine Ligand 13, and CSF Interleukin 10 in the Diagnosis of Central Nervous System Lymphoma

M.C. Mabray, R.F. Barajas, J.E. Villanueva-Meyer, C.A. Zhang, F.E. Valles, J.L. Rubenstein, and S. Cha

ABSTRACT

BACKGROUND AND PURPOSE: CXC chemokine ligand 13 and interleukin 10 have emerged as CSF biomarkers for the diagnosis of CNS lymphoma. Our hypothesis is that the combined use of ADC, CXC chemokine ligand 13, and interleukin 10 will result in increased diagnostic performance compared with the use of ADC values alone.

MATERIALS AND METHODS: Eighty-seven patients were included in this study, including 43 with CNS lymphoma and 44 without CNS lymphoma (21 metastases, 14 high-grade gliomas, 9 tumefactive demyelinating lesions) who had undergone CSF proteomic analysis and had a new enhancing mass on brain MR imaging. Average ADC was derived by contouring the contrast-enhancing tumor volume. Group means were compared via *t* tests for average ADC, CXC chemokine ligand 13, and interleukin 10. Receiver operating characteristic analysis was performed for each individual variable. Multiple-variable logistic regression with receiver operating characteristic analysis was performed, and the multiple-variable receiver operating characteristic was compared with single-variable receiver operating characteristics.

RESULTS: The average ADC was lower and CSF CXC chemokine ligand 13 and interleukin 10 values were higher in CNS lymphoma ($P < .001$). Areas under the curve ranged from 0.739 to 0.832 for single-variable ROC. Multiple-variable logistic regression yielded statistically significant individual effects for all 3 variables in a combined model. Multiple-variable receiver operating characteristics (area under the curve, 0.928) demonstrated statistically significantly superior diagnostic performance compared with the use of single variables alone.

CONCLUSIONS: The combined use of ADC, CSF CXC chemokine ligand 13, and interleukin 10 results in increased diagnostic performance for the diagnosis of CNS lymphoma. This finding highlights the importance of CSF analysis when the diagnosis of CNS lymphoma is considered on the basis of MR imaging.

ABBREVIATIONS: ADCavg = average ADC; CNSL = central nervous system lymphoma; CXCL-13 = CXC chemokine ligand 13; IL-10 = interleukin 10; ROC = receiver operating characteristic; AUC = area under the curve

Central nervous system lymphoma (CNSL) may be primary CNSL when isolated to the central nervous system or secondary CNSL in the setting of systemic lymphoma.[1-3] Patients who are immunocompromised are at an increased risk of developing CNSL (primary or secondary); however, the rates of primary CNSL are increasing among immunocompetent patients.[4-8] CNSL now accounts for approximately 1%–5% of all brain tumors and thus should be considered in the differential diagnosis of a patient with a new brain mass lesion.[4,6,7]

Arriving at a consistently accurate preoperative diagnosis for a patient with a brain mass lesion encountered on MR imaging remains an overall difficult task.[9] There is considerable overlap in the clinical presentation and appearance of brain mass lesions on MR imaging, including CNSL, and there is much research into using advanced imaging techniques to arrive at a diagnosis.[9-13] Ultimately, most patients with a newly encountered brain mass lesion will undergo stereotactic brain biopsy to arrive at a diagnosis, an invasive procedure with a rate of diagnostic failure that may be as high as 35%.[14,15] The diagnosis of CNSL may be further complicated by its response to glucocorticoids, which may com-

Received February 26, 2015; accepted after revision May 12.

From the Departments of Radiology and Biomedical Imaging (M.C.M., R.F.B., J.E.V.-M., C.A.Z., F.E.V., S.C.), Medicine Division of Hematology/Oncology (J.L.R.), Epidemiology and Biostatistics (C.A.Z.), and Neurological Surgery (S.C.), University of California San Francisco, San Francisco, California.

M.C.M. and R.F.B. contributed equally to this study and are considered co-first authors. J.L.R. and S.C. contributed equally to this study and are considered co-senior authors.

M.C.M. and R.F.B. were supported by a National Institutes of Health T32 training grant (5T32EB001631–10).

Paper previously presented at: Annual Meeting of the Radiological Society of North America, November 30 to December 5, 2014; Chicago, Illinois.

Please address correspondence to Marc C. Mabray, MD, Radiology and Biomedical Imaging, 505 Parnassus Ave, M391, University of California, San Francisco, San Francisco, CA 94143; e-mail: marc.mabray@ucsf.edu, marccm7@gmail.com

Indicates open access to non-subscribers at www.ajnr.org

http://dx.doi.org/10.3174/ajnr.A4450

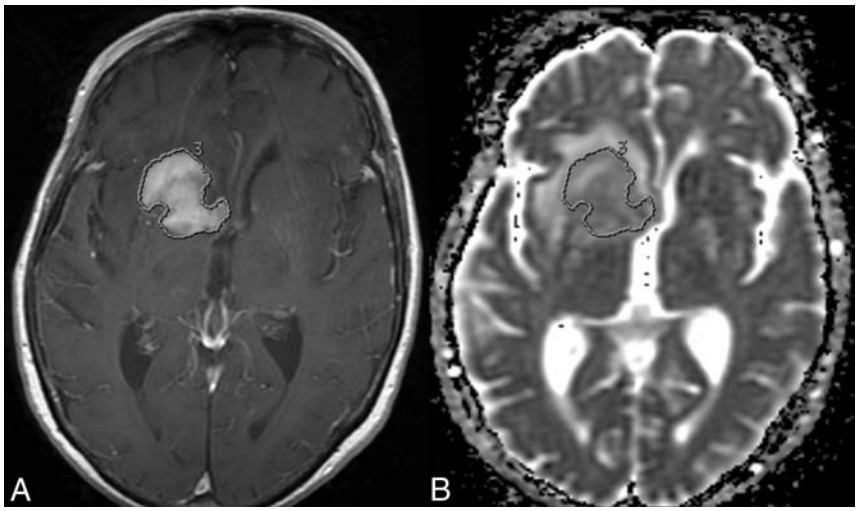

FIG 1. An axial postgadolinium T1-weighted MR image (*A*) and a coregistered axial ADC map (*B*) demonstrate manual contouring of the contrast-enhancing CNSL on this section, which allows the measurement of ADCavg. This is performed on every section of the contrast-enhancing tumor.

plicate diagnosis by both MR imaging and stereotactic biopsy.[16,17] tk;4Ideally, an accurate diagnosis of a new brain mass lesion could be offered before brain biopsy to facilitate treatment planning and surgical triage, and potentially even obviate biopsy in some cases.

Multiple MR imaging features have been reported useful for distinguishing CNSL from the more common high-grade glioma, including relatively low ADC values on DWI, relatively low cerebral blood volume and high permeability on MR perfusion, lipid peaks and high choline-to-creatinine ratios on MR spectroscopy, and the absence of foci of susceptibility on high-resolution susceptibility imaging.[10-13,18,19] ADC derived from DWI is of particular interest because this sequence is routinely performed on all brain MRI. Low ADC values in CNSL are related to high cellularity, which theoretically interferes with the diffusion of water within the tumor.[20,21] These MR imaging findings may be helpful but are also present in numerous other conditions and are ultimately nonspecific.

CXC chemokine ligand 13 (CXCL-13), a mediator of B-cell migration, and interleukin 10 (IL-10), an anti-inflammatory cytokine, are produced by lymphocytes in CNSL, can be detected in the CSF, and have emerged as CSF biomarkers for the diagnosis of CNSL.[22-25] These CSF biomarkers should be considered in the evaluation of a brain mass detected on MR imaging. The aim of our study was to investigate the performance of the combined use of ADC derived from the preoperative clinical MR imaging and CSF CXCL-13 and IL-10 concentrations for the diagnosis of CNSL. Our hypothesis is that the combined use of ADC, CSF CXCL-13, and CSF IL-10 will result in increased diagnostic performance compared with the diagnostic performance of ADC values alone.

MATERIALS AND METHODS

Study Subjects

Eighty-seven patients were included in this cohort study compliant with the institutional review board and Health Insurance Portability and Accountability Act. We performed a retrospective review of a prospectively built cohort data base of patients who had undergone CSF sampling from 2003 to 2011 at our institution as part of a multiinstitutional study.[22,24] We cross-referenced this data base with MR imaging. Inclusion criteria for our study were CSF sampling with CXCL-13 and IL-10 and a preoperative brain MR imaging showing an enhancing mass lesion. Exclusion criteria were age younger than 12 years, traumatic CSF collection, or therapeutic intervention within 3 weeks. Eighty-seven patients were included in this study, including 43 with CNSL (38 primary CNSL, 5 secondary CNSL) and 44 without CNSL (21 metastases, 14 high-grade gliomas, 9 tumefactive demyelinating lesions). All diagnoses were pathologically confirmed following surgical biopsy. None of the patients were HIV-positive. The medical record was retrospectively reviewed to determine whether patients received corticosteroids before CSF sampling.

CSF Proteomic Analysis

These methods have been previously described.[22,24] Briefly, CSF samples were frozen within 2 hours of collection and stored at −70°C until analysis, at which point they were thawed and CSF concentrations of CXCL-13 and IL-10 were determined in duplicate by using an enzyme-linked immunoabsorbent assay. All CSF CXCL-13 and IL-10 concentrations are reported in picograms per milliliter.

MR Imaging and ADC Measurements

Standard clinical MR imaging was performed at 1.5T ($n = 68$) or 3T ($n = 19$). Axial DWI (TR/TE, 10,000/99 ms; section thickness/intersection gap, 5/0 mm; matrix size, 256 × 256; FOV, 24 cm × 24 cm; 3 orthogonal diffusion gradient directions; b-values, 0 and 1000 s/mm^2) was performed in the transverse plane covering the whole brain. Contrast-enhanced 3D spoiled gradient-recalled T1-weighted imaging (TR/TE, 34/8 ms; section thickness/intersection gap, 1.5/0 mm) was performed in the axial plane. Slight variations in the scanning protocol were allowed as changes were made in the departmental protocol with time, as long as the patients had diffusion-weighted imaging performed at b=0 and 1000 s/mm^2.

All MR images were initially reviewed on the clinical PACS. We performed additional image processing and analysis in a blinded fashion off-line from the clinical PACS workstation using the FuncTool application (Version 9.4.05a; GE Healthcare, Milwaukee, Wisconsin) of an Advantage Workstation (Version 4.5; GE Healthcare). ADC maps were constructed from the diffusion-weighted images and coregistered to the postcontrast T1-weighted images. Each lesion was manually segmented on each section of the ADC map by contouring the contrast-enhancing lesion on the postcontrast T1-weighted images (Fig 1) by using established methods.[21,26] Manual adjustments were made on the ADC map if there was any misregistration. Average ADC (ADCavg) was calculated for each lesion volume in units of 10^{-6} mm^2/s (all ADC values in this article are reported in units of 10^{-6} mm^2/s). All ROIs were performed by a neuroradiology trainee

(R.F.B.) and secondarily approved by an attending neuroradiologist (S.C.) certified by the American Board of Radiology with a Certificate of Added Qualification in neuroradiology.

Statistical Analysis

Statistical analysis and line art production were performed by using MedCalc for Windows, Version 14.8.1 (MedCalc Software, Mariakerke, Belgium) and the R statistical computing software (http://www.r-project.org). The mean and SD of age were calculated for all patients and for the 2 patient groups, which were compared with a Welch 2-tailed *t* test. Corticosteroid administration was compared between the 2 patient groups with a Fisher exact test. Mean and 95% confidence intervals for the CNSL and non-CNSL groups were calculated for ADCavg, CXCL-13, and IL-10, and means were compared with Welch 2-tailed *t* tests. Single-variable receiver operating characteristic (ROC) analysis was then conducted for each variable for the diagnosis of CNSL. Multiple-variable logistic regression with ROC was then performed for the identification of CNSL by using the predictive variables ADCavg, CXCL-13, and IL-10. Optimized sensitivities and specificities were identified by using the maximum Youden J Index (maximum vertical distance to the null hypothesis AUC = 0.5 line or sensitivity [1-specificity]). Additionally, thresholds required for 95% specificity were calculated along with the sensitivity at this threshold. Pair-wise comparisons of the multiple-variable ROC curve AUCs were made to the single-variable ROC curves by using the ROC compare function of MedCalc, which uses the method of Delong et al,[27] accounting for correlated variables. A two-tailed $P < .05$ was considered statistically significant.

Table 1: Patient characteristics[a]

	Overall (*n* = 87)	CNSL (*n* = 43)	Non-CNSL (*n* = 44)
Mean age (yr) (SD)	56.03 (16.97)	61.84 (15.20)	49.95 (16.57)
Age range (yr)	15–85	24–84	15–85
Male/female ratio	43:44	20:23	23:21

[a] The patients with CNSL were statistically significantly older than the patients without CNSL ($P = .001$).

Table 2: Variables for the CNSL and non-CNSL groups with *P* values[a]

	Variable Means by Patient Group		
Factor	CNSL (*n* = 43)	Non-CNSL (*n* = 44)	*P* Value
ADCavg	864.81	1071.65	<.001
95% CI	(832.50–897.13)	(981.23–1162.04)	
CXCL-13	2960.49	72.54	<.001
95% CI	(1124.96–4796.01)	(9.02–136.05)	
IL-10	557.48	5.93	<.001
95% CI	(167.49–947.47)	(3.42–8.43)	

[a] The patients with CNSL had lower ADC values and higher CSF CXCL-13 and IL-10 values than those without CNSL.

RESULTS

Patient Characteristics

Patient characteristics are reported in Table 1. The CNSL group (mean age, 61.84 years) was statistically significantly older than the non-CNSL group (mean age, 49.95 years) ($P = .001$). Corticosteroid administration information before CSF sampling was

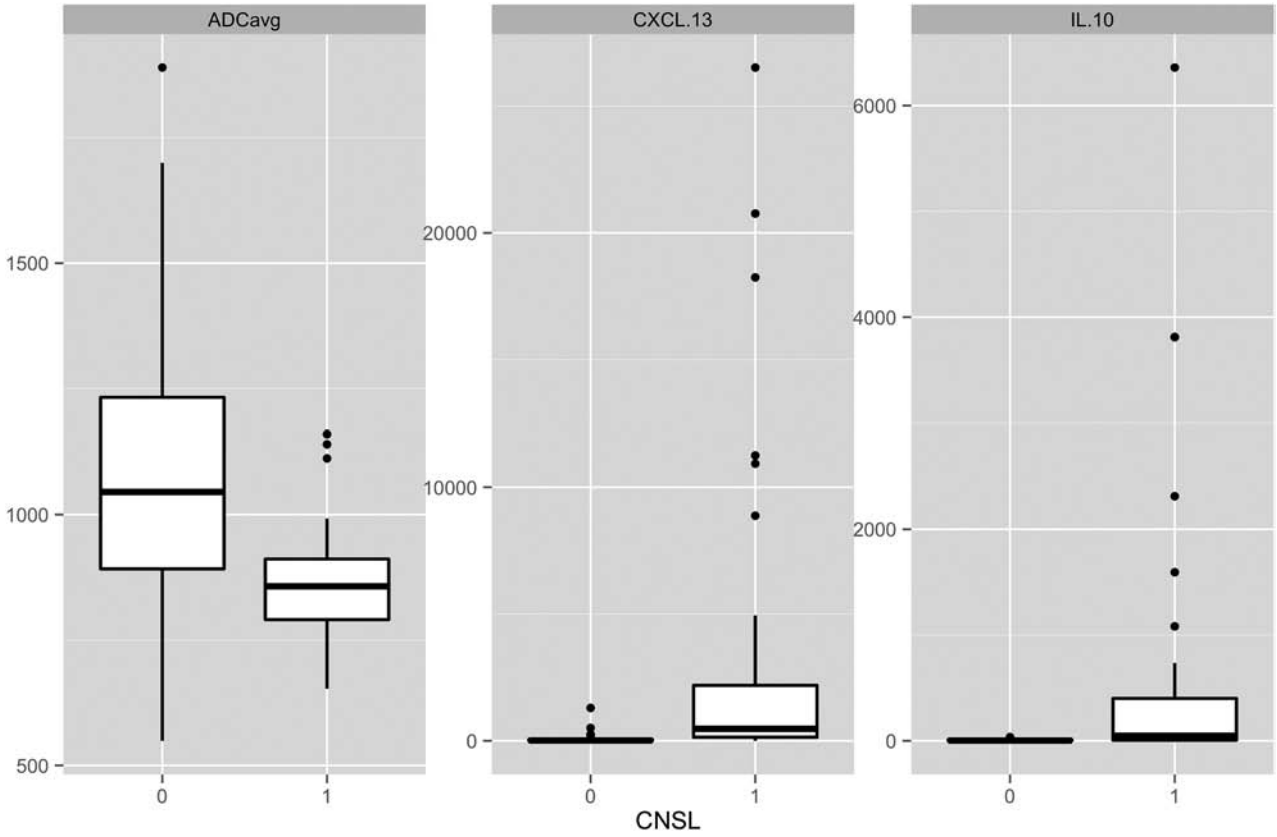

FIG 2. Boxplots of ADCavg, CSF CXCL-13, and CSF IL-10. ADCavg is statistically significantly lower, and CSF CXCL-13 and IL-10 are statistically significantly higher in patients with CNSL ($P < .001$).

Table 3: Results of individual and multiple-variable ROCs for the diagnosis of CNSL[a]

Factor and *P* Value	ROC Results with Optimized Thresholds				
	AUC (95% CI)	Maximum Youden Index J	Threshold Sensitivity/Specificity	Threshold ± Likelihood Ratios	Threshold PPV/NPV
ADCavg ($P < .001$)	0.739 (0.634–0.827)	0.521 at ≤971	90.70/61.36	2.35/0.15	69.64/87.10
CXCL-13 ($P < .001$)	0.832 (0.737–0.904)	0.677 at <106.0	76.74/90.91	8.44/0.26	89.19/80.00
IL-10 ($P < .001$)	0.792 (0.692–0.872)	0.583 at >21.77	62.79/95.45	13.81/0.39	93.10/72.41
ADCavg, CXCL-13, IL-10 ($P < .001$)	0.928 (0.851–0.972)	0.723 at probability of >0.527	81.40/90.91	11.26/0.25	89.74/83.33

Note:—NPV indicates negative predictive value; PPV, positive predictive value.

[a] All ROC curves were statistically significant. Optimized thresholds were selected by using the maximum Youden Index J, the maximum vertical distance from the AUC = 0.5 null hypothesis line (sensitivity [1-specificity]). PPV and NPV should be interpreted with caution because they are highly dependent on the prevalence of the disease in the tested population, and as CSF testing becomes more common, this may not be reflective of our study population.

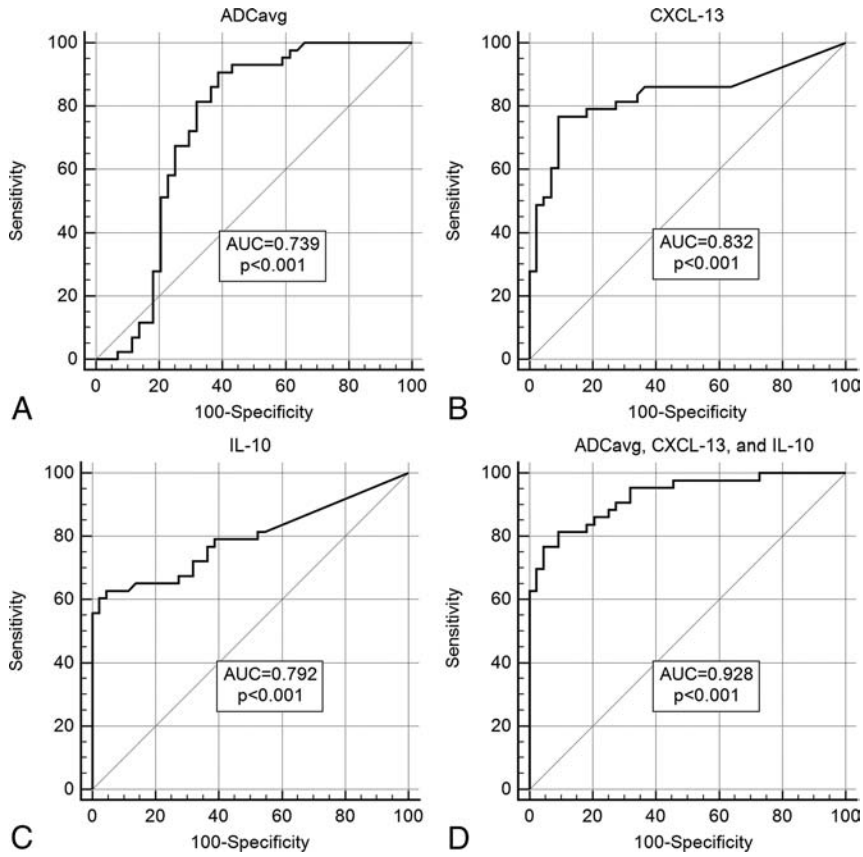

FIG 3. ROC curves of ADCavg (*A*), CXCL-13 (*B*), IL-10 (*C*), and ADCavg with CXCL-13 and IL-10 (*D*). All ROCs are statistically significant ($P < .001$). Diagnostic performance measured by AUC is statistically significantly superior in the multiple-variable model (*D*) compared with the single-variable models (*A–C*).

retrospectively available for 64/87 patients (30/43 patients with CNSL and 34/44 without it). More patients with CNSL were confirmed to have received corticosteroids ($n = 24$) before CSF sampling than those in the non-CNSL group ($n = 14$, $P = .005$). The corticosteroid administered was dexamethasone in 22 and hydrocortisone in 2 of the patients with CNSL and dexamethasone in 11, methylprednisolone in 2, and prednisone in 1 of the patients without CNSL.

ADCavg and CSF Values by Group

ADCavg, CSF CXCL-13, and CSF IL-10 values are reported in Table 2 and depicted in Fig 2. ADCavg was statistically significantly lower and CSF CXCL-13 and IL-10 values were higher in CNSL than in non-CNSL ($P < .001$).

Single-Variable ROC for the Identification of CNSL

ROC curves for all 3 variables analyzed were statistically significant for the identification of CNSL ($P < .001$). Results with AUC and optimized thresholds with the maximum Youden Index J, sensitivities, specificities, likelihood ratios, and predictive values are reported in Table 3 and depicted in Fig 3. AUCs ranged from 0.739 (ADCavg) to 0.832 (CXCL-13), and maximum Youden Index J values ranged from 0.521 (ADCavg) to 0.677 (CXCL-13). Threshold values for 95% specificity with associated sensitivity are reported in Table 4. Sensitivity at 95% specificity ranged from 0.00% (ADCavg, ≤598.2) to 62.79% (IL-10 > 20.65).

Multiple Variable Logistic Regression for the Identification of CNSL

The results of multiple-variable logistic regression are presented in Table 5. The model was overall statistically significant ($P < .001$), and the 3 individual variables were each individually statistically significant. The logistic regression equation can be represented as: probability of CNSL $= 1/[1 + e^{(2.617 - 0.0048\,(\mathrm{ADCavg}) + 0.0024\,(\mathrm{CXCL\text{-}13}) + 0.0626\,(\mathrm{IL\text{-}10})}]$. The multiple-variable ROC results are presented in Table 3, and the curve is depicted in Fig 3. The AUC was 0.928, and the maximum Youden Index J was 0.723, with sensitivity and specificity of 81.40% and 90.91% at a probability threshold of >0.527. Results at set 95% specificity are reported in Table 4. Sensitivity at set 95% specificity was 76.74 at a probability threshold of >.639.

ROC Comparisons

Results of ROC curve comparisons are reported in Table 6. The multiple-variable ROC demonstrated statistically significantly better diagnostic performance than the single-variable AUCs.

DISCUSSION

While the diagnosis of CNSL can be suggested on the basis of MR imaging findings, arriving at a consistently accurate preoperative

diagnosis for a patient with a brain mass lesion encountered on MR imaging remains an overall difficult task and an active area of research.[9-13,18-20] Considerable advances, however, have been made in the field of CSF proteomics that have yielded 2 CSF biomarkers for CNSL, CXCL-13 and IL-10.[22-25] In this study, we have examined the individual diagnostic performances of ADC, CSF CXCL-13, and IL-10 and the combined diagnostic performances in a multiple-variable model considering ADC, CSF CXCL-13, and CSF IL-10 in cohorts of patients with and without CNSL. We found that the combined use of ADC, CSF CXCL-13, and CSF IL-10 results in a statistically significantly increased diagnostic performance for the diagnosis of CNSL and that each variable has a statistically significant individual effect. CSF CXCL-13 and CSF IL-10 values should be considered when a brain mass with reduced ADC values is encountered and when the diagnosis of CNSL is considered. This study provides the statistical basis for considering all 3 variables in clinical practice. Consideration of these factors could potentially be used in the future to make the diagnosis of CNSL without the need for stereotactic biopsy.

Our study supports the observations in the literature that ADC values are decreased and CSF CXCL-13 and IL-10 values are increased in CNSL, while demonstrating the combined use of these variables in multiple-variable diagnostic models.[9-13,18-26] ADCavg demonstrated a moderate diagnostic performance for CNSL in ROC analysis with an AUC of 0.739 (Fig 3) and was relatively sensitive compared with specificity, with an optimized sensitivity/specificity pair of 90.70/61.36 at a threshold of ≤971. CSF CXCL-13 and CSF IL-10 also demonstrated moderate diagnostic performance as previously shown for CNSL in ROC analysis with AUCs of 0.832 for CXCL-13 and 0.792 for IL-10 (Fig 3). In agreement with our prior analysis and the literature, these CSF biomarkers (particularly IL-10) were found to be more specific than sensitive, with optimized sensitivity/specificity pairs of 76.74/90.91 for CXCL-13 (at >106) and 62.79/95.45 for IL-10 (at >21.77).[22-25]

Our multiple-variable model takes advantage of the different sensitivity/specificity profiles offered by each variable with resulting improved and optimized diagnostic performance demonstrated by a statistically significantly larger AUC (0.928) on ROC analysis (Tables 3 and 6). The logistic regression results demonstrated that each of these variables had a statistically significant individual effect in the model and thus contributed to the probability of CNSL after the other variables had been taken into account. Our logistic regression equation can thus be used to calculate the probability of CNSL, given IL-10, CXCL-13, and ADCavg, and demonstrates that higher IL-10 and CXCL-13 values and lower ADC values should increase the diagnostic confidence for CNSL. Conversely, lower CXCL-13 and IL-10 values and higher ADC values should decrease diagnostic confidence for CNSL. These results statistically demonstrate the importance of considering CSF analysis in these patients and not relying solely on the presence of a mass with reduced diffusion in making the diagnosis of CNSL.

Our study contains several important limitations. The size of our study is relatively modest, and it was performed at only 1 institution. Clinical factors such as corticosteroid administration were not controlled, and more of the patients with CNSL received corticosteroids before CSF sampling than the patients without CNSL, the effect of which is unknown. A larger, prospective, multi-institutional study could be considered to further evaluate the results of this study. The quantitative measurement of ADC values as performed in this study may pose a limitation to adoption into clinical workflow; however, we routinely use a similar processing method on the same platform for perfusion analysis. Possible future directions to address this limitation could include evaluating the performance of subjectively "restricted diffusion" with CSF CXCL-13 and IL-10. Our multiple-variable models are limited by the variables that we included. With the CNSL group being older that the non-CNSL group, age could have been added to the model and likely would have had an effect; age was, however, omitted for simplicity in comparison of the ROC curves with the corresponding single-variable ROCs. Likewise, additional imaging features could have also been investigated but were omitted for model simplicity. Furthermore, the predictive model that we present is unlikely to be easily adopted in clinical practice; however, a version of the regression equation could conceivably be combined with automatic lesion segmentation to measure ADC and automated data extraction from the medical record for use in computer-aided diagnosis and decision support in the future. We likely have the computing power to accomplish this automated

Table 4: Sensitivities and corresponding threshold values from the ROC analysis for a set specificity of 95%[a]

Factor	Sensitivity at Set 95% Specificity (95% CI)	Threshold Value for 95% Specificity
ADCavg	0.00 (0.00–2.33)	≤598.2
CXCL-13	51.16 (18.60–79.07)	>262.82
IL-10	62.79 (48.84–79.07)	>20.65
ADCavg, CXCL-13, IL-10	72.09 (55.81–86.05)	Probability of >.616

[a] ADCavg alone was essentially unable to reach a specificity of 95% (the sensitivity at the calculated threshold is 0%); however, with the addition of the CSF variables in the combined model, we can reach a specificity of 95% with a sensitivity of 72.09%. The highest sensitivity at 95% specificity is reached in the multiple-variable model.

Table 6: Comparisons of the multiple-variable ROC with the single-variable ROCs[a]

Model	ADCavg	CXCL-13	IL-10
ADCavg, CXCL-13, IL-10	$P < .001$	$P = .016$	$P = .002$

[a] The multiple-variable ROC demonstrated a statistically significantly larger AUC than the corresponding single-variable AUCs, signifying statistically significantly superior diagnostic performance.

Table 5: Results of multiple-variable logistic regression with the ADCavg and CSF CXCL-13 and IL-10[a]

Model	Overall *P*	Intercept	ADCavg Effect and (OR)	CXCL-13 Effect and (OR)	IL-10 Effect and (OR)
ADCavg, CXCL-13, IL-10	<001	2.617	−0.0048 $P = .012$ (0.995)	0.0024 $P = .022$ (1.002)	0.0626 $P = .017$ (1.065)

[a] The model was overall statistically significant, and all individual variables were individually statistically significant. This result demonstrates that all 3 variables should be factored into the diagnostic confidence that a lesion is a CNSL.

analysis, though these features are not currently incorporated into clinical PACS workstations.

CONCLUSIONS

In this study, we have demonstrated that the combined use of ADC, CSF CXCL-13, and CSF IL-10 results in statistically significantly increased diagnostic performance for the diagnosis of CNSL compared with the diagnostic performance of ADC alone. Our multiple-variable diagnostic model demonstrated excellent diagnostic performance (AUC of 0.928 and optimized sensitivity/specificity of 81.40/90.91), which was statistically significantly superior to the diagnostic performance of the individual variable models. Within this multiple-variable model, we found statistically significant individual effects for ADCavg (OR, 0.995; $P = .012$), CXCL-13 (OR, 1.002; $P = .022$), and IL-10 (OR, 1.065; $P = .017$) demonstrating that each variable contributed individually to the probability of CNSL. This study statistically demonstrates the importance of corroborating with CSF CXCL-13 and CSF IL-10 values (or suggesting they be obtained) when a brain mass with reduced ADC values is encountered and when the diagnosis of CNSL is considered. Higher CXCL-13 and IL-10 values and lower ADC values should all individually increase the diagnostic confidence that a lesion is a CNSL. A combined diagnostic model incorporating ADCavg, CSF CXL-13, and CSF IL-10 could potentially be used in the future to make the diagnosis of CNSL without the need for stereotactic biopsy.

Disclosures: Marc C. Mabray—*RELATED*: *Grant*: National Institutes of Health, *Comments*: Supported by National Institutes of Health T32 Grant while working on this project. Francisco E. Valles—*RELATED*: *Grant*: University of California, San Francisco Doris Duke Charitable Foundation Clinical Research Fellowship (Independent Cancer Research Foundation).

REFERENCES

1. Ferreri AJ. **Risk of CNS dissemination in extranodal lymphomas.** *Lancet Oncol* 2014;15:e159–169 CrossRef Medline
2. Hochberg FH, Baehring JM, Hochberg EP. **Primary CNS lymphoma.** *Nat Clin Pract Neurol* 2007;3:24–35 CrossRef Medline
3. van Besien K, Gisselbrecht C, Pfreundschuh M, et al. **Secondary lymphomas of the central nervous system: risk, prophylaxis and treatment.** *Leuk Lymphoma* 2008;49(suppl 1):52–58 CrossRef Medline
4. van der Sanden GA, Schouten LJ, van Dijck JA, et al; Working Group of Specialists in Neuro-Oncology in the Southern and Eastern Netherlands. **Primary central nervous system lymphomas: incidence and survival in the Southern and Eastern Netherlands.** *Cancer* 2002;94:1548–56 CrossRef Medline
5. Besson C, Goubar A, Gabarre J, et al. **Changes in AIDS-related lymphoma since the era of highly active antiretroviral therapy.** *Blood* 2001;98:2339–44 CrossRef Medline
6. Haldorsen IS, Krossnes BK, Aarseth JH, et al. **Increasing incidence and continued dismal outcome of primary central nervous system lymphoma in Norway 1989–2003: time trends in a 15-year national survey.** *Cancer* 2007;110:1803–14 CrossRef Medline
7. Olson JE, Janney CA, Rao RD, et al. **The continuing increase in the incidence of primary central nervous system non-Hodgkin lymphoma: a surveillance, epidemiology, and end results analysis.** *Cancer* 2002;95:1504–10 CrossRef Medline
8. Coté TR, Manns A, Hardy CR, et al. **Epidemiology of brain lymphoma among people with or without acquired immunodeficiency syndrome: AIDS/Cancer Study Group.** *J Natl Cancer Inst* 1996;88:675–79 CrossRef Medline
9. Cha S. **Update on brain tumor imaging: from anatomy to physiology.** *AJNR Am J Neuroradiol* 2006;27:475–87 Medline
10. Kickingereder P, Sahm F, Wiestler B, et al. **Evaluation of microvascular permeability with dynamic contrast-enhanced MRI for the differentiation of primary CNS lymphoma and glioblastoma: radiologic-pathologic correlation.** *AJNR Am J Neuroradiol* 2014;35:1503–08 CrossRef Medline
11. Zacharia TT, Law M, Naidich TP, et al. **Central nervous system lymphoma characterization by diffusion-weighted imaging and MR spectroscopy.** *J Neuroimaging* 2008;18:411–17 CrossRef Medline
12. Haldorsen IS, Espeland A, Larsson EM. **Central nervous system lymphoma: characteristic findings on traditional and advanced imaging.** *AJNR Am J Neuroradiol* 2011;32:984–92 CrossRef Medline
13. Kickingereder P, Wiestler B, Sahm F, et al. **Primary central nervous system lymphoma and atypical glioblastoma: multiparametric differentiation by using diffusion-, perfusion-, and susceptibility-weighted MR imaging.** *Radiology* 2014;272:843–50 CrossRef Medline
14. Josephson SA, Papanastassiou AM, Berger MS, et al. **The diagnostic utility of brain biopsy procedures in patients with rapidly deteriorating neurological conditions or dementia.** *J Neurosurg* 2007;106:72–75 CrossRef Medline
15. Hall WA. **The safety and efficacy of stereotactic biopsy for intracranial lesions.** *Cancer* 1998;82:1749–55 Medline
16. Weller M. **Glucocorticoid treatment of primary CNS lymphoma.** *J Neurooncol* 1999;43:237–39 CrossRef Medline
17. Geppert M, Ostertag CB, Seitz G, et al. **Glucocorticoid therapy obscures the diagnosis of cerebral lymphoma.** *Acta Neuropathol* 1990;80:629–34 CrossRef Medline
18. Calli C, Kitis O, Yunten N, et al. **Perfusion and diffusion MR imaging in enhancing malignant cerebral tumors.** *Eur J Radiol* 2006;58:394–403 CrossRef Medline
19. Horger M, Fenchel M, Nägele T, et al. **Water diffusivity: comparison of primary CNS lymphoma and astrocytic tumor infiltrating the corpus callosum.** *AJR Am J Roentgenol* 2009;193:1384–87 CrossRef Medline
20. Guo AC, Cummings TJ, Dash RC, et al. **Lymphomas and high-grade astrocytomas: comparison of water diffusibility and histologic characteristics.** *Radiology* 2002;224:177–83 CrossRef Medline
21. Barajas RF Jr, Rubenstein JL, Chang JS, et al. **Diffusion-weighted MR imaging derived apparent diffusion coefficient is predictive of clinical outcome in primary central nervous system lymphoma.** *AJNR Am J Neuroradiol* 2010;31:60–66 CrossRef Medline
22. Roy S, Josephson SA, Fridlyand J, et al. **Protein biomarker identification in the CSF of patients with CNS lymphoma.** *J Clin Oncol* 2008;26:96–105 CrossRef Medline
23. Sasagawa Y, Akai T, Tachibana O, et al. **Diagnostic value of interleukin-10 in cerebrospinal fluid for diffuse large B-cell lymphoma of the central nervous system.** *J Neurooncol* 2015;121:177–83 CrossRef Medline
24. Rubenstein JL, Wong VS, Kadoch C, et al. **CXCL13 plus interleukin 10 is highly specific for the diagnosis of CNS lymphoma.** *Blood* 2013;121:4740–48 CrossRef Medline
25. Sasayama T, Nakamizo S, Nishihara M, et al. **Cerebrospinal fluid interleukin-10 is a potentially useful biomarker in immunocompetent primary central nervous system lymphoma (PCNSL).** *Neuro Oncol* 2012;14:368–80 CrossRef Medline
26. Valles FE, Perez-Valles CL, Regalado S, et al. **Combined diffusion and perfusion MR imaging as biomarkers of prognosis in immunocompetent patients with primary central nervous system lymphoma.** *AJNR Am J Neuroradiol* 2013;34:35–40 CrossRef Medline
27. DeLong ER, DeLong DM, Clarke-Pearson DL. **Comparing the areas under two or more correlated receiver operating characteristic curves: a nonparametric approach.** *Biometrics* 1988;44:837–45 CrossRef Medline

On the Use of DSC-MRI for Measuring Vascular Permeability

J.T. Skinner, P.L. Moots, G.D. Ayers, and C.C. Quarles

ABSTRACT

BACKGROUND AND PURPOSE: Contrast agent extravasation has been shown to confound brain tumor perfusion measurements with DSC–MR imaging, necessitating the use of correction techniques (eg, Weisskoff, Bjornerud). Leakage parameters (K_2 and K_a) postulated to reflect vessel permeability can be extracted from these correction methods; however, the biophysical interpretation of these parameters and their relationship to commonly used MR imaging measures of vascular permeability (eg, contrast agent volume transfer constant, [K^{trans}]) remain unclear. Given that vascular density, as assessed by blood volume, and vascular permeability, as reflected by K^{trans} (and potentially K_2 or K_a), report on unique and clinically informative vascular characteristics, there is a compelling interest to simultaneously assess these features.

MATERIALS AND METHODS: We acquired multiecho DSC–MR imaging data, allowing the simultaneous computation and voxelwise comparison of single- and dual-echo derived measures of K_2, K_a and K^{trans} in patients with glioma. This acquisition enabled the investigation of competing T1 and T2* leakage effects and TE dependency on these parameters.

RESULTS: K_2 and K_a displayed nonsignificant ($P = .150$ and $P = .060$, respectively) voxelwise linear correlations with K^{trans}, while a significant ($P < .001$) inverse relationship was observed between K_2 and K_a (coefficient of determination [r^2] = 0.466–0.984). Significantly different ($P < .005$) mean estimates were found between voxels exhibiting predominately T1 and T2* effects for K_2 and K_a. K^{trans}, however, was observed to be similar between these voxels (0.109 versus 0.092 minutes^{-1}). Significant differences ($P < .001$) in extracellular-extravascular volume fraction (v_e) (0.285 versus 0.167) were also observed between cohorts. Additionally, K_2 and K_a were found to have a significant quadratic relationship ($P = .031$ and $P = .005$, respectively) with v_e.

CONCLUSIONS: Estimates of vascular permeability in brain tumors may be simultaneously acquired from multiple-echo DSC–MR imaging via K^{trans}; however, caution should be used in assuming a similar relationship for K_2 and K_a.

ABBREVIATIONS: CA = contrast agent; DCE = dynamic contrast-enhanced; Gd = gadolinium; K_a = apparent transfer constant; K_2 = leakage parameter; K^{trans} = volume transfer constant; R_1 = longitudinal relaxation rate; R_2 = transverse relaxation rate; v_e = extracellular extravascular volume fraction; R_2^* = effective transverse relaxation rate

Brain tumors are characterized by abnormal, poorly constructed vasculature that is often permeable,[1] making them identifiable on contrast-enhanced MR images. With dynamic contrast-enhanced (DCE)–MR imaging methods, contrast agent (CA) wash-in and extravasation alter the tissue T1 relaxation time, and kinetic analysis of the associated signal change permits the computation of the CA volume transfer constant (K^{trans}), which reflects vascular permeability and perfusion. In dynamic susceptibility contrast MR imaging studies, CA flowing through blood vessels decreases tissue T2*, and the acquired signal changes can be used to estimate tumor blood volume. However, CA extravasation has been shown to confound measurements of tissue perfusion (eg, underestimation of blood volume), particularly in high-grade brain tumors.[2-4] When corrected for CA leakage effects, DSC–MR imaging measures of blood volume correlate with brain tumor grade and may be useful for monitoring treatment response.[2,5]

CA extravasation leads to simultaneous and competing T1 and

Received March 26, 2015; accepted after revision May 12.

From the Vanderbilt University Institute of Imaging Science (J.T.S., C.C.Q.), Departments of Cancer Biology (C.C.Q.), and Biomedical Engineering (C.C.Q.), Vanderbilt University, Nashville, Tennessee; and Departments of Radiology and Radiological Sciences (J.T.S., C.C.Q.), Neurology (P.L.M.), and Biostatistics (G.D.A.), Vanderbilt University School of Medicine, Nashville, Tennessee.

This work was supported by National Institutes of Health R01CA158079, National Cancer Institute 2R25CA092043, and Vanderbilt-Ingram Cancer Center's Young Ambassadors Grant (C.C.Q.).

Please address correspondence to C. Chad Quarles, PhD, Division of Neuroimaging Research Barrow Neurological Institute, St. Joseph's Hospital and Medical Center, 350 W Thomas Rd, Phoenix, AZ 85013; e-mail: christopher.quarles@dignityhealth.org

Indicates open access to non-subscribers at www.ajnr.org

http://dx.doi.org/10.3174/ajnr.A4478

Table 1: Patient demographics

Patient	Age (yr)	Sex	Prior Resection	Pathology	OS (mo)
1	61	Female	Yes	Grade IV glioblastoma	17.9
2	66	Male	Yes	Grade IV glioblastoma	18.2
3	65	Male	Yes	Grade III anaplastic astrocytoma	NA
4	51	Male	Yes	Grade IV glioblastoma	4.3
5	55	Male	No	Grade III oligodendroglioma	13.1
6	40	Male	Yes	Grade IV glioblastoma	11.0
7	42	Female	Yes	Grade IV glioblastoma	NA

Note:—OS indicates overall survival after radiologically confirmed tumor recurrence/progression; NA, not applicable.

T2* effects that can substantially alter the temporal dynamics of DSC–MR imaging signals[2,6] and necessitate the use of correction techniques. One such technique, developed by Weisskoff et al[7] and Boxerman et al,[2] incorporates knowledge of the average signal time course across the brain in nonenhancing voxels to model and correct time courses in tumor voxels. As a result, a leakage parameter termed "K_2" can be extracted and reflects the degree of CA extravasation. Although initially developed to correct T1 leakage effects, the Weisskoff method has been adapted to also account for T2* leakage effects.[8] A known limitation of this method, however, is that it assumes that the mean transit times of both healthy and diseased tissue are equal; this has been observed to not be true in gliomas.[9] To address this issue, Bjornerud et al[10] recently developed an MTT-insensitive approach for correcting both T1 and T2* leakage effects on DSC–MR imaging signals.[11] In this method, the tissue residue function, which describes the CA passage through a voxel, is separated into an intravascular and an extravascular component, from which an apparent transfer constant "K_a" (similar to K_2) can be estimated. A third technique aims to remove T1-based CA leakage effects through the use of multiple gradient-echo acquisitions.[3,12-14] A feature of this approach is that dynamic T1-weighted information can be separated and quantified.[15-17] Traditional pharmacokinetic modeling[18,19] can then be applied to these data to extract a measure of K^{trans} in a manner similar to that in DCE–MR imaging. This approach has been validated in animal brain tumor models and has been recently applied in patients with high-grade gliomas.[16,17,20] For one to collect both DCE–MR imaging and DSC–MR imaging datasets, an alternative strategy is to acquire traditional DCE–MR imaging data during a preload injection of contrast agent, which is a technique also commonly used to reduce T1 leakage effects in single-echo-based DSC–MR imaging data.[3]

In the case of brain tumors, K^{trans} is largely considered to reflect vascular permeability[19] and has demonstrated promise in tumor grading[21,22] and identifying disease progression and treatment response.[23-26] It has been postulated that measures of K_2 and K_a may also directly report on vascular permeability; however, their relationship with imaging biomarkers such as K^{trans} is not entirely clear and may be dependent on CA kinetics, tissue microstructure, and imaging parameters. Preliminary studies have also investigated the use of K_2 and K_a for assessing tumor type,[27] grade,[28,29] and treatment response.[11]

Inherent to the aforementioned DSC–MR imaging correction techniques, estimates of K_2 and K_a may assume positive or negative values depending on whether T1 ($+K_2$, $-K_a$) or T2* ($-K_2$, $+K_a$) leakage effects are the dominating source of signal error. Unlike K_2 and K_a, estimates of K^{trans} assume the use of a "purely" T1-weighted signal and, therefore, presume insensitivity to competing T1 and T2* leakage effects. In this regard, a previous simulation study reported a nonlinear relationship between K_a and K^{trans} when large flip angles (>70°) were used.[10] In a follow-up in vivo study,[11] a positive quadratic relationship between K_a and K^{trans} was observed. A more recent study found a positive linear correlation between K_2 and K^{trans} when comparing maximum whole-tumor values across patients.[30] These studies, however, were limited to ROI-based estimates and measures of K^{trans} acquired from separate DCE–MR imaging acquisition and did not take into consideration the dominating CA leakage effect.

As suggested by previous works, the presence of simultaneous T1 and T2* leakage effects within a tumor may influence the magnitude and interpretation of K_2 and K_a. The overarching goal of this study, therefore, was to investigate the contribution of both T1 and T2* effects on K_2 and K_a, while evaluating these parameters as imaging biomarkers of vascular permeability in brain tumors. This goal was achieved through voxelwise comparisons of DSC–MR imaging–derived measures of K_2, K_a, and K^{trans} using the previously described methods. The multiecho nature of this study allowed simultaneous measurement of these parameters from the same dataset, permitting a more accurate comparison free of registration errors and/or sequence-specific differences. In addition, the multiecho data allowed further exploration of potential TE dependencies of both Weisskoff and Bjornerud correction techniques.

MATERIALS AND METHODS

MR imaging data were acquired in patients with high-grade gliomas (n = 7, Table 1) under Vanderbilt University Institutional Review Board guidelines at 3T (Achieva; Philips Healthcare, Best, the Netherlands) using a 32-channel head coil. Multiple flip angle data (TR = 7.6 ms, TE = 4.6 ms, flip angle = 2°–20° in 2° increments) were acquired to compute precontrast longitudinal relaxation rate (R_{10}) maps. Dual-echo DSC–MR imaging data were then acquired by using either a dual gradient-echo EPI or spin- and gradient-echo EPI protocol[17,31] with the following parameters: TR = 1.5 seconds (dual gradient-echo) or 1.8 seconds (spin- and gradient-echo), TE_1/TE_2 = 7.0/31.0 ms (dual gradient-echo) or 8.3/25 ms (spin- and gradient-echo), sensitivity encoding = 2, FOV = 240 × 240 mm^2, reconstructed voxel size = 2.5 × 2.5 × 5.0 mm^3, and sections = 15. For spin- and gradient-echo data, only the first 2 echoes were used in the analysis. Measurements were made before, during, and after administration of Gd-DTPA (0.1 mmol/kg, 4-mL/s infusion rate followed by a 20-mL saline flush). The scan duration was 7.5 minutes, including 80 seconds of prebolus baseline data. A high-resolution T1-weighted dataset was collected following the DSC–MR imaging experiment. Dynamic estimates of ΔR_2^* were computed for each echo ($\Delta R^*_{2,TE1}$ and $\Delta R^*_{2,TE2}$) and for the dual-echo data ($\Delta R^*_{2,DE}$) as previously described.[12,13]

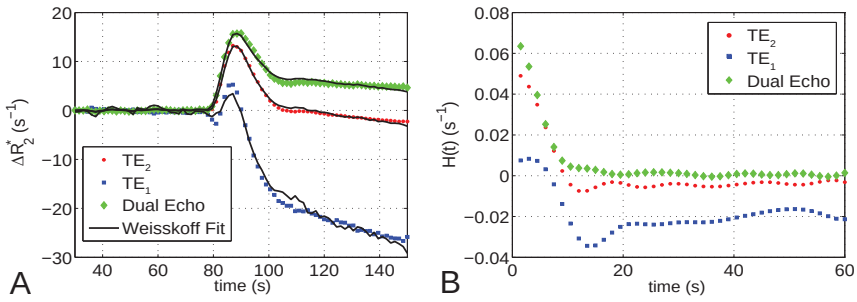

FIG 1. *A*, Representative uncorrected tumor ΔR_2^* time course and the associated Weisskoff model fit (*solid*) used to compute K_2 at TE$_1$ (*square*), TE$_2$ (*dot*), and dual-echo (*diamond*). *B*, Corresponding tissue residue functions used to compute K_a at TE$_1$, TE$_2$, and dual-echo.

K_2 Computation

The method proposed by Weisskoff et al[7] allows the extraction of K_2 from Equation 1,

$$1)\qquad \Delta\widetilde{R_2^*}(t) \approx K_1 \times \overline{\Delta R_2^*(t)} - K_2 \int_0^t \overline{\Delta R_2^*(t')dt'},$$

where $\overline{\Delta R_2^*}$ is the average ΔR_2^* from a mask of nonenhancing brain voxels and $\Delta\widetilde{R_2^*}$ is the leakage affected estimate of ΔR_2^*. A voxelwise least squares fit to Equation 1 was performed to extract K_2 by using 80 seconds of prebolus baseline data and 70 seconds of postbolus data (2.5 minutes total), consistent with previous reports.[2,3,29]

K_a Computation

In the presence of CA extravasation, the tissue concentration time course, $C_t(t)$, can be represented as

$$2)\qquad C_t(t) = f\int_0^t R(t) \times C_p(t-\tau)d\tau + K_a\int_{T_c}^{t'} C_p(t'-\tau) \times \exp(-K_a(\tau - T_c)/v_e)d\tau,$$

where f is proportional to tissue blood flow, $R(t)$ is defined as the tissue-specific residue function, T_c is the capillary transit time of the CA, v_e is the extracellular extravascular volume fraction (v_e), and C_p is the CA concentration in plasma (computed from an arterial input function extracted from the dual-echo data by using an automated selection process[32,33]). In DSC–MR imaging, $C_t(t)$ is estimated in relative terms through measurements of $\Delta R_{2,t}^*(t)$,[10] where $\Delta R_{2,t}^*(t) \alpha\, r_2^* \times C_t(t)$ and r_2^* is the effective transverse relaxivity. Circular deconvolution of Equation 2 with the arterial input function[34] (during the same time course used in the Weisskoff correction) results in a composite residue function $H(t)$ described by an early vascular phase ($0 \le t < T_c$) and an extravasation phase ($t \ge T_c$)[10]:

$$3)\qquad \begin{aligned} H(t) &\approx f \times R(t) & 0 \le t < T_c \\ H(t) &\approx K_a \times \exp(-K_a(t-T_c)/v_e) & t \ge T_c \end{aligned}.$$

In the context of a single-echo DSC–MR imaging acquisition, $H(t) \approx K_a$ for $t \gg T_c$. In this study, K_a was estimated as the mean value from $H(t = T_c)$, where T_c is equal to 1.5 × the mean transit time, to $H(t =$ 60 seconds).

K^{trans} Computation

To compute an estimate of K^{trans} from multiecho DSC–MR imaging data, a T1-weighted signal time course $[S_{T1w}(t)]$ was first extracted from dual-echo data via Equation 4.[15,16,35]

$$4)\qquad S_{T1W}(t) = S_{TE_1}(t) \times e^{ln\left(\frac{S_{TE_1}(t)}{S_{TE_2}(t)}\right)} \times \left(\frac{TE_1}{TE_2 - TE_1}\right).$$

A R_{10} map was combined with the $S_{T1w}(t)$ data to produce dynamic longitudinal relaxation rate time courses $[R_{1t}(t)]$ for each voxel.[36,37] K^{trans} and v_e were estimated by fitting $R_{1t}(t)$ and $C_p(t)$ (arterial input function) with the standard Tofts model.[18,19]

Voxel Selection

Voxels selected for this analysis were obtained from enhancing regions on the postgadolinium (Gd) T1-weighted images, determined using a 50% signal threshold (based on the maximum signal intensity in tumor-containing sections) over a manually drawn tumor ROI. These voxels were further categorized by the predominate leakage effect (T1 or T2*) exhibited in their dynamic ΔR_2^* time course. In this study, "T2* voxels" were defined by a positive mean ΔR_2^* during the last 20 seconds of the time course used for computation of K_a and K_2. "T1 voxels" were defined as those in which this estimate was negative.

Statistical Analysis

Voxelwise measures of K_2 and K_a were compared with K^{trans} and v_e to examine the relationship between these parameters. Associations between the aforementioned parameters were first analyzed on an individual basis by using simple linear regression and reported using the r^2 statistic (coefficient of determination). Unless otherwise noted, group voxelwise comparisons were conducted using analysis of covariance in a generalized linear model for repeated measures. Generalized estimating equations were used with an exchangeable covariance structure to model the correlation among voxels across patients.

RESULTS

Figure 1*A* shows a representative uncorrected tumor ΔR_2^* time course for each TE and the dual-echo signal, along with the associated Weisskoff model fit. Figure 1*B* shows the corresponding tissue residue functions used to compute K_a from the same patient. The computed K^{trans}, K_2, and K_a maps (overlaid on post-Gd T1-weighted images) for this patient (at TE$_2$) can be seen in Fig 2*B–D*, respectively, along with the corresponding post-Gd T1-weighted image (Fig 2*A*). Figure 3*A*, -*B* shows a sample voxelwise comparison of K_2 and K_a (computed at TE$_2$) with the parameter K^{trans}. The range of correlations at TE$_2$ were $r^2 = 0.014–0.430$ for K_2 and $r^2 = 0.0001–0.403$ for K_a. Across patients, both K_2 and K_a were found to have nonsignificant ($P = .150$ and $P = .060$, respectively) linear correlations with K^{trans}. A significant ($P < .001$) inverse relationship was observed (Fig 3*C*), however, between K_2

and K_a ($r^2 = 0.466–0.984$). To help elucidate these observed relationships, further analysis was performed.

With the availability of multiecho data, the effect of TE on K_2 and K_a was investigated. Figure 4 shows boxplots using the median values of K_2 and K_a across all patients. A statistically significant difference (Mann-Whitney *U* test) was observed between K_2 at TE_1 and TE_2 ($P < .001$), K_2 at TE_1 and dual-echo ($P < .001$), and K_2 at TE_2 and dual-echo ($P < .01$) acquisitions. Similar differences were observed for K_a. For TE_2, voxelwise estimates of K_2 were observed to be predominately positive for high-grade gliomas, whereas K_a was predominately negative. A decrease in TE_1 resulted in a broader voxelwise distribution of values across patients, with estimates of K_2 becoming increasingly positive and K_a becoming increasingly negative. The computation of K_2 using the $\Delta R^*_{2,DE}$ time course resulted in a negative shift in the distribution of values, with an increase in the number of voxels near $K_2 = 0$. A similar shift in the distribution toward positive values was observed for K_a.

Figure 5 shows the contribution of both T1 and T2* leakage effects on the relaxation rate time courses. Figure 5*A* shows the mean ΔR_2^* time course (TE_2) for a tumor ROI from patient 2. The resulting ΔR_1 time course from the same tumor can be seen in Fig 5*B*. Although the ΔR_2^* time course appears to show no appreciable signs of CA leakage, the ΔR_1 time course exhibits large changes in R_1 with bolus passage. This indicates CA extravasation and results in a moderate estimate of K^{trans}. Similarly, focusing on the smallest 10% of all voxels (based on the magnitude of K_a) in a given patient results in $K_a = -0.043 \pm 0.050$ minutes^{-1}, $K_2 = 0.113 \pm 0.553$ minutes^{-1}, and $K^{trans} = 0.060 \pm 0.099$ minutes^{-1} (weighted mean ± pooled standard deviation). Figure 5*C*, -*D* shows mean ΔR_2^* and ΔR_1 time courses from the same tumor with voxels separated by predominate T1 or T2* leakage effects. Note that in Fig 5*C*, -*D*, voxels from the same tumor exhibited positive and negative values of K_2 and K_a, while K^{trans} was observed to be almost identical between the 2 cohorts.

Table 2 displays the mean estimates of K_2, K_a, and K^{trans} (separated by T1 and T2* voxels) across all patients. On average, 63% of voxels in the high-grade gliomas were found to predominately exhibit T1 leakage effects. In addition, a significant difference ($P < .005$, paired *t* test) was observed across patients between mean estimates from T1 and T2* voxel cohorts for both K_2 and K_a. While the difference between T1 and T2* cohorts for K^{trans} trended toward significance ($P \approx .05$), the weighted mean for each cohort across patients was similar (0.109 minutes^{-1} versus 0.092 minutes^{-1}). In all voxels across patients, we observed $v_e = 0.241 \pm 0.207$. When separated by leakage effect, a significant difference ($P < .001$, paired *t* test) in mean estimates of v_e was also observed. Additionally, both K_2 and K_a were found

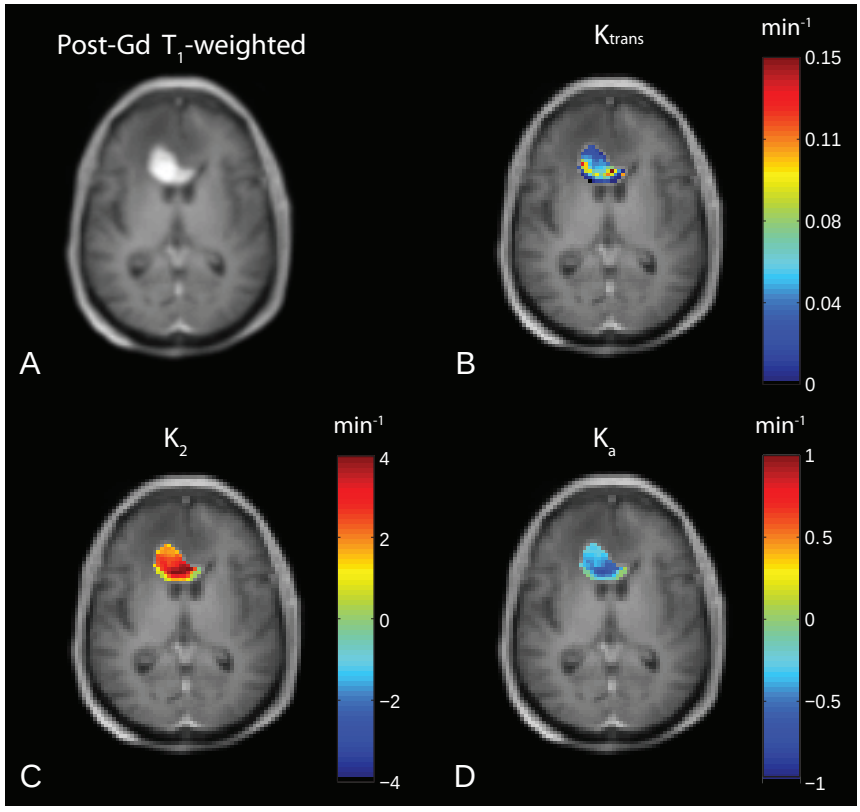

FIG 2. *A*, T1-weighted post-Gd anatomic image showing a high-grade brain tumor. Sample computed permeability maps (units in minute^{-1}), K^{trans} (*B*), K_2 (*C*), and K_a (*D*).

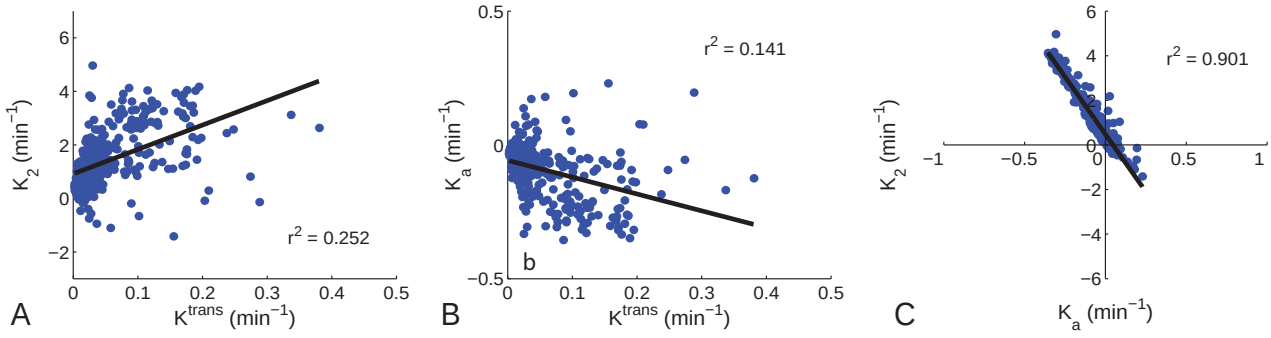

FIG 3. *A*, Sample voxelwise comparison between K_2 at TE_2 and K^{trans}. *B*, Sample voxelwise comparison between K_a at TE_2 and K^{trans}. *C*, Voxelwise comparison between K_2 (y-axis) and K_a (x-axis). *Linear regression line* shown in black.

to have a significant quadratic relationship ($P = .031$ and $P = .005$, respectively) with v_e.

DISCUSSION

DCE–MR imaging estimates of vascular permeability, often reported via K^{trans}, have been shown to be helpful in deciphering brain tumor grade[21] and in predicting disease prognosis.[25,38] Unlike DCE–MR imaging, DSC–MR imaging acquisitions can actually be confounded by the increased vascular permeability present in brain tumors, requiring strategies for leakage correction of the MR imaging signal time courses. Rate constants (K_2 and K_a) computed from these correction techniques have been suggested to reflect vessel permeability.[7,28] To evaluate this relationship, we performed a simultaneous comparison between K^{trans} and the parameters K_2 and K_a using multiecho DSC–MR imaging. In general, the range of K_2 and K_a estimates in this study was observed to be larger than that of K^{trans}, though they were consistent with previous measures in brain tumors.[8,10,28] Voxelwise linear relationships between K_2 and K_a and the parameter K^{trans} were found to be nonsignificant when computed from the same dataset. Although a nonlinear relationship between K_a and K^{trans} was previously presented in simulations,[10] this work provides additional in vivo confirmation. The individual correlations observed here between K_2 and K^{trans} in gliomas were similar to those observed by Bonekamp et al[30] using maximum K^{trans} and K_2 values from whole-tumor ROIs. Although the lack of a strong linear correlation with K^{trans} suggests potential limitations with extracting permeability estimates from DSC–MR imaging correction methods themselves, it should not, however, be interpreted as a failure of these techniques to reliably correct CBV measures for CA leakage.

The effect of TE on K_2 and K_a was also studied. From Fig 4, we observed a significant increase (decrease) in estimates of K_2 (K_a) with a shorter TE. This is due, in part, to the decrease in T2* weighting with decreasing TE and subsequent dominance of T1 leakage effects. Liu et al[8] previously explored the effect of TE on K_2 in numeric simula-

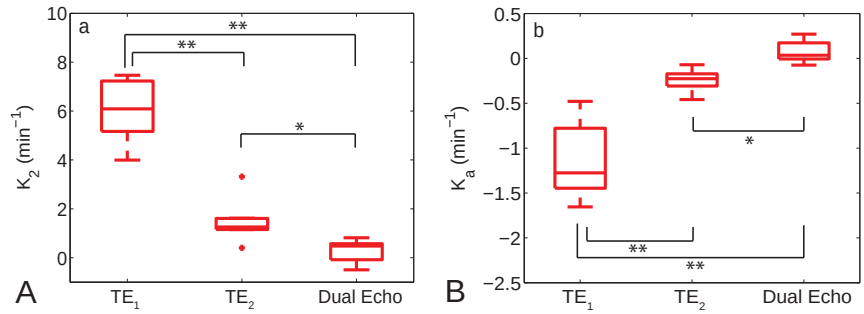

FIG 4. Boxplots of median parameter estimates (from all patients) calculated at various TEs for K_2 (*A*) and K_a (*B*). Boxplots display the median, 25th, and 75th percentiles (edges of box) and extreme data points (whiskers). Outliers are plotted individually (plus sign). Significance was determined by the Mann-Whitney *U* test. * indicates $P < .01$; **, $P < .001$. Note: Positive outlier for K_2 at TE$_1$ not pictured.

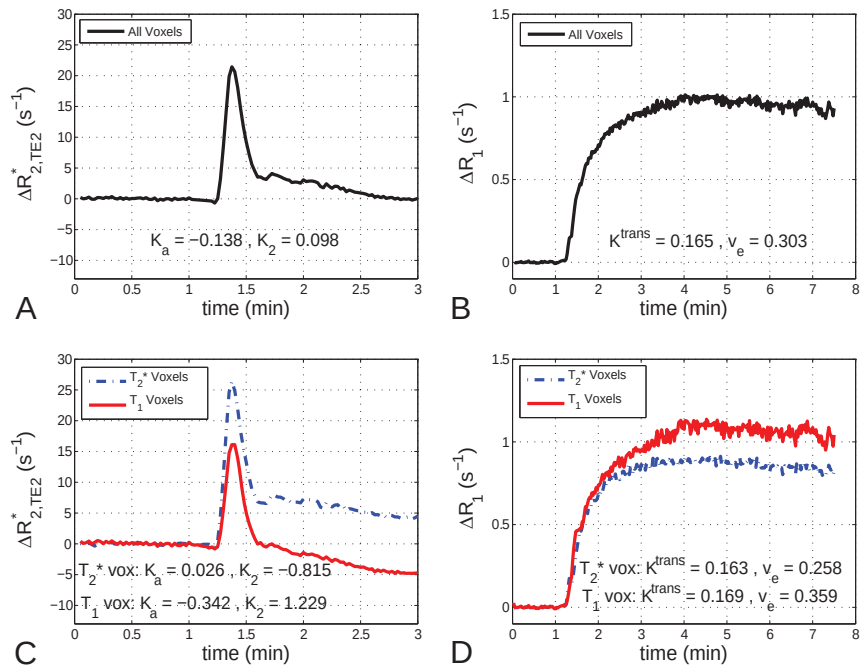

FIG 5. Sample mean ΔR_2^* time course (TE = 31 ms) for a tumor ROI (*A*) and the resulting ΔR_1 time course (*B*). Mean ΔR_2^* (*C*) and ΔR_1 (*D*) time courses from the same tumor with voxels separated by whether they predominately exhibit T2* leakage effects (T2* voxels) or T1 leakage effects (T1 voxels).

Table 2: Patient-specific estimates of DSC-MRI and DCE-MRI parameters separated by the predominant leakage effect

	No. of Voxels (%)		K_2 (min^{-1})		K_a (min^{-1})		K^{trans} (min^{-1})		v_e	
Patient No.	T1	T2*	T1	T2*	T1	T2*	T1	T2*	T1	T2*
1	44 (79%)	12 (21%)	1.807	1.205	−0.373	−0.250	0.223	0.066	0.221	0.072
2	214 (45%)	265 (55%)	1.229	−0.815	−0.342	0.026	0.169	0.163	0.359	0.258
3	126 (61%)	79 (39%)	2.374	0.822	−0.372	−0.117	0.089	0.038	0.328	0.150
4	368 (47%)	417 (53%)	1.767	0.700	−0.536	−0.469	0.104	0.078	0.228	0.140
5	187 (56%)	147 (44%)	1.975	0.787	−0.149	−0.025	0.069	0.044	0.284	0.107
6	734 (93%)	52 (7%)	3.726	0.240	−0.256	0.004	0.099	0.050	0.290	0.138
7	16 (64%)	9 (36%)	2.591	0.025	−0.418	0.024	0.200	0.179	0.203	0.107
Mean$_w$			2.627	0.289	−0.329	−0.208	0.109	0.092	0.285	0.167

Note:—Mean$_w$ indicates weighted mean.

tions and noted that changes in the actual vascular permeability should not affect the polarity of K_2, though changes in imaging parameters (eg, TE) could. Before the current study, a similar analysis with K_a had not yet been performed, to our knowledge.

In addition to TE, the intrinsic presence of competing and simultaneous T1 and T2* leakage effects, within a given voxel, were integral in determining the value of K_2 and K_a. As shown in Fig 5, competing T1 and T2* leakage effects can produce a ΔR_2^* time course that paradoxically appears to be free of CA extravasation effects. This is misleading because the dynamic ΔR_1 information reveals appreciable CA leakage, resulting in moderate estimates of K^{trans}. As noted by Bjornerud et al,[10] the presence of both T1 and T2* relaxation effects in the extracellular extravascular space may drive K_a (and K_2) toward zero, resulting in artifactually low estimates. As an example, in the smallest 10% of all voxels (based on the magnitude of K_a), the mean K^{trans} was observed to be 50% larger than $|K_a|$. Conversely, the magnitude of the mean K_a was $\approx 3\times$ larger than K^{trans} when computed using all voxels. Additionally, the mean value of K_2 and K_a, computed from the aforementioned subset of voxels (smallest 10%), was almost an order of magnitude smaller than the respective mean K_2 and K_a computed using all voxels. These findings clearly have implications for the reliability of these parameters as measures of vascular permeability.

In general, the relationship of K_2 and K_a with K^{trans} may indicate an inaccurate assumption that these parameters solely reflect vessel permeability in brain tumors. When separated into T1 and T2* voxel cohorts, the mean values of K_2 and K_a across patients were found to be significantly different from one another (Table 2). The same was true for v_e. Similar to the previous observation between K_a and K^{trans} in vivo,[11] a significant quadratic relationship was observed between K_2 and K_a and v_e across all patients. To this end, a recent theoretic study by Liu et al[39] demonstrated a potential relationship between v_e and the ratio of the parameters K_1 and K_2 from the Weisskoff correction method. These results indicate that K_2 and K_a may also be influenced by the extravasation space of the CA.

The data in Table 2 also revealed that T1 voxels demonstrated larger v_e values than those found in T2* voxels. This result likely originates from the underlying biophysical basis of T1 and T2* leakage effects. As in DCE–MR imaging, T1 leakage effects result from the direct interaction of CA with the extracellular extravascular water. Accordingly, the physiologic factors that drive the tissue CA concentration (compartmental volume fractions, perfusion, and vascular permeability) and physical properties (CA T1 relaxivity, precontrast T1) and pulse sequence parameters (TR, flip angle) all influence the shape and magnitude of T1 leakage effects on DSC–MR imaging signals. In addition to physiologic factors and imaging parameters, T2* leakage effects are influenced by intravoxel susceptibility differences created by the spatial distribution of the CA within a voxel. Recently, Semmineh et al[40] demonstrated that these effects are predominantly influenced by cellular properties, including density, size, distribution, and shape. Consistent with the results presented herein, stronger T2* leakage effects were observed for tissues with higher cell density (or lower v_e). In general, the dependency of T2* leakage effects on tumor cellularity manifests as changes in the effective T2* relaxivity of the CA. So unlike T1 leakage effects, where the T1 relaxivity of the CA is essentially constant within and across tumors, the T2* relaxivity may vary from voxel to voxel as the cellular properties change.[41]

The variable CA T2* relaxivity also has important implications for the interpretation of the extracted K_2 and K_a parameters. Although voxels were designated as predominantly exhibiting either T1 or T2* leakage effects, the signal of each voxel is the summation of these competing effects, as previously discussed. In the limiting case in which T2* leakage effects are absent and the signals only reflect T1 leakage effects, the K_2 and K_a parameters are primarily driven by the underlying CA kinetics and the assumptions built into the correction models and can be understood accordingly. However, when there are competing T1 and T2* effects, K_2 and K_a represent a complex balance between the CA kinetics and the tissue microstructure. Practically, this implies that a positive and negative estimate of K_2 or K_a of the same absolute value may not reflect the same combination of vascular permeability, tissue compartment size, or microstructural geometry. Similarly, K_2 and K_a values that are equivalent within or across tumors may not reflect the same underlying physiologic environment because they could originate from unique combinations of competing T1 and T2* effects. This observation may help further explain the discrepancies in using K_2 and K_a to evaluate tumor grade and to assess treatment response.[11,28,29] Computational studies that account for the underlying biophysical basis of the DSC–MR imaging signal could be used to systematically investigate and provide insight into the complex interaction between T1 and T2* leakage effects and the derived K_2 and K_a values.

The use of multiecho DSC–MR imaging in this study enabled measures of DCE–MR imaging signals and, subsequently, computation of the associated K^{trans} maps. As mentioned above, an alternative approach to collect both datasets in the same examination is to acquire DCE–MR imaging data during a preload of CA. This step enables the use of traditional DCE–MR imaging pulse sequences, ones that typically have higher spatial (and lower temporal) resolution. For the purpose of the study, this approach would have enabled the comparison of more conventionally derived K^{trans} values with K_2 and K_a. However, the addition of a preload to this study would have reduced T1 leakage effects and increased T2* leakage effects. It is unclear how this change would influence the correlation among K^{trans}, K_2, and K_a. Another limitation of this study is the small sample size. While the findings are likely to hold in a larger population of patients with gliomas, it would be valuable to expand the tumor types considered (eg, primary central nervous system lymphoma and brain metastasis) as different histologic subtypes have been shown to express varying degrees of T1 and T2* leakage effects.

CONCLUSIONS

This study investigated the use of DSC–MR imaging for estimating vascular permeability in brain tumors. Implementation of common DSC–MR imaging leakage-correction techniques afforded the computation of rate constants (K_2 and K_a) postulated to report on vessel permeability. Additionally, the acquisition of multiecho data allowed the computation of the DCE–MR imaging pharmacokinetic parameter K^{trans}. A voxelwise comparison among the parameters K_2, K_a, and K^{trans} revealed nonsignificant linear correlations that may be attributed, in part, to competing

T1 and T2* leakage effects and the effect of TE on K_2 and K_a. Further investigation also revealed a significant quadratic relationship between K_2 and K_a and the DCE–MR imaging parameter v_e. On the basis of these findings, caution should be used in assuming a direct relationship between K_2 and K_a and vascular permeability in brain tumors. Furthermore, the acquisition of K^{trans} from multiecho DSC–MR imaging data may provide a convenient method for simultaneously measuring vascular permeability and perfusion in brain tumors.

Disclosures: Jack T. Skinner—*RELATED*: *Grant*: National Institutes of Health.* C. Chad Quarles—*RELATED*: *Grant*: National Institutes of Health.* *Money paid to the institution.

REFERENCES

1. Shubik P. **Vascularization of tumors: a review.** *J Cancer Res Clin Oncol* 1982;103:211–26 CrossRef Medline
2. Boxerman JL, Schmainda KM, Weisskoff RM. **Relative cerebral blood volume maps corrected for contrast agent extravasation significantly correlate with glioma tumor grade, whereas uncorrected maps do not.** *AJNR Am J Neuroradiol* 2006;27:859–67 Medline
3. Paulson ES, Schmainda KM. **Comparison of dynamic susceptibility-weighted contrast-enhanced MR methods: recommendations for measuring relative cerebral blood volume in brain tumors.** *Radiology* 2008;249:601–13 CrossRef Medline
4. Quarles CC, Gochberg DF, Gore JC, et al. **A theoretical framework to model DSC-MRI data acquired in the presence of contrast agent extravasation.** *Phys Med Biol* 2009;54:5749–66 CrossRef Medline
5. Schmainda KM, Prah M, Connelly J, et al. **Dynamic-susceptibility contrast agent MRI measures of relative cerebral blood volume predict response to bevacizumab in recurrent high-grade glioma.** *Neuro Oncol* 2014;16:880–88 CrossRef Medline
6. Paulson E, Prah DE, Schmainda KM. **Compensation of confounding T1 and T2 dipolar and residual susceptibility effects in DSC-MRI using dual-echo SPIRAL.** In: *Proceedings of the Annual Meeting of the International Society for Magnetic Resonance in Medicine*, Berlin, Germany. May 19–25, 2007:2811
7. Weisskoff RM, Boxerman JL, Sorensen AG. **Simultaneous blood volume and permeability mapping using a single Gd-based contrast agent.** In: *Proceedings of the Annual Meeting of the International Society for Magnetic Resonance in Medicine*, San Francisco, California. August 6–12, 1994:279
8. Liu HL, Wu YY, Yang WS, et al. **Is Weisskoff model valid for the correction of contrast agent extravasation with combined T1 and T2* effects in dynamic susceptibility contrast MRI?** *Med Phys* 2011; 38:802–09 CrossRef Medline
9. Quarles CC, Ward BD, Schmainda KM. **Improving the reliability of obtaining tumor hemodynamic parameters in the presence of contrast agent extravasation.** *Magn Reson Med* 2005;53:1307–16 CrossRef Medline
10. Bjornerud A, Sorensen AG, Mouridsen K, et al. **T1- and T2*-dominant extravasation correction in DSC-MRI: part I—theoretical considerations and implications for assessment of tumor hemodynamic properties.** *J Cereb Blood Flow Metab* 2011;31:2041–53 CrossRef Medline
11. Emblem KE, Bjornerud A, Mouridsen K, et al. **T(1)- and T(2)(*)-dominant extravasation correction in DSC-MRI: part II—predicting patient outcome after a single dose of cediranib in recurrent glioblastoma patients.** *J Cereb Blood Flow Metab* 2011;31:2054–64 CrossRef Medline
12. Vonken EJ, van Osch MJ, Bakker CJ, et al. **Measurement of cerebral perfusion with dual-echo multi-slice quantitative dynamic susceptibility contrast MRI.** *J Magn Reson Imaging* 1999;10:109–17 Medline
13. Miyati T, Banno T, Mase M, et al. **Dual dynamic contrast-enhanced MR imaging.** *J Magn Reson Imaging* 1997;7:230–35 CrossRef Medline
14. Uematsu H, Maeda M, Sadato N, et al. **Blood volume of gliomas determined by double-echo dynamic perfusion-weighted MR imaging: a preliminary study.** *AJNR Am J Neuroradiol* 2001;22: 1915–19 Medline
15. Vonken EP, van Osch MJ, Bakker CJ, et al. **Simultaneous quantitative cerebral perfusion and Gd-DTPA extravasation measurement with dual-echo dynamic susceptibility contrast MRI.** *Magn Reson Med* 2000;43:820–27 Medline
16. Quarles CC, Gore JC, Xu L, et al. **Comparison of dual-echo DSC-MRI- and DCE-MRI-derived contrast agent kinetic parameters.** *Magn Reson Imaging* 2012;30:944–53 CrossRef Medline
17. Skinner JT, Robison RK, Elder CP, et al. **Evaluation of a multiple spin- and gradient-echo (SAGE) EPI acquisition with SENSE acceleration: applications for perfusion imaging in and outside the brain.** *Magn Reson Imaging* 2014;32:1171–80 CrossRef Medline
18. Tofts PS. **Modeling tracer kinetics in dynamic Gd-DTPA MR imaging.** *J Magn Reson Imaging* 1997;7:91–101 CrossRef Medline
19. Tofts PS, Brix G, Buckley DL, et al. **Estimating kinetic parameters from dynamic contrast-enhanced T(1)-weighted MRI of a diffusable tracer: standardized quantities and symbols.** *J Magn Reson Imaging* 1999;10:223–32 Medline
20. Schmiedeskamp H, Andre JB, Straka M, et al. **Simultaneous perfusion and permeability measurements using combined spin- and gradient-echo MRI.** *J Cereb Blood Flow Metab* 2013;33:732–43 CrossRef Medline
21. Zhang N, Zhang L, Qiu B, et al. **Correlation of volume transfer coefficient Ktrans with histopathologic grades of gliomas.** *J Magn Reson Imaging* 2012;36:355–63 CrossRef Medline
22. Cha S, Yang L, Johnson G, et al. **Comparison of microvascular permeability measurements, K(trans), determined with conventional steady-state T1-weighted and first-pass T2*-weighted MR imaging methods in gliomas and meningiomas.** *AJNR Am J Neuroradiol* 2006;27:409–17 Medline
23. Ah-See ML, Makris A, Taylor NJ, et al. **Early changes in functional dynamic magnetic resonance imaging predict for pathologic response to neoadjuvant chemotherapy in primary breast cancer.** *Clin Cancer Res* 2008;14:6580–89 CrossRef Medline
24. George ML, Dzik-Jurasz AS, Padhani AR, et al. **Non-invasive methods of assessing angiogenesis and their value in predicting response to treatment in colorectal cancer.** *Br J Surg* 2001;88:1628–36 CrossRef Medline
25. Armitage PA, Schwindack C, Bastin ME, et al. **Quantitative assessment of intracranial tumor response to dexamethasone using diffusion, perfusion and permeability magnetic resonance imaging.** *Magn Reson Imaging* 2007;25:303–10 CrossRef Medline
26. Batchelor TT, Sorensen AG, di Tomaso E, et al. **AZD2171, a pan-VEGF receptor tyrosine kinase inhibitor, normalizes tumor vasculature and alleviates edema in glioblastoma patients.** *Cancer Cell* 2007;11:83–95 CrossRef Medline
27. Toh CH, Wei KC, Chang CN, et al. **Differentiation of primary central nervous system lymphomas and glioblastomas: comparisons of diagnostic performance of dynamic susceptibility contrast-enhanced perfusion MR imaging without and with contrast-leakage correction.** *AJNR Am J Neuroradiol* 2013;34:1145–49 CrossRef Medline
28. Provenzale JM, Wang GR, Brenner T, et al. **Comparison of permeability in high-grade and low-grade brain tumors using dynamic susceptibility contrast MR imaging.** *AJR Am J Roentgenol* 2002;178: 711–16 CrossRef Medline
29. Donahue KM, Krouwer HG, Rand SD, et al. **Utility of simultaneously acquired gradient-echo and spin-echo cerebral blood volume and morphology maps in brain tumor patients.** *Magn Reson Med* 2000;43:845–53 Medline
30. Bonekamp D, Deike K, Wiestler B, et al. **Association of overall survival in patients with newly diagnosed glioblastoma with contrast-enhanced perfusion MRI: comparison of intraindividually matched T1- and T2 (*)-based bolus techniques.** *J Magn Reson Imaging* 2015;42:87–96 CrossRef Medline
31. Schmiedeskamp H, Straka M, Newbould RD, et al. **Combined spin-**

and gradient-echo perfusion-weighted imaging. *Magn Reson Med* 2012;68:30–40 CrossRef Medline
32. Carroll TJ, Rowley HA, Haughton VM. **Automatic calculation of the arterial input function for cerebral perfusion imaging with MR imaging.** *Radiology* 2003;227:593–600 CrossRef Medline
33. Newton AT, Skinner JT, Quarles CC. **Automatic AIF estimation in multi-echo DSC-MRI of pediatric patieints: avoiding the noise floor.** In: *Proceedings of the Annual Meeting of the International Society for Magnetic Resonance in Medicine*, Salt Lake City, Utah. April 20–26, 2013
34. Liu HL, Pu Y, Liu Y, et al. **Cerebral blood flow measurement by dynamic contrast MRI using singular value decomposition with an adaptive threshold.** *Magn Reson Med* 1999;42:167–72 Medline
35. Kuperman VY, Karczmar GS, Blomley MJ, et al. **Differentiating between T1 and T2* changes caused by gadopentetate dimeglumine in the kidney by using a double-echo dynamic MR imaging sequence.** *J Magn Reson Imaging* 1996;6:764–68 CrossRef Medline
36. Landis CS, Li X, Telang FW, et al. **Determination of the MRI contrast agent concentration time course in vivo following bolus injection: effect of equilibrium transcytolemmal water exchange.** *Magn Reson Med* 2000;44:563–74 Medline
37. Skinner JT, Yankeelov TE, Peterson TE, et al. **Comparison of dynamic contrast-enhanced MRI and quantitative SPECT in a rat glioma model.** *Contrast Media Mol Imaging* 2012;7:494–500 CrossRef Medline
38. Mills SJ, Patankar TA, Haroon HA, et al. **Do cerebral blood volume and contrast transfer coefficient predict prognosis in human glioma?** *AJNR Am J Neuroradiol* 2006;27:853–58 Medline
39. Liu Y, Ding W, Bensheng Q. **Extravascular extracellular space fraction measurement by DSC-MRI: a theoretical study.** In: *Proceedings of the Annual Meeting of the International Society for Magnetic Resonance in Medicine and European Society for Magnetic Resonance in Medicine*, Milan, Italy. May 10–16, 2014
40. Semmineh NB, Xu J, Boxerman JL, et al. **An efficient computational approach to characterize DSC-MRI signals arising from three-dimensional heterogeneous tissue structures.** *PLoS One* 2014;9:e84764 CrossRef Medline
41. Semmineh NB, Xu J, Skinner JT, et al. **Assessing tumor cytoarchitecture using multiecho DSC-MRI derived measures of the transverse relaxivity at tracer equilibrium (TRATE).** *Magn Reson Med* 2015;74:772–84 CrossRef Medline

Favorable Bridging Therapy Based on DWI-FLAIR Mismatch in Patients with Unclear-Onset Stroke

I. Mourand, D. Milhaud, C. Arquizan, K. Lobotesis, R. Schaub, P. Machi, X. Ayrignac, O.F. Eker, A. Bonafé, and V. Costalat

ABSTRACT

BACKGROUND AND PURPOSE: Standard selection criteria for revascularization therapy usually exclude patients with unclear-onset stroke. Our aim was to evaluate the efficacy and safety of revascularization therapy in patients with unclear-onset stroke in the anterior circulation and to identify the predictive factors for favorable clinical outcome.

MATERIALS AND METHODS: We retrospectively analyzed 41 consecutive patients presenting with acute stroke with unknown time of onset treated by intravenous thrombolysis and/or mechanical thrombectomy. Only patients without well-developed fluid-attenuated inversion recovery changes of acute diffusion lesions on MR imaging were enrolled. Twenty-one patients were treated by intravenous thrombolysis; 19 received, simultaneously, intravenous thrombolysis and mechanical thrombectomy (as a bridging therapy); and 1 patient, endovascular therapy alone. Clinical outcome was evaluated at 90 days by using the mRS. Mortality and symptomatic intracranial hemorrhage were also reported.

RESULTS: Median patient age was 72 years (range, 17–89 years). Mean initial NIHSS score was 14.5 ± 5.7. Successful recanalization (TICI 2b–3) was assessed in 61% of patients presenting with an arterial occlusion, symptomatic intracranial hemorrhage occurred in 2 patients (4.9%), and 3 (7.3%) patients died. After 90 days, favorable outcome (mRS 0–2) was observed in 25 (61%) patients. Following multivariate analysis, initial NIHSS score (OR, 1.43; 95% CI, 1.13–1.82; $P = .003$) and bridging therapy (OR, 37.92; 95% CI, 2.43–591.35; $P = .009$) were independently associated with a favorable outcome at 3 months.

CONCLUSIONS: The study demonstrates the safety and good clinical outcome of acute recanalization therapy in patients with acute stroke in the anterior circulation and an unknown time of onset and a DWI/FLAIR mismatch on imaging. Moreover, bridging therapy versus intravenous thrombolysis alone was independently associated with favorable outcome at 3 months.

ABBREVIATIONS: FAT = first found abnormal time; GRAPPA = generalized autocalibrating partially parallel acquisition; IVT = intravenous thrombolysis; sICH = symptomatic intracranial hemorrhage

Acute ischemic strokes with an unknown time of symptom onset occur in approximately 25% of patients.[1] Hence, these patients are usually excluded from intravenous thrombolysis (IVT).[2] However, many patients with an unknown stroke onset could also benefit from this treatment. In a subset of these patients, it has been shown that the clinical features and imaging characteristics do not differ significantly from those in patients with a known time of onset.[1] MR imaging could be helpful if it is used as a "clock" for stroke of unknown time onset; indeed, in a recent multicenter observational study of patients with stroke with known time of symptom onset, the DWI-FLAIR mismatch, defined by positive findings on DWI and negative findings on FLAIR, was effective in identifying patients within 4.5 hours of symptom onset.[3]

To date, limited studies have focused on the safety and effectiveness of IVT in patients with a stroke of unknown onset time, especially by using MR imaging–specific eligibility criteria.[4-9] Only a few reports have evaluated the feasibility of endovascular therapies in patients with wake-up stroke.[10-12] Recently, randomized studies have demonstrated that mechanical thrombectomy is an alternative and synergistic method of treatment to IVT in acute ischemic stroke, with a higher recanalization rate (66%–100%) and a more favorable outcome (32.6%–71%).[13-17]

The aim of this study was to describe the experience of our

Received January 6, 2015; accepted after revision June 2.

From Departments of Neurology (I.M., D.M., C.A., X.A.), Neuroradiology (K.L., P.M., O.F.E., A.B., V.C.), and Medical Information (R.S.), University Hospital Center of Montpellier, Gui de Chauliac Hospital, Montpellier, France.

A.B. and V.C. contributed equally to this work.

Please address correspondence to I. Mourand, MD, Neurology Department, CHRU, Gui de Chauliac Hospital, 80 Avenue Augustin Fliche, 34295 Montpellier Cedex 5, France; e-mail: i-mourand@chu-montpellier.fr

Indicates article with supplemental on-line table.

http://dx.doi.org/10.3174/ajnr.A4574

center with 41 patients presenting with a stroke of an unknown time of symptom onset in the anterior circulation, who were treated by using a coalescent stroke-management protocol with IVT, mechanical thrombectomy, or bridging therapy based on DWI/FLAIR mismatch. We also assessed predictive factors for favorable outcome at 3 months and evaluated the feasibility, safety, and efficacy of revascularization therapy in these patients.

MATERIALS AND METHODS

All consecutive patients admitted in our stroke unit with a stroke of unknown time of onset and treated by reperfusion therapy between October 2010 and October 2013 were included in this study. The patient demographics, risk factors, and clinical and imaging data were prospectively registered in our stroke databank. The NIHSS score was systematically assessed by a stroke neurologist on admission. This study was approved by the local ethics committee. Consent for treatment was obtained from the patients or their family before the endovascular procedure.

The inclusion criteria were as follows: 1) patients with acute stroke without a known time of symptom onset, presenting to our emergency department within 4 hours after the first found abnormal time (FAT); 2) acute ischemic lesions within the anterior circulation on DWI; 3) an ASPECTS of ≥5; 4) the presence of a DWI/FLAIR mismatch according to Thomalla et al[3]; 5) the presence of a clinically relevant impairment in social, occupational, or other important areas of functioning following a physician evaluation; and 6) the presence of clinical-diffusion mismatch between stroke severity and volume of DWI lesions assessed by visual inspection. For mechanical thrombectomy, patients were selected if they had the following additional criteria: 1) the presence of a proximal intracranial artery occlusion in the stroke territory; 2) an NIHSS score of ≥8; 3) a premorbid mRS of <1; and 4) initiation of endovascular treatment within 6 hours of FAT.

In cases of anterior cerebral artery stroke, the MR imaging eligibility criterion was an infarct volume <50% of the arterial territory.

MR Imaging Protocol

Multimodal MR imaging was performed in all patients by using a 1.5T magnet (Gyroscan Intera, Release 10; Philips Healthcare, Best, the Netherlands; 33-mT/m hypergradients). The MR imaging protocol included the following sequences: T2 gradient echo (TR/TE = 900/27 ms; flip angle = 15°; 1 repetition; generalized autocalibrating partially parallel acquisition [GRAPPA] = 2; 5.0-mm section thickness with no intersection gap; voxel size = 1.3 × 0.9 × 5 mm); DWI (TR/TE = 3600/83 ms; b-values = 0 and 1000 s/mm^2; 2 repetitions; GRAPPA = 2; 5.0-mm section thickness with no intersection gap; voxel size = 1.8 × 1.8 × 5 mm); an ADC map; FLAIR (TR/TE = 8000/94 ms; TI = 2500 ms; turbo factor = 15; GRAPPA = 2; 5.0-mm section thickness with no intersection gap; voxel size = 0.6 × 0.6 × 5 mm); and T1 contrast-enhanced MRA (3D coronal gradient echo: TR/TE = 3.45/1.28 ms; flip angle = 25°; GRAPPA = 2; 144 sections; voxel size = 0.7 × 0.7 × 0.7 mm; gadolinium contrast agent, 0.5 mmol/mL, 0.2 mL/kg; flow rate = 2 mL/sec) of the supra-aortic trunks and intracranial vessels.

The DWI/FLAIR mismatch was defined according to Thomalla et al.[3] It was diagnosed when a visible acute ischemic lesion was present on DWI with no traceable parenchymal hyperintensity in the corresponding region on FLAIR imaging. Collateral blood flow in the distal cerebral artery territory was defined on FLAIR by linear or serpentine vascular hyperintensities relative to gray matter in the MCA territory subarachnoid space. It was graded as "present" if vascular hyperintensities in the sulci were seen on FLAIR images or as "absent" if they were not detectable.

Revascularization Protocol

IVT (0.9 mg/kg) was administered to patients within a maximum of 4.5 hours of FAT. Conventional clinical and laboratory inclusion and exclusion criteria for IVT were applied.[2] In cases of bridging therapy, patients were transferred to the angiographic suite for thrombectomy as soon as possible. Among patients with contraindications to IVT, thrombectomy alone was performed.

Mechanical thrombectomy was performed via a femoral artery approach with the patient under general anesthesia with the Solitaire FR device (Covidien, Irvine, California). General anesthesia included urinary bladder catheterization and endotracheal intubation without neuromuscular blockade.

An 8F or 9F Merci balloon-guide catheter (Concentric Medical, Mountain View, California) was inserted through a sheath. A 0.21-inch-internal-diameter microcatheter (Prowler Select Plus; Codman & Shurtleff, Raynham, Massachusetts; or Vasco 21; Balt, Montmorency, France) was navigated distal to the occlusion over a 0.014-inch steerable guidewire, which was then exchanged with the thrombectomy device. During the retrieval, the balloon-guide catheter was inflated to interrupt anterograde flow. Manual aspiration with a 50-mL syringe was performed through the hemostatic valve during the retrieval, to reverse the flow and aspirate clot debris possibly lost in the guide catheter lumen. The number of attempts to retrieve the thrombus was limited to 5 passes by the occluded vessel. Neither IV heparin nor intra-arterial fibrinolytics were administered at any time during the procedure. Blood pressure was carefully monitored during anesthetic induction and during the procedure, with a minimal threshold set at 90 mm Hg (mean arterial pressure). Hypotension was rapidly corrected if needed. Following any complications, extubation was planned at the end of the procedure and the patient was transferred to the intensive care unit.

Follow-up CT or MR imaging was performed 24 hours after the acute therapy to assess the extent of the infarction and/or hemorrhagic complications. If no hemorrhage was present, antiplatelet drugs were administered.

Outcome Measures

Successful recanalization, defined as TICI 2b or 3, was assessed at the end of the procedure in patients treated with thrombectomy. In patients treated with IVT, recanalization at 1 day was considered successful if follow-up MRA or angio-CT demonstrated complete visualization of the occluded artery, without residual stenosis of >50%.

"Symptomatic intracranial hemorrhage" (sICH) was defined as a documented hemorrhage on CT or MR imaging with a decline of ≥4 points in the NIHSS score. Device-related complications were also reported. Clinical outcome was quantified by mRS

and mortality at day 90. Favorable outcome at 90 days was defined as an mRS score of ≤2.

Statistical Analysis

Patients with a favorable or poor outcome were compared by using the Student *t* or Mann-Whitney test for continuous variables and the χ^2 or Fisher test for categoric variables. Bivariate logistic regressions were used to identify predictors of favorable outcome. Potential independent predictors ($P < .25$ in bivariate logistic regressions) were included in a multivariate logistic regression, built by stepwise procedure. Adjusted odds ratios and their 95% confidence intervals were calculated. The statistical significance threshold was set at 5%. Statistical analyses were conducted by using SAS software 9.2 (SAS Institute, Cary, North Carolina).

RESULTS

Population Data

Overall, 41 patients with unclear-onset stroke in the anterior circulation (median age, 72 years; range, 17–89 years; female/male ratio, 26:15) were included. Baseline clinical and radiologic features and main clinical outcomes at day 90 are presented in the Online Table.

The median time interval between last-seen-normal time and hospital admission was 490 minutes (interquartile range, 255–641 minutes). The mean NIHSS score was 14.5 ± 5.7. The median time interval from FAT to MR imaging was 135 minutes (interquartile range, 109–158 minutes) and 517 minutes (interquartile range, 314–678 minutes) from last-seen-normal time. The median DWI ASPECTS was 8 (range, 5–10). Thirty-six patients (88%) showed an arterial occlusion in the anterior circulation. Occlusion sites were the proximal MCA (M1) in 28 cases (68.3%), the distal MCA (M2, M3) in 5 cases (12.1%), and the anterior cerebral artery in 3 cases (7.3%). The internal carotid artery was occluded in 14 patients (34.1%), including 9 patients with tandem cervical ICA and intracranial occlusions and 5 carotid bifurcation occlusions.

Stroke-Management Protocol

Nineteen patients (46.3%) underwent bridging therapy, and 21 patients (51.2%), IVT alone. In these patients, the exclusion criteria for thrombectomy included the following: no occluded intracranial artery (5 patients), NIHSS score of <8 (4 patients), distal cerebral artery occlusion (5 patients), premorbid mRS of >1 (3 patients), fast recovery symptoms after IVT administration (1 patient), and delay beyond 6 hours after FAT (3 patients). The mean time from initial MR imaging to the start of IVT was 51 ± 24 minutes. One patient with uncontrolled hypertension was treated by mechanical thrombectomy alone.

For the 20 patients treated by mechanical thrombectomy, the median number of passes with the thrombectomy device was 2 (range, 1–5). The thrombectomy procedure failed in 2 cases because of an inability to advance the microcatheter in the proximal ICA. Immediate successful recanalization (TICI ≥2b) was achieved in 15 patients (75%), and TICI 3 was achieved in 40% (8/20). The mean time from MR imaging to groin puncture was 81 ± 38 minutes. The median time from groin puncture to maximum final TICI was 60 minutes (range, 21–248 minutes). The mean time from FAT to recanalization was 295 ± 75 minutes and 686 ± 196 minutes from last-seen-normal-time.

Outcome

Four device-related complications occurred without neurologic deterioration or clinical sequelae, including 1 vessel perforation, 1 cervical ICA dissection, and 2 distal asymptomatic embolizations. Two (4.9%) patients had sICH related to the acute therapy within the first 24 hours with a favorable outcome. Three (7.3%) patients died during their hospital stay. Favorable outcome (mRS ≤2) was observed in 25 (61%) patients, including 14 (70%) patients of the 20 treated by mechanical thrombectomy and 11 (52%) of the 21 treated by IVT alone. A representative case is shown in Fig 1.

Predictive Factors for Clinical Outcome

Compared with patients treated by IVT alone, patients treated with bridging therapy showed a statistically significant difference in a number of parameters. Patients were younger ($P = .041$) with a lower systolic blood pressure level at admission ($P = .017$), a higher NIHSS score ($P = .007$), and a lower ASPECTS ($P = .022$). Their recanalization rate ($P = .023$) was better (On-line Table).

The variables entered in the multivariate logistic regression analysis exploring predictive factors associated with a favorable outcome at day 90 (mRS ≤2) were age, initial systolic blood pressure, initial blood glucose level, initial NIHSS score, IVT versus bridging therapy, and time interval from FAT to treatment initiation. In the final adjusted model, each 1-point decrease of the initial NIHSS score was independently associated with a favorable outcome at day 90 (OR, 1.43; 95% CI, 1.13–1.82; $P = .003$) in patients with unclear-onset stroke and bridging therapy versus IV thrombolysis (OR, 37.92; 95% CI, 2.43–591.35; $P = .009$) (Table).

DISCUSSION

Our study provided 2 important findings: 1) Reperfusion therapy based on DWI/FLAIR mismatch in patients with unclear-onset stroke seems to be efficient and safe, and 2) bridging therapy versus IVT alone is independently associated with favorable outcome at 3 months.

Our results are comparable with those of studies of IVT by using MR imaging variables (DWI/PWI, DWI/FLAIR mismatch) for patient selection, which showed favorable clinical outcome (40%–56.3% for mRS 0–2) and acceptable mortality (0%–10.3%) and sICH (0%–10.3%) rates.[6-9] In contrast, CT-based thrombolysis in patients with wake-up stroke showed variable results. The only randomized controlled trial with thrombolytic treatment based on CT selection was stopped early because the rate of sICH was significantly higher in patients with wake-up stroke (13.6%) than in the other patients with stroke (4.0%).[18] Barreto et al,[4] by using noncontrast cranial CT, found, retrospectively, that 46 patients with intravenous thrombolysis and wake-up stroke had a significantly higher rate of favorable outcome (28% versus 13%; $P = .006$) but a higher mortality rate (15% versus 0%) than 34 patients with wake-up stroke treated without thrombolysis.

In the literature, there are only a few reports of patients with an

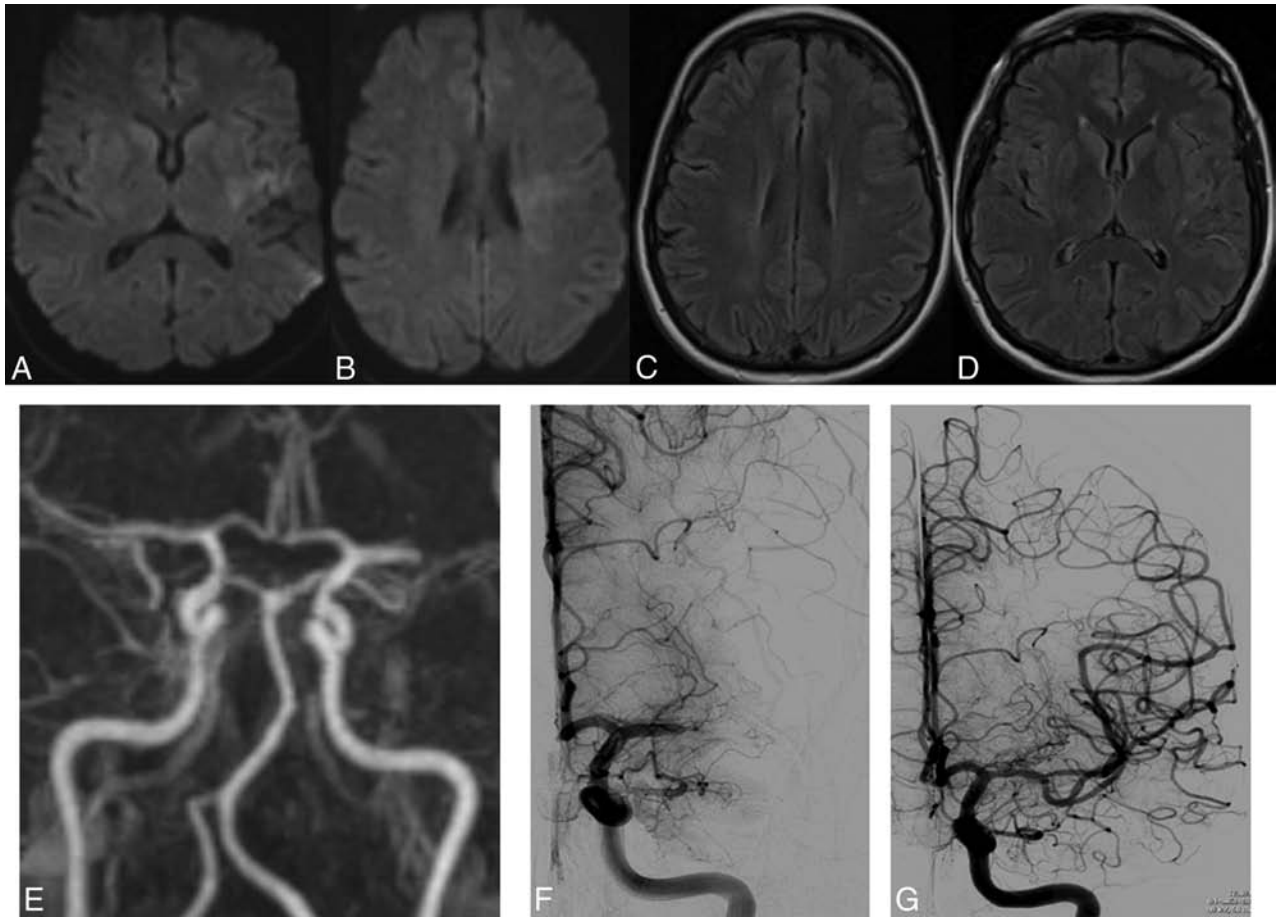

FIG 1. A 49-year-old woman presented with right hemiplegia and dysarthria (NIHSS score, 13). The patient arrived at the emergency department 72 minutes after symptom detection. MR imaging showed an acute ischemic lesion in the left MCA territory on DWI (*A* and *B*) without parenchymal signal changes on FLAIR (*C* and *D*) and occlusion of the left MCA (M1 segment) with collateral blood flow in the distal cerebral artery territory on MRA (*E*). Intravenous thrombolysis was started (0.9 mg/kg) 140 minutes after symptom detection. On DSA, the left MCA was still occluded on the M1 segment (*F*) and was recanalized after mechanical thrombectomy (TICI 3) (*G*). Time from symptom detection to recanalization was 189 minutes (3 hours 9 minutes). The mRS score at 3 months was zero.

Predictive factors associated with favorable outcome at day 90 (mRS ≤2)

		Bivariate Logistic Regression				Multivariate Logistic Regression			
Variable		OR	95% CI		*P*	OR	95% CI		*P*
Initial NIHSS	For each 1-point decrease	1.19	1.03	1.37	.017	1.43	1.13	1.82	.003
Treatment group	Bridging versus thrombolysis	2.95	0.72	12.11	.132	37.91	2.43	591.35	.009
Blood glucose	For each 0.5-mmol/L increase	0.82	0.66	1.02	.081				
Age	For each 5-year increase	0.79	0.60	1.04	.094				
Systolic blood pressure	For each 10-mm Hg increase	0.80	0.59	1.09	.160				
FAT-to-treatment delay	For each 30-minute increase	0.81	0.50	1.30	.377				

acute stroke of unknown time of onset who underwent multimodal reperfusion therapy or endovascular therapy. In the Reperfusion Therapy in Unclear-Onset Stroke Based on MRI Evaluation trial, a prospective study using MR imaging criteria in 83 patients with an unknown time of onset,[19] more than two-thirds of patients received endovascular treatment and approximately 10% received IVT alone. Favorable outcome (mRS 0–2) was achieved in 44.6%, and sICH was seen in 3.6%. Natarajan et al[11] performed a retrospective review of 30 patients with significant salvageable brain tissue identified on CT perfusion who underwent endovascular recanalization (intra-arterial thrombolysis, mechanical thrombectomy, or angioplasty) ≥8 hours after last-seen-normal time, including those with wake-up stroke; partial/complete recanalization was achieved in 66.7% of patients, with 20% presenting with mRS 0–2 at 3 months. Overall mortality was 33.3%, and sICH was 10%.

Recently, Stampfl et al[12] retrospectively analyzed clinical and angiographic data in 19 patients with wake-up stroke and diffusion/perfusion mismatch on MR or CT imaging treated with stent-retriever devices. Despite successful and rapid recanalization (94.7% of TICI ≥2), clinical outcome remained poor (10.5% of mRS 0–2; 36.8% died), and sICH occurred in 21.1% of patients. The authors underlined the difficulty of patient selection for endovascular therapy. Despite a lower recanalization rate, our results are better than those previously published for multimodal reperfusion therapy[11,19] or endovascular treatment[12] in terms of the frequency of good outcome (61% versus 10.5%–44.6%), mortality (7.3% versus 33.3%–36.8%), and sICH (4.9% versus 3.6%–21.1%) rates.

Recently 3 randomized studies[13-17] reported the superiority of rapid thrombectomy, compared with IVT alone, in patients with acute ischemic stroke with a proximal intracranial occlusion and improving reperfusion (66%–100% for intervention versus 31.2%–37% for controls) and functional outcome at 90 days (32.6%–71% for intervention versus 19.1%–40% for controls). There were no significant differences in mortality (9%–18.9% for intervention versus 12%–20% for controls) or the occurrence of symptomatic intracerebral hemorrhage (0%–7.7% for intervention versus 1.9%–6.4% for controls).

In our study, patients treated with bridging therapy had more favorable outcome compared with patients treated with IVT alone. These results were shown despite the conditions of patients treated with bridging being more severe (worst NIHSS and ASPECTS at admission). Indeed, after adjusting for the initial NIHSS score, bridging therapy versus IVT alone was independently associated with favorable outcome at 3 months in patients with unclear-onset stroke. Even if there is a statistically significant difference between these 2 groups of patients, our results suggest that IVT followed by endovascular therapy combines the advantages of a rapid start of treatment with IVT[2] and a greater likelihood of early recanalization.

Recently, several trials emphasized the importance of patient selection for reperfusion therapy, with the tissue clock shown by multiparametric MR imaging techniques.[6-9,12] We selected, in our study, patients using DWI/FLAIR mismatch and clinical-diffusion mismatch among MR imaging criteria. As reported by Thomalla et al,[3] a patient with an acute ischemic lesion detected with DWI but not with FLAIR imaging is likely to be within 4.5 hours of symptom onset with high specificity (78%; 95% CI, 72%–84%) and high positive predict value (83%; 95% CI, 79%–88%). Moreover, clinical-diffusion mismatch, which predicts the presence of PWI-DWI mismatch, may be associated with neurologic improvement in patients treated with IVT as reported by Terasawa et al.[20] Indeed, a number of studies have provided support for penumbral-imaging selection, by using the perfusion-diffusion mismatch criteria for the treatment of acute ischemic stroke[7-9,12] because salvage of the ischemic penumbra has formed the theoretic basis of recanalization therapies. This criterion may be particularly helpful in late time windows, when the proportion of patients with penumbral tissue steadily decreases. Last, the results of Diffusion and Perfusion Imaging Evaluation for Understanding Stroke Evolution Study 2 demonstrated that reperfusion was associated with increased good functional outcome at day 9 in a defined target mismatch profile.[21]

Obvious limitations of our monocentric observational study were the small number of patients, a retrospective analysis of our prospective dataset performed, and no control group. Using predefined imaging criteria, several ongoing prospective clinical trials are testing the safety and efficiency of thrombolytic treatment in patients with stroke with an unknown time of onset.[22]

CONCLUSIONS

Our preliminary results suggest that MR imaging–based reperfusion therapy can safely and efficiently be applied to patients with acute stroke with an unknown time of onset (based on DWI/FLAIR mismatch). Moreover, this study underlines the fact that IVT combined with endovascular mechanical thrombectomy seems to be associated with favorable clinical outcome when patients are carefully selected. Nevertheless, multicenter randomized trials are required to confirm these results and to determine the optimal multimodal MR imaging criteria for patient selection and the optimal treatment strategies.

Disclosures: Alain Bonafé—*UNRELATED*: *Consultancy*: Covidien (consultant for ev3), Stryker; *Grants/Grants Pending*: Covidien.* Vincent Costalat—*Consultancy*: Balt, Codman Neuro-DePuy Synthes, Stryker, MicroVention; *Payment for Lectures (including service on Speakers Bureaus)*: Stryker, Balt; *Payment for Development of Educational Presentations*: Covidien, Stryker. *Money paid to the institution.

REFERENCES

1. Fink JN, Kumar S, Horkan C, et al. **The stroke patient who woke up: clinical and radiological features, including diffusion and perfusion MRI.** *Stroke* 2002;33:988–93 CrossRef Medline
2. Hacke W, Kaste M, Bluhmki E, et al; ECASS Investigators. **Thrombolysis with alteplase 3 to 4.5 hours after acute ischemic stroke.** *N Engl J Med* 2008;359:1317–29 CrossRef Medline
3. Thomalla G, Cheng B, Ebinger M, et al; STIR and VISTA Imaging Investigators. **DWI-FLAIR mismatch for the identification of patients with acute ischaemic stroke within 4.5 h of symptom onset (PRE-FLAIR): a multicentre observational study.** *Lancet Neurol* 2011;10:978–86 CrossRef Medline
4. Barreto AD, Martin-Schild S, Hallevi H, et al. **Thrombolytic therapy for patients who wake-up with stroke.** *Stroke* 2009;40:827–32 CrossRef Medline
5. Cortijo E, García-Bermejo P, Calleja AI, et al. **Intravenous thrombolysis in ischemic stroke with unknown onset using CT perfusion.** *Acta Neurol Scand* 2014;129:178–83 CrossRef Medline
6. Aoki J, Kimura K, Iguchi Y, et al. **Intravenous thrombolysis based on diffusion-weighted imaging and fluid-attenuated inversion recovery mismatch in acute stroke patients with unknown onset time.** *Cerebrovasc Dis* 2011;31:431–41 CrossRef Medline
7. Breuer L, Schellinger PD, Huttner HB, et al. **Feasibility and safety of magnetic resonance imaging-based thrombolysis in patients with stroke on awakening: initial single-centre experience.** *Int J Stroke* 2010;5:68–73 CrossRef Medline
8. Cho AH, Sohn SI, Han MK, et al. **Safety and efficacy of MRI-based thrombolysis in unclear-onset stroke: a preliminary report.** *Cerebrovasc Dis* 2008;25:572–79 CrossRef Medline
9. Kim JT, Park MS, Nam TS, et al. **Thrombolysis as a factor associated with favorable outcomes in patients with unclear-onset stroke.** *Eur J Neurol* 2011;18:988–94 CrossRef Medline
10. Kuruvilla A, Norris GM, Xavier AR. **Acute endovascular recanalization therapy in wake-up stroke.** *J Neurol Sci* 2011;300:148–50 CrossRef Medline
11. Natarajan SK, Snyder KV, Siddiqui AH, et al. **Safety and effective-**

ness of endovascular therapy after 8 hours of acute ischemic stroke onset and wake-up strokes. *Stroke* 2009;40:3269–74 CrossRef Medline
12. Stampfl S, Ringleb PA, Haehnel S, et al. **Recanalization with stent-retriever devices in patients with wake-up stroke.** *AJNR Am J Neuroradiol* 2013;34:1040–43 CrossRef Medline
13. Berkhemer OA, Fransen PSS, Beumer D, et al. **A randomized trial of intraarterial treatment for acute ischemic stroke.** *N Engl J Med* 2015; 372:11–20 CrossRef Medline
14. Campbell BCV, Mitchell PJ, Kleinig TJ, at al; EXTEND-IA Investigators. **Endovascular therapy for ischemic stroke with perfusion-imaging selection.** *N Engl J Med* 2015;372:1009–18 CrossRef Medline
15. Goyal M, Demchuk AM, Menon BK, et al; ESCAPE Trial Investigators. **Randomized assessment of rapid endovascular treatment of ischemic stroke.** *N Engl J Med* 2015;372:1019–30 CrossRef Medline
16. Jovin TG, Chamorro A, Cobo E, et al; REVASCAT Trial Investigators. **Thrombectomy within 8 hours after symptom onset in ischemic stroke.** *N Engl J Med* 2015;372:2296–306 CrossRef Medline
17. Saver JL, Goyal M, Bonafe A, et al; SWIFT PRIME Investigators. **Stent-retriever thrombectomy after intravenous t-PA vs. t-PA alone in stroke.** *N Engl J Med* 2015;372:2285–95 CrossRef Medline
18. Adams HP Jr, Leira EC, Torner JC, et al; AbESTT-II Investigators. **Treating patients with 'wake-up' stroke: the experience of the AbESTT-II trial.** *Stroke* 2008;39:3277–82 CrossRef Medline
19. Kang DW, Sohn SI, Hong KS, et al. **Reperfusion therapy in unclear-onset stroke based on MRI evaluation (RESTORE): a prospective multicenter study.** *Stroke* 2012;43:3278–83 CrossRef Medline
20. Terasawa Y, Kimura K, Iguchi Y, et al. **Could clinical diffusion-mismatch determined using DWI ASPECTS predict neurological improvement after thrombolysis before 3 h after acute stroke?** *J Neurol Neurosurg Psychiatry* 2010;81:864–68 CrossRef Medline
21. Lansberg MG, Straka M, Kemp S, et al; DEFUSE 2 study investigators. **MRI profile and response to endovascular reperfusion after stroke (DEFUSE 2): a prospective cohort study.** *Lancet Neurol* 2012;11: 860–67 CrossRef Medline
22. Kang DW, Kwon JY, Kwon SU, et al. **Wake-up or unclear-onset strokes: are they waking up to the world of thrombolysis therapy?** *Int J Stroke* 2012;7:311–20 CrossRef Medline

Quantitative MRI for Analysis of Active Multiple Sclerosis Lesions without Gadolinium-Based Contrast Agent

I. Blystad, I. Håkansson, A. Tisell, J. Ernerudh, Ö. Smedby, P. Lundberg, and E.-M. Larsson

ABSTRACT

BACKGROUND AND PURPOSE: Contrast-enhancing MS lesions are important markers of active inflammation in the diagnostic work-up of MS and in disease monitoring with MR imaging. Because intravenous contrast agents involve an expense and a potential risk of adverse events, it would be desirable to identify active lesions without using a contrast agent. The purpose of this study was to evaluate whether pre-contrast injection tissue-relaxation rates and proton density of MS lesions, by using a new quantitative MR imaging sequence, can identify active lesions.

MATERIALS AND METHODS: Forty-four patients with a clinical suspicion of MS were studied. MR imaging with a standard clinical MS protocol and a quantitative MR imaging sequence was performed at inclusion (baseline) and after 1 year. ROIs were placed in MS lesions, classified as nonenhancing or enhancing. Longitudinal and transverse relaxation rates, as well as proton density were obtained from the quantitative MR imaging sequence. Statistical analyses of ROI values were performed by using a mixed linear model, logistic regression, and receiver operating characteristic analysis.

RESULTS: Enhancing lesions had a significantly ($P < .001$) higher mean longitudinal relaxation rate (1.22 ± 0.36 versus 0.89 ± 0.24), a higher mean transverse relaxation rate (9.8 ± 2.6 versus 7.4 ± 1.9), and a lower mean proton density (77 ± 11.2 versus 90 ± 8.4) than nonenhancing lesions. An area under the receiver operating characteristic curve value of 0.832 was obtained.

CONCLUSIONS: Contrast-enhancing MS lesions often have proton density and relaxation times that differ from those in nonenhancing lesions, with lower proton density and shorter relaxation times in enhancing lesions compared with nonenhancing lesions.

ABBREVIATIONS: AUC = area under the curve; Gd = gadolinium; NAWM = normal-appearing white matter; PD = proton density; qMRI = quantitative MRI; ROC = receiver operating characteristic; R_1 = longitudinal relaxation rate; R_2 = transverse relaxation rate

MR imaging of the CNS is of great importance in the diagnostic evaluation of multiple sclerosis and in the follow-up and monitoring of disease activity and treatment response.[1] With the use of MR imaging, dissemination of lesions in time and space is evaluated according to the revised McDonald criteria.[2] New lesions at follow-up scans represent disease activity and may indicate a need for a therapy switch.[3] Even though patients with MS are monitored with MR imaging, lesion load does not have a strong predictive value for disability.[4] Injection of a gadolinium (Gd)-based contrast agent is included in routine MS MR imaging protocols and is used to detect active MS lesions on the basis of a local disruption of the blood-brain barrier due to acute inflammation. Even though uncommon, Gd administration may be associated with nephrogenic systemic fibrosis[5] in patients with reduced renal function, and there is a potential risk for immediate adverse events.[6] Furthermore, 2 recent studies reported signal changes in the deep nuclei of the brain with a relationship to an increasing cumulative dose of Gd-based contrast material,[7,8] which has been shown to indicate deposition of Gd in the body.[9] Apart from the potential adverse events, contrast agents also constitute an additional expense (cost of contrast agent and prolongation of scanning time). Intravenous injections of contrast agents may also cause patient discomfort during MR imaging examinations.

Overall, it would be desirable to develop a method to identify

Received April 23, 2015; accepted after revision June 15.

From the Departments of Radiology and Medical and Health Sciences (I.B., Ö.S.), Centre for Medical Image Science and Visualization (I.B., A.T., Ö.S., P.L., E.-M.L.), Departments of Neurology and Clinical and Experimental Medicine (I.H.), Departments of Radiation Physics and Medical and Health Sciences (A.T., P.L., E.-M.L.), and Departments of Clinical Immunology and Transfusion Medicine and Clinical and Experimental Medicine (J.E.), Linköping University, Linköping Sweden; and Department of Surgical Sciences/Radiology (E.-M.L.), Uppsala University, Uppsala, Sweden.

This work was supported by the National Science and Engineering Research Council, University of Linköping, and University Hospital Research Funds.

Please address correspondence to Ida Blystad, MD, Department of Radiology, University Hospital Linköping, 581 85 Linköping, Sweden; e-mail: ida.blystad@regionostergotland.se

Indicates open access to non-subscribers at www.ajnr.org

http://dx.doi.org/10.3174/ajnr.A4501

Table 1: Patient demographics

Demographics	
No. of subjects	44
Median age at inclusion (yr)	31 (range, 21–62)
Sex (M/F)	8:36
Diagnosis at inclusion (possible MS/MS)	23/21
Diagnosis at 1-year follow-up (possible MS/MS)	16/28
Relapse[a] at inclusion (yes/no)	22/22
Relapse at 1-year follow-up (yes/no)	4/40
Median EDSS at inclusion	2 (range, 0–5)
Median EDSS at 1-year follow-up	1.25 (range, 0–4)

Note:—EDSS indicates Expanded Disability Status Scale.

[a] A "relapse" was defined as new symptoms or worsening of previous symptoms, lasting >24 hours and in the absence of increased body temperature and infection.

active MS lesions without the administration of contrast agents. Previous studies have reported changes in acute MS lesions regarding MR imaging frequency shift,[10] magnetization transfer ratio,[11] and relaxation values,[12] suggesting the possibility of using quantitative methods to distinguish and characterize the acute lesions. However, so far no method has met the requirements necessary to be considered fully clinically applicable. A new sequence for quantitative MR imaging, quantitative MRI (qMRI), with a clinically acceptable scanning time of approximately 5 minutes has been developed.[13,14] The qMRI sequence makes it possible to measure the longitudinal relaxation rate (R_1), the transverse relaxation rate (R_2), and proton density (PD) from the same scan and also takes the normalized radiofrequency B1 field into account.

This study was performed to compare the relaxation rates and PD of active MS lesions before contrast agent injection with quantitative values from nonenhancing lesions to determine whether active MS lesions can be identified by qMRI without the administration of a Gd-based contrast agent.

MATERIALS AND METHODS

Subjects

Forty-six patients with a clinical suspicion of MS were consecutively enrolled in a prospective longitudinal cohort study of early MS at the Department of Neurology at the University Hospital in Linköping, Sweden. Two patients were excluded, 1 due to withdrawal of consent and 1 due to the finding of a trigeminal schwannoma, which explained the patient's clinical findings. The patients were classified as having possible MS or MS according to the revised McDonald criteria.[2] Table 1 shows details of patient demographics. MR imaging according to a standard clinical MS protocol with the addition of qMRI before and after administration of a Gd-based contrast agent was performed at inclusion (baseline) and after 1 year. In addition, 4 MR imaging examinations were performed in relation to clinical relapses. Ninety-two MR imaging examinations were performed. The local institutional review board approved the study, and informed written consent was obtained from all patients.

MR Imaging Acquisition

Images were acquired on a 1.5T MR imaging scanner (Achieva; Philips Healthcare, Best, the Netherlands) by using an 8-channel phased array head coil. The sequence parameters for conventional images were as follows:

- T2-weighted fluid-attenuated inversion recovery: axial; FOV, 230 × 183 mm; 43 sections; voxel size, 0.9 × 1.14 × 3 mm; TE, 120 ms; TR, 6000 ms; TI, 2000 ms; scan time, 6 minutes
- T1-weighted spin-echo before and after Gd contrast agent injection: axial; FOV, 230 × 183 mm; 43 sections; voxel size, 0.9 × 1.13 × 3 mm; TE, 15 ms; TR, 596 ms; scan time, 5:08 minutes
- T2-weighted spin-echo; axial; FOV, 230 × 184 mm; 43 sections; voxel size, 0.6 × 0.78 mm; TE, 100 ms; TR, 4452 ms; scan time, 3:42 minutes.

The quantitative sequence, QMAP,[13,14] is a multisection, multiecho, and multisaturation delay qMRI technique, with the following parameters in this study:

- qMRI: axial; FOV, 230 × 182; 43 sections; voxel size, 1.5 × 1.5 mm; TE, 14, 28, 42, 56, 70 ms; TR, 4244 ms; TI, 0.0974, 0.5846, 1.8511, 4.0919 seconds; saturation flip angle, 120°; scan time, 6:09 minutes.

All images had a section thickness of 3 mm without an intersection gap. Postcontrast qMRI images were acquired approximately 15 minutes after intravenous injection of 0.2 mL/kg body weight of a 0.5-mmol/mL Gd-based contrast agent (gadopentetate dimeglumine, Magnevist; Bayer HealthCare Pharmaceuticals, Wayne, New Jersey).

Postprocessing and ROI Placement

The qMRI sequence yields quantitative maps of R_1, R_2, and PD (Fig 1), which are used for measurements and to create synthetic images matching the conventional ones (Fig 2). The postprocessing time of the raw image dataset was approximately 1 minute on an ordinary PC by using SyMRI Diagnostic software (SyntheticMR, Linköping, Sweden) to create the synthetic images. Relaxation time values (T-values) were obtained from R_1 and R_2 by calculating $T = 1/R$. Using the software MevisLab, Version 2.4 (MeVis Medical Solutions, Bremen, Germany), we anonymized the synthetic images with corresponding conventional images and presented them to a neuroradiologist in random order. For each patient, synthetic T2-weighted, T2-FLAIR, T1-weighted, and T1-weighted Gd images were displayed side by side. MS lesions were identified by conventional neuroradiologic criteria, described in the McDonald criteria for MS. The MS lesions were then classified by visual assessment as enhancing or nonenhancing. The neuroradiologist had access to the conventional images for confirmation of the findings (Fig 3*A*).

ROIs were placed in the synthetic images within MS lesions of >3 mm in diameter, slightly inside the visual outer rim of the lesion in order to avoid partial volume effects from surrounding tissue. Thus ROI size varied depending on the size of the lesion. ROIs in nonenhancing lesions were drawn in synthetic T2-weighted images. ROIs in enhancing lesions were drawn on the synthetic T1-weighted Gd images (Fig 3*B*). A transformation matrix between the qMRI volume after contrast agent injection and the qMRI volume before contrast agent injection was calculated. This calculation was done by a registration of the synthetic T1-weighted Gd imaging to the synthetic T1WI by using rigid body registration with the image registration toolkit in MeVisLab. The transformation matrix was then used to register the T1-weighted Gd imaging ROIs of active lesions to the precontrast qMRI volume (Fig 3*A*).

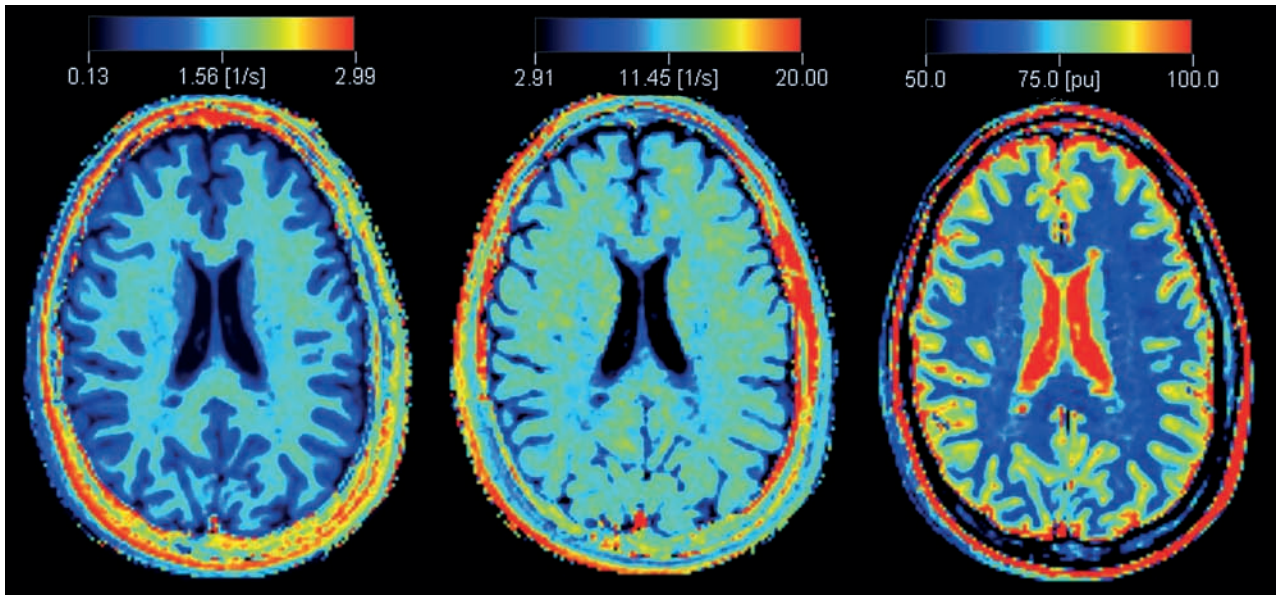

FIG 1. An example of quantitative R_1 (*left*), R_2 (*middle*), and proton density (*right*) maps derived from the qMRI scan in a patient with MS.

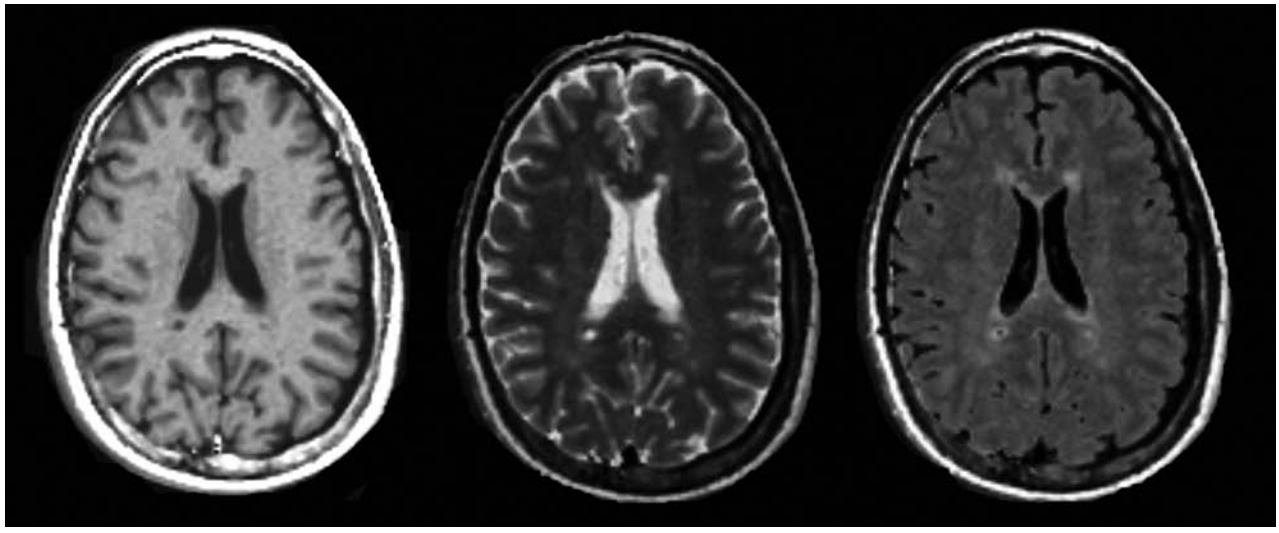

FIG 2. Synthetic T1WI (*left*), T2WI (*middle*), and T2-weighted FLAIR (*right*) imaging, postsynthesized from the quantitative MR imaging scan in a patient with MS.

In the same patients, ROIs were also placed in synthetic T2-weighted images in the normal-appearing white matter (NAWM) in an area in the contralateral hemisphere that corresponded as far as possible to the location of the lesion. However, NAWM ROIs tended to be located more subcortical in the hemisphere due to diffuse signal changes in the periventricular white matter, "dirty appearing white matter" (Fig 4).

Statistics

After forming mean values of R_1, R_2, and PD in each ROI, these means were compared by using a mixed linear model. The fixed effects were the type of ROI (NAWM, enhancing lesion, or nonenhancing lesion) and the time (in years) from the first examination, whereas patient identity was a random effect. For comparisons between types of ROIs, we used the Tukey *t* test.

In addition, receiver operating characteristic (ROC) analysis was performed after aggregating data to the ROI level and excluding ROIs representing NAWM. Lesions were classified as nonenhancing or Gd-enhancing by using each of the measured entities (R_1, R_2, and PD) and a linear combination of the 3, obtained with a logistic regression model; the corresponding area under the ROC curve (AUC) was reported.

All statistical calculations were performed in JMP 9.0 (SAS, Cary, North Carolina).

RESULTS

Of the 92 examinations, 14 contained both contrast-enhancing and nonenhancing MS lesions. Forty-four examinations had nonenhancing MS lesions only. These 58 examinations were obtained from 29 individuals. Thirty examinations had no lesions or MS lesions that were <3 mm. Four examinations had white matter

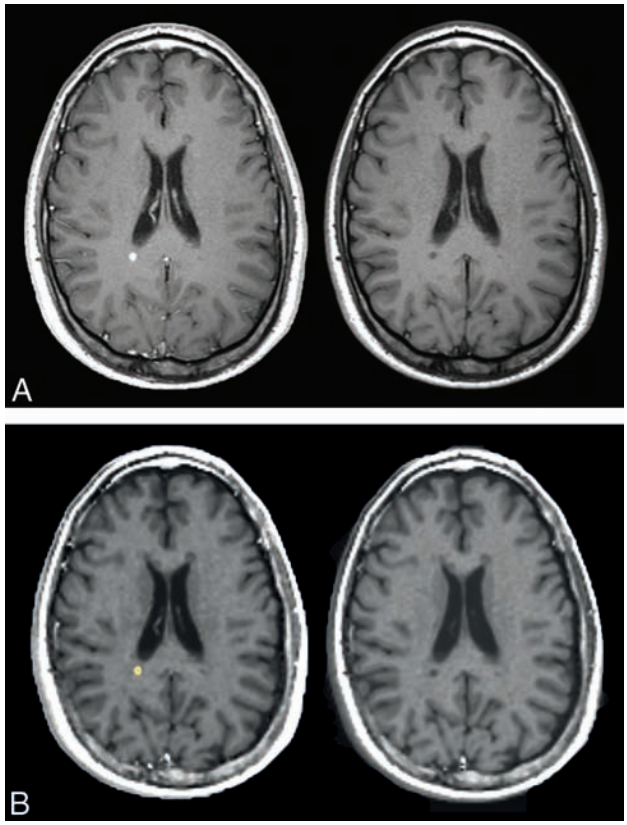

FIG 3. *A*, Conventional T1WI images corresponding to the synthetic images in *B*. Postgadolinium imaging is on the *left* and native on the *right*. *B*, An active lesion with ROI placement in the synthetic T1WI after gadolinium-based contrast agent injection (*left image*). The ROI was then registered onto the synthetic precontrast injection T1WI (*right image*).

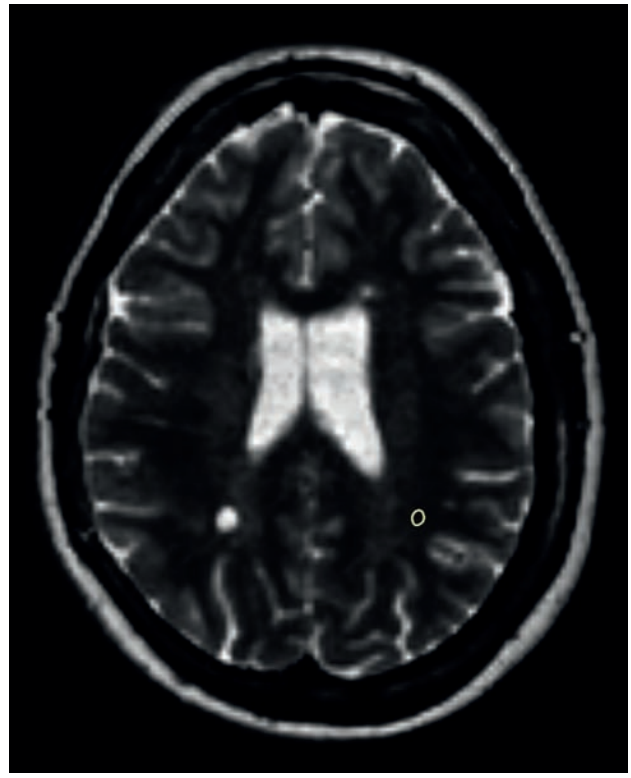

FIG 4. An example of a synthetic T2WI with an ROI placed in the NAWM in the left hemisphere contralateral to a nonenhancing lesion in the right hemisphere.

Table 2: Quantitative measurements of normal-appearing white matter and enhancing and nonenhancing MS lesions before gadolinium-based contrast agent injection[a]

	R_1 (1/s)	R_2 (1/s)	PD (%)
NAWM ($n = 102$)	1.71 ± 0.09	13.1 ± 0.67	62.4 ± 1.9
Enhancing lesions ($n = 43$)	1.22 ± 0.36	9.8 ± 2.6	77.0 ± 11.2
Nonenhancing lesions ($n = 622$)	0.89 ± 0.24	7.4 ± 1.9	89.8 ± 8.4
Difference between enhancing and nonenhancing lesions	+0.33[b]	+2.43[b]	−12.8[b]

[a] Data are means. Differences are estimated as least squares means and are tested with the Tukey *t* test.
[b] $P < .001$.

lesions assessed as not having a typical MS lesion appearance (unspecific white matter lesions); thus, these examinations were not a part of the quantitative analysis. Forty-three ROIs were drawn in enhancing MS lesions, and 622 ROIs were drawn in nonenhancing MS lesions. In all, 102 ROIs were drawn in NAWM, approximately 2 ROIs per patient with certain MS lesions.

Enhancing MS lesions had significantly higher precontrast mean R_1, higher mean R_2, and lower mean PD than nonenhancing lesions (Table 2). Precontrast relaxation times for the enhancing lesions were thus shorter than those for the nonenhancing lesions. For enhancing lesions, the mean R_1 value was 1.22 s^{-1} (T1 = 820 ms) and the mean R_2 value was 9.8 s^{-1} (T2 = 102 ms). For nonenhancing lesions, a mean R_1 value of 0.89 s^{-1} (T1 = 1126 ms) and a mean R_2 of 7.4 s^{-1} (T2 = 135 ms) were found. NAWM had a mean R_1 of 1.71 s^{-1} (T1 = 584 ms), and mean R_2 was 13.1 s^{-1} (T2 = 76 ms).

Distributions of mean R_1, mean R_2, and mean PD for enhancing and nonenhancing lesions are shown in Fig 5. As can be seen in Fig 5*A*, enhancement was rare in lesions with a mean R_1 value below 0.8 s^{-1} (sensitivity, 0.884). On the other hand, above this threshold, enhancing lesions were still less frequent than nonenhancing ones, and the specificity was only 0.360. Very few enhancing lesions had a mean R_2 value below 6 s^{-1} (sensitivity, 0.954), whereas higher mean R_2 values were not specific for enhancing lesions (specificity, 0.249) (Fig 5*B*). Mean PD values above 95% were very seldom found in enhancing lesions (sensitivity, 0.977), but even below this threshold, the enhancing lesions made up a minority of the findings (specificity, 0.317) (Fig 5*C*). Table 3 shows the sensitivity and specificity for a few different cutoff values in the same parameters for predicting enhancing MS lesions.

When sensitivity and specificity for all possible thresholds were combined in a receiver operating characteristic analysis, the area under the ROC curve was 0.764 for mean R_1, 0.760 for mean R_2, and 0.811 for mean PD. For the optimal linear combination of the 3 measurements obtained by logistic regression [−3.93 mean (R_1) + 0.210 mean (R_2) − 0.194 mean (PD)], the AUC was only slightly higher (0.832).

DISCUSSION

There have been attempts to predict the breakdown of the BBB in MS lesions without contrast agents by using conventional images,[15,16] but the accuracy has not been satisfactory so far. Previ-

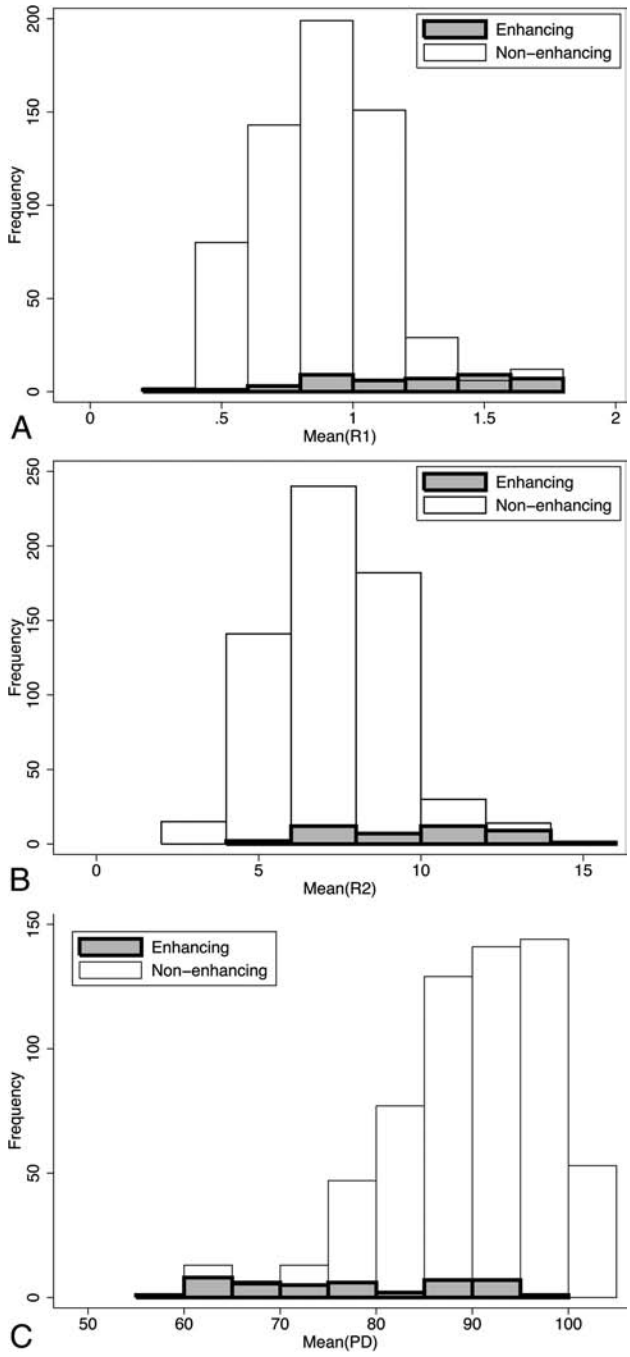

FIG 5. *A*, Histograms of mean R_1 for enhancing and nonenhancing lesions. *B*, Histograms of mean R_2 for enhancing and nonenhancing lesions. *C*, Histograms of mean PD for enhancing and nonenhancing lesions.

ous studies have used features of conventional images (eg, T2 peripheral rim hypointensities[16]) and mathematic modeling of voxel-based T1 and T2 intensities[15] in an attempt to identify active lesions, but they did not attain the desired sensitivity and specificity to fully identify active lesions without a contrast agent. Quantification of diffusion characteristics of acute lesions by using ADC values was previously thought to be a discriminator of acute-versus-chronic MS lesions, but a recent study showed variable diffusion values in acute MS lesions.[17] Most previous quantitative relaxation methods yielded measurements of either T1 or T2 relaxation. Some methods do quantify T1 and T2, but they

Table 3: Sensitivity and specificity for different cutoffs for relaxation values to predict enhancing MS lesions

Relaxation Value	Sensitivity (%)	Specificity (%)	Youden Index[a]
R_1 measurement			
1.28	47	95	42
1.17	58	90	48
1.10	60	82	42
R_2 measurement			
10	51	93	44
9.34	63	87	50
8.70	65	78	43
PD measurement			
77.69	54	92	46
79.96	61	87	48
82.53	63	82	45

[a] Youden index = sensitivity + specificity − 100.

have not been clinically applicable, due to either long scan times, lack of robustness, or complicated and cumbersome postprocessing procedures,[18] and relaxation values are thus not part of the clinical routine assessment of MR imaging examinations today.

Previous reports of relaxation time measurements in MS lesions have shown variable results. In the present study, with the use of qMRI, we found significant differences between the quantitative values of enhancing lesions and nonenhancing lesions, which is in line with other studies that have found a difference in quantitative characteristics in acute MS lesions compared with nonenhancing lesions.[10-12.] We found that enhancing lesions had shorter T2 than nonenhancing lesions but longer T2 than NAWM. This finding is consistent with those in other studies,[11,19] whereas some early studies on relaxation times in MS lesions showed a longer T2 in acute than in chronic lesions.[20] However, looking at the original studies, Larsson et al[21] did not find a difference in T1 and T2 measurements between acute and chronic plaques, but a tendency toward a slight increase in T1 and T2 in the acute plaques and a very high T2 value in the center of the plaque at a later stage. Ormerod et al[22] reported a decrease in T1 and T2 relaxation times in serial studies of acute lesions; however the classification of acute or chronic MS lesions of the brain stem was based on the duration of symptoms, not on contrast enhancement in lesions.

Our finding of a shorter T1 in enhancing lesions than in nonenhancing lesions is not in line with the findings of Jurcoane et al.[12] However, they used a method for voxel-based automatic calculation of T1 shortening after contrast agent administration, defining all FLAIR hyperintense areas, including dirty-appearing white matter, as lesions. Lesion voxels were then defined as contrast-enhancing if T1 shortening was 2 SDs above the T1 shortening in NAWM. Thus, dirty-appearing white matter would constitute a great part of the nonenhancing lesions, explaining the higher T1 values in enhancing lesions because the relaxation time values of dirty-appearing white matter are lower than those in lesions but higher than those in NAWM.[23] In our study, the comparison was made between enhancing and nonenhancing lesions, not including the dirty-appearing white matter.

The finding of shorter T1 and T2 in enhancing lesions than in chronic lesions could be understood on the basis of the pathology involved,[24] with the acute lesions being hypercellular due to an accumulation of inflammatory cells. The subsequent edema, intra- and intercellular in origin, results in a slight increase in the

relaxation values compared with normal tissue. In chronic lesions, there are hypocellularity, demyelination, and naked axons, and the free water fraction increases, yielding a higher relaxation time value. This is also reflected in the higher PD values in nonenhancing lesions compared with the enhancing lesions.

Despite the significant differences demonstrated, the overlap in T1-, T2-, and PD values between enhancing and nonenhancing lesions results in an imperfect prediction of enhancement from qMRI values. Even after forming an optimal linear combination of the 3 measurements, the AUC was only slightly higher than that for PD, which yielded the best prediction out of the 3 measurements.

In this study, the relaxation measurements in the lesions were made irrespective of their time point in the disease, which means that the age of the lesion was not a factor in the analysis and the dynamics of the evolution of the lesions were not considered. However, Cotton et al[25] showed that the acute phase with contrast enhancement has a median duration of 1–2 weeks for most lesions. Patients in this cohort were newly diagnosed with possible MS or MS, and most were in the early stages of the disease.

The ROC analysis gave a maximal AUC of 0.832, which is comparable with that in other studies,[15] but the result does not support the use of relaxation time measurements alone for clinical evaluation of the status of the BBB in MS lesions, because the clinical setting requires a higher sensitivity and specificity. Nevertheless, qMRI is a potentially useful complement in the event of contraindications to contrast agents and in combination with the visual assessment of the images with regard to new lesions and in association with clinical findings of a relapse. The quantitative measurement of lesions is clearly a more objective tool than the visual assessment of a radiologist and could be of value in the longitudinal monitoring of patients with MS.

Because the qMRI sequence enables quantitative assessment of tissue relaxation values,[26] other uses for this sequence are performing segmentation and volumetric measurements.[27,28] The automated volumetric technique could also be an objective tool for the evaluation of brain atrophy development in patients with MS,[29] which today is usually performed by visual assessment by the neuroradiologist in the clinical setting. qMRI could therefore complement conventional MR images in the examination of patients with MS regarding brain volume measurements.

This study was performed on a 1.5T scanner, and a previous study[27] has shown that the results of tissue segmentation from the qMRI sequence may differ between 1.5T and 3T. This means that the relaxation values of this study cannot be extrapolated to a 3T MR imaging setting. However, the higher field strength at 3T gives a higher signal-to-noise ratio. This enables a higher resolution that potentially could decrease the partial volume effect, which would be beneficial for quantitative measurements. Even if care was taken to place ROIs within the MS lesions to avoid partial volume effects, this study would have been strengthened by an MR imaging protocol with isotropic voxels and even thinner sections for higher accuracy of ROI placement.

In this work, the number of contrast-enhancing lesions was limited, and future work will include follow-up MR imaging at 2 and 4 years, including scans from relapses, which will yield larger subject matter for analysis, looking at the quantitative properties of the brain after Gd-based contrast agent injection, in lesions and in the gray and white matter. In addition, a long-term prospective study could evaluate the predictive prognostic value of qMRI compared with traditional contrast-based assessment. One possibility would be that changes in the quantitative characteristics in acute MS lesions might better represent the pathologic process than visual assessment of contrast enhancement, which merely reflects the damaged BBB. Quantitative MR imaging with relaxation measurements may help elucidate more of the complex mechanisms behind multiple sclerosis.

CONCLUSIONS

Contrast-enhancing MS lesions have PD and relaxation times that differ from those in nonenhancing lesions, with lower PD and shorter relaxation times in enhancing lesions compared with nonenhancing lesions. PD, which had the highest AUC value, still had only a moderate ability to predict Gd enhancement. Even though qMRI can provide additional information about the changes occurring in MS, it does not seem to be able to replace Gd injection in the evaluation of MS lesions.

ACKNOWLEDGMENTS

The authors wish to thank Anders Grönqvist at Centre for Medical Image Science and Visualization for technical support.

REFERENCES

1. Rocca MA, Anzalone N, Falini A, et al. **Contribution of magnetic resonance imaging to the diagnosis and monitoring of multiple sclerosis.** *Radiol Med* 2013;118:251–64 CrossRef Medline
2. Polman CH, Reingold SC, Banwell B, et al. **Diagnostic criteria for multiple sclerosis: 2010 revisions to the McDonald criteria.** *Ann Neurol* 2011;69:292–302 CrossRef Medline
3. Coyle PK. **Switching therapies in multiple sclerosis.** *CNS Drugs* 2013;27:239–47 CrossRef Medline
4. Barkhof F. **The clinico-radiological paradox in multiple sclerosis revisited.** *Curr Opin Neurol* 2002;15:239–45 CrossRef Medline
5. Thomsen HS, Morcos SK, Almén T, et al; ESUR Contrast Medium Safety Committee. **Nephrogenic systemic fibrosis and gadolinium-based contrast media: updated ESUR Contrast Medium Safety Committee guidelines.** *Eur Radiol* 2013;23:307–18 CrossRef Medline
6. Prince MR, Zhang H, Zou Z, et al. **Incidence of immediate gadolinium contrast media reactions.** *AJR Am J Roentgenol* 2011;196: W138–43 CrossRef Medline
7. Kanda T, Ishii K, Kawaguchi H, et al. **High signal intensity in the dentate nucleus and globus pallidus on unenhanced T1-weighted MR images: relationship with increasing cumulative dose of a gadolinium-based contrast material.** *Radiology* 2014;270:834–41 CrossRef Medline
8. Errante Y, Cirimele V, Mallio CA, et al. **Progressive increase of T1 signal intensity of the dentate nucleus on unenhanced magnetic resonance images is associated with cumulative doses of intravenously administered gadodiamide in patients with normal renal function, suggesting dechelation.** *Invest Radiol* 2014;49:685–90 CrossRef Medline
9. McDonald RJ, McDonald JS, Kallmes DF, et al. **Intracranial gadolinium deposition after contrast-enhanced MRI.** *Radiology* 2015;275: 772–82 CrossRef Medline
10. Wiggermann V, Hernández Torres E, Vavasour IM, et al. **Magnetic resonance frequency shifts during acute MS lesion formation.** *Neurology* 2013;81:211–18 CrossRef Medline
11. Levesque IR, Giacomini PS, Narayanan S, et al. **Quantitative magnetization transfer and myelin water imaging of the evolution of acute**

multiple sclerosis lesions. *Magn Reson Med* 2010;63:633–40 CrossRef Medline
12. Jurcoane A, Wagner M, Schmidt C, et al. **Within-lesion differences in quantitative MRI parameters predict contrast enhancement in multiple sclerosis.** *J Magn Reson Imaging* 2013;38:1454–61 CrossRef Medline
13. Warntjes JB, Dahlqvist O, Lundberg P. **Novel method for rapid, simultaneous T1, T*2, and proton density quantification.** *Magn Reson Med* 2007;57:528–37 CrossRef Medline
14. Warntjes JB, Leinhard OD, West J, et al. **Rapid magnetic resonance quantification on the brain: optimization for clinical usage.** *Magn Reson Med* 2008;60:320–29 CrossRef Medline
15. Shinohara RT, Goldsmith J, Mateen FJ, et al. **Predicting breakdown of the blood-brain barrier in multiple sclerosis without contrast agents.** *AJNR Am J Neuroradiol* 2012;33:1586–90 CrossRef Medline
16. Treabă CA, Bălaşa R, Podeanu DM, et al. **Cerebral lesions of multiple sclerosis: is gadolinium always irreplaceable in assessing lesion activity?** *Diagn Interv Radiol* 2014;20:178–84 CrossRef Medline
17. Eisele P, Szabo K, Griebe M, et al. **Reduced diffusion in a subset of acute MS lesions: a serial multiparametric MRI study.** *AJNR Am J Neuroradiol* 2012;33:1369–73 CrossRef Medline
18. Deoni SC, Peters TM, Rutt BK. **High-resolution T1 and T2 mapping of the brain in a clinically acceptable time with DESPOT1 and DESPOT2.** *Magn Reson Med* 2005;53:237–41 CrossRef Medline
19. Papanikolaou N, Papadaki E, Karampekios S, et al. **T2 relaxation time analysis in patients with multiple sclerosis: correlation with magnetization transfer ratio.** *Eur Radiol* 2004;14:115–22 CrossRef Medline
20. MacKay AL, Vavasour IM, Rauscher A, et al. **MR relaxation in multiple sclerosis.** *Neuroimaging Clin N Am* 2009;19:1–26 CrossRef Medline
21. Larsson HB, Frederiksen J, Petersen J, et al. **Assessment of demyelination, edema, and gliosis by in vivo determination of T1 and T2 in the brain of patients with acute attack of multiple sclerosis.** *Magn Reson Med* 1989;11:337–48 CrossRef Medline
22. Ormerod IE, Bronstein A, Rudge P, et al. **Magnetic resonance imaging in clinically isolated lesions of the brain stem.** *J Neurol Neurosurg Psychiatry* 1986;49:737–43 CrossRef Medline
23. West J, Aalto A, Tisell A, et al. **Normal appearing and diffusely abnormal white matter in patients with multiple sclerosis assessed with quantitative MR.** *PLoS One* 2014;9:e95161 CrossRef Medline
24. Filippi M, Rocca MA, Barkhof F, et al; Attendees of the Correlation between Pathological MRI Findings in MS Workshop. **Association between pathological and MRI findings in multiple sclerosis.** *Lancet Neurol* 2012;11:349–60 CrossRef Medline
25. Cotton F, Weiner HL, Jolesz FA, et al. **MRI contrast uptake in new lesions in relapsing-remitting MS followed at weekly intervals.** *Neurology* 2003;60:640–46 CrossRef Medline
26. West J, Warntjes JB, Lundberg P. **Novel whole brain segmentation and volume estimation using quantitative MRI.** *Eur Radiol* 2012;22:998–1007 CrossRef Medline
27. West J, Blystad I, Engström M, et al. **Application of quantitative MRI for brain tissue segmentation at 1.5 T and 3.0 T field strengths.** *PLoS One* 2013;8:e74795 CrossRef Medline
28. Warntjes JB, Tisell A, Landtblom AM, et al. **Effects of gadolinium contrast agent administration on automatic brain tissue classification of patients with multiple sclerosis.** *AJNR Am J Neuroradiol* 2014;35:1330–36 CrossRef Medline
29. Vågberg M, Lindqvist T, Ambarki K, et al. **Automated determination of brain parenchymal fraction in multiple sclerosis.** *AJNR Am J Neuroradiol* 2013;34:498–504 CrossRef Medline

Presurgical Assessment of the Sensorimotor Cortex Using Resting-State fMRI

F.C. Schneider, M. Pailler, I. Faillenot, F. Vassal, J. Guyotat, F.-G. Barral, and C. Boutet

ABSTRACT

BACKGROUND AND PURPOSE: The functional characterization of the motor cortex is an important issue in the presurgical evaluation of brain lesions. fMRI noninvasively identifies motor areas while patients are asked to move different body parts. This task-based approach has some drawbacks in clinical settings: long scanning times and exclusion of patients with severe functional or neurologic disabilities and children. Resting-state fMRI can avoid these difficulties because patients do not perform any goal-directed tasks.

MATERIALS AND METHODS: Nineteen patients with diverse brain pathologies were prospectively evaluated by using task-based and resting-state fMRI to localize sensorimotor function. Independent component analyses were performed to generate spatial independent components reflecting functional brain networks or noise. Three radiologists identified the motor components and 3 portions of the motor cortex corresponding to the hand, foot, and face representations. Selected motor independent components were compared with task-based fMRI activation maps resulting from movements of the corresponding body parts.

RESULTS: The motor cortex was successfully and consistently identified by using resting-state fMRI by the 3 radiologists for all patients. When they subdivided the motor cortex into 3 segments, the sensitivities of resting-state and task-based fMRI were comparable. Moreover, we report a good spatial correspondence with the task-based fMRI activity estimates.

CONCLUSIONS: Resting-state fMRI can reliably image sensorimotor function in a clinical preoperative routine. It is a promising opportunity for presurgical localization of sensorimotor function and has the potential to benefit a large number of patients affected by a wide range of pathologies.

ABBREVIATIONS: IC = independent component; ICA = independent component analysis; rs-fMRI = resting-state fMRI; tb-fMRI = task-based fMRI

Mapping of cerebral function in neurosurgery patients aims to predict the efficacy of the neurosurgical treatment, estimate the operation risk, and avoid neurologic deficits. Several techniques have been used to identify brain activity in tissue surrounding the regions planned for resection, including neuronavitaged transcranial magnetic stimulation,[1] magnetoencephalography,[2] and fMRI,[3] each having advantages and drawbacks over the others.

Received December 18, 2014; accepted after revision May 29, 2015.

From the Departments of Radiology (F.C.S., M.P., F.-G.B., C.B.), Neurology (I.F.), and Neurosurgery (F.V.), University Hospital of Saint-Etienne, Saint-Etienne, France; Thrombosis Research Group EA 3065 (F.C.S., F.-G.B., C.B.) and Central Integration of Pain Institut National de la Santé et de la Recherche Médicale U1028 (I.F.), Jean Monnet University, Saint-Etienne, France; Image-Guided Clinical Neurosciences and Connectomics EA 7282 (F.V.), Auvergne University, Clermont-Ferrand, France; and Department of Neurosurgery (J.G.), Hospices Civils de Lyon, Claude Bernard University, Lyon, France.

Please address correspondence to Fabien Schneider, PhD, Service de Radiologie, Hôpital Nord, 42055 Saint-Etienne Cedex 2, France; e-mail: fabien.schneider@univ-st-etienne.fr

http://dx.doi.org/10.3174/ajnr.A4472

The clinical criterion standard for localization of functional brain areas is intraoperative electrical stimulation in the awake patient.[4] Although electrical stimulation provides unique assistance during surgery, it is an invasive technique that requires expertise of the surgical team and a cooperative and motivated subject. It also adds considerable time to the surgical procedure for an investigation limited to a few cortical areas. Therefore, fMRI has been seen as very promising for clinical applications. However, its integration into preoperative surgical planning has been relatively slow because of several practical constraints: the dedicated experimental setup, long scanning time, and a high cognitive demand on the patient. Moreover, localizing the sensorimotor cortex with fMRI at the individual level can be challenging in some cases when the patient has paresis or paralysis. Furthermore, >1 acquisition is necessary whenever the lesion is bordering on several motor representations.

Techniques measuring functional connectivity can address several of the limitations faced by stimulus-driven or task-based fMRI (tb-fMRI). Resting-state fMRI (rs-fMRI) uses slow, sponta-

Table 1: Patient characteristics

Case	Age (yr)	Sex	Diagnosis	Localization	Lateralization	tb-fMRI
1	67	M	3 Metastases	SFG	2 R, 1 L	RH, RF, face
2	28	F	Low-grade glioma	SFG	L	RH, face
3	39	M	Low-grade glioma	RG	L	RH
4	53	M	AVM	IFG, insula	R	LH, face
5	28	M	AVM	FG	L	Face
6	43	F	Stroke	PP	R	RH, LH, RF, LF, face
7	45	M	High-grade glioma	SPL	L	RH, LH, RF
8	50	M	Stroke	IOG, cerebellum	R	RH, LH, LF, face
9	12	M	Low-grade glioma	SFG, PrG	L	RH, LH, RF, LF
10	66	M	Metastasis	PoG	R	RH, LH, LF
11	58	M	Stroke	Brain stem	L	RH, LH, RF, face
12	68	M	Stroke	Brain stem	R	RH, LH, LF, face
13	26	F	Low-grade glioma	SFG, CG	R	Face
14	77	M	Metastasis	PoG	R	RH, LH
15	70	F	Metastasis	PoG	L	RH
16	58	M	Low-grade glioma	PrG, PoG	R	LH, LF
17	28	M	Low-grade glioma	SFG	L	RH, LH
18	31	F	Low-grade glioma	SFG	R	RH, LH
19	23	M	Low-grade glioma	SFG, PrG	R	RH, LH

Note:—L indicates left; R, right; RH, right hand; LH, left hand; RF, right foot; LF, left foot; SFG, superior frontal gyrus; RG, rectus gyrus; IFG, inferior frontal gyrus; FG, fusiform gyrus; PP, periventricular parietal white matter; SPL, superior parietal lobule; IOG, inferior occipital gyrus; PrG, precentral gyrus; PoG, postcentral gyrus; CG, cingulate gyrus.

neous fluctuations in the blood oxygen level–dependent signal to characterize networks of distant brain regions.[5] The subject simply "rests" in the scanner without any specific task to perform. rs-fMRI has been successfully applied in groups of healthy volunteers,[6] provides a means of mapping several functional networks in a single acquisition, appears robust across individuals,[7] and is less-demanding than tb-fMRI because it requires less cooperation from the patient and can be used in individuals with neurologic deficits or cognitive dysfunction or in children. Additionally, spontaneous activity continues in the primary sensory and motor cortices even when subjects are asleep[8] or anesthetized.[9] This feature suggests that complete patient compliance may not be necessary. Resting-state networks have been extensively explored in recent years at the group level in populations of healthy subjects and patients. In the case of neurosurgery patients with brain damage,[10] precise functional network estimation at the individual level is essential for surgery planning and/or intraoperative navigation. The conclusions of previous pioneering studies were limited to the feasibility of rs-fMRI for presurgical mapping by using small patient samples.[11-15]

In this study, we investigated the sensitivity of extracting the sensorimotor network from rs-fMRI at the individual level in patients with brain damage scheduled for surgery. Because brain lesions can appear at any segment of the motor cortex, we divided our investigations into 3 portions of the somatotypy (foot, hand, and face). rs-fMRI was then compared with tb-fMRI acquired when corresponding body parts were moved.

MATERIALS AND METHODS

Subjects

Nineteen patients (14 men; mean age, 46 years) intended for neurosurgery were prospectively enrolled in this study (Table 1) and underwent both tb- and rs-fMRI. tb-fMRI results were used for surgical planning. Pathologies included low-grade glioma (n = 8), high-grade glioma (n = 1), metastasis (n = 4), AVM (n = 2), and chronic stroke lesions (n = 4) causing medically refractory neuropathic pain (stimulator positioning was guided by tb-fMRI for chronic electrical stimulation of the motor cortex). Patients gave written informed consent, and the study was approved by the local ethics committee.

Image Acquisition

Nine patients (cases 1–6, 8, 16, 17) were imaged by using a 1.5T MR imaging scanner (Achieva; Philips Healthcare, Best, the Netherlands) equipped with an 8-channel head coil. Single-shot gradient-echo EPI was used for functional acquisitions with the following parameters: TR/TE/flip angle, 2700 ms/50 ms/90°, 28 contiguous sections of 3.5 mm, FOV of 230 × 230 mm^2, and an acquisition matrix of 64 × 64; 105 dynamic scans per run were acquired for tb-fMRI acquisitions, and 130, for rs-fMRI. A 3D T1-weighted turbo field echo sequence was performed for anatomic localization: TR/TE/flip angle, 7.84 ms/3.81 ms/8°, 140 sections of 1 mm, acquisition matrix of 256 × 256, FOV of 256 × 256 mm^2, and a turbo field echo factor of 180.

The images of the 10 remaining patients were acquired by using a 3T scanner (Magnetom Verio; Siemens, Erlangen, Germany) and a 12-channel head coil. Single-shot gradient-echo EPI parameters were the following: TR/TE/flip angle, 2690 ms/30 ms/90°, 40 contiguous sections of 3.5 mm, FOV of 224 × 224 mm^2, and an acquisition matrix of 64 × 64. tb-fMRI comprised 110 dynamic scans per run and rs-fMRI, 155. A 3D T1-weighted magnetization-prepared rapid acquisition of gradient echo sequence was also performed with the following parameters: TR/TI/TE/flip angle, 1800 ms/900 ms/3.3 ms/9°, acquisition matrix of 256 × 192, FOV of 256 × 192 mm^2.

Behavioral Paradigm

For rs-fMRI, subjects were instructed to stay quiet and fixate on a white cross on a black screen. The tb-fMRI examination included 1–5 motor runs, each containing only 1 type of movement (which involved either the right/left hand, right/left foot, or face). Hand movements were self-paced hand tapping. Face movements consisted of stretching and pushing forward the lips. Foot movements included rotations of the ankle (dorsiflexion-extension). Each tb-

fMRI acquisition consisted of 30-second blocks of motor movement alternating with 30-second blocks of resting.

Data Preprocessing

The 3 initial brain volumes of each run were discarded to eliminate nonequilibrium effects of magnetization. Image preprocessing was performed with SPM8 (http://www.fil.ion.ucl.ac.uk/spm/software/spm8). Images were time- and motion-corrected and then smoothed by using a spatial Gaussian kernel of 8 mm of full width at half maximum.

Independent Component Analysis of rs-fMRI

To investigate resting-state networks for each patient, we performed retrospective analyses of single-subject independent component analysis (ICA) by using the Group ICA of fMRI Toolbox software (GIFT; http://mialab.mrn.org/software/gift/). The number of independent components (ICs) was estimated individually for each subject by using the minimum description length criteria.[16] Before the ICA procedure, a data-reduction step was performed by using principal component analysis. The ICs were then estimated by using the Infomax algorithm.[17] Stable estimation was achieved by rerunning the ICA analyses 20 times by using the ICASSO[18] toolbox implemented in GIFT. In case of ICs with an ICASSO stability index of <0.9, the ICA analysis was recomputed by using fewer ICs (the number of ICs estimated by minimum description length minus the number of ICs with an ICASSO stability index of ≤ 0.9). Eighteen-to-34 ICs were then estimated in our patient sample. The spatial maps of the components were converted into z score maps and thresholded at $z \geq 2$. The mean image of the rs-fMRI time-series (estimated during the motion-correction procedure) was used to coregister the z score maps on the anatomic MR imaging acquisition to allow a precise spatial localization of the resting-state networks by using SPM8.

Manual Selection of Individual Motor Components by Experts

For each patient, 3 independent experts (C.B., F.C.S., and M.P.), blinded to tb-fMRI results, visualized all thresholded ICs superimposed on T1 images and selected any number of motor-related components. Of note, F.C.S. participated in both the prospective interpretation of 13 patients explored with tb-fMRI and the retrospective readings of the rs-fMRI. The time interval between the 2 tasks was 2 months for 2 patients and >1 year for 17 patients. The IC selection criteria were based on the shape of spatial maps, temporal profiles, and anatomic landmarks (eg, central sulcus). The central sulcus was reported as difficult or impossible to detect in 6 cases, either because of the presence of extensive edema (cases 1, 10, and 16) or the tumor itself (cases 9, 14, and 15). Readers were also asked to locate IC clusters within the motor cortex and whether they could be attributed to the foot, the hand, or the face representation.

In the case of different motor IC selection among the experts, a consensus was reached after consultation to select which IC most likely reflects the motor cortex for both hemispheres.

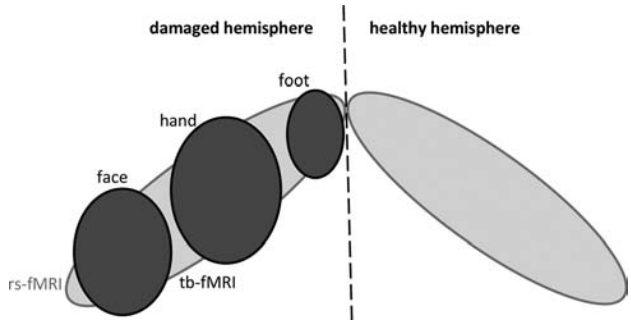

FIG 1. Illustration of expected findings by using rs-fMRI (light gray) and tb-fMRI (dark gray). rs-fMRI is presumed to show the whole motor cortex (possibly bilaterally), whereas a single motor cortex representation (face, hand, or foot) would be obtained by using tb-fMRI.

General Linear Modeling of tb-fMRI

The tb-fMRI data were high-pass-filtered (1/128 Hz) and analyzed through the general linear formulation of SPM8. The model also included the 6 movement parameters estimated from the motion-correction procedure to capture residual movement-related artifacts. Statistical parametric maps were thresholded at $P < .05$, corrected for multiple comparisons (controlling for the family-wise error) by using 2 different procedures: The first method tested each voxel time course (called the "voxel" correction), and the second combined the spatial extent of each cluster of estimated activity and each voxel intensity (termed hereafter "cluster,"[19]). The mean image of the tb-fMRI dataset was used to coregister the activation maps on the anatomic MR imaging acquisition to allow a precise localization of the activated areas and a direct comparison with rs-fMRI results (see below).

tb-fMRI and rs-fMRI Sensitivities

The sensitivity of rs-fMRI was estimated by dividing the number of times a motor cortex representation (hand, face, or foot) was detected by the total number of patients. The sensitivity of tb-fMRI was calculated as the ratio of detections for a given motor cortex representation (hand, face, or foot) by the number of patients for whom this investigation was performed (Table 1).

Overlap between rs-fMRI and tb-fMRI

To reduce the influence of voxels outside the motor cortex on the results, we segmented both rs- and tb-fMRI spatial maps around the cluster defined by experts as the motor cortex (spm_clusters function; http://www.fil.ion.ucl.ac.uk/spm/software/spm8/). The result of this procedure gave a single cluster for the motor IC and a single cluster for tb-fMRI (called rs-motor and tb-motor). Then, we calculated a concurrence ratio by dividing the number of voxels within the intersection of rs- and tb-motor by the number of voxels of tb-motor (Figs 1 and 2).

RESULTS

Nine patients had lesions in the left hemisphere. For consistency of the data presentation, we hereafter refer to healthy and damaged sides. For 1 patient, metastases were detected in both hemispheres (case 1). The left side was then defined as the altered one because the corresponding tumor was considered

the most likely to have caused the patient deficits (because of its location, size, and edema). We tested the motoricity of the hand for 17 patients, the foot for 9 patients, and the face for 9 patients (Table 1). Figure 2 illustrates typical rs- and tb-fMRI results.

tb-fMRI and rs-fMRI Sensitivities

The rs-motor component was identified for all patients and by all experts. A consensus was reached in all patients for the hand area, in 15 patients for the face area, and in 13 for the foot representation (Table 2). tb-fMRI investigations led to significant activity estimates, in most cases independent of the thresholding strategy (voxel or cluster).

Overlap between rs-fMRI and tb-fMRI

We did not observe any significant interactions among the hand, face, or foot representations and the overlap between rs- and tb-fMRI (Fig 3). Moreover, their similarity did not significantly differ between the 2 hemispheres. In contrast, we observed a better correspondence between rs- and tb-fMRI when using the voxel correction for multiple testing (31% versus 23%, $P = .003$). This advantage was more pronounced on the lesion side ($P = .009$) and for the hand representation ($P = .01$).

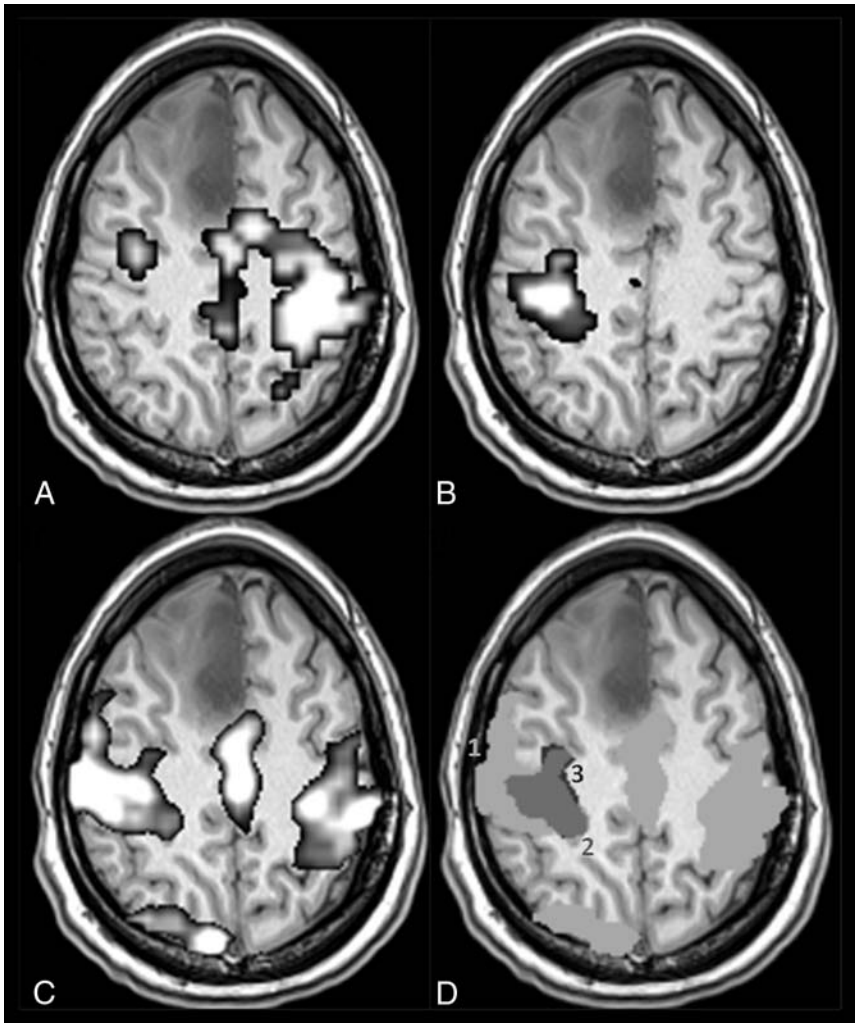

FIG 2. A patient with a right medial frontal low-grade glioma (case 18 in Table 1). Activity estimates from right (*A*) and left (*B*) hand movements by using tb-fMRI ($P < .05$, family-wise error–corrected at the voxel level) are shown and are compared with the motor IC of rs-fMRI (*C*, $z \geq 2$). The overlap between rs-and tb-fMRI results is illustrated in *D*, where spatial maps of *B* and *C* are superimposed after binarization and segmentation of the motor clusters (see "Materials and Methods"): 1 (light gray) and 3 (black), respectively, indicate rs- and tb-spatial maps, and their intersection is labeled 2 (dark gray). The concurrent ratio is 92% for this patient.

Comparison of the 2 MR Imaging Acquisition Systems

The overall rs-fMRI sensitivity of the 3T system was higher than that for the 1.5T system ($P = .0029$, Table 3). Moreover, the intersection between tb- and rs-fMRI results did not differ significantly between the 2 MR imaging systems, though there was a trend toward higher concurrent ratios at 3T when using both the voxel (35% versus 27%, $P = .33$) or the cluster correction (27% versus 20%, $P = .29$) for multiple testing of tb-fMRI statistical maps.

DISCUSSION

Presurgical localization of the eloquent cortex is clearly one of the keys to reducing postsurgery motor deficits and reaching an optimal patient outcome. Among the functional imaging techniques, rs-fMRI has been commonly used in neuroscience and has now attracted interest for clinical applications.[20,21] Compared with tb-fMRI, rs-fMRI has some practical advantages: shorter scanning times and a simple setup. It is less sensitive to subject-related deficiencies such as paresis, paralysis, or lack of attention, and it is easier to apply to children. Here, we demonstrated that rs-fMRI is capable of consistently mapping the motor cortex with a spatial precision that is necessary in clinical settings (ie, discrimination of foot, hand, and face representations). The probability of identifying different body representations by using rs-fMRI is

Table 2: Sensitivity of rs- and tb-fMRI

	Foot		Hand		Face	
	Healthy Side	Damaged Side	Healthy Side	Damaged Side	Healthy Side	Damaged Side
rs-fMRI	68% (13/19)	68% (13/19)	100% (19/19)	100% (19/19)	79% (15/19)	79% (15/19)
tb-fMRI cluster-correction	50% (1/2)	89% (8/9)	100% (11/11)	94% (16/17)	100% (9/9)	100% (9/9)
tb-fMRI voxel-correction	50% (1/2)	89% (8/9)	100% (11/11)	94% (16/17)	89% (8/9)	89% (8/9)

equivalent to that of tb-fMRI. Nevertheless, unequal results were obtained in different parts of the motor cortex: The largest body part representation (hand) was the easiest to detect and the most consistent among readers (Table 2). Our findings are in line with those of Liu et al,[13] who studied 6 patients with tumors or epileptic foci near the motor cortex before surgery. The visual evaluation of their results led to good agreement between rs-fMRI and tb-fMRI, which included hand and tongue movements. We also measured the overlap between rs- and tb-fMRI through concurrent ratios. The average value was approximately 30%, which is in agreement with the findings of Tie et al,[22] who assessed concurrent ratios in healthy individuals.

Of several methods that can be used to analyze tb-fMRI data,[23] we used SPM, and dissimilar results may be obtained with other software. Particularly, different strategies can be applied to deal with the multiple-testing problem when analyzing tb-fMRI data.[24,25] No consensus has been reached on which one to use in the context of individual patient analysis. We investigated 2 different approaches to correct for multiple comparisons in our work: a test based on the cluster size and another based on voxel intensity. The cluster size correction is known to have increased sensitivity when the signal is spatially extended[19,25]; this result is likely when attempting to detect the activity of the sensorimotor cortex. The sensitivity of both tests was similar and approximately 95% in our data (Table 2). However, when comparing tb- and rs-fMRI spatial maps, we observed different overlap depending on the multiple-comparison technique; concurrent ratios were larger with the correction at the voxel level.

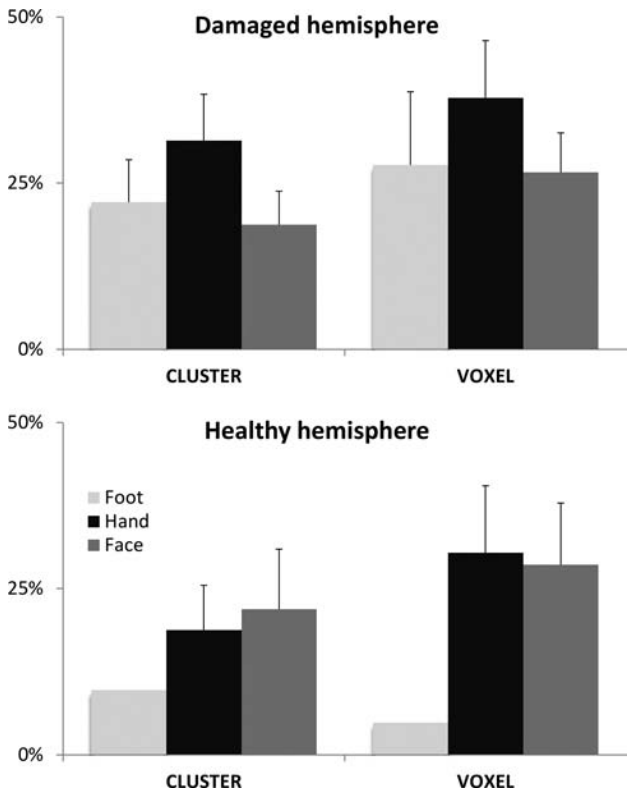

FIG 3. Overlap between tb-fMRI and rs-fMRI. Average (and standard error of the mean) concurrent ratios are displayed for the damaged hemisphere and the healthy hemisphere. Different body parts were moved during tb-fMRI, leading to 3 ratio calculations: foot (light gray), hand (black), and face (dark gray). Two different thresholding strategies were tested for tb-fMRI analysis: a test based on the cluster size (cluster) and another one based on the voxel intensity (voxel).

Table 3: Sensitivity of rs-fMRI for the 2 MR imaging systems

	Foot		Hand		Face	
	Healthy Side	Damaged Side	Healthy Side	Damaged Side	Healthy Side	Damaged Side
1.5T	55% (5/9)	55% (5/9)	100% (9/9)	100% (9/9)	67% (6/9)	67% (6/9)
3T	80% (8/10)	80% (8/10)	100% (10/10)	100% (10/10)	90% (9/10)	90% (9/10)

Of note, both the rs-ICs and the tb-activation maps did not exclusively show the motor cortex. tb-fMRI revealed a somatotopic segment of the motor cortex and can display nonspecific activations. rs-fMRI motor components showed the whole motor cortex and were typically bilateral (Fig 1). To limit the impact of this problem, we segmented the spatial maps resulting from rs- and tb-fMRI analyses. However, the outcome usually showed regions larger than the primary motor cortex (Fig 2). This effect frequently occurred when using the cluster correction because it is more likely to expose large clusters of activity and may explain the lower concurrent ratios obtained when using this test.

Most previous studies testing rs-fMRI clinical feasibility used cross-correlation techniques.[11,13-15] This approach requires the definition of a seed region based on anatomy or additional functional exploration, to reveal correlations between the average signal time course of voxels within the ROI and the time courses of the other brain voxels. The approach we used here (ICA) does not require any prior knowledge of the temporal or spatial patterns of brain responses. ICA is a popular mathematic approach that maximizes statistical independence among its components to identify distinct resting-state networks. A practical drawback that can be attributed to ICA is that the user must choose among dozens of functional components, which most probably reflect neurofunctional systems over noise. This selection is often made by visual inspection. Other strategies have been imagined to assist the IC selection. Kokkonen et al[12] used a template-matching method, for which each IC was spatially correlated to a motor tb-fMRI template. The authors reported successful results in 8 patients with brain tumors. Nevertheless, to avoid adding any prior spatial knowledge in our analyses, we chose another strategy to analyze our rs-fMRI data. Visual review of the calculated ICs for every patient was thus made by 3 radiologists blinded to each other and to the results of tb-fMRI. Additionally, a novel data-driven method has been recently tested at the individual level in patients with epilepsy and tumors.[26] It showed promising results and may resolve some of the limitations of cross-correlation analysis (structural seed definition) and ICA (postanalysis IC selection).

A tb-fMRI examination including movement of the hand, face, and foot gives satisfactory coverage of the motor cortex for many clinical purposes. The number of studied body parts has to be adapted to the lesion location. Nonetheless, when considering a large lesion, one must examine the entire motor cortex of the injured hemisphere and one may also be interested in mapping the normal motor representation in the contralateral hemisphere. This process leads to long scanning times and may not be adapted to every

patient, especially when the functional exploration is combined with morphologic and/or spectroscopic acquisitions.

Case 9 relates to a 12-year-old child with a glioma, for whom the whole MR imaging examination may have been too long and too demanding to be entirely and satisfactorily completed. Indeed, the tb-fMRI explorations of both feet did not give any significant results. Alternatively, both complete motor cortices were then identified by using rs-fMRI in <7 minutes. Because a long scanning time is the most frequent difficulty for the schedule of tb-fMRI examinations, rs-fMRI is a convincing surrogate and can be more easily integrated with other MR imaging investigations. For another case (15), the patient had difficulty performing the task because of a Dupuytren contracture. This led to nonsignificant and uninterpretable results by using tb-fMRI. This case illustrates the limits of tb-fMRI in a clinical environment where it is difficult to design a specific task for each patient. In contrast, rs-fMRI results were informative.

Additionally, we showed that rs-fMRI can be successfully performed by using 2 different MR imaging systems (1.5T and 3T). Nevertheless, we report a better ability to detect the motor cortex at 3T and a trend toward a better similarity between rs-and tb-fMRI spatial maps at 3T (Table 3). Indeed, the spatial specificity of tb-fMRI increases with the strength of the magnetic field.[27] Moreover, because the amplitude of spontaneous blood oxygen level–dependent fluctuations is also likely to increase with field strength, it is then not surprising to find a better intersection between rs- and tb-fMRI results at 3T.

Generalizability in real-life clinical settings is usually a critical step when developing new techniques. Here, we successfully tested rs-fMRI in a prospective study, involving a typical patient list of our department by using 2 different clinical MR imaging systems. Sensitivity was comparable with that of tb-fMRI with fewer practical acquisition issues. The IC selection process still needs to be standardized and automated in some way to allow rs-fMRI to be largely used for clinical planning before surgery. Moreover, preliminary studies characterizing the accuracy of rs-fMRI showed promising results.[15,26] These findings constitute the groundwork for the establishment of rs-fMRI in surgical planning. However, improved patient outcome has yet to be demonstrated, to firmly establish the clinical utility of rs-fMRI.

CONCLUSIONS

We showed that rs-fMRI can reliably image the sensorimotor function in preoperative routine. Different motor cortex representations were successfully and consistently identified by 3 radiologists. Moreover, we report good spatial correspondence with tb-fMRI activity estimates. rs-fMRI is a promising opportunity for presurgical localization of sensorimotor function and can resolve most of the tb-fMRI issues in clinical settings. Moreover, rs-fMRI can be easily integrated with other MR imaging investigations. Our study brings new advances in the clinical utility of rs-fMRI.

Disclosures: Fabrice-Guy Barral—*RELATED*: *Support for Travel to Meetings for the Study or Other Purposes*: ALN Compagny,* *Comments*: Cardiovascular and Interventional Radiological Society European Congress 2014. Claire Boutet—*UNRELATED*: *Payment for Development of Educational Presentations*: Boehringer Ingelheim, *Comments*: 300 euros for a teaching communication for 1 day on stroke imaging; *Travel/Accommodations/Meeting Expenses Unrelated to Activities Listed*: Guerbet, Ipsen Pharma, Biogen, St Jude Medical France, Toshiba, GE Medical System and Genzyme, *Comments*: payment directly of accommodation and transport for my participation in a national congress. *Money paid to the institution.

REFERENCES

1. Weiss C, Tursunova I, Neuschmelting V, et al. **Improved nTMS- and DTI-derived CST tractography through anatomical ROI seeding on anterior pontine level compared to internal capsule.** *Neuroimage Clin* 2015;7:424–37 CrossRef Medline
2. Stufflebeam SM. **Clinical magnetoencephalography for neurosurgery.** *Neurosurg Clin N Am* 2011:22:153–67, vii–viii
3. Mueller WM, Yetkin FZ, Hammeke TA, et al. **Functional magnetic resonance imaging mapping of the motor cortex in patients with cerebral tumors.** *Neurosurgery* 1996;93:515–20; discussion 520–21
4. Haglund MM, Berger MS, Shamseldin M, et al. **Cortical localization of temporal lobe language sites in patients with gliomas.** *Neurosurgery* 1994;34:567–76; discussion 576 CrossRef Medline
5. Fox MD, Raichle ME. **Spontaneous fluctuations in brain activity observed with functional magnetic resonance imaging.** *Nat Rev Neurosci* 2007;8:700–11 CrossRef Medline
6. Auer DP. **Spontaneous low-frequency blood oxygenation level-dependent fluctuations and functional connectivity analysis of the "resting" brain.** *Magn Reson Imaging* 2008;26:1055–64 CrossRef Medline
7. Damoiseaux JS, Rombouts SA, Barkhof F, et al. **Consistent resting-state networks across healthy subjects.** *Proc Natl Acad Sci U S A* 2006;103:13848–53 CrossRef Medline
8. Fukunaga M, Horovitz SG, van Gelderen P, et al. **Large-amplitude, spatially correlated fluctuations in BOLD fMRI signals during extended rest and early sleep stages.** *Magn Reson Imaging* 2006;24:979–92 CrossRef Medline
9. Kiviniemi VJ, Haanpää H, Kantola JH, et al. **Midazolam sedation increases fluctuation and synchrony of the resting brain BOLD signal.** *Magn Reson Imaging* 2005;23:531–37 CrossRef Medline
10. Holodny AI, Schulder M, Liu WC, et al. **The effect of brain tumors on BOLD functional MR imaging activation in the adjacent motor cortex: implications for image-guided neurosurgery.** *AJNR Am J Neuroradiol* 2000;21:1415–22 Medline
11. Böttger J, Margulies DS, Horn P, et al. **A software tool for interactive exploration of intrinsic functional connectivity opens new perspectives for brain surgery.** *Acta Neurochir (Wien)* 2011;153:1561–72 CrossRef Medline
12. Kokkonen SM, Nikkinen J, Remes J, et al. **Preoperative localization of the sensorimotor area using independent component analysis of resting-state fMRI.** *Magn Reson Imaging* 2009;27:733–40 CrossRef Medline
13. Liu H, Buckner RL, Talukdar T, et al. **Task-free presurgical mapping using functional magnetic resonance imaging intrinsic activity.** *J Neurosurg* 2009;111:746–54 CrossRef Medline
14. Quigley M, Cordes D, Wendt G, et al. **Effect of focal and nonfocal cerebral lesions on functional connectivity studied with MR imaging.** *AJNR Am J Neuroradiol* 2001;22:294–300 Medline
15. Zhang D, Johnston JM, Fox MD, et al. **Preoperative sensorimotor mapping in brain tumor patients using spontaneous fluctuations in neuronal activity imaged with functional magnetic resonance imaging: initial experience.** *Neurosurgery* 2009:5(6 suppl):226–36 CrossRef Medline
16. Li YO, Adali T, Calhoun VD. **Estimating the number of independent components for functional magnetic resonance imaging data.** *Hum Brain Mapp* 2007;28:1251–66 CrossRef Medline
17. Bell AJ, Sejnowski TJ. **An information-maximization approach to blind separation and blind deconvolution.** *Neural Comput* 1995;7:1129–59 CrossRef Medline
18. Himberg J, Hyvärinen A, Esposito F. **Validating the independent components of neuroimaging time series via clustering and visualization.** *Neuroimage* 2004;22:1214–22 CrossRef Medline

19. Poline JB, Worsley KJ, Evans AC, et al. **Combining spatial extent and peak intensity to test for activations in functional imaging.** *Neuroimage* 1997;5:83–96 CrossRef Medline
20. Castellanos FX, Di Martino A, Craddock RC, et al. **Clinical applications of the functional connectome.** *Neuroimage* 2013;80:527–40 CrossRef Medline
21. Lee MH, Smyser CD, Shimony JS. **Resting-state fMRI: a review of methods and clinical applications.** *AJNR Am J Neuroradiol* 2013;34:1866–72 CrossRef Medline
22. Tie Y, Rigolo L, Norton IH, et al. **Defining language networks from resting-state fMRI for surgical planning: a feasibility study.** *Hum Brain Mapp* 2014;3:1018–30 CrossRef Medline
23. Carp J. **The secret lives of experiments: methods reporting in the fMRI literature.** *Neuroimage* 2012;63:289–300 CrossRef Medline
24. Nichols TE. **Multiple testing corrections, nonparametric methods, and random field theory.** *Neuroimage* 2012;62:811–15 CrossRef Medline
25. Hayasaka S, Nichols TE. **Validating cluster size inference: random field and permutation methods.** *Neuroimage* 2003;20:2343–56 CrossRef Medline
26. Mitchell TJ, Hacker CD, Breshears JD, et al. **A novel data-driven approach to preoperative mapping of functional cortex using resting-state functional magnetic resonance imaging.** *Neurosurgery* 2013;73:969–82; discussion 982–83 CrossRef Medline
27. Ogawa S, Menon RS, Tank DW, et al. **Functional brain mapping by blood oxygenation level-dependent contrast magnetic resonance imaging: a comparison of signal characteristics with a biophysical model.** *Biophys J* 1993;64:803–12 CrossRef Medline

Association between *CYP2C19* Polymorphisms and Outcomes in Cerebral Endovascular Therapy

M. Lin, M. Todaro, J. Chan, L. Churilov, W.S. Zhu, S. Ramdave, P.J. Mitchell, R.J. Dowling, P. Kwan, and B. Yan

ABSTRACT

BACKGROUND AND PURPOSE: Differing responses to clopidogrel following endovascular treatment of cerebrovascular diseases may increase the risk of vascular complications. *CYP2C19* gene polymorphisms influence clopidogrel activity. We aimed to study the clinical impact of *CYP2C19* gene polymorphisms in patients undergoing endovascular treatment.

MATERIALS AND METHODS: This was a prospective, longitudinal, observational study. Information on demographics and cerebrovascular status was collected as baseline. Clopidogrel response was tested by the VerifyNow P2Y12 assay. *CYP2C19* genotyping was undertaken by polymerase chain reaction–restriction fragment length polymorphism. Three-month follow-up data included vascular complications, mortality, and modified Rankin Scale score. Associations were investigated among *CYP2C19* genotypes, clopidogrel responsiveness, and clinical outcomes.

RESULTS: One hundred and eight participants were included. Median age was 56 years (interquartile range, 48.8–65.0 years), and 35 (32.4%) were male. Forty-four participants were classified into group 1 (homozygous *CYP2C19*1/*1*); 31, into group 2 (25 with *CYP2C19*1/*2*, two with *CYP2C19*1/*3*, three with *CYP2C19*3/*3*, one with *CYP2C19*2/*3*); 28, into group 3 (24 with *CYP2C19*1/*17*, four with *CYP2C19*17/*17*); and 5, into group 4 (*CYP2C19*2/*17*). A significantly higher proportion of participants in group 3 experienced ischemic events (9 of 28, 32.1%) compared with group 1 (5 of 44, 11.4%; $P = .04$; odds ratio, 3.7; 95% confidence interval, 1.1–12.6). There was no significant difference in clopidogrel response among the 4 genotype groups.

CONCLUSIONS: Individuals with *CYP2C19*17* may have increased risk of ischemic events following endovascular treatment, independent of clopidogrel responsiveness. Larger studies are required to confirm the influence of *CYP2C19*17* on clinical outcomes and to understand the mechanisms for increased ischemic events.

ABBREVIATIONS: IQR = interquartile range; PRU = platelet reactivity unit

Endovascular treatment of cerebrovascular diseases, for example intracranial aneurysms and large artery stenosis, involves the placement of metallic coils or stents.[1] These procedures are followed by increased thrombotic activity and platelet aggregation, resulting in ischemic complications.[2,3]

Clopidogrel is a commonly used antiplatelet drug to reduce the rate of procedure-related thrombosis.[4,5]

Clopidogrel is a prodrug and requires hepatic metabolism mediated by the cytochrome P450 2C19 (*CYP2C19*) enzyme to produce the active R-130964 constituents.[6] Active R-130964 permanently binds to P2Y12 G-protein-coupled platelet surface receptors to block the effects of adenosine diphosphate, leading to inhibition of platelet aggregation.[7]

The response to clopidogrel varies widely among individuals. Up to 66% of patients with cerebrovascular disease have a reduced response to clopidogrel,[8-11] placing them at higher risk of thrombosis,[12] while 14.9%–38% of patients are hyper-responsive to

Received February 1, 2015; accepted after revision June 4.

From the Melbourne Brain Centre (M.L., W.S.Z., B.Y.), and Departments of Radiology (P.J.M., R.J.D., B.Y.), and Neurology (M.T., P.K., B.Y.), The Royal Melbourne Hospital, University of Melbourne, Parkville, Victoria, Australia; Department of Medicine (M.T., J.C., S.R., P.K.), University of Melbourne, Melbourne, Victoria, Australia; and Florey Institute of Neurosciences and Mental Health (L.C.), Melbourne Brain Centre, Heidelberg, Victoria, Australia.

The corresponding authors, Drs Kwan and Yan, had full access to all of the data in the study and take responsibility for the integrity of the data and the accuracy of the data analysis.

Our institution has received research support and grants across the years from Stryker, Covidien, MicroVention, and Codman Johnson & Johnson. No shares, money for talks, commissions, money for papers, and so forth have been received.

Please address correspondence to Patrick Kwan, MD, PhD, Department of Neurology, Royal Melbourne Hospital, Parkville, Victoria 3050, Australia; e-mail: kwanp@unimelb.edu.au; and Bernard Yan, MD, Department of Neurology, Royal Melbourne Hospital, Parkville, Victoria 3050, Australia; e-mail: bernard.yan@mh.org.au

Evidence-Based Medicine Level 2.

http://dx.doi.org/10.3174/ajnr.A4481

clopidogrel.[13,14] Differing responses to clopidogrel may be related to *CYP2C19* gene polymorphisms.[6,9] Of particular clinical importance are the *CYP2C19*2* and *CYP2C19*3* alleles, more commonly seen in Asian descent than African and Caucasian descent, which reduce enzyme activity and have been associated with an increased incidence of stent thrombosis in coronary intervention studies.[8,12] In contrast, *CYP2C19*17* may increase hemorrhagic complications,[14] but its impact on ischemic events and clinical outcome has not been definitively clarified.[14,15]

The influence of *CYP2C19* polymorphisms on outcomes to clopidogrel treatment has been poorly studied in patients with cerebrovascular disease compared with cardiovascular disease. Results from studies in coronary artery disease cannot be readily extrapolated to cerebrovascular disease owing to their different pathophysiology. Coronary artery studies focus mainly on clopidogrel hyporesponsiveness and ischemia as phenotypic outcomes because hemorrhagic complications are rare.[16] However, both ischemia and hemorrhage are considerable risks for patients undergoing endovascular neurointervention.[17]

We prospectively investigated the relationship among common *CYP2C19* variants, clopidogrel response, and clinical outcomes in patients following neurointerventional procedures. We hypothesized that *CYP2C19* variants were associated with clinical outcomes.

MATERIALS AND METHODS

Subjects

This was a prospective cohort study. Consecutive patients who underwent elective neurointervention for intracranial aneurysms or intracranial stenosis were prospectively recruited from The Royal Melbourne Hospital. The neurointervention procedures included simple coiling, balloon-assisted coiling, stent-assisted coiling, balloon and stent-assisted coiling, and Pipeline Embolization Device (Covidien, Irvine, California) flow-diversion stent placement of intracranial aneurysms and intracranial stenosis.

Inclusion criteria were the following: age older than 18 years, imaging evidence of intracranial aneurysms or intracranial stenosis intended for neurointervention, and ongoing use of clopidogrel on recruitment. Participants were excluded if there was significant coagulopathy, such as hemophilia, or other terminal medical comorbidities. All participants provided written informed consent in accordance with the Declaration of Helsinki. The study was approved by the Royal Melbourne Hospital Human Research and Ethics Committee (HREC 2006.155).

Baseline demographic information for each participant included the following: age, sex, ethnicity (African, Asian, Caucasian), cerebrovascular risk factors (smoking history, diabetes, hypertension, hypercholesterolemia, atrial fibrillation, and peripheral vascular disease), size and location of the aneurysms, and indication for the procedure (stent placement or coiling of aneurysm or stenosis). All participants were prescribed clopidogrel, 75 mg/day, and aspirin, 150 mg/day, for at least 3 days before the procedures. Concomitant use of heparin, warfarin, and proton-pump inhibitors was noted.

Ex Vivo Clopidogrel Response Testing

Arterial blood samples were collected perioperatively through the angiographic puncture site of the femoral artery. Samples collected in sodium citrate tubes were rested at room temperature (25°C) for 30 minutes to 4 hours. After resting, the samples were tested for clopidogrel responsiveness by using the VerifyNow P2Y12 assay (Accumetrics, San Diego, California) in accordance with the manufacturer's instructions. The assay produces a value for inhibition of platelet activity in a percentage (percentage inhibition). This value indicates the level of active clopidogrel metabolite-P2Y12 receptor interaction, which inhibits platelet aggregation.[18] According to the manufacturer's manual, percentage inhibition is derived by the VerifyNow P2Y12 assay from the platelet reactivity unit (PRU) and baseline platelet thrombosis activity (BASE). The formula used to calculate percentage inhibition is Percentage Inhibition $= (\text{BASE} - \text{PRU}) \times 100/\text{BASE}$.

CYP2C19 Genotyping

For each patient, a second blood sample was collected, from which genomic DNA was extracted by using the Gentra Puregene Blood Kit (Qiagen, Hilden, Germany) and suspended in DNA Hydration Solution (Qiagen).

Genotyping for *CYP2C19*2*, **3*, and **17* was performed by using polymerase chain reaction–restriction fragment length polymorphism as previously described (**2* and **3*[19]; **17*[20]). Each polymerase chain reaction contained GoTaq Hot Start Mastermix (Promega, Madison, Wisconsin; 400-μmol/L deoxyadenosine triphosphate, 400-μmol/L deoxyguanosine triphosphate, 400-μmol/L deoxycytidine triphosphate, 400-μmol/L deoxythymidine triphosphate, and 4-mmol/L magnesium chloride), 20-μM forward and reverse primers, nuclease-free water, and 50-ng DNA for **2* and **17* and 100-ng DNA for **3*.

For *CYP2C19*2*, the 169-bp polymerase chain reaction product was digested by 200-U SmaI (New England Biolabs, Ipswich, Massachusetts) at 25°C overnight. The *CYP2C19 *1* (wild type) yields a 120- and 49-bp product, whereas the *CYP2C19*2* (681 G>A) variant is resistant to digestion.[19]

The 636 G>A region for *CYP2C19*3* identification was analyzed by digesting the 329-bp polymerase chain reaction product with 16-U BamHI (New England Biolabs) at 37°C for 2 hours. The *CYP2C19*1* yields a 233- and 96-bp product, while the *CYP2C19*3* variant was resistant to digestion.[19]

For the *CYP2C19*17* variant, the 470-bp polymerase chain reaction product (containing the 806 C>T region) was digested with 40-U SfaNI (New England Biolabs) at 37°C for 3 hours followed by enzyme inactivation at 65°C for 20 minutes. *CYP2C19*1* yielded 3 products of 183, 142, and 113 bp. The *CYP2C19*17* variant yielded 3 products of 217, 142, and 113 bp after digestion.[20] The digested patterns for each genotype were separated on a 3% gel by electrophoresis.

To investigate the potential effect of different types of *CYP2C19* polymorphisms, we classified the participants into 4 mutually exclusive genotype groups based on their expected phenotypic behavior.

Clinical Outcomes

A neurologist (B.Y.) specializing in cerebrovascular disease assessed the participants at 3 months after the procedure. Participants who were unable to attend clinics were contacted by telephone.

Clinical end points included cerebral ischemic events and intracerebral hemorrhage periprocedurally and at 3 months postprocedure, and 3-month postprocedural modified Rankin Scale score and mortality. Periprocedural complications included intraoperative clot formations. Three-month ischemic end points included transient ischemic attack (TIA) and symptomatic and asymptomatic (without symptoms but evident on repeat imaging) ischemic stroke. TIA was defined by an acute neurologic deficit that resolved within 1 hour without evidence of ischemia on neuroimaging. Ischemic stroke was defined by an acute neurologic deficit with evidence of ischemia on neuroimaging, without hemorrhage. Hemorrhagic complications included intracranial hemorrhages and any hemorrhage outside the cranium. Major hemorrhagic complications were defined if the participant required surgical intervention. Brain CT and angiography were performed as clinically indicated to identify vascular events.

The modified Rankin Scale score is a 6-scale score used to describe functional status. mRS 0–1 is generally regarded as good functional outcome, and mRS 2–6, poor functional outcome.[21]

Statistical Analysis

Group 1 comprised wild type carriers (*CYP2C19*1/*1*), who also acted as the control group. Group 2 comprised participants who carried *CYP2C19*2* or *CYP2C19*3* (presumed hypofunctioning alleles) in the absence of *CYP2C19*17* (presumed hyperfunctioning allele). Group 3 comprised participants with *CYP2C19*17* in the absence of *CYP2C19*2* and *CYP2C19*3*. Group 4 comprised *CYP2C19*2/*17* individuals (combination of hypo- and hyperfunctioning alleles). Group 1 was used as a reference group (because *CYP2C19*1* is known to be the wild type variant) to facilitate the estimation of the effect of the inheritance of other polymorphisms on individual clopidogrel response and clinical outcome compared with the wild type.

Distribution of age and clopidogrel response among the 4 genotype groups was examined by using the Kruskal-Wallis test equality-of-population rank test. Imbalances in the proportion of vascular risk factors in the 4 genotype groups were tested by the Fisher exact test. Logistic regression analysis was used to investigate the association between the group membership and the categoric outcomes (ischemia, hemorrhage, good functional outcome [mRS 0–1]). The effect sizes for each outcome were estimated as odds ratios by using group 1 as a reference.

The statistical analyses were conducted by using STATA, Version 13 IC (StataCorp, College Station, Texas) and SPSS, Version 19 software (IBM, Armonk, New York). Due to the exploratory nature of this study, no adjustment for multiplicity of comparisons was made, and the value of $P = .05$ was the threshold for statistical significance for all the comparisons.

RESULTS

Baseline Characteristics

A total of 108 participants recruited from 2010 to 2013 were included in this study. Among them, 93 (86.1%) underwent endovascular treatment for unruptured aneurysms; 13, (12.0%) for intracranial stenosis; and 2 (1.9%), for venous sinus stenosis. Eleven (10.2%) participants underwent coiling alone, 26 (24.1%) underwent balloon-assisted coiling, and 13 (12.0%) underwent concurrent stent placement and coiling, while 7 (6.5%) required balloon-assisted stent placement and coiling. The median age was 56 years (interquartile range [IQR], 48.8–65.0), and 35 participants (32.4%) were men. Most (91.7%) were of white descent.

Table 1: Clopidogrel response by genotype groups[a]

	Group 1 (*n* = 38)	Group 2 (*n* = 25)	Group 3 (*n* = 25)	Group 4 (*n* = 5)	Fisher Exact Test, *P* Value
Percentage inhibition[b]					
Median	37.5	17.0	30.0	30.0	.32
IQR	17.0–70.0	6.0–47.0	12.0–47.0	24.0–54.0	

[a] Group 1: *CYP2C19*1/*1*; Group 2: *CYP2C19*1/*2,*1/*3, *2/*2, *2/*3*; Group 3: *CYP2C19*1/*17,*17/*17*; Group 4: *CYP2C19*2/*17*.
[b] Percentage inhibition = (BASE − PRU) × 100/BASE.

There was no significant difference in the age distribution among the 4 groups (Kruskal-Wallis, $P = .93$). There was also no significant difference in the distribution of sex in the genotype groups (Fisher exact test, $P = .06$). No significant difference was found among the 4 genotype groups for cerebrovascular risk factors, such as history of cerebrovascular disease (transient ischemic attack, ischemic and hemorrhagic stroke), cigarette smoking, diabetes, hypertension, hypercholesterolemia, and atrial fibrillation or peripheral vascular disease (Fisher exact test $P = .13$, $P = .73$, $P = .72$, $P = .61$, $P = .96$, $P = .91$, $P = .12$, respectively).

CYP2C19 *Genotypes*

On the basis of the *CYP2C19* genotypes, 44 participants were classified into group 1 (homozygous *CYP2C19*1/*1*); 31, into group 2 (25 with *CYP2C19*1/*2*, two with *CYP2C19*1/*3*, three with *CYP2C19*3/*3*, one with *CYP2C19*2/*3*; none had *CYP2C19*2/*2*). Twenty-eight were classified into group 3 (24 with *CYP2C19*1/*17*, four with *CYP2C19*17/*17*); and 5, into group 4 (*CYP2C19*2/*17*; none had *CYP2C19*3/*17*). There was no significant difference in the distribution of age, sex, and other cerebrovascular risk factors among the 4 *CYP2C19* genotype groups.

CYP2C19 *Genotypes and Outcomes*

At 3 months postprocedure, 18 of 108 (16.7%) participants had experienced ischemic events, 16 (14.8%) had hemorrhagic complications (5 major and 11 minor), and 4 (3.7%) had complications of both a hemorrhagic and ischemic nature. Two of the ischemic complications occurred in the periprocedural period. Ninety-nine of 108 (91.7%) participants had good functional outcome at 3 months. One participant, who carried *CYP2C19*1/*1*, died (Tables 1 and 2).

A significantly higher proportion of participants in group 3 (*CYP2C19*1/*17* or **17/*17*) experienced ischemic events (9 of 28, 32.1%) compared with group 1 (*CYP2C19*1/*1*) individuals (5 of 44, 11.4%; $P = .04$; odds ratio, 3.7; 95% confidence interval, 1.1–12.6). The difference remained significant after adjustment for age ($P = .03$; OR, 4.0; 95% CI, 1.1–14.3) and ex vivo clopidogrel response ($P = .04$; OR, 4.5; 95% CI, 1.1–17.9). No significant differences between group 1 (5 of 44, 11.4%) and the other genotype groups, groups 2 (3 of 25, 9.7%) and 4 (1 of 5, 20%), were identified in the incidence of ischemia. Other adjustments for sex, history of cerebrovascular disease, and peripheral vascular disease did not have a significant influence on the results.

Table 2: Postprocedural clinical outcomes by genotype groups[a]

	Group 1 (*n* = 44)	Group 2 (*n* = 31)	Group 3 (*n* = 28)	Group 4 (*n* = 5)	Fisher Exact Test, *P* Value
Ischemic complication (No.) (%)	5 (11.4)	3 (9.7)	9 (32.1)	1 (20.0)	.08
Hemorrhagic complication (No.) (%)	8 (18.2)	1 (3.2)	5 (17.9)	2 (40.0)	.06
mRS ≥2 (No.) (%)	5 (11.4)	1 (3.2)	2 (7.1)	1 (20.0)	.35

[a] Group 1: *CYP2C19*1/*1*; Group 2: *CYP2C19*1/*2,*1/*3, *2/*2, *2/*3*; Group 3: *CYP2C19*1/*17,*17/*17*; Group 4: *CYP2C19*2/*17*.

No significant differences between group 1 and the other genotype groups were identified in the incidence of hemorrhage. Age is a known influencing factor on mRS. However, there was no significant difference in age-adjusted mRS between group 1 and the other genotype groups.

CYP2C19 *Genotypes and Ex Vivo Clopidogrel Response*

Clopidogrel response was available in 93 participants. Of these participants, 38 of 44 (86.4%) were from group 1; 25 of 31 (80.1%), from group 2; 25 of 28 (89.3%), from group 3; and 5 of 5 (100%), from group 4. The median clopidogrel response was 37.5% inhibition (IQR, 12.0%–70.0%) for group 1, 17.0% (IQR, 6.0%–47.0%) for group 2, 30.0% (IQR, 12.0%–47.0%) for group 3, and 30.0% (IQR, 24.0%–54.0%) for group 4. Overall, there was no significant difference in clopidogrel response in terms of percentage inhibition among the 4 genotype groups (Kruskal-Wallis, $P = .32$). There was no significant difference in percentage inhibition among patients with no complications (26.0%; IQR, 12.0%–53.0%) compared with ischemic events (30.6%; IQR, 2.75%–51.0%; $P = .5$) and hemorrhagic events (47.9%; IQR, 31.5%–70.8%; $P = .9$).

PRU values were also compared between the genotype groups 2, 3, and 4 and group 1. The median PRU between group 1 and group 2 was not significant (237; IQR, 105–291 versus 261; IQR, 184–316; $P = .78$). Similarly, no significance was found between group 1 and group 4 (237; IQR, 105–291 versus 246; IQR, 195–281; $P = .88$). There appeared to be a significant difference between the median PRUs of group 1 and group 3 (237; IQR, 105–291 versus 232; IQR, 209–245; $P = .03$).

Ex Vivo Clopidogrel Response and Clinical Outcomes

Among the 93 participants with clopidogrel-response testing, 16 (17.2%) experienced ischemic events. There was no significant difference between the median clopidogrel response of participants who developed ischemic events ([$n = 16$] 15.5%; IQR, 2.5%–55.0%) compared with participants without ischemic events ([$n = 77$] 30.0%; IQR, 13.0%–65.0%) ($P = .3$).

Of the 93 participants with clopidogrel-response results, 14 (15.1%) experienced hemorrhagic events. The median clopidogrel response of participants who experienced hemorrhagic events was significantly higher ([$n = 14$] 46.0%; IQR, 30.0%–72.0%) compared with those who did not experience hemorrhages ([$n = 22$] 22.0%; IQR, 1.0%–53.0%) ($P = .03$).

There was no significance between the median PRU values for the ischemic-versus-nonischemic participants (253; IQR, 151.75–313.75 versus 244; IQR, 172–295; $P = .44$). Similarly, the median PRU evaluation was made for hemorrhagic-versus-nonhemorrhagic participants (211; IQR, 100–242 versus 249; IQR, 172.5–306.5; $P = .60$). These results showed no statistical significance.

DISCUSSION

Clopidogrel is a common antiplatelet prescribed to prevent secondary ischemia for patients with cerebrovascular conditions treated by endovascular techniques. However, variations in clopidogrel response associated with *CYP2C19* polymorphisms may have a negative impact on treatment results.

Our investigation suggests increased risk of ischemic events in individuals carrying the *CYP2C19*17* allele (group 3) compared with homozygous *CYP2C19*1/*1* wild type carriers (group 1). *CYP2C19*17* is generally thought to be hyperfunctioning[20]; this feature should suggest an increased risk of hemorrhage. However, our study shows *CYP2C19*17* to be significantly associated with ischemic events, despite no significant association with platelet activity. This novel finding is unexpected and leads us to suspect involvement of other pathways in the association between the *CYP2C19* gene and clinical outcomes. Our study did not obtain data from imaging sources to interpret clinical outcomes but, instead, defined ischemic events evidenced by stroke or transient ischemic attacks in clinical follow-up only.

Correlation between *CYP2C19*17* and secondary ischemic events following endovascular treatment of cerebrovascular disease has not been reported previously, to our knowledge. However, studies investigating the phenotypic effects of *CYP2C19*17* are limited, and the influence of this polymorphism on the activity of clopidogrel, and hence clinical outcomes, remains controversial. Although a recent study in patients with myocardial infarction has suggested a significantly increased incidence of bleeding events and 1-year mortality rate among *CYP2C19*17* carriers,[15] others have found that *CYP2C19*17* has minimal influence on clopidogrel response.[21] The lack of association between *CYP2C19*17* and the ex vivo clopidogrel response in the present study, along with conflicting findings in previous studies, suggests that the polymorphism may influence clinical outcomes via mechanisms independent of measured clopidogrel response in this patient population. This influence has not been previously investigated and deserves further exploration in future studies.

Compared with *CYP2C19*17*, *CYP2C19*2* and *CYP2C19*3* are well-documented as hypofunctioning alleles in healthy subjects and patients with coronary artery and cerebrovascular diseases.[9,12,22–24] These alleles have also been reported to be significantly associated with subacute stent thrombosis and myocardial infarction following percutaneous coronary intervention.[8,25] This correlation is understood to be a leading cause for increased risk of ischemic complications.[26] Our results did not find *CYP2C19*2* or *CYP2C19*3* to be significantly associated with clinical outcome and clopidogrel response. However, the trends indicated in our results are reflective of those in previous literature.

In this study, *CYP2C19* polymorphism was not associated significantly with mRS, a commonly used functional outcome in interventional studies of cerebrovascular disease. The inclusion of primarily participants undergoing elective procedures may explain the small number of poor functional outcomes recorded, with mRS ≥2 recorded in only 8.5% (7 of 106). This low incidence

of poor clinical outcome limited our ability to draw conclusions concerning the influence of *CYP2C19* genotypes on functional outcomes. Further studies to validate the association between *CYP2C19* polymorphisms and functional outcomes are needed because cerebrovascular complications (ischemia and hemorrhage) are major contributors of morbidity.

Our results did not show a significant association between clopidogrel response and *CYP2C19* polymorphisms and clinical outcome. Point-of-care clopidogrel response testing platforms such as the VerifyNow P2Y12 assay could add clinical benefits for patients receiving endovascular neurointervention, provided that standardized values predicting response (ischemia and hemorrhage) can be defined. However, there is currently no standard definition for VerifyNow P2Y12 assay values. Values assigned to define clopidogrel hyporesponsiveness in previous studies vary widely between 15%[18] and 40%,[27] though the cutoff value of 20% is commonly used.[10,28] Likewise, there is no standard VerifyNow P2Y12 value to define clopidogrel hyperresponsiveness. The rare occurrence of hemorrhagic complications in coronary artery disease may have resulted in limited research being conducted on clopidogrel hyper-responsiveness. PRU values are also useful in defining clopidogrel responsiveness. However, the PRU values were not found to be statistically significant for the clinical outcomes of our study, ischemia and hemorrhage, compared to no complications. Similarly, no significance was found in PRU values of *CYP2C19*2* and *CYP2C19*3* compared with the wild type. However, the PRU values in *CYP2C19*17* carriers were significantly lower compared with the wild type. The influence of *CYP2C19*17* on platelet reactivity is an area that requires more research.

The findings in our study were novel. However, the mechanism by which *CYP2C19*17* influenced clinical outcomes remains undefined because we did not find a significant correlation between the *CYP2C19*17* genotype and platelet activity. The main limitation of the present study was the small sample size, and the elective nature of the endovascular treatments was likely a contributing factor to low rates of poor functional outcomes.

CONCLUSIONS

Our results suggest an increased risk of ischemic events in carriers of *CYP2C19*17* who undergo neurointervention. Further research to validate the association and to understand the underlying biologic mechanisms is warranted.

Disclosures: Patrick Kwan—*UNRELATED*: *Grants/Grants Pending*: UCB (research grants)*; *Payment for Lectures (including service on Speakers Bureaus)*: Eisai, GlaxoSmithKline, UCB, *Comments*: lecture fees; *OTHER RELATIONSHIPS*: He received research grants from the National Health and Medical Research Council of Australia, Australian Research Council, Hong Kong Research Grants Council, and Health and Medical Research Fund. He and his institution also received speaker's or consultancy fees and/or research grants from Eisai, GlaxoSmithKline, and UCB. Bernard Yan—*UNRELATED*: research and educational grants from Bayer, Codman (Johnson & Johnson); *Payment for Lectures (including service on Speakers Bureaus)*: Stryker, bioCSL, and Boehringer Ingelheim. *Money paid to the institution.

REFERENCES

1. Molyneux A, Kerr R, Stratton I, et al; International Subarachnoid Aneurysm Trial (ISAT) Collaborative Group. **International Subarachnoid Aneurysm Trial (ISAT) of neurosurgical clipping versus endovascular coiling in 2143 patients with ruptured intracranial aneurysms: a randomised trial.** *Lancet* 2002;360:1267–74 CrossRef Medline
2. Lee DH, Kim HS, Kim SM, et al. **Change of platelet reactivity to antiplatelet therapy after stenting procedure for cerebral artery stenosis: VerifyNow antiplatelet assay before and after stenting.** *Neurointervention* 2012;7:23–26 CrossRef Medline
3. Zhang QY, Li Y, Guan SY, et al. **Incidence and predictors of definite stent thrombosis after coronary stent implantation.** *Chin Med J (Engl)* 2012;125:1547–51 Medline
4. Yamada NK, Cross DT 3rd, Pilgram TK, et al. **Effect of antiplatelet therapy on thromboembolic complications of elective coil embolization of cerebral aneurysms.** *AJNR Am J Neuroradiol* 2007;28:1778–82 CrossRef Medline
5. Kang HS, Han MH, Kwon BJ, et al. **Is clopidogrel premedication useful to reduce thromboembolic events during coil embolization for unruptured intracranial aneurysms?** *Neurosurgery* 2010;67:1371–76; discussion 1376 CrossRef Medline
6. Kazui M, Nishiya Y, Ishizuka T, et al. **Identification of the human cytochrome P450 enzymes involved in the two oxidative steps in the bioactivation of clopidogrel to its pharmacologically active metabolite.** *Drug Metab Dispos* 2010;38:92–99 CrossRef Medline
7. Grau AJ, Reiners S, Lichy C, et al. **Platelet function under aspirin, clopidogrel, and both after ischemic stroke: a case-crossover study.** *Stroke* 2003;34:849–54 CrossRef Medline
8. Collet JP, Hulot JS, Pena A, et al. **Cytochrome P450 2C19 polymorphism in young patients treated with clopidogrel after myocardial infarction: a cohort study.** *Lancet* 2009;373:309–17 CrossRef Medline
9. Brandt JT, Close SL, Iturria SJ, et al. **Common polymorphisms of CYP2C19 and CYP2C9 affect the pharmacokinetic and pharmacodynamic response to clopidogrel but not prasugrel.** *J Thromb Haemost* 2007;5:2429–36 CrossRef Medline
10. Rho GJ, Shin WR, Kong TS, et al. **Significance of clopidogrel resistance related to the stent-assisted angioplasty in patients with atherosclerotic cerebrovascular disease.** *J Korean Neurosurg Soc* 2011;50:40–44 CrossRef Medline
11. Pandya DJ, Fitzsimmons BF, Wolfe TJ, et al. **Measurement of antiplatelet inhibition during neurointerventional procedures: the effect of antithrombotic duration and loading dose**. *J Neuroimaging* 2010;20:64–69 CrossRef Medline
12. Shuldiner AR, O'Connell JR, Bliden KP, et al. **Association of cytochrome P450 2C19 genotype with the antiplatelet effect and clinical efficacy of clopidogrel therapy.** *JAMA* 2009;302:849–57 CrossRef Medline
13. Goh C, Churilov L, Mitchell P, et al. **Clopidogrel hyper-response and bleeding risk in neurointerventional procedures.** *AJNR Am J Neuroradiol* 2013;34:721–26 CrossRef Medline
14. Sibbing D, Koch W, Gebhard D, et al. **Cytochrome 2C19*17 allelic variant, platelet aggregation, bleeding events, and stent thrombosis in clopidogrel-treated patients with coronary stent placement.** *Circulation* 2010;121:512–18 CrossRef Medline
15. Cresci S, Depta JP, Lenzini PA, et al. **Cytochrome P450 gene variants, race, and mortality among clopidogrel-treated patients after acute myocardial infarction.** *Circ Cardiovasc Genet* 2014;7:277–86 CrossRef Medline
16. Dias V, Cabral S, Gomes C, et al. **Intramyocardial dissecting haematoma: a rare complication of acute myocardial infarction.** *Eur J Echocardiogr* 2009;10:585–87 CrossRef Medline
17. Darweesh SK, Leening MJ, Akoudad S, et al. **Clopidogrel use is associated with an increased prevalence of cerebral microbleeds in a stroke-free population: the Rotterdam study.** *J Am Heart Assoc* 2013;2:e000359 CrossRef Medline
18. Godino C, Mendolicchio L, Figini F, et al. **Comparison of VerifyNow-P2Y12 test and Flow Cytometry for monitoring individual platelet response to clopidogrel: what is the cut-off value for identifying patients who are low responders to clopidogrel therapy?** *Thromb J* 2009;7:4 CrossRef Medline
19. De Morais SM, Wilkinson GR, Blaisdell J, et al. **Identification of a new**

genetic defect responsible for the polymorphism of (S)-mephenytoin metabolism in Japanese. *Mol Pharmacol* 1994;46:594–98 Medline
20. Rudberg I, Mohebi B, Hermann M, et al. **Impact of the ultrarapid CYP2C19*17 allele on serum concentration of escitalopram in psychiatric patients.** *Clin Pharmacol Ther* 2008;83:322–27 CrossRef Medline
21. Huang Y, Guo JW; Project Group for Demonstration Study of Syndrome Differentiation Protocol and Effect Evaluation of Acute Ischemic Stroke. **Outcome and safety assessment of an herbal medicine treatment protocol for yin pattern of acute ischemic stroke.** *Zhong Xi Yi Jie He Xue Bao* 2010;8:417–26 CrossRef Medline
22. Geisler T, Schaeffeler E, Dippon J, et al. **CYP2C19 and nongenetic factors predict poor responsiveness to clopidogrel loading dose after coronary stent implantation.** *Pharmacogenomics* 2008;9:1251–59 CrossRef Medline
23. Lee JB, Lee KA, Lee KY. **Cytochrome P450 2C19 polymorphism is associated with reduced clopidogrel response in cerebrovascular disease.** *Yonsei Med J* 2011;52:734–38 CrossRef Medline
24. Hulot JS, Bura A, Villard E, et al. **Cytochrome P450 2C19 loss-of-function polymorphism is a major determinant of clopidogrel responsiveness in healthy subjects.** *Blood* 2006;108:2244–47 CrossRef Medline
25. Harmsze AM, van Werkum JW, Ten Berg JM, et al. **CYP2C19*2 and CYP2C9*3 alleles are associated with stent thrombosis: a case-control study.** *Eur Heart J* 2010;31:3046–53 CrossRef Medline
26. Ryu DS, Hong CK, Sim YS, et al. **Anti-platelet drug resistance in the prediction of thromboembolic complications after neurointervention.** *J Korean Neurosurg Soc* 2010;48:319–24 CrossRef Medline
27. Prabhakaran S, Wells KR, Lee VH, et al. **Prevalence and risk factors for aspirin and clopidogrel resistance in cerebrovascular stenting.** *AJNR Am J Neuroradiol* 2008;29:281–85 CrossRef Medline
28. Nordeen JD, Patel AV, Darracott RM, et al. **Clopidogrel resistance by P2Y12 platelet function testing in patients undergoing neuroendovascular procedures: incidence of ischemic and hemorrhagic complications.** *J Vasc Interv Neurol* 2013;6:26–34 Medline

Mechanical Thrombectomy Using the New ERIC Retrieval Device Is Feasible, Efficient, and Safe in Acute Ischemic Stroke: A Swiss Stroke Center Experience

T. Kahles, C. Garcia-Esperon, S. Zeller, M. Hlavica, J. Añon, M. Diepers, K. Nedeltchev, and L. Remonda

ABSTRACT

BACKGROUND AND PURPOSE: Intravenous thrombolysis and mechanical thrombectomy predominantly using stent retrievers have been shown to effectively restore cerebral blood flow and improve functional outcome in patients with acute ischemic stroke. We sought to determine the safety and feasibility of mechanical thrombectomy using the new ERIC retrieval device.

MATERIALS AND METHODS: We identified 36 consecutive patients from our Stroke Center registry with acute ischemic stroke who were treated with the new ERIC retriever from September 2013 to December 2014. Patients with ischemic stroke meeting the following criteria were eligible: onset-to-treatment time of ≤4.5 hours or wake-up stroke ($n = 10$) with relevant CT perfusion mismatch, NIHSS score of ≥4, and proof of large-vessel occlusion in the anterior circulation on CT angiography. We assessed the baseline characteristics including age, sex, comorbidities, stroke severity, site of vessel occlusion, presence of tissue at risk, and treatment-related parameters such as onset-to-treatment time, recanalization grade, and outcome.

RESULTS: The mean age was 70 ± 13 years, and the median NIHSS score on admission was 18 (interquartile range, 10–20). Seventeen of 36 patients were on platelet inhibitors or anticoagulants before endovascular treatment (47.2%); 20 patients received intravenous thrombolysis (55.5%). The ERIC was used as the sole retriever in 28 patients (77.8%) and as a rescue device in 8. Excellent recanalization was achieved in 30/36 patients (83.3%) with TICI 3 in 19/36 and 2b in 11/36, respectively. Median procedural time in these patients was 90 minutes (interquartile range, 58–133 minutes). No intraprocedural complications occurred.

CONCLUSIONS: In this observational study, the new ERIC retrieval device was technically feasible, safe, and effective in acute ischemic stroke with large-vessel occlusion.

ABBREVIATIONS: ERIC = Embolus Retriever with Interlinked Cages; IQR = interquartile range; IVT = intravenous thrombolysis; sICH = symptomatic intracerebral hemorrhage

Early restoration of cerebral blood flow is crucial to prevent persistent brain damage in acute ischemic stroke. Intravenous thrombolysis (IVT) with tPA has been shown to increase recanalization rates[1] and improve clinical outcome within 4.5 hours after symptom onset.[2,3] Still, its effectiveness in large-vessel occlusion is rather limited.[4] In contrast, endovascular interventions, in particular mechanical thrombectomy, have revealed high rates of recanalization in proximal artery occlusion (reviewed by Jansen and Rohr[5]). In the past decade, various devices have been introduced for this purpose (reviewed by Spiotta et al[6]). Just recently, new-generation stent retrievers were launched and proved to be even more effective than previous approaches.[7-9]

However, even the latest devices need to be deployed for several minutes before retrieving the thrombus and thus require precious time. Moreover, 1 device does not fit all occlusion types, and alternative effective devices are warranted. In this pilot study, we sought to determine the feasibility, efficacy, and safety of mechanical thrombectomy in patients with acute ischemic stroke by using the new Embolus Retriever with Interlinked Cages (ERIC; MicroVention, Tustin, California) (Fig 1*B*).

MATERIALS AND METHODS

Patients

We identified 36 consecutive patients with acute stroke who were treated with the new ERIC device from September 2013 to December 2014 at the Cantonal Hospital Aarau Stroke Center. Ethical approval was obtained from the local ethics committee.

Patients with ischemic stroke were eligible if they met the fol-

Received March 10, 2015; accepted after revision May 15.

From the Departments of Neurology (T.K., C.G.-E., S.Z., K.N.) and Neuroradiology (M.H, J.A., M.D., L.R.), Cantonal Hospital Aarau, Aarau, Switzerland.

Please address correspondence to Luca Remonda, MD, Department of Neuroradiology, Cantonal Hospital Aarau, Tellstr, CH- 5001 Aarau, Switzerland; e-mail: luca.remonda@ksa.ch

Indicates article with supplemental on-line tables.

http://dx.doi.org/10.3174/ajnr.A4463

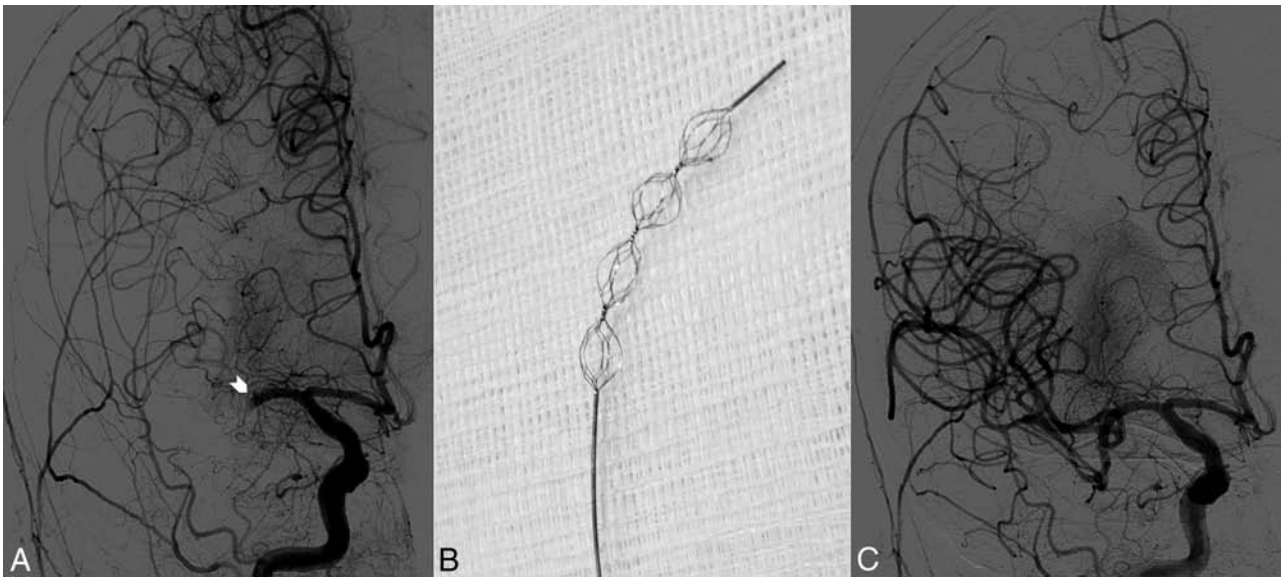

FIG 1. *A*, MCA M1 occlusion (*white arrowhead*). *B*, ERIC retriever tip. *C*, MCA M1 recanalized.

Table 1: Baseline characteristics of treated patients

Characteristics	
Age (mean) (yr)	70 ± 13
Female sex (%)	47.2
Hypertension (%)	69.4
Diabetes (%)	13.9
Hypercholesterolemia (%)	44.4
Smoking (%)	24.5
Prior TIA/stroke (%)	8.3
Modified Charlson Index (median) (IQR)	1 (0–2)
Prior PI/OAC (%)	47.2
Baseline NIHSS (median) (IQR)	18 (10–20)
Intravenous thrombolysis (%)	55.5
Site of vessel occlusion (%)	
MCA-M1	52.8
MCA-M2	25.0
ICA-T	11.1
Other	11.1
	$n = 36$

Note:—PI indicates platelet inhibitor; OAC, oral anticoagulant; ICA-T, intracranial internal carotid artery bifurcation.

lowing criteria: 18 years of age or older; onset-to treatment time of ≤4.5 hours or wake-up-stroke with relevant CT perfusion mismatch, NIHSS score of ≥4, and proof of large-vessel occlusion in anterior circulation arteries (ICA, MCA, anterior cerebral artery) on CT angiography. As mentioned above, patients with unknown onset of symptoms (wake-up stroke) underwent a CTP series, which included a time-to-peak map with a threshold of ≥6 seconds and a cerebral blood volume map. A TTP/CBV area ratio of ≥2 was considered a relevant CTP mismatch.

IVT with 0.9 mg/kg of body weight was started immediately in eligible patients in-house or at the referring hospital if applicable. Intra-arterial urokinase (1.000.000 IU/60 minutes) was used in certain cases at the treating physician's discretion ($n = 2$).

We determined baseline characteristics, including age, sex, comorbidities, cardiovascular risk factors, previous medication, stroke severity, and site of vessel occlusion (Table 1).

Outcome Measures

We assessed treatment-related parameters such as onset-to-treatment time (last seen normal to groin puncture), procedural time (groin puncture to final recanalization), recanalization grade (Thrombolysis in Cerebral Infarction score), intra-/postprocedural complications (eg, symptomatic intracerebral hemorrhage [sICH]), and functional outcome at discharge (NIHSS/mRS) and at 3 months (mRS).

Recanalization was defined as being "satisfactory" with TICI 2–3 and "excellent" with TICI 2b/3. Intraprocedural complications included vessel dissection or perforation, embolic events in previously unaffected territories, or sICH during the procedure.[10] Intraprocedural symptomatic intracerebral hemorrhage was defined as proof of intracerebral hemorrhage on final tomography in the angiography suite and a decline in the NIHSS score of ≥4 points. Functional outcome at 3 months was considered "favorable" with an mRS of ≤2 (independent) and "satisfactory" with an mRS of ≤3 (ambulatory without help).

Endovascular Procedure

The new ERIC is formed by 3–5 interlinked cages with diameters ranging from 3 to 6 mm and a resulting working length of 15–44 mm (Fig 1). Thus, the number of working cages can be adjusted to the required working length. The ERIC is designed to retract the clot coaxially and prevent the captured clot from shearing off during retraction. All procedures were performed on an Allura Xper FD20/20 biplane angiography system (Philips Healthcare, Best, the Netherlands) according to the departmental protocol with intraprocedural modification if required. Briefly, an 8F balloon-guide catheter was placed in the distal common carotid artery. A heparinized saline solution was continuously perfused through the catheter during the procedure. With the balloon of the guide catheter deflated, a 0.0014-inch guidewire was advanced coaxially over a Headway 17 Advanced Microcatheter (MicroVention) within the occluded intracranial vessel and navigated distal to the clot. The Headway 17 microcatheter was then advanced over the wire

through the clot and the guidewire was exchanged for the embolectomy device. The ERIC was advanced and deployed a few millimeters distal to the clot. The balloon of the guide catheter was inflated, and the microcatheter and the embolectomy device were gently withdrawn under continuous proximal aspiration with a syringe. A control angiography was performed to confirm recanalization and reperfusion. Modifications of the standard procedure are reported in On-line Table 1.

RESULTS

Baseline Data

Patient baseline characteristics are presented in detail in Table 1. The mean age was 70 ± 13 years, and 47.2% were female patients. The median NIHSS score on admission was 18 (interquartile range [IQR], 10–20). Twenty-five patients had hypertension, 16 had hypercholesterolemia, and 5 had diabetes mellitus, and 9 were active cigarette smokers. In addition, the modified Charlson Index as a measure of comorbidities showed a light-to-moderate burden with a median modified Charlson Index of 1 (IQR, 0–2). Strokes of 36 patients were considered wake-up with undetermined onset of symptoms.

Procedural Data

CT angiography on admission revealed the following occlusion types: MCA M1 segment (n = 19), MCA M2 segment (n =9), terminal carotid-T (n =4), tandem (intracranial internal carotid artery bifurcation–MCA, n = 3), and combined MCA M1 and anterior cerebral artery (n = 1) (Table 1).

In 20 patients, intravenous tPA was started before mechanical thrombectomy. Intra-arterial urokinase was administered in another 2 patients without prior intravenous thrombolytic therapy. ERIC was used as the single retriever in 28 patients (77.8%) and as a rescue device in 8. Excellent recanalization was achieved in 30 of 36 patients (83.3%) with TICI 3 in 19/36 and 2b in 11/36, respectively. Median procedural time was 90 minutes (IQR, 58–133 minutes) in these patients. General anesthesia was required in 13/36 patients, whereas 23/36 procedures were performed with the patient under conscious sedation. No intraprocedural switch from conscious sedation to general anesthesia was necessary, and no intraprocedural complications occurred. The median time from symptom onset to groin puncture was 4 hours 57 minutes (IQR, 3 hours 36 minutes to 7 hours 47 minutes).

Clinical Outcome

The median NIHSS score at discharge was 9 (IQR, 2–16), corresponding to a decrease of 9 points compared with the median NIHSS score on admission (Table 2). One-third of patients achieved favorable outcome (mRS ≤2) at 90 days after the ischemic event. Satisfactory outcome (mRS ≤3) was achieved in 14/36 when leaving the hospital, with an increase to 21/36 (58%) 3 months later.

Three sICHs (8.3%) were documented in the early course of hospitalization, all in patients with successful recanalization. No intraprocedural intracerebral hemorrhage occurred.

There was a 19.4% in-hospital mortality (7/36) due to the development of fulminant cerebral edema despite successful recanalization in 3 patients (all TICI 3), followed by decompressive surgery in 2 of them and sICH in 1 of the latter. A fourth patient had vessel reocclusion on the same day after incomplete recanalization (TICI 2a) and developed a large MCA infarct. Because of considerable pre-stroke comorbidities with metastatic lung cancer and multiple myeloma, the latter patient's relatives and the treating physicians agreed to not extend diagnostic and therapeutic procedures according to the patient's presumed decision, with death on day 3. Accordingly, 3 patients with severe systemic infections (pneumonia in 2 and unidentified focus in 1) during hospitalization were continued on palliative care due to severe neurologic deficits, advanced age, and the poor prognosis. No intraprocedural deaths occurred.

During the 3-month follow-up, mortality further increased to 27.8% (10/36). One patient died 54 days after stroke during rehabilitation, with bacterial pneumonia and septicemia resulting in multiorgan failure. In the other 2 patients, therapeutic procedures were terminated in agreement with the patient's relatives and the patient's presumed decision due to age, stroke severity, and fatal prognosis.

One patient (patient 29, On-line Table 1) with successful recanalization and considerable clinical benefit, with an improvement from NIHSS 19 on admission to NIHSS 2 (and mRS 3) at discharge, underwent aortic arch replacement due to an incidental aortic arch aneurysm 10 weeks later. Perioperatively, he developed new focal neurologic deficits with proof of new ischemic infarcts on cranial CT, resulting in an mRS score of 5 at 3-month follow-up.

DISCUSSION

Retrieving thrombi with the new ERIC device was technically feasible, effective, and safe in this pilot study of acute ischemic stroke with large-vessel occlusion in anterior circulation arteries. The ERIC is designed to adapt to different vessel diameters and thrombus lengths and is thus available in diameters ranging from 3 to 6 mm and a working length of 15–44 mm with 3–5 spheres. The minimal required microcatheter internal diameter is 0.017 inches for all ERIC types. Proximal vessel occlusions, such as carotid-T occlusions, could be reached as easily as M2 branch occlusions in this pilot study.

Satisfactory recanalization with TICI grades 2–3 was demonstrated in 94.4%, being excellent in 83.3% (TICI 2b–3). Additional thrombus aspiration at the end of the procedure further enhanced recanalization efficacy in 1 patient (patient 8). These high rates of successful recanalization also resulted in a substantial proportion of patients with an independent outcome (mRS ≤2, 33.3%). Of note, as many as 21 patients were ambulatory without help (mRS ≤3, 58.3%) 3 months after the index event. These findings are in line with the recently published Multicenter Randomized Clinical Trial of Endovascular Treatment for Acute Ischemic Stroke in the Netherlands (MR CLEAN) trail,[11] predominantly using the Solitaire stent retriever (Covidien, Irvine, California) (mRS 2, 33%; mRS 3, 51%), and they are close to the results of the Spanish multicenter Endovascular Revascularization with Solitaire Device versus Best Medical Therapy in Anterior Circulation Stroke within 8 Hours (REVASCAT) trial[12] (mRS 2, 44%; mRS 3, 62%). The higher rates of favorable functional outcome in the Endovascular Treatment for Small Core and Anterior

Table 2: Procedural and outcome characteristics of treated patients

Characteristics	
LSN to GP (median) (IQR)	4 hr 57 min (3 hr 36 min to 7 hr 47 min)
Procedural time (TICI 2b/3) (median) (IQR)	90 min (58–133 min)
Postprocedural TICI (%)	
2b/3	83.3
2a	11.1
1	5.5
NIHSS at discharge (median) (IQR)	9 (2–16)
mRS at discharge (%)	
0–2	27.8
0–3	38.9
6	19.4
mRS at 3 mo (%)	
0–2	33.3
0–3	58.3
6	27.8
sICH (%)	8.3

Note:—LSN to GP indicates time from last seen normal to groin puncture.

Circulation Proximal Occlusion with Emphasis on Minimizing CT to Recanalization Times (ESCAPE) trial,[13] Extending the Time for Thrombolysis in Emergency Neurological Deficits–Intra-Arterial (EXTEND-IA) trial,[14] and Solitaire With the Intention For Thrombectomy as PRIMary Endovascular Treatment (SWIFT PRIME) trial[15] are most likely attributable to a shorter time from stroke onset to mechanical thrombectomy (difference median, >60 minutes).

Overall, the median NIHSS score decreased from 18 points on admission to 9 points at discharge. The median NIHSS score on admission was 20 (range, 16–27) in patients who died during the 3-month follow-up period compared with 15 points (range, 5–21) in survivors. A high NIHSS score on admission is a known predictor of poor outcome,[16] and despite the small numbers currently studied, our data further support this finding. Less than one-third of patients (10/36) died before the end of the 3-month follow-up period. None of those deaths could be directly attributed to the endovascular procedure or the retrieval device. The fulminant development of cerebral edema with or without sICH during hospitalization and the consequences of stroke severity and advanced age during follow-up explained the reported deaths. Moreover, the mortality rate was in line with previously published data of mechanical thrombectomy studies by using the Merci retriever (Concentric Medical, Mountain View, California), Penumbra System (Penumbra, Alameda, California), Revive device (Codman Neurovascular, Raynham, Massachusetts), or Trevo device (Stryker, Kalamazoo, Michigan), and it tended to slightly exceed mortality rates reported in many trials using the Solitaire stent retriever (compare On-line Table 2). However, until recently, these trials lacked power and were not designed to show the superiority of one device or the other. In particular, the study designs were very heterogeneous among those trials; small numbers were studied in most of the trials; and regarding the present observational single-arm study, more than one-third of the patients were treated in an extended time window, even beyond 6 hours from symptom onset based on CT mismatch.

In fact, given the promising results in terms of favorable and satisfactory outcome with the new ERIC retrieval device (mRS ≤2, 33.3%; mRS ≤3, 58.3% at 90 days), even in the light of a comparatively longer onset-to-treatment time by using advanced imaging protocols, the new ERIC adds a great asset to the existing armamentarium of recanalization devices. In addition, it further encourages research dealing with the use of advanced imaging techniques for patient selection.

Also in terms of safety, the ERIC appeared to be reliable and was free of intraprocedural complications. The rate of sICH (8.3%) during hospitalization was comparable with that in previously reported trials using mechanical thrombectomy devices (On-line Table 2). Most interesting, all 3 sICHs in our pilot study occurred after the intervention and were associated with intravenous thrombolysis, successful recanalization, massive edema formation, and the need for decompressive surgery, indicating a common mechanism with underlying blood-brain barrier disruption.

Conscious sedation was chosen if possible. General anesthesia was required in 13/36 patients due to persisting vomiting, agitation, or impaired consciousness. However, the best anesthesiology management in endovascular stroke therapy is not known to date and is being investigated in a large randomized controlled trial (https://www.clinicaltrials.gov/; Sedation vs. Intubation for Endovascular Stroke TreAtment [SIESTA], NCT 02126085).

Our pilot study certainly has some limitations: the retrospective monocenter single-arm design, a rather small number of patients, and the lack of formally independent assessment of TICI score and procedural complications. Thus, the results should be interpreted with caution.

However, to our knowledge, this is the first report on consecutive patients with stroke treated with the new ERIC retrieval device. Our findings support the safety and effectiveness of mechanical thrombectomy in terms of vessel recanalization and show a clinical benefit. Moreover, despite the rather extended period from stroke onset to intervention and the lower rate of IVT, our results are promising and in line with previously published data by using other recanalization devices with a shorter time to treatment and higher rates of IVT.

After the stunning results of the Interventional Management of Stroke (IMS) III trial, SYNTHESIS expansion, and Mechanical Retrieval and Recanalization of Stroke Clots Using Embolectomy (MR RESCUE) trials,[17-19] showing no benefit of endovascular treatment compared with standard care including IVT, the news from the latest trials, ie, MR CLEAN,[11] ESCAPE,[13] EXTEND-IA,[14] SWIFT PRIME,[15] and REVASCAT, [12] clearly demonstrated the safety and effectiveness of an intra-arterial approach for acute stroke treatment in selected patients within the first hours of symptom onset.

CONCLUSIONS

The new ERIC retrieval device appears to be technically safe and effective in removing thrombi in large-vessel occlusion. Moreover, despite substantial focal neurologic deficits on admission and an onset-to-treatment time of, on average, >6 hours (mean, 6 hours 13 minutes; median, 4 hours 57 minutes), almost one-third of patients achieved an independent functional outcome

and almost 60% were ambulatory without help 90 days after the ischemic event.

ACKNOWLEDGMENTS

We appreciate the professional cooperation of physicians, nurses, and technical assistants from the Departments of Anesthesiology, Neuroradiology, and Neurology in the specialized treatment of our patients with stroke.

Disclosures: Michael Diepers—*UNRELATED*: *Consultancy*: TETEC AG, Reutlingen, *Comments*: no connections to stroke therapies. Krassen Nedeltchev—*UNRELATED*: *Board Membership*: Advisory Boards: Bayer (Schweiz) AG, Boehringer Ingelheim (Schweiz) GmbH, Bristol Myers Squibb, Pfizer, AstraZeneca AG, GlaxoSmithKline, St. Jude Medical, Lundbeck (Schweiz) AG, Medtronic (Schweiz) AG, Sanofi-Aventis (Schweiz) AG, Genzyme, Shire, Biogen-Idec, Merck Serono, Teva Pharmaceutical Industries Ltd, Novartis Pharmaceuticals; *Grants/Grants Pending*: Swiss National Research Foundation, Swiss Heart Foundation, Research Council of the Cantonal Hospital of Aarau, *Comments*: grants outside the scope of the present work; *Payment for Lectures (including service on Speakers Bureaus)*: Speakers Bureaus: Boehringer Ingelheim (Schweiz) GmbH, Bristol Myers Squibb, Pfizer, AstraZeneca AG, St. Jude Medical, Teva Pharmaceutical Industries Ltd.

REFERENCES

1. Rha JH, Saver JL. **The impact of recanalization on ischemic stroke outcome: a meta-analysis.** *Stroke* 2007;38:967–73 CrossRef Medline
2. The Neurological Disorers and Stroke rt-PA Stroke Study Group. **Tissue plasminogen activator for acute ischemic stroke: Neurological Disorders and Stroke rt-PA Stroke Study Group.** *N Engl J Med* 1995;333:1581–87 CrossRef Medline
3. Hacke W, Kaste M, Bluhmki E, et al; ECASS Investigators. **Thrombolysis with alteplase 3 to 4.5 hours after acute ischemic stroke.** *N Engl J Med* 2008;359:1317–29 CrossRef Medline
4. Saqqur M, Uchino K, Demchuk AM, et al; CLOTBUST Investigators. **Site of arterial occlusion identified by transcranial Doppler predicts the response to intravenous thrombolysis for stroke.** *Stroke* 2007;38:948–54 CrossRef Medline
5. Jansen O, Rohr A. **Neurothrombectomy in the treatment of acute ischaemic stroke.** *Nat Rev Neurol* 2013;9:645–52 CrossRef Medline
6. Spiotta AM, Chaudry MI, Hui FK, et al. **Evolution of thrombectomy approaches and devices for acute stroke: a technical review.** *J Neurointerv Surg* 2015;7:2–7 CrossRef Medline
7. Ribo M, Molina CA, Jankowitz B, et al. **Stentrievers versus other endovascular treatment methods for acute stroke: comparison of procedural results and their relationship to outcomes.** *J Neurointerv Surg* 2014;6:265–69 CrossRef Medline
8. Nogueira RG, Lutsep HL, Gupta R, et al; TREVO 2 Trialists. **Trevo versus Merci retrievers for thrombectomy revascularisation of large vessel occlusions in acute ischaemic stroke (TREVO 2): a randomised trial.** *Lancet* 2012;380:1231–40 CrossRef Medline
9. Saver JL, Jahan R, Levy EI, et al; SWIFT Trialists. **Solitaire flow restoration device versus the Merci retriever in patients with acute ischaemic stroke (SWIFT): a randomised, parallel-group, non-inferiority trial.** *Lancet* 2012;380:1241–49 CrossRef Medline
10. Nedeltchev K, Pattynama PM, Biaminoo G, et al; DEFINE Group. **Standardized definitions and clinical endpoints in carotid artery and supra-aortic trunk revascularization trials.** *Catheter Cardiovasc Interv* 2010;76:333–44 CrossRef Medline
11. Berkhemer OA, Fransen PS, Beumer D, et al. **A randomized trial of intraarterial treatment for acute ischemic stroke.** *N Engl J Med* 2015; 372:11–20 CrossRef Medline
12. Jovin TG, Chamorro A, Cobo E, et al; REVASCAT Trial Investigators. **Thrombectomy within 8 hours after symptom onset in ischemic stroke.** *N Engl J Med* 2015;372:2296–306 CrossRef Medline
13. Goyal M, Demchuk AM, Menon BK, et al; ESCAPE Trial Investigators. **Randomized assessment of rapid endovascular treatment of ischemic stroke.** *N Engl J Med* 2015;372:1019–30 CrossRef Medline
14. Campbell BC, Mitchell PJ, Kleinig TJ, et al; EXTEND-IA Investigators. **Endovascular therapy for ischemic stroke with perfusion-imaging selection.** *N Engl J Med* 2015;372:1009–18 CrossRef Medline
15. Saver JL, Goyal M, Bonafe A, et al; SWIFT PRIME Investigators. **Stent-retriever thrombectomy after intravenous t-PA vs. t-PA alone in stroke.** *N Engl J Med* 2015;372:2285–95 CrossRef Medline
16. Adams HP Jr, Davis PH, Leira EC, et al. **Baseline NIH Stroke Scale score strongly predicts outcome after stroke: a report of the Trial of Org 10172 in Acute Stroke Treatment (TOAST).** *Neurology* 1999;53: 126–31 CrossRef Medline
17. Broderick JP, Palesch YY, Demchuk AM, et al; Interventional Management of Stroke (IMS) III Investigators. **Endovascular therapy after intravenous t-PA versus t-PA alone for stroke.** *N Engl J Med* 2013;368:893–903 CrossRef Medline
18. Ciccone A, Valvassori L, Nichelatti M, et al; SYNTHESIS Expansion Investigators. **Endovascular treatment for acute ischemic stroke.** *N Engl J Med* 2013;368:904–13 CrossRef Medline
19. Kidwell CS, Jahan R, Gornbein J, et al; MR RESCUE Investigators. **A trial of imaging selection and endovascular treatment for ischemic stroke.** *N Engl J Med* 2013;368:914–23 CrossRef Medline
20. Wardlaw JM, Murray V, Berge E, et al. **Recombinant tissue plasminogen activator for acute ischaemic stroke: an updated systematic review and meta-analysis.** *Lancet* 2012;379:2364–72 CrossRef Medline
21. Furlan A, Higashida R, Wechsler L, et al. **Intra-arterial prourokinase for acute ischemic stroke: the PROACT II study: a randomized controlled trial—Prolyse in Acute Cerebral Thromboembolism.** *JAMA* 1999;282:2003–11 CrossRef Medline
22. Ogawa A, Mori E, Minematsu K, et al; MELT Japan Study Group. **Randomized trial of intraarterial infusion of urokinase within 6 hours of middle cerebral artery stroke: the middle cerebral artery embolism local fibrinolytic intervention trial (MELT) Japan.** *Stroke* 2007;38:2633–39 CrossRef Medline
23. IMS Study Investigators. **Combined intravenous and intra-arterial recanalization for acute ischemic stroke: the Interventional Management of Stroke Study.** *Stroke* 2004;35:904–11 CrossRef Medline
24. IMS II Trial Investigators. **The Interventional Management of Stroke (IMS) II Study.** *Stroke* 2007;38:2127–35 CrossRef Medline
25. Mazighi M, Serfaty JM, Labreuche J, et al; RECANALISE investigators. **Comparison of intravenous alteplase with a combined intravenous-endovascular approach in patients with stroke and confirmed arterial occlusion (RECANALISE study): a prospective cohort study.** *Lancet Neurol* 2009;8:802–09 CrossRef Medline
26. Smith WS, Sung G, Starkman S, et al; MERCI Trial Investigators. **Safety and efficacy of mechanical embolectomy in acute ischemic stroke: results of the MERCI trial.** *Stroke* 2005;36:1432–38 CrossRef Medline
27. Smith WS, Sung G, Saver J, et al. **Mechanical thrombectomy for acute ischemic stroke: final results of the Multi MERCI trial.** *Stroke* 2008;39:1205–12 CrossRef Medline
28. Penumbra Pivotal Stroke Trial Investigators. **The Penumbra pivotal stroke trial: safety and effectiveness of a new generation of mechanical devices for clot removal in intracranial large vessel occlusive disease.** *Stroke* 2009;40:2761–68 CrossRef Medline
29. Menon BK, Hill MD, Eesa M, et al. **Initial experience with the Penumbra stroke system for recanalization of large vessel occlusions in acute ischemic stroke.** *Neuroradiology* 2011;53:261–66 CrossRef Medline
30. Castaño C, Dorado L, Guerrero C, et al. **Mechanical thrombectomy with the Solitaire AB device in large artery occlusions of the anterior circulation: a pilot study.** *Stroke* 2010;41:1836–40 CrossRef Medline
31. Roth C, Papanagiotou P, Behnke S, et al. **Stent-assisted mechanical recanalization for treatment of acute intracerebral artery occlusions.** *Stroke* 2010;41:2559–67 CrossRef Medline
32. Miteff F, Faulder KC, Goh AC, et al. **Mechanical thrombectomy with a self-expanding retrievable intracranial stent (Solitaire AB): experience in 26 patients with acute cerebral artery occlusion.** *AJNR Am J Neuroradiol* 2011;32:1078–81 CrossRef Medline

33. Wehrschuetz M, Wehrschuetz E, Augustin M, et al. **Early single center experience with the Solitaire thrombectomy device for the treatment of acute ischemic stroke.** *Interv Neuroradiol* 2011;17:235–40 Medline
34. Dorn F, Stehle S, Lockau H, et al. **Endovascular treatment of acute intracerebral artery occlusions with the Solitaire stent: single-centre experience with 108 recanalization procedures.** *Cerebrovasc Dis* 2012;34:70–77 CrossRef Medline
35. Pereira VM, Gralla J, Davalos A, et al. **Prospective, multicenter, single-arm study of mechanical thrombectomy using Solitaire Flow Restoration in acute ischemic stroke.** *Stroke* 2013;44:2802–07 CrossRef Medline
36. San Román L, Obach V, Blasco J, et al. **Single-center experience of cerebral artery thrombectomy using the TREVO device in 60 patients with acute ischemic stroke.** *Stroke* 2012;43:1657–59 CrossRef Medline
37. Mendonça N, Flores A, Pagola J, et al. **Trevo system: single-center experience with a novel mechanical thrombectomy device.** *J Neuroimaging* 2013;23:7–11 CrossRef Medline
38. Rohde S, Haehnel S, Herweh C, et al. **Mechanical thrombectomy in acute embolic stroke: preliminary results with the Revive device.** *Stroke* 2011;42:2954–56 CrossRef Medline
39. Kurre W, Aguilar-Pérez M, Schmid E, et al. **Clinical experience with the pREset stent retriever for the treatment of acute ischemic stroke: a review of 271 consecutive cases.** *Neuroradiology* 2014;56:397–403 CrossRef Medline

3D Printing of Intracranial Aneurysms Using Fused Deposition Modeling Offers Highly Accurate Replications

A.M.J. Frölich, J. Spallek, L. Brehmer, J.-H. Buhk, D. Krause, J. Fiehler, and A. Kemmling

ABSTRACT

BACKGROUND AND PURPOSE: As part of a multicenter cooperation (Aneurysm-Like Synthetic bodies for Testing Endovascular devices in 3D Reality) with focus on implementation of additive manufacturing in neuroradiologic practice, we systematically assessed the technical feasibility and accuracy of several additive manufacturing techniques. We evaluated the method of fused deposition modeling for the production of aneurysm models replicating patient-specific anatomy.

MATERIALS AND METHODS: 3D rotational angiographic data from 10 aneurysms were processed to obtain volumetric models suitable for fused deposition modeling. A hollow aneurysm model with connectors for silicone tubes was fabricated by using acrylonitrile butadiene styrene. Support material was dissolved, and surfaces were finished by using NanoSeal. The resulting models were filled with iodinated contrast media. 3D rotational angiography of the models was acquired, and aneurysm geometry was compared with the original patient data.

RESULTS: Reproduction of hollow aneurysm models was technically feasible in 8 of 10 cases, with aneurysm sizes ranging from 41 to 2928 mm^3 (aneurysm diameter, 3–19 mm). A high level of anatomic accuracy was observed, with a mean Dice index of 93.6% ± 2.4%. Obstructions were encountered in vessel segments of <1 mm.

CONCLUSIONS: Fused deposition modeling is a promising technique, which allows rapid and precise replication of cerebral aneurysms. The porosity of the models can be overcome by surface finishing. Models produced with fused deposition modeling may serve as educational and research tools and could be used to individualize treatment planning.

ABBREVIATIONS: FDM = fused deposition modeling; ID = identification

Endovascular aneurysm treatment is a continuously evolving field in which new treatment modalities are rapidly being developed and techniques are being refined, such as the recent introduction of intravascular flow diverters and intrasaccular flow disruptors.[1,2] The safe and effective practice of endovascular neuroradiology demands an intimate understanding of the way devices work and interact with a given patient's vascular anatomy. In this regard, vascular models provide an ideal environment to allow familiarization with a given device.[3] In addition, specific treatment challenges can be created to assess the behavior of devices in predefined situations. To enhance the applicability of such models for dedicated research and open the field of patient-individualized treatment planning, we aimed to develop patient-individual, anatomically precise vascular models that can be accessed with clinical endovascular devices. Multiple previous investigations have described the production of vascular models based on silicone casts.[4-8] As part of a multicenter cooperation (Aneurysm-Like Synthetic bodies for Testing Endovascular devices in 3D Reality), we systematically assessed the technical feasibility and accuracy of different additive manufacturing methods for this purpose. With the primary goal of increasing production speed and decreasing costs, we evaluated the method of fused deposition modeling (FDM) for the production of hollow aneurysm models. The FDM material extrusion technology is one of the most widely installed and least cost-intensive among several additive manufacturing techniques.[9] Our goal was to assess the

Received May 8, 2015; accepted after revision June 17.

From the Department of Diagnostic and Interventional Neuroradiology (A.M.J.F., L.B., J.-H.B., J.F., A.K.), University Medical Center Hamburg-Eppendorf, Hamburg, Germany; and Technical University Hamburg-Harburg (D.K., J.S.), Institute of Product Development and Mechanical Engineering Design, Hamburg, Germany.

This work was supported by a grant from the Forschungszentrum Medizintechnik Hamburg.

Preliminary data on 4 aneurysm models were previously presented at: Annual Meeting of the German Society for Neuroradiology, October 23–25, 2014; Cologne, Germany.

Please address correspondence to Andreas M.J. Frölich, MD, Department of Diagnostic and Interventional Radiology, University Medical Center Hamburg-Eppendorf, Martinistr 52, 20246 Hamburg, Germany; e-mail: a.froelich@gmail.com

http://dx.doi.org/10.3174/ajnr.A4486

Aneurysm and model characteristics

Model ID	Aneurysm Geometry and Location	Patient Aneurysm Volume (mm^3)	Model Aneurysm Volume (mm^3)	Dice Index of Similarity (%)
A	Saccular, basilar tip	68.0	69.8	94.6%
B	Saccular, ICA	220.2	180.1	90.0%
C	Fusiform, ICA	731.8	722.5	91.7%
D	Saccular, VA	278.0	263.4	95.9%
E	Giant, ICA	2927.3	2843.0	97.3%
F	Fusiform, VA	62.9	NA	NA
G	Saccular, ACA	36.9	40.9	91.3%
H	Saccular, AICA	23.9	NA	NA
I	Saccular, ICA	153.6	153.6	95.3%
J	Saccular, ACA	145.5	160.0	92.5%

Note:—ACA indicates anterior cerebral artery; VA, vertebral artery; NA, not applicable.

principal technical feasibility of FDM aneurysm model production and determine the geometric accuracy of the model and its potential use for treatment simulations.

MATERIALS AND METHODS

Study Design

In this institutional review board–approved, single-center, retrospective study with waived individual consent, 3D rotational angiographic data from 10 aneurysms were manually selected to represent common aneurysm configurations. We included saccular ($n = 7$), fusiform ($n = 2$), and giant ($n = 1$) aneurysms with different dimensions and neck configurations (Table).

Image Acquisition

All clinical 3D rotational angiography data were acquired by using an Allura Xper FD 20/20 angiography system (Philips Healthcare, Best, the Netherlands) with the following acquisition parameters: 5-second-rotational acquisition, 220° rotation, 150 single frames at a frame rate of 30/s, 15- to 48-cm-detector FOV, 512 acquisition matrix. Images were reconstructed by using a soft-tissue kernel with an isotropic voxel size (edge length range, 0.1–0.3 mm).

Model Fabrication

After patient selection, all image data were anonymized. 3D rotational angiographic data were processed by using Analyze software, Version 11.0 (AnalyzeDirect, Overland Park, Kansas). Vessels were segmented semiautomatically with supervision by using a region-growing algorithm with seeds placed in main arteries proximal to the aneurysm. Redundant vascular structures were isolated and stripped to finally obtain binary images representing the aneurysm and a short segment of the adjacent parent vessel. Small vascular branches such as the anterior choroidal artery were digitally shortened or removed if not immediately relevant to the aneurysm access route, to improve the physical stability of the models. Binary images of segmented vessels were inverted to obtain a vessel lumen model and converted to volumetric surface files suitable for additive manufacturing. Connectors for silicone tubes were digitally attached with the software CATIA V5 (Dassault Systèmes SA, Vélizy-Villacoublay, France). Using a Designjet Color 3D printer (Hewlett-Packard Development Company, Palo Alto, California), we fabricated a hollow aneurysm model from acrylonitrile butadiene styrene with 254-μm-layer thickness. Support material was removed mechanically and dissolved by using the Designjet 3D Removal System (Hewlett-Packard Development Company). Surfaces needed to be finished to overcome the inherent porosity of the raw models. We used 2 different methods for surface finishing: 1) placing the models in an acetone vapor bath for 90–120 seconds, and 2) infiltrating the models in a water-based impregnation agent NanoSeal (JELN Imprägnierung GmbH, Schwalmstadt, Germany) for 15 minutes. The final models used for analysis were finished by using NanoSeal.

Model Evaluation

The resulting models were connected to silicone tubing and filled with iodinated contrast media (iopamidol, Iomeron 150; Bracco, Milan, Italy). 3D rotational angiography of the models was acquired on an Allura Xper FD 20 angiography system. Acquisition parameters were identical to the those in the clinical scan, with the exception of a fixed-detector FOV of 15 cm.

The resulting images were again transformed to binary images and then coregistered with the original patient images by using a semiautomatic, rigid transformation matrix in Analyze 11.0. The volume of overlapping voxels was calculated. Aneurysm volumes were obtained and compared by using a paired t test. The Dice index, which relates the amount of overlap to the overall object size, was calculated as a measure of anatomic precision of the models as follows: $S = (2 \times OL) / (A + B)$, where A and B are the aneurysm volumes in the model and patient data, OL is the volume of overlapping voxels, and S is the index of similarity, which ranges from zero for no overlap to 1 for identical, completely overlapping geometries. In addition, we subjectively compared aneurysm and parent vessel configuration for any noticeable differences in geometry. Contrast material leakage through porous parts of the models was noted, if present. Statistical analyses were performed by using MedCalc for Windows, Version 13 (MedCalc Software, Mariakerke, Belgium).

RESULTS

Aneurysm Characteristics

Morphologic characteristics of all aneurysms and corresponding vascular models are summarized in the Table. Model fabrication typically took approximately 3–6 days: Image segmentation and preparation took approximately 1–2 hours, the printing process took 2–5 hours, removal of support material required 1–3 days (depending on the geometric complexity of the model), and finally, 1–2 further days were required for infusion of NanoSeal and drying. Among the selected aneurysm geometries, models could be successfully produced in 8 of 10 cases. In the remaining 2 cases, vascular segments in the access path or distal to the aneurysm were occluded. Occlusion occurred only in vascular segments with a diameter of <1 mm. The corresponding aneurysms were a 2-mm AICA aneurysm, which was not completely patent after manufacturing, and a 4-mm aneurysm arising from a hypoplastic V4 segment of the vertebral artery, measuring <1 mm; this vessel segment was occluded.

After manufacturing and removal of support material, the models were permeable to water. Surface finishing with both acetone vapor and infiltration made the models impermeable. However, some leakage of contrast occurred at the tube connectors with some of the models finished by using acetone vapor due

to loss of contour of the tube connectors during the finishing process. All models in the final analysis were finished by using NanoSeal infiltration.

Anatomic Precision

Aneurysms with volumes ranging from 40.9 to 2927.3 mm^3 and maximum diameters ranging from 3 to 19 mm were successfully reproduced (Figs 1 and 2). Mean aneurysm volumes were not significantly different for patient data versus vascular models (570 and 540 mm^3, $P = .2$). The mean Dice index was 93.6% ± 2.4%. In 1 model, a small bleb on the aneurysm surface was observed, related to an imperfection in the fabrication process and was similar in appearance to a small daughter aneurysm. No other significant anatomic discrepancies were observed. No contrast leakage of the model wall was observed in the models produced for the final analysis. Integration of the models into a vascular model with flow was easy, and models could be accessed with a microcatheter. Due to the surface properties, wire and catheter navigation within the models was somewhat impeded by a relatively high friction.

DISCUSSION

The current analysis shows that aneurysm models produced with FDM offer a high level of accuracy. The method is applicable over a wide range of aneurysm geometries and sizes. After surface finishing, the models are rendered impermeable to water and can be easily incorporated into vascular flow models; the incorporation is facilitated by the digital addition of tube connectors. The resulting setup can be used to familiarize operators with a specific aneurysm geometry or to study the behavior of vascular implants in a given anatomy. Vessel segments <1 mm were not reliably reproduced or were obstructed; this problem may be related to the printer and building material used and the surface-finishing procedure. It may represent a limitation of the FDM technique for manufacturing very small vascular branches and aneurysms. Currently available printers offer layer thicknesses below the 254-μm-layer thickness used in our project, which may allow manufacturing of even small vascular branches that were not patent with our current approach, but the current lower range is approximately 100 μm (eg, 127 μm on the Fortus printer; Stratasys, Eden Prairie, Minnesota). This range may be a drawback of FDM compared with other manufacturing methods, such as stereolithography and material jetting, which offer spatial resolutions of approximately 25 μm. Another limitation of FDM is the relatively slow build speed due to the inertia of the plotting heads and the required frequent changes in direction of the plotting heads.[10]

Advantages of FDM include the wide availability and relatively low cost of printers and building materials. One of the most interesting roles for additive manufacturing in interventional neuroradiology is the idea of in-hospital, on-demand production of aneurysm models directly available to physicians involved in aneurysm treatment. Our data show that FDM is principally suitable for this purpose but needs to be further compared with other additive manufacturing techniques for aneurysm model production.

Previously described neurovascular models have commonly used silicone; these models are typically produced by using a dissolvable core and casting liquid silicone around it.[3,5] For patient-specific models, the core can be produced as a solid replica of the vessel lumen by direct additive manufacturing or by producing a mold that is then used to obtain wax replicas of the vessel lumen, which can be subsequently coated with silicone to produce the final model.[5,7,8] This multistep manufacturing process has been reported to last approximately 2 weeks,[4] whereas direct manufacturing of hollow models by using FDM and surface finishing in our study took approximately 3–6 days. If surface finishing could be avoided, possibly with new building materials, production speed may be further increased. The continuing development of additive manufacturing machines and technologies, such as printing a single object with different building materials,[11] will further expand the tools available for producing vascular models and necessitates continuous evaluation of different printers and techniques.

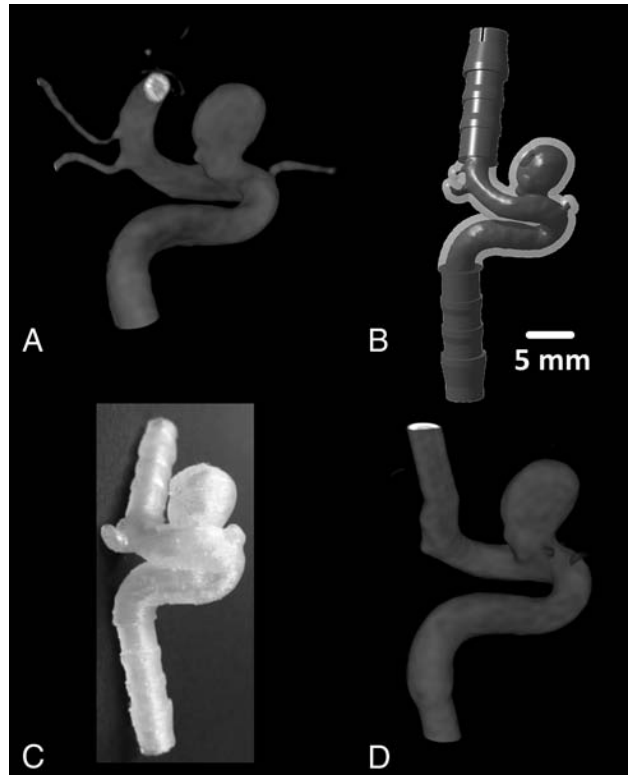

FIG 1. Model construction. In this case of a saccular supraophthalmic ICA aneurysm (model identification [ID] B), panels demonstrate 3D rotational angiography from the original patient data (*A*), the digitized model with attached silicone tube connectors (*B*), a photograph of the resulting FDM model (*C*), and 3D rotational angiography obtained from this model (*D*).

Not all aneurysm geometries could be successfully produced. Particularly small vessel segments with an inner diameter of <1 mm were prone to short-segmental occlusions (Fig 3). Due to the layer-by-layer manufacturing process, vessel segments that run diagonally to the x–y plane of the model are particularly susceptible to these occlusions, while those running parallel to the z-axis should be less affected. Due to the complex geometry of the aneurysm models, occlusions can be difficult to predict. A different potential cause of interior occlusions or alteration of the interior surface is residue after surface finishing. Imperfections of the inner surface can impede wire and catheter movement and promote turbulent flow, which could affect hemodynamic measurements

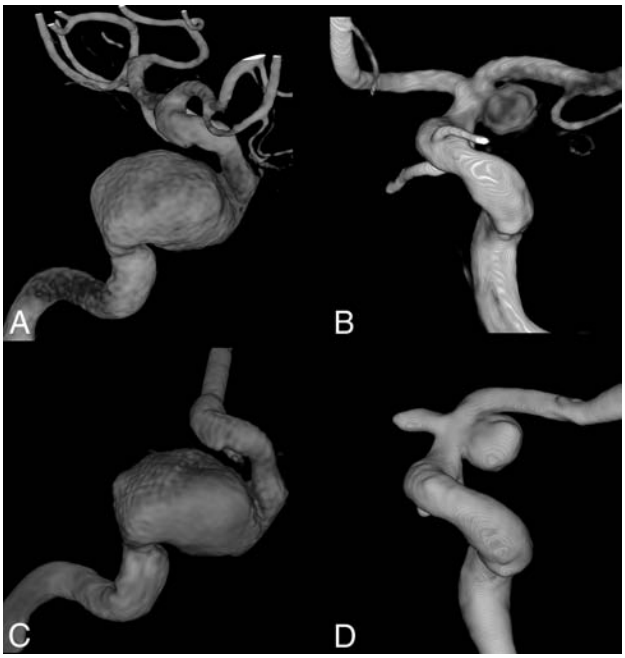

FIG 2. Sample aneurysm geometries. 3D rotational angiography demonstrates a giant fusiform ICA aneurysm (model ID E, *left*) and a supraophthalmic saccular ICA aneurysm (model ID A, *right*). Patient anatomy (*A* and *B*) and corresponding vascular models (*C* and *D*) are shown. Note that the anterior cerebral artery was purposely shortened in model ID A.

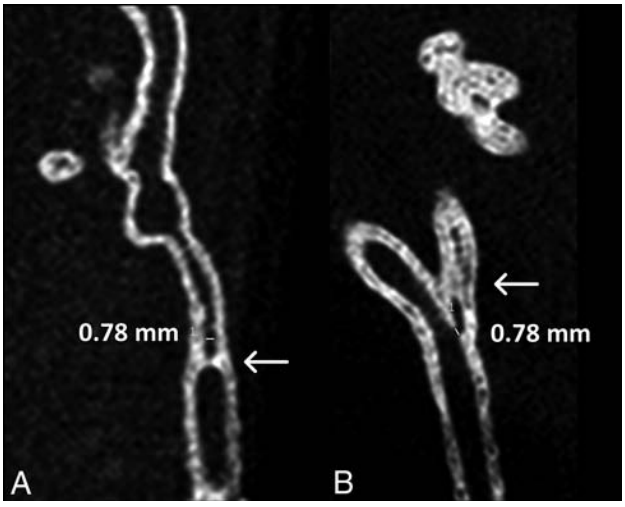

FIG 3. Small vascular branch occlusions. Multiplanar reformation from nonenhanced 3D rotational angiography of model ID F (*A*) shows a short-segment occlusion (*arrow*) of the lumen. A similar, somewhat longer occlusion was encountered in model ID H (*arrow* in *B*).

performed in the models compared with the real endothelial surface.

Another limitation of the current models is the use of a semitranslucent building material. This currently restricts their use to an environment with fluoroscopic capabilities because catheter movement can barely be directly observed through the material; thus, the use of camera equipment instead of fluoroscopy is not currently feasible. However, transparent building materials for FDM are available commercially, and their use for aneurysm models should be further assessed. Other additive manufacturing methods, such as stereolithography, may offer an improved transparency and higher spatial resolution compared with FDM due to differences in optical properties of the resulting models.[10] Another limitation of the presented approach is the rigidity of the models. This means they will not realistically respond to catheter or coil forces, limiting the degree of realism when simulating procedures such as coil embolization. A growing understanding of the forces that occur inside the aneurysm and catheters during endovascular procedures[12] and the mechanical properties of the vessel wall[5] will help define the required properties for producing elastic aneurysm models with 3D printing.

Several critical parts of neurointerventional procedures depend heavily on the elasticity of the anatomic structures, such as the dislocation of catheters or coils, rupture of the aneurysm, and movement of vessels in the access path. Accurate replication of these properties will greatly increase the degree of realism. Elastic building materials are available for different additive manufacturing techniques including FDM, and their properties should be assessed. A further limitation of our study is its retrospective design with manual selection of different aneurysm morphologies. However, this approach allowed us to assess the feasibility of the technique by using a relatively small sample.

The clinical goal for the development of vascular models is improvement of patient safety by helping physicians acquire and maintain the necessary interventional skills. Apart from using physical models, neurointerventional procedures can also be practiced by using commercially available virtual reality simulators, which generate angiography-like images in a computer simulation controlled by specialized catheters and wires. The advantages of this approach are its great flexibility, broad range of available procedures, and practically limitless repeatability.[13] However, haptic feedback is limited, and the behavior of catheters, coils, and other implants is simulated; these features severely affect the degree of realism, particularly in critical situations such as dislocation of implants and catheters. Furthermore, each device has to be specifically integrated into the simulation; this step limits the available interventional tools. In this regard, physical vascular models offer the advantage of using real catheter materials with realistic haptic feedback, which allows detailed studies of catheter and implant behavior. To our knowledge, no study exists directly comparing the effects of training for neurointerventional procedures with virtual reality simulators versus vascular models. Further assessment of the way these training environments help develop and maintain procedural skills and evaluation of their impact on procedural duration and complications seem highly promising targets for improving patient safety.

Possibly the most exciting prospect for patient-individual models is the idea of individualized treatment planning. If it could be shown that coils and other implants behave similarly in a 3D model compared with reality, an entire neurointerventional procedure could be performed in vitro to help plan the actual operation. The principal feasibility of this technique has recently been demonstrated by using a patient-specific silicone model.[4] This approach may offer exciting advances with regard to patient safety. For inclusion into clinical practice, the speed of production and the cost of the models will be highly relevant, which may argue in favor of additive manufacturing over silicone-based

model manufacturing. Furthermore, the ability to repetitively "treat" an individual aneurysm model or treat several models of the same aneurysm in parallel with different therapeutic approaches could improve our understanding of the suitability of the plethora of currently available aneurysm treatment modalities and may help in standardizing indications. An increased use of vascular models may also reduce the need for using animals as part of neurointerventional training courses and for a variety of research endeavors.

CONCLUSIONS

Hollow aneurysm models manufactured by FDM offer a high level of anatomic accuracy and can be easily integrated into vascular flow models for training and research purposes. Further assessment of FDM and comparison with other additive manufacturing techniques seems promising, particularly regarding the use of elastic and transparent building materials and the behavior of the models during simulated procedures.

Disclosures: Andreas M.J. Frölich—*RELATED*: Forschungszentrum Medizintechnik,* *Comments*: The work was supported by a grant from the Forschungszentrum Medizintechnik Hamburg, Hamburg, Germany; *UNRELATED*: *Payment for Lectures (including service on Speakers Bureaus)*: speaker's honoraria from Siemens, Forchheim, Germany. Jan-Hendrik Buhk—*UNRELATED*: *Board Membership*: Clinical Advisory Board, Codman Neurovascular. Jens Fiehler—*RELATED*: *Grant*: BMBF, Hansestadt Hamburg.* *Money paid to the institution.

REFERENCES

1. Papagiannaki C, Spelle L, Januel AC, et al. **WEB intrasaccular flow disruptor—prospective, multicenter experience in 83 patients with 85 aneurysms.** *AJNR Am J Neuroradiol* 2014;35:2106–11 CrossRef Medline
2. Brinjikji W, Murad MH, Lanzino G, et al. **Endovascular treatment of intracranial aneurysms with flow diverters: a meta-analysis.** *Stroke* 2013;44:442–47 CrossRef Medline
3. Paramasivam S, Baltsavias G, Psatha E, et al. **Silicone models as basic training and research aid in endovascular neurointervention: a single-center experience and review of the literature**. *Neurosurg Rev* 2014;37:331–37; discussion 337 CrossRef Medline
4. Kono K, Shintani A, Okada H, et al. **Preoperative simulations of endovascular treatment for a cerebral aneurysm using a patient-specific vascular silicone model.** *Neurol Med Chir (Tokyo)* 2013;53:347–51 CrossRef Medline
5. Chueh JY, Wakhloo AK, Gounis MJ. **Neurovascular modeling: small-batch manufacturing of silicone vascular replicas.** *AJNR Am J Neuroradiol* 2009;30:1159–64 CrossRef Medline
6. Wetzel SG, Ohta M, Handa A, et al. **From patient to model: stereolithographic modeling of the cerebral vasculature based on rotational angiography.** *AJNR Am J Neuroradiol* 2005;26:1425–27 Medline
7. Suzuki Y, Fujitsuka M, Chaloupka JC. **Simulation of endovascular neurointervention using silicone models: imaging and manipulation.** *Neurol Med Chir (Tokyo)* 2005;45:567–72; discussion 572–73 CrossRef Medline
8. Knox K, Kerber CW, Singel SA, et al. **Rapid prototyping to create vascular replicas from CT scan data: making tools to teach, rehearse, and choose treatment strategies.** *Catheter Cardiovasc Interv* 2005;65:47–53 CrossRef Medline
9. Wohlers T. *Wohlers Report 2014: Additive Manufacturing and 3D Printing State of the Industry—Annual Worldwide Progress Report*. Fort Collins: Wohlers Associates; 2014
10. Gibson I, Rosen D, Stucker B. *Additive Manufacturing Technologies: 3D Printing, Rapid Prototyping, and Direct Digital Manufacturing*. New York: Springer; 2015
11. Wurm G, Lehner M, Tomancok B, et al. **Cerebrovascular biomodeling for aneurysm surgery: simulation-based training by means of rapid prototyping technologies.** *Surg Innov* 2011;18:294–306 CrossRef Medline
12. Lamano JB, Bushnell GG, Chen H, et al. **Force characterization of intracranial endovascular embolization: coil type, microcatheter placement, and insertion rate**. *Neurosurgery* 2014;75:707–15; discussion 715–16 CrossRef Medline
13. Ahmed K, Keeling AN, Fakhry M, et al. **Role of virtual reality simulation in teaching and assessing technical skills in endovascular intervention.** *J Vasc Interv Radiol* 2010;21:55–66 CrossRef Medline

Therapeutic Internal Carotid Artery Occlusion for Large and Giant Aneurysms: A Single Center Cohort of 146 Patients

R.S. Bechan, C.B. Majoie, M.E. Sprengers, J.P. Peluso, M. Sluzewski, and W.J. van Rooij

ABSTRACT

BACKGROUND AND PURPOSE: At our institution, patients with large or giant ICA aneurysms are preferably treated with endovascular ICA balloon occlusion. Alternative treatment or conservative treatment is offered only for patients who cannot tolerate permanent ICA occlusion. In this observational study, we report the clinical and imaging results of ICA occlusion for aneurysms in a large single-center patient cohort.

MATERIALS AND METHODS: Between January 1995 and January 2015, occlusion of the ICA was considered in 146 patients with large or giant ICA aneurysms. Ninety-six patients (66%) passed the angiographic test occlusion, and, in 88 of these 96 patients (92%), the ICA was permanently occluded. In 11 of 88 patients with angiographic tolerance, ICA occlusion was performed with the patient under general anesthesia without clinical testing.

RESULTS: There was 1 hypoperfusion infarction after hypovolemic shock from a large retroperitoneal hematoma (complication rate 1.1% [95% CI, 1%–6.8%]). The mean imaging and clinical follow-up was 35 months (median 18 months; range, 3–180 months). On the latest MR imaging, 87 of 88 aneurysms (99%) were completely occluded and 61 of 80 aneurysms (76%) were decreased in size or completely obliterated. Of 62 patients who presented with cranial nerve dysfunction by mass effect of the aneurysm, 30 (48%) were cured, 25 (40%) improved, 6 (10%) were unchanged, and 1 patient (2%) was hemiplegic after a complication.

CONCLUSIONS: ICA occlusion for large and giant aneurysms after angiographic test occlusion was safe and effective. Two-thirds of eligible patients passed the angiographic test. Most aneurysms shrunk, and most cranial nerve dysfunctions were cured or improved.

Large and giant aneurysms of the internal carotid artery can be located intradurally from the ophthalmic segment upward or extradurally in the cavernous sinus. Intradural aneurysms may be symptomatic by SAH or decreased visual acuity by mass effect on the optic nerve or chiasm. Large and giant cavernous sinus aneurysms may be symptomatic by mass effect on cranial nerves III–VII or by carotid cavernous fistula, epistaxis, or, rarely, SAH when ruptured.[1-3]

In general, treatment of large and giant ICA aneurysms is indicated after rupture to prevent recurrent SAH. Treatment is also indicated in symptomatic or asymptomatic unruptured intradural aneurysms to prevent first-time SAH or to alleviate symptoms of mass effect. Cavernous sinus aneurysms generally exhibit a benign clinical course. For both symptomatic and asymptomatic cavernous aneurysms, the risk profile of treatment should be balanced against the benign natural history.

Treatment of large and giant ICA aneurysms can be surgical, endovascular, or a combination. Surgery consists of direct clipping or bypass construction followed by parent ICA occlusion.[4,5] During the past decades, endovascular techniques have largely replaced surgery for these aneurysms. Endovascular treatment can consist of ICA balloon occlusion, selective coiling with or without balloon or stent assistance, or parent ICA reconstruction with flow diverters.[6-9]

At the Sint Elisabeth Ziekenhuis, therapeutic ICA occlusion has been the preferred treatment for large and giant ICA aneurysms since 1995, despite the availability in the last decade of new endovascular devices, such as stents and flow diverters, intended to spare the parent ICA. We report the clinical and imaging results of ICA occlusion for aneurysms in a large single-center patient cohort. Although some data of our cohort have been published previously, in this article we intend to give a comprehensive and complete overview of our results with narrowed confidence intervals.

Received May 5, 2015; accepted after revision June 8.

From Sint Elisabeth Ziekenhuis (R.S.B., J.P.P., M.S., W.J.v.R.), Tilburg, the Netherlands; and Academisch Medisch Centrum (C.B.M., M.E.S.), Amsterdam, the Netherlands.

Please address correspondence to W.J. van Rooij, PhD, Department of Radiology, Sint Elisabeth Ziekenhuis, Hilvarenbeekseweg 60, 5022GC Tilburg, the Netherlands; e-mail: wjjvanrooij@gmail.com

http://dx.doi.org/10.3174/ajnr.A4487

MATERIALS AND METHODS

General

The indication for treatment of large and giant ICA aneurysms was discussed jointly with neurosurgeons and neurologists. Treatment was tailored to the individual patient by accounting for clinical presentation, aneurysm characteristics, patient age, comorbidity, and the patient's wishes. At our institution, patients with large or giant ICA aneurysms were preferably treated with endovascular ICA balloon occlusion. Selective coiling, flow-diverter treatment, bypass surgery, or conservative therapy was offered only for patients who could not tolerate permanent ICA occlusion. Large or giant ICA aneurysms in patients who presented with SAH were generally coiled first to prevent secondary hemorrhage, and, in a later stage, ICA occlusion was considered as definitive therapy. ICA occlusion in the acute phase of SAH was preferably not performed because vasospasm could induce ischemic events by decreasing reserve capacity after ICA occlusion.

ICA Occlusion

The protocol for therapeutic ICA occlusion has been described previously.[10,11] In short, during ICA balloon test occlusion, angiography of the contralateral ICA and/or vertebral artery was performed to assess collateral flow via the anterior and posterior communicating arteries. Apart from clinical tolerance in awake patients, synchronous opacification of the cortical cerebral veins in the territories of the examined and occluded vessels was considered indicative of tolerance to permanent occlusion. We considered synchronicity if the relative delay in contrast filling of the cortical veins was ≤1 second (2 frames in an angiographic run of 2 frames/second). This was best appreciated in forward and backward cine-loop with enhanced image contrast. After tolerance was determined, the ICA was permanently occluded proximal to the aneurysm with detachable balloons (Gold Valve no. 16 balloon; Nycomed, Paris, France, or Balt, Montmorency, France) or, in a short period when balloons were not available, with detachable coils. Aneurysm trapping was never performed. In the second half of the study period, therapeutic ICA occlusion was also performed in selected patients under general anesthesia without clinical testing. After permanent ICA occlusion, the patient was monitored for 24 hours in a medium care unit with special attention to blood pressure and fluid balance.

Patients Without Tolerance for ICA Occlusion

Patients who could not tolerate ICA occlusion were discussed again in a joint meeting with neurosurgeons and neurologists. Bypass surgery, selective coiling with or without stent assistance, or flow-diverter treatment was offered in symptomatic patients or asymptomatic patients with intradural aneurysms. In selected patients with asymptomatic or symptomatic cavernous sinus aneurysms, conservative treatment was recommended.

Follow-Up Assessment

After ICA occlusion, MR imaging was performed within 72 hours to evaluate thrombosis of the aneurysm and to detect (clinically silent) ischemic events in the watershed areas. In addition to T1- and T2-weighted images, diffusion-weighted images were included in the protocol in later years. A clinical outpatient visit and MR imaging were scheduled at 3 months and, in many patients, at various intervals thereafter. A substantial proportion of patients were the subject of several long-term MR imaging follow-up studies.[12-15]

Location of 146 large and giant ICA aneurysms in 146 patients

Extradural	87 (60%)
Cavernous segment	86 (59%)
Petrosal segment	1 (1%)
Intradural	59 (40%)
Hypophyseal segment	15 (10%)
Ophthalmic segment	15 (10%)
Posterior communicating artery	4 (3%)
Supraclinoid ICA dissection	4 (3%)
Supraclinoid other	18 (12%)
ICA bifurcation	3 (2%)

Statistical Analysis

Quantitative variables were expressed as mean (standard deviation), and categoric variables were expressed as frequencies or percentages. Statistical analysis was performed with MedCalc statistical software (version 14.12.0; MedCalc Software, Mariakerke, Belgium).

RESULTS

Patients

Between January 1995 and January 2015 occlusion of the ICA was considered in 146 patients with large or giant ICA aneurysms. There were 126 women (86%) and 20 men (14%), with a mean age of 57.8 years (median, 59 years; range, 16–91 years). The locations of the 146 ICA aneurysms are displayed in the Table. There were 87 extradural aneurysms (60%) and 59 intradural aneurysms (40%).

Clinical presentation was oculomotor dysfunction in 74 (50%); SAH in 22 (15%); decreased visual acuity in 19 (13%); carotid cavernous fistula in 9 (6%); hemiplegia in 2 (1%); and trigeminal neuralgia, panhypopituitarism, and epistaxis each in 1 patient. In 17 patients (12%), the aneurysm was an incidental finding.

Patients with Tolerance for ICA Occlusion

Of 146 patients who underwent ICA test occlusion, venous filling was synchronous in 96 (66%). In 88 of these 96 patients (92%), the ICA was permanently occluded. In 11 of 88 patients with angiographic tolerance, ICA occlusion was performed with the patient under general anesthesia without clinical testing. Six patients with SAH were treated with coiling first and were later treated with ICA occlusion for the same aneurysm. Of the remaining 8 aneurysms in 8 patients, 6 were selectively coiled, 1 was treated with a flow diverter, and 1 was left untreated. In 7 of these 8 patients (6 with ruptured cavernous sinus aneurysms and 1 with carotid cavernous fistula), ICA test occlusion was performed before parent vessel sparing treatment in order to be informed beforehand about tolerance and the possibility of carotid sacrifice as a potential bailout during treatment.

Patients with Nontolerance for ICA Occlusion

In 50 of 146 patients (34%), cortical venous filling during ICA test occlusion was not synchronous. Nineteen of 42 patients (45%)

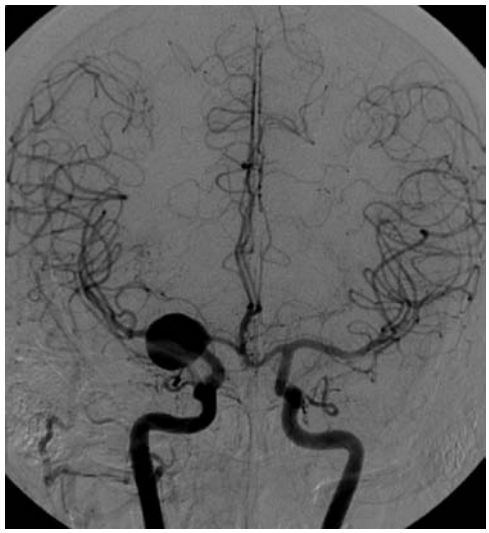

FIG 1. Large carotid tip aneurysm incidentally found in a 45-year-old woman. This aneurysm failed to thrombose after right ICA occlusion and was surgically treated 10 months later.

who were awake during test occlusion had neurologic symptoms. Twenty-one patients were treated with selective coiling, in 13 with stent or balloon assistance. Five patients had uncomplicated bypass surgery before ICA occlusion. One patient was treated with a flow diverter. One patient with severe head trauma and carotid cavernous fistula died soon after test occlusion. Twenty-two patients (with cavernous sinus aneurysms) were treated conservatively.

Procedural and Postprocedural Complications

There were no complications of the test occlusion in 146 patients (0% [95% CI, 0%–3%]). Of 88 patients treated by ICA occlusion, 6 (6.8%) had small hypoperfusion infarctions in the watershed zone between the anterior and middle cerebral artery on MR imaging 1–3 days after the occlusion. In 3 patients, this was subclinical; the other 3 patients had a mild transient hemiparesis. There were no thromboembolic ischemic complications. In another patient, a detachable balloon detached prematurely, and the empty balloon migrated with the blood flow into a left M3 branch. MR imaging after ICA occlusion demonstrated a localized ischemic area in the insula without clinical symptoms. There was 1 permanent neurologic complication in a 78-year-old woman who developed hypoperfusion infarction with hemiparesis as a result of hypovolemic shock due to a large retroperitoneal hematoma. The permanent complication rate was 1 of 88 (1.1% [95% CI, 1%–6.8%]).

Imaging Follow-Up

Mean imaging and clinical follow-up was 35 months (median, 18 months; range, 3–180 months). Angiographic and MR imaging follow-up showed complete occlusion of 86 of 88 aneurysms (97.7%) treated by ICA occlusion. In 2 patients (1.4%), the aneurysm was not completely occluded on short-term follow-up. One patient with a supraclinoid ICA aneurysm had persistent filling of the aneurysm via the posterior communicating artery; this patient later underwent bypass surgery and clipping (Fig 1). The other patient had persistent filling of the giant carotid tip aneurysm at the 10-month follow-up angiogram, but MR imaging 3 months later demonstrated complete thrombosis (Fig 2).

At the latest MR imaging, 61 of 80 aneurysms (76%) were decreased in size or were completely obliterated.

Recovery of Cranial Nerve Function after ICA Occlusion

Of the 62 patients who presented with cranial nerve dysfunction by mass effect of the aneurysm and were treated with ICA occlusion, 30 (48%) were cured, 25 (40%) improved, 6 (10%) were unchanged, and 1 patient (2%) was hemiplegic after a complication.

DISCUSSION

In this large cohort of consecutive patients with large and giant ICA aneurysms and therapeutic carotid artery occlusion after angiographic testing, the risk of permanent neurologic complications was extremely low. This study confirmed previous data from the same cohort and demonstrated that good clinical and anatomic results were sustained over time in a growing cohort of patients. These new data were more robust, with incremental narrowing of confidence intervals.

The only permanent neurologic complication was the result of hypovolemic shock due to an undetected retroperitoneal hematoma during ambulance transportation back to the referring hospital. Thus, the angiographic test occlusion as a predictor for tolerance to ICA occlusion proved to be very accurate, with no false-positives. The negative predictive value of the angiographic test occlusion could not be assessed because no ICA occlusion was performed when the test indicated nontolerance. Data from the era of surgical ICA clamp occlusion without previous tolerance testing indicate that approximately three-fourths of patients can tolerate ICA occlusion.[16-18] In our cohort, the angiographic test indicated tolerance to permanent ICA occlusion in two-thirds of patients, which indicates that the proportion of false-negatives is probably limited.

After ICA occlusion, all aneurysms thrombosed completely except one, which makes the treatment very effective. The one exception was a large carotid tip aneurysm in a patient with a patent ipsilateral posterior communicating artery aneurysm that was not appreciated on angiography during test occlusion. Apparently, hemodynamic changes in the circle of Willis after ICA occlusion induced increased flow over the posterior communicating artery that prevented intraluminal thrombosis of the aneurysm. In aneurysms located distal to the posterior communicating artery, one should be aware of this phenomenon. We never encountered persistent aneurysm filling through collaterals via the ophthalmic artery. The effectiveness of our protocol of ICA balloon occlusion proximal to the aneurysm is comparable with the protocol of trapping the aneurysm with coils used by Labeyrie et al.[19] However, we are in favor of our protocol because it is much easier to perform and definitely much cheaper. In addition, trapping in aneurysms located close to the ICA bifurcation is not possible because the distal ICA segment is too short to accommodate the coils.

During follow-up of at least 3 months in all the patients and much longer in most, three-fourths of the aneurysms decreased in size and almost 90% of the patients who presented with cranial

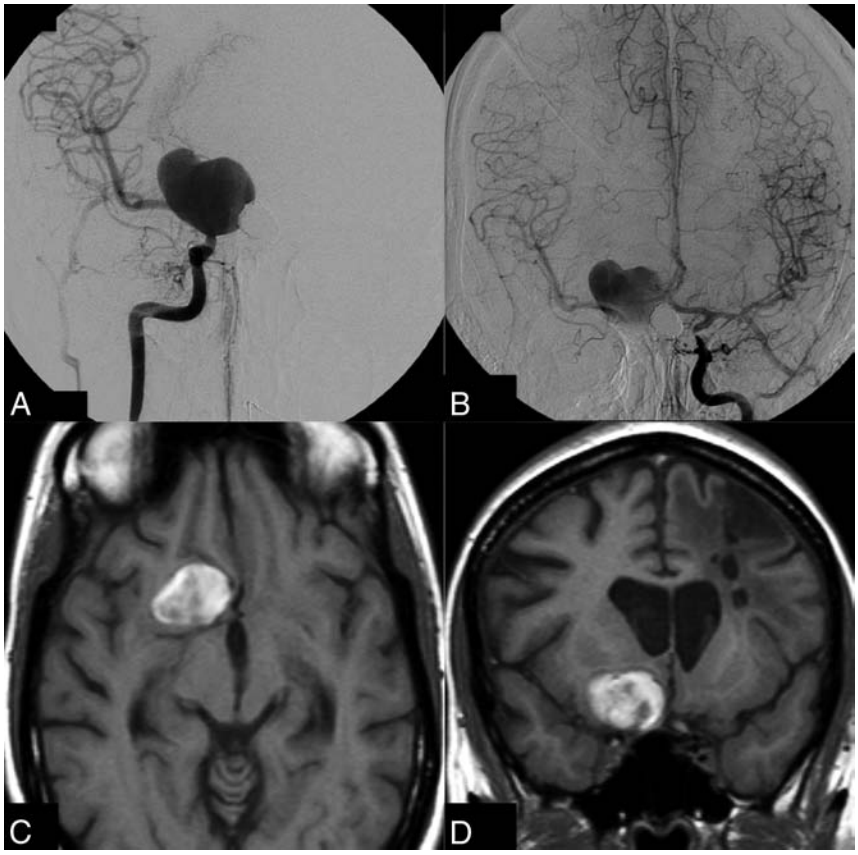

FIG 2. Giant unruptured right carotid tip aneurysm in a 36-year-old woman with multiple aneurysms. *A*, Right ICA angiogram shows the giant aneurysm; test occlusion showed ample collateral circulation via the anterior communicating artery. *B*, Left ICA angiogram 6 months after right ICA occlusion demonstrates that the aneurysm is still not occluded. *C* and *D*, T1-weighted MR imaging 10 months after right ICA occlusion reveals complete thrombosis of the aneurysm lumen.

nerve dysfunction were cured or improved. These favorable results on aneurysm size and symptoms of mass effect are in concordance with other studies.[7,20,21]

Our data confirmed that ICA occlusion for large and giant carotid artery aneurysms was a very safe and effective therapy in patients with adequate collateral circulation. The angiographic test occlusion accurately predicted tolerance to ICA occlusion with probably only a few false-negatives but no false-positives. The angiographic test occlusion obviates the need for clinical testing and can be safely performed in patients under general anesthesia. After ICA occlusion and confirmation of aneurysm thrombosis on MR imaging, the aneurysm can be considered cured, and further imaging follow-up is not necessary. In a previous 3T MRA follow-up study in a selection of 26 patients of the present cohort, there were no de novo aneurysms after a mean follow-up of >50 months. In conjunction with other follow-up studies of patients with clipped aneurysms, there was no reason to believe that there is an increased risk of developing de novo aneurysms in patients with aneurysms treated by ICA occlusion compared with patients with clipped aneurysms.[13] In another follow-up study by using MR arterial spin-labeling in 11 patients from this cohort after a mean 39-month follow-up, CBF values were within normal range and there was no significant CBF difference between hemispheres ipsilateral and contralateral to carotid sacrifice.[15]

Several investigators advocate ICA sparing therapy with flow diverters for ICA aneurysms, also in patients who can tolerate ICA occlusion.[22] However, recent meta-analyses that concern flow-diverter stents show that the combined morbidity and mortality rate is approximately 10%, regardless of the type of aneurysm.[23-29] Mortality was 4% in the study of Briganti et al[24] in 76 patients with cavernous aneurysms treated with flow diverters. Many fatal complications with stent-assisted techniques are due to major hemorrhagic or ischemic complications, which are completely absent from carotid occlusion series. Because long-term imaging follow-up studies after flow-diverter treatment of ICA aneurysms are not yet available, complication rates may be underestimated: delayed in-stent occlusion may go clinically undetected in the three-fourths of patients who can tolerate ICA occlusion.[30] In our opinion, supported by others,[19] the safety profile of flow diverters is not good enough to justify treatment of ICA aneurysms in patients who can tolerate carotid occlusion, especially not in patients with cavernous aneurysms that generally exhibit a benign natural history.

ICA occlusion according to our protocol is also cost effective: angiographic test occlusion, followed by permanent ICA occlusion, is a straightforward procedure that takes 45–120 minutes. Occlusion balloons are cheap, and the patient is discharged home the next day. Prolonged imaging follow-up beyond the 3-month interval is usually not needed.

For patients with large and giant ICA aneurysms who cannot tolerate ICA occlusion, parent vessel sparing therapies should be considered with caution. In balancing the risks and benefits of these alternative therapies, it should be kept in mind that complications that lead to acute or delayed ICA occlusion in these patients certainly will cause neurologic deficit or even death. With the use of stents or flow diverters, this risk is not negligible: in-stent stenosis and occlusion occurs in approximately 10% of cases in the short term and the midterm.[23] With bypass surgery, the risk of occlusion of the bypass is certainly present.[4] The safest option to treat an aneurysm in a patient who cannot tolerate ICA occlusion seems to be selective coiling with or without balloon assistance. In patients with cavernous sinus aneurysms, conservative therapy can be the best option in a substantial proportion.

CONCLUSIONS

In patients with large and giant ICA aneurysms, ICA occlusion, when tolerated, remains a very safe and effective therapy. Tolerance to ICA occlusion can be reliably predicted by the angiographic test occlusion, also in patients under general anesthesia. In patients who cannot tolerate ICA occlusion, alternative treat-

ments sparing the ICA should be offered only after careful benefit to risk analysis because complication rates of these therapies are substantially higher.

Disclosures: Charles Majoie—*UNRELATED*: *Grants/Grants Pending*: Dutch Heart Foundation*; *Payment for Lectures (including service on speakers bureaus)*: Stryker.* *Money paid to the institution.

REFERENCES

1. van Rooij WJ. **Endovascular treatment of cavernous sinus aneurysms.** *AJNR Am J Neuroradiol* 2012;33:323–26 CrossRef Medline
2. van der Schaaf IC, Brilstra EH, Buskens E, et al. **Endovascular treatment of aneurysms in the cavernous sinus: a systematic review on balloon occlusion of the parent vessel and embolization with coils.** *Stroke* 2002;33:313–38 CrossRef Medline
3. van Rooij WJ, Sluzewski M, Beute GN. **Ruptured cavernous sinus aneurysms causing carotid cavernous fistula: incidence, clinical presentation, treatment, and outcome.** *AJNR Am J Neuroradiol* 2006;27:185–89 Medline
4. Brilstra EH, Rinkel GJ, Klijn CJ, et al. **Excimer laser-assisted bypass in aneurysm treatment: short-term outcomes.** *J Neurosurg* 2002;97: 1029–35 CrossRef Medline
5. Langer DJ, Van Der Zwan A, Vajkoczy P, et al. **Excimer laser-assisted nonocclusive anastomosis: an emerging technology for use in the creation of intracranial-intracranial and extracranial-intracranial cerebral bypass.** *Neurosurg Focus* 2008;24:E6 CrossRef Medline
6. van Rooij WJ, Sluzewski M. **Endovascular treatment of large and giant aneurysms.** *AJNR Am J Neuroradiol* 2009;30:12–18 CrossRef Medline
7. Lubicz B, Gauvrit JY, Leclerc X, et al. **Giant aneurysms of the internal carotid artery: endovascular treatment and long-term follow-up.** *Neuroradiology* 2003;45:650–55 CrossRef Medline
8. Lanzino G, Crobeddu E, Cloft HJ, et al. **Efficacy and safety of flow diversion for paraclinoid aneurysms: a matched-pair analysis compared with standard endovascular approaches.** *AJNR Am J Neuroradiol* 2012;33:2158–61 CrossRef Medline
9. D'Urso PI, Karadeli HH, Kallmes DF, et al. **Coiling for paraclinoid aneurysms: time to make way for flow diverters?** *AJNR Am J Neuroradiol* 2012;33:1470–74 CrossRef Medline
10. van Rooij WJ, Sluzewski M, Slob MJ, et al. **Predictive value of angiographic testing for tolerance to therapeutic occlusion of the carotid artery.** *AJNR Am J Neuroradiol* 2005;1:175–78 Medline
11. van Rooij WJ, Sluzewski M, Metz NH, et al. **Carotid balloon occlusion for large and giant aneurysms: evaluation of a new test occlusion protocol.** *Neurosurgery* 2000;47:116–21; discussion 122 CrossRef Medline
12. van Rooij WJ, Sluzewski M. **Unruptured large and giant carotid artery aneurysms presenting with cranial nerve palsy: comparison of clinical recovery after selective aneurysm coiling and therapeutic carotid artery occlusion.** *AJNR Am J Neuroradiol* 2008;29:997–1002 CrossRef Medline
13. de Gast AN, Sprengers ME, van Rooij WJ, et al. **Long-term 3T MR angiography follow-up after therapeutic occlusion of the internal carotid artery to detect possible de novo aneurysm formation.** *AJNR Am J Neuroradiol* 2007;28:508–10 Medline
14. de Gast AN, Sprengers ME, van Rooij WJ, et al. **Midterm clinical and magnetic resonance imaging follow-up of large and giant carotid artery aneurysms after therapeutic carotid artery occlusion.** *Neurosurgery* 2007;60:1025–29; discussion 1029–31 CrossRef Medline
15. Gevers S, Heijtel D, Ferns SP, et al. **Cerebral perfusion long term after therapeutic occlusion of the internal carotid artery in patients who tolerated angiographic balloon test occlusion.** *AJNR Am J Neuroradiol* 2012;33:329–35 CrossRef Medline
16. Linskey ME, Jungreis CA, Yonas H, et al. **Stroke risk after abrupt internal carotid artery sacrifice: accuracy of preoperative assessment with balloon test occlusion and stable xenon-enhanced CT.** *AJNR Am J Neuroradiol* 1994;15:829–43 Medline
17. Drake CG, Peerless SJ, Ferguson GG. **Hunterian proximal arterial occlusion for giant aneurysms of the carotid circulation.** *J Neurosurg* 1994;81:656–65 CrossRef Medline
18. Fox AJ, Viñuela F, Pelz DM, et al. **Use of detachable balloons for proximal artery occlusion in the treatment of unclippable cerebral aneurysms.** *J Neurosurg* 1987;66:40–46 CrossRef Medline
19. Labeyrie MA, Lenck S, Bresson D, et al. **Parent artery occlusion in large, giant, or fusiform aneurysms of the carotid siphon: clinical and imaging results.** *AJNR Am J Neuroradiol* 2015;36:140–45 CrossRef Medline
20. Abud DG, Spelle L, Piotin M, et al. **Venous phase timing during balloon test occlusion as a criterion for permanent internal carotid artery sacrifice.** *AJNR Am J Neuroradiol* 2005;26:2602–09 Medline
21. Zhang Z, Lv X, Wu Z, et al. **Clinical and angiographic outcome of endovascular and conservative treatment for giant cavernous carotid artery aneurysms.** *Interv Neuroradiol* 2014;20:29–36 CrossRef Medline
22. Tanweer O, Raz E, Brunswick A, et al. **Cavernous carotid aneurysms in the era of flow diversion: a need to revisit treatment paradigms.** *AJNR Am J Neuroradiol* 2014;35:2334–40 CrossRef Medline
23. Velioglu M, Kizilkilic O, Selcuk H, et al. **Early and midterm results of complex cerebral aneurysms treated with Silk stent.** *Neuroradiology* 2012;54:1355–65 CrossRef Medline
24. Briganti F, Napoli M, Tortora F, et al. **Italian multicenter experience with flow-diverter devices for intracranial unruptured aneurysm treatment with periprocedural complications–a retrospective data analysis.** *Neuroradiology* 2012;54:1145–52 CrossRef Medline
25. Berge J, Biondi A, Machi P, et al. **Flow-diverter Silk stent for the treatment of intracranial aneurysms: 1-year follow-up in a multicenter study.** *AJNR Am J Neuroradiol* 2012;33:1150–55 CrossRef Medline
26. Nelson PK, Sahlein D, Shapiro M, et al. **Recent steps toward a reconstructive endovascular solution for the orphaned, complex-neck aneurysm.** *Neurosurgery* 2006;59(5 suppl 3):S77-92; discussion S3-13 CrossRef Medline
27. Kallmes DF, Hanel R, Lopes D, et al. **International retrospective study of the Pipeline embolization device: a multicenter aneurysm treatment study.** *AJNR Am J Neuroradiol* 2015;36:108–15 CrossRef Medline
28. Arrese I, Sarabia R, Pintado R, et al. **Flow-diverter devices for intracranial aneurysms: systematic review and meta-analysis.** *Neurosurgery* 2013;73:193–99; discussion 199–200 CrossRef Medline
29. Brinjikji W, Murad MH, Lanzino G, et al. **Endovascular treatment of intracranial aneurysms with flow diverters: a meta-analysis.** *Stroke* 2013;44:442–47 CrossRef Medline
30. Fiorella D, Hsu D, Woo HH, et al. **Very late thrombosis of a Pipeline embolization device construct: case report**. *Neurosurgery* 2010; 67(suppl operative):onsE313–34; discussion onsE314 CrossRef Medline

PulseRider Stent-Assisted Coiling of Wide-Neck Bifurcation Aneurysms: Periprocedural Results in an International Series

B. Gory, A.M. Spiotta, S. Mangiafico, A. Consoli, A. Biondi, E. Pomero, M. Killer-Oberpfalzer, W. Weber, R. Riva, P.E. Labeyrie, and F. Turjman

ABSTRACT

SUMMARY: The PulseRider is a novel endovascular device specifically designed to treat bifurcation intracranial aneurysms with wide necks. In an international series, we report the results of PulseRider stent-assisted coiling of 15 patients (9 women and 6 men; mean age, 62.6 years) with 15 unruptured wide-neck (median dome size, 8 mm; median neck size, 5 mm) bifurcation aneurysms. Failure of PulseRider treatment occurred in 1 case, and 1 intraprocedural thromboembolic complication was observed. There was no mortality or neurologic permanent morbidity at discharge and at 1 month. Immediate angiographic outcome showed 12 complete occlusions and 2 neck remnants. Follow-up at 6 months was available for 3 aneurysms and demonstrated 2 complete aneurysm occlusions and 1 growing neck remnant. In this small series of selected patients, PulseRider stent-assisted coiling of wide-neck bifurcation aneurysms was feasible with low procedural complication rates. Angiographic follow-up will be required to evaluate the efficacy of the PulseRider device.

ABBREVIATION: IA = intracranial aneurysm

Endovascular treatment with coils is the reference therapy for ruptured intracranial aneurysms (IAs).[1-3] Although no randomized study demonstrated the superiority of endovascular treatment compared with clipping for unruptured IAs, endovascular treatment is also often the preferred therapeutic option.[3] However, endovascular treatment with coils of IAs with wide necks is difficult or simply not feasible. In this specific situation, balloon-assisted and stent-assisted techniques have widened the indications for endovascular treatment.[4-7] Endovascular treatment of bifurcation IAs often requires stent placement with double stents in "Y" or "X" configurations, which could increase the risk of clinical complications,[7,8] whereas some authors reported low rates of complications compared with the balloon-remodeling technique.[9,10]

Recently, 3 devices have been specifically developed for the endovascular treatment of such aneurysms arising at bifurcations: the WEB (Sequent Medical, Aliso Viejo, California), the pCONus (phenox, Bochum, Germany), and the PulseRider device (Pulsar Vascular, San Jose, California). The WEB is an intrasaccular braided-wire flow disruptor,[11,12] and the pCONus is a new stent-like self-expanding nitinol implant with 4 distal petals allowing coiling of the aneurysmal sac.[13] The PulseRider has a unique frame configuration that opens to conform to the vessel walls. It is specifically designed to preserve luminal patency and hemodynamic flow through the parent vessel bifurcation, while minimizing exposed metal to encourage early endothelialization while securely retaining coils within the aneurysm sac. It received a CE mark for intracranial aneurysms but has not been approved by the FDA. To date, a single published article on aneurysms treated with the PulseRider reported a series including 3 IAs.[14] The aim of this study was to evaluate the results of the treatment of wide-neck bifurcation IAs with the PulseRider in an international series.

Case Series

The PulseRider is a self-expanding nitinol implant (Fig 1) that is delivered via a standard microcatheter with an inner diameter of 0.021 inches. The device is retrievable and may be repositioned by retracting it into the microcatheter at any time during or after deployment. It is deployed at the parent vessel bifurcation and across the aneurysm neck to provide a supporting framework, bridging the aneurysm neck while retaining coils within the aneurysm. The PulseRider is electrolytically detached from the delivery wire. The T or Y configurations are available according to

Received April 10, 2015; accepted after revision June 8.

From the DHU IRIS, Department of Interventional Neuroradiology (B.G., R.R., P.E.L., F.T.), Hôpital Neurologique Pierre Wertheimer, Hospices Civils de Lyon, Lyon, France; Department of Neurosciences (A.M.S.), Division of Neurosurgery, Medical University of South Carolina, Charleston, South Carolina; Department of Neuroradiology (S.M., A.C.), Careggi University Hospital, Florence, Italy; Department of Neuroradiology and Endovascular Therapy (A.B., E.P.), Jean-Minjoz Hospital, Franche-Comté University, Besançon, France; Neuroscience Institute/Department of Neurology (M.K.-O.), Paracelsus Medical University, Christian Doppler Clinic, Salzburg, Austria; and Department of Neuroradiology (W.W.), Knappschaftskrankenhaus, Recklinghausen, Germany.

Please address correspondence to Benjamin Gory, MD, MSc, DHU IRIS, Department of Interventional Neuroradiology, Hôpital Neurologique Pierre Wertheimer, Hospices Civils de Lyon, 59 Blvd, 69677 Bron, France; e-mail: benjamin.gory@chu-lyon.fr

http://dx.doi.org/10.3174/ajnr.A4506

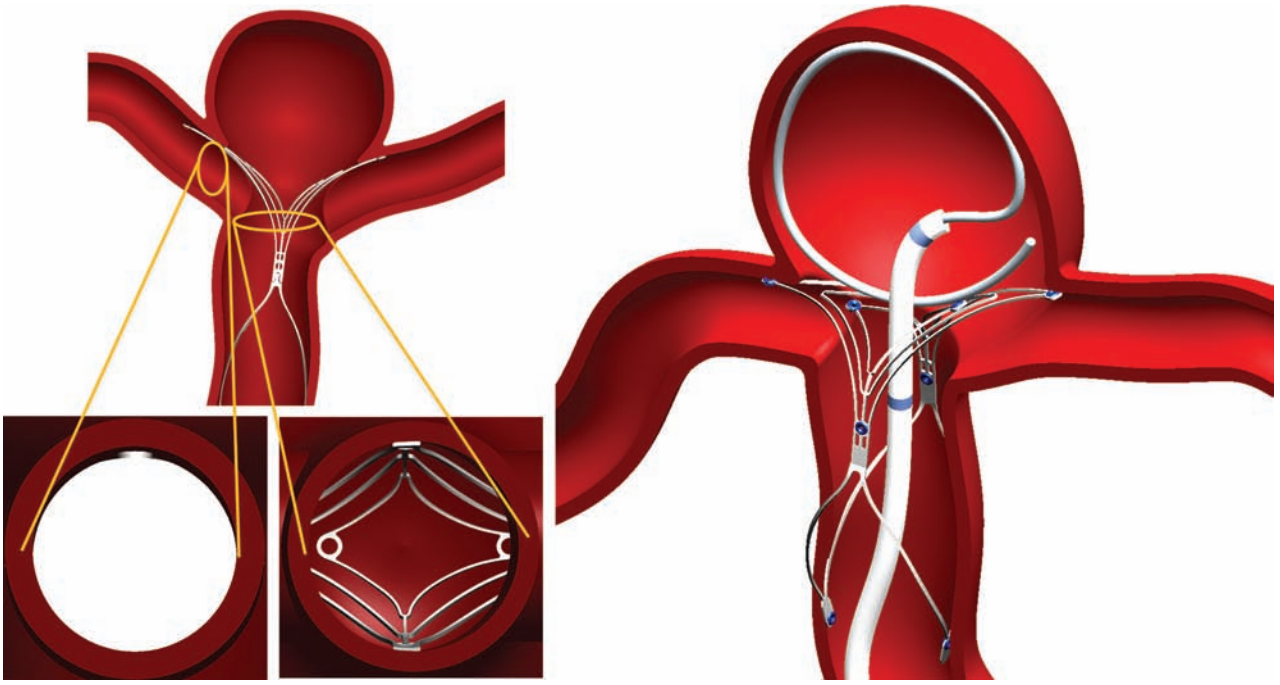

FIG 1. The PulseRider device is intended for use with embolic coils for the treatment of unruptured wide-neck intracranial aneurysms originating on or near a vessel bifurcation. The PulseRider has a unique arch design with concentrated coverage at the neck allowing attenuated coil packing, and open architecture in the branch vessels eliminates struts crossing through the lumen of the branch vessels. Reproduced with permission from PulsarVascular.

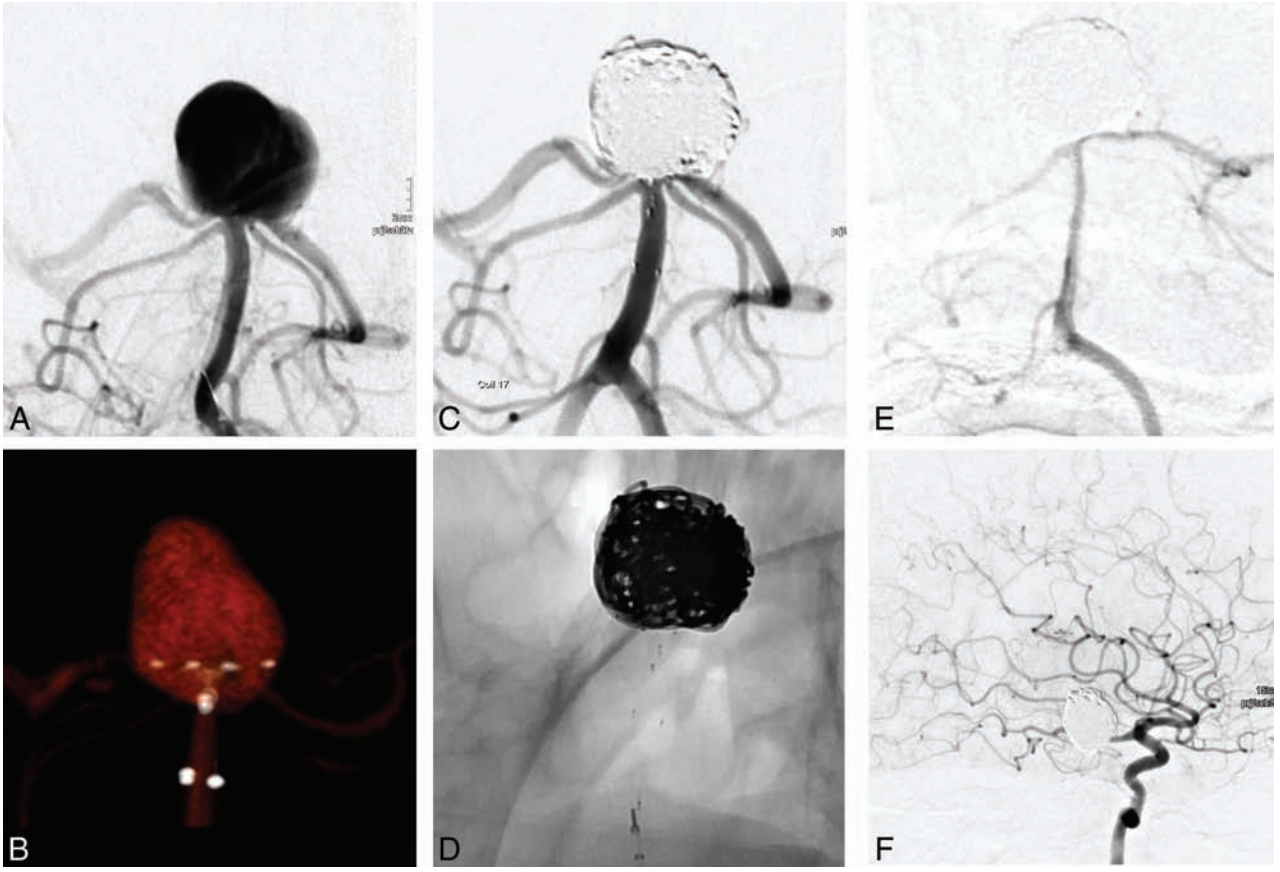

FIG 2. Incidental large basilar artery aneurysm in a 60-year-old woman (case 1). *A*, The angiogram shows a 17-mm aneurysm with an 8-mm neck. *B*, 3D reconstruction after rotational angiography shows the PulseRider device placement before coiling. *C* and *D*, An angiogram at the end of the procedure shows final complete aneurysm occlusion. *E*, Angiographic follow-up at 6 months reveals complete aneurysm occlusion with an occlusion of the P1 segment of the posterior cerebral artery, which was supplied by the internal carotid artery via the posterior communicating artery (*F*). The patient was asymptomatic.

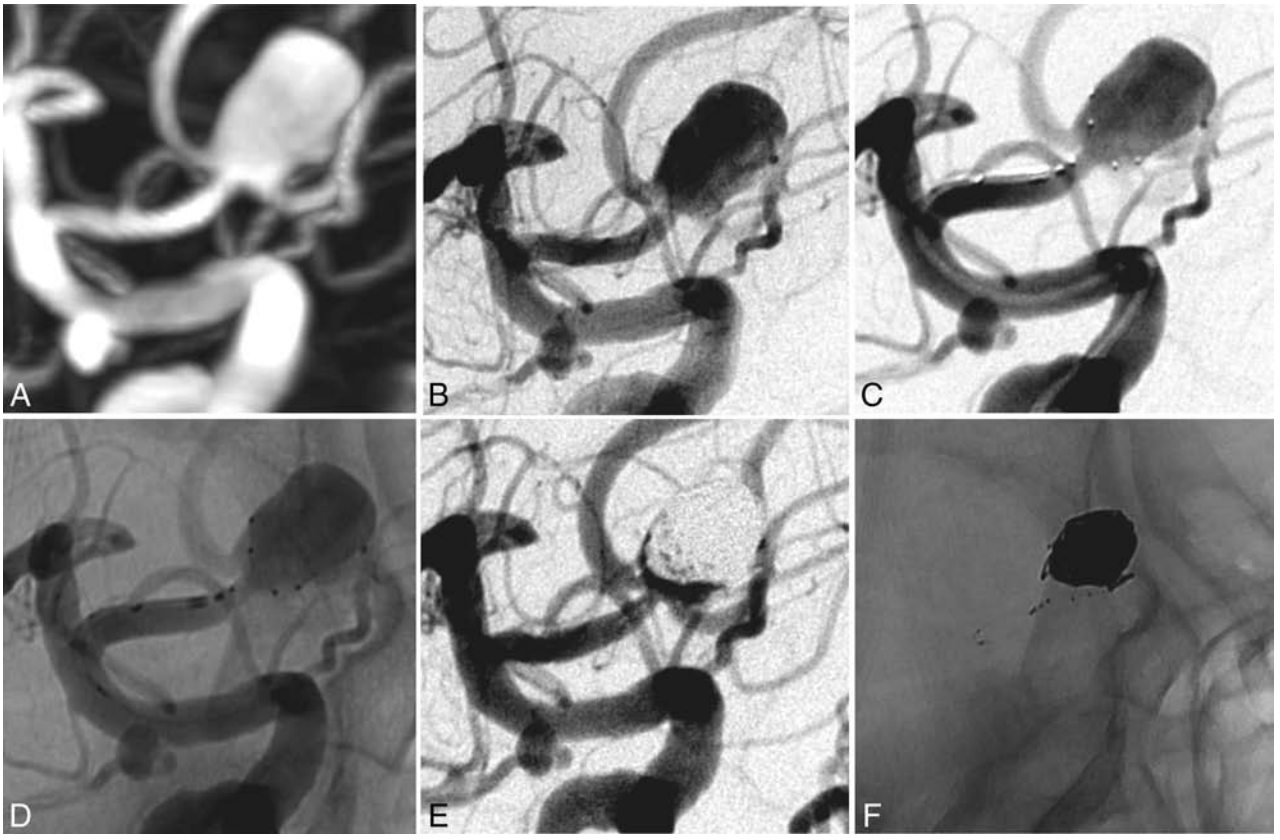

FIG 3. A wide-neck anterior communicating artery aneurysm in a 50-year-old woman (case 2). *A*, 3D reconstruction after rotational angiography shows a large anterior communicating artery with a 4.2-mm neck. *B*, Subtracted angiography shows a large anterior communicating artery. *C* and *D*, PulseRider stent-assisted coiling was performed. *E* and *F*, Subtracted angiographies at the end of the procedure show a neck remnant. The PulseRider device retained coils within the aneurysm sac.

the geometry of the daughter vessels arising at the bifurcation with 8- or 10-mm diameters.

From June 2014 to February 2015, 15 consecutive patients (9 women and 6 men; mean age, 62.6 years) with 15 unruptured bifurcation IAs (median dome size, 8 mm; median neck size, 5 mm) at 1 US center (Charleston, South Carolina) and 5 European institutions (Lyon and Besançon, France; Florence, Italy; Recklinghausen, Germany; Salzburg, Austria) who were treated with the PulseRider device for IAs were retrospectively analyzed (under institutional review board approved protocol in United States and without approved ethics committee protocols in the European Union). The decision to assist coiling by a PulseRider device was made at the discretion of the senior author. All patients were treated under general anesthesia and full anticoagulation. In addition, double antiplatelet therapy was administered preoperatively according to the operator's protocol.

Endovascular Procedure

A Prowler Select Plus 0.021-inch microcatheter (Codman & Shurtleff, Raynham, Massachusetts) was navigated over a 0.014-inch microwire and positioned at the neck of the aneurysm. In a suitable working projection, the appropriately sized PulseRider was then deployed across the neck of the aneurysm with limbs in the daughter vessels arising at the bifurcation or in the aneurysm, or in a hybrid fashion with one limb in the branch vessel and the other limb in the aneurysm. Thereafter, a second microcatheter was inserted through the shaft into the aneurysm fundus, and coiling was performed. The PulseRider was detached either at or near the final coiling.

Treatment Failure

Treatment failure with the PulseRider occurred in 1 patient (patient 11) with a wide-neck carotid terminus aneurysm and a 4.5-mm dome. The deployment of the PulseRider was achieved, but on control angiograms, suboptimal positioning of the device was seen with incomplete protection of the neck. The PulseRider was replaced several times without success, and the aneurysm was then treated with stent-assisted coiling (Y-stent placement).

Procedural Complications

One thromboembolic event after detachment of the device occurred. After successful PulseRider-assisted coiling of a right MCA aneurysm, a thrombus formation occurred at the limbs of the device and caused a stenosis of the distal M1 segment. After immediate administration of glycoprotein IIb/IIIa inhibitors, the stenosis remained but the patient woke up without neurologic deficits and remained in this status at 1 month follow-up. No intraoperative rupture was observed.

Outcome

Among the 14 patients treated with the PulseRider, no neurologic impairment was observed at discharge and at 1-month follow-up

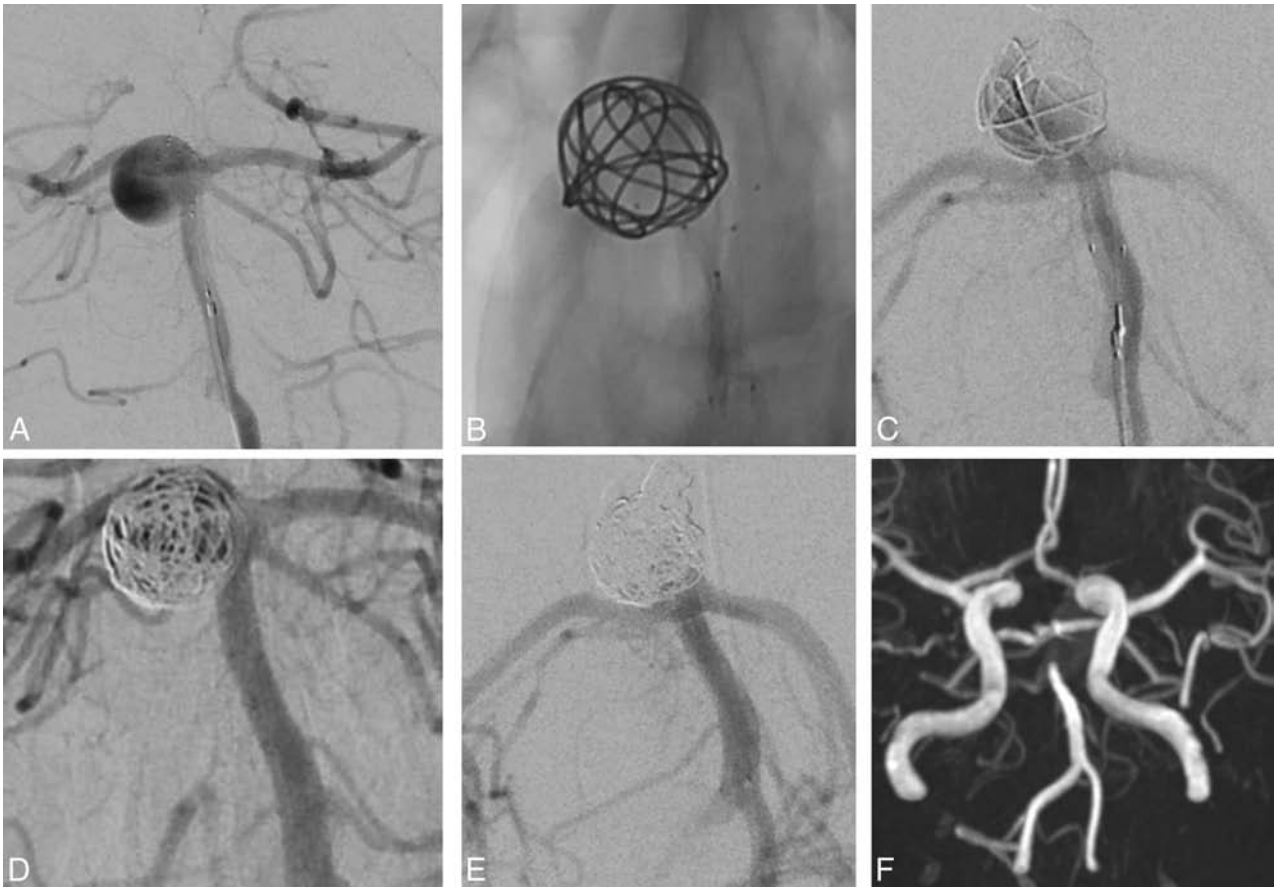

FIG 4. An unruptured basilar tip aneurysm in a 60-year-old man (case 3). *A*, Subtracted angiography shows a large basilar tip aneurysm with a 4-mm-wide neck. *B–D*, Endovascular treatment was performed by using a PulseRider device. *E*, Subtracted angiography at the end of the procedure shows complete aneurysm occlusion. *F*, MRA at 1 day shows complete occlusion.

(11 patients). There were no delayed neurologic deficits or deaths at follow-up.

One reader (B.G.) independently evaluated all the angiograms by using a simplified 3-point scale (total occlusion, neck remnant, aneurysm remnant).[15] Immediate angiograms showed complete occlusion in 12 patients and neck remnant in 2 patients. Angiographic follow-up at 6 months was available for 3 patients and demonstrated 2 complete aneurysm occlusions and 1 growing neck remnant. During follow-up, retreatment was performed in 1 case due to a significant increase in the size of the neck remnant, with complete occlusion at the end of procedure. No in-stent stenosis and 1 jailed branch occlusion were observed.

Illustrative Cases

Case 1. A 60-year-old woman (Fig 2, patient 9) presented with an incidental large basilar artery aneurysm. Angiography revealed a 17-mm aneurysm with an 8-mm neck. Endovascular treatment was performed by using a PulseRider device with final complete aneurysm occlusion. Angiographic follow-up at 6 months revealed complete aneurysm occlusion with an occlusion of the P1 segment of the posterior cerebral artery, which was supplied by the internal carotid artery via the posterior communicating artery. The patient was asymptomatic.

Case 2. A 50-year-old woman (Fig 3, patient 6) presented with an incidental finding of a 4.2-mm wide-neck anterior communicating artery aneurysm. Endovascular PulseRider deployment and then coiling was performed. The final angiogram showed a neck remnant.

Case 3. A 60-year-old woman (Fig 4, patient 14) presented with an unruptured basilar tip aneurysm. Angiography showed a large basilar tip aneurysm with a 4-mm-wide neck. Endovascular treatment was performed by using a PulseRider. The final angiogram showed complete aneurysm occlusion, and MRA at 1 day showed complete aneurysm occlusion.

DISCUSSION

This initial study reports a series of patients with unruptured bifurcation IAs with wide necks treated by PulseRider stent-assisted coiling.

Feasibility and Patient Selection

This report suggests that PulseRider-assisted coiling of IAs with wide necks is feasible; however, the selection of patients should be well-considered before deciding on a PulseRider treatment. In fact, in this small series of 15 patients, the rate of failure was 6.7% (patient 11). This patient presented with a wide-neck terminus carotid aneurysm with a small-size dome. The PulseRider deployment was feasible, but it did not provide protection of the aneu-

Clinical and angiographic outcomes

No.	Age (yr), Sex	Location	D (mm)	N (mm)	Failure	PulseRider Diameter (mm)	Immediate Angiographic Outcome	6-Month Angiographic Outcome	Modified Rankin Scale		
									Initial	Discharge	1 Month
1	74, F	Basilar tip	16.3	10.9	No	10	Complete		1	1	3
2	69, M	Carotid terminus	4.2	3.5	No	8	Complete		0	0	1
3	69, F	Basilar tip	7.9	4.1	No	8	Complete		0	0	0
4	57, F	Carotid terminus	4.1	2.3	No	8	Complete		1	0	
5	65, F	Basilar tip	9.5	5.7	No	10	Complete		0	1	
6	50, F	AcomA	8.4	4.2	No	8	Neck remnant		0	0	0
7	82, M	MCA	5.6	3.9	No	8	Complete		1	1	1
8	54, F	Basilar tip	4.5	11	No	8	Neck remnant	Neck remnant (w)	0	0	0
9	60, F	Basilar tip	17	8	No	10	Complete	Complete	0	0	0
10	51, F	MCA	5.5	4	No	8	Complete	Complete	0	0	0
11	64, M	Carotid terminus	4.5	4	Yes	8	–	–	–	–	–
12	67, M	MCA	8	5	No	8	Complete		0	0	0
13	56, M	AcomA	15	5	No	10	Complete		0	0	0
14	60, M	Basilar tip	7	4	No	8	Complete	Complete[a]	0	0	
15	74, F	MCA	6	5	No	8	Complete		0	0	0

Note:—AcomA indicates anterior communicating artery; D, dome; N, neck; w, worsening; –, not applicable because the treatment failed with PulseRider.
[a] MRA at 1 day.

rysmal neck even after several attempted placements. The pCONus device was placed and not detached due to the same problem occurring repeatedly; the aneurysm was then successfully treated with Y-stent-assisted coiling without complications.

Selection of patients is also important when using a WEB device. In the recent series of Gherasim et al[11] dealing with 10 patients with unruptured anterior communicating artery aneurysms (mean dome size, 5.8 mm; range, 3.8–8.2 mm; mean neck size, 5.4 mm; range, 3.6–8 mm), WEB deployment failed in 3 of 10 patients because of unfavorable anatomy and the use of a much larger and stiffer microcatheter for the WEB device than usually used for coiling.[11]

Periprocedural Complications

Our results show that endovascular treatment of IAs with the PulseRider is safe despite the very specific population with a median neck size of 5 mm. There was neither device-related mortality nor permanent morbidity. Similar results have also been reported in the first published series.[14] The safety of the PulseRider was also highlighted because no clinically evident complications were associated with its use in 3 wide-neck aneurysms.[14] Contrary to sidewall IAs, bifurcation IAs with wide necks are difficult or impossible to treat with simple coiling and often need double stent placement in "Y" and "X" configurations. However, the risk of procedure-related morbidity and mortality is not negligible. The rate of procedure-related permanent neurologic deficits was 10% in 97 patients with complex and wide-neck bifurcation aneurysms.[8] Compared with regular intracranial stent placement, PulseRider treatment also needed dual antiplatelet therapy during the perioperative period despite a very low amount of metal. The safety of this device seems very good in our small series. However, the safety of PulseRider stent-assisted coiling remains to be assessed in larger series.

Anatomic Results

As previously reported in the small series of Spiotta et al,[14] complete initial aneurysm occlusion was achieved in most cases (84.6%). These immediate anatomic results are encouraging, given the unfavorable angiographic aspects of IAs included in our series. In this series of Spiotta et al with 3 wide-neck bifurcations aneurysms, complete aneurysm occlusion was observed in all cases.[14] In fact, large or giant IAs treated with coils presented low initial angiographic occlusion rates and high rates of recanalization.[3,15,16] However, in our series, angiographic control at follow-up was obtained in only 3/13 patients (23%). A follow-up is mandatory to evaluate the efficacy of this treatment. Although angiography remains the criterion standard, there is a role for MRA in following up these patients because small artifacts were introduced by metal as illustrated in Fig 4 (patient 14).[17] Much more data with the PulseRider device are clearly required to evaluate the mid- and long-term results of this new endovascular approach.

The limitations of our study were a small number of patients with a relatively short follow-up period to evaluate the efficacy of the PulseRider device. In addition, a small percentage of patients were followed in our series. However, we believe it is important to have a preliminary evaluation for this new endovascular treatment device dedicated to challenging IAs with wide necks and/or complex anatomy. So far, the preliminary results are encouraging.

Disclosures: Alejandro M. Spiotta—*UNRELATED*: *Consultancy*: Penumbra, Pulsar, MicroVention, Stryker; *Grants/Grants Pending*: MicroVention (research grant)*; *Travel/Accommodations/Meeting Expenses Unrelated to Activities Listed*: Penumbra, Pulsar, MicroVention, Stryker. *Money paid to the institution.

REFERENCES

1. Molyneux A, Kerr R, Stratton I, et al; International Subarachnoid Aneurysm Trial (ISAT) Collaborative Group. **International Subarachnoid Aneurysm Trial (ISAT) of neurosurgical clipping versus endovascular coiling in 2143 patients with ruptured intracranial aneurysms: a randomised trial.** *Lancet* 2002;360:1267–74 CrossRef Medline
2. Molyneux AJ, Birks J, Clarke A, et al. **The durability of endovascular coiling versus neurosurgical clipping of ruptured cerebral aneurysms: 18 year follow-up of the UK cohort of the International Subarachnoid Aneurysm Trial (ISAT).** *Lancet* 2015;385:691–97 CrossRef Medline
3. Gory B, Turjman F. **Endovascular treatment of 404 intracranial aneurysms treated with Nexus detachable coils: short-term and mid-term results from a prospective, consecutive, European multicenter study.** *Acta Neurochir* 2014;156:831–37 CrossRef Medline

4. Gory B, Kessler I, Seizem Nakiri G, et al. **Initial experience of intracranial aneurysm embolization using the balloon remodeling technique with Scepter C, a new double-lumen balloon.** *Interv Neuroradiol* 2012;18:284–87 CrossRef Medline
5. Gory B, Klisch J, Bonafé A, et al. **Solitaire AB stent-assisted coiling of wide-necked intracranial aneurysms: short-term results from a prospective, consecutive, European multicentric study.** *Neuroradiology* 2013;55:1373–78 CrossRef Medline
6. Gory B, Klisch J, Bonafé A, et al. **Solitaire AB stent-assisted coiling of wide-necked intracranial aneurysms: mid-term results from the SOLARE study.** *Neurosurgery* 2014;75:215–19; discussion 219 CrossRef Medline
7. Gory B, Rouchaud A, Saleme S, et al. **Endovascular treatment of middle cerebral artery aneurysms for 120 nonselected patients: a prospective cohort study.** *AJNR Am J Neuroradiol* 2014;35:715–20 CrossRef Medline
8. Bartolini B, Blanc R, Pistocchi S, et al. **"Y" and "X" stent-assisted coiling of complex and wide-neck intracranial bifurcation aneurysms.** *AJNR Am J Neuroradiol* 2014;35:2153–58 CrossRef Medline
9. Consoli A, Vignoli C, Renieri L, et al. **Assisted coiling of saccular wide-necked unruptured intracranial aneurysms: stent versus balloon.** *J Neurointerv Surg* 2014 Nov 26. [Epub ahead of print] CrossRef Medline
10. Limbucci N, Renieri L, Nappini S, et al. **Y-stent assisted coiling of bifurcation aneurysms with Enterprise stent: long-term follow-up.** *J Neurointerv Surg* 2014 Dec 11. [Epub ahead of print] CrossRef Medline
11. Gherasim DN, Gory B, Sivan-Hoffmann R, et al. **Endovascular treatment of wide-neck anterior communicating artery aneurysms using WEB-DL and WEB-SL: short-term results in a multicenter study.** *AJNR Am J Neuroradiol* 2015;36:1150–54 CrossRef Medline
12. Bozzetto Ambrosi P, Gory B, Sivan-Hoffman R, et al. **Endovascular treatment of bifurcation intracranial aneurysms with the WEB SL/SLS: 6-month clinical and angiographic results.** *Interv Neuroradiol* 2015;21:462–69 CrossRef Medline
13. Gory B, Aguilar-Pérez M, Pomero E, et al. **pCONus device for the endovascular treatment of wide-neck middle cerebral artery aneurysms.** *AJNR Am J Neuroradiol* 2015 Jul 23. [Epub ahead of print] CrossRef Medline
14. Spiotta AM, Chaudry MI, Turk AS, et al. **Initial experience with the PulseRider for the treatment of bifurcation aneurysms: report of first three cases in the USA.** *J Neurointerv Surg* 2015 Jan 5. [Epub ahead of print] CrossRef Medline
15. Raymond J, Guilbert F, Weill A, et al. **Long-term angiographic recurrences after selective endovascular treatment of aneurysms with detachable coils.** *Stroke* 2003;34:1398–403 CrossRef Medline
16. Campi A, Ramzi N, Molyneux AJ, et al. **Retreatment of ruptured cerebral aneurysms in patients randomized by coiling or clipping in the International Subarachnoid Aneurysm Trial (ISAT).** *Stroke* 2007;38:1538–44 CrossRef Medline
17. Choi JW, Roh HG, Moon WJ, et al. **Optimization of MR parameters of 3D TOF-MRA for various intracranial stents at 3.0T MRI.** *Neurointervention* 2011;6:71–77 CrossRef Medline

Postoperative Imaging Findings following Sigmoid Sinus Wall Reconstruction for Pulse Synchronous Tinnitus

P. Raghavan, Y. Serulle, D. Gandhi, R. Morales, K. Quinn, K. Angster, R. Hertzano, and D. Eisenman

ABSTRACT

BACKGROUND AND PURPOSE: Transmastoid sigmoid sinus wall reconstruction is a surgical technique increasingly used for the treatment of pulsatile tinnitus arising from sigmoid sinus wall anomalies. The imaging appearance of the temporal bone following this procedure has not been well-characterized. The purpose of this study was to evaluate the postoperative imaging appearance in a group of patients who underwent this procedure.

MATERIALS AND METHODS: The medical records of 40 consecutive patients who underwent transmastoid sigmoid sinus wall reconstruction were reviewed. Thirteen of 40 patients underwent postoperative imaging. Nineteen CT and 7 MR imaging examinations were assessed for the characteristics of the materials used for reconstruction, the impact of these on the adjacent sigmoid sinus, and complications.

RESULTS: Tinnitus resolved in 38 of 40 patients. Nine patients were imaged postoperatively for suspected complications, including dural sinus thrombosis, facial swelling, and wound drainage. Two patients underwent imaging for persistent tinnitus, and 2, for development of tinnitus on the side contralateral to the side of surgery. The materials used for reconstruction (NeuroAlloderm, HydroSet, bone pate) demonstrated characteristic imaging appearances and could be consistently identified. In 5 of 13 patients, there was extrinsic compression of the sigmoid sinus by graft material. Dural sinus thrombosis occurred in 2 patients.

CONCLUSIONS: The imaging findings following sigmoid sinus wall repair are characteristic. Graft materials may result in extrinsic compression of the sigmoid sinus, and this finding may be confused with dural venous thrombosis. Awareness of the imaging characteristics of the graft materials used enables this differentiation.

ABBREVIATIONS: PST = pulse synchronous tinnitus; SSWR = sigmoid sinus wall reconstruction

Tinnitus may be categorized as subjective, when it originates in either the peripheral or central auditory system and is perceived only by the patient, or objective, when it arises from a mechanical somatosound.[1] Pulsatile, or pulse synchronous, tinnitus (PST) usually arises from the abnormal self-perception of one's vascular flow. PST is a potentially disabling symptom, which may profoundly impact daily functioning.[2] Although PST can arise from a number of venous and arterial abnormalities,[2,3] venous PST accounts for most cases encountered in clinical practice.[4]

It is increasingly recognized that sigmoid sinus wall anomalies, which include thinning and dehiscence of the sigmoid sinus plate with or without an associated diverticulum, are a frequently encountered and surgically correctable cause of PST.[5-7] Both open surgical and endovascular interventions have proved successful in the amelioration of PST in such patients.[8-10] Sigmoid sinus wall reconstruction (SSWR) is increasingly being performed via an extraluminal, transmastoid approach.[11] The goal of the procedure is to bridge the bony dehiscence and reconstruct the wall of the sinus, thereby eliminating audible turbulence and interrupting the transmission of mural vibrations via the mastoid air cells. The purpose of this study was to describe the imaging findings in patients who have undergone SSWR and to evaluate the imaging characteristics of complications arising from this procedure.

MATERIALS AND METHODS

Patients

This retrospective, anonymized, single-center study was performed in accordance with the Health Insurance Portability and Accountability Act. Requirement for informed consent was waived by the institutional review board. The medical records of 40 consecutive patients (35 females; median age, 38 years; range,

Received May 3, 2015; accepted after revision June 9.

From the Departments of Radiology (P.R., Y.S., D.G., R.M.) and Otolaryngology (K.Q., K.A., R.H., D.E.), University of Maryland Medical Center, Baltimore, Maryland.

Prashant Raghavan and Yafell Serulle shared equally in the authorship of this article and are co-first authors.

Please address correspondence to Prashant Raghavan, MBBS, Department of Radiology, University of Maryland Medical Center, 22 S Greene St, Baltimore, MD 21201; e-mail: Prashant.raghavan@gmail.com

http://dx.doi.org/10.3174/ajnr.A4511

14–70 years) who underwent sigmoid sinus repair between May 2007 and January 2015 were reviewed. Patients were selected for the procedure after comprehensive clinical, audiometric, and tympanometric evaluations. All patients had undergone preoperative CT imaging examinations demonstrating the presence of sigmoid sinus wall anomalies (Fig 1). Postoperative imaging was obtained in 13 of the 40 patients, either for persistent or recurrent PST following surgery (4/40) or when there was concern for surgical complications (9/40).

Surgical Technique

The standardized technique of SSWR has been previously described (Fig 2).[5] Briefly, an extended mastoidectomy is performed, followed by skeletonization of the sigmoid sinus. The affected area is then decompressed to a normal-appearing sinus wall. The surrounding sinus wall and dura are undermined away from the posterior petrous face. Ectatic portions of the sinus are reduced with bipolar cautery. A soft-tissue graft of the temporalis fascia or AlloDerm (LifeCell, Branchburg, New Jersey), an acellular collagen matrix, is appropriately sized and inserted between the dura and posterior fossa bony plate, reconstructing the soft-tissue sinus wall. The graft is held in place without suturing by the intracranial and intravascular pressure. For hemostasis, especially if there is violation of the diverticulum intraoperatively, Surgicel (Ethicon, Somerville, New Jersey) is sometimes inserted deep into the soft-tissue graft. The bony defect is reconstructed with HydroSet Injectable HA Bone Substitute (Stryker, Kalamazoo, Michigan), a calcium phosphate cement that converts to hydroxyapatite. Autologous bone pate, derived from bone dust produced by drilling of the mastoid temporal bone that mixes with blood oozing in the surgical field to form a jellylike layer, is added for additional reinforcement, external to the HydroSet. The rationale behind reinforcing the soft-tissue reconstruction with the addition of a rigid layer (HydroSet and bone pate) is to diminish transmission of vibration of the exposed venous wall.[5] In summary, the reconstruction comprises 3 layers: soft-tissue graft, HydroSet, and bone pate, from innermost to outermost.

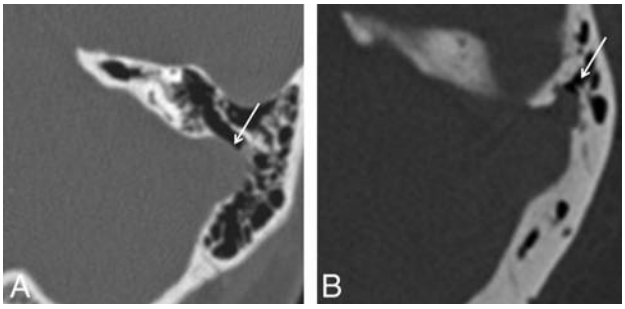

FIG 1. CT features of sigmoid wall anomalies. *A*, Axial CT image of the temporal bone demonstrates dehiscence of the left sigmoid sinus wall (*arrow*). *B*, Axial CT image of the temporal bone in a different patient demonstrates a small left sigmoid sinus diverticulum (*arrow*). Both patients presented with left pulse synchronous tinnitus.

Imaging Studies

Nineteen postoperative CT examinations were reviewed. Seven patients had a single CT, and 6 patients had 2 CT examinations following surgery. Iodinated intravenous contrast was administered in 8 patients. Seven MR imaging examinations were performed in 4 patients following surgery (1 nonenhanced MR imaging in conjunction with a 2D time-of-flight MR venogram and 6 gadolinium-enhanced MR imaging examinations, 3 of which included contrast-enhanced MR venography). Preoperative temporal bone CTs were available in all patients for comparison.

Scanning parameters for temporal bone CT examinations were as follows: section thickness, 0.67 mm at a 0.33-mm interval, 140 kV(peak), 350 mAs at 64 × 0.625 mm collimation, a 0.358 pitch, rotation time of 0.5, and FOV of 200 mm. Images were reconstructed in axial and coronal planes. Intravenous contrast (100 mL of iohexol injection, Omnipaque; GE Healthcare, Piscataway, New Jersey) was administered at 1.5 mL/s followed by a 50-mL saline flush, with automatic image acquisition 20 seconds after the appearance of contrast in the common carotid arteries. MR images were obtained by using a 1.5T (Avanto; Siemens, Erlangen, Germany) MR imaging scanner. Protocols included standard T1, T2, FLAIR, and susceptibility- and diffusion-weighted images of the brain and 2D time-of-flight venography.

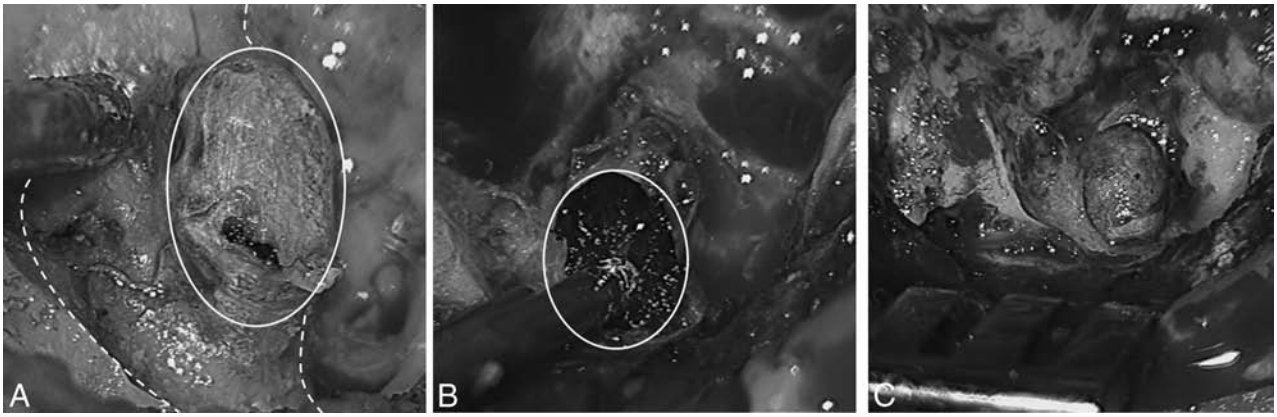

FIG 2. Intraoperative findings in sigmoid sinus wall repair. *A*, Appearance of a right sigmoid sinus diverticulum during transmastoid surgery. *Dashed lines* show the outline of a normal sigmoid sinus; the *oval* indicates a diverticulum. *B*, Postreduction of diverticulum. *C*, Postrepair of a sinus wall. Note the soft-tissue graft reinforcing the wall of the sigmoid sinus. Following this step, the bone defect is repaired with synthetic bone cement (HydroSet) and autologous bone pate. In all images, the left of the figure corresponds to the back of the patient (posterior head).

Summary of patient demographics and clinical, imaging, and surgical features

No.	Age (yr)	Sex	Side	Indication for SSWR	Indication for Postoperative Imaging	Mass Effect on SS	Dural Venous Sinus Thrombus	Other Findings
1	59	F	L	Dehiscence	Persistent tinnitus	−	−	Dehiscent left jugular bulb
2	57	F	L	Dehiscence	Persistent tinnitus	+[a]	−	
3	41	F	R	Dehiscence + encephalocele	Leak from wound	−	−	Tegmen tympani encephalocele + fluid collection
4	62	F	L	Dehiscence	Headache + visual changes	−	−	
5	31	F	R>L	Diverticulum	L tinnitus	−	−	L dehiscence
6	37	F	L	Dehiscence	Headache + neck pain	+	−	
7	38	F	R	Diverticulum	Headache	−	+	
8	14	M	R	Dehiscence	L tinnitus	−	−	L dehiscence
9	21	F	R	Dehiscence	Headache + visual changes	−	−	
10	44	M	R	Diverticulum	Headache	−	−	
11	20	F	L	Dehiscence	Headache	+[a]	−	
12	46	F	R	Diverticulum	Intraoperative diverticulum rupture	+	−	
13	65	F	R	Diverticulum	Right facial swelling	+	+	

Note:—SS indicates sigmoid sinus; R, right; L, left.
[a] CT was initially interpreted as dural sinus thrombosis.

Image Analysis

A qualitative examination was performed by 2 neuroradiologists, with 10 and 15 years of experience, blinded to clinical data, who reviewed all images individually. In case of disagreement, the radiologists reviewed the images together on the same workstation, to reach a consensus. All findings pertaining to graft materials were confirmed by the operating surgeon.

Preoperative temporal bone CTs were evaluated for the presence of diverticula or dehiscences. The maximal transverse dimensions of the diverticula and the maximal transverse width of the dehiscences were documented. The postoperative images were evaluated for the presence and appearance (thickness, attenuation) of the surgical material used. These included the soft-tissue materials (temporalis fascia graft, AlloDerm, and Surgicel), HydroSet, and bone pate. Density was measured by placing ROIs at the center of each type of graft material (soft tissue, HydroSet, bone pate), ensuring that adjacent structures were not inadvertently included. The maximal transverse dimension of the surgical soft-tissue materials was measured in the axial plane. The presence of mass effect on the sigmoid sinus by the soft-tissue graft was also determined. Mass effect was defined when there was direct apposition of the soft-tissue material on the sigmoid sinus, resulting in >50% reduction of the caliber of the sinus lumen in the transverse plane. Also evaluated were the presence of dural venous sinus thrombosis, fluid collections at the operative site, and any other findings that explained symptomatology.

RESULTS

Forty patients underwent SSWR for PST (5 male, 35 female; 14–70 years of age; median age, 38 years). There were 24 patients with dehiscence and 16 with diverticula. Average dehiscence width was 5 mm (range, 2–9 mm), and the average maximal diverticulum size was 6 mm (range, 3–10 mm). The standardized surgical procedure (see "Materials and Methods") was used in all patients. Resolution of PST immediately following surgery occurred in 38/40 patients. Postoperative imaging was performed in those patients who had persistent PST following surgery ($n = 2$), late recurrence (or new occurrence) of tinnitus on the contralateral side ($n = 2$) within 2 years of surgery, or in those cases in which there was concern for surgical complications ($n = 9$). These indications included headache with or without visual disturbances ($n = 6$), concern for dural thrombus from intraoperative diverticulum rupture ($n = 1$), fluid collection at the operative site ($n = 1$), and facial swelling and erythema ($n = 1$).

Of the 13 patients with postoperative imaging, 2 were male and 11 were female, with ages ranging from 14 to 65 years (median age, 41 years) (Table). The time interval between operative intervention and first postoperative examination ranged from 1 day to 2 years (median interval, 14 days). Seven patients presented with right PST; 5, with left PST; and 1 had bilateral PST with right-sided dominance. Imaging findings on preoperative CT scans included sigmoid sinus dehiscence ($n = 8$) and sigmoid sinus diverticulum ($n = 5$). Average dehiscence width was 4 mm (range, 2–7 mm), and average maximal diverticulum size was 5 mm (range, 2–10 mm).

In all 13 patients, SSWR was performed with soft-tissue and rigid reinforcement as previously described. In 6 patients, reconstruction was performed with AlloDerm; in 6, with temporalis fascia graft; and in 1 patient, both AlloDerm and temporalis fascia were used. Surgicel was used for hemostasis, especially when there was violation of the diverticulum during surgical reduction. In all patients, HydroSet was used to reconstruct the osseous defect, and in 11 patients, autologous bone pate was used for additional reinforcement. One patient underwent simultaneous mesh reconstruction of a tegmen tympani meningocele.

Imaging Findings

The 3 layers used in SSWR were consistently identified in all patients on imaging. Soft-tissue material between the sigmoid sinus and the sigmoid plate, comprising AlloDerm and/or temporalis fascia graft with or without Surgicel, was identified in all postoperative scans (Fig 3*A*) as crescentic, extraluminal, low-attenuation material relative to the enhanced sigmoid sinus (approximately 30–60 HU [Hounsfield units]). It was not possible to differentiate the individual soft-tissue components on the basis of CT imaging characteristics. Although the thickness of the temporalis fascia and AlloDerm used in surgery is only between 1 and 2 mm, the average thickness of the soft-tissue material on CT was 5.1 mm

(range, 2–8 mm). This difference may be attributed to a number of factors including variability of blood absorption by the Surgicel when used, granulation tissue, and focal hemorrhage.

HydroSet was identified as sharply demarcated hyperattenuated material (1400–1500 HU) conforming to the size and shape of dehiscence (Fig 3*B*). Bone pate was identified as amorphous ill-defined hyperattenuation (400–500 HU) placed external to the HydroSet (Fig 3*B*).

The soft-tissue graft demonstrated intermediate-to-high signal on T1- and T2-weighted MR imaging (Fig 4) and intermediate signal on gradient-echo sequences (Fig 5*D*). On gadolinium-enhanced images, no enhancement was observed in the immediate postoperative period. Four weeks following surgery, however, enhancement was present, presumably due to the formation of granulation tissue (Fig 4*B*, -*C*).

The degree of mass effect exerted by the soft-tissue material on the adjacent sigmoid sinus was variable. In 5/13 patients, there was narrowing of the lumen (>50% decrease in caliber compared with preoperative images) (Fig 5). Two of these patients presented with headaches; 1, with persistent PST; and 1, with unrelated facial cellulitis (see below). In 1 patient who was imaged due to intraoperative diverticulum violation, the mass effect resulted in no symptoms.

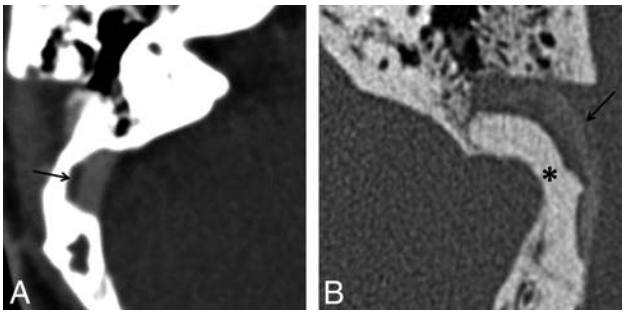

FIG 3. Postoperative CT imaging. Axial CT image of the temporal bone in a soft-tissue window (*A*) demonstrates relatively hypoattenuated material (*arrow*) lateral to the contrast-enhanced sigmoid sinus representing soft tissue graft. *B*, On bone window (different patient), HydroSet is identified as sharply demarcated attenuated material (*asterisk*) conforming to the size and shape of the dehiscence. Bone pate is identified lateral to the HydroSet as amorphous ill-defined hyperattenuation (*arrow*).

One of the 6 patients with postoperative headache had thrombosis of the right transverse sinus, ipsilateral to the surgery (Fig 6). This patient responded rapidly to anticoagulation and had no neurologic deficit. In 2 other patients experiencing postoperative headaches, imaging indicated mass effect by the soft-tissue graft on the sigmoid sinus, as described above. In the remaining 2 patients who had headache and/or visual disturbances, no significant findings were evident.

The patient who had facial swelling presented 2 days following surgery with right facial edema, pain, and erythema. CT showed mass effect from the temporalis fascia graft on the sigmoid sinus and, additionally, a small, nonocclusive thrombus within the sigmoid sinus. The patient, already on an anticoagulation regimen, was diagnosed with facial cellulitis, treated with antibiotics, and discharged.

In the first of 2 patients who had persistent PST immediately following surgery, the symptoms were attributed to coexistent jugular bulb dehiscence. In the second patient, significant mass effect on the sigmoid sinus by the soft-tissue graft was identified. This was thought to be unrelated to the tinnitus because the PST persisted even though a follow-up CT demonstrated that the mass effect had resolved.

Two patients had new PST on the side contralateral to the surgery. One patient initially presented with right-greater-than left PST, with CT demonstrating right sigmoid sinus diverticulum and a small left sigmoid sinus wall dehiscence. This patient underwent bilateral, staged SSWR a few months apart. The second patient presented with left-sided PST approximately 2 years after right SSWR, and repair of the left-sided dehiscences resulted in cessation of the tinnitus.

One patient demonstrated a fluid collection at the operative site. No peripheral enhancement to imply infection was seen.

DISCUSSION

Sigmoid sinus wall anomalies have been increasingly recognized as a cause of pulsatile tinnitus. According to some reports, between 22% and 48% of patients clinically diagnosed with pulsatile tinnitus of venous origin have a diverticulum or dehiscence of the sigmoid sinus that is detectable on contrast-enhanced CT.[6,12] Although treatment for sigmoid sinus wall

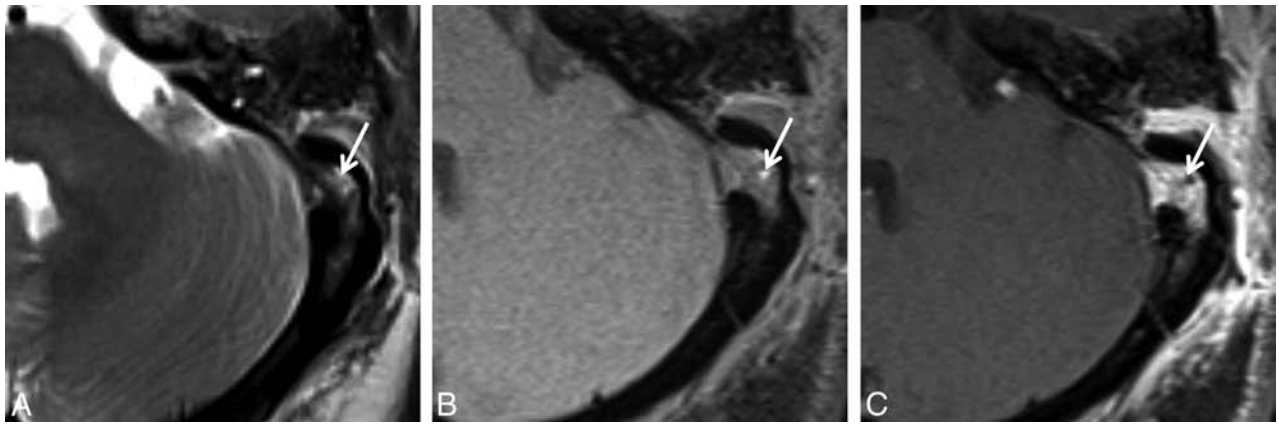

FIG 4. Postoperative MR imaging. Axial T2- (*A*), precontrast T1- (*B*), and postcontrast T1-weighted (*C*) images demonstrate a temporalis fascia graft (*arrow*) between the sigmoid sinus and the reconstructed sigmoid sinus wall. The graft demonstrates intermediate-to-high signal on both T1- and T2-weighted images and contrast enhancement. These images were obtained 28 days following surgery.

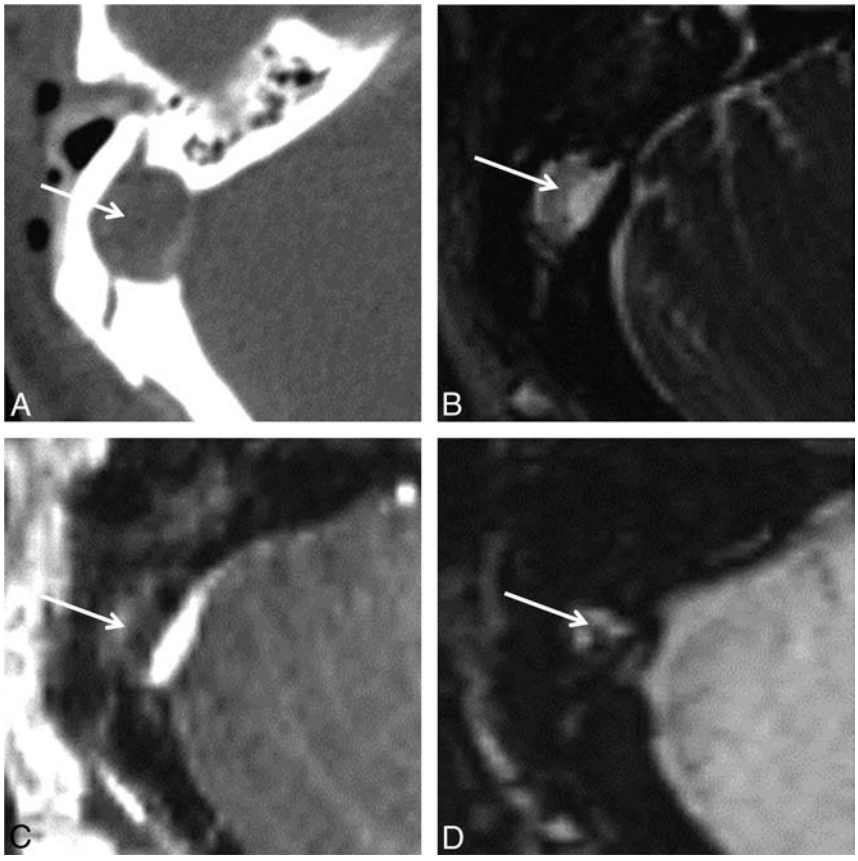

FIG 5. Mass effect on the sigmoid sinus following sigmoid sinus wall repair. A 46-year-old woman status post right diverticulum repair. Images were obtained 1 day following surgery. Postcontrast axial CT image (*A*) demonstrates significant mass effect caused by the soft-tissue graft (*arrow*), resulting in severe narrowing of the sigmoid sinus. Axial T2 (*B*) and postcontrast T1-weighted (*C*) images. The graft is intermediate-to-high signal on T2-weighted images. Note the lack of enhancement of the graft in the immediate postoperative period. The soft-tissue material, unlike thrombus, is not hypointense on the susceptibility-weighted image (*D*).

abnormalities historically has been endovascular embolization,[13] more recently, the open transmastoid approach has become the norm.[5,14,15] Otto et al[14] described 5 patients with unilateral or bilateral PST with sigmoid sinus wall abnormalities on imaging, 3 of whom underwent surgical intervention with resurfacing of the sinus with resolution of symptoms. More recently, Harvey et al[11] reported a series of 33 patients with sigmoid sinus wall abnormalities who underwent treatment by using the transmastoid approach, 30 of whom responded favorably to the procedure.

The expected imaging appearance of the temporal bone following sigmoid sinus reconstruction has not been previously described, to our knowledge. Given that postoperative imaging is not routinely performed and is only indicated to rule out postsurgical complications, it behooves the radiologist to become familiar with the appearance of the various materials used to repair and reinforce the sigmoid sinus wall to distinguish normal findings from potential disease. Our observations indicate that the 3 layers used in SSWR (soft-tissue graft, HydroSet, and bone pate) are consistently recognizable and demonstrate characteristic imaging appearances.

Recovery from transmastoid SSWR is generally uneventful. In our study, the most common symptom that warranted imaging following surgery was headache with or without visual disturbances. Thrombosis of the sigmoid/transverse sinus is the most worrisome complication of this procedure. Manipulation of the sigmoid sinus wall entails a risk for thrombosis, and sigmoid sinus thrombosis is not infrequently encountered following translabyrinthine and suboccipital craniectomy.[16] Although the surgical technique used in this study does not require significant exposure or retraction of the sigmoid sinus, the risk for thrombosis does exist. To avoid this, all patients at our institution are placed on an anticoagulation regimen comprising aspirin preoperatively and aspirin and clopidogrel postoperatively. Symptomatic postoperative thrombosis was only encountered in 1 patient, and that patient was noncompliant with the regimen.

Mass effect on the sigmoid sinus from extraluminal soft-tissue material at the operative site was commonly seen in our study and is a finding that may be confused with thrombosis. Five patients of the 13 evaluated in this series had this finding, 3 of whom had headaches. Patients with mass effect were closely monitored and reported resolution of their headaches with conservative management. The mass effect likely arises from a combination of soft-tissue material (AlloDerm/temporalis fascia); Surgicel, which likely undergoes expansion in the operative bed; and a localized hematoma. Differentiation of these individual components is not possible on imaging. However, it is important to distinguish this extraluminal process (which requires close clinical observation, but is self-limiting) from intraluminal thrombosis (which may require prompt anticoagulation). A combination of CT and MR imaging characteristics may be useful in this regard (Figs 5 and 6). Acute thrombus is hyperattenuated on noncontrast CT, whereas extraluminal soft-tissue material typically appears as relatively hypoattenuating material and is focal, being confined to the site of repair. On MR imaging, on gradient-echo or susceptibility-weighted images, thrombus, unlike graft material, is markedly hypointense and may propagate along the course of the transverse/sigmoid sinus. If there are equivocal findings, a combination of both CT and MR imaging may be used to distinguish intraluminal thrombus from extraluminal surgical material.

Two of the 13 patients reported persistent tinnitus after surgery. In 1 patient, this was attributed to a coexistent dehiscence of the ipsilateral jugular bulb. In the second patient, no additional findings were identified that could explain persistent symptomatology. In both patients, the postoperative scans indicated that the dehiscent sigmoid sinus had been fully reconstructed. In addition, in 2 patients, PST resolved in the immediate postoperative

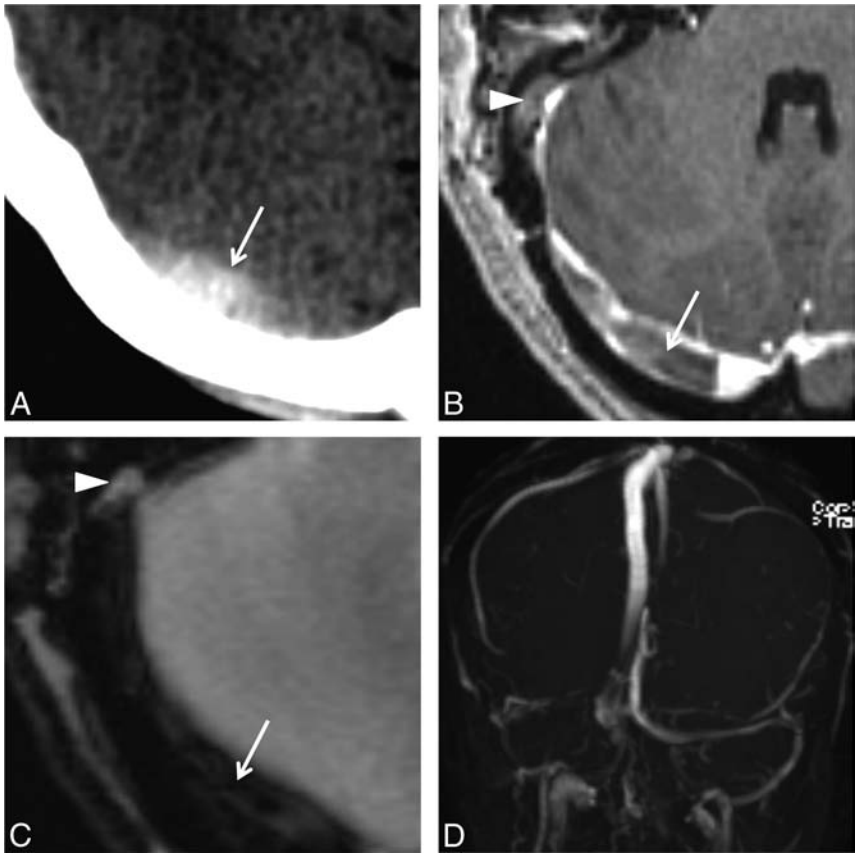

FIG 6. Transverse sinus thrombosis following SSWR. Images were obtained 11 days following surgery after the patient reported severe headaches. Noncontrast axial CT (*A*) demonstrates hyperattenuation (*arrow*) within the right transverse sinus. On postcontrast T1-weighted MR imaging (*B*), there is a filling defect (*arrow*) within the right transverse sinus, which is hypointense on the gradient-echo image (*C*). Note the presence of a soft-tissue graft lateral to the sigmoid sinus (*arrowhead*), which demonstrates no susceptibility. Maximum-intensity projection reconstruction (*D*) demonstrates right transverse sinus thrombosis.

period but later recurred on the contralateral side: In 1 patient, this recurrence was attributed to subtle dehiscence on the other side, which was detectable on the preoperative CT scan. These cases stress the importance of careful evaluation of preoperative imaging studies for other anomalies that can cause PST, even after a sigmoid sinus wall abnormality has been identified. In a recent study, up to 70% of patients analyzed for causes of PST were found to have >1 vascular anomaly or variant on the symptomatic side.[7]

Limitations

The relatively small number of patients represents a key limitation of our study. This is because postoperative imaging was only performed in those patients who presented with worrisome symptoms following surgery. In addition, a more detailed understanding of how graft materials evolve with time will require long-term follow-up imaging. Also, although the technique described is increasingly recognized as a standard approach to SSWR, variations in the use of materials across institutions may exist. It is important, therefore, for radiologists to communicate with the surgeons performing the technique to be able to interpret postoperative studies in an accurate manner.

CONCLUSIONS

Symptoms requiring postoperative imaging after SSWR include headaches, visual disturbances, and persistent/recurrent tinnitus. A variety of soft and rigid materials is used to reconstruct the sigmoid sinus wall in patients with PST arising from sigmoid sinus wall abnormalities, and these surgical materials can be easily recognized and differentiated on imaging studies. The surgical material may exert mass effect the on sinus wall, a finding that must not be mistaken for sinus thrombosis and does not require anticoagulation. Symptomatic sinus thrombosis is rare and may be distinguished from such compression by an awareness of the typical imaging appearances of the materials used in the procedure.

ACKNOWLEDGMENTS

We thank Brigitte Pocta, MLA, for assistance with revision and preparation of the manuscript.

Disclosures: Dheeraj Gandhi—*UNRELATED*: *Royalties*: Cambridge Press. Ronna Hertzano—*UNRELATED*: *Grants/Grants Pending*: National Institutes of Health,* Department of Defense,* *Comments*: National Institutes of Health, transcription factors in inner ear development, RO1DC013817; Department of Defense, the molecular basis of noise induced hearing loss, MR130240. *Money paid to the institution.

REFERENCES

1. Levine SB, Snow JB Jr. **Pulsatile tinnitus.** *Laryngoscope* 1987;97:401–06 CrossRef Medline
2. Liyanage SH, Singh A, Savundra P, et al. **Pulsatile tinnitus.** *J Laryngol Otol* 2006;120:93–97 CrossRef Medline
3. Sismanis A. **Pulsatile tinnitus: a 15-year experience.** *Am J Otol* 1998; 19:472–77 Medline
4. Sonmez G, Basekim CC, Ozturk E, et al. **Imaging of pulsatile tinnitus: a review of 74 patients.** *Clin Imaging* 2007;31:102–08 CrossRef Medline
5. Eisenman DJ. **Sinus wall reconstruction for sigmoid sinus diverticulum and dehiscence: a standardized surgical procedure for a range of radiographic findings.** *Otol Neurotol* 2011;32:1116–19 CrossRef Medline
6. Mattox DE, Hudgins P. **Algorithm for evaluation of pulsatile tinnitus.** *Acta Otolaryngol* 2008;128:427–31 CrossRef Medline
7. Dong C, Zhao PF, Yang JG, et al. **Incidence of vascular anomalies and variants associated with unilateral venous pulsatile tinnitus in 242 patients based on dual-phase contrast-enhanced computed tomography.** *Chin Med J (Engl)* 2015;128:581–85 CrossRef Medline
8. Grewal AK, Kim HY, Comstock RH 3rd, et al. **Clinical presentation and imaging findings in patients with pulsatile tinnitus and sigmoid sinus diverticulum/dehiscence.** *Otol Neurotol* 2014;35:16–21 CrossRef Medline
9. Wang GP, Zeng R, Liu ZH, et al. **Clinical characteristics of pulsatile tinnitus caused by sigmoid sinus diverticulum and wall dehiscence: a study of 54 patients.** *Acta Otolaryngol* 2014;134:7–13 CrossRef Medline

10. Baomin L, Yongbing S, Xiangyu C. **Angioplasty and stenting for intractable pulsatile tinnitus caused by dural venous sinus stenosis: a case series report.** *Otol Neurotol* 2014;35:366–70 CrossRef Medline
11. Harvey RS, Hertzano R, Kelman SE, et al. **Pulse-synchronous tinnitus and sigmoid sinus wall anomalies: descriptive epidemiology and the idiopathic intracranial hypertension patient population.** *Otol Neurotol* 2014;35:7–15 CrossRef Medline
12. Schoeff S, Nicholas B, Mukherjee S, et al. **Imaging prevalence of sigmoid sinus dehiscence among patients with and without pulsatile tinnitus.** *Otolaryngol Head Neck Surg* 2014;150:841–46 CrossRef Medline
13. Houdart E, Chapot R, Merland JJ. **Aneurysm of a dural sigmoid sinus: a novel vascular cause of pulsatile tinnitus.** *Ann Neurol* 2000; 48:669–71 CrossRef3.3.CO%3B2-Y Medline
14. Otto KJ, Hudgins PA, Abdelkafy W, et al. **Sigmoid sinus diverticulum: a new surgical approach to the correction of pulsatile tinnitus.** *Otol Neurotol* 2007;28:48–53 CrossRef Medline
15. Gologorsky Y, Meyer SA, Post AF, et al. **Novel surgical treatment of a transverse-sigmoid sinus aneurysm presenting as pulsatile tinnitus: technical case report.** *Neurosurgery* 2009;64:E393–94; discussion E394 CrossRef Medline
16. Keiper GL Jr, Sherman JD, Tomsick TA, et al. **Dural sinus thrombosis and pseudotumor cerebri: unexpected complications of suboccipital craniotomy and translabyrinthine craniectomy.** *J Neurosurg* 1999;91:192–97 CrossRef Medline

Advanced Modeled Iterative Reconstruction in Low-Tube-Voltage Contrast-Enhanced Neck CT: Evaluation of Objective and Subjective Image Quality

J.-E. Scholtz, M. Kaup, K. Hüsers, M.H. Albrecht, B. Bodelle, S.C. Metzger, J.M. Kerl, R.W. Bauer, T. Lehnert, T.J. Vogl, and J.L. Wichmann

ABSTRACT

BACKGROUND AND PURPOSE: Dose-saving techniques in neck CT cause increased image noise that can be counteracted by iterative reconstruction. Our aim was to evaluate the image quality of advanced modeled iterative reconstruction (ADMIRE) in contrast-enhanced low-tube-voltage neck CT.

MATERIALS AND METHODS: Sixty-one patients underwent 90-kV(peak) neck CT by using third-generation 192-section dual-source CT. Image series were reconstructed with standard filtered back-projection and ADMIRE strength levels 1, 3, and 5. Attenuation and noise of the sternocleidomastoid muscle, internal jugular vein, submandibular gland, tongue, subscapularis muscle, and cervical fat were measured. Signal-to-noise and contrast-to-noise ratios were calculated. Two radiologists assessed image noise, image contrast, delineation of smaller structures, and overall diagnostic acceptability. Interobserver agreement was calculated.

RESULTS: Image noise was significantly reduced by using ADMIRE compared with filtered back-projection with the lowest noise observed in ADMIRE 5 (filtered back-projection, 9.4 ± 2.4 Hounsfield units [HU]; ADMIRE 1, 8.3 ± 2.8 HU; ADMIRE 3, 6.7 ± 2.0 HU; ADMIRE 5, 5.4 ± 1.7 HU; all, $P < .001$). Sternocleidomastoid SNR and internal jugular vein–sternocleidomastoid contrast-to-noise ratios were significantly higher for ADMIRE with the best results in ADMIRE 5 (all, $P < .001$). Subjective image quality and image contrast of ADMIRE 3 and 5 were consistently rated better than those for filtered back-projection and ADMIRE 1 (all, $P < .001$). Image noise was rated highest for ADMIRE 5 (all, $P < .005$). Delineation of smaller structures was voted higher in all ADMIRE strength levels compared with filtered back-projection ($P < .001$). Global interobserver agreement was good (0.75).

CONCLUSIONS: Contrast-enhanced 90-kVp neck CT is feasible, and ADMIRE 5 shows superior objective image quality compared with filtered back-projection. ADMIRE 3 and 5 show the best subjective image quality.

ABBREVIATIONS: ADMIRE = advanced modeled iterative reconstruction; CNR = contrast-to-noise ratio; DSCT = dual-source CT; FBP = filtered back-projection; HU = Hounsfield units

Contrast-enhanced CT is a well-established initial cross-sectional imaging technique for examination of the head and neck region.[1-3] Several strategies have been developed for both radiation dose reduction and improvement of image quality. These typically involve adjusting CT acquisition parameters such as tube voltage, tube current, tube rotation time, pitch, and collimation to the patient body and examined body region.[4-6] The interaction of these parameters is complex, and manual adjustments may result in nondiagnostic images. Thus, commercially available techniques, including tube current modulation,[7] automatic exposure control,[8,9] automated tube voltage adaptation,[10,11] iterative reconstruction,[12-15] and selective in-plane shielding (thyroid, eye lens, breast, and gonads),[16] have been introduced to support the radiologic technologist, physicist, and radiologist team in developing appropriate CT protocols.

Reduced tube voltage can increase contrast-to-noise ratio (CNR) of iodine enhancing soft-tissue structures, while the radiation dose is substantially reduced.[4] The drawback of an increased image noise in low-tube-voltage examinations can be counteracted by iterative reconstruction, which reduces image noise compared with filtered back-projection (FBP).[12,14] Recently introduced advanced modeled iterative reconstruction (ADMIRE) performs detailed modeling in the projection data domain, result-

Received May 4, 2015; accepted after revision June 10.

From the Department of Diagnostic and Interventional Radiology (J.-E.S., M.K., K.H., M.H.A., B.B., S.C.M., J.M.K., R.W.B., T.L., T.J.V., J.L.W.), University Hospital Frankfurt, Frankfurt, Germany; and Department of Radiology and Radiological Science (J.L.W.), Medical University of South Carolina, Charleston, South Carolina.

Jan-Erik Scholtz and Moritz Kaup contributed equally and share first authorship.

Neither Ralf W. Bauer nor J. Matthias Kerl analyzed or controlled any data in this study.

Please address correspondence to Jan-Erik Scholtz, MD, Universitätsklinikum Frankfurt am Main, Institut für Diagnostische und Interventionelle Radiologie, Theodor-Stern-Kai 7, 60590 Frankfurt; e-mail: janerikscholtz@gmail.com

http://dx.doi.org/10.3174/ajnr.A4502

Table 1: Results of objective image analysis[a]

	FBP	ADMIRE 1	ADMIRE 3	ADMIRE 5
Attenuation (HU)				
Sternocleidomastoid muscle	79.4 ± 13.2	80.1 ± 13.4	79.9 ± 13.6	79.2 ± 13.7
Internal jugular vein	288.5 ± 71.4	290.5 ± 72.6	289.0 ± 71.6	287.3 ± 72.2
Submandibular gland	131.4 ± 47.1	131.2 ± 48.2	131.6 ± 47.8	131.1 ± 47.2
Tongue	97.4 ± 14.1	97.5 ± 13.9	96.2 ± 13.5	95.7 ± 13.5
Subscapularis muscle	69.8 ± 12.9	69.9 ± 12.8	68.8 ± 12.6	69.0 ± 12.4
Fat	−105.7 ± 9.3	−106.4 ± 11.3	−107.2 ± 10.9	−106.0 ± 11.3
Image noise (HU)				
Sternocleidomastoid muscle	9.4 ± 2.4	8.3 ± 2.8	6.7 ± 2.0	5.4 ± 1.7
Internal jugular vein	12.6 ± 6.3	11.2 ± 5.9	10.3 ± 7.1	8.5 ± 5.5
Submandibular gland	11.9 ± 2.6	11.2 ± 2.5	9.4 ± 2.9	7.5 ± 3.0
Tongue	10.3 ± 2.4	9.8 ± 2.6	8.6 ± 2.8	6.9 ± 3.2
Subscapularis muscle	15.3 ± 2.8	13.7 ± 2.7	11.8 ± 2.6	8.6 ± 2.8
Fat	15.1 ± 5.1	14.9 ± 4.5	12.6 ± 4.8	9.8 ± 4.0

[a] Data are means.

ing in less noise and improved artifact suppression.[17] ADMIRE includes a local signal-to-noise relationship analysis and decomposes the image data into information and noise.[18] Further technical details have been described in recent studies.[14,17,18] Thus, neck CT may potentially be performed with a reduced tube voltage and therefore lower radiation dose without impairing image quality.

The purpose of our study was to evaluate the impact of ADMIRE on image quality in low-tube-voltage contrast-enhanced neck CT compared with FBP on a 192-section third-generation dual-source CT (DSCT).

MATERIALS AND METHODS

Patient Population

This retrospective study was approved by the ethics committee of our hospital, and the requirement for written informed consent was waived. Sixty-four patients (54.6 ± 16.4 years of age; range, 24–82 years) underwent contrast-enhanced neck CT between November 2014 and February 2015. These time intervals were chosen due to a change in tube voltage to 90 kV in the standard protocol for contrast-enhanced neck CT in adults on the DSCT scanner used in October 2014. Our study population consisted of 38 males (58.1 ± 16.1 years of age; range, 24–82 years) and 26 females (49.5 ± 16.1 years of age; range, 26–75 years). Indications for contrast-enhanced neck CT included detection or exclusion ($n = 26$) or follow-up ($n = 10$) of a tumor or lymphoma in the head and neck region or the visualization or exclusion of a clinically suspected inflammatory process ($n = 28$).

CT angiography and noncontrast examinations were excluded from this study. Furthermore, nondiagnostic studies due to severe motion or metal artifacts were excluded. Underage patients (younger than 18 years of age) were excluded because they are examined with different scan protocols at our institution. Contraindications for CT imaging were any known previous reactions to iodinated contrast medium, renal impairment with a glomerular filtration rate lower than 60 mL/min, and known pregnancy.

Examination Protocol

All examinations were performed on a 192-section third-generation DSCT (Somatom Force; Siemens, Erlangen, Germany) in single-energy mode. The examinations were planned according to our current protocol for head and neck imaging of 90 kV and 197 reference mAs. Further scan parameters were as follows: pitch, 0.8; rotation time, 1.0 seconds; collimation, 192 × 0.6 mm. Dedicated automated real-time attenuation-based tube current modulation software (CARE Dose 4D; Siemens) was activated.

CT examinations were performed in a craniocaudal direction with the patient in the supine position and in expiratory breathhold. Data acquisition started 70 seconds after the start of intravenous administration of 100 mL of nonionic iodinated contrast medium (iopamidol, Imeron 400; Bracco, Milan, Italy) with a flow rate of 2 mL/s.

CT Data Reconstruction

Image series were reconstructed in axial views with a section thickness of 2 mm (2-mm increment) by using an FBP algorithm with a soft-tissue convolution kernel (B30f) and ADMIRE with a soft-tissue convolution kernel (Br30f). The technical features of ADMIRE have been described previously.[14,19] ADMIRE provides 5 strength levels (1–5); each examination was reconstructed in strength levels 1, 3, and 5. We chose these reconstruction levels because level 3 is recommended as the standard for most contrast-enhanced CT examinations by the vendor, and we could compare the impact of image reconstruction, with very little ADMIRE contribution (level 1) and maximum ADMIRE influence (level 5), with the standard. We omitted the levels in-between (levels 2 and 4) because we assumed that differences in image quality may be less apparent. Images were series reconstructed in clinical routine with an average reconstruction time of 0.5–1 minute for each parameter without differences in time required among the different ADMIRE levels.

Objective Image Analysis

All measurements were performed on a commercially available PACS workstation. We evaluated the following anatomic structures: the sternocleidomastoid muscle, internal jugular vein, tongue, submandibular gland, cervical fat, and the subscapularis muscle. Circular ROIs (10–30 mm^2) were drawn as large as possible in these structures while carefully avoiding inclusion of adjacent anatomic structures or focal regions of inhomogeneity. Signal attenuation and image noise were measured in Hounsfield units (HU). Values averaged of 3 measurements were calculated to ensure data consistency. Image noise was quantified as the SD of each measured anatomic structure. Signal-to-noise ratio was calculated for the sternocleidomastoid muscle and submandibular gland by using the following formula:

$$\mathrm{SNR} = \frac{\text{Mean Signal Intensity}}{\mathrm{SD}}.$$

The sternocleidomastoid muscle–fat contrast-to-noise ratio and submandibular gland–fat CNR were calculated as follows:

$$CNR = \frac{HU\ (Soft\text{-}Tissue\ Structure) - HU\ (Fat)}{Image\ Noise\ (Fat)}.$$

The internal jugular vein (IJV)–sternocleidomastoid muscle CNR was calculated as follows:

$$CNR = \frac{Attenuation\ (IJV) - Attenuation\ (Sternocleidomastoid\ Muscle)}{Image\ Noise\ (Sternocleidomastoid\ Muscle)}.$$

Subjective Image Analysis

Patients were evaluated in a randomized manner independently by 2 radiologists with 3 and 4 years of experience in neck CT, respectively. Observers were blinded to the reconstruction technique used. All CT images were preadjusted to the same soft-tissue window setting (width, 400; level, 60). Reviewers were allowed to scroll through the complete presented axial image series with the possibility of freely adjusting the window width and level. Subjective image analyses were performed on rating scales of 1–5 for overall image quality (5 = excellent, 4 = good, 3 = sufficient, 2 = poor, 1 = nondiagnostic); delineation of small structures of the pharynx (wall, mucosal margin, parapharyngeal fat, parapharyngeal muscle), larynx (mucosal folds, intrinsic laryngeal muscles, paralaryngeal muscles), and salivary glands (glandular tissue, paraglandular fat spaces); delineation of lymphatic tissue of Waldeyer tonsillar ring and cervical lymph (5 = excellent visibility, 4 = above average, 3 = acceptable, 2 = suboptimal, 1 = very poor); image contrast (5 = excellent image contrast, 4 = above average, 3 = acceptable, 2 = suboptimal, 1 = very poor); and image noise (5 = very low, 4 = low, 3 = average, 2 = considerable, 1 = high).

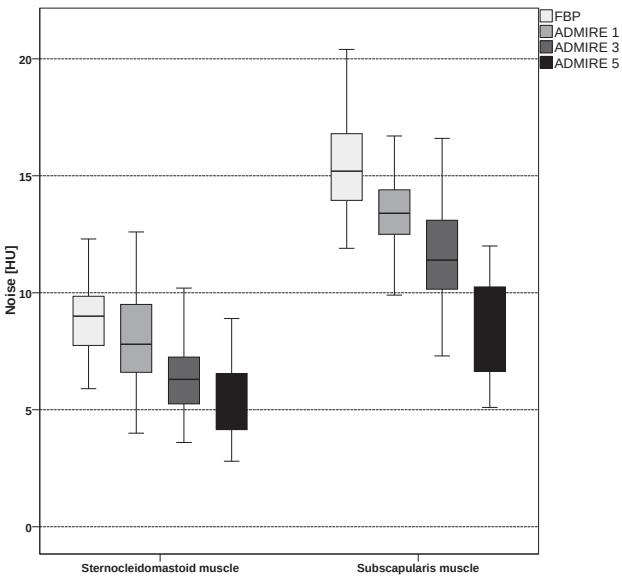

FIG 1. Boxplot graph shows comparison of image noise of the sternocleidomastoid and subscapularis muscles between the different image reconstruction settings. Image noise of the sternocleidomastoid muscle and subscapularis muscle was significantly lower with all ADMIRE levels, with the best results for ADMIRE 5 (all, $P < .001$). Noise in the lower part of the neck, represented by the subscapularis muscle, was significantly increased within each reconstruction mode compared with the upper part of the neck, represented by the sternocleidomastoid muscle (all, $P < .001$).

Radiation Dose

Radiation exposure was expressed as CT dose index volume ($CTDI_{vol}$) and dose-length product, and it was provided automatically by the CT scanner. The estimated effective dose was calculated by using a standard conversion factor of 0.0051 for 100-kV neck CT. In addition, size-specific dose estimates were calculated. To calculate specific dose estimates, we measured the effective diameter from the anteroposterior (AP) and lateral (LAT) dimensions at the fourth cervical vertebra.

$$Effective\ Diameter\ (cm) = \sqrt{AP \times LAT}.$$

A conversion factor based on the effective diameter and the 32-cm diameter polymethylmethacrylate phantom provided by the American Association of Physicists in Medicine Report No. 204 was selected for each patient.[20] Size-specific dose estimate (SSDE) was calculated as follows:

$$SSDE\ (mGy) = CTDI_{vol} \times Conversion\ Factor.$$

Statistical Analysis

For statistical analysis, dedicated software (SPSS, Version 19; IBM Armonk, New York) was used. A P value $< .05$ was significant for all tests. Data sphericity was assessed with the Greenhouse-Geisser and the Huynh-Feldt methods. Continuous variables were expressed as means ± SDs. Quantitative image analysis was evaluated by using repeated measures of ANOVA. Statistical analysis of qualitative image analysis was performed by using the nonparametric Wilcoxon test for the intraindividual comparison.

The interobserver acceptance of subjective image analysis was expressed by Cohen weighted analysis: $\kappa < 0.30$ indicated slight agreement; $\kappa = 0.3–0.7$, moderate agreement; $\kappa > 0.7$, good agreement.

Table 2: Signal-to-noise ratio and contrast-to-noise ratio calculations[a]

	FBP	ADMIRE 1	ADMIRE 3	ADMIRE 5
Signal-to-noise ratio				
Sternocleidomastoid muscle	9.0 ± 2.5	10.8 ± 4.1	13.0 ± 4.4	16.4 ± 6.2
Submandibular gland	11.6 ± 4.6	12.3 ± 4.7	15.3 ± 6.8	19.6 ± 8.2
Contrast-to-noise ratio				
Sternocleidomastoid muscle–fat	14.5 ± 8.1	13.8 ± 4.9	17.3 ± 7.7	22.6 ± 11.4
Submandibular gland–fat	19.1 ± 11.6	17.9 ± 8.2	22.6 ± 11.7	28.6 ± 17.1
IJV–sternocleidomastoid muscle	24.1 ± 10.1	28.7 ± 13.5	34.8 ± 16.3	41.2 ± 22.1

Note:—IJV indicates internal jugular vein.
[a] Data are means.

Table 3: Subjective image-quality assessment[a]

	FBP	ADMIRE 1	ADMIRE 3	ADMIRE 5
Overall image quality	3.2 ± 0.5 (0.58)	3.3 ± 0.6 (0.57)	4.4 ± 0.9 (0.12)	4.7 ± 0.5 (0.67)
Image noise	3.4 ± 0.5 (0.79)	3.8 ± 0.4 (0.83)	4.6 ± 0.5 (0.52)	4.9 ± 0.3 (0.32)
Delineation of smaller structures	3.3 ± 0.4 (0.74)	3.7 ± 0.5 (0.78)	3.8 ± 0.4 (0.50)	3.8 ± 0.4 (0.74)
Image contrast	3.5 ± 0.5 (0.80)	3.4 ± 0.5 (0.78)	4.8 ± 0.4 (0.34)	4.8 ± 0.4 (0.47)

[a] Data are means ± SD. Interobserver agreement (slight [$\kappa < 0.3$], moderate [$\kappa = 0.3–0.7$], good [$\kappa > 0.7$]).

RESULTS

All examinations were performed without any complications. No examinations

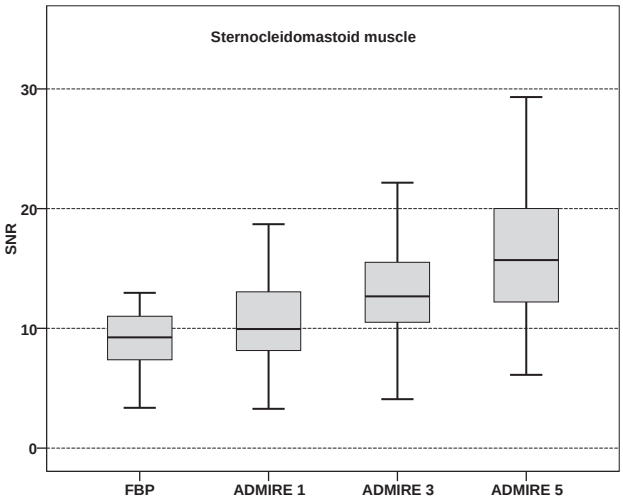

FIG 2. Boxplot graphs show comparison of signal-to-noise ratios of the sternocleidomastoid muscle. SNR was significantly higher for ADMIRE compared with FBP with the highest results observed for ADMIRE strength level 5 (all, $P < .001$). Significant differences were also shown within ADMIRE strength levels (all, $P < .001$).

were excluded because of severe motion or metal artifacts. Due to submandibular gland removal, evaluation of the submandibular gland was not possible in 2 cases.

The mean CT dose index volume was 6.57 ± 0.75 mGy. The mean dose-length product was 174.4 ± 31.3 mGy × cm, and the mean calculated effective dose was 0.89 ± 0.16 mSv. The average effective diameter was 15.8 ± 1.9 cm, and the mean effective tube current was 227.0 ± 26.1 mAs. The calculated average size-specific dose estimate was 13.59 ± 1.23 mGy.

Objective Image Analysis

Attenuation of the sternocleidomastoid muscle (all, $P > .405$) and submandibular gland (all $P > .245$) in FBP and all ADMIRE strength levels did not differ significantly. Image noise of the sternocleidomastoid muscle was significantly reduced by using ADMIRE compared with FBP with the lowest noise observed in ADMIRE 5 (all, $P < .001$). Image noise of the subscapularis muscle, representing noise levels in the lower part of the neck, was increased compared with noise of the sternocleidomastoid muscle, representing the upper part of the neck, within each reconstruction method (all, $P < .001$). Attenuation and image noise measurements are summarized in Table 1. Figure 1 illustrates a comparison of image noise between FBP and ADMIRE 1, 3, and 5 of the sternocleidomastoid muscle and subscapularis muscle.

SNR calculations are summarized in Table 2. The sternocleidomastoid muscle SNR was significantly higher for all reconstructed ADMIRE strength levels compared with FBP, with the best results in ADMIRE 5 and significant differences within all ADMIRE strength levels (all, $P < .001$). Comparisons of the sternocleidomastoid muscle SNR are illustrated in Fig 2.

Sternocleidomastoid muscle–fat CNR was significantly higher in ADMIRE 3 and 5 compared with FBP and ADMIRE 1, with the highest CNR in ADMIRE 5 (all, $P < .001$). Sternocleidomastoid muscle–fat CNR in FBP was slightly higher than that in ADMIRE 1 ($P = .256$). Submandibular gland–fat CNR was highest in ADMIRE 5 compared with FBP and ADMIRE 1 and 3 ($P < .001$).

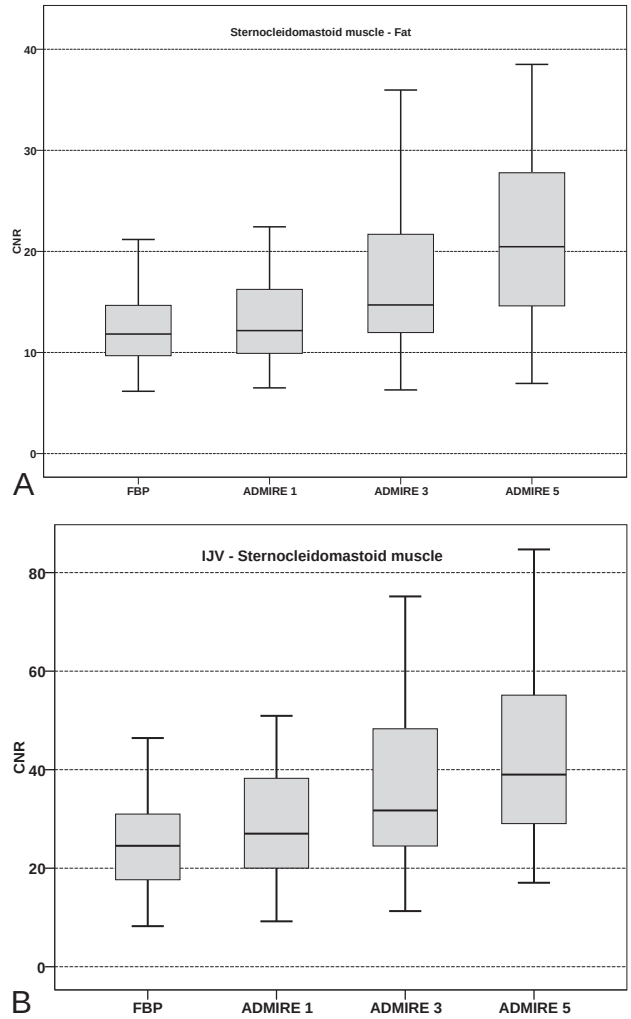

FIG 3. Boxplot graphs show contrast-to-noise ratios of sternocleidomastoid muscle-to-fat (*A*) with significantly higher results in ADMIRE strength levels 3 and 5 compared with FBP and ADMIRE 1 ($P < .001$), while internal jugular vein–sternocleidomastoid muscle CNR (*B*) is significantly increased in all ADMIRE strength levels compared with FBP (all, $P < .001$).

Submandibular gland–fat CNR in FBP was nonsignificantly higher compared with ADMIRE 1 ($P = .430$) but was significantly lower compared with ADMIRE 3 ($P = .004$). Internal jugular vein–sternocleidomastoid CNR was significantly higher in all ADMIRE strength levels compared with FBP, with the highest CNR in ADMIRE 5 and significant differences within the ADMIRE strength levels (all, $P < .001$). Results of CNR calculations are summarized in Table 2, and comparisons of CNR calculations are shown in Fig 3. Figure 4 shows axial images of a bilateral T2 glottic larynx cancer by using FBP and ADMIRE 1, 3, and 5.

Subjective Image Analysis

Results from subjective ratings including interobserver agreement are summarized in Table 3. Overall image quality was voted best in ADMIRE 5, with moderate interobserver agreement and slightly but not significantly better results compared with ADMIRE 3 ($P = .088$). Both ADMIRE 3 and 5 were voted significantly higher than FBP and ADMIRE 1 ($P < .001$). ADMIRE 1 was rated slightly better than FBP ($P = .109$).

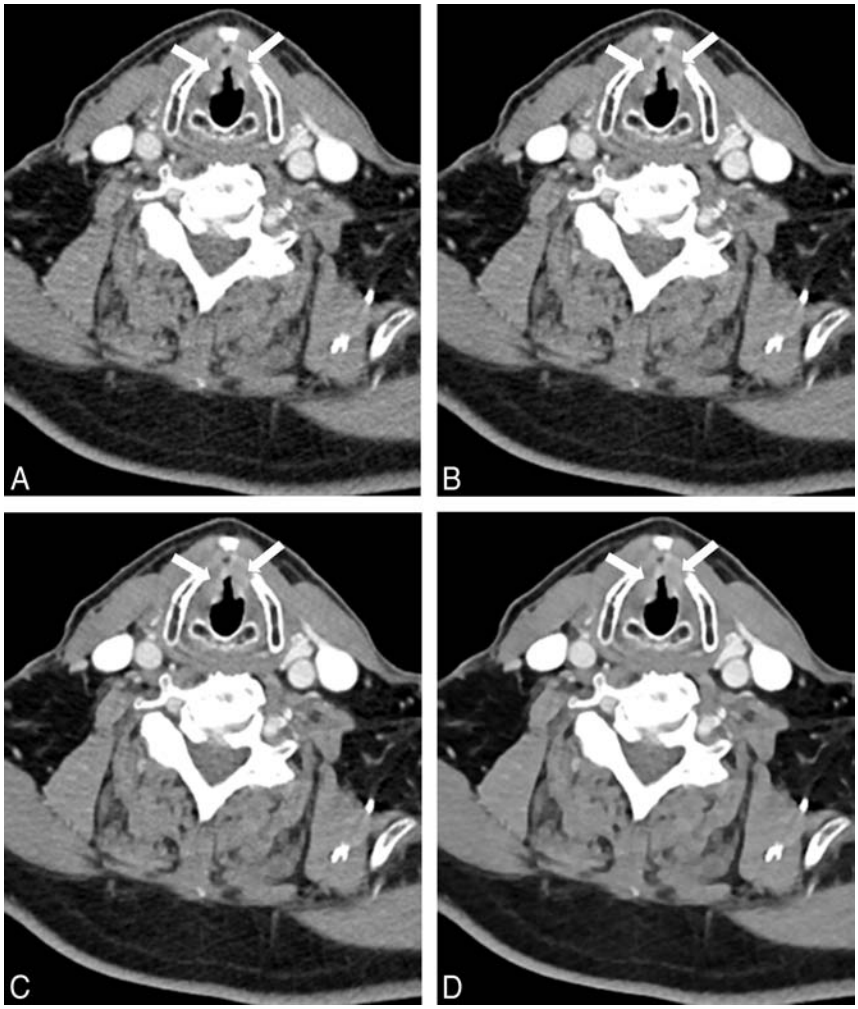

FIG 4. Images of a 46-year-old male patient examined with a low tube voltage of 90 kV on 192-section DSCT (window settings: width, 400 HU; level, 80 HU). Images were reconstructed by using filtered back-projection (*A*) and advanced modeled iterative reconstruction with strength levels 1 (*B*), 3 (*C*), and 5 (*D*). Axial images show histologically proved bilateral T2 squamous cell carcinoma of the glottic larynx (*arrows*). Image noise was highest by using FBP (*A*). The higher ADMIRE strength levels show consistently lower image noise (*B–D*). The internal jugular vein–sternocleidomastoid muscle CNR is highest by using ADMIRE 5 (*D*). Delineation of smaller structures was considered good by both observers in all images.

Image noise of all ADMIRE strength levels was voted significantly better than FBP with significant differences within ADMIRE strength levels and the highest ratings for ADMIRE 5 (all, $P < .005$).

Delineation of smaller structures was voted significantly better in all ADMIRE strength levels compared with FBP (all, $P \leq .001$) without significant differences among the ADMIRE levels (ADMIRE 1 versus 3, $P = .071$; ADMIRE 1 versus 5, $P = .285$; ADMIRE 3 versus 5, $P = .316$). Interobserver agreement of the delineation of smaller structures was moderate to good ($\kappa = 0.50-0.78$). Figure 5 shows axial images of a bilateral T4 glottic larynx cancer.

Image contrast was rated highest in ADMIRE 3 and 5 ($P = .769$). Both ADMIRE 3 and 5 were voted significantly better than FBP and ADMIRE 1 (all, $P < .001$). FBP was voted slightly better than ADMIRE 1 ($P = .157$). Global interobserver agreement was good ($\kappa = 0.75$).

DISCUSSION

The results of our study indicate that ADMIRE improves image quality for low-tube-voltage contrast-enhanced neck CT compared with FBP. Image noise was reduced significantly, and SNR and CNR were increased with ADMIRE. Objective image quality peaked with ADMIRE 5, while subjective image quality was superior in ADMIRE 3 and 5. Our protocol may be beneficial in clinical routine for reducing radiation exposure in patients undergoing neck CT without impairing image quality.

Repetitive use of CT may result in a substantial radiation exposure with a generally rising cumulative radiation dose in the population that may potentially increase the risk for radiation-induced carcinogenesis.[21,22] Tube-voltage reduction is one of several opportunities to reduce radiation exposure substantially in contrast-enhanced neck CT.[11,23] A potential drawback of a reduced tube voltage is an increase in image noise.[4,5,11,23,24] Due to increased image noise, 70 kV(peak) neck CT has compromised image quality in the lower part of the neck.[23] As a consequence of limited diagnostic acceptability, May et al[11] excluded 80-kVp acquisitions by using automated tube voltage adaptation in contrast-enhanced neck CT in combination with FBP on a second-generation 128-section DSCT. Nevertheless, an average radiation dose reduction of 8%–9% was measured in automated tube voltage adaptation ranging from 100 to 140 kVp.[11] In contrast and despite an increased image noise, prior studies investigating 80-kVp contrast-enhanced neck CT in combination with FBP on the same second-generation DSCT reported an increased tumor delineation and good diagnostic accuracy of benign and malignant pathologies.[4,5,24] The average size-specific dose estimate in our study was 13.59 ± 1.23 mGy, which corresponds to a dose reduction of approximately 35.4% compared with standard 120 kVp.

Iterative reconstruction has quickly become a standard feature on modern CT scanners, providing image noise reduction.[18,25] Gaddikeri et al[12] recently reported a substantial image noise reduction and increased SNR and CNR in 140-kV contrast-enhanced neck CT by using model-based iterative reconstruction compared with FBP. Nevertheless, image acquisition with 100 or 120 kV is more commonly encountered due to a lower radiation dose and improved iodine attenuation. Prior studies have reported that the combination of a reduced tube voltage and an iterative reconstruction algorithm may allow substantial radia-

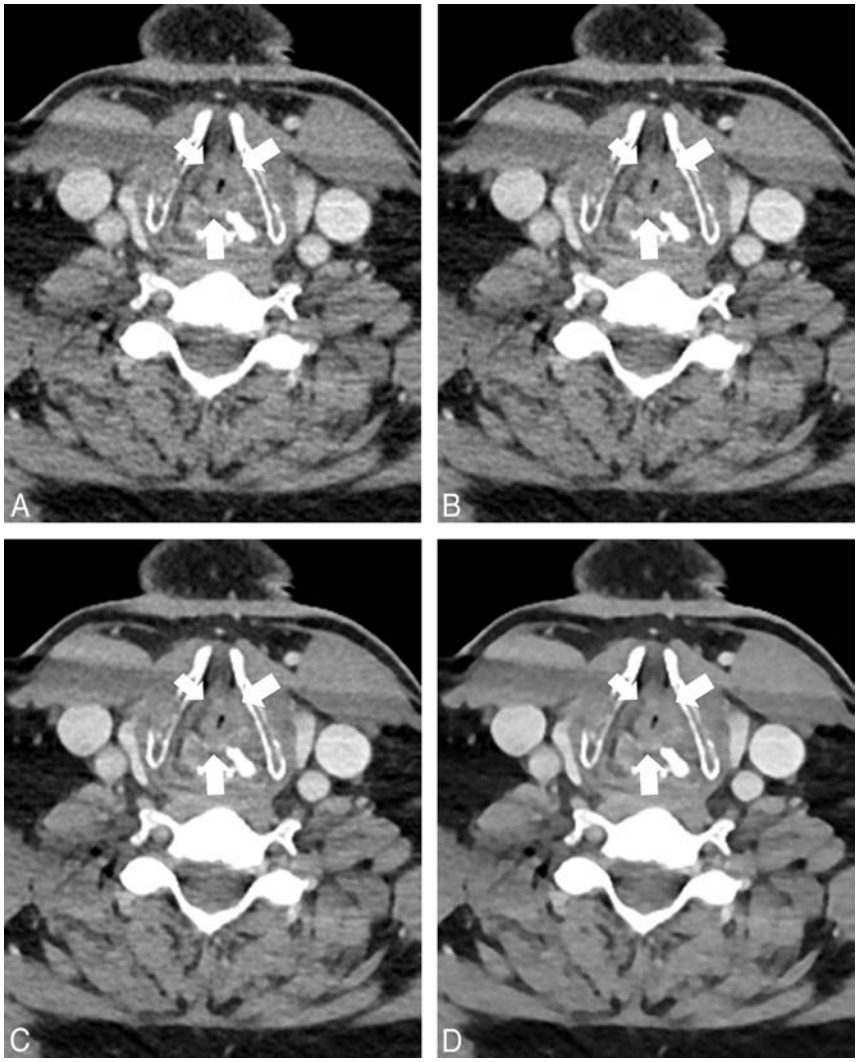

FIG 5. A 58-year-old male patient with sudden dyspnea. CT was performed with a tube voltage of 90 kV (window settings: width, 400 HU; level, 80 HU). Images were reconstructed by using filtered back-projection (*A*) and advanced modeled iterative reconstruction with strength levels 1 (*B*), 3 (*C*), and 5 (*D*). Images show histologically proved bilateral T4 laryngeal squamous cell carcinoma (*arrows*). The tumor reaches to the left thyroid cartilage but is separated from the right thyroid cartilage by a thin fat line. Image noise was lower in ADMIRE compared with FBP with the lowest image noise in ADMIRE 5 (*D*). Streak artifacts in the sternocleidomastoid muscle on both sides are visible in all images due to the shoulder region in the lower part of the neck.

tion dose reduction without impairment of image quality.[12-14,26] Third-generation DSCT has improved tube efficiency at lower tube voltages and is equipped with a model-based ADMIRE algorithm to provide adequate image quality in low-tube-voltage acquisitions. ADMIRE has been shown to provide an improved 3D regularization process, which results in better noise reduction in the image domain.[14] Furthermore, fewer noise streaks and better artifact suppression are facilitated by detailed modeling in the projection data domain. Initial results were reported by Gordic et al,[14] who observed reduced image noise with higher ADMIRE strength levels in 90–120 kV abdominal CT. Furthermore, SNR and CNR were significantly increased in all measured abdominal soft-tissue structures with the best results for ADMIRE strength levels 4 and 5. In our study, similar results were observed for 90-kV acquisitions: Attenuation of anatomic structures of the neck was constant between FBP and ADMIRE, while objectively and subjectively measured image noise was significantly reduced with ADMIRE compared with FBP, with lowest noise observed in ADMIRE 5. This result is in accordance with those reported by Gordic et al[14] measuring the lowest image noise in 90-kV abdominal CT for ADMIRE 5. Solomon et al[18] reported a substantial radiation dose reduction in ADMIRE compared with FBP while preserving detectability in a low-contrast acquisition in a phantom study.

Image noise in the lower part of the neck is significantly higher compared with the upper part due to superimposition of the shoulder region.[12,23] Gnannt et al[23] reported worse visualization in the lower third of the neck in a 70-kVp acquisition when combined with FBP on a 64-section CT. Our results demonstrate that ADMIRE is unable to compensate for image noise differences between the upper and lower parts of the neck, but it significantly reduces image noise in both upper and lower neck space with the lowest noise observed with ADMIRE 5. Similar findings were reported by Gaddikeri et al[12] for model-based iterative reconstruction compared with FBP in 140-kVp contrast-enhanced neck CT. Thus, the lower part of the neck remains a critical area to evaluate when applying dose-saving scan protocols, and application of these protocols should be considered on the basis of the indication for imaging.

In line with previously published studies, SNR and CNR were increased in ADMIRE with the highest results in ADMIRE 5.[14,18] Nevertheless, we also observed higher variations in both parameters with ADMIRE 5. Because attenuation values of all soft-tissue structures were constant in FBP and ADMIRE, the cause of the increase in SNR and CNR is the reduction of image noise. A further reduction of tube voltage may result in an increase of attenuation of ionic soft-tissue structures with the additional increase of SNR. However, the performance of ADMIRE reconstruction in such imaging protocols should be investigated in future studies.

Subjective image results were also favorable for higher ADMIRE levels, similar to the objectively measured results. Image noise was rated best in ADMIRE 5 compared with FBP and ADMIRE 1 and 3. Delineation of smaller neck structures was voted better in all ADMIRE strength levels compared with FBP. Slight differences within ADMIRE strength levels did not reach statistical significance. Image contrast and overall image quality were voted excellent in both ADMIRE 3 and 5, with significantly

better ratings compared with FBP and ADMIRE 1. Although ADMIRE 5 has been thought to provide an artificially smoothed image impression in prior studies, both image contrast and overall image quality were rated slightly but not significantly better in ADMIRE 5 compared with ADMIRE 3.

Due to the low image noise and the excellent image quality in 90-kVp acquisitions in combination with ADMIRE in contrast-enhanced neck CT in our study, which is the current standard protocol at our institution, we suggest additional investigations on the diagnostic accuracy of benign and malignant neck pathologies in 90-kVp acquisitions. Furthermore, the feasibility of tube voltage reduction to 80 and 70 kVp with respect to the patient's anatomy, such as a short neck, should be further evaluated.

Some limitations of our study need to be addressed. First, we performed a comparison of ADMIRE versus FBP. Together with the implementation of ADMIRE, a new third-generation 192-section DSCT was implemented in our system. An additional comparison of different generations of iterative reconstruction techniques and DSCT systems would have been favorable. However, an intraindividual comparison in follow-up examinations would have been influenced by hardware differences between second-generation 128-section and third-generation 192-section DSCT and additional differences in standard scan protocol parameters, including tube voltage and potential. Second, while a cohort of 64 patients is sufficient for an initial feasibility study, additional evaluation in a larger, more diversified cohort is necessary. Third, we did not investigate the combination of a standard 120-kV acquisition with ADMIRE, because 90-kV is our current protocol for contrast-enhanced neck CT by using 192-section DSCT. Furthermore, we did not focus on specific neck pathologies separately but evaluated subsequent patients with clinical indications for head and neck CT. Further studies should focus on specific neck pathologies, including visualization of squamous cell carcinoma or cervical lymphoma staging and follow-up, and inflammation of soft-tissue structures. In addition, low-tube-voltage CT may result in suboptimal image quality in patients with a short neck with a wide diameter. Our technique should be re-evaluated in this specific patient population for its impact on the detection of laryngeal or hypopharyngeal cancer. Finally, we did not evaluate differences in the diagnostic performance of the various ADMIRE reconstruction levels. The initial goal of our study was to demonstrate the feasibility of the low-tube-voltage 90-kV acquisition and to find the best reconstruction parameters to achieve optimal image quality by applying ADMIRE to reduce image noise caused by CT scanning with a low tube voltage. Performing multireader evaluations of 3 different ADMIRE reconstructions in each patient to assess diagnostic performance would have led to recall bias. Nevertheless, we plan to directly compare low-tube-voltage ADMIRE reconstructions with standard 120-kV FBP scans in the near future for the diagnostic performance for the detection of head and neck malignancy.

CONCLUSIONS

Our results demonstrate that low-tube-voltage acquisitions in combination with ADMIRE significantly reduce image noise and increase SNR and CNR in contrast-enhanced 192-section neck CT. Objective image quality peaked by using ADMIRE 5, while ADMIRE 3 and 5 showed the best subjective image quality. Dose-saving low-tube-voltage 90-kVp contrast-enhanced neck CT in combination with ADMIRE strength levels 3 or 5 may be routinely applied to enhance image quality and reduce the radiation dose in clinical routine.

Disclosures: Ralf W. Bauer—*UNRELATED: Payment for Lectures (including service on Speakers Bureaus)*: Siemens, *Comments*: Speakers Bureau, CT division. J. Matthias Kerl—*UNRELATED: Payment for Lectures (including service on Speakers Bureaus)*: Siemens, *Comments*: Speakers Bureau, CT division.

REFERENCES

1. Dammann F, Bootz F, Cohnen M, et al. **Diagnostic imaging modalities in head and neck disease.** *Dtsch Arztebl Int* 2014;111:417–23 CrossRef Medline
2. Gonzalez-Beicos A, Nunez D. **Imaging of acute head and neck infections.** *Radiol Clin North Am* 2012;50:73–83 CrossRef Medline
3. Griauzde J, Srinivasan A. **Imaging of vascular lesions of the head and neck.** *Radiol Clin North Am* 2015;53:197–213 CrossRef Medline
4. Scholtz JE, Kaup M, Kraft J, et al. **Objective and subjective image quality of primary and recurrent squamous cell carcinoma on head and neck low-tube-voltage 80-kVp computed tomography.** *Neuroradiology* 2015;57:645–51 CrossRef Medline
5. Wichmann JL, Kraft J, Nöske EM, et al. **Low-tube-voltage 80-kVp neck CT: evaluation of diagnostic accuracy and interobserver agreement.** *AJNR Am J Neuroradiol* 2014;35:2376–81 CrossRef Medline
6. Schulz B, Potente S, Zangos S, et al. **Ultra-low dose dual-source high-pitch computed tomography of the paranasal sinus: diagnostic sensitivity and radiation dose.** *Acta Radiol* 2012;53:435–40 CrossRef Medline
7. Greess H, Wolf H, Baum U, et al. **Dose reduction in computed tomography by attenuation-based on-line modulation of tube current: evaluation of six anatomical regions.** *Eur Radiol* 2000;10:391–94 CrossRef Medline
8. Papadakis AE, Perisinakis K, Damilakis J. **Automatic exposure control in pediatric and adult multidetector CT examinations: a phantom study on dose reduction and image quality.** *Med Phys* 2008;35:4567–76 CrossRef Medline
9. Söderberg M, Gunnarsson M. **Automatic exposure control in computed tomography–an evaluation of systems from different manufacturers.** *Acta Radiol* 2010;51:625–34 CrossRef Medline
10. Lurz M, Lell MM, Wuest W, et al. **Automated tube voltage selection in thoracoabdominal computed tomography at high pitch using a third-generation dual-source scanner: image quality and radiation dose performance.** *Invest Radiol* 2015;50:352–60 CrossRef Medline
11. May MS, Kramer MR, Eller A, et al. **Automated tube voltage adaptation in head and neck computed tomography between 120 and 100 kV: effects on image quality and radiation dose.** *Neuroradiology* 2014;56:797–803 CrossRef Medline
12. Gaddikeri S, Andre JB, Benjert J, et al. **Impact of model-based iterative reconstruction on image quality of contrast-enhanced neck CT.** *AJNR Am J Neuroradiol* 2015;36:391–96 CrossRef Medline
13. Bodelle B, Klein E, Naguib NN, et al. **Acute intracranial hemorrhage in CT: benefits of sinogram-affirmed iterative reconstruction techniques.** *AJNR Am J Neuroradiol* 2014;35:445–49 CrossRef Medline
14. Gordic S, Desbiolles L, Stolzmann P, et al. **Advanced modelled iterative reconstruction for abdominal CT: qualitative and quantitative evaluation.** *Clin Radiol* 2014;69:e497–504 CrossRef Medline
15. Korn A, Fenchel M, Bender B, et al. **Iterative reconstruction in head CT: image quality of routine and low-dose protocols in comparison with standard filtered back-projection.** *AJNR Am J Neuroradiol* 2012;33:218–24 CrossRef Medline
16. Curtis JR. **Computed tomography shielding methods: a literature review.** *Radiol Technol* 2010;81:428–36 Medline
17. Ramirez-Giraldo J, Primak A, Grant K, et al. **Radiation dose optimi-**

zation technologies in multidetector computed tomography: a review. *Med Phys* 2014;2:420–30
18. Solomon J, Mileto A, Ramirez-Giraldo JC, et al. **Diagnostic performance of an advanced modeled iterative reconstruction algorithm for low-contrast detectability with a third-generation dual-source multidetector CT scanner: potential for radiation dose reduction in a multireader study.** *Radiology* 2015;275:735–45 CrossRef Medline
19. Gordic S, Morsbach F, Schmidt B, et al. **Ultralow-dose chest computed tomography for pulmonary nodule detection: first performance evaluation of single energy scanning with spectral shaping.** *Invest Radiol* 2014;49:465–73 CrossRef Medline
20. Computed Tomography Subcommittee Task Group #204. **Size specific dose estimates (SSDE) in pediatric and adult body CT examinations.** *American Association of Physicists in Medicine Reports*. 2011. http://www.aapm.org/pubs/reports/default.asp. Accessed June 7, 2015
21. Berrington de González A, Mahesh M, Kim KP, et al. **Projected cancer risks from computed tomographic scans performed in the United States in 2007.** *Arch Intern Med* 2009;169:2071–77 CrossRef Medline
22. Brenner DJ, Hall EJ. **Computed tomography: an increasing source of radiation exposure.** *N Engl J Med* 2007;357:2277–84 CrossRef Medline
23. Gnannt R, Winklehner A, Goetti R, et al. **Low kilovoltage CT of the neck with 70 kVp: comparison with a standard protocol.** *AJNR Am J Neuroradiol* 2012;33:1014–19 CrossRef Medline
24. Scholtz JE, Hüsers K, Kaup M, et al. **Evaluation of image quality and dose reduction of 80 kVp neck computed tomography in patients with suspected peritonsillar abscess.** *Clin Radiol* 2015;70:e67–73 CrossRef Medline
25. Beister M, Kolditz D, Kalender WA. **Iterative reconstruction methods in x-ray CT.** *Phys Med* 2012;28:94–108 CrossRef Medline
26. May MS, Wüst W, Brand M, et al. **Dose reduction in abdominal computed tomography: intraindividual comparison of image quality of full-dose standard and half-dose iterative reconstructions with dual-source computed tomography.** *Invest Radiol* 2011;46:465–70 CrossRef Medline

Endolymphatic Hydrops Reversal following Acetazolamide Therapy: Demonstration with Delayed Intravenous Contrast-Enhanced 3D-FLAIR MRI

A.R. Sepahdari, N. Vorasubin, G. Ishiyama, and A. Ishiyama

ABSTRACT

SUMMARY: Endolymphatic hydrops, the primary pathologic alteration in Menière disease, can be visualized by using delayed intravenous contrast-enhanced 3D-FLAIR MR imaging. It is not known whether MR imaging–demonstrable changes of hydrops fluctuate with disease activity or are fixed. We describe the results of baseline and posttreatment MR imaging studies in a group of subjects with Menière disease with hydrops who were treated with acetazolamide. Seven subjects with untreated Menière disease with MR imaging evidence of hydrops had repeat MR imaging during acetazolamide treatment. Symptoms and imaging findings were assessed at each time point. Five subjects showed symptom improvement, of whom 3 had improvement or resolution of hydrops. One subject had recurrent symptoms with recurrent hydrops after discontinuing therapy. Two had unchanged hydrops despite symptom improvement. Subjects with unchanged symptoms had unchanged hydrops. Hydrops reversal may be seen with acetazolamide treatment in Menière disease. MR imaging may provide an additional biomarker of disease.

ABBREVIATIONS: hT2WI-FLAIR = heavily T2-weighted 3D FLAIR; MD = Menière disease; SPACE = sampling perfection with application-optimized contrasts by using different flip angle evolutions

Meniere disease (MD) is an incompletely understood condition characterized by symptoms of hearing loss, aural fullness, vertigo, and tinnitus.[1] The clinical phenotype and severity of symptoms vary among patients, and symptoms commonly fluctuate, typically presenting with fluctuating hearing loss that progresses and vertigo spells that eventually are associated with peripheral vestibular damage.[2] A variety of treatments are available, including low-salt diet, oral diuretics, intratympanic steroid injection, and endolymphatic sac shunt surgery.[3] The efficacy of these treatments has not been proved, and the mechanism of their effects is speculative.

MD is characterized by endolymphatic hydrops (ie, ballooning of the endolymphatic system), which has been described in human temporal bone postmortem studies.[4,5] Recent advances in MR imaging technology have allowed in vivo imaging of endolymphatic hydrops, which has the potential to advance our understanding of the natural history of the disease and assess changes in response to treatment. Several groups have confirmed the ability of delayed intravenous contrast-enhanced MR imaging to detect hydrops,[6-8] but no prior studies have assessed serial changes in hydrops during diuretic treatment by using delayed intravenous contrast-enhanced MR imaging, to our knowledge. One study that followed patients treated with betahistine by using intratympanic contrast-enhanced MR imaging did not show hydrops reversal despite symptomatic improvement.[9] Another study by using contrast administered through the eustachian tube showed decreased endolymphatic space size following endolymphatic sac decompression in a small group of patients.[10]

Our goal was to evaluate baseline and posttreatment MR imaging changes of endolymphatic hydrops in a group of patients with MD treated with oral acetazolamide, with the goal of developing a noninvasive objective biomarker for disease activity.

MATERIALS AND METHODS

Subjects

This institutional review board–approved study was performed with a waiver of informed consent and a waiver of Health Insurance Portability and Accountability Act authorization. A clinical data base of 356 subjects with hearing loss and/or vestibular

Received March 9, 2015; accepted after revision May 25.

From the Departments of Radiological Sciences (A.R.S.), Head and Neck Surgery (N.V., A.I.), and Neurology (G.I.), David Geffen School of Medicine, University of California, Los Angeles, Los Angeles, California.

Drs Vorasubin and Sepahdari contributed equally to this work.

Preliminary results of this work were previously presented at: Annual Meeting of the American Otological Society, May 16–17, 2014; Las Vegas, Nevada.

Please address correspondence to Ali Sepahdari, MD, Department of Radiological Sciences, David Geffen School of Medicine, University of California, Los Angeles, 757 Westwood Plaza, Suite 1621D, Los Angeles, CA 90095; e-mail: alisepahdari@gmail.com

Indicates article with supplemental on-line table.

http://dx.doi.org/10.3174/ajnr.A4462

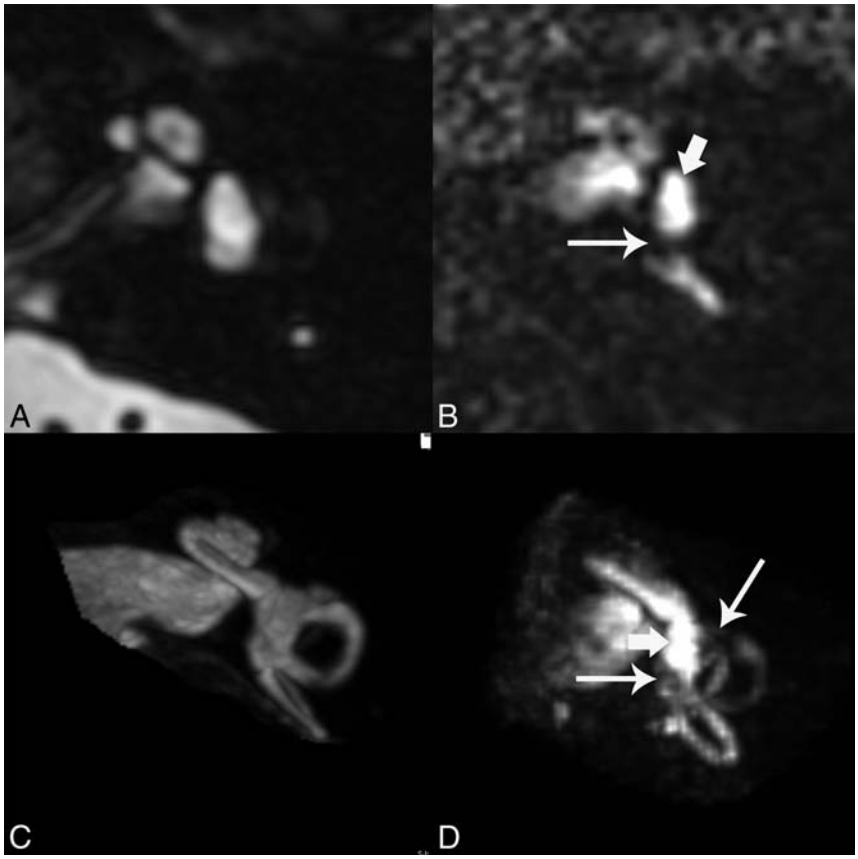

FIG 1. Normal appearance of cisternographic T2 (T2 SPACE) and heavily T2-weighted 3D FLAIR. *A*, Axial T2 SPACE source image through the midmodiolar level shows normal bright signal of fluid in the vestibule. Both endolymph and perilymph are bright by this technique. *B*, Axial hT2WI-FLAIR source image at the same level shows predominantly bright perilymphatic fluid in this part of the vestibule (*short arrow*), with a small signal void reflecting normal endolymphatic space near the ampulla of the posterior semicircular canal (*long arrow*). *C*, 3D maximum intensity projection of the T2 SPACE sequence shows the cochlea, vestibule, and semicircular canals in the same image, all with normal bright fluid signal. *D*, 3D MIP of the hT2WI-FLAIR sequence shows 2 small signal voids in the vestibule reflective of normal endolymphatic spaces (*long arrows*). The vestibule is predominantly filled with bright perilymph (*short arrow*).

symptoms imaged with hydrops-protocol MR imaging (4-hour delayed double-dose intravenous contrast-enhanced MR imaging using 3D-FLAIR sequences) was queried. Seven subjects met the following inclusion criteria: 1) clinical diagnosis of definite or probable MD, as determined by American Academy of Otolaryngology–Head and Neck Surgery guidelines[11]; 2) pretreatment MR imaging showing evidence of endolymphatic hydrops; and 3) posttreatment MR imaging during treatment with acetazolamide. Acetazolamide treatment was initiated at a dose of 250 mg by mouth daily. Treatment was continued indefinitely if there was a response.

Imaging

MR imaging was performed on a 3T Magnetom Skyra unit (Siemens, Erlangen, Germany) by using a 16-channel head and neck coil, 4 hours following an intravenous injection of 0.2 mmol/kg of either gadopentetate dimeglumine (Magnevist; Bayer HealthCare Pharmaceuticals, Wayne, New Jersey) or gadobutrol (Gadavist; Bayer Schering Pharma, Berlin, Germany). Scanning consisted of a "cisternographic" heavily T2-weighted 3D turbo spin-echo sequence (sampling perfection with application-optimized contrasts by using different flip angle evolutions [T2 SPACE]; Siemens) and a heavily T2-weighted 3D FLAIR sequence (hT2WI-FLAIR).[12] All sequences were performed as volumetric axial scans through the inner ear and internal auditory canals. The hT2WI-FLAIR sequence was performed with the following parameters: section thickness, 0.8 mm; TR/TE, 9000/534 ms; TI, 2350 ms; number of averages, 2; echo-train length, 144; flip angle, 120; matrix, 320 × 260; FOV, 200 × 167 mm; acquisition time, 6 minutes 45 seconds.

The hT2WI-FLAIR images normally show bright signal in the perilymph due to accumulation of dilute contrast in this space and dark signal in the endolymph, which remains protected from the contrast due to the presence of tight junctions. The T2 SPACE sequence shows bright signal within both endolymph and perilymph. The hT2WI-FLAIR images were reformatted in an axial plane parallel to the lateral semicircular canal to standardize interpretation and were also reconstructed as 3D maximum intensity projections. Figure 1 shows the normal appearance of T2 SPACE and hT2WI-FLAIR images. The images were evaluated with respect to the presence of endolymphatic hydrops. The qualitative criteria described by Baráth et al[7] were used to assess the 2D images for the presence of hydrops in the vestibule. 3D MIPs were also reviewed, and the criteria described by Sepahdari et al[8] were used to assess these images for hydrops in the vestibule. Cochlear hydrops was not specifically assessed because it was not thought that the cochlea is consistently evaluated due to the limitations of spatial resolution.

RESULTS

Of the 7 patients who met the inclusion criteria, all were diagnosed with definite MD. One of these patients was clinically diagnosed as having delayed endolymphatic hydrops, a subset of MD. All patients had unilateral clinical symptoms and unilateral hydrops on MR imaging. Five experienced improvement in symptoms; 3 of these 5 also showed either complete or partial reversal of hydrops (Fig 2). Two patients with symptomatic improvement did not have any change in hydrops. The 2 patients whose symptoms did not reverse showed unchanged hydrops. Clinical data are summarized in the On-line Table. Patient 3 required a dose increase to 250 mg twice daily before achieving a response. Patient 4 was only able to tolerate a dose of 62.5 mg daily due to medical comorbidities and did not have a response. Patient 1 had a return of vertigo and hydrops after attempting discontinuation of acet-

azolamide, and his symptoms improved after resuming treatment. A subsequent attempt to taper to 125 mg daily resulted in a return of vertigo.

The average duration of symptoms before initial MR imaging in all patients was 7.4 months. The average duration of treatment before follow-up imaging was 4.5 months. The average follow-up period was 19 months. Among the 3 patients whose symptoms and hydrops reversed, 2 continued acetazolamide treatment and were followed for an average of 9.5 months without recurrent symptoms. One patient discontinued acetazolamide and experienced recurrent symptoms with recurrent MR imaging evidence of hydrops (Fig 3). The 2 patients who had symptom improvement without hydrops reversal were imaged an average of 4 months after initiating treatment. The 3 patients with hydrops reversal were imaged an average of 6 months after treatment.

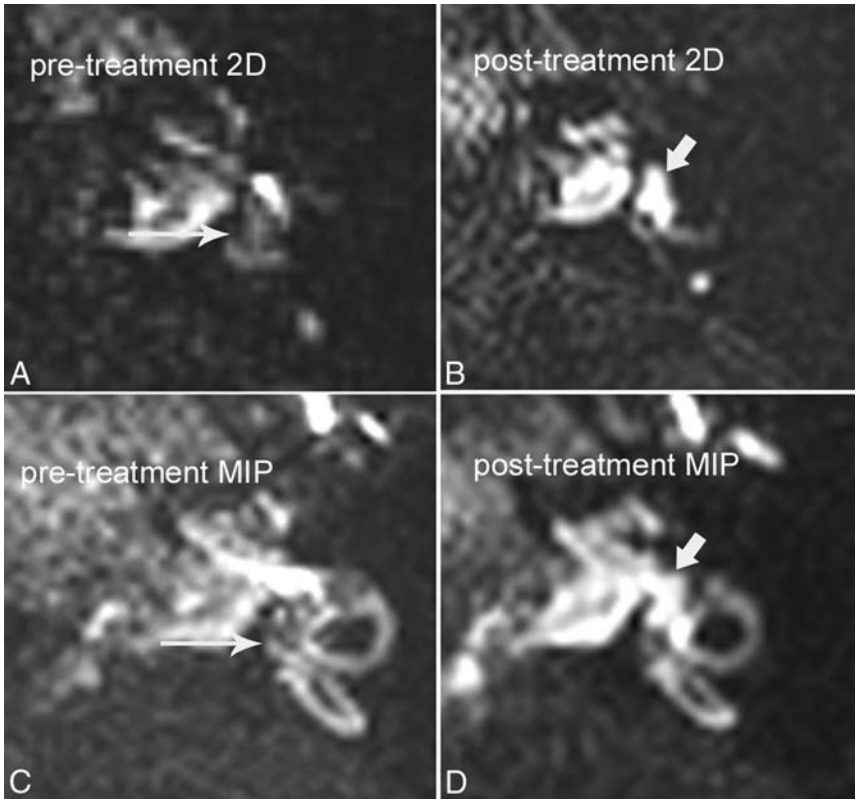

FIG 2. A 42-year-old man with grade I vestibular hydrops, with reversal of symptoms and reversal of hydrops after treatment with acetazolamide. *A*, Pretreatment axial hT2WI-FLAIR source image through the vestibule shows dilated endolymphatic spaces effacing the vestibular perilymph (*long arrow*). Compare with the normal appearance of the inner ear in Fig 1*B*. *B*, Posttreatment axial hT2WI-FLAIR source image through the vestibule shows interval resolution of endolymphatic hydrops, with normal bright perilymph signal in the vestibule (*short arrow*). *C*, Pretreatment hT2WI-FLAIR 3D MIP shows dilated endolymphatic spaces effacing >50% of the vestibule (*long arrow*). *D*, Posttreatment hT2WI-FLAIR 3D MIP shows interval resolution of hydrops, with normal bright perilymph (*short arrow*) occupying >50% of the vestibule.

DISCUSSION

Delayed intravenous contrast-enhanced MR imaging is an emerging technique for evaluating patients with MD. The ability to visualize hydrops with this technique has been confirmed by multiple groups on different continents.[6-8,13] To date, however, no strong clinical application has been established for this technique, and existing research is mostly limited to showing a connection between a clinical diagnosis of MD and imaging evidence of hydrops.

By showing reversibility of hydrops, we demonstrate that MR imaging can provide a biomarker of disease. This is critical for evaluating the effects of various treatments, particularly when exploring new therapies. Symptoms are known to fluctuate in MD and hence do not provide a sufficient marker of treatment effectiveness on their own. Audiometric testing and vestibular evoked myogenic potentials offer added objective measures of disease severity in MD but may also be confounded by other variables, such as presbyacusis or additional pathology such as otosclerosis.[14] MR imaging visualization of hydrops provides a unique, quantifiable marker of a direct effect of the disease.

One patient experienced reversal of

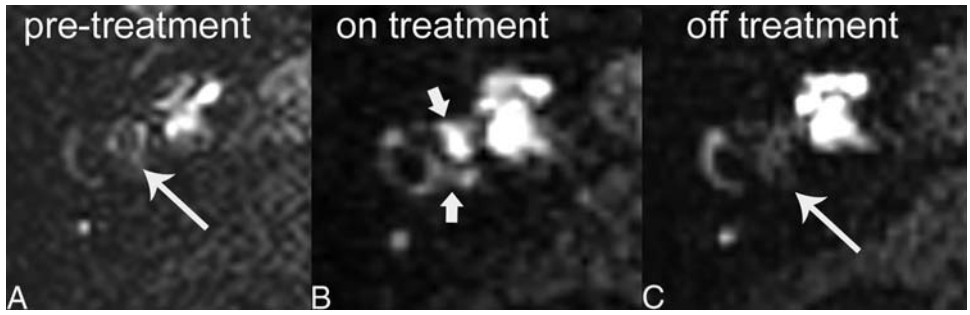

FIG 3. A 72-year-old man with hydrops responsive to acetazolamide and recurrence after discontinuation of treatment. *A*, Pretreatment axial hT2WI-FLAIR source image through the vestibule shows marked hydrops with complete effacement of the normal bright vestibular perilymphatic fluid by dilated, dark endolymphatic space (*long arrow*). *B*, Posttreatment axial hT2WI-FLAIR, during treatment with acetazolamide, shows reversal of hydrops. Normal bright perilymphatic fluid is now visible (*short arrows*). *C*, Following discontinuation of acetazolamide and recurrence of symptoms, follow-up axial hT2WI-FLAIR image shows recurrence of hydrops (*long arrow*).

symptoms and reversal of MR imaging–evident hydrops while on acetazolamide and re-emergence of symptoms with re-emergence of hydrops after stopping diuretics. Although this was just a single case, it shows a promising connection among acetazolamide treatment, symptoms, and hydrops.

Notably, 2 of 5 patients in our study who had symptom reversal did not have hydrops reversal. The reasons for this result are unclear because the small number of subjects does not permit a robust statistical analysis. However, factors such as the duration of disease before treatment and the length of time between treatment and repeat imaging may influence the results. Alternatively, the symptomatic improvement in these patients may have been a coincidence related to normal symptom fluctuation rather than an effect of the treatment. Rather than considering this phenomenon as a limitation of MR imaging, we view it as evidence that MR imaging provides unique information that is not duplicated by eliciting a clinical history from the patient.

The primary limitation of this study is the small number of subjects. Although a high volume of hydrops-protocol MRI is performed at our institution, only a small number of subjects met the inclusion criteria for this analysis. Despite the small number of subjects, the results provide support for the use of pre- and post-treatment hydrops-protocol MR imaging in prospective investigations of treatments for MD. There are also inherent technical limitations of the MR imaging technique and limits of image interpretation. Although our MR imaging technique has equal or superior resolution to other techniques reported in the literature, further technical improvements are needed to confidently visualize the entire membranous labyrinth. The method of image assessment, categorizing each ear as normal, grade I hydrops, or grade II hydrops, may be insensitive to subtle changes among scans. Further advancements in image acquisition and image interpretation techniques are needed to fully realize the potential of hydrops imaging.

CONCLUSIONS

Pilot data from a group of patients imaged with hydrops-protocol MR imaging before and during acetazolamide treatment show that endolymphatic hydrops is a reversible feature of Menière disease. Hydrops-protocol MR imaging provides a unique biomarker of disease in MD and may be valuable in assessing the effects of treatment.

REFERENCES

1. Andrews JC, Honrubia V. **Menière's disease**. In: Baloh RW, Halmagyi GM, eds. *Disorders of the Vestibular System.* New York: Oxford University Press; 1996: 300–17
2. Paparella MM, Sajjadi H. **The natural history of Menière's disease**. In: Harris JP, ed. *Menière's Disease.* Amsterdam: Kugler Publications; 1999:29–40
3. Chung JW, Fayad J, Linthicum F, et al. **Histopathology after endolymphatic sac surgery for Ménière's syndrome.** *Otol Neurotol* 2011;32:660–64 CrossRef Medline
4. Paparella MM. **Pathogenesis and pathophysiology of Menière's disease.** *Acta Otolaryngol Suppl* 1991;485:26–35 Medline
5. Merchant SN, Adams JC, Nadol JB Jr. **Pathophysiology of Menière's syndrome: are symptoms caused by endolymphatic hydrops?** *Otol Neurotol* 2005;26:74–81 CrossRef Medline
6. Pyykko I, Nakashima T, Yoshida T, et al. **Menière's disease: a reappraisal supported by a variable latency of symptoms and the MRI visualisation of endolymphatic hydrops.** *BMJ Open* 2013;3:pii: e001555 CrossRef Medline
7. Baráth K, Schuknecht B, Naldi AM, et al. **Detection and grading of endolymphatic hydrops in Menière disease using MR imaging.** *AJNR Am J Neuroradiol* 2014;35:1387–92 CrossRef Medline
8. Sepahdari AR, Ishiyama G, Vorasubin N, et al. **Delayed intravenous contrast-enhanced 3D FLAIR MRI in Menière's disease: correlation of quantitative measures of endolymphatic hydrops with hearing.** *Clin Imaging* 2015;39:26–31 CrossRef Medline
9. Gürkov R, Flatz W, Keeser D, et al. **Effect of standard-dose betahistine on endolymphatic hydrops: an MRI pilot study.** *Eur Arch Otorhinolaryngol* 2013;270:1231–35 CrossRef Medline
10. Liu F, Huang W, Meng X, et al. **Comparison of noninvasive evaluation of endolymphatic hydrops in Menière's disease and endolymphatic space in healthy volunteers using magnetic resonance imaging.** *Acta Otolaryngol* 2012;132:234–40 CrossRef Medline
11. **Committee on Hearing and Equilibrium guidelines for the diagnosis and evaluation of therapy in Menière's disease: American Academy of Otolaryngology-Head and Neck Foundation, Inc.** *Otolaryngol Head Neck Surg* 1995;113:181–85 CrossRef Medline
12. Naganawa S, Yamazaki M, Kawai H, et al. **Visualization of endolymphatic hydrops in Ménière's disease with single-dose intravenous gadolinium-based contrast media using heavily T(2)-weighted 3D-FLAIR.** *Magn Reson Med Sci* 2010;9:237–42 CrossRef Medline
13. Naganawa S, Nakashima T. **Visualization of endolymphatic hydrops with MR imaging in patients with Ménière's disease and related pathologies: current status of its methods and clinical significance.** *Jpn J Radiol* 2014;32:191–204 CrossRef Medline
14. Mukaida T, Sone M, Yoshida T, et al. **Magnetic resonance imaging evaluation of endolymphatic hydrops in cases with otosclerosis.** *Otol Neurotol* 2015;36:1146–50 CrossRef Medline

Evolution of T1 Relaxation, ADC, and Fractional Anisotropy during Early Brain Maturation: A Serial Imaging Study on Preterm Infants

J. Schneider, T. Kober, M. Bickle Graz, R. Meuli, P.S. Hüppi, P. Hagmann, and A.C. Truttmann

ABSTRACT

BACKGROUND AND PURPOSE: The alteration of brain maturation in preterm infants contributes to neurodevelopmental disabilities during childhood. Serial imaging allows understanding of the mechanisms leading to dysmaturation in the preterm brain. The purpose of the present study was to provide reference quantitative MR imaging measures across time in preterm infants, by using ADC, fractional anisotropy, and T1 maps obtained by using the magnetization-prepared dual rapid acquisition of gradient echo technique.

MATERIALS AND METHODS: We included preterm neonates born at <30 weeks of gestational age without major brain lesions on early cranial sonography and performed 3 MRIs (3T) from birth to term-equivalent age. Multiple measurements (ADC, fractional anisotropy, and T1 relaxation) were performed on each examination in 12 defined white and gray matter ROIs.

RESULTS: We acquired 107 MRIs (35 early, 33 intermediary, and 39 at term-equivalent age) in 39 cerebral low-risk preterm infants. Measures of T1 relaxation time showed a gradual and significant decrease with time in a region- and hemispheric-specific manner. ADC values showed a similar decline with time, but with more variability than T1 relaxation. An increase of fractional anisotropy values was observed in WM regions and inversely a decrease in the cortex.

CONCLUSIONS: The gradual change with time reflects the progressive maturation of the cerebral microstructure in white and gray matter. Our study provides reference trajectories from 25 to 40 weeks of gestation of T1 relaxation, ADC, and fractional anisotropy values in low-risk preterm infants. We speculate that deviation thereof might reflect disturbed cerebral maturation; the correlation of this disturbed maturation with neurodevelopmental outcome remains to be addressed.

ABBREVIATIONS: FA = fractional anisotropy; GA = gestational age; MP2RAGE = magnetization-prepared dual rapid acquisition of gradient echo; PLIC = posterior limb of the internal capsule; R_{adj}^2 = correlation coefficient adjusted for the degree of freedom; TEA = term-equivalent age; GRAPPA = generalized autocalibrating partially parallel acquisition

Offering a prognosis for the neurodevelopment of very preterm infants remains a challenge, as has recently been shown.[1] Yet, prematurity still carries a high burden of impairment in survivors, affecting motor, cognitive, and socioemotional development.[2,3] While the motor deficits are frequently linked to moderate or severe WM lesions such as cystic periventricular leukomalacia or large intraparenchymal hemorrhage, the cognitive abnormalities are probably more related to the mixed picture of brain injury and alteration of cerebral development,[4] coined by Volpe as diffuse encephalopathy of prematurity.[5] A large body of work in the past decades has been devoted to new techniques of

Received April 7, 2015; accepted after revision June 11.

From the Clinic of Neonatology and Follow-up (J.S., M.B.G., A.C.T.), Department of Pediatrics, and Department of Radiology (T.K., R.M., P.H.), University Hospital Center and University of Lausanne, Lausanne, Switzerland; Advanced Clinical Imaging Technology (T.K.), Siemens Healthcare IM BM PI, Lausanne, Switzerland; LTS5 (T.K.), École Polytechnique Fédérale de Lausanne, Lausanne, Switzerland; and Division of Development and Growth (P.S.H.), Department of Pediatrics, University Hospital of Geneva, Geneva, Switzerland.

Patric Hagmann and Anita C. Truttmann contributed equally to the study as last coauthors.

This work was funded by a Special Program University Medicine from the Swiss National Science Foundation (number 33CM30–124101). Patric Hagmann is financially supported by the Leenaards Foundation. This work was supported by the Centre d'Imagerie BioMédicale of the University of Lausanne, the Swiss Federal Institute of Technology Lausanne, the University of Geneva, the Centre Hospitalier Universitaire Vaudois, the Hôpitaux Universitaires de Genève, and the Leenaards and the Jeantet Foundations.

Paper previously presented at: Annual Meeting of the European Society of Paediatric Research, October 11–14, 2013; Porto, Portugal; and Annual Meeting of the Pediatric Academic Societies, April 28 to May 1, 2012; Boston, Massachusetts.

Please address correspondence to Anita C. Truttmann, MD, Service de Néonatologie, Département médico-chirurgical de Pédiatrie, Maternité–CHUV, Ave Pierre-Decker 2, 1011 Lausanne, Switzerland; e-mail: Anita.Truttmann@chuv.ch

Indicates open access to non-subscribers at www.ajnr.org

Indicates article with supplemental on-line tables.

Indicates article with supplemental on-line photo.

http://dx.doi.org/10.3174/ajnr.A4510

MR imaging, specifically addressing the question of the maturation of the preterm brain.

Longitudinal imaging of the growing brain between 25 and 40 weeks of gestation allows assessing neuronal differentiation, gyral maturation, connecting fiber development, and early myelination.[6] To analyze these features of normal/abnormal maturation, efficient tools and reference values are still lacking. Several authors have described serial quantitative measures by using apparent diffusion coefficients and fractional anisotropy (FA) in various cohorts.[7-11] These sequences probe tissue microstructure and are used as markers of maturation, especially for axonal and dendritic organization and myelination. Recently, magnetization-prepared dual rapid acquisition of gradient echo (MP2RAGE) emerged as a new technique, which, by obtaining a purely T1-weighted image, allows the extraction of whole-brain T1 tissue relaxation time maps to provide quantitative tissue characterization.[12] The descriptive properties of T1 relaxometry are of particular interest in the preterm population because they give structural information about tissue, such as water content and lipid and macromolecule composition, and draw a picture of the chronologic maturation of myelin. Moreover, there is a lack of quantitative T1 values for the assessment of brain development.[11,13-15]

In this serial imaging study in very preterm infants with cerebral low risk, we aimed to provide, for the first time, reference values for T1 relaxation time, and we hypothesized that their evolution is comparable with that of ADC and FA values, conferring greater and more precise information about tissue structure.

MATERIALS AND METHODS

Patients

Neonates born before 30 weeks of gestation between February 2011 and May 2013 in our level III neonatology unit were considered for inclusion during the first days of life. Noninclusion criteria were the following: severe cardiorespiratory instability, intraventricular hemorrhage grade III and/or parenchymal hemorrhagic infarction on early sonography, severe congenital malformations, and genetic abnormalities. Patients who subsequently developed severe lesions on MR imaging, who died during the study, or who had abnormal neurologic assessment at term equivalent age (TEA) according to the Hammersmith Neonatal Neurologic Examination[16] were excluded from the final analysis. We thus defined the remaining patients as "cerebral low-risk." Neonatal variables were registered prospectively from the medical records.

Ethics approval was provided by the local committee, and written informed consent was obtained. Specific risks arising from imaging children younger than 2 years of age were assessed by the medical team and the institutional review board before the MR imaging examination.

MR Imaging

We planned 3 sequential MRIs: The first was during the first 2–3 weeks of life, the third at TEA, and the second in-between (from 10 to 20 days of life for the first part of the cohort and at 34–35 weeks of gestational age for the second part). All MRIs were performed on a 3T Magnetom Trio system (Siemens, Erlangen, Germany). A neonatal MR imaging–compatible incubator (Nomag; LMT Medical Systems, Luebeck, Germany) equipped with a dedicated 8-channel neonatal head coil was used. Monitoring was provided during scanning (temperature, heart rate, oxygen saturation), and respiratory support was applied when necessary. Patients received no sedation and wore protective earmuffs (MiniMuffs; Natus Medical, San Carlos, California). A neonatologist and a neonatal nurse were present throughout the examination. The cerebral MR imaging protocol included the following: 1) inversion recovery T1-weighted TSE axial (in-plane resolution, 0.6 mm; section thickness, 3 mm with 10% gap; 35 sections; TR, 8000 ms; TE, 17 ms; FOV, 160 mm; acceleration factor generalized autocalibrating partially parallel acquisition (GRAPPA) = 2; measurement time, 3 minutes 14 seconds); 2) T2-weighted TSE axial (in-plane resolution, 0.2 mm; section thickness, 2.5 mm with a 10% gap; 35 sections; TR, 4520 ms; TE, 143 ms; FOV, 160 mm; acceleration factor GRAPPA = 2; measurement time, 4 minutes 15 seconds); 3) T2-weighted TSE coronal (in-plane resolution, 0.4 mm; section thickness, 1.2 mm with a 10% gap; 100 sections; TR, 5410 ms; TE, 159 ms; FOV, 200 mm; acceleration factor GRAPPA = 2; measurement time, 4 minutes 59 seconds); 4) 3D MP2RAGE (in-plane resolution, 0.7 mm; section thickness, 1.2 mm; TR, 4000 ms; TE, 3.17 ms; FOV, 190 mm; TI 1, 900 ms; TI 2, 2200 ms; acceleration factor GRAPPA = 2; measurement time, 4 minutes 58 seconds); 5) DTI (in-plane resolution, 2 mm; section thickness, 2 mm with no gap; 43 sections; TR, 5200 ms; TE, 84 ms; FOV, 192 mm; b-value 1, 0 s/mm^2; b-value 2, 1000 s/mm^2; diffusion encoding directions, 82 and 5 B0 images; acceleration factor GRAPPA = 3; measurement time, 7 minutes 29 seconds). The standard ADC and FA maps generated by the scanner software were used in this study. No additional motion and eddy current corrections were performed. The vendor computes ADC and FA maps according to Basser et al[17] by using a least square estimation of the tensor.

Using T2, inversion recovery T1, and MP2RAGE, we calculated scores for severity at TEA according to Kidokoro et al,[18] including 6 items in the WM and 7 items in the GM and cerebellum. A global score (WM + GM and cerebellum score) was calculated and classified as normal (0–3), mild (4–7), moderate (8–11), and severe (≥12). Two neonatologists experienced in reading MR imaging calculated the score. Intraventricular hemorrhages were graded according to Papile,[19] and WM and cerebellar lesions were also described.

Twelve ROIs were identified with anatomic landmarks on 5 different sections for the WM (frontal, central, parietal, posterior limb of internal capsule [PLIC]; corpus callosum genu and splenium; and optic radiations) and the GM (frontal, perirolandic, and parietal cortices; thalamus; and lentiform nucleus). Freehand ROIs were drawn to maximize the size and avoid the risk of GM/WM contamination, as shown in On-line Fig 1. Each ROI was placed on the DTI sequence to measure ADC and FA and on the T1 map obtained from the MP2RAGE sequence to calculate the effective T1 relaxation time.[12]

Neurodevelopmental Outcome

The patients were offered neurodevelopmental follow-up at 6 and 18 months of corrected age. A developmental pediatrician blinded to the neuroimaging findings performed a developmental assessment by using the Bayley Scales of Infant Development II, which entails a mental developmental index and a psychomotor devel-

Clinical variables describing the total population, the low-risk cohort, and the excluded patients[a]

	Total Cohort	Low-Risk Cohort	Excluded	*P* Value[b]
No. of patients (%)	51	39 (76.5)	12 (23.5)	
GA (weeks, days) (median) (range)	27 4/7 (25 0/7–31 4/7)	27 4/7 (25 5/7–30)	28 1/7 (25 0/7–31 4/7)	NS
Female (No.) (%)	29 (56.9)	19 (48.7)	10 (83)	<.05
Weight (g) (median) (range)	889 (517–1590)	900 (560–1485)	727.5 (517–1590)	NS
Small for GA (weight <10th percentile) (No.) (%)	12 (23.5)	8 (20.5)	4 (33.3)	NS
Multiple births (No.) (%)	12 (23.5)	6 (15.4)	6 (50)	<.05
Chorioamnionitis (No.) (%)	21 (41.2)	16 (41.0)	5 (41.7)	NS
Antenatal steroids (No.) (%)	45 (88.2)	34 (87.2)	11 (91.7)	NS
All BPD/severe BPD (No.) (%)	26 (51.0)/9 (17.6)	17 (43.6)/5 (12.8)	9 (75.0)/4 (33.3)	NS
Postnatal steroids (No.) (%)	7 (13.7)	2 (5.1)	5 (41.7)	<.05
Treated patent ductus arteriosus (No.) (%)	25 (49.0)	17 (43.6)	8 (66.7)	NS
Early-onset sepsis (No.) (%)	13 (25.5)	11 (28.2)	2 (16.7)	NS
Late-onset sepsis (No.) (%)	17 (33.3)	13 (33.3)	4 (33.3)	NS
Necrotizing enterocolitis (No.) (%)	2 (3.9)	0 (0)	2 (16.7)	NS
Treated retinopathy of prematurity (No.) (%)	3 (5.9)	1 (2.6)	2 (16.7)	NS
Death (No.) (%)	2 (3.9)	0 (0)	2 (16.7)	NS
6-Mo MDI (median) (range)	98 (74–118)	98 (86–118)	93 (74–102)	<.05
6-Mo PDI (median) (range)	88 (49–111)	88 (62–111)	78.5 (49–88)	<.05
18-Mo MDI (median) (range)	93 (65–127)	93 (65–127)	87 (79–101)	NS
18-Mo PDI (median) (range)	83 (49–103)	84 (55–103)	71 (49–95)	<.05

Note:—MDI indicates mental developmental index; PDI, psychomotor developmental index; BPD, bronchopulmonary dysplasia; NS, nonsignificant.

[a] Bronchopulmonary dysplasia: O_2 supplementation for 28 days. Severe BPD: respiratory support at 36 weeks of GA. Necrotizing enterocolitis: Bell stage >2.

[b] Between low-risk cohort and excluded patients.

opmental index. The test mean is 100 ± 15; a score <2 SDs means a severe delay.

Statistical Analyses

Statistical analyses were performed by using Matlab R2014b (MathWorks, Natick, Massachusetts) and STATA 13.0 (StataCorp, College Station, Texas). The different associations were analyzed with linear and quadratic regression. The correlation coefficient adjusted for the *df* (R_{adj}^2) was used to identify the model with the best explanatory power. The Pearson linear correlation (R) was used to compare T1 relaxation time and ADC or FA values. The dispersion of ADC and T1 values was compared with a 1-sided *t* test applied on the normalized root mean square error of each marker. Demographic and neonatal variables were compared with the Student *t* test (continuous variables) and with the Fisher exact test (categoric variables). Statistical significance was defined as $P < .05$.

RESULTS

Description of the Population

Among 126 eligible patients, 51 preterm neonates were recruited. Reasons for not being included were parental refusal ($n = 26$), early death ($n = 9$), cardiorespiratory instability ($n = 13$), early transfer to peripheral hospital ($n = 11$), or absent recruiting person ($n = 16$). Twelve patients were excluded from the final analysis because of severe lesions on brain MR imaging (MR imaging scores ≥8 or parenchymal hemorrhagic infarction), death, withdrawal of consent, or abnormal neurologic examination findings at TEA. We thus show the characteristics of the population based on 39 cerebral low-risk preterm neonates (Table).

Conventional MR Imaging and Scoring System

One hundred seven MR imaging examinations were performed; 35 early, 33 intermediary, and 39 at TEA. Thirty patients underwent 3 serial MRIs, 8 patients had 2, and 1 patient had only 1. The assessment of the image quality allowed considering 86% of the scans as good or with minimal motion artifacts.

Several mild cerebral lesions were diagnosed on the conventional sequences, including intraventricular hemorrhages grade I ($n = 5$) and grade II ($n = 2$), punctuate WM lesions ($n = 3$), and punctuate cerebellar hemorrhages ($n = 4$). Two patients had 2 types of lesions (intraventricular hemorrhage grade I and punctuate WM lesions).

The scoring system could be applied on 37 MRIs at TEA: The global score was within the normal range for 16 and mildly abnormal for 21 patients, and no patient had a moderate or severe score. The MR images and scoring system, including brain metrics, are detailed in On-line Table 1.

Quantitative Measures

T1 Relaxation. In Fig 1*A*, T1 relaxation values (milliseconds) measured in the 12 ROIs of the right and left hemispheres on the serial images of the 39 patients are presented. Maturation in the different cerebral regions was reflected by a gradual decrease of T1 with time. The PLIC matured the fastest ($R_{adj}^2 = 0.8242$, $P = 8.09 \times 10^{-81}$). The values in the WM of the corona radiata showed a fast and continuous decrease until TEA ($R_{adj}^2 = 0.663$, $P = 1.61 \times 10^{-51}$). The parietal ($R_{adj}^2 = 0.2833$, $P = 2.00 \times 10^{-17}$) and frontal WM ($R_{adj}^2 = 0.0803$, $P = 5.65 \times 10^{-6}$) matured along a shouldered curve, which peaks around 30 weeks of gestational age (GA). The deep GM matured simultaneous to WM, especially the thalamus ($R_{adj}^2 = 0.6814$, $P = 5.66 \times 10^{-49}$) and the lentiform nucleus ($R_{adj}^2 = 0.3747$, $P = 1.06 \times 10^{-24}$). The cortex showed little change with time. The maturation in the different areas of the cortex at TEA was gradual: first in the perirolandic, then in the parietal, and finally in the frontal cortex (see On-line Table 2 for T1 values).

ADC values are represented in Fig 1*B*, and strengths of the correlations were less strong in almost all the regions (PLIC: $R_{adj}^2 = 0.4816$, $P = 8.31 \times 10^{-32}$; central WM: $R_{adj}^2 = 0.566$, $P =$

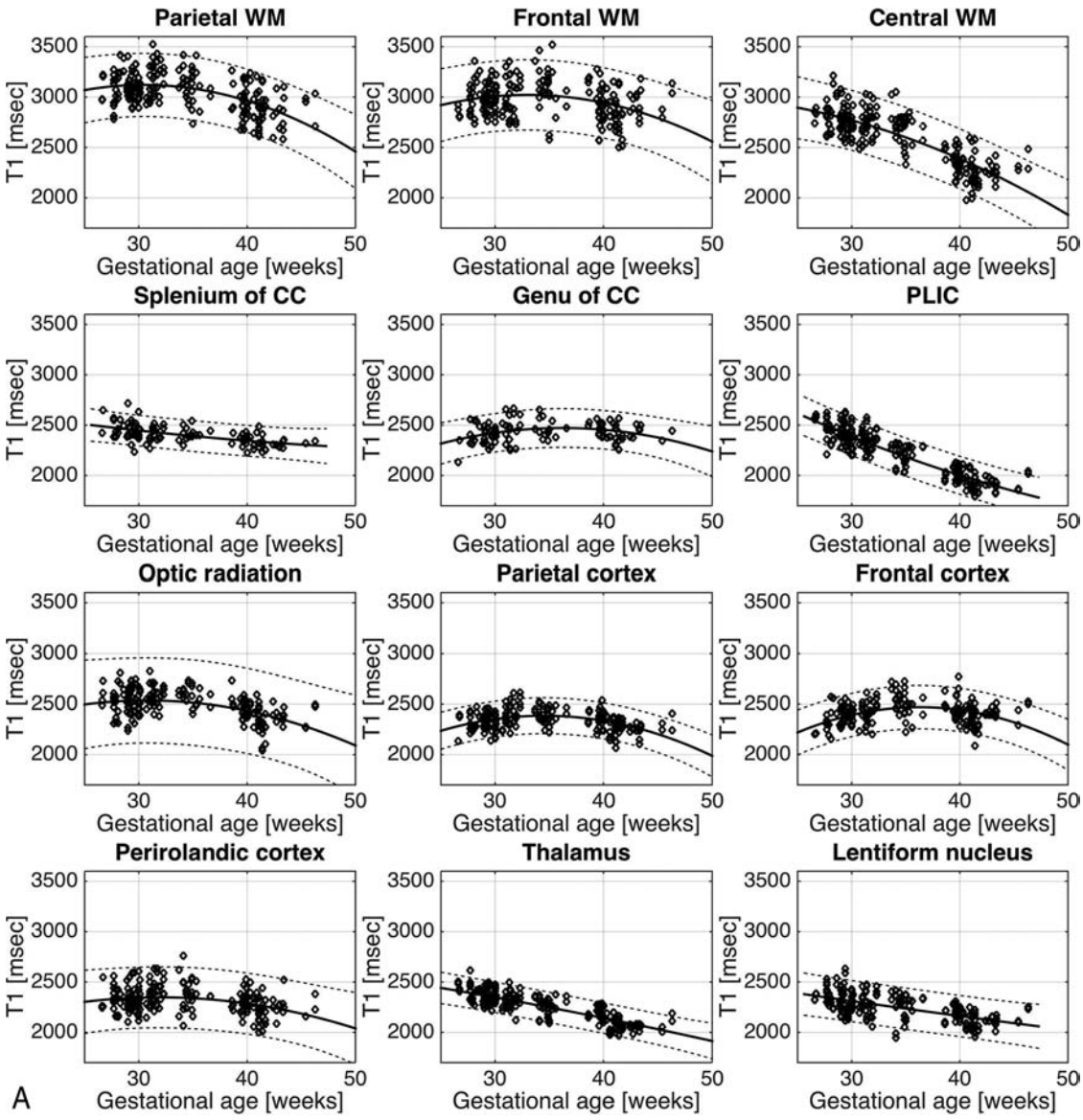

FIG 1. MR imaging values measured in the right and left hemispheres between 25 and 40 weeks of gestational age in 12 ROIs for the low-risk cohort of 39 patients. *Dotted lines* indicate 95% confidence interval. CC indicates corpus callosum. T1 values (*A*), ADC values (*B*), FA values (*C*).

2.54×10^{-40}; thalamus: $R_{adj}^2 = 0.4855$, $P = 9.42 \times 10^{-32}$), except for parietal WM ($R_{adj}^2 = 0.3048$, $P = 1.20 \times 10^{-18}$), frontal WM ($R_{adj}^2 = 0.312$, $P = 4.05 \times 10^{-19}$), and the lentiform nucleus ($R_{adj}^2 = 0.6718$, $P = 3.20 \times 10^{-52}$).

The evolution of FA with time is shown in Fig 1*C*. The maturation was most visible in the PLIC ($R_{adj}^2 = 0.5386$, $P = 5.19 \times 10^{-37}$), the optic radiation ($R_{adj}^2 = 0.3465$, $P = 3.05 \times 10^{-21}$), and the corpus callosum (splenium: $R_{adj}^2 = 0.2159$, $P = 5.24 \times 10^{-7}$; genu: $R_{adj}^2 = 0.1126$, $P = 9.27 \times 10^{-5}$), with a gradual increase in these regions. At the same time, FA decreased in the cortical GM (parietal: $R_{adj}^2 = 0.4535$, $P = 1.70 \times 10^{-31}$; frontal: $R_{adj}^2 = 0.199$, $P = 3.67 \times 10^{-12}$; perirolandic: $R_{adj}^2 = 0.4889$, $P = 7.50 \times 10^{-32}$).

For each ROI, we produced reference values stratified by gestational weeks, expressed as mean ± SD for T1, ADC, and FA (On-line Table 2).

There was a significant and strong correlation between the T1 relaxation time and ADC values for all the ROIs and all MR images at different gestational ages (Pearson correlation $R^2 = 0.616$, $P < .001$). Furthermore, T1 values exhibited a significantly lower dispersion than ADC values ($P = 1.06 \times 10^{-4}$). The correlation between T1 relaxation and FA (Pearson correlation $R^2 = -0.128$) was negative and less significant.

DISCUSSION

The present study provides quantitative reference values for cerebral development, based on 107 MRIs acquired between 25 and 40 weeks in 39 very preterm infants. We used a newly developed sequence, MP2RAGE, which gives the T1 relaxation time, and compared it with MR imaging markers, ADC and FA. The selected cohort can be considered cerebral-low-risk, according to the exclusion criteria. Our findings were comparable with existing data (On-line Tables 3 and 4) issued from fetuses and preterm infants, detailed below.

Given fetal diffusion values and maturation curves obtained between 22 and 36 weeks, our findings of ADC and FA values were comparable with the ones presented by different groups,[20-22]

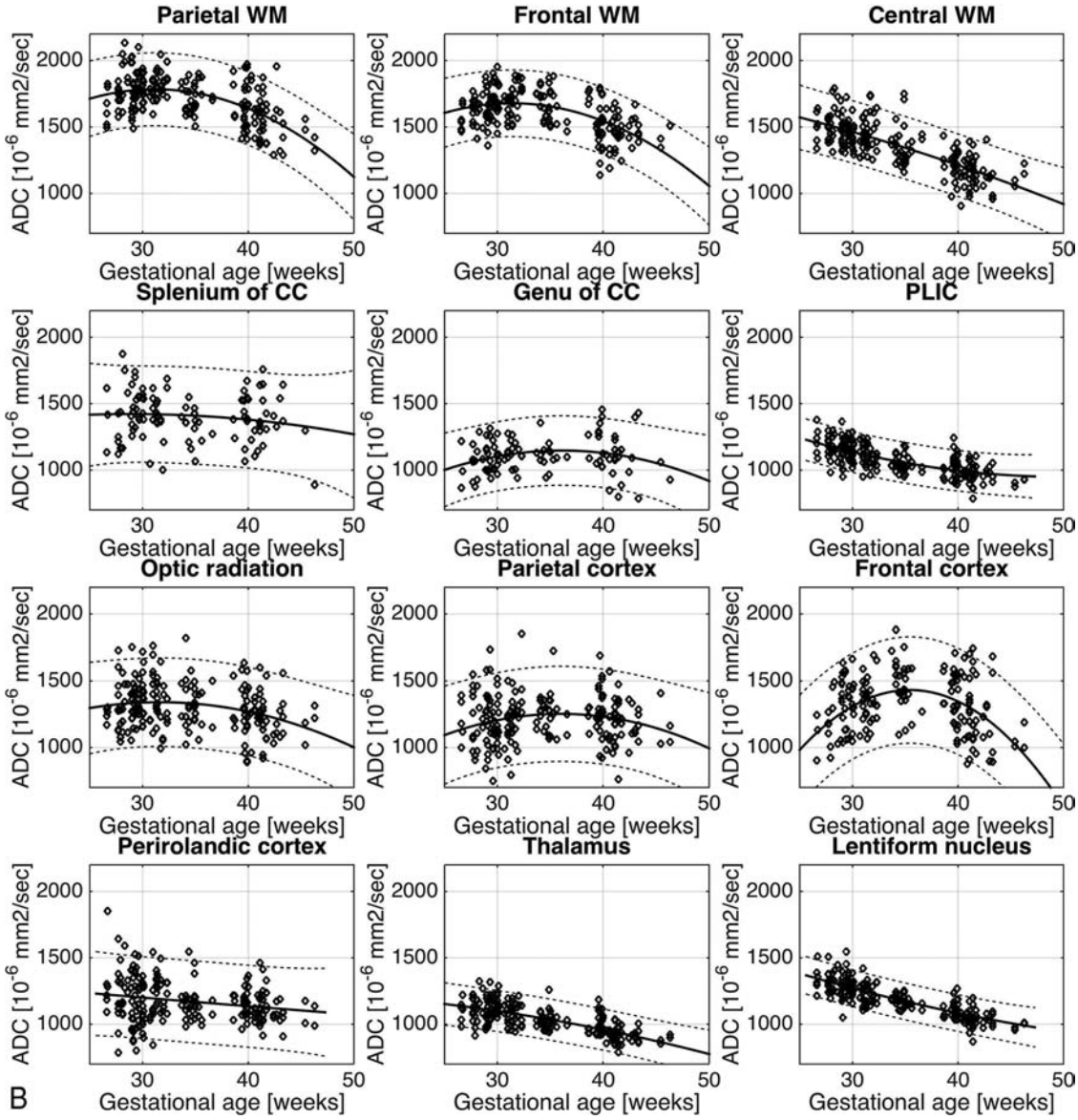

FIG 1. Continued. ADC values.

though subtle differences between fetuses at 37 weeks of gestation and preterm infants at TEA were reported.[23] No fetal data of T1 values are available.

While a multitude of data exist for preterm infants at TEA,[24,25] only a few studies have described the longitudinal evolution of quantitative brain MR imaging markers. In the late 1990s, Hüppi et al[9] reported changes of ADC and FA in the WM of preterm infants between early life and TEA. Their group showed differences in WM fiber organization and delay of development at TEA compared with term. Miller et al,[7] by using DTI, also showed serial differences in maturation in 23 infants with and without WM injury. Later, Nossin-Manor et al[11] assessed tissue organization longitudinally and were able to show a difference in maturation according to the different ROIs and the different techniques used, such as magnetization transfer, DTI, and T1 imaging. Recently Kersbergen et al[8] provided reference diffusivity values from scans obtained between 30 weeks and TEA. Compared with these studies, our ADC and FA values were similar to those in Nossin-Manor[11] and Partridge et al,[26] and FA values were slightly higher than those reported by other groups.[8,24] The relatively large heterogeneity of FA values in the literature is difficult to explain with certainty. However, it may involve several potential confounders: 1) b-value ranges from 600 to 1000 s/mm^2,[27] 2) slightly different tensor reconstruction strategies, 3) drawing and selection of the ROIs (this may actually be the main causative agent), and 4) some unsuspected systematic differences between the cohorts.

Concerning T1 relaxometry, only a few studies relate T1 values in infancy,[13] neonates[15] and premature infants,[11,14] albeit it provides reliable quantitative measures and high contrast images. We were able not only to measure T1 relaxometry serially in premature brains but also to show a strong correlation between ADC and T1 values, enhancing its validity toward clinical use. Moreover, we described a closer distribution of T1 values compared with ADC, in particular at TEA. Compared with existing data,[11,14] our findings were similar.

When performing serial imaging of preterm brain by using specific MR imaging markers, it is important to understand the different

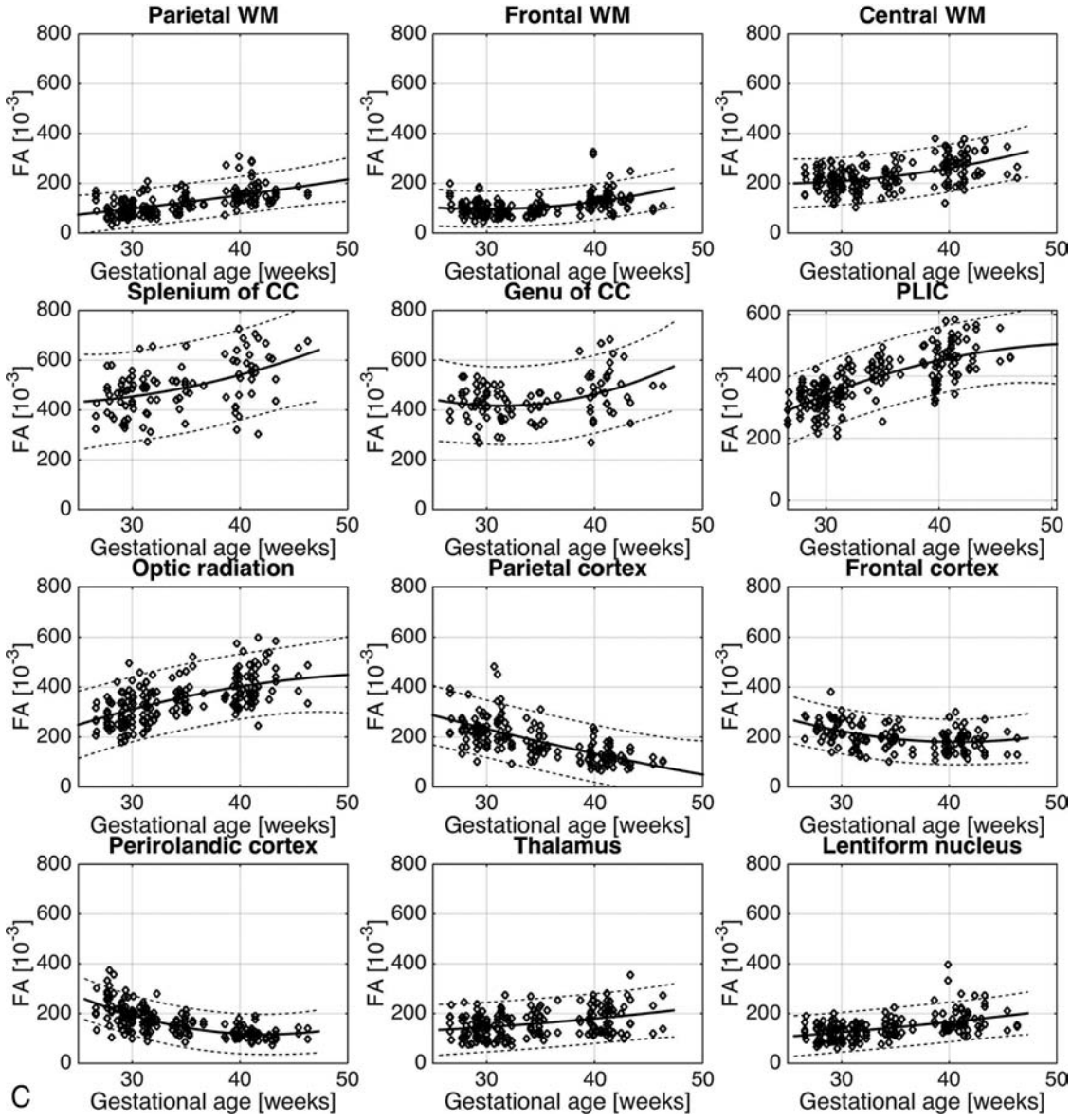

FIG 1. Continued. FA values.

processes involved in brain maturation during the last trimester of gestation, such as neuronal differentiation, premyelination with water-content reduction, increase of lipid concentration, maturation of preoligodendrocytes, and finally the beginning of axonal myelination and development of connecting fibers.[5,28]

Diffusion and T1 relaxation time are sensitive to changes in tissue water content and compartmentalization. Mean diffusivity reflects intra- and extracellular water mobility and provides information about cellular and axonal density and myelination. Moreover, T1 relaxation time also provides information about lipid concentration associated with myelin production, cholesterol, and macromolecules (galactocerebrosides)[11,13] and can, therefore, be considered as an optimal marker of brain maturation. FA represents a measure of tissue directionality sensitive to the degree of axonal alignment, fiber diameter, and consecutive early processes of premyelination.[9]

To draw brain maturational trajectories in very preterm infants, we used the above-mentioned 3 imaging biomarkers. In the WM fiber tracts (PLIC, optic radiation, and corona radiata), the linear decline of ADC and T1 reflects reduction in water content, fiber packaging, and early processes of myelination, especially for the PLIC from 36 weeks onward. In these structures, the steep slope of FA represents the progressive development of unidirectional (PLIC) or multidirectional (corona radiata) fibers. The splenium and genu of the corpus callosum consist of tightly packed fibers with a high degree of coherent parallel organization, which myelinate only at 3 and 5 months after term, respectively.[11,29] This feature accounts for little change with time for ADC and T1 values and high absolute FA values. In the frontal and parietal WM, we observed a shouldered curve on ADC and T1 maps that could be explained by the inclusion of the subplate zone that peaks between 29 to 32 gestational weeks and then gradually disappears. The subplate has a high water content,[5,30,31] is particularly voluminous in the frontal WM,[21,32] and accounts for elevated ADC and T1 values.

In the basal ganglia and thalamus, the ADC and T1 values showed a gradual decrease due to fast neuronal densification with

ongoing myelination, as described starting around 26 weeks.[29] In FA, these subcortical GM structures exhibited little change with time because of the low directionality of neuronal and glial content. In the frontal and parietal cortex, the evolution of ADC and T1 values showed a shouldered curve with maximum values around 35 weeks, possibly related to programmed cell death and additional neuropil before 35 weeks[33,34] and higher neuronal attenuation afterward. The perirolandic cortex seemed to mature faster than other cortical regions, and this accelerated maturation has been described in areas with primary function, such as the sensorimotor cortex.[34,35] The observed decline of the FA is attributed to the preferential reduction in the radial component of water diffusivity, reflecting the loss of the radial glial cells and the extension of dendrites of pyramidal cells.[32-35]

The present study has a number of limitations. We assumed that our cohort was at cerebral low-risk, given their clinical evolution and the absence of major cerebral lesions. Neurodevelopmental outcome at 6 and 18 months showed that no patient had cerebral palsy, blindness, or hearing loss, and the distribution of developmental scores was typical for this population of preterm infants. Furthermore, because patients with moderate or severe brain lesions were scarce, we could not compare their values with those obtained from the selected low-risk patients. Finally, comparison with healthy control fetuses and term neonates was not available.

In this study, we propose reference values of T1 relaxometry, which could represent a precise and complementary tool to investigate brain development with time. We speculate that deviation of the described trajectories might reflect disturbed maturation, and this could add valuable information for the diagnosis of encephalopathy of prematurity.[4,5] Kinney and Volpe[28] described "altered developmental trajectories, combined with acquired insults and reparative phenomena" to characterize this entity, in which all the structures detailed above are affected. Oligodendrocyte differentiation, axonal growth, subplate organization, and maturation of the subcortical structures represent features that are likely to be affected by prematurity.

CONCLUSIONS

Our study evaluated, longitudinally and serially, the cerebral developmental trajectories of a cohort of cerebral low-risk preterm infants born at fewer than 30 weeks of gestation. On the successive MP2RAGE and DTI sequences, we observed a gradual decline with time of ADC and T1 relaxation time and changes of FA in the described 12 ROIs, reflecting the specific and sequential maturational changes occurring during development in the WM and GM microstructures. T1 maps confer high contrast, are easy to analyze, and thus appear as a promising complementary biomarker of cerebral maturation. We provide reference values for T1 relaxation, ADC, and FA, and we speculate that deviation thereof might reflect disturbed cerebral maturation; the correlation of this disturbed maturation with neurodevelopmental outcome remains to be addressed.

ACKNOWLEDGMENTS

We thank Professor J.-F. Tolsa for his tremendous support.

Disclosures: Juliane Schneider—*RELATED*: Swiss National Science Foundation, *Comments*: National Grant (No. 33CM30–124101) allocated to a multidisciplinary project on brain development in preterm infants, performed in 3 academic sites, of which the University Hospital of Lausanne is 1 partner; *Support for Travel to Meetings for the Study or Other Purposes*: Swiss National Science Foundation (National Grant (No. 33CM30–124101). Tobias Kober—*UNRELATED*: *Employment*: I have been an employee of Siemens Healthcare Switzerland since 2011. Petra S. Hüppi—*RELATED*: *Grant*: Swiss National Science Foundation*; *UNRELATED*: *Grants/Grants Pending*: Swiss National Science Foundation,* European Commission,* Nestlé Research Center.* Patric Hagmann—*RELATED*: *Grant*: Leenaards Foundation*; *UNRELATED*: *Grants/Grants Pending*: Swiss National Science Foundation.* Anita Truttmann—*RELATED*: *Grant*: Swiss National Science Foundation.* *Money paid to the institution.

REFERENCES

1. Van't Hooft J, van der Lee JH, Opmeer BC, et al. **Predicting developmental outcomes in premature infants by term equivalent MRI: systematic review and meta-analysis.** *Syst Rev* 2015;4:71 CrossRef Medline
2. Moore T, Hennessy EM, Myles J, et al. **Neurological and developmental outcome in extremely preterm children born in England in 1995 and 2006: the EPICure studies.** *BMJ* 2012;345:e7961 CrossRef Medline
3. Marret S, Marchand-Martin L, Picaud JC, et al; EPIPAGE Study Group. **Brain injury in very preterm children and neurosensory and cognitive disabilities during childhood: the EPIPAGE cohort study.** *PLoS One* 2013;8:e62683 CrossRef Medline
4. Back SA, Miller SP. **Brain injury in premature neonates: a primary cerebral dysmaturation disorder?** *Ann Neurol* 2014;75:469–86 CrossRef Medline
5. Volpe JJ. **Brain injury in premature infants: a complex amalgam of destructive and developmental disturbances.** *Lancet Neurol* 2009;8:110–24 CrossRef Medline
6. Volpe JJ. **Neuronal proliferation, migration, organization, and myelination.** In: *Neurology of the Newborn.* 5th ed. New York: Saunders; 2008:51–117
7. Miller SP, Vigneron DB, Henry RG, et al. **Serial quantitative diffusion tensor MRI of the premature brain: development in newborns with and without injury.** *J Magn Reson Imaging* 2002;16:621–32 CrossRef Medline
8. Kersbergen KJ, Leemans A, Groenendaal F, et al. **Microstructural brain development between 30 and 40 weeks corrected age in a longitudinal cohort of extremely preterm infants.** *Neuroimage* 2014;103:214–24 CrossRef Medline
9. Hüppi PS, Maier SE, Peled S, et al. **Microstructural development of human newborn cerebral white matter assessed in vivo by diffusion tensor magnetic resonance imaging.** *Pediatr Res* 1998;44:584–90 CrossRef Medline
10. Chau V, Synnes A, Grunau RE, et al. **Abnormal brain maturation in preterm neonates associated with adverse developmental outcomes.** *Neurology* 2013;81:2082–89 CrossRef Medline
11. Nossin-Manor R, Card D, Morris D, et al. **Quantitative MRI in the very preterm brain: assessing tissue organization and myelination using magnetization transfer, diffusion tensor and T_1 imaging.** *Neuroimage* 2013;64:505–16 CrossRef Medline
12. Marques JP, Kober T, Krueger G, et al. **MP2RAGE, a self bias-field corrected sequence for improved segmentation and T1-mapping at high field.** *Neuroimage* 2010;49:1271–81 CrossRef Medline
13. Deoni SC, Dean DC 3rd, O'Muircheartaigh J, et al. **Investigating white matter development in infancy and early childhood using myelin water faction and relaxation time mapping.** *Neuroimage* 2012;63:1038–53 CrossRef Medline
14. Williams LA, Gelman N, Picot PA, et al. **Neonatal brain: regional variability of in vivo MR imaging relaxation rates at 3.0 T—initial experience.** *Radiology* 2005;235:595–603 CrossRef Medline
15. Maitre NL, Slaughter JC, Stark AR, et al. **Validation of a brain MRI relaxometry protocol to measure effects of preterm birth at a flexible postnatal age.** *BMC Pediatr* 2014;14:84 CrossRef Medline
16. Dubowitz LM, Dubowitz V, Palmer P, et al. **A new approach to the**

neurological assessment of the preterm and full-term newborn infant. *Brain Dev* 1980;2:3–14 CrossRef Medline
17. Basser PJ, Mattiello J, LeBihan D. **MR diffusion tensor spectroscopy and imaging.** *Biophys J* 1994;66:259–67 CrossRef Medline
18. Kidokoro H, Neil JJ, Inder TE. **New MR imaging assessment tool to define brain abnormalities in very preterm infants at term.** *AJNR Am J Neuroradiol* 2013;34:2208–14 CrossRef Medline
19. Papile LA, Burstein J, Burstein R, et al. **Incidence and evolution of subependymal and intraventricular hemorrhage: a study of infants with birth weights less than 1,500 gm.** *J Pediatr* 1978;92:529–34 CrossRef Medline
20. Schneider MM, Berman JI, Baumer FM, et al. **Normative apparent diffusion coefficient values in the developing fetal brain.** *AJNR Am J Neuroradiol* 2009;30:1799–803 CrossRef Medline
21. Schneider JF, Confort-Gouny S, Le Fur Y, et al. **Diffusion-weighted imaging in normal fetal brain maturation.** *Eur Radiol* 2007;17:2422–29 CrossRef Medline
22. Trivedi R, Gupta RK, Husain N, et al. **Region-specific maturation of cerebral cortex in human fetal brain: diffusion tensor imaging and histology.** *Neuroradiology* 2009;51:567–76 CrossRef Medline
23. Viola A, Confort-Gouny S, Schneider JF, et al. **Is brain maturation comparable in fetuses and premature neonates at term equivalent age?** *AJNR Am J Neuroradiol* 2011;32:1451–58 CrossRef Medline
24. Rose J, Vassar R, Cahill-Rowley K, et al. **Brain microstructural development at near-term age in very-low-birth-weight preterm infants: an atlas-based diffusion imaging study.** *Neuroimage* 2014;86:244–56 CrossRef Medline
25. Oishi K, Mori S, Donohue PK, et al. **Multi-contrast human neonatal brain atlas: application to normal neonate development analysis.** *Neuroimage* 2011;56:8–20 CrossRef Medline
26. Partridge SC, Mukherjee P, Henry RG, et al. **Diffusion tensor imaging: serial quantitation of white matter tract maturity in premature newborns.** *Neuroimage* 2004;22:1302–14 CrossRef Medline
27. Chung AW, Thomas DL, Ordidge RJ, et al. **Diffusion tensor parameters and principal eigenvector coherence: relation to b-value intervals and field strength.** *Magn Reson Imaging* 2013;31:742–47 CrossRef Medline
28. Kinney HC, Volpe JJ. **Modeling the encephalopathy of prematurity in animals: the important role of translational research.** *Neurol Res Int* 2012;2012:295389 CrossRef Medline
29. Counsell SJ, Maalouf EF, Fletcher AM, et al. **MR imaging assessment of myelination in the very preterm brain.** *AJNR Am J Neuroradiol* 2002;23:872–81 Medline
30. Kostović I, Jovanov-Milošević N, Radoš M, et al. **Perinatal and early postnatal reorganization of the subplate and related cellular compartments in the human cerebral wall as revealed by histological and MRI approaches.** *Brain Struct Funct* 2014;219:231–53 CrossRef Medline
31. Raybaud C, Ahmad T, Rastegar N, et al. **The premature brain: developmental and lesional anatomy.** *Neuroradiology* 2013;55(suppl 2):23–40 CrossRef Medline
32. Dudink J, Buijs J, Govaert P, et al. **Diffusion tensor imaging of the cortical plate and subplate in very-low-birth-weight infants.** *Pediatr Radiol* 2010;40:1397–404 CrossRef Medline
33. McKinstry RC, Mathur A, Miller JH, et al. **Radial organization of developing preterm human cerebral cortex revealed by non-invasive water diffusion anisotropy MRI.** *Cereb Cortex* 2002;12:1237–43 CrossRef Medline
34. Ball G, Srinivasan L, Aljabar P, et al. **Development of cortical microstructure in the preterm human brain.** *Proc Natl Acad Sci U S A* 2013;110:9541–46 CrossRef Medline
35. Deipolyi AR, Mukherjee P, Gill K, et al. **Comparing microstructural and macrostructural development of the cerebral cortex in premature newborns: diffusion tensor imaging versus cortical gyration.** *Neuroimage* 2005;27:579–86 CrossRef Medline
36. Rose J, Butler EE, Lamont LE, et al. **Neonatal brain structure on MRI and diffusion tensor imaging, sex, and neurodevelopment in very-low-birthweight preterm children.** *Dev Med Child Neurol* 2009;51:526–35 CrossRef Medline
37. Cheong JL, Thompson DK, Wand HX, et al. **Abnormal white matter signal on MR Imaging is related to abnormal tissue microstructure.** *AJNR Am J Neuroradiol* 2009;30:623–28 CrossRef Medline
38. Jones RA, Palasis S, Grattan-Smith JD. **MRI of the neonatal brain: optimization of spin-echo parameters.** *AJR Am J Roentgenol* 2004;182:367–72 Medline

Parenchymal Brain Laceration as a Predictor of Abusive Head Trauma

L.A. Palifka, L.D. Frasier, R.R. Metzger, and G.L. Hedlund

ABSTRACT

BACKGROUND AND PURPOSE: Accurate differentiation of abusive head trauma and accidental head injury in infants and young children is critical and impacts clinical care, patient prognosis, forensic investigations, and medicolegal proceedings. No specific finding seen on cross-sectional brain imaging has been reported to distinguish abusive head trauma from accidental injury. Our study investigated whether a specific imaging finding, parenchymal brain laceration, is unique to children diagnosed with abusive head trauma.

MATERIALS AND METHODS: We retrospectively identified 137 patients with abusive head trauma and 28 patients who incurred moderate to severe accidental brain injury. Brain MR imaging represented the imaging standard for characterizing intracranial injuries.

RESULTS: Among the abusive head trauma cohort, parenchymal brain lacerations were identified in 18 patients, while none were identified in any patients with accidental injury.

CONCLUSIONS: Our findings are in concurrence with the existing forensic, pathology, and imaging literature, which suggests that parenchymal brain lacerations may be related to abusive injury mechanisms.

ABBREVIATIONS: AHT = abusive head trauma; AI = accidental injury; GRE = gradient-echo imaging; SDH = subdural hematoma; SCWM = subcortical white matter

Abusive head trauma (AHT) is an important cause of neurologic morbidity and mortality in children, being most common in infants younger than 1 year of age. Moreover, the fatal consequences and long-term sequelae of AHT are mainly related to primary and secondary parenchymal brain injury, including contusions, axonal shear injury, lacerations, cerebral edema, hypoxia, ischemia, and infarction.

Early signs and symptoms of AHT in infants may be nonspecific, such as irritability, lethargy, or vomiting. Without a history of trauma, these infants are often diagnosed with other conditions that cause similar symptoms in infants. With AHT, historical information regarding the cause of injury may be difficult to obtain or falsely attributed to an accidental cause, with as many as 30% of AHT cases being unrecognized as inflicted injury.[1] Many of those children, if not accurately diagnosed, present later with more serious or even fatal brain injuries.

The clinical and imaging features of inflicted injury, such as retinal hemorrhages, subdural hematoma (SDH), and brain injury resulting in encephalopathy, are highly suggestive of AHT, warranting a comprehensive evaluation for abuse, though they are neither pathognomonic nor always present.[2] Each case is complex and may have varying features of abusive injury. Therefore, characterizing injuries that are predictive of AHT provides critical information to child abuse specialists who are responsible for the diagnosis and management of AHT. An intracranial finding observed only in AHT, which is lacking in children with witnessed accidental injury (AI), has considerable medicolegal implications. In this observational report, the authors describe a distinct form of inflicted brain injury, parenchymal lacerations, also referred to as subcortical clefts, contusional tears, cerebral contusional white matter clefts, and gliding contusions.[1-13]

Parenchymal brain lacerations have been reported in AHT in conjunction with many of the more specific findings of this condition; however, it is not known at what frequency they occur, if at all, in severe accidental head trauma. Since the initial descriptions

Received April 13, 2015; accepted after revision June 4.

From the Department of Radiology (L.A.P.), Dartmouth-Hitchcock Medical Center, Lebanon, New Hampshire; Division of Child Abuse Pediatrics (L.D.F.), Penn State Milton S. Hershey Children's Hospital, Hershey, Pennsylvania; Division of Pediatric Surgery (R.R.M.), University of Utah, Salt Lake City, Utah; and Department of Medical Imaging (G.L.H.), Primary Children's Medical Center, Salt Lake City, Utah.

Paper previously presented in part at: Annual Meeting of the American Society of Neuroradiology and the Foundation of the ASNR Symposium, May 17–22, 2014; Montreal, Quebec, Canada.

Please address correspondence to L. Palifka, MD, Department of Radiology, Dartmouth-Hitchcock Medical Center, One Medical Center Dr, Lebanon, NH 03756; e-mail: lpalifka@hitchock.org

Indicates article with supplemental on-line table.

http://dx.doi.org/10.3174/ajnr.A4519

Table 1: Age and sex of AHT and AI cohorts

	Abusive Head Trauma (*n* = 137)	Accidental Injury (*n* = 28)	*P* Value
Age, y (median [IQR], range)	0.50 (0.24–0.92), 0.05–2.92	1.37 (0.83–2.38), 0.04–2.83	<.001
Male	64%	68%	NS

Note:—NS indicates not significant; IQR, interquartile range.

of traumatic lacerations, there have been no population comparison studies directed at these important predictive lesions, to our knowledge. The purpose of this study was to determine the comparative frequency of lacerations in AHT versus AI and improve our understanding of the pattern of brain injury in AHT among victims younger than 3 years of age. Lacerations may represent a pattern of injury unique to AHT and are likely the result of angular acceleration, deceleration, and rotational forces that occur when infants have AHT whether through shaking and/or impact or even crushing injuries. With this information, we aim to establish additional imaging features that, in some cases, could be specific for AHT.

MATERIALS AND METHODS

Patients

This study was approved by the University of Utah review board. Retrospective review of the medical records and cross-sectional brain imaging (NCCT and MR imaging) were performed in 2 patient cohorts of infants and children younger than 3 years of age treated between January 2005 and May 2013 at a pediatric hospital verified by the American College of Surgeons as a Level I Pediatric Trauma Center.

For the AHT group, a search of the hospital Child Protective Services data base identified records of 291 patients who either by confession and/or evaluation by the institutional child abuse medical evaluation team were determined to have inflicted trauma. Cases were excluded if brain MR imaging was not performed because MR imaging served to confirm and characterize intracranial injury. Cases were also excluded if no brain pathology was observed on imaging. One case was excluded for suspected meningoencephalitis. Patients who had extensive birth trauma (forceps or failed forceps delivery) were also excluded.

For the AI cohort, a search of the hospital trauma data base identified 214 patients who were coded as having moderate-to-severe traumatic brain injury, as indicated by a presenting Glasgow Coma Scale score of <13. Eighty-seven cases were subsequently determined to have been AHT and were excluded from the AI cohort. Of the remaining 127 cases, we further excluded the following: cases of drowning ($n = 5$); underlying vascular or congenital malformation ($n = 2$); and brain imaging not performed or no brain pathology observed on NCCT/MR imaging ($n = 92$).

Imaging

All imaging was reviewed by a pediatric neuroradiologist and a radiology resident. The reviewers were not blinded to the cohorts. NCCT brain imaging was performed and reviewed for calvarial/skull base fracture, extra-axial hemorrhage, parenchymal injury, and extracalvarial soft-tissue injury. It was noted whether a laceration was suspected on NCCT by a parenchymal linear focus of high or low attenuation, which was carefully evaluated by subsequent MR imaging.

Brain MR imaging was conducted at 1.5T or 3T by using commercially available platforms. In most cases, a routine trauma protocol was used, consisting of sagittal T1; axial T1, FLAIR, dual-echo proton density, and T2; coronal gradient-echo imaging (GRE) and FSE T2 sequences. In some cases, postcontrast T1WI axial and coronal sequences and 3D sagittal spoiled gradient-recalled with isotropic axial and coronal reformations were acquired. MR images were reviewed for extra-axial collections and parenchymal injuries, including edema, ischemia, parenchymal hemorrhage/contusion, shear injury, or lacerations. MR imaging was typically performed on the day of or up to 5 days after presentation.

MR imaging was deemed the criterion standard for identifying a parenchymal laceration. The MR imaging criteria for diagnosing a laceration included the following: 1) a parenchymal cleft containing CSF, hemorrhage, or a CSF-hemorrhage fluid level; 2) a linear or oval cleft lined with a paramagnetic substance (ie, ferritin, hemosiderin) demonstrating gradient-echo imaging or SWI hypointensity or a perimeter of diffusion restriction; and 3) a linear signal alteration of >5 mm (including T2/FLAIR hyperintense signal and/or T1 shortening) that did not conform to a sulcus or perivascular space.

Skeletal surveys, CT of the abdomen and pelvis, and clinical records were also reviewed to document the presence of non-CNS injuries such as musculoskeletal and solid organ injuries.

Data Analysis

Tests for association were conducted by using the Fisher exact test, and differences in group distributions were compared by using the Wilcoxon rank sum test. Statistical differences were considered significant if the probability of type 1 error was <5%. Statistical analyses were performed by using STATA, Version 12.1 (StataCorp, College Station, Texas).

RESULTS

A total of 137 patients met the eligibility criteria for inclusion into the AHT group, and 28 patients met the criteria for the AI group. The almost 5-fold difference in group size was mainly due to the infrequent use of MR imaging for patients with accidental head injury. Patients of the AHT group were younger than those of the AI group (median, 0.50 versus 1.37 years, respectively; $P < .001$) though the sex was similar, as reported in Table 1. Patients within the AI cohort presented to the emergency department with a mean Glasgow Coma Scale score of 5.9 (18 of 28 scores were affected by paralytics).

Lacerations were identified in 18 (13.1%) of the 137 cases of AHT, while none (0%) were detected in the patients with AI. This finding represents a 13% difference in the risk of brain laceration between the groups and may indicate an association between head injury mechanism and laceration ($P = .045$). These results suggest that the presence of a laceration can indicate an abusive cause of brain injury with a sensitivity and negative predictive value of only 13.1% and 19.0%, respectively, but with both specificity and positive predictive values of 100%.

Of the AHT cohort found to have lacerations, 10 cases had

documented emergency department Glasgow Coma Scale scores with an average of 4.5 (7 of 10 were affected by paralytics). Eleven of 18 (60%) cases demonstrated physical evidence of impact to the head such as calvarial fractures ($n = 9$) or extracalvarial soft-tissue swelling ($n = 2$). Eleven cases also had imaging evidence of extra-CNS injuries, including solid organ or musculoskeletal injuries. Variably present were findings of other parenchymal injuries, including contusion (20%), shear injury (40%), and ischemic injury (40%). Only 3 cases (17%) had no extracranial evidence of head impact and no imaging evidence for extra-CNS injury.

Half (9/18) of the AHT cohort with lacerations demonstrated evidence of retinal hemorrhages on MR imaging. In the AI cohort, only 3 of 28 (11%) patients with accidental trauma had retinal hemorrhages by funduscopic examination.

The exact mechanisms of injury for the AHT cohort are largely unknown. A summary of patient characteristics and mechanisms of injury among the AI group are listed in Table 2.

Table 2: Summary of characteristics of patients with AHT/PBL and AI and imaging findings

	AHT Cohort with PBLs (n = 18)	AI Cohort (n = 28)
Type of accident		
MVA		8
Pedestrian vs auto		6
Fall		9
Crush		2
Horse		2
Unknown	16	1
Shaking injury	2	
Calvarial fracture	9	20
Suture diastasis	9	1
Extra-axial hematoma		
Epidural	1	3
Subdural	17	21
Subarachnoid	11	17
Contusion	4	8
Shear injury	7	14
Ischemic injury	7	4
Laceration	18	0
Extra-CNS injuries	10	10
Deceased	3	1

Note:—PBLs = parenchymal brain lacerations; MVA, motor vehicle accident.

Of the 18 cases of patients with AHT with lacerations, 7 (39%) demonstrated multiple lacerations. Most lacerations were hemorrhagic linear tears or clefts in the subcortical white matter (SCWM) (Fig 1). Lacerations were present in various regions, with frontal lobes predominating. In half of the cases (9/18), lacerations were suspected on NCCT (generally lesions longer than 1.5 cm or fluid-filled clefts), whereas the remaining were only identified by MR imaging. MR imaging characteristics include GRE blooming or diffusion restriction along the margins of the tear or a cleft with a fluid-hematocrit level (Figs 2 and 3). A few lacerations were surrounded by vasogenic edema. The On-line Table summarizes imaging characteristics of lacerations and details on which particular MR imaging sequence the lacerations were optimally visualized.

When available, brain imaging remote from presentation was reviewed to evaluate the evolution of the injury and characterize the appearance of chronic lacerations. The most common remote imaging finding in patients with both AHT and AI was resolution of extra-axial blood products and regional or diffuse encephalomalacia or cortical atrophy. Some lacerations healed without obvious residual parenchymal alteration that would meet the criteria for a laceration. Other lacerations of ≥2 months remote from presentation were clearly identified as clefts with central T2 hyperintense signal or a persistent fluid-fluid level or hemosiderin-lined tear (Fig 4).

DISCUSSION

Imaging plays a crucial role in the characterization of pediatric head trauma. The differentiation of abusive from accidental head injury relies heavily on imaging observations, accumulated experience, and peer-reviewed literature. Our review of AHT and AI cohorts suggests that parenchymal brain lacerations should be considered proxies for AHT.

As early as 1957, Freytag and Lindenberg[14] described the pathomorphology of cortical cleft contusions (lacerations) and their association with trauma. In 1969, these authors reported postmortem findings in 16 infants with reported trauma ($n = 9$) or postmortem evidence of injury ($n = 7$).[3] All had SAH, SDH, and evidence of bodily violence, including bruising. These infants

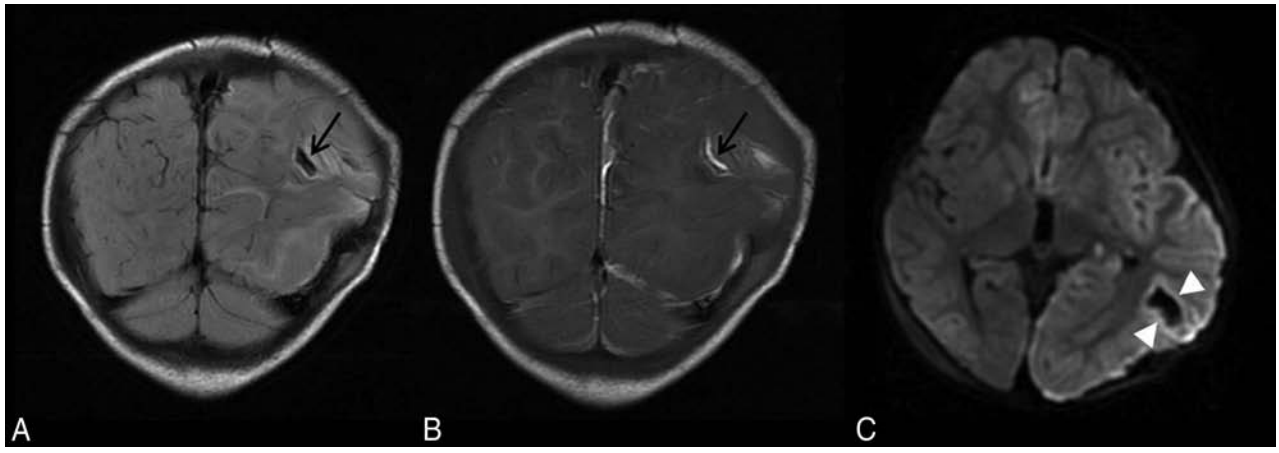

FIG 1. Parenchymal brain lacerations. Case 135. Coronal T2 FLAIR (*A*) and T1WI (*B*) demonstrate a curvilinear cleft (*black arrows*) in the left posterior temporoparietal region containing blood products consistent with acute laceration. *C*, Axial DWI demonstrates marginal diffusion hyperintensity (*white arrowheads*).

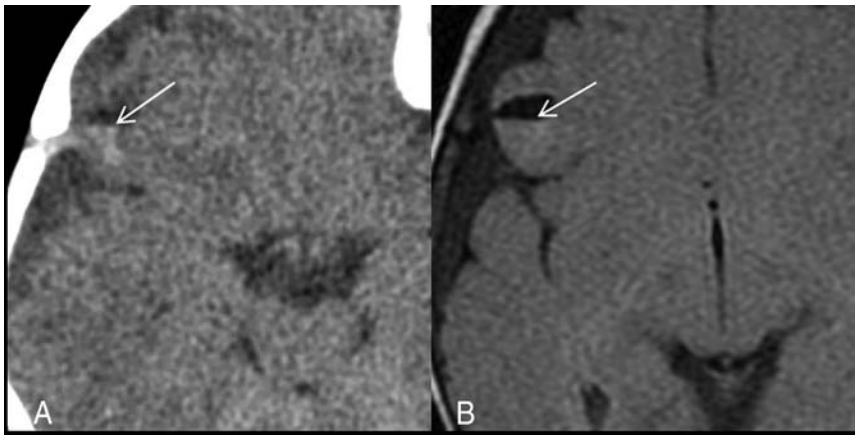

FIG 2. Parenchymal brain laceration with a fluid level. Case 18. *A*, Axial NCCT image demonstrates an SCWM cleft with a CSF-hemorrhage fluid level. *B*, Axial T2 FLAIR image depicts a fluid level with layering blood products isointense to gray matter.

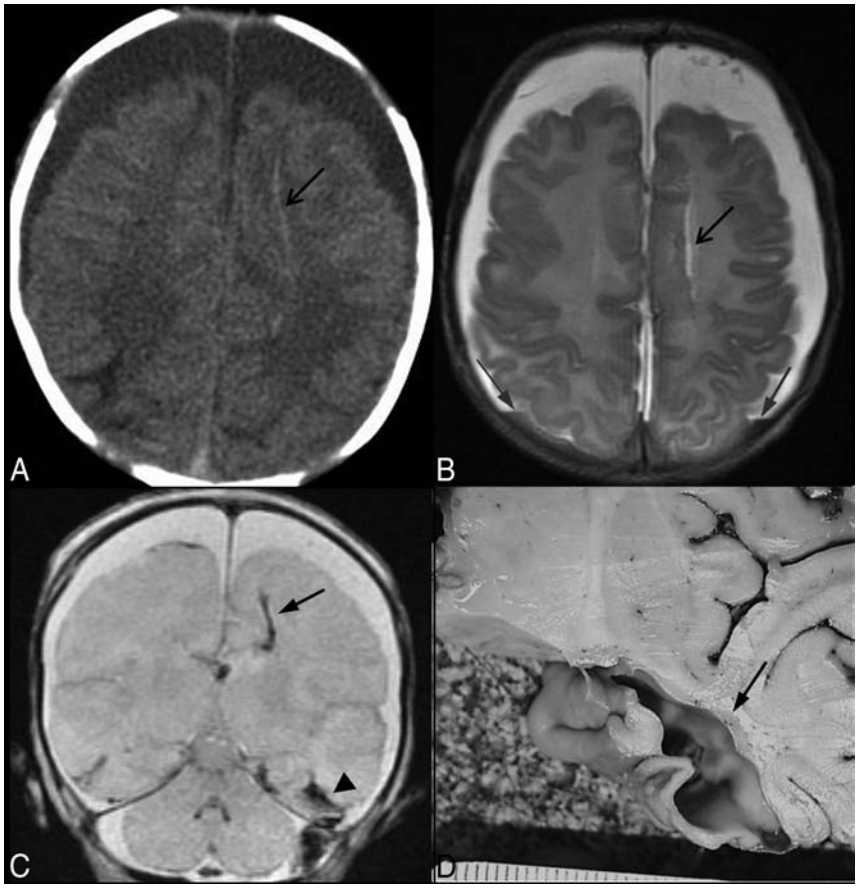

FIG 3. Parenchymal brain lacerations. Case 59. *A*, Axial NCCT image depicts long linear high-attenuation laceration in the left frontal SCWM (*black arrow*) and bifrontal CSF-attenuation extra-axial collections. *B*, The corresponding level on an axial T2WI demonstrates a linear parenchymal tear with a fluid signal (*black arrow*) and hematocrit level within bilateral subdural hemorrhages (*gray arrows*). *C*, Coronal GRE image demonstrates blooming from blood products within left frontal (*black arrow*) and bilateral (*black arrowhead*) temporal lacerations. A subdural hemorrhage is present above and below the cerebellar tentorium. *D*, A photograph of specimen from brain cutting demonstrates the left temporal SCWM laceration (*black arrow*).

exhibited macroscopic cerebral hemispheric white matter tears. The white matter tears were described as smooth-walled, with "fresh" tears containing blood and "older" tears demonstrating faint or no blood-product staining. The authors speculated that the gelatin-like consistency of the poorly myelinated infant brain predisposed to parenchymal tearing in the context of shear force generated from trauma.

Calder et al[5] reported their results in 12 patients with inflicted head injury. In their study, brains of victims younger than 5 months of age ($n = 9$) showed SCWM tears, while patients older than 5 months of age ($n = 3$) showed more adult-like white matter injury with diffuse axonal injury, axonal retraction balls, and axonal swelling. The authors concluded that the white matter tears represented the manifestation of mechanical damage produced by trauma. They reported that "these clefting lesions of the white matter are important because they represent primary evidence of brain trauma in early infancy."[5]

Imaging

Jaspan et al,[13] in a series of 6 infants proved to have experienced AHT, reported their cranial sonographic findings of cerebral contusional tears. Frontoparietal and posterior frontal locations of the tears were most common, and SDH was commonly observed. All patients had retinal hemorrhages and fractures, and most had bruising. These authors proposed that the infant's smooth cranial fossae floors, pliable calvaria, patent sutures, and gelatin-like white matter represented the substrate whereby the differential movement of gray matter and white matter in the setting of trauma led to clefting white matter tears. These authors reinforced the earlier observations by Calder et al,[5] who, a decade earlier, recognized these tears as a proxy for brain trauma in young infants.

Our data recapitulate the pathomorphologic observations of Lindenberg et al,[3] including the association of lacerations with evidence of AHT, such as SDH and SAH. All cases with lacerations demonstrated extra-axial blood products: Epidural hematoma ($n = 1$), SDH alone ($n = 6$), and both SAH and a subdural collection such as acute SDH and/or chronic SDH/hygroma ($n = 11$). Seven cases demonstrated purely acute SDH, while 2 cases had evidence of growing traumatic hygromas. Eight of the 17 cases with SDH $\pm$ SAH demonstrated mixed-attenuation collections.

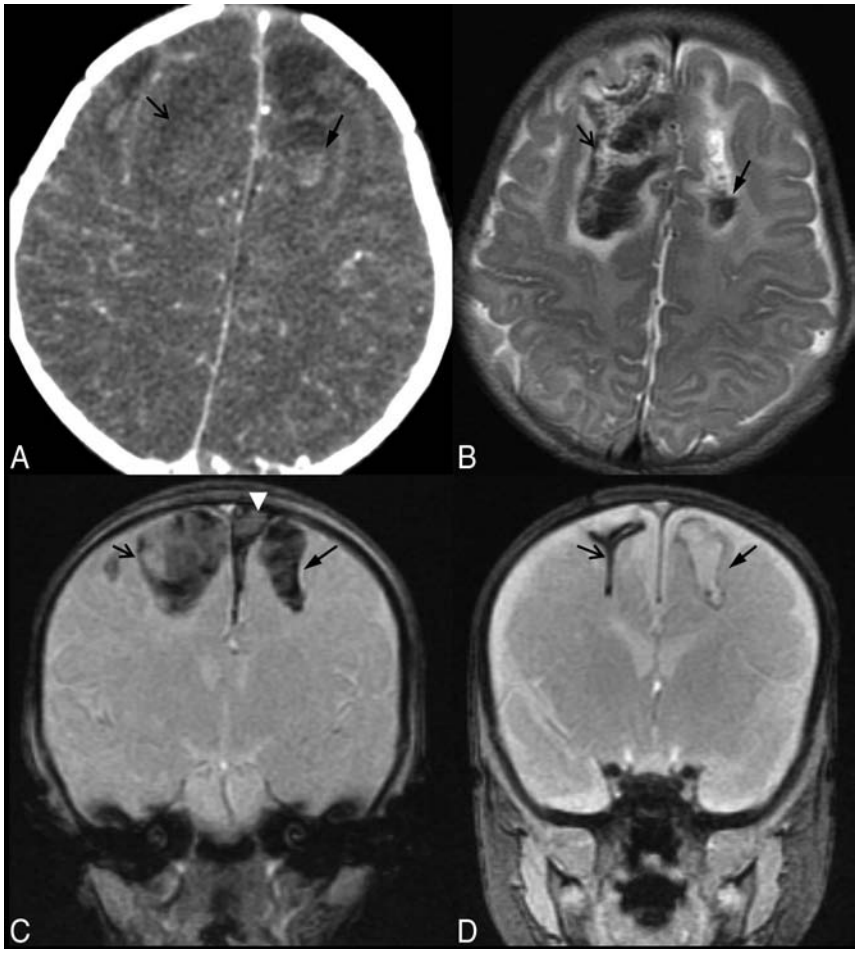

FIG 4. Parenchymal brain lacerations. Case 53. *A*, Axial NCCT image depicts a bifrontal parenchymal clefting injury with a hematocrit level within the left frontal laceration. *B*, The corresponding level on an axial T2WI better demonstrates the acute hemorrhagic SCWM parenchymal clefts with a fluid-hematocrit level and mild surrounding edema. *C*, Coronal GRE image 1 day after the acute injury demonstrates blooming artifacts of the blood-filled wide parenchymal clefts in the SCWM of the frontal lobes. Note the left parasagittal SDH (*white arrowhead*). *D*, Coronal GRE image 2 months following injury demonstrates blooming from hemosiderin-lined clefts (*arrows*). There has been marked retraction of the blood clot and near-apposition of the walls of the cleft within the right frontal lobe parenchymal brain laceration, while the cleft in the left SCWM remains wide and fluid-filled.

In 1 case, the collection was surgically evacuated and found to be consistent with acute hemorrhage; 3 cases had evidence of loculated clots or membranes suggestive of acute or chronic SDH; and 4 had low-attenuation collections that could have represented either hygroma or chronic SDH.

In our study, there were 2 laceration cases with perpetrator confession of shaking injury, both of which also had signs of impact. Evidence of impact, such as calvarial fracture or extra-calvarial soft-tissue swelling, was not always present in the cases with lacerations. Of the AHT cases with lacerations, a minimum of 9 (50%) cases had retinal hemorrhages, and 7 (39%) cases lacked signs of impact to the head, suggesting that shaking injury could result in parenchymal laceration.

During the study period, we incidentally encountered head NCCT imaging of a patient presenting for a reason other than acute trauma, which demonstrated findings of chronic bifrontal lacerations. This finding emphasizes that radiologists should be aware of encountering lacerations remote from trauma, such as in a child presenting with seizures or developmental delay without a history of reported trauma. Thus, the interpreting radiologist should appreciate the finding of a parenchymal brain laceration as a proxy for AHT.

Differential Diagnosis

In the setting of suspected pediatric head trauma, a review of the health history, appropriate laboratory testing, and cross-sectional brain imaging allow the child abuse pediatrician to develop a focused differential diagnosis. Despite clinical, imaging, and forensic evidence of AHT as a cause of parenchymal brain laceration, there are individuals who posit that such lacerations found in neonates and young infants lack diagnostic specificity.

An association between instrumented delivery and neurologic injury is well-recognized. Au-Yong et al[15] reported 5 children with cerebral cortical tears, 4 of which had a history of difficult deliveries (4 forceps, 1 episode of antepartum hemorrhage). A combination of ultrasound, NCCT, and MR imaging was used in the investigation of neurologic abnormality (seizures, hypertonia, eye deviation, and increasing head circumference). All patients were studied with MR imaging. Most interesting, MR imaging in these 5 patients depicted clefting lesions extending through the cerebral cortex.[15] This finding differs from the subcortical clefting reported from postmortem series of injured infants and the imaging manifestations of AHT-associated brain parenchymal clefts, including our data showing parenchymal brain lacerations only in the AHT cohort.[1,2,11-13,16]

Multicystic encephalomalacia reflects the underlying subcortical necrosis of white matter and diffuse loss of the cerebral cortical neurons. It is most commonly observed following a perinatal hypoxic-ischemic injury. Less commonly, multicystic encephalomalacia may follow AHT. Other intracranial injuries (SAH, SDH) are often detected in the acute and subacute periods following AHT. The imaging characteristics of multicystic encephalomalacia, including diffuse cerebral cortical atrophy and multiple subcortical cysts, are not likely to be confused with the parenchymal brain lacerations seen in AHT.[17]

The cystic and cavitary necrotic white matter findings of late neonatal and early infantile CNS infections (agents such as congenital cytomegalovirus infections, Parechovirus encephalitis, and *Citrobacter* meningoencephalitis) are characterized by their distinctive clinical presentations, CSF chemistries, microbiologic assays, polymerase chain reaction results, and imaging character-

istics, which bear no resemblance to the lacerations that have been reported among victims of AHT.[18]

Limitations

Because this was a retrospective study conducted at a single institution, certain inherent limitations may apply, such as generalizability and bias in patient selection. In addition, interpretations of images were not conducted in a blinded fashion with respect to study cohorts.

Setting a high standard for imaging evaluation by using MR imaging to determine the presence of lacerations limited the size of our cohorts. This limitation was especially true for the AI cohort because serial neurologic examinations and negative NCCT results did not warrant brain MR imaging. MR imaging would be even less frequent for cases of mild traumatic brain injury.

Although the age range of both groups was similar, the median age of patients in the AHT cohort was younger than those in the AI cohort; this difference suggests that age-related brain maturation, along with the mechanism of injury, may play a role in the prevalence of lacerations between the 2 cohorts. Sixteen of 18 patients with laceration were younger than 1 year. However, 8 of 28 patients with AI were also younger than 1 year of age. It has been postulated that lacerations only occur in the youngest patients, when brain substance is more gelatinous, due to lack of mature myelination. Brain turgor has been estimated to mature by 2–3 years of age (personal communication by phone, L.B. Rorke-Adams, MD, August 2, 2013). The oldest patient with a laceration was 29 months, suggesting that lacerations are not exclusive to the immature brain substance of infants. Further studies with larger sample sizes, particularly of very young patients, are warranted to more thoroughly address this potential confounder.

CONCLUSIONS

In our observational review of young pediatric head trauma groups (AHT and AI), brain parenchymal lacerations were only identified in the AHT cohort. When present, lacerations were always associated with other findings of CNS trauma, including retinal hemorrhages and SDHs with SAH. The median age in the AHT cohort was substantially younger than that in the AI cohort; this finding confirms prior reports that child abuse is most common in the first year of life.

Only half of the lacerations characterized by MR imaging were visualized by NCCT, emphasizing the importance of MR imaging for the detection of parenchymal injury. Even with a normal head NCCT examination, and especially in a child younger than 1 year of age, we strongly encourage MR imaging to evaluate for parenchymal injury and extra-axial hemorrhage, which are important diagnostic and prognostic considerations. Hemosiderin-lined or fluid-filled brain parenchymal clefts or linear blooming (SWI and GRE) parenchymal abnormalities observed in an infant or young child evaluated for reasons other than acute trauma should raise concern for prior inflicted brain injury.

Disclosures: Lori D. Frasier—*UNRELATED*: *Expert Testimony*: compensated legal consultation and testimony in various jurisdictions in the United States. *Consultancy*: legal consultation without testimony in various jurisdictions in the United States; Children's Healthcare of Minnesota (peer-review and quality improvement consultant). *Honoraria*: for invited lectures, including service on Speaker's bureaus. Gary L. Hedlund—*UNRELATED*: *Expert Testimony*: compensated legal consultation and testimony in various jurisdictions in the United States. *Honoraria*: for invited lectures.

REFERENCES

1. Jenny C, Hymel KP, Ritzen A, et al. **Analysis of missed cases of abusive head trauma.** *JAMA* 1999;281:621–26 CrossRef Medline
2. Hedlund GL, Frasier LD. **Neuroimaging of abusive head trauma.** *Forensic Sci Med Pathol* 2009;5:280–90 CrossRef Medline
3. Lindenberg R, Freytag E. **Morphology of brain lesions from blunt trauma in early infancy.** *Arch Pathol* 1969;87:298–305 Medline
4. Ordia IJ, Strand R, Gilles F, et al. **Computerized tomography of contusional clefts in the white matter of infants: report of two cases.** *J Neurosurg* 1981;54:696–98 CrossRef Medline
5. Calder IM, Hill I, Scholtz CL. **Primary brain trauma in non-accidental injury.** *J Clin Pathol* 1984;37:1095–1100 CrossRef Medline
6. Hausdorf G, Helmke K. **Sonographic demonstration of contusional white matter clefts in an infant.** *Neuropediatrics* 1984;15:110–12 CrossRef Medline
7. Sato Y, Yuh WT, Smith WL, et al. **Head injury in child abuse: evaluation with MR imaging.** *Radiology* 1989;173:653–57 CrossRef Medline
8. Kleinman PK. *Diagnostic Imaging of Child Abuse*. 2nd ed. St Louis: Mosby-Year Book; 1998:315–18
9. Tung GA, Kumar M, Richardson RC, et al. **Comparison of accidental and nonaccidental traumatic head injury in children on noncontrast computed tomography.** *Pediatrics* 2006;118:626–33 CrossRef Medline
10. Bechtel K, Stoessel K, Leventhal JM, et al. **Characteristics that distinguish accidental from abusive injury in hospitalized young children with head trauma.** *Pediatrics* 2004;114:165–68 CrossRef Medline
11. Ewing-Cobbs L, Prasad M, Kramer L, et al. **Acute neuroradiologic findings in young children with inflicted or noninflicted traumatic brain injury.** *Childs Nerv Syst* 2000;16:25–33; discussion 34 CrossRef Medline
12. Kemp AM, Jaspan T, Griffiths J, et al. **Neuroimaging: what neuroradiological features distinguish abusive from non-abusive head trauma? A systematic review.** *Arch Dis Child* 2011;96:1103–12 CrossRef Medline
13. Jaspan T, Narborough G, Punt JA, et al. **Cerebral contusional tears as a marker of a child abuse: detection by cranial sonography.** *Pediatr Radiol* 1992;22:237–45 CrossRef Medline
14. Freytag E, Lindenberg R. **Morphology of cortical contusions.** *AMA Arch Pathol* 1957;63:23–42 Medline
15. Au-Yong IT, Wardle SP, McConachie NS, et al. **Isolated cerebral cortical tears in children: aetiology, characterisation and differentiation from non-accidental head injury.** *Br J Radiol* 2009;82:735–41 CrossRef Medline
16. Duhaime AC, Gennarelli TA, Thibault LE, et al. **The shaken baby syndrome: a clinical, pathological, and biomechanical study.** *J Neurosurg* 1987;66:409–15 CrossRef Medline
17. Matlung SE, Bilo RA, Kubat B, et al. **Multicystic encephalomalacia as an end-stage finding in abusive head trauma.** *Forensic Sci Med Pathol* 2011;7:355–63 CrossRef Medline
18. Hedlund G, Bale JF, Barkovich AJ. **Infections of the developing and mature nervous system.** In: Barkovich AJ, Raybaud C, eds. *Pediatric Neuroimaging*. 5th ed. Philadelphia: Lippincott Williams & Wilkins; 2012:954–1050

The Arcuate Fasciculus and Language Development in a Cohort of Pediatric Patients with Malformations of Cortical Development

M.J. Paldino, K. Hedges, and F. Golriz

ABSTRACT

BACKGROUND AND PURPOSE: Patients with epilepsy and malformations of cortical development have a high prevalence of language deficits. The purpose of this study was to investigate whether the status of the arcuate fasciculus at diffusion tractography could provide a clinically meaningful marker of language function in patients with cortical malformations.

MATERIALS AND METHODS: Thirty-seven patients 3–18 years of age who had DTI performed at 3T and language evaluation by a pediatric neurologist were retrospectively identified. Twenty-two age-matched children without any neurologic, language, or MR imaging abnormalities who had identical DTI performed for an indication of headache were selected as a control cohort. The arcuate fasciculi were constructed and segmented by deterministic tractography for all subjects.

RESULTS: Twenty-one patients had intact language; 11 had mild-to-moderate and 5, profound language impairment. All patients with normal language and all control subjects had an identifiable left arcuate. The left arcuate was absent in 11 patients; all 11 were language-impaired. Failure to identify the left arcuate was strongly associated with some degree of language impairment ($P < .001$). Sensitivity, specificity, and positive predictive value for language dysfunction were 65%, 100%, and 100%, respectively. The absence of the arcuate bilaterally was associated with complete failure to develop oral language ($P < .015$).

CONCLUSIONS: Failure to identify the left arcuate fasciculus at diffusion tractography was a highly specific marker of language dysfunction in a cohort of pediatric patients with malformations of cortical development. Failure to identify the arcuate fasciculus on either side was associated with failure to develop oral language.

ABBREVIATION: MCD = malformation of cortical development

Most higher order functions of the human brain are not accomplished by individual functional centers compartmentalized to a particular region of the cortex. Rather, they emerge from parallel processing within subspecialized, but distributed, functional systems. A complex neural network, formed by some 10 billion neurons, forms the structural substrate for efficient interaction between local and distributed areas of the cerebrum. Diffusion tractography is an extension of DTI, which uses the directional tendencies of water diffusion to construct 3D trajectories of white matter tracts based on their structural coherence.[1-3] The functional importance of many such fiber systems has now been described; this description has allowed assessment of brain white matter abnormalities in terms of functional systems.[4,5] Despite the obvious promise of this technique, the ability to apply quantitative information derived from DTI toward management of an individual patient has, to date, proved elusive.

Epilepsy is a common neurologic condition defined by recurrent, unprovoked seizures, which affects 1% of the population, including 1 in 200 children.[6,7] Unlike in adults, developmental lesions predominate as the source of seizures in children; in particular, malformations of cortical development (MCDs) are the most common anatomic substrate for intractable epilepsy in children.[8] Patients with epilepsy and MCDs are at high risk for language and other cognitive impairments. Although the work-up has traditionally centered on detecting localized dysplastic abnormalities, patients with MCDs experience a wide range of deficits, which often cannot be explained on the basis of the location of the structural abnormality.[9-13] The cortical structure outside the region of MCD is normal, at least in the sense that it does not demonstrate the same histopathologic abnormalities that characterize a dysplastic cortex. Therefore, the occurrence of such a wide

Received March 6, 2015; accepted after revision May 12.

From the Department of Radiology (M.J.P., K.H.), Children's Hospital Boston and Harvard Medical School, Boston, Massachusetts; and Department of Radiology (F.G.), Texas Children's Hospital, Houston, Texas.

Please address correspondence to Farahnaz Golriz, MD, Department of Radiology, Texas Children's Hospital, 6701 Fannin St, Houston, TX 77030; e-mail: fxgolriz@texaschildrens.org

http://dx.doi.org/10.3174/ajnr.A4461

range of functional abnormalities implies the importance of aberrant cortico-cortical interaction or connectivity. Regardless of whether such aberrant connectivity is established by genetic/developmental processes or by activity-dependent reorganization, and there is evidence to support a role for each, such abnormalities have obvious potential implications for neurocognitive development.[14-19]

Recent work has demonstrated the potential for machine learning to translate quantitative data from whole-brain tractography into phenotypic information regarding language function in an individual patient.[20] Although highly accurate, this technique is time-consuming and requires substantial expertise in image processing and mathematics/statistics. These issues constitute a barrier to widespread adoption of such approaches into clinical practice, especially outside academic centers. There is a need for more practical imaging markers of language dysfunction.

The arcuate fasciculus is a major intrahemispheric association pathway that connects important receptive and expressive speech areas in the frontal and temporal lobes.[4,21] Although the exact roles of this pathway remain the subject of debate, strong evidence suggests an important contribution to language function.[22,23] Furthermore, the absence of the arcuate fasciculus has been reported in several neurodevelopmental disorders that manifest language impairment.[24] Together with recent work demonstrating that absence of the arcuate fasciculus at diffusion tractography is a highly reproducible binary finding, these results make the arcuate a very attractive target as a potential imaging marker of language function.[25] Hence, the goal of this study was to define the relationship between the arcuate fasciculi at diffusion tractography and the function of the language network in pediatric patients with MCD.

MATERIALS AND METHODS

This Health Insurance Portability and Accountability Act–compliant study was approved by the local institutional review board. Patients were identified retrospectively with the following inclusion criteria: 1) pediatric age group (18 years of age or younger); 2) diagnosis of a MCD established by MR imaging; 3) MR imaging of the brain performed at 3T, including DTI; and 4) language development characterized by a pediatric neurologist, within 1 month of the above brain imaging examination. Refinements to the above-defined population were based on the following exclusion criteria: 1) motion or other degradation to image quality, and 2) exclusion of patients younger than 3 years of age to increase confidence in the clinical determination of language function.

An age- and sex-matched control group was also retrospectively identified with the following inclusion criteria: 1) clinical indication of headache; 2) MR imaging of the brain performed at 3T, including DTI (identical to DTI performed in the patient group); and 3) language characterized as normal by a pediatric neurologist. Exclusion criteria were the following: 1) any neurologic abnormality by history or physical examination, 2) any degree of language impairment, 3) any MR imaging abnormality, and 4) marked motion or other degradation to image quality.

Patients were divided into 3 groups based on characterization of their language development by a pediatric neurologist: 1) intact: age-appropriate; 2) mild-to-moderate impairment: delayed by comparison with peers (either expressive or receptive); and 3) profound impairment: absent oral language. This categorization was made retrospectively at the time of this study on the basis of the subjective assessment made by a pediatric neurologist at the time of clinical examination. This 3-point scale was selected because it has been used to provide both a clinically meaningful and reproducible estimate of language function.[26]

MR Imaging

All imaging was performed on two 3T magnets (2 Tim Trio; Siemens, Erlangen, Germany). We performed the following sequences: 1) sagittal magnetization-prepared rapid acquisition of gradient echo (TR/TE, 2530 /3.39 ms; 1 acquisition; flip angle, 7°; TI, 1100 ms; acceleration, 2; voxel size, $1 \times 1 \times 1$ mm); 2) axial fast spin-echo T2-weighted (TR/TE, 11,730/89 ms; 2 acquisitions; flip angle, 120°; acceleration, 2; voxel size, $0.6 \times 0.4 \times 2.5$ mm); 3) axial fluid-attenuated inversion recovery (TR/TE, 9000/137 ms; 1 acquisition; flip angle, 150°; FOV, 22 cm; voxel size, $0.7 \times 0.7 \times 4$ mm); and 4) axial single-shot echo-planar imaging DTI (TR/TE, 7000/90 ms; flip angle, 90°; 1 acquisition; voxel size, $2 \times 2 \times 2$ mm). For DTI, 35 image sets were acquired, 5 without diffusion weighting (B0) and 30 with noncollinear diffusion-weighting gradients (b=1000 s/mm^2). All images were visually inspected for artifacts, including subject motion.

Image Processing and Analysis

Maps of mean diffusivity and fractional anisotropy were created by using the Diffusion Toolkit (www.Trackvis.org/dtk). For each voxel, a tensor matrix was derived. After diagonalization of the matrix, we obtained eigenvalues, and mean diffusivity and fractional anisotropy were quantified for each pixel according to standard equations.[27] Two users experienced in tractography performed tract reconstruction, segmentation, and analysis. The Diffusion Toolkit was used for deterministic tract reconstruction by using a fiber association by continuous tracking algorithm (35° angular threshold). A DWI mask was used to remove CSF, a process that has been shown to effectively prevent spurious tract reconstruction.[5] TrackVis (www.trackvis.org) was then used for segmentation and analysis of the arcuate fasciculus. ROIs for tract segmentation were placed manually on the color fractional anisotropy maps cross-referenced to the B0 images according to previously described methods.[28] The arcuate fasciculus in each subject was categorized as present on the left only, right only, or bilaterally. This method has been shown previously to provide a highly reliable classification of the arcuate fasciculus with respect to its absence versus presence.[25] Mean fractional anisotropy and mean diffusivity were then calculated for each identifiable arcuate fasciculus.

Statistics

Statistical testing was performed by using SAS software, Version 9.2 (SAS Institute, Cary, North Carolina). Proportions of subjects with-versus-without the absence of the arcuate fasciculus and with-versus-without language impairment were compared by using the Fisher exact test (α = .05). The Wilcoxon rank sum test

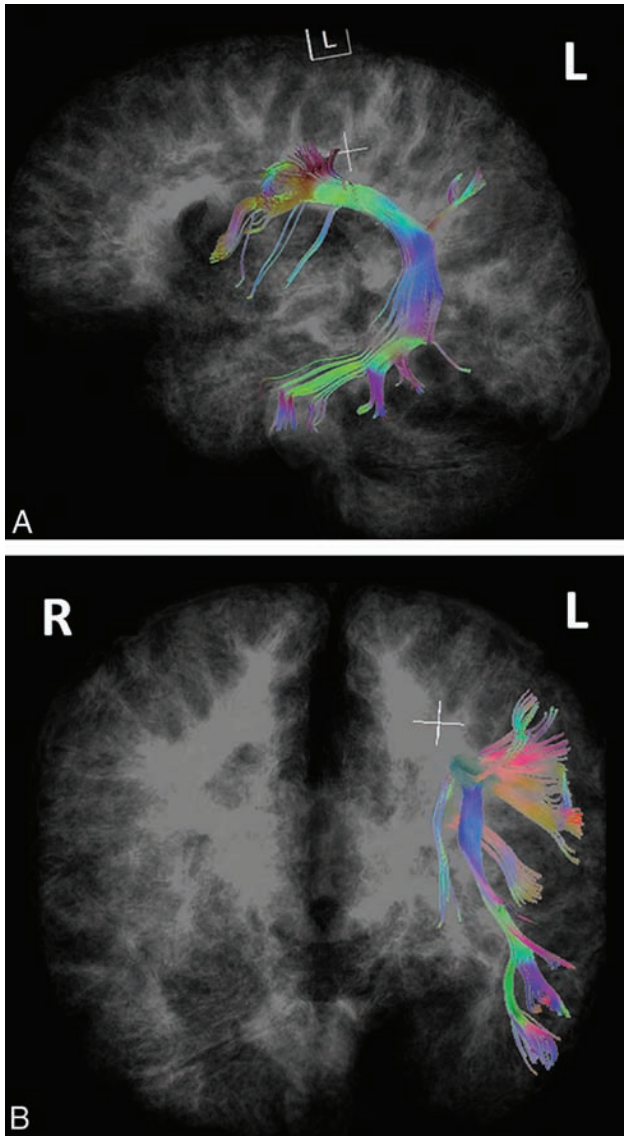

FIG 1. Left lateral (*A*) and posterior (*B*) views of a 3D tract reconstruction of the arcuate fasciculi in a control subject. Images demonstrate the presence of the arcuate fasciculus in the left hemisphere only. R indicates, right, L, left. The *cursors* reflect the center of the image space.

($\alpha = .05$) was used to compare continuous variables (mean fractional anisotropy and mean diffusivity) between groups.

RESULTS

Patients

Imaging was performed from January 2009 to April 2011. Of the 49 patients with MCD identified as meeting the inclusion criteria, 1 was excluded on the basis of motion and 11, on the basis of age (younger than 3 years). Thirty-seven patients with MCD (age range, 3–18 years; median, 10 years; 20 males, 17 females) and 22 age- and sex-matched controls (age range, 3–18 years; median, 10 years; 10 males, 12 females) composed the final study group. Cerebral malformations in the patient group included the following: polymicrogyria ($n = 16$), focal cortical dysplasia ($n = 15$), schizencephaly ($n = 4$), and gray-matter heterotopia ($n = 2$). Twenty-one patients with MCD had intact language; 11 had mild-to-moderate impairment (4 with polymicrogyria, 4 with focal cortical dysplasia, 3 with schizencephaly); and 5 had profound impairment (3 with polymicrogyria, 1 with schizencephaly, 1 with focal cortical dysplasia).

Left Arcuate Fasciculus

All control subjects had intact language and an identifiable left arcuate fasciculus (see representative example in Fig 1). Similarly, all (21/21) patients with MCD with intact language had an identifiable left arcuate fasciculus (see example in Fig 2). By contrast, all (11/11) patients with MCD without an identifiable left arcuate fasciculus manifested some degree of language impairment (6 mild-to-moderate, 5 profound; see example in Fig 3). The frequency of language impairment in patients with MCD with no identifiable left arcuate fasciculus was significantly greater than that of those with a left arcuate fasciculus ($P < .001$). Conversely, the frequency of the absence of the left arcuate fasciculus in patients with some degree of language impairment was significantly greater than that in patients with intact language ($P < .001$). The diagnostic performance of an absent left arcuate fasciculus for some degree of language impairment is presented in Table 1. Although the patient number was insufficient to address statistically, all 4 left-handers with no identifiable left arcuate were impaired with respect to language.

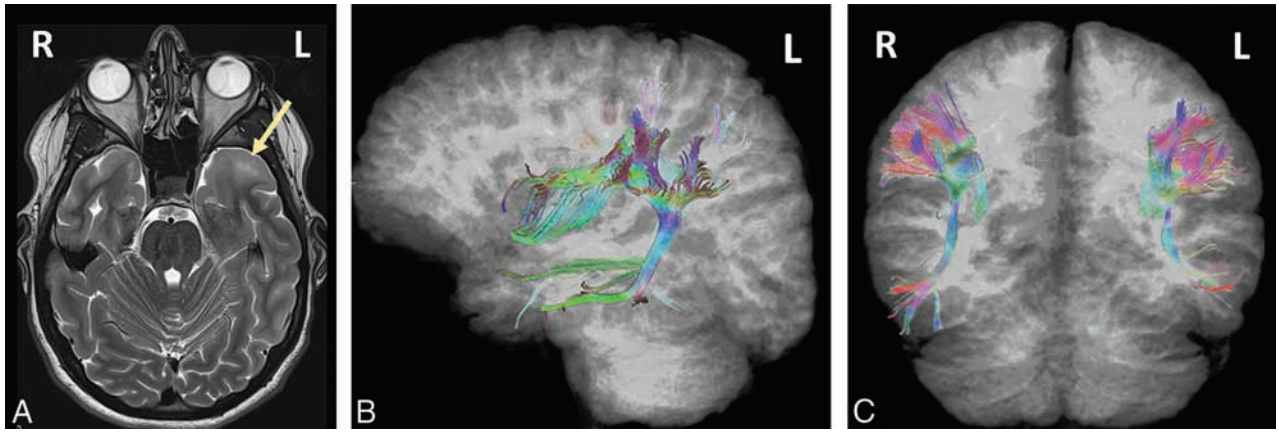

FIG 2. Axial T2-weighted image (*A*) demonstrates focal cortical dysplasia (*arrow*) centered in the left anterior temporal lobe in a right-handed patient. Left lateral (*B*) and posterior (*C*) views of a 3D reconstruction demonstrate the appearance of the arcuate fasciculus in each hemisphere. This patient has normal language.

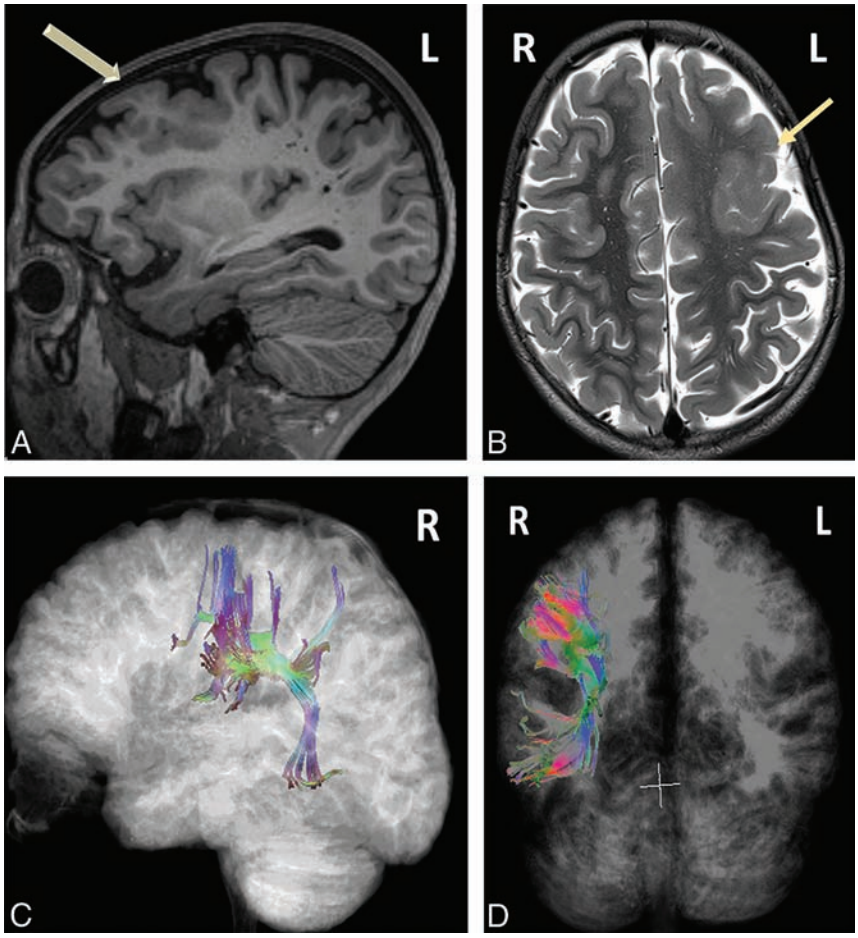

FIG 3. Sagittal MPRAGE (*A*) and axial T2-weighted (*B*) images demonstrate extensive focal cortical dysplasia (*arrow*) involving most of the visualized left frontal lobe. Right lateral (*C*) and posterior (*D*) views of the arcuate fasciculi demonstrate the presence of the arcuate fasciculus in the right hemisphere only. This right-handed patient was impaired with respect to language.

Table 1: Diagnostic performance of the absence of the left arcuate fasciculus with respect to language impairment

	Diagnostic Performance	95% LCI	95% UCI
Sensitivity (%)	64.7	38.6	84.9
Specificity (%)	100	78.1	100
PPV (%)	100	67.8	100
NPV (%)	75	52.9	89.3

Note:—LCI indicates lower limit of the 95% confidence interval; UCI, upper limit of the 95% confidence interval; PPV, positive predictive value; NPV, negative predictive value.

Aside from its absence/presence, no significant differences in the character of the left arcuate fasciculus were observed when patients with MCD were compared with the control cohort. Specifically, there was no significant difference in tract diffusion metrics (either fractional anisotropy or mean diffusivity) within the identifiable left arcuate fasciculi in patients with MCD versus controls. Trends toward higher fractional anisotropy in the left-versus-right arcuate fasciculus in both patients with MCD and controls did not meet statistical significance. There was no significant sex difference in tract metrics in either subject group, and the frequency of language impairment was not associated with sex.

Right Arcuate Fasciculus

Seventy-seven percent (17/22) of control subjects demonstrated an identifiable right arcuate fasciculus. Similarly, the right arcuate fasciculus was variably present in both the language-impaired (11/17) and language-intact (15/20) patients with MCD. There was no difference in the frequency of right arcuate fasciculus absence in patients with MCD with versus without language impairment ($P = .722$), and there was not a significant difference between the frequency of language impairment in patients with MCD with (10/26) versus without (7/11) a right arcuate fasciculus ($P = .283$).

Of the 11 patients with MCD with absent left arcuate fasciculi, all of whom were language-impaired to some degree (see above), 4 also had no identifiable right arcuate fasciculus. All 4 of these patients with no identifiable arcuate fasciculus in either hemisphere were profoundly impaired with respect to language (see example in Fig 4). Of those remaining patients without a left arcuate fasciculus who had an identifiable right arcuate fasciculus, 6 were mild-to-moderately impaired, while only 1 was profoundly impaired. The frequency of profound language impairment among those with an absent left arcuate fasciculus was significantly greater in those patients whose right arcuate fasciculus was also absent ($P < .015$). The diagnostic performance of failure to identify both the left and right arcuate fasciculi for profound language impairment is presented in Table 2.

DISCUSSION

On the basis of this study in pediatric patients with MCD, we report 2 main findings: 1) Failure to identify the left arcuate fasciculus at diffusion tractography was universally associated with language impairment; and 2) in patients with no identifiable left arcuate fasciculus, failure to identify the right arcuate fasciculus was strongly associated with a complete absence of oral language.

Although incompletely understood, the fluent comprehension and production of language are best conceptualized as an emergent property that results from complex interaction between distributed cortical regions across the cerebrum. Traditionally, it was thought to be predicated primarily on Wernicke and Broca areas, located in the left posterior temporal and left inferior frontal lobes, respectively, interacting via the arcuate fasciculus. However, current understanding suggests that Wernicke and Broca areas are but a part of a richly interconnected, large-scale language network that extends to additional frontal, parietal, and temporal association areas in both hemispheres.[29] Furthermore, optimal network function relies on interaction with cortical areas, primarily in the frontal and parietal lobes, which are not directly involved in language but rather facilitate cognitive function through working memory, attention, and other executive processes.[21] A dual-stream architecture of white matter pathways that promotes such

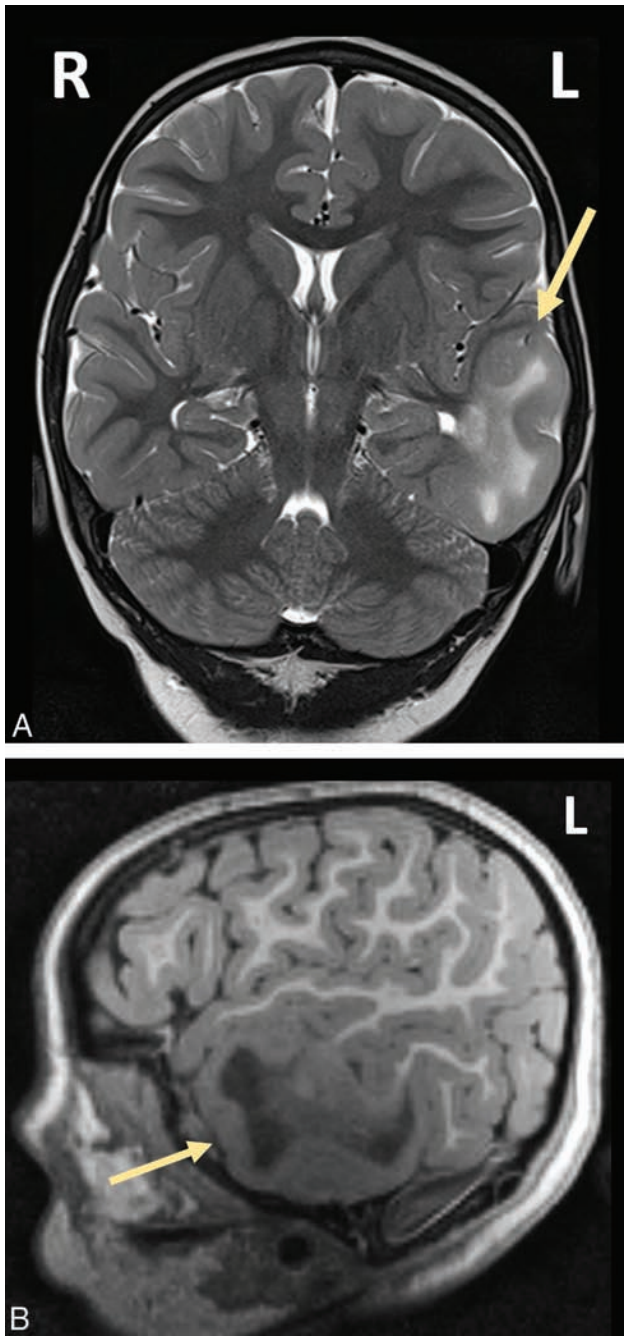

FIG 4. Coronal T2-weighted (*A*) and sagittal MPRAGE (*B*) images demonstrate a large focal cortical dysplasia (*arrow*) in the left temporal lobe. This patient has no identifiable arcuate fasciculus in either hemisphere (data not shown) and no language development.

cortico-cortical interaction and, therefore, subserves language function has been proposed.[30] In general terms, the ventral stream is believed to link phonemic information with conceptual knowledge. Although the pathways that form the anatomic basis for this "stream" remain the subject of debate, roles for the uncinate, inferior longitudinal, and inferior fronto-occipital fasciculi have all been proposed.[31] Specific functional attributes of the dorsal stream are less well-documented but generally are thought to involve the linkage between auditory and motor representations.[30] The arcuate/superior longitudinal fasciculus is generally considered to form the anatomic basis of the dorsal stream.[32]

Table 2: Diagnostic performance of the absence of both left and right arcuate fasciculi with respect to profound language impairment

	Diagnostic Performance	95% LCI	95% UCI
Sensitivity (%)	80	29.8	98.9
Specificity (%)	100	86.7	100
PPV (%)	100	39.6	100
NPV (%)	96.9	82.4	99.8

Note:—LCI indicates lower limit of the 95% confidence interval; UCI, upper limit of the 95% confidence interval; PPV, positive predictive value; NPV, negative predictive value.

We found that failure to identify the left arcuate fasciculus at diffusion tractography was consistently associated with language dysfunction in our patient population. This finding highlights the importance of formation of the left arcuate fasciculus and, furthermore, suggests that it may be a prerequisite for normal language development. The right arcuate, by contrast, was variably identified in both patients and control subjects and was not clearly associated with language function in our cohort. However, in patients with no left arcuate, the inability to identify the right arcuate fasciculus was strongly associated with a complete failure to develop oral language. This finding suggests that the right arcuate fasciculus may, in fact, play an important role in language function, particularly in the setting of suboptimal development of more central network components. Together, our findings suggest the potential for diffusion tractography to provide clinically meaningful markers of network function in an individual patient. Absence versus presence of the arcuate fasciculus has recently been shown to be highly reliable; this finding adds to its appeal as a potential biomarker.[25]

Formation of association pathways involves numerous developmental processes that act in a coordinated fashion to establish mature patterns of cerebral connectivity. These include, but are not limited to, differentiation and maturation of pyramidal cells in cortical layer 3, axonal genesis and guidance to the subplate, synapse formation and establishment of connectivity with the developing cortical plate, and selection (or pruning) of connections.[33] The last of these steps seems to involve activity-dependent stabilization of functionally useful synapses.[34] Our observations suggest a frequent impact on the establishment and/or preservation of cortico-cortical connections in patients with MCD. One possible explanation for this finding is that such patients frequently exhibit abnormalities within the cortical layers involved in cortico-cortical connectivity. It would follow that abnormal cortical lamination could result in a diminished and/or abnormal contribution to the arcuate fasciculus and, therefore, failure to detect it at tractography. As an alternative explanation, disordered genetic regulation of molecular events involved in the formation of cortico-cortical connections could also account for the reported findings. In this scenario, absence of a detectable arcuate fasciculus need not be associated with histologic abnormality of any particular cortical layer.

The histopathologic significance of failure to identify a tract at tractography is yet to be established. In addition to the absence of the tract in an absolute sense, this finding could reflect marked disorganization of white matter structures, resulting in a profound loss of tissue coherence. As an additional possibility, research in epilepsy has demonstrated the presence of relatively

widespread abnormal and epileptogenic networks in patients with focal structural lesions and, furthermore, has suggested the potential for ongoing seizure activity to establish and/or potentiate these networks.[14,15,19] Aberrant connectivity resulting from such activity-dependent reorganization could also account for the findings in this study.

Although it has not been well-studied to date, the idea that cortico-cortical connections may be abnormal in patients with MCD is consistent with a report by Munakata et al,[35] in which a case of unilateral left-sided polymicrogyria was associated with the absence of the left arcuate fasciculus. Similarly, Bernal et al[36] reported the absence of the arcuate fasciculus in 2 cases of bilateral perisylvian polymicrogyria. More recently, Saporta et al[24] suggested the functional relevance of such a finding after failing to identify the arcuate in 3 patients with congenital perisylvian syndrome and severe language dysfunction. Our results are also in line with work by Paldino et al,[20] who used a machine-learning approach to predict language phenotype on the basis of whole-brain tractography data in a cohort of patients with epilepsy and MCDs. Specifically, they found that the left arcuate fasciculus was an important contributor to the language phenotype. Although the sensitivity for language impairment in our study was inferior to that attained by the machine, this difference might be explained, at least in part, by the access of the machine-learning algorithm to metrics related to all major white matter tracts in the left hemisphere and not only the arcuate.

In our study, the absence of the left arcuate fasciculus was highly specific for language impairment and, in our opinion, would be more easily generalized to clinical practice. The importance of the arcuate fasciculus to language function has also been suggested in other neurodevelopmental disorders. Abnormal, though identifiable, arcuate fasciculi have been reported in a range of disorders manifesting speech delay.[37-39] Along similar lines, Wilson et al[40] reported the absence of the left arcuate fasciculus in 6 of 7 patients with Angelman syndrome, a developmental disorder characterized by pervasive developmental delay and failure to develop speech. Sundaram et al[41] reported the absence of the left arcuate fasciculus in 11 of 20 patients with global developmental delay. Both of the latter studies reported the presence of the left arcuate fasciculus in all healthy control subjects. These results are in line with ours and suggest that the absence of the left arcuate fasciculus may be a marker of language impairment in other patient populations. Of note, a study by Lebel and Beaulieu[42] reported a small frequency of the absence of the left arcuate fasciculus in healthy patients. In our control population, by contrast, all subjects had an identifiable left arcuate fasciculus. This discrepancy could be accounted for by the relatively small number of subjects in our study. Alternatively, it could reflect differences in image acquisition (including field strength and directional scheme for diffusion weighting) or methods of image processing. Further studies designed to rigorously define the normal character of the arcuate fasciculus at 3T will be a necessary adjunct to future investigation.

This study has several limitations. First, it was a study of a selected cohort of patients with MCD. Extrapolation of these results to other patient groups at risk for language impairment may not be valid. Second, because fMRI was not performed, the actual locations of receptive and expressive language were not definitively ascertained. This limitation, however, is substantially mitigated by corroboration with language function. In particular, if there was a significant frequency of ectopic or right hemispheric–dominant language function, it did not seem, in this study, to impact the prognostic significance of the imaging findings. Finally, functional assessment of language in this study was limited to a gross 3-point scale, chosen to reflect clinically relevant differences in language function while maximizing reproducibility of the assessment. Detailed neuropsychologic evaluation was not performed but would be of great potential value to future studies. In particular, such an evaluation might allow the identification of specific domains of language dysfunction in each patient, which could further elucidate functional subspecialization within the language network.

CONCLUSIONS

We report 2 main findings in pediatric patients with MCD: 1) Failure to identify the left arcuate fasciculus at diffusion tractography was consistently associated with language impairment; and 2) in patients with no left arcuate, failure to identify the right arcuate fasciculus was strongly associated with a complete absence of oral language. These findings suggest that the ability to form and/or maintain cortico-cortical connections is frequently impaired in patients with cortical malformations and, furthermore, is closely related to network function. In sum, our findings suggest the potential for diffusion tractography to provide clinically meaningful markers of network function in an individual patient.

REFERENCES

1. Basser PJ, Pajevic S, Pierpaoli C, et al. **In vivo fiber tractography using DT-MRI data.** *Magn Reson Med* 2000;44:625–32 CrossRef Medline
2. Melhem ER, Mori S, Mukundan G, et al. **Diffusion tensor MR imaging of the brain and white matter tractography.** *AJR Am J Roentgenol* 2002;178:3–16 CrossRef Medline
3. Lee SK, Kim DI, Kim J, et al. **Diffusion-tensor MR imaging and fiber tractography: a new method of describing aberrant fiber connections in developmental CNS anomalies.** *Radiographics* 2005;25:53–65, discussion 66–68 Medline
4. Catani M, Thiebaut de Schotten M. **A diffusion tensor imaging tractography atlas for virtual in vivo dissections.** *Cortex* 2008;44:1105–32 CrossRef Medline
5. Vishwas MS, Chitnis T, Pienaar R, et al. **Tract-based analysis of callosal, projection, and association pathways in pediatric patients with multiple sclerosis: a preliminary study.** *AJNR Am J Neuroradiol* 2010;31:121–28 CrossRef Medline
6. Boyle CA, Decouflé P, Yeargin-Allsopp M. **Prevalence and health impact of developmental disabilities in US children.** *Pediatrics* 1994;93:399–403 Medline
7. Cascino GD. **Improving quality of life with epilepsy surgery: the seizure outcome is the key to success.** *Neurology* 2007;68:1967–68 CrossRef Medline
8. Phi JH, Cho BK, Wang KC, et al. **Longitudinal analyses of the surgical outcomes of pediatric epilepsy patients with focal cortical dysplasia.** *J Neurosurg Pediatr* 2010;6:49–56 CrossRef Medline
9. Krsek P, Maton B, Jayakar P, et al. **Incomplete resection of focal cortical dysplasia is the main predictor of poor postsurgical outcome.** *Neurology* 2009;72:217–23 CrossRef Medline
10. Klein B, Levin BE, Duchowny MS, et al. **Cognitive outcome of chil-**

dren with epilepsy and malformations of cortical development. *Neurology* 2000;55:230–35 CrossRef Medline
11. Lee SK, Kim DI, Mori S, et al. **Diffusion tensor MRI visualizes decreased subcortical fiber connectivity in focal cortical dysplasia.** *Neuroimage* 2004;22:1826–29 CrossRef Medline
12. Widjaja E, Blaser S, Miller E, et al. **Evaluation of subcortical white matter and deep white matter tracts in malformations of cortical development.** *Epilepsia* 2007;48:1460–69 CrossRef Medline
13. Widjaja E, Zarei Mahmoodabadi S, Otsubo H, et al. **Subcortical alterations in tissue microstructure adjacent to focal cortical dysplasia: detection at diffusion-tensor MR imaging by using magnetoencephalographic dipole cluster localization.** *Radiology* 2009; 251:206–15 CrossRef Medline
14. Galicia E, Imai K, Mohamed IS, et al. **Changing ictal-onset EEG patterns in children with cortical dysplasia.** *Brain Dev* 2009;31:569–76 CrossRef Medline
15. Jayakar P, Dunoyer C, Dean P, et al. **Epilepsy surgery in patients with normal or nonfocal MRI scans: integrative strategies offer long-term seizure relief.** *Epilepsia* 2008;49:758–64 CrossRef Medline
16. Jonas R, Asarnow RF, LoPresti C, et al. **Surgery for symptomatic infant-onset epileptic encephalopathy with and without infantile spasms.** *Neurology* 2005;64:746–50 CrossRef Medline
17. Jonas R, Nguyen S, Hu B, et al. **Cerebral hemispherectomy: hospital course, seizure, developmental, language, and motor outcomes.** *Neurology* 2004;62:1712–21 CrossRef Medline
18. Koh S, Mathern GW, Glasser G, et al. **Status epilepticus and frequent seizures: incidence and clinical characteristics in pediatric epilepsy surgery patients.** *Epilepsia* 2005;46:1950–54 CrossRef Medline
19. Lerner JT, Salamon N, Hauptman JS, et al. **Assessment and surgical outcomes for mild type I and severe type II cortical dysplasia: a critical review and the UCLA experience.** *Epilepsia* 2009;50:1310–35 CrossRef Medline
20. Paldino MJ, Hedges K, Zhang W. **Independent contribution of individual white matter pathways to language function in pediatric epilepsy patients.** *Neuroimage Clin* 2014;6:327–32 CrossRef Medline
21. Dronkers NF, Wilkins DP, Van Valin RD Jr, et al. **Lesion analysis of the brain areas involved in language comprehension.** *Cognition* 2004;92:145–77 CrossRef Medline
22. Yeatman JD, Dougherty RF, Rykhlevskaia E, et al. **Anatomical properties of the arcuate fasciculus predict phonological and reading skills in children.** *J Cogn Neurosci* 2011;23:3304–17 CrossRef Medline
23. Marchina S, Zhu LL, Norton A, et al. **Impairment of speech production predicted by lesion load of the left arcuate fasciculus.** *Stroke* 2011;42:2251–56 CrossRef Medline
24. Saporta AS, Kumar A, Govindan RM, et al. **Arcuate fasciculus and speech in congenital bilateral perisylvian syndrome.** *Pediatr Neurol* 2011;44:270–74 CrossRef Medline
25. Paldino MJ, Hedges K, Rodrigues KM, et al. **Repeatability of quantitative metrics derived from MR diffusion tractography in paediatric patients with epilepsy.** *Br J Radiol* 2014;87:20140095 CrossRef Medline
26. Im K, Paldino MJ, Poduri A, et al. **Altered white matter connectivity and network organization in polymicrogyria revealed by individual gyral topology-based analysis.** *Neuroimage* 2014;86: 182–93 CrossRef Medline
27. Basser PJ, Pierpaoli C. **Microstructural and physiological features of tissues elucidated by quantitative-diffusion-tensor MRI.** *J Magn Reson B* 1996;111:209–19 CrossRef Medline
28. Wakana S, Caprihan A, Panzenboeck MM, et al. **Reproducibility of quantitative tractography methods applied to cerebral white matter.** *Neuroimage* 2007;36:630–44 CrossRef Medline
29. Turken AU, Dronkers NF. **The neural architecture of the language comprehension network: converging evidence from lesion and connectivity analyses.** *Front Syst Neurosci* 2011;5:1 CrossRef Medline
30. Hickok G, Poeppel D. **Dorsal and ventral streams: a framework for understanding aspects of the functional anatomy of language.** *Cognition* 2004;92:67–99 CrossRef Medline
31. Dick AS, Tremblay P. **Beyond the arcuate fasciculus: consensus and controversy in the connectional anatomy of language.** *Brain* 2012; 135:3529–50 CrossRef Medline
32. Ellmore TM, Beauchamp MS, O'Neill TJ, et al. **Relationships between essential cortical language sites and subcortical pathways.** *J Neurosurg* 2009;111:755–66 CrossRef Medline
33. Friederici AD. **Pathways to language: fiber tracts in the human brain.** *Trends Cogn Sci* 2009;13:175–81 CrossRef Medline
34. Innocenti GM, Price DJ. **Exuberance in the development of cortical networks.** *Nat Rev Neurosci* 2005;6:955–65 CrossRef Medline
35. Munakata M, Onuma A, Takeo K, et al. **Morphofunctional organization in three patients with unilateral polymicrogyria: combined use of diffusion tensor imaging and functional magnetic resonance imaging.** *Brain Dev* 2006;28:405–09 CrossRef Medline
36. Bernal B, Rey G, Dunoyer C, et al. **Agenesis of the arcuate fasciculi in congenital bilateral perisylvian syndrome: a diffusion tensor imaging and tractography study.** *Arch Neurol* 2010;67:501–05 CrossRef Medline
37. Peters SU, Kaufmann WE, Bacino CA, et al. **Alterations in white matter pathways in Angelman syndrome.** *Dev Med Child Neurol* 2011;53:361–67 CrossRef Medline
38. Gopal SP, Tiwari VN, Veenstra AL, et al. **Sensitive diffusion tensor imaging quantification method to identify language pathway abnormalities in children with developmental delay.** *J Pediatr* 2012; 160:147–51 CrossRef Medline
39. Jeong JW, Sundaram SK, Kumar A, et al. **Aberrant diffusion and geometric properties in the left arcuate fasciculus of developmentally delayed children: a diffusion tensor imaging study.** *AJNR Am J Neuroradiol* 2011;32:323–30 CrossRef Medline
40. Wilson BJ, Sundaram SK, Huq AH, et al. **Abnormal language pathway in children with Angelman syndrome.** *Pediatr Neurol* 2011;44: 350–56 CrossRef Medline
41. Sundaram SK, Sivaswamy L, Makki MI, et al. **Absence of arcuate fasciculus in children with global developmental delay of unknown etiology: a diffusion tensor imaging study.** *J Pediatr* 2008;152: 250–55 CrossRef Medline
42. Lebel C, Beaulieu C. **Lateralization of the arcuate fasciculus from childhood to adulthood and its relation to cognitive abilities in children.** *Hum Brain Mapp* 2009;30:3563–73 CrossRef Medline

Asymmetry of the Odontoid Lateral Mass Interval in Pediatric Trauma CT: Do We Need to Investigate Further?

A. Eran, D.M. Yousem, and I. Izbudak

ABSTRACT

BACKGROUND AND PURPOSE: Odontoid lateral mass interval asymmetry can be within the normal spectrum or the result of traumatic atlantoaxial injury. We sought to set radiographic guidelines for further investigation of odontoid lateral mass interval asymmetry in cervical spine CT studies of pediatric trauma patients.

MATERIALS AND METHODS: Fourteen children with C1–2 ligamentous injury or atlantoaxial rotational fixation/subluxation were retrospectively identified. We identified an additional 56 children fulfilling the following inclusion criteria: 1) They underwent C-spine CT to exclude traumatic injury, and 2) C-spine clearance and follow-up. Those were matched for age, sex, and severity of traumatic insult with the injured group. Clinical data were collected, and we measured the following parameters: anterior atlantodental interval; odontoid lateral mass interval; and the rotation of the head, C1, and C2.

RESULTS: A significant difference ($P < .001$) was found between the groups in cervical tenderness and torticollis. There was a significant difference in the atlantodental interval value (3.3 ± 0.8 mm in injured and 2.2 ± 0.5 mm in noninjured). The directionality of head, C1, and C2 rotation was significantly ($P < .05$) more toward the same direction in the noninjured group. We found significant linear correlation between head rotation and ipsilateral odontoid lateral mass interval asymmetry only in the noninjured at C1–2. With multivariant analysis, the presence of cervical tenderness and an abnormal atlantodental interval were the most significant variables.

CONCLUSIONS: Odontoid lateral mass interspace asymmetry in the absence of cervical tenderness and with a normal atlantodental interval is likely in the normal range and need not be further investigated.

ABBREVIATIONS: ADI = atlantodental interval; OLMI = odontoid lateral mass interval

Cervical spine injury in children is rare relative to adults, with a reported incidence of 1%–2%.[1,2] In children 8–10 years of age and younger, the upper cervical spine is more vulnerable to injury due to anatomic and developmental considerations.[1,3,4] From a clinical perspective, exclusion of cervical spine injury in young children might be challenging because clinical decision tools are not as accurate as in adults.[5] Although radiographs are advocated as the first line of screening for cervical spine injury in children with Glasgow Coma Scale >8 to reduce radiation, multidetector CT is often performed.

Odontoid lateral mass interval (OLMI) asymmetry was reported present in healthy adult and pediatric populations whether traumatized or not.[6-12] It is thought to arise from anatomic variation, head rotation, and muscle spasm. Nevertheless OLMI asymmetry might also imply ligamentous injury or atlantoaxial rotational fixation/subluxation at the C1–C2 level which, if present, could potentially lead to a catastrophic sequela.[4,13,14] Therefore, when facing a CT study of a trauma victim with pure OLMI asymmetry and no fracture, radiologists and clinicians may find such injury difficult to exclude.

The differential diagnostic possibilities of OLMI asymmetry without fracture in trauma settings include C1–2 ligamentous injury and atlantoaxial rotational fixation/subluxation. Consequently, further work-up in such cases includes dynamic CT with head rotation,[4] which leads to increased radiation exposure, or MR imaging with the added risk of child sedation and increasing costs. To our knowledge, no prior study has compared injured and noninjured populations with OLMI asymmetry to define which children could be cleared and which need additional work-up.

Received March 22, 2015; accepted after revision May 18.

From the Department of Radiology (A.E.), Rambam Health Care Campus, Haifa, Israel; and Department of Radiology (D.M.Y., I.I.), Johns Hopkins Medical Institutions, Baltimore, Maryland.

Paper previously presented at: Annual Meeting of the American Society of Neuroradiology, June 4–9, 2011; Seattle, Washington.

Please address correspondence to Ayelet Eran, MD, Rambam Health Care Campus, Radiology Department, PO Box 9602, Haifa 31096, Israel; e-mail: a_eran@rambam.health.gov.il

http://dx.doi.org/10.3174/ajnr.A4492

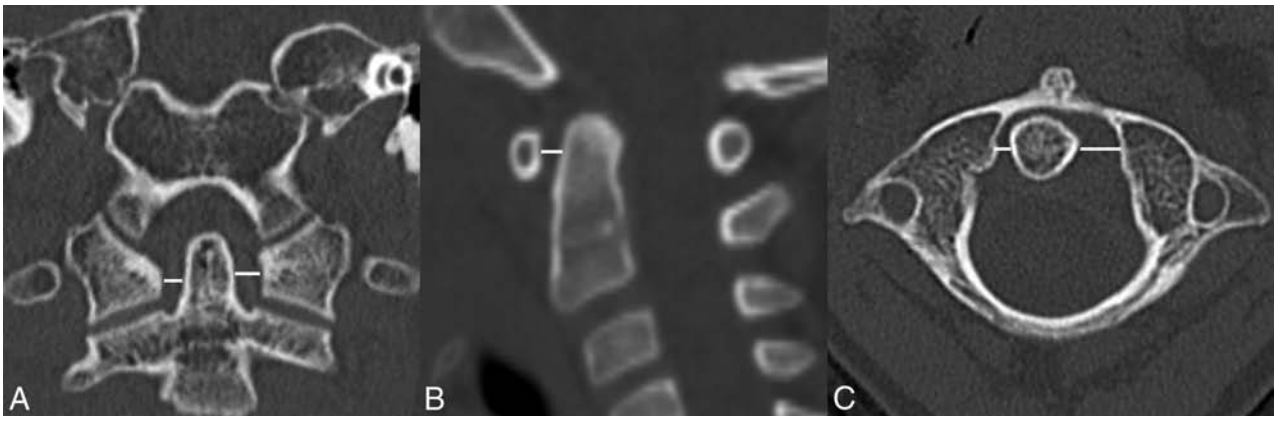

FIG 1. Coronal, sagittal, and axial CT sections at the craniocervical junction that show OLMI measurement (*white line*) at the midlateral mass level (*A* and *C*) and ADI measurement (*B*).

In this study, we sought to find radiologic and clinical parameters that could differentiate injured and noninjured patients with OLMI asymmetry in the scenario of acute trauma.

MATERIALS AND METHODS

The study was approved by the institutional review board with a waiver of informed consent.

Patients

For this retrospective study, we included children 2–18 years of age. Children younger than 2 years of age were excluded to avoid inaccurate measurements due to insufficient vertebral ossification.

We reviewed our clinical data base during a 4-year time frame and identified 14 children diagnosed with C1–2 ligamentous injury without fracture or with atlantoaxial rotational fixation/subluxation. Patients with insufficient clinical data, no CT scans, and congenital malformations or diseases affecting the upper cervical spine were excluded. All patients underwent either MR imaging or dynamic CT to confirm the diagnosis. These 14 patients constitute the injured group.

During the same time frame, 2730 cervical spine CTs were performed to rule out traumatic injury. We reviewed the CT results and medical records of those patients and identified 381 children fulfilling the following inclusion criteria: 1) They underwent cervical spine CT to rule out traumatic injury, and 2) had eventual cervical spine clearance based on CT results, physical examination, and documented uneventful clinical follow-up. From this group, we selected 56 consecutive children matched for age, sex, and severity of traumatic insult with the injured group; these children constituted a control, noninjured group.

For each individual, relevant clinical data were collected from the patient's electronic records.

CT Technique and Measurements

CT scans were performed by using 16- to 64-section machines (GE Healthcare; Milwaukee, Wisconsin) with section widths ranging from 1 to 2.5 mm. All CT studies included had CT data appropriate for performance of MPR.

Measurements were performed on a PACS workstation. Axial, coronal, and sagittal reformats were constructed on the PACS to allow maximal symmetry. All measurements were performed by a single investigator (A.E.) to eliminate the possibility of interobserver variability.

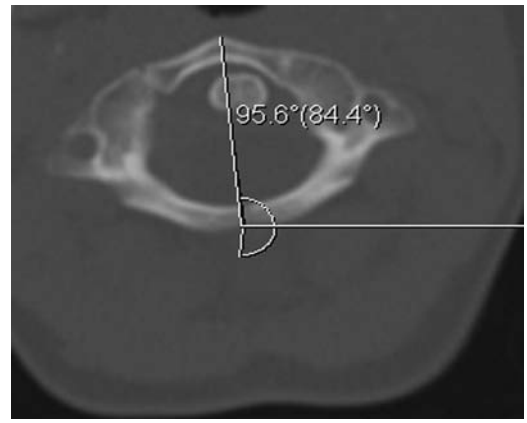

FIG 2. Axial CT image at the C1 level shows measurement of C1 rotation.

Each individual right and left OLMI interspace was measured on the axial and coronal planes at the midlateral mass level (Fig 1). OLMI asymmetry was calculated in the coronal and axial planes by subtracting the value of the right interspace from that of the left one. The values were noted in absolute and real numbers to determine the degree and directionality of the asymmetry.

For each individual, the atlantodental interval (ADI) was also measured on the midsagittal plane (Fig 1).

Head rotation was measured in degrees by using the angle tool of the PACS toolbox. The rotation of the head, C1, and C2 relative to the CT table was measured by drawing an angle in which 1 ray was a line along the midline axis of each structure (head/C1/C2) and the second ray was parallel to the CT table, pointing toward the right side of the screen (Fig 2). The rotation of each structure relative to the other was calculated by subtracting the angle of the lower structure from that of the upper one (eg, rotation of C2 relative to C1 equals the C1 angle minus the C2 angle). Therefore, rightward rotation was given a negative value, and left head rotation had a positive value. Those measurements were noted in absolute and real values to evaluate the degree and directionality of the rotation.

Demographics and clinical characteristics of the study groups

Variable	Injured[a]	Noninjured[a]	*P* Value
Age (yr) (average)	7.6 ± 2.8	7.66 ± 2.79	NS
Sex F/M	8:6	33:23	NS
LOC	4 (28.6%)	16 (28.6%)	NS
Neurologic deficit	1 (7.1%)	10 (17.9%)	NS
Cervical tenderness	11 (78.6%)	4 (8.7%)	<.001
Torticollis	8 (61.5%)	0	<.001

Note:—LOC indicates loss of consciousness; NS, not significant.
[a] Values for categoric variables are given in numbers (percentages).

Statistical Analysis

The data were analyzed with SPSS, Version 17 (IBM, Armonk, New York). The differences between the 2 groups in quantitative variables were analyzed by Mann-Whitney *U* and *t* tests. The differences between the 2 groups in the categoric variables were tested by Fisher exact and Pearson χ^2 tests. The Pearson correlation was used to find the relation between the degree and directionality of head rotation and OLMI asymmetry. Multivariate analysis by logistic regression was used to study the parameters that determined whether the patient was in the noninjured or the injured group. $P \leq .05$ was considered significant.

RESULTS

The demographics and clinical data of the injured and noninjured groups are summarized in the Table. There was no statistically significant difference between the groups in age, sex, and percentage of patients with loss of consciousness. Cervical tenderness was present in 78.6% of patients in the injured group compared with 8.7% of the noninjured group. Torticollis was present in 61.5% of the injured patients and absent in the noninjured group. Those differences were statistically significant ($P < .001$) (Table).

OLMI asymmetry was 3.8 ± 2.2 mm (mean) in the injured group and 1.4 ± 0.7 mm in the noninjured group; this difference was statistically significant ($P < .001$). There was no significant difference between measurements in the coronal or axial planes, and the values represent the average of the 2 measurements. ADI was significantly different between the groups: −3.3 ± 0.8 mm in the injured group and 2.2 ± 0.5 mm in the noninjured group ($P < .001$).

During head rotation, the directionality of the head, C1, and C2 rotation was significantly ($P < .05$) more toward the same direction in the noninjured group. In the 2 groups, there was a trend toward OLMI increase during head rotation. We found a significant linear correlation between head rotation and OLMI asymmetry only in the noninjured group at the C1–2 level. During head rotation to the right, there was a significant increase in OLMI asymmetry toward the right (the right OLMI was larger) ($P < .05$) and vice versa on head rotation to the left. No such correlation was found in other levels and in the injured group.

On multivariate analysis, cervical tenderness and an abnormal ADI were the most significant variables that differentiated the injured and noninjured groups ($P < .001$).

DISCUSSION

The dilemma concerning whether additional work-up is needed for a child with OLMI asymmetry is encountered almost on a daily basis in busy trauma centers. Accumulating data show that OLMI asymmetry can be a normal variant in adults[6-9,11,12] and children,[10] or it can be related to head positioning. Nevertheless, OLMI asymmetry can also imply ligamentous cervical spine injury at the craniocervical junction, which can be considerably disabling and even lethal.[4,13,14] In this study, we compared injured and noninjured children who presented to the emergency department similarly to enable us to find parameters that will differentiate between the groups. Such comparison has not been performed before in the literature, to the best of our knowledge.

In our study, we compared OLMI asymmetry and head rotation in pediatric patients with known traumatic injury without fracture at the C1–2 level with matched pediatric trauma patients without cervical spine injury. We found significant differences between injured and noninjured patients in the following parameters: Cervical tenderness and torticollis were significantly more common in the injured patients; OLMI asymmetry and ADI were significantly larger in the injured group. Analysis of head rotation parameters showed that rotation of the head, C1, and C2 was significantly more toward the same direction in the noninjured group and there was linear correlation between the direction of head rotation and OLMI asymmetry at the C1–2 level only in noninjured patients.

The mean OLMI asymmetry in the noninjured patients was 1.4 ± 0.7 mm, which is similar to results obtained in prior studies in children,[10] therefore confirming the validity of our data. The asymmetry in the injured group was 3.8 ± 2.2 mm, which overlaps with the noninjured group. In a study by Wolansky et al,[8] an asymmetry >3 mm was found to be abnormal in adults. On the other hand, Billmann et al[12] did not find a significant correlation between OLMI asymmetry and traumatic injury in adults. It seems that on the basis of our results and prior studies, a division of normal and abnormal based on OLMI asymmetry alone cannot be applied.

ADI was found to be one of the significant parameters in multivariate analysis that differentiated injured from noinjured children. The maximal interval in the noninjured group was 2.7 mm, and the minimal interval in the injured group was 2.5 mm, giving almost complete separation between the groups. Bertozzi et al[15] studied cervical spine parameters at the craniocervical junction in noninjured children and found a similar maximal ADI of 2.6 mm.

The analysis of head rotation parameters gives additional tools to differentiate the groups. In the noninjured group, we found increasing OLMI distance on head rotation ipsilateral to the rotation side. Those normal relations were also shown by Sutherland et al[16] in postmortem examinations. Pang and Li,[17] in a study of head rotation in children, found that most of the rotation occurs at the C1–2 level and has a predictable behavior. This behavior is disturbed when the child has an atlantoaxial rotatory fixation.[18] Possibly the ligamentous disruption in the injured group in our study prevented normal motion. Additional studies of head rotation parameters in patients with ligamentous injury at the C1–2 level may confirm this finding.

One of the limitations in this study is excluding ligamentous injury in the noninjured patients without MR imaging. However, other studies also used normal CT findings and no evidence of cervical spine injury on emergency department discharge as tools for confirming "no injury."[19] MR imaging is an expensive tool, and screening every patient with cervical spine trauma by using

MR imaging is not justified. We additionally confirmed clearance of cervical spine injury on a clinic follow-up visit in our noninjured group. Another limitation of our study is its retrospective nature. Finally, the relatively small number of injured patients in our study is another limitation and probably reflects low prevalence of C1–C2 injury in children, at least at our institution. Further multicenter prospective studies that use the parameters we suggest for injury exclusion are needed.

CONCLUSIONS

OLMI asymmetry in the absence of cervical tenderness and with normal ADI (<2.6 mm) is likely due to head positioning and should not be further investigated unless high clinical suspicion exists.

Disclosures: David M. Yousem—*UNRELATED*: *Expert Testimony*: medicolegal cases, self-employed; *Payment for Lectures (including service on Speakers Bureaus)*: American College of Radiology Education Center Course Director*; *Royalties*: 3 books with Elsevier; *Payment for Development of Educational Presentations*: CMEInfo.com for Continuing Medical Education courses.* Izlem Izbudak—*UNRELATED*: *Grants/Grants Pending*: Siemens,* *Comments*: MRI DTI research grant. *Money paid to the institution.

REFERENCES

1. Booth TN. **Cervical spine evaluation in pediatric trauma.** *AJR Am J Roentgenol* 2012;198:W417–25 CrossRef Medline
2. Platzer P, Jaindl M, Thalhammer G, et al. **Cervical spine injuries in pediatric patients.** *J Trauma* 2007;62:389–96; discussion 394–96 CrossRef Medline
3. Khanna G, El-Khoury GY. **Imaging of cervical spine injuries of childhood.** *Skeletal Radiol* 2007:36:477–94 CrossRef Medline
4. Lustrin ES, Karakas SP, Ortiz AO, et al. **Pediatric cervical spine: normal anatomy, variants, and trauma.** *Radiographics* 2003;23:539–60 CrossRef Medline
5. Viccellio P, Simon H, Pressman BD, et al; NEXUS Group. **A prospective multicenter study of cervical spine injury in children.** *Pediatrics* 2001;108:E20 CrossRef Medline
6. Lee S, Joyce S, Seeger J. **Asymmetry of the odontoid-lateral mass interspaces: a radiographic finding of questionable clinical significance.** *Ann Emerg Med* 1986;15:1173–76 CrossRef Medline
7. Iannacone WM, DeLong WG Jr, Born CT, et al. **Dynamic computerized tomography of the occiput-atlas-axis complex in trauma patients with odontoid lateral mass asymmetry.** *J Trauma* 1990;30:1501–05 CrossRef Medline
8. Wolansky LJ, Rajaraman V, Seo C, et al. **The lateral atlanto-dens interval: normal range of asymmetry.** *Emerg Radiol* 1999;6:290–93 CrossRef
9. Harty JA, Lenehan B, O'Rourke SK. **Odontoid lateral mass asymmetry: do we over-investigate?** *Emerg Med J* 2005;22:625–27 CrossRef Medline
10. Borders HL, Junewick JJ, Sherwood JM, et al. **Pediatric lateral atlantodental interval: how much asymmetry is normal?** *J Comput Assist Tomogr* 2011;35:557–59 CrossRef Medline
11. Chen Y, Zhuang Z, Qi W, et al. **A three-dimensional study of the atlantodental interval in a normal Chinese population using reformatted computed tomography.** *Surg Radiol Anat* 2011;33:801–06 CrossRef Medline
12. Billmann F, Bokor-Billmann T, Burnett C, et al. **Occurrence and significance of odontoid lateral mass interspace asymmetry in trauma patients.** *World J Surg* 2013;37:1988–95 CrossRef Medline
13. Roche C, Carty H. **Spinal trauma in children.** *Pediatr Radiol* 2001;31:677–700 CrossRef Medline
14. Mirvis SE. **How much lateral atlantodental interval asymmetry and atlantoaxial lateral mass asymmetry is acceptable on an open-mouth odontoid radiograph, and when is additional investigation necessary?** *AJR Am J Roentgenol* 1998;170:1106–07 CrossRef Medline
15. Bertozzi JC, Rojas CA, Martinez CR. **Evaluation of the pediatric craniocervical junction on MDCT.** *AJR Am J Roentgenol* 2009;192:26–31 CrossRef Medline
16. Sutherland JP Jr, Yaszemski MJ, White AA. **Radiographic appearance of the odontoid lateral mass interspace in the occipitoatlantoaxial complex.** *Spine* 1995;20:2221–25 CrossRef Medline
17. Pang D, Li V. **Atlantoaxial rotatory fixation: part 1—biomechanics of normal rotation at the atlantoaxial joint in children.** *Neurosurgery* 2004;55:614–25; discussion 625–26 CrossRef Medline
18. Pang D, Li V. **Atlantoaxial rotatory fixation: part 2—new diagnostic paradigm and a new classification based on motion analysis using computed tomographic imaging.** *Neurosurgery* 2005;57:941–53; discussion 941–53 CrossRef Medline
19. Rojas CA, Hayes A, Bertozzi JC, et al. **Evaluation of the C1–C2 articulation on MDCT in healthy children and young adults.** *AJR Am J Roentgenol* 2009;193:1388–92 CrossRef Medline

Proton Density MRI Increases Detection of Cervical Spinal Cord Multiple Sclerosis Lesions Compared with T2-Weighted Fast Spin-Echo

A.L. Chong, R.V. Chandra, K.C. Chuah, E.L. Roberts, and S.L. Stuckey

ABSTRACT

BACKGROUND AND PURPOSE: There is a paucity of literature that supports the Consortium of Multiple Sclerosis Centers guideline that proton density MR imaging is a core spinal cord sequence. We hypothesized that proton density fast spin-echo imaging is superior to T2 fast spin-echo MR imaging for the detection of cervical cord MS lesions. This study compared the detection rate and conspicuity of cervical cord MS lesions on sagittal 1.5T proton density fast spin-echo and T2 fast spin-echo MR imaging.

MATERIALS AND METHODS: One hundred consecutive patients with MS imaged with 1.5T sagittal proton density fast spin-echo and T2 fast spin-echo cervical cord MR imaging between September 2012 and October 2013 were retrospectively included. The number of MS lesions detected on each sequence was recorded; conspicuity was assessed quantitatively with the lesion-to-cord contrast ratio and lesion-contrast-to-noise ratio. Statistical analysis was performed by using the Wilcoxon signed rank test.

RESULTS: Seventy-eight patients had MS cord lesions detected. Proton density fast spin-echo imaging detected a greater number of lesions ($n = 181$) compared with T2 fast spin-echo imaging ($n = 137$, $P < .001$). Fifteen patients (19%) with abnormal findings on proton density fast spin-echo imaging had normal findings on T2 fast spin-echo imaging; no patient with abnormal T2 fast spin-echo imaging findings had normal proton density fast spin-echo imaging findings. Although proton density fast spin-echo and T2 fast spin-echo imaging had similar lesion-to-cord contrast ratios (proton density fast spin-echo, 0.32 ± 0.01, versus T2 fast spin-echo, 0.33 ± 0.01; $P = .43$), proton density fast spin-echo had greater lesion-contrast-to-noise ratio (proton density fast spin-echo, 82 ± 3.0, versus T2 fast spin-echo, 64 ± 2.6; $P < .001$).

CONCLUSIONS: Proton density fast spin-echo imaging is superior to T2 fast spin-echo MR imaging for the detection of cervical cord MS lesions. Proton density fast spin-echo detects cord lesions in patients in whom T2 fast spin-echo findings appear normal. This study forms the evidentiary base for the current Consortium of Multiple Sclerosis Centers guideline that proton density imaging is a core spinal cord sequence.

ABBREVIATIONS: CMSC = Consortium of Multiple Sclerosis Centers; FSE = fast spin-echo; GRE = gradient recalled-echo; LCCR = lesion-to-cord contrast ratio; LCNR = lesion-contrast-to-noise ratio; PD = proton density; SE = spin-echo

Spinal cord involvement is common in MS, particularly in the cervical cord.[1-3] The detection of cord abnormality is diagnostically useful because silent cord lesions are rare in other neurologic disorders and in normal aging.[4] Since the integration of MR imaging into the International Panel (McDonald) criteria in 2001,[5] there is increasing international effort to standardize MR imaging protocols. Clinical guidelines from the Consortium of Multiple Sclerosis Centers (CMSC) recommend the use of sagittal T2-weighted and sagittal T1-weighted MR imaging and either sagittal proton density (PD) or STIR as core spinal cord sequences.[6]

However, a caveat of the CMSC guidelines is that the selection of spinal cord sequences was based on the experience of the consensus group, rather than large studies.[7] This was not surprising due to few studies comparing pulse sequences and the disparate study designs in the literature.[8-11] Perhaps the discrepancy in study designs are related to the marked variability in adherence to guideline recommendations in routine clinical practice.[12] While previous studies have examined the diagnostic benefit of additional STIR imaging,[9,13,14] no previous study has assessed whether there is a diagnostic benefit to the addition of sagittal PD imaging to T2-weighted imaging of the cord. Thus, the purpose of

Received March 14, 2015; accepted after revision May 22.

From Monash Imaging (A.L.C., R.V.C., K.C.C., E.L.R., S.L.S.), Monash Health, Melbourne, Victoria, Australia; and Departments of Medicine (R.V.C., S.L.S.), Surgery (R.V.C.), and Imaging (S.L.S.), Monash University, Melbourne, Victoria, Australia.

Please address correspondence to Ronil V. Chandra, MBBS, MMed, FRANZCR, Monash Imaging, Monash Health, Department of Medicine and Department of Surgery, Monash University, 246 Clayton Rd, Clayton, Victoria 3168, Australia; e-mail: ronil.chandra@monashhealth.org or ronilvchandra@gmail.com

Indicates article with supplemental on-line table.

http://dx.doi.org/10.3174/ajnr.A4476

our study was to compare cervical cord MS lesion detection and conspicuity on sagittal 1.5T PD fast spin-echo (FSE) and T2-FSE MR imaging.

MATERIALS AND METHODS

Subjects

Institutional review board approval was obtained. The requirement for informed patient consent was waived by the institutional review board. An academic teaching hospital institutional data base was retrospectively reviewed between September 2012 and October 2013. A total of 1444 patients underwent the institutional protocol for cervical cord MS lesion detection across 4 different MR imaging scanners. The study sample was formed by the first 100 consecutive patients who satisfied the following inclusion criteria: 1) cervical cord MR imaging on a single 1.5T MR scanner, 2) both sagittal PD-FSE and T2-FSE cervical cord MR imaging performed, and 3) definite MS according to the 2010 revised McDonald criteria.[15] Exclusion criteria were the following: 1) MR imaging with motion artifacts reducing diagnostic quality, and 2) sagittal PD-FSE and T2-FSE cervical cord MR imaging performed during separate MR imaging examinations. Thus only single MR imaging examinations were included for each patient.

MR Image Acquisition

All patients were examined on a 1.5T Magnetom Avanto (Siemens, Erlangen, Germany) MR imaging scanner equipped with an SQ-engine gradient system (45 mT/m with slew rate of 200 T/m/s) by using a 16-channel neck matrix coil. All patients underwent an institutional protocol for MS lesion detection consistent with the CMSC clinical guidelines: sagittal T2-FSE, sagittal T1-FSE, sagittal PD-FSE, and axial multiecho data image combination gradient recalled-echo (GRE) through the cervical cord from C1/2 to T1, with supplementary axial T2-FSE cervical cord imaging as required. No STIR imaging was performed. The Online Table summarizes the acquisition parameters of the index PD-FSE and reference T2-FSE sequences.

Qualitative Lesion Detection and Analysis

The cervical cord was divided into 7 segments (C1, C2, C3, C4, C5, C6, and C7). Two fellowship-trained neuroradiologists (R.V.C. and K.C.C. with 5 and 12 years' experience in neuroradiologic MR imaging interpretation, respectively) identified MS lesions in each segment. "MS lesions" were defined as hyperintense compared with normal-appearing cord and at least 3 mm in greatest dimension.[16] A "long lesion" was defined as contiguous involvement of >2 segments. MS lesions detected on both sagittal PD-FSE and T2-FSE were included; if an MS lesion was detected on only 1 sagittal sequence, then it was included only if the same MS lesion was also detected on 1 axial sequence. This requirement minimized the inclusion of potential artifacts.

Reviewers were blinded to patient identification, clinical information, and the results of the alternate sagittal MR imaging. Blinding to image type (PD-FSE or T2-FSE) could not be performed because the imaging sequence could be easily distinguished. To maximize lesion detection, we allowed variation of window widths and levels. Recall bias was minimized by separation of each review session by 2 weeks and presentation of images in a randomized order. Performance bias due to viewer fatigue was minimized by dividing the image review into 6 separate sessions. Discrepancies between the reviewers were examined in additional review sessions and were resolved by consensus. The PD-FSE MR image was considered the index test, and the T2-FSE MR image was considered the reference standard, consistent with previous literature.[8,17] The interobserver agreement was determined by using the κ statistic.

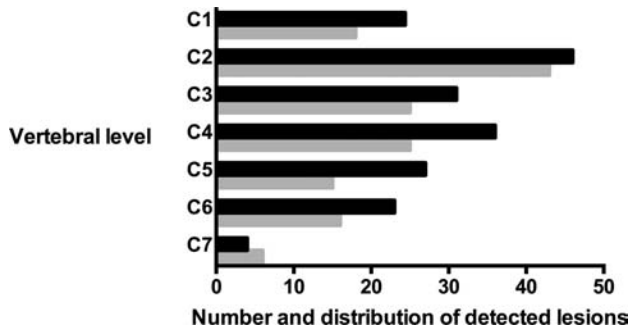

FIG 1. Comparison of the number and distribution of MS lesions detected in the cervical cord in PD-FSE (black) and T2-FSE (gray) imaging.

Quantitative Lesion Analysis

Lesion conspicuity was assessed quantitatively by using a normalized lesion-to-cord contrast ratio (LCCR) and a lesion-contrast-to-noise ratio (LCNR). ROIs were obtained within MS lesions, normal-appearing cord, and background air by using the OsiriX Imaging Software, Version 4.0 (http:// www.osirix-viewer.com). The LCCR was calculated for each sequence by applying the mean signal intensities generated in the ROIs in the equation below, where S_{lesion} is the signal intensity of the lesion and S_{cord} is the signal intensity of normal-appearing cord[18]:

$$\text{LCCR} = \frac{S_{\text{lesion}} - S_{\text{cord}}}{S_{\text{cord}}}$$

The LCNR was calculated for each sequence by assessing the difference between the S_{lesion} and S_{cord} against the level of background noise expressed as the SD of background air (SD_{air}) as measured in the equation below[18]:

$$\text{LCNR} = \frac{S_{\text{lesion}} - S_{\text{cord}}}{SD_{\text{air}}}$$

The Wilcoxon signed rank test was used for statistical analysis. $P < .05$ was considered statistically significant. All statistical calculations were performed by using STATA software, Version 11 (StataCorp, College Station, Texas).

RESULTS

Demographic Data

The median age of included patients was 44.5 years (interquartile range, 37–52 years), with a female/male ratio of 3:1. No patient was excluded due to motion artifacts. The majority of patients (78/100, 78%) had MS lesions. The mean number of lesions per patient was 2.3 (range, 0–6) for PD-FSE and 1.8 (range, 0–5) for T2-FSE imaging.

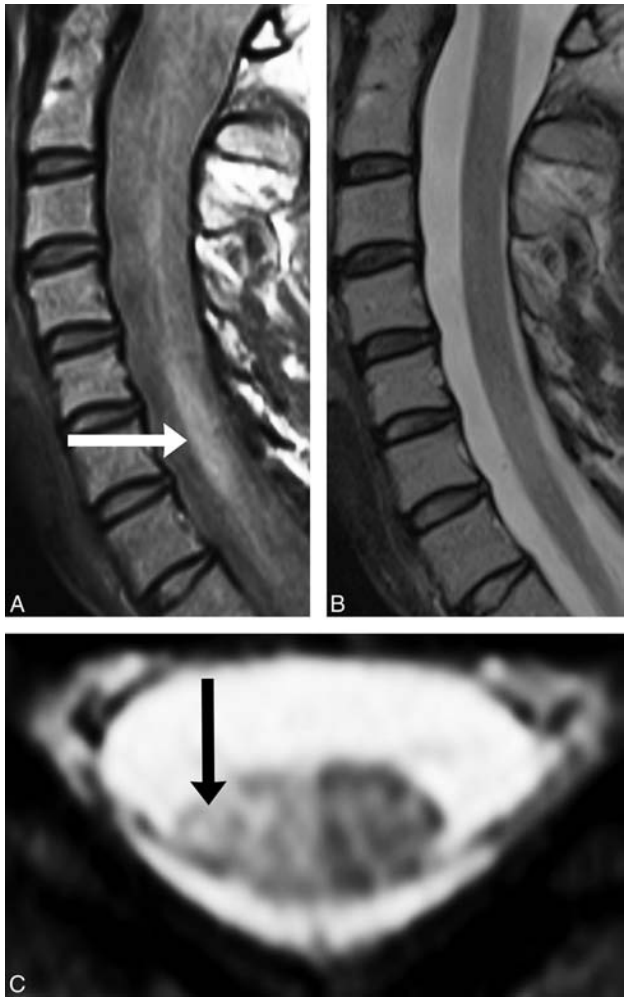

FIG 2. Sagittal PD-FSE imaging (*A*) demonstrates a lesion at C5–C7 (*white arrow*), which correlates with axial GRE imaging (*C*, *black arrow*). *B*, No lesion is detected at the C5–C7 cervical cord segments on sagittal T2-FSE imaging.

Qualitative Lesion Detection

PD-FSE imaging depicted a greater number of lesions compared with T2-FSE imaging (PD, $n = 181$, versus T2, $n = 137$; $P < .001$). This was evident at every vertebral segment, except at the C7 level (Fig 1). There was almost perfect interobserver agreement for lesion detection on both PD-FSE ($\kappa = 0.92$; 95% CI, 0.82–1.0) and T2-FSE ($\kappa = 0.92$; 95% CI, 0.84–0.99) imaging.

Long lesions were detected in 21 patients (21/78, 27%) on PD-FSE imaging and 10 patients (10/78, 13%) on T2-FSE imaging. In 5 patients, long lesions on PD-FSE corresponded with ≥2 discontinuous, discrete lesions detected on sagittal T2-FSE imaging. In all cases, axial GRE or T2 imaging also depicted contiguous involvement. In 15 patients (15/78, 19%), ≥1 lesion was detected on PD-FSE imaging with no lesions detected on sagittal T2-FSE imaging (Figs 2–5). All sagittal PD-FSE lesions not seen on sagittal T2-FSE imaging were confirmed on axial imaging. All PD-detected lesions were confirmed on either sagittal T2-FSE or axial imaging. One PD-detected cord lesion at C1 could not be confirmed on axial imaging due to lack of axial coverage and was excluded. No patients with abnormal T2-FSE imaging findings had normal PD-FSE imaging findings.

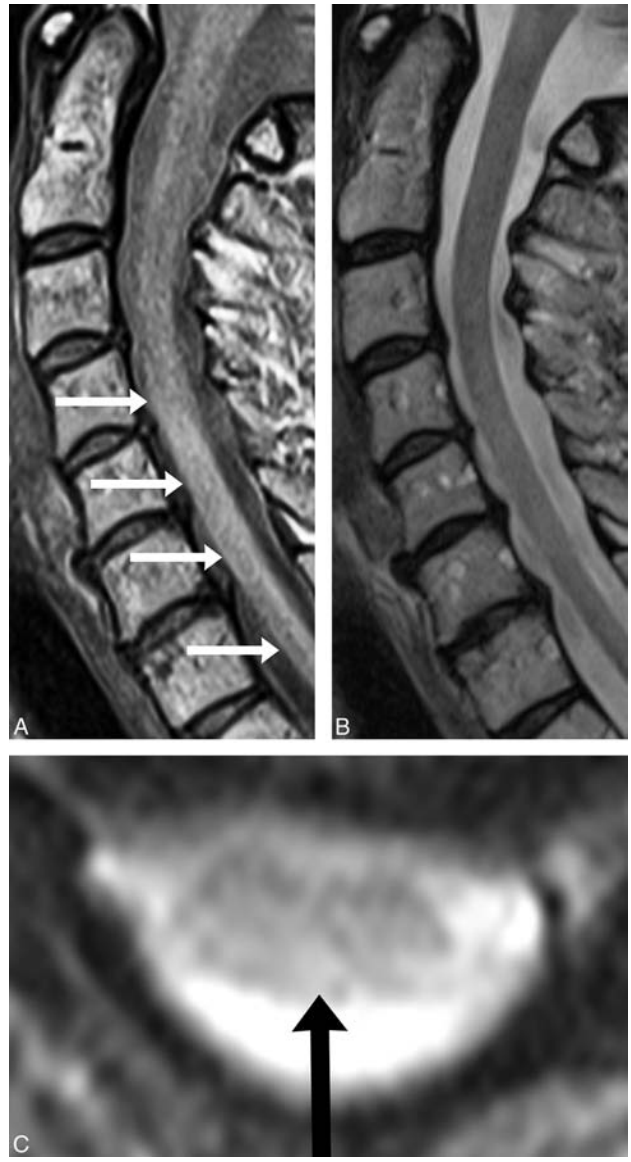

FIG 3. A C5–C7 lesion (*A*, *white arrows*) is seen on sagittal PD-FSE imaging and correlates with axial GRE imaging (*C*, *black arrow*). *C*, No lesion is detected on sagittal T2-FSE imaging.

Quantitative Lesion Analysis

Although PD-FSE and T2-FSE imaging had similar LCCR (PD-FSE, 0.32 ± 0.01, versus T2-FSE, 0.33 ± 0.01; $P = .43$), PD-FSE had significantly greater LCNR (PD-FSE, 82 ± 3.0, versus T2-FSE, 64 ± 2.6; $P < .001$).

DISCUSSION

This study demonstrates that sagittal PD-FSE imaging is superior to sagittal T2-FSE MR imaging for the detection of cervical cord MS lesions at 1.5T. PD-FSE imaging detects 32% more lesions; improved performance is evident at almost all vertebral level segments without an increase in the false-positive rate. This may be related to the greater LCNR compared with T2-FSE imaging, providing superior diagnostic confidence. The higher lesion-detection rate of PD-FSE imaging is further emphasized by the finding that PD-FSE imaging detects long lesions that are depicted as multiple smaller lesions on sagittal T2-FSE imaging.

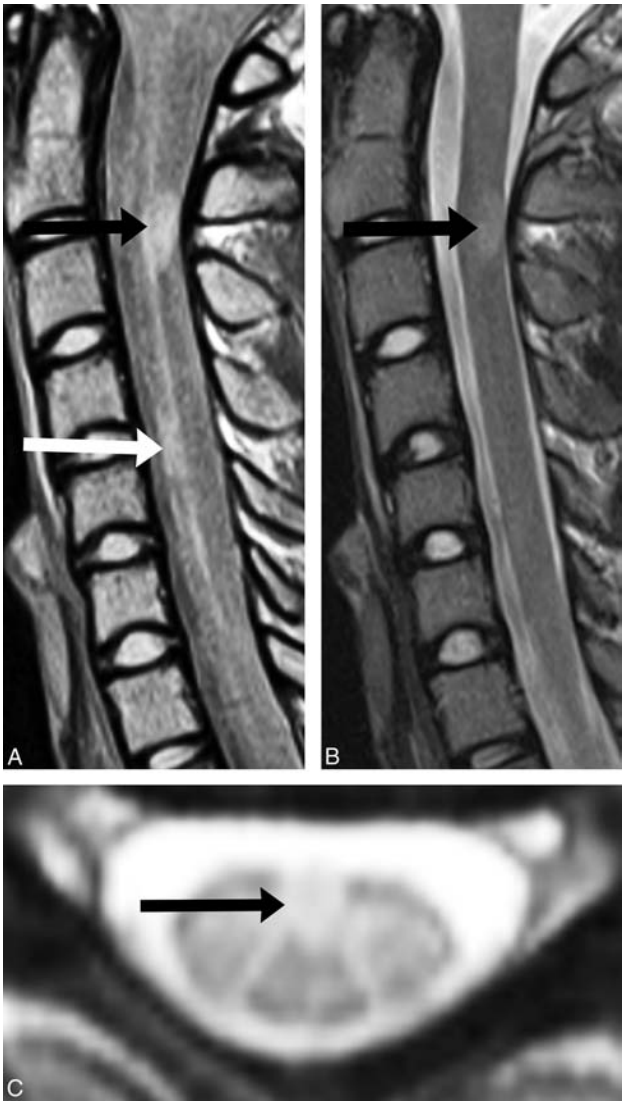

FIG 4. *A,* Sagittal PD-FSE imaging demonstrates a lesion at C2 (*black arrow*) and one at C4 (*white arrow*). *B,* Sagittal T2-FSE imaging demonstrates the same C2 lesion (*black arrow*), but not the C4 lesion. *C,* Axial GRE imaging confirms the C4 lesion (*black arrow*).

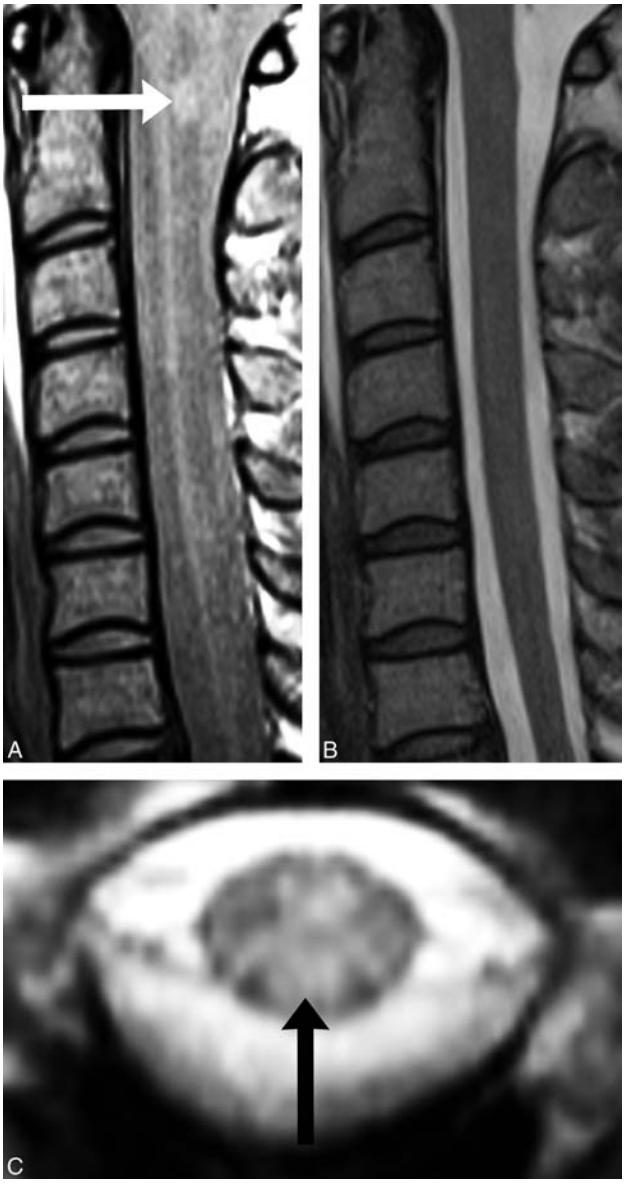

FIG 5. Sagittal PD-FSE imaging (*A*) demonstrates a lesion at C1 (*white arrow*), which correlates with axial GRE imaging (*C*, *black arrow*). *B*, No lesion is detected at the C1 cord segment on sagittal T2-FSE imaging.

This result is very important since sagittal T2-FSE sequences are the most commonly used in clinical institutions for cord MS lesion detection.

In addition, almost 1 in 6 patients with definite MS had cervical cord lesions detected on PD-FSE imaging but not on T2-FSE imaging. This difference has important implications for clinical practice, as cervical cord involvement may be missed if only sagittal T2WI is performed. Most surprising, this scenario is not uncommon. A prospective case study of 14 Australian institutions by Curley et al[12] found that 75% of spinal cord examinations did not comply with the CMSC MR imaging guidelines and relied on T2WI only. Specifically, PD-weighted imaging was performed in only 2 of 79 (2.5%) cord examinations, and STIR imaging was performed in 18 of 79 (23%) cord examinations (A. Coulthard, MBBS FRANZR, personal written communication, November 10, 2014).

To our knowledge, no previous studies have directly compared the lesion detection rate of PD-FSE with T2-FSE for cervical cord MS lesions. Most studies are designed to assess either dual-echo (PD and T2-weighted) conventional spin-echo (SE) and dual-echo FSE or T2-FSE MR imaging against other novel sequences such as STIR.[8,13,17,19] Discordant study designs and variability in data presentation and analyses preclude a substantive and useful comparison of our findings with those in these alternate studies. However, T2-weighted imaging was consistently outperformed by alternate MR sequences in all of these studies.[8,13,17,19] Moreover, there are good histopathologic data to support the use of PD-weighted imaging.[20]

A postmortem study of 19 patients with MS assessed the correlation between histopathology and 4.7T and 1T PD-SE MR imaging. All areas of the spinal cord scored as abnormal by the neuropathologist were rated as abnormal on PD-SE MR imaging; all abnormal specimens were identified by both 4.7T and 1T PD-SE MR imaging. In addition, no abnormalities were

detected in the 3 control patients on either histopathology or PD-SE MR imaging.[20]

The significantly improved LCNR in our large cohort has not been previously reported. In a smaller prospective study of 20 patients with MS, a higher contrast-to-noise ratio with PD conventional SE compared with T2 conventional SE imaging was reported, but the result did not reach statistical significance.[10] Another study of 60 patients with MS measured the contrast-to-noise ratio by using 1T PD SE and T2-SE imaging. Although statistical comparison was not performed, reported contrast-to-noise ratio values were approximately twice as high for PD-SE imaging as for T2-SE imaging.[11] Conversely, an alternate smaller study found that T2 conventional SE had a greater contrast-to-noise ratio than PD conventional SE imaging at 1.5T in 20 patients with MS.[9] This difference may simply reflect our larger cohort and imaging results on modern 1.5T MR imaging scanners compared with this previous study, which recruited almost 20 years ago.

Our study confirms the diagnostic benefit of PD-FSE MR imaging in addition to T2-FSE cervical cord imaging, as recommended by the CMSC guidelines. PD-FSE is easy to implement; our PD sequence was performed in <3 minutes and was well-tolerated by patients. The strengths of our study include the large cohort of patients with definite MS, minimization of recall and performance bias, and the use of both qualitative and quantitative analyses. The limitations of our study are the retrospective study design and use of 1.5T MR imaging, which was chosen to increase the generalizability of the study results to smaller institutions and clinical practices without 3T MR imaging availability. Although 3T MR imaging improves the PD lesion volume detection rate in the brain compared with 1.5T,[21] no such data are yet available for the spinal cord. In addition, STIR sequences were not performed and/or examined in this cohort. This is our institutional practice, which is in line with the CMSC guidelines, in which sagittal PD or STIR may be performed as the core spinal cord sequences.

CONCLUSIONS

Sagittal PD-FSE imaging is superior to T2-FSE MR imaging for the detection of cervical cord MS lesions. PD-FSE detects cord lesions in patients in whom sagittal T2-FSE imaging appears normal. This study forms the evidentiary base for the current CMSC guideline that PD imaging is a core spinal cord imaging sequence.

ACKNOWLEDGMENTS

We thank Eldho Paul, School of Public Health, Monash University, for his assistance with statistical analysis.

REFERENCES

1. Tartaglino LM, Friedman DP, Flanders AE, et al. **Multiple sclerosis in the spinal cord: MR appearance and correlation with clinical parameters.** *Radiology* 1995;195:725–32 CrossRef Medline
2. Kidd D, Thorpe JW, Thompson AJ, et al. **Spinal cord MRI using multi-array coils and fast spin echo, II: findings in multiple sclerosis.** *Neurology* 1993;43:2632–37 CrossRef Medline
3. Uldry PA, Regli F, Uské A. **Magnetic resonance imaging in patients with multiple sclerosis and spinal cord involvement: 28 cases.** *J Neurol* 1993;240:41–45 CrossRef Medline
4. Bot JC, Barkhof F, Lycklama à Nijeholt G, et al. **Differentiation of multiple sclerosis from other inflammatory disorders and cerebrovascular disease: value of spinal MR imaging.** *Radiology* 2002;223:46–56 CrossRef Medline
5. McDonald WI, Compston A, Edan G, et al. **Recommended diagnostic criteria for multiple sclerosis: guidelines from the International Panel on the Diagnosis of Multiple Sclerosis.** *Ann Neurol* 2001;50:121–27 CrossRef Medline
6. Consortium of Multiple Sclerosis Centers. **MRI Protocol for the Diagnosis and Follow-up of MS 2009 Revised Guidelines.** November 10, 2012. http://c.ymcdn.com/sites/www.mscare.org/resource/collection/9C5F19B9-3489-48B0-A54B-623A1ECEE07B/mriprotocol2009.pdf. Accessed March 31, 2013
7. Simon JH, Li D, Traboulsee A, et al. **Standardized MR imaging protocol for multiple sclerosis: Consortium of MS Centers Consensus Guidelines.** *AJNR Am J Neuroradiol* 2006;27:455–61 Medline
8. Philpott C, Brotchie P. **Comparison of MRI sequences for evaluation of multiple sclerosis of the cervical spinal cord at 3 T.** *Eur J Radiol* 2011;80:780–85 CrossRef Medline
9. Hittmair K, Mallek R, Prayer D, et al. **Spinal cord lesions in patients with multiple sclerosis: comparison of MR pulse sequences.** *AJNR Am J Neuroradiol* 1996;17:1555–65 Medline
10. Bot JC, Barkhof F, Lycklama à Nijeholt GJ, et al. **Comparison of a conventional cardiac-triggered dual spin-echo and a fast STIR sequence in detection of spinal cord lesions in multiple sclerosis.** *Eur Radiol* 2000;10:753–58 CrossRef Medline
11. Lycklama à Nijeholt GJ, Barkhof F, Scheltens P, et al. **MR of the spinal cord in multiple sclerosis: relation to clinical subtype and disability.** *AJNR Am J Neuroradiol* 1997;18:1041–48 Medline
12. Curley M, Josey L, Lucas R, et al. **Adherence to MRI protocol consensus guidelines in multiple sclerosis: an Australian multi-centre study.** *J Med Imaging Radiat Oncol* 2012;56:594–98 CrossRef Medline
13. Rocca MA, Mastronardo G, Horsfield MA, et al. **Comparison of three MR sequences for the detection of cervical cord lesions in patients with multiple sclerosis.** *AJNR Am J Neuroradiol* 1999;20:1710–16 Medline
14. Campi A, Pontesilli S, Gerevini S, et al. **Comparison of MRI pulse sequences for investigation of lesions of the cervical spinal cord.** *Neuroradiology* 2000;42:669–75 CrossRef Medline
15. Polman CH, Reingold SC, Banwell B, et al. **Diagnostic criteria for multiple sclerosis: 2010 revisions to the McDonald criteria.** *Ann Neurol* 2011;69:292–302 CrossRef Medline
16. Geurts JJ, Roosendaal SD, Calabrese M, et al; MAGNIMS Study Group. **Consensus recommendations for MS cortical lesion scoring using double inversion recovery MRI.** *Neurology* 2011;76:418–24 CrossRef Medline
17. Dietemann JL, Thibaut-Menard A, Warter JM, et al. **MRI in multiple sclerosis of the spinal cord: evaluation of fast short-tau inversion-recovery and spin-echo sequences.** *Neuroradiology* 2000;42:810–13 CrossRef Medline
18. Geurts JJ, Pouwels PJ, Uitdehaag BM, et al. **Intracortical lesions in multiple sclerosis: improved detection with 3D double inversion-recovery MR imaging.** *Radiology* 2005;236:254–60 CrossRef Medline
19. Poonawalla AH, Hou P, Nelson FA, et al. **Cervical spinal cord lesions in multiple sclerosis: T1-weighted inversion-recovery MR imaging with phase-sensitive reconstruction.** *Radiology* 2008;246:258–64 CrossRef Medline
20. Nijeholt GJ, Bergers E, Kamphorst W, et al. **Post-mortem high-resolution MRI of the spinal cord in multiple sclerosis: a correlative study with conventional MRI, histopathology and clinical phenotype.** *Brain* 2001;124:154–66 CrossRef Medline
21. Sicotte NL, Voskuhl RR, Bouvier S, et al. **Comparison of multiple sclerosis lesions at 1.5 and 3.0 Tesla.** *Invest Radiol* 2003;38:423–27 CrossRef Medline

Predicting High-Flow Spinal CSF Leaks in Spontaneous Intracranial Hypotension Using a Spinal MRI-Based Algorithm: Have Repeat CT Myelograms Been Reduced?

J.T. Verdoorn, P.H. Luetmer, C.M. Carr, J.I. Lane, V.T. Lehman, J.M. Morris, K.R. Thielen, J.T. Wald, and F.E. Diehn

ABSTRACT

BACKGROUND AND PURPOSE: We adopted an imaging algorithm in 2011 in which extradural fluid on spinal MR imaging directs dynamic CT myelography. We assessed algorithm compliance and its effectiveness in reducing repeat or unnecessary dynamic CT myelograms.

MATERIALS AND METHODS: CT myelograms for CSF leaks from January 2011 to September 2014 were reviewed. Patients with iatrogenic leaks, traumatic brachial plexus injuries, or prior CT myelography within 2 years were excluded. Completion and results of spinal MR imaging, CT myelographic technique, and the need for repeat CT myelography or unnecessary dynamic CT myelograms were recorded.

RESULTS: The algorithm was followed in 102 (79%) of 129 patients. No extradural fluid was detected in 75 (74%), of whom 70 (93%) had no leak, 4 (5%) had a slow leak, and 1 (1%) had a fast leak. Extradural fluid was detected in 27 (26%): 24 (89%) fast leaks, 1 (4%) slow leak, and 2 (7%) with no leaks. When the algorithm was followed, 1 (1%) required repeat CT myelography and 3 (3%) had unnecessary dynamic CT myelograms. The algorithm was breached in 27 (21%) cases, including no pre-CT myelogram MR imaging in 11 (41%), performing conventional CT myelography when extradural fluid was present in 13 (48%), and performing dynamic CT myelography when extradural fluid was absent in 3 (11%). Algorithm breaches resulted in 4 (15%) repeat CT myelograms and 3 (12%) unnecessary dynamic CT myelograms, both higher than with algorithm compliance.

CONCLUSIONS: Using spinal MR imaging to direct CT myelography resulted in significant reduction in repeat CT myelograms to localize fast leaks with minimal unnecessary dynamic CT myelograms.

ABBREVIATION: CTM = CT myelogram

Extradural fluid on spinal MR imaging has been reported to predict fast spinal CSF leaks for which the leak site may not be localized on conventional CT myelograms (CTMs).[1] We adopted an imaging algorithm in January 2011 for the evaluation of patients with clinical suspicion of spinal CSF leak. The first step of this algorithm is to perform MR imaging of the entire spinal canal, and the results of the MR imaging are then used to guide the type of CTM initially performed. Specifically, if extradural fluid is present on MR imaging, dynamic CTM is performed. Our current technique used for dynamic CTM has been previously reported.[2] If extradural fluid is not present, conventional CTM is performed.

The goal of adopting this algorithm was to attempt to reduce the number of repeat dynamic CTMs for leak localization in patients with fast spinal CSF leaks who initially underwent conventional CTM with the leak identified but not localizable. Averaged over the previous 8 years, repeat dynamic CTM for leak localization was performed in 21% of patients at our institution.[1] Reducing repeat CTM is desirable for several reasons, including radiation reduction, cost savings, and fewer invasive procedures.

The purpose of this study was to retrospectively evaluate our compliance with the algorithm and determine its effectiveness in reducing repeat dynamic CTM performed for leak localization.

MATERIALS AND METHODS

After obtaining institutional review board approval, a retrospective review was performed of all patients referred to CTM for suspected spinal CSF leak between January 2011 and September 2014, as determined by a radiology information system data base search. Referral to CTM was based on a working clinical diagnosis of spontaneous intracranial hypotension, typically with a history of orthostatic headache, as determined following evaluation by a headache neurologist.

Received March 15, 2015; accepted after revision May 21.

From the Department of Radiology, Mayo Clinic Rochester, Rochester, Minnesota.

Paper previously presented at: Annual Meeting of the American Society of Neuroradiology and the Foundation of the ASNR Symposium; April 24–30, 2015; Chicago, Illinois.

Please address correspondence to Patrick H. Luetmer, MD, Department of Radiology, Mayo Clinic Rochester, 200 First St SW, Rochester, MN 55905; e-mail: luetmer.patrick@mayo.edu

http://dx.doi.org/10.3174/ajnr.A4465

Patients with spinal CSF leaks secondary to an iatrogenic cause or traumatic brachial plexus injuries, as determined by review of radiology reports and the electronic medical record, were excluded. Patients with a prior CTM within 2 years, as determined by review of prior radiology examinations performed at our institution or an outside facility, were also excluded because the presence and rate of a CSF leak on the prior study could bias selection of CTM examination type.

The radiology report from each CTM was reviewed to determine the type of CTM performed. This was categorized as either conventional or dynamic. The report was also reviewed to determine whether a spinal CSF leak was present or absent. If a leak was present, it was categorized as either a fast or slow leak. A "fast leak" was defined as a leak that required the initial dynamic series of a dynamic CTM for leak localization. The initial dynamic series of a dynamic CTM includes up to 6 serial CT scans of the spine obtained during intrathecal contrast injection over the course of approximately 75 seconds, as previously described by our group.[2] All other leaks were defined as slow leaks.

Whether a spinal MR imaging examination was completed within the year preceding the CTM was recorded. The spinal MR imaging could have been from our institution or from an outside facility, if electronically available. If a spinal MR imaging examination was completed, the presence or absence of an extradural fluid collection on that examination was recorded on the basis of review of the radiology report. Each of these spinal MR imaging examinations had been interpreted by a staff neuroradiologist from our institution. If no report was available for a spinal MR imaging performed at an outside facility, the images were reviewed by a staff neuroradiologist from our institution to determine the presence or absence of an extradural fluid collection. The segments of the spine imaged on MR imaging were also recorded. These were divided into cervical, thoracic, lumbar, and each possible combination thereof. The number of days elapsed between the spinal MR imaging and the CTM was also noted. Any interventional treatment performed for spontaneous intracranial hypotension between the spinal MR imaging and the CTM was also recorded.

On the basis of whether spinal MR imaging was performed, the presence or absence of extradural fluid on MR imaging, the type of CTM performed, whether a spinal CSF leak was identified on the CTM, and whether that leak was fast or slow, the algorithm was analyzed for compliance and success as described below.

The number of patients in whom the algorithm was followed (ie, compliance) included all patients who had pre-CTM spinal MR imaging of any segments and who were appropriately triaged for dynamic CTM if extradural fluid was present on the MR imaging or conventional CTM if extradural fluid was not present.

Algorithm success was defined as patients in whom the algorithm was followed, did not require repeat imaging with a dynamic CTM for leak localization, and did not undergo unnecessary dynamic CTM for a slow or absent CSF leak. Algorithm failure was defined as patients in whom the algorithm was followed but either required repeat imaging with dynamic CTM for leak localization or underwent initial dynamic CTM for a slow or absent CSF leak.

The number of patients in whom the algorithm was not followed included all patients with one of the following breaches: patients without pre-CTM spinal MR imaging, patients inappropriately triaged for dynamic CTM if extradural fluid was not present on the MR imaging, or patients inappropriately triaged for conventional CTM if extradural fluid was present on the MR imaging.

The number of unnecessary dynamic CTMs for slow or absent CSF leaks and nonlocalized fast leaks on conventional CTM was recorded for cases in which the algorithm was breached and also for cases in which it was followed. These were compared by using a 2-tailed Fisher exact test.

RESULTS

Study Population

We identified 181 patients who were referred to CTM for a suspected spinal CSF leak. Of those, 52 (29%) were excluded. Reasons for exclusion in these patients were the following: 37 (71%) for prior CTM within 2 years, 12 (23%) for iatrogenic leaks, and 3 (6%) for leaks related to traumatic brachial plexus injuries. The remaining 129 patients were included in the study population.

In the 118 patients who underwent spinal MR imaging, the average number of days between spinal MR imaging and CTM was 50.4 (range, 0–351 days). Fifteen of 118 (13%) patients underwent interventional treatment between the spinal MR imaging and CTM. Of these, 12 received nontargeted epidural blood patches, 2 received nontargeted epidural injections of blood and fibrin glue, and 1 underwent surgical dural repair.

Algorithm Compliance

The algorithm was followed in 102 (79%) of 129 patients. In these patients, spinal MR imaging segments included the following: cervical/thoracic/lumbar in 82 (80%), cervical/thoracic in 8 (8%), cervical/lumbar in 2 (2%), thoracic/lumbar in 2 (2%), cervical in 2 (2%), thoracic in 4 (4%), and lumbar in 2 (2%).

Of the 20 patients with only a portion of the spine imaged with MR imaging, 18 had no extradural fluid present. These patients all underwent conventional CTM with no leak identified in 16 (89%) and slow leaks identified in 2 (11%). In the 2 patients with slow leaks, the imaged portion of the spine on MR imaging included the suspected site of leak identified on CTM. The 2 patients with extradural fluid present were appropriately triaged to dynamic CTM with fast leaks identified.

In the 102 patients in whom the algorithm was followed, extradural fluid was present on spinal MR imaging in 27 (26%) and absent in 75 (74%). When extradural fluid was present, dynamic CTM was performed and demonstrated a fast leak in 24 (89%) of 27 patients (Fig 1), a slow leak in 1 (4%), and no identifiable leak in 2 (7%). When extradural fluid was absent, conventional CTM was performed and demonstrated no identifiable leak in 70 (93%) of 75 patients, a slow leak in 4 (5%), and a fast leak that could not be localized in 1 (1%).

Algorithm Success

When the algorithm was followed, algorithm success was present in 98 (96%) of 102 patients, and algorithm failure, in 4 (4%).

As for the failures, 3 (3%) of 102 patients underwent unnecessary dynamic CTM for a slow or absent CSF leak and 1 (1%)

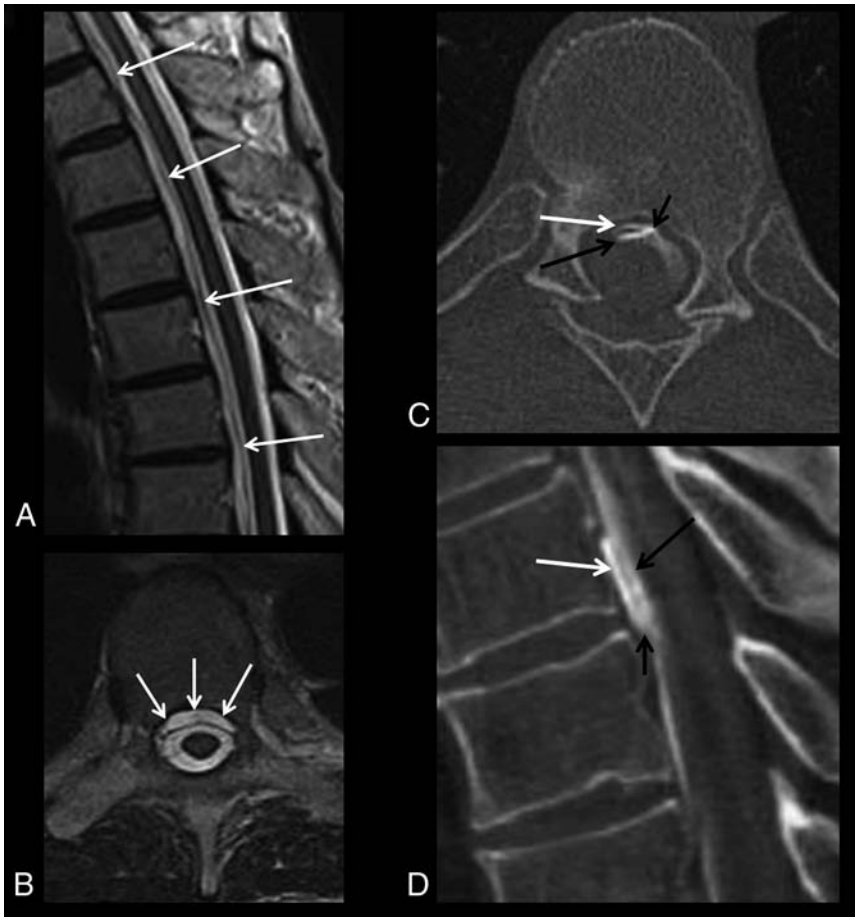

FIG 1. Example of a patient with algorithm compliance and success. Initial spinal MR imaging demonstrates a ventral epidural fluid collection in the midthoracic spine on sagittal (*white arrows*, *A*) and axial (*white arrows*, *B*) T2-weighted images. The patient was appropriately triaged to dynamic CTM, in which a fast CSF leak is identified on initial dynamic axial (*C*) and sagittal reformatted (*D*) CT scans. *C* and *D*, *Short black arrows* indicate the CSF leak site; *white arrows*, ventral epidural contrast; and *long black arrows*, contrast in the ventral thecal sac.

required repeat imaging with a dynamic CTM for localization of a fast leak.

Algorithm Noncompliance, Breach Types, and Clinical Impact

The algorithm was not followed in 27 (21%) of 129 patients. Breaches included no pre-CTM spinal MR imaging in 11 (41%), performing a conventional CTM when extradural fluid was present on spinal MR imaging in 13 (48%), and performing an unnecessary dynamic CTM for a slow or absent CSF leak when extradural fluid was absent on spinal MR imaging in 3 (11%).

Algorithm breaches resulted in 8 (30%) of 27 patients having nonlocalized fast leaks, in 1 (13%) of 8 due to no pre-CTM MR imaging, and in 7 (87%) due to performing a conventional CTM when extradural fluid was present on spinal MR imaging. Repeat imaging with dynamic CTM was performed in 4 (15%) of 27 patients for leak localization.

Overall, algorithm breaches resulted in significantly more repeat imaging with dynamic CTM ($P = .007$, 2-tailed Fisher exact test) and a non-statistically significant trend toward more unnecessary initial dynamic CTMs ($P = .11$, 2-tailed Fisher exact test) than cases in which the algorithm was followed.

Because extradural fluid could have potentially been present in patients with only partial spinal MR imaging performed, statistical analysis was repeated with exclusion of these patients. This analysis demonstrated similar results, with algorithm breaches resulting in significantly more repeat imaging with dynamic CTM ($P = .013$, 2-tailed Fisher exact test) and a non-statistically significant trend toward more unnecessary initial dynamic CTMs ($P = .16$, 2-tailed Fisher exact test) than cases in which the algorithm was followed.

DISCUSSION

While some patients with spontaneous intracranial hypotension have a self-limited course and can be treated with conservative measures, including bedrest, hydration, and caffeine, many do require an invasive therapeutic intervention.[3] In those patients who do not respond to ≥1 nontargeted epidural blood patch, targeted epidural injections or surgical repair may be required. In these patients, localization of the spinal leak becomes necessary to provide targeted therapy. CTM remains the primary technique for localization of spinal CSF leaks.

This study demonstrates that the imaging algorithm we have adopted for the evaluation of patients with suspected spinal CSF leak, when followed at our institution, results in significantly decreased repeat dynamic CTM performed for leak localization as opposed to cases in which the algorithm is not followed. In addition, when the algorithm has been followed, rates of repeat dynamic CTM have decreased to 1% as opposed to an average of 21% during the 8 years before using the algorithm. Additionally, fewer unnecessary dynamic CTMs for slow or absent CSF leaks have been performed when the algorithm has been followed as opposed to when it has been breached.

Important benefits result from reducing repeat dynamic CTMs. One obvious benefit is a decrease in radiation dose to the patient from only having a single CTM performed rather than a conventional CTM followed by a dynamic CTM. This is particularly significant given the increased awareness and public concern about medical radiation in recent years, with focused effort to keep radiation doses as low as reasonably achievable.[4] The estimated effective dose for a conventional CT myelogram at our institution is 21.5 mSv compared with 70.6 mSv (range, 21.5–182.9 mSv) for a dynamic CT myelogram.[2] Three patients in the current study underwent digital subtraction myelography with an average effective dose of 32.2 mSv. Another benefit of reducing repeat dynamic CTM is improved patient care, in that the patient

has to undergo only a single invasive examination rather than 2, which leads to lower risk, less discomfort, and cost savings for the patient. In the patient population with spontaneous intracranial hypotension, the risk of post-lumbar puncture headache should particularly be minimized, including avoiding unnecessary dural puncture. Although this outcome is speculative, referring clinician and patient satisfaction is presumably heightened because the clinical question is more quickly answered, with the opportunity to enact prompt targeted therapy if necessary. Finally, in a time when health care spending is expected to rise at faster rates in the United States compared with previous years,[5] judicious use of our resources and elimination of any potentially superfluous examinations are desirable.

Our study did have limitations. Inherent limitations include the retrospective nature of the study and its performance at a single large referral center. Another limitation is that 20% of patients who underwent pre-CTM spinal MR imaging and whose procedures were considered to have followed the algorithm had only a portion of the spinal canal rather than the entire spinal canal scanned by MR imaging. Extradural fluid could not be entirely excluded in such patients with partial spine MR imaging negative for leak. While it is unclear why these cases occurred, it is postulated that MR imaging examinations were occasionally targeted for clinically suspected symptoms at a specific level. However, the algorithm was successful in all these patients; they either had no extradural fluid detected in the imaged portion of the spine and underwent conventional CTM with slow or no CSF leak identified or had extradural fluid and underwent dynamic CTM with a fast leak identified. In the patients with leaks identified, the spinal segment including the leak level was included on each of the MR imaging examinations. Additionally, repeat statistical analysis with exclusion of patients with only a portion of the spinal canal scanned on MR imaging yielded similar statistically significant results in terms of repeat dynamic CTM and unnecessary initial dynamic CTM between the algorithm-compliant and -noncompliant groups. Ideally, though, each patient would undergo MR imaging of the entire spine to look for extradural fluid before the type of CTM to perform was decided. Timing between MR imaging and CTM was not standardized. An additional limitation of our study is that we could not determine the precise reasons for algorithm breaches, given the retrospective analysis.

Although algorithm success was quite high, several patients had algorithm failure. The reasons for algorithm failure are unclear and may be related to changes in rate/presence of CSF leak between MR imaging and CTM and/or individual patient variability in the ability to absorb CSF from the epidural space. Interventional therapy for the treatment of spontaneous intracranial hypotension, present in 15 patients between spinal MR imaging and CTM, could also potentially have altered the rates of algorithm success and failure. However, most patients who underwent interval treatment had no extradural fluid on MR imaging, were appropriately triaged to conventional CTM, and had no leak identified. Algorithm failure could additionally be secondary to the low sensitivity or specificity of spinal MR imaging for the detection of extradural fluid. No attempt was made to determine the sensitivity, specificity, or interobserver variability of detection of extradural fluid on spinal MR imaging because this study was focused on the effectiveness of the algorithm in routine clinical practice.

Given the high rate of algorithm success, future effort could be dedicated to ensuring compliance with the algorithm. The noncompliance rate of 21% over the study timeframe could have several causes, one of which may be the lack of awareness or education of referring clinicians in regard to the algorithm. The most common causes of algorithm breach were no pre-CTM spinal MR imaging and performing a conventional CTM when extradural fluid was present. It may be instructive to investigate why these algorithm breaches occurred. A possible solution to these most common breaches would be to require entire spine MR imaging before scheduling CTM for suspected spinal CSF leak and to require a dynamic CTM as the initial CTM if extradural fluid is present on the MR imaging, assuming that there are not contraindications to these examinations. Much of the responsibility for ensuring algorithm compliance also falls on the neuroradiologist performing the CTM, who should be aware of the algorithm and follow it unless there is a compelling reason to proceed otherwise.

CONCLUSIONS

If targeted therapy is being considered in a patient with a suspected spinal CSF leak, use of the presence or absence of extradural fluid on spinal MR imaging to determine whether a patient should initially undergo dynamic or conventional CTM to localize the leak has been a useful algorithm at our institution, with a relatively high degree of compliance. The algorithm has resulted in a significant reduction in the necessity for repeat CTM with a dynamic technique to localize fast leaks, with a minimal number of unnecessary initial dynamic CTMs performed.

ACKNOWLEDGMENTS

The authors acknowledge Vicki C. Schmidt and Suson M. Walsh for assistance with the radiology information system data base searches.

REFERENCES

1. Luetmer PH, Schwartz KM, Eckel LJ, et al. **When should I do dynamic CT myelography? Predicting fast spinal CSF leaks in patients with spontaneous intracranial hypotension.** *AJNR Am J Neuroradiol* 2012;33:690–94 CrossRef Medline
2. Thielen KR, Sillery JC, Morris JM, et al. **Ultrafast dynamic computed tomography myelography for the precise identification of high-flow cerebrospinal fluid leaks caused by spiculated spinal osteophytes.** *J Neurosurg Spine* 2015;22:324–31 CrossRef Medline
3. Mokri B. **Spontaneous intracranial hypotension.** *Curr Neurol Neurosci Rep* 2001;1:109–17 CrossRef Medline
4. Huda W. **Radiation risks: what is to be done?** *AJR Am J Roentgenol* 2015;204:124–27 CrossRef Medline
5. Sisko AM, Keehan SP, Cuckler GA, et al. **National health expenditure projections, 2013–23: faster growth expected with expanded coverage and improving economy.** *Health Aff (Millwood)* 2014;33:1841–50 CrossRef

Spine Cryoablation: Pain Palliation and Local Tumor Control for Vertebral Metastases

A. Tomasian, A. Wallace, B. Northrup, T.J. Hillen, and J.W. Jennings

ABSTRACT

BACKGROUND AND PURPOSE: Percutaneous cryoablation has emerged as a minimally invasive technique for the management of osseous metastases. The purpose of this study was to assess the safety and effectiveness of percutaneous imaging-guided spine cryoablation for pain palliation and local tumor control for vertebral metastases.

MATERIALS AND METHODS: Imaging-guided spine cryoablation was performed in 14 patients (31 tumors) with vertebral metastases refractory to conventional chemoradiation therapy or analgesics, to achieve pain palliation and local tumor control in this retrospective study. Spinal nerve and soft-tissue thermal protection techniques were implemented in all ablations. Patient response was evaluated by a pain numeric rating scale administered before the procedure and 1 week, 1 month, and 3 months after the procedure. Pre- and postprocedural analgesic requirements (expressed as morphine-equivalent dosages) were also analyzed at the same time points. Pre- and postprocedural cross-sectional imaging was evaluated in all patients to assess local control (no radiographic evidence of disease at the treated sites). Complications were monitored. Analysis of the primary end points was undertaken via paired-comparison procedures by using the Wilcoxon signed rank test.

RESULTS: Thirty-one tumors were ablated in 14 patients (9 women and 5 men; 20–73 years of age; mean age, 53 years). The most common tumor location was in the lumbar spine ($n = 14$, 45%), followed by the thoracic spine ($n = 8$, 26%), sacrum ($n = 6$, 19%), coccyx ($n = 2$, 6%), and cervical spine ($n = 1$, 3%). There were statistically significant decreases in the median numeric rating scale score and analgesic usage at 1-week, 1-month, and 3-month time points ($P < .001$ for all). Local tumor control was achieved in 96.7% (30/31) of tumors (median follow-up, 10 months). Two patients had transient postprocedural unilateral lower extremity radiculopathy and weakness.

CONCLUSIONS: Percutaneous imaging-guided spine cryoablation is a safe and effective treatment for pain palliation and local tumor control for vertebral metastases.

ABBREVIATIONS: NRS = numeric rating scale; RFA = radiofrequency ablation

The vertebral column is the most common site for bone metastases, with an incidence of 30%–70% in patients with metastatic cancer, and is a major cause of morbidity in these patients.[1-3]

The current standard of care for the management of painful osseous metastases is external beam radiation.[4] Generally, external beam radiation achieves at least partial pain palliation, but often, there is a delay in the relief of symptoms.[5] In addition, painful osseous metastatic disease is often refractory to systemic therapies such as chemotherapy, hormonal therapy, radiopharmaceuticals, and bisphosphonates.[6] Surgical intervention is of limited value in patients with spinal metastases, owing to its morbidity and the often poor functional status and short life span of the patients, and is typically reserved for lesions with consequent neurologic compromise or spinal instability. Pain palliation with systemic analgesics, including nonsteroidal anti-inflammatory drugs and opioids, remains the only alternative option for many patients.[7]

Investigators have explored several alternative strategies for the treatment of painful metastases, including minimally invasive percutaneous imaging-guided tissue ablative methods using ethanol,[8] laser-induced interstitial thermotherapy,[9] radiofrequency ablation (RFA),[10-13] and, most recently, cryoablation.[14-23] Two multicenter clinical trials have demonstrated that percutaneous RFA is effective in reducing pain due to osseous metastatic dis-

Received April 14, 2015; accepted after revision May 26.

From the Mallinckrodt Institute of Radiology, Washington University School of Medicine, St Louis, Missouri.

Please address correspondence to Anderanik Tomasian, MD, Mallinckrodt Institute of Radiology, Washington University School of Medicine, 510 South Kingshighway Blvd, St Louis, MO 63110; e-mail: tomasian.andy@gmail.com

http://dx.doi.org/10.3174/ajnr.A4521

ease.[12,13] Although effective at reducing pain, RFA has important limitations, including nonvisualization of the ablation margin with CT, pain associated with the procedure, and, frequently, increased pain during the immediate posttreatment period.

Similar to RFA, an important limitation of microwave ablation is nonvisualization of the ablation zone with CT. In contrast to RFA or microwave ablation, cryoablation results in formation of a hypoattenuating ice ball, which is readily identified by CT, beyond which tissues are safe from thermal injury.[24] Additional advantages of cryoablation compared with RFA or microwave ablation are decreased intraprocedural and postprocedural pain, the ability to use multiple probes in various orientations to achieve additive overlapping ablation zones,[6,18] and efficiency in the treatment of osteoblastic metastases when high impedance often renders RFA ineffective.

The purpose of this single-center study was to retrospectively evaluate the safety and effectiveness of percutaneous imaging-guided spine cryoablation for pain palliation and local tumor control for patients with painful vertebral metastatic disease.

MATERIALS AND METHODS

This retrospective study was approved by our institutional review board and was Health Insurance Portability and Accountability Act–compliant. Consent was waived for retrospective study participation. Percutaneous imaging-guided cryoablation of 31 vertebral metastases was performed in 14 patients with lesions refractory to conventional chemotherapy, radiation therapy, and analgesics following interdisciplinary consultation in the setting of a committee involving medical oncologists, radiation oncologists, surgical oncologists, and interventional musculoskeletal radiologists. Resistance to radiation therapy and chemotherapy was determined by the radiation oncologists and medical oncologists, respectively. Only patients with substantial pain as indicated by a score of at least 4 on a scale of 0–10 for the question "Please rate your pain by circling the one number that best describes your worst pain over the past 24 hours" were treated.[25] Informed consent for the procedure was obtained from all patients. The study population included 9 women and 5 men with a mean age of 53 years (range, 20–73 years).

The most common primary tumor was lung cancer in 4 patients (28.5%) and colorectal carcinoma in 3 patients (21.5%). Other tumors included breast cancer and follicular thyroid carcinoma in 2 patients each (14%) and head and neck squamous cell carcinoma, pancreatic adenocarcinoma, and epithelioid hemangioendothelioma in 1 patient each (7%). Eighteen of 31 lesions underwent directed optimized radiation therapy before the cryoablation procedure, ranging from 28 months to 1 month before the procedure. Preprocedural imaging studies were reviewed in all patients for ablation planning. Postcryoablation MR imaging and PET/CT imaging were available for all patients (range, 1–24 months following the procedures) and were evaluated to determine the following: 1) the extent of ablation and degree of local tumor control, 2) baseline for subsequent PET/CT or MR imaging and the potential cryoablation retreatment, and 3) possible complications. Postablation imaging was independently reviewed by 2 attending interventional musculoskeletal radiologists (J.W.J. and T.J.H.) for all patients and agreement regarding local tumor control was achieved on consensus. Local tumor control was defined as no radiographic evidence of active tumor based on the following criteria: 1) no new or residual nodular or masslike enhancement in the ablation bed, and 2) lack of hypermetabolism in the ablation bed on PET/CT.

Cryoablation Procedure

The procedures were performed with the patient under conscious sedation in 13 patients (28 lesions) and under general anesthesia in 1 patient (3 lesions) by 2 interventional musculoskeletal radiologists (J.W.J. and T.J.H.) with 10 and 5 years of spine ablation experience, respectively. CT was used for imaging guidance in all patients. Local and periosteal anesthesia was achieved with a combination of 1% lidocaine and 0.25% bupivacaine for all patients.

Cryoablation was performed on each lesion following coaxial (bone component) or single-axial (soft-tissue component or bone–soft tissue interface) placement of Endocare (HealthTronics, Austin, Texas) or Galil (Galil Medical, Yokneam, Israel) cryoprobes. Cryoprobe type, number of probes, duration of the ablation cycle, number of ablations, and the percutaneous approach were preoperatively determined by the operator in each individual case on the basis of tumor size, location, and goal of therapy. The vertebral body lesions were accessed by using a unipedicular or bipedicular approach, depending on the size of the lesion. A bipedicular approach was used if the lesion involved >50% of the vertebral body width. The vertebral posterior element lesions and sacrococcygeal lesions were accessed directly. The Galil cryoprobes used were 13–17 ga with predicted ablation zones ranging from 2 × 1 to 4 × 2 cm in diameter at −40°C. The Endocare Perc-15 and Perc-17 (both 1.7 mm in diameter) were used with predicted ablation zones of 15 × 15 and 15 × 35 mm at −40°C, respectively. At least 1 freeze/active thaw/freeze cycle was performed on each lesion, with duration times of at least 10 minutes, 5 minutes, and 10 minutes, respectively. Intraprocedural ablation imaging was performed at 5- and 10-minute intervals during the freeze cycles. Ice ball size and extent were evaluated on standard body (window of 400 HU and level of 40 HU) settings on unenhanced CT as a hypoattenuating region arising from the probe tips to envelope the neoplastic tissue.

With primarily osteolytic lesions, the hypoattenuating ice ball was clearly visualized and used to determine the adequacy of ablation. With primarily osteoblastic lesions and lack of a large lytic component, the intraosseous ice ball was not well seen. The size of the ablation zone was determined by a combination of the hypoattenuating ice ball extending beyond the cortex and preclinical testing data demonstrating ice ball size with a given cryoprobe. The duration of the freezing portion of the ablation cycle was adjusted on the basis of the adequacy of lesion coverage and the proximity of adjacent critical structures on interval imaging. There were no probe manipulations between cycles.

Thermal Protection Techniques

Neuroforaminal thermal monitoring was performed in all cases, owing to the close proximity of the neural foramen and/or central canal to the margins of the ablation zone. Neural thermal protection techniques involving epidural or neuroforaminal injection of

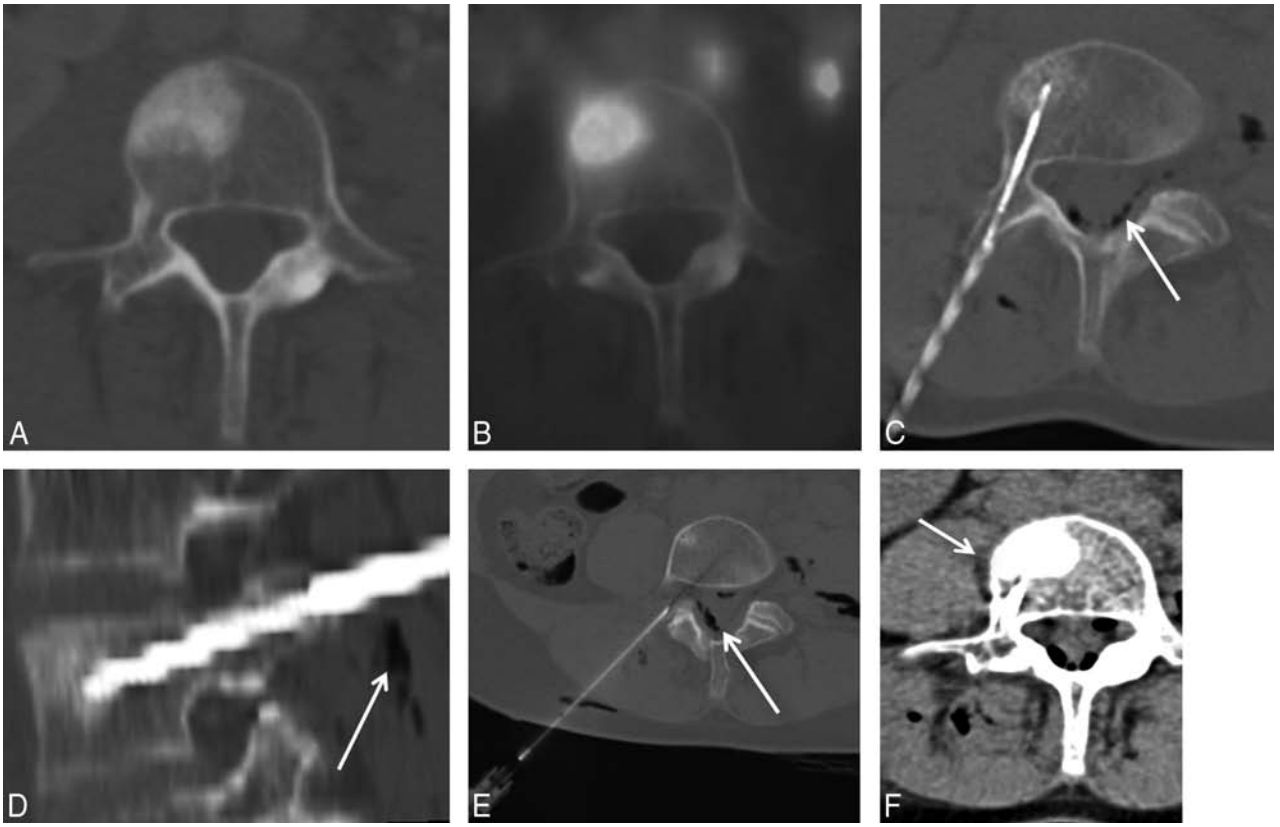

FIG 1. A 59-year-old woman with non-small cell lung cancer and painful osteoblastic L4 vertebral body metastasis. Transaxial CT (*A*) and FDG PET/CT (*B*) images demonstrate a hypermetabolic osteoblastic L4 vertebral body metastasis. Transaxial (*C*) and sagittal (*D*) intraprocedural CT images demonstrate coaxial placement of a single Ice Rod Plus 17-gauge cryoprobe (Galil) within the L4 sclerotic lesion via a right transpedicular approach. To achieve thermal protection, an 18-ga spinal needle is placed at the right L4–L5 neuroforamen (*E*), and carbon dioxide is injected in the neuroforamen and epidural space before cryoablation (*C–E*, *arrows*). Postablation CT demonstrates a thin rim of hypoattenuating ice ball extending beyond intact vertebral body cortex (*F*, *arrow*), marking the margin of the ablation zone.

carbon dioxide or warmed 5% dextrose water were implemented. This was performed by placing an 18-ga spinal needle (Becton, Dickinson and Company, Franklin Lakes, New Jersey) in the region of the neuroforamen, connected to a Passage Hemostasis Valve (Merit Medical, South Jordan, Utah), and coaxial placement of a thermocouple (St. Jude Medical, St. Paul, Minnesota) into the neuroforamen to measure temperatures. If the temperatures began to approach 10°C, the thermoprotective agents were injected into the neuroforamen. Because carbon dioxide is one of the most effective thermoprotecive agents, it is always injected first. In addition, thermal protection of abdominal and pelvic soft tissues, including nerves and bowel, was achieved by injection of carbon dioxide via a 22-gauge spinal needle (Becton, Dickinson and Company) placed adjacent to critical structures in close proximity to the ablation zone, and adequacy of thermal protection was verified with CT before cryoablation.

Intraprocedural motor-evoked potential monitoring was performed during 1 ablation, which was performed with the patient under general anesthesia.[26,27]

The cutaneous thermal protection technique consisted of a surface application of warm saline solution in all cases. After ablation, the patients were transferred to a recovery unit for 1 hour of postprocedural observation before being discharged to the patient care division.

Pre- and Posttreatment Patient Assessment

On the day of the procedure, preprocedural pain was determined by a numeric rating scale (NRS) score (scaled from a minimum of 0 to a maximum of 10),[25] and analgesic requirements were recorded by the musculoskeletal nurse coordinator. The subsequent NRS scores and analgesic requirements were then obtained by telephone 1 week, 1 month, and 3 months after the procedure by the musculoskeletal nurse coordinator. Patients were asked about potential postprocedural complications, including questions about the wound, nerve pain, and muscle weakness. Chart reviews were also undertaken, and evidence of complications was recorded.

Primary End Points and Statistical Analysis

The primary end points analyzed were pain relief, analgesic and/or opioid usage, local tumor control on postprocedural cross-sectional imaging, and complication rates. Preprocedural NRS scores and analgesics usage expressed as morphine equivalent dosages by using established tables,[28] as well as postprocedural NRS scores and analgesics usage at 1 week, 1 month, and 3 month intervals, were analyzed for median differences by using the Wilcoxon signed rank test. Results are reported as median ± absolute deviation, to analyze the nonnormal data distribution appropriately. Postprocedural cross-sectional imaging was evalu-

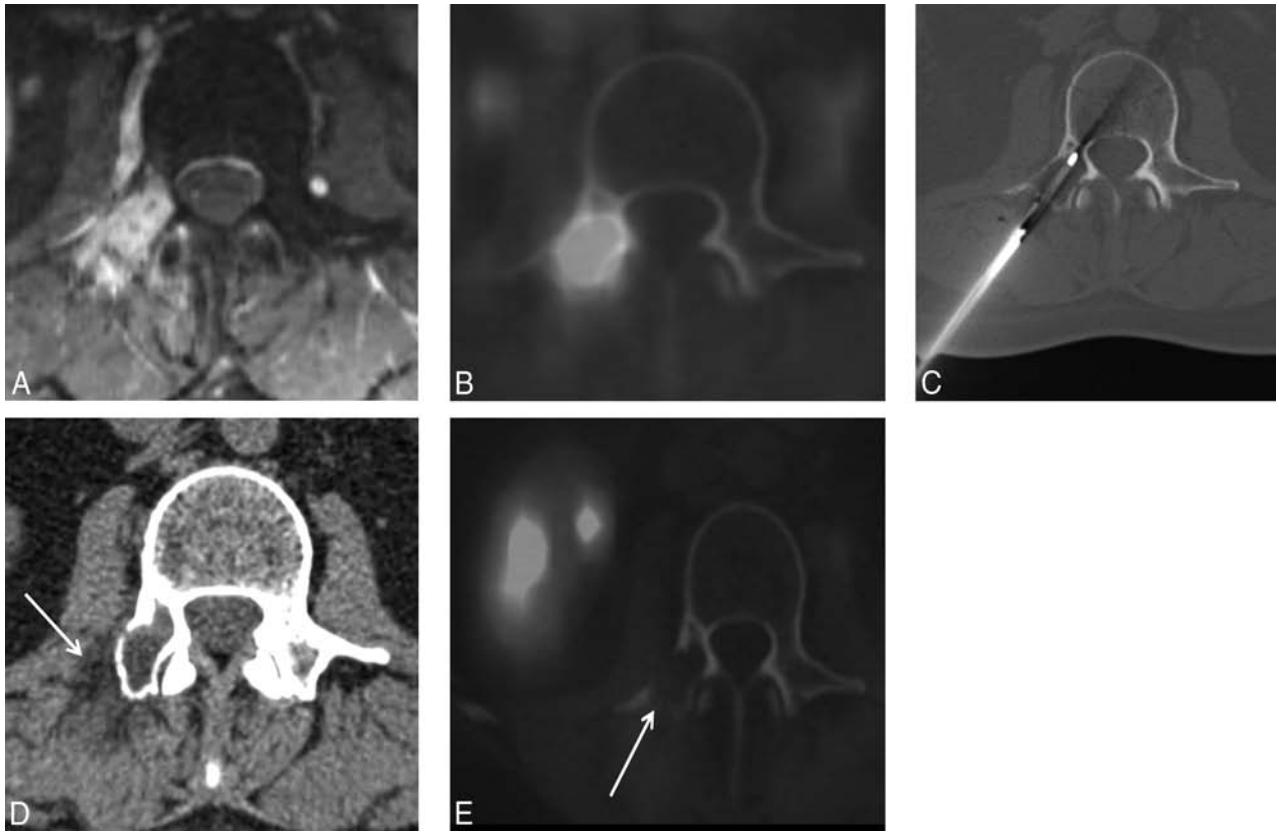

FIG 2. A 54-year-old woman with metastatic breast cancer and painful right L2 pedicle and transverse process osteolytic metastasis. Transaxial T1-weighted fat-saturated postcontrast MR (*A*) and FDG PET/CT (*B*) images demonstrate right L2 pedicle and transverse process metastasis that demonstrates homogeneous contrast enhancement and marked FDG uptake. Transaxial CT image (*C*) demonstrates coaxial placement of the Perc-17 Endocare cryoprobe within the right L2 pedicle and transverse process osteolytic lesion. Postcryoablation transaxial CT image (*D*) demonstrates the hypoattenuating ice ball encompassing the lesion and extending beyond the cortical margin (*arrow*). A 14-month postcryoablation FDG PET/CT demonstrates complete local tumor control with no evidence of metabolically active tumor (*E*, *arrow*).

ated and compared with preprocedural imaging by the authors to determine local tumor control. Complications were identified and classified according to the Society of Interventional Radiology classification system for complications by outcome.[29] All statistical analyses were performed by using SPSS Statistics, Release 22.0 (IBM, Armonk, New York). An α value of .05 was statistically significant.

RESULTS

All cryoablation procedures were performed as preoperatively planned and were technically successful. Thirty-one metachronous tumors (22 osteolytic and 9 osteoblastic lesions) were ablated in 14 patients (Figs 1–3). The most common tumor location was in the lumbar spine ($n = 14$, 45%), followed by thoracic spine ($n = 8$, 26%), sacrum ($n = 6$, 19%), coccyx ($n = 2$, 6%), and cervical spine ($n = 1$, 3%). The anatomic locations of treated lesions were in vertebral body (lumbar spine, $n = 8$, and thoracic spine, $n = 4$), pedicle (lumbar spine, $n = 3$, and thoracic spine, $n = 2$), lamina (lumbar spine, $n = 2$, and thoracic spine, $n = 2$), and spinous process (lumbar spine, $n = 1$). The treated lesion in the cervical spine involved the lamina and spinous process. One lesion underwent cementoplasty (sacrum), and 1 lesion underwent vertebroplasty (lumbar spine) as part of the procedure. According to the Society of Interventional Radiology guidelines,[29] no major complication, such as permanent neural thermal injury, occurred as a result of the cryoablation procedure. Two of the 14 patients had postprocedural radicular lower extremity nerve pain (a minor complication) and received nerve root steroid and/or anesthetic injections. These patients remained asymptomatic following 1 transforaminal nerve root block (follow-up of 10 and 15 months). Local tumor control (no radiographic evidence of active tumor at the treated sites) was achieved in 96.7% (30/31) of tumors (median follow-up, 10 months; range, 1–24 months), as evaluated on postprocedural cross-sectional imaging. One patient with sacral metastases developed progression of disease despite technically adequate cryoablation.

Effect of Cryoablation on Patient Pain and Analgesic Use

There were statistically significant decreases in the median NRS scores at 1 week, 1 month, and 3 months following the procedure ($P < .001$ for all). The preprocedural NRS score was 8 ± 1 (median ± absolute deviation). The postprocedural NRS score at 1-week, 1-month, and 3-month time points was 3 ± 1 (median ± absolute deviation) (Fig 4*A*). Two patients had slightly improved, but persistent, pain at all postprocedural time points, of whom 1 patient died 5 months after the procedure with progression of disease. There were statistically significant decreases in the median morphine-equivalent dosages at 1-week, 1-month, and

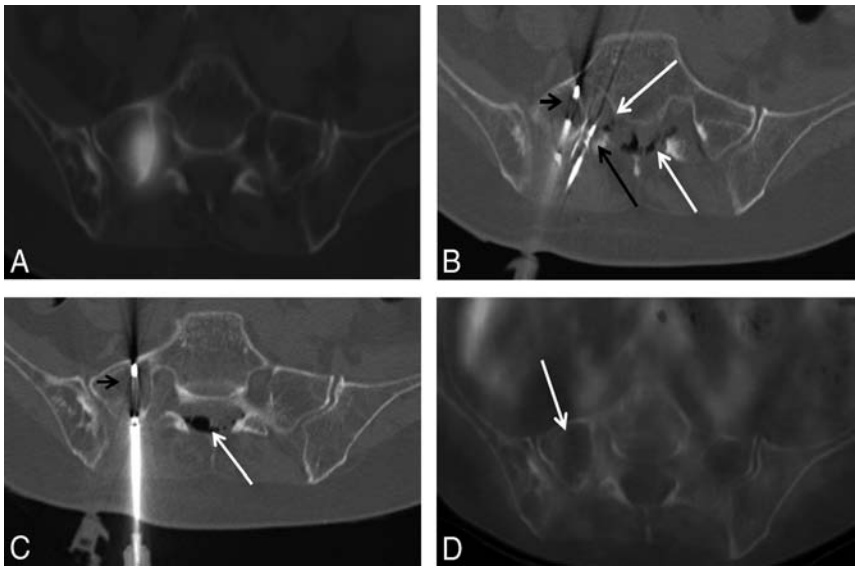

FIG 3. A 69-year-old man with metastatic follicular thyroid carcinoma and painful right S1 metastasis. Transaxial iodine-131 SPECT CT image demonstrates increased radiopharmaceutical uptake in the right S1, compatible with metastasis (*A*). Transaxial intraprocedural CT images demonstrate coaxial placement of 2 Perc-17 Endocare cryoprobes within the right S1 lesion (*B* and *C*, *short arrow*). Thermal protection is performed by placement of a thermocouple and a spinal needle within the right S1 neuroforamen (*B*, *long black arrow*) and injection of carbon dioxide into the right S1 neuroforamen with epidural extension (*B* and *C*, *white arrows*). A 24-month postcryoablation FDG PET/CT demonstrates complete local tumor control with no evidence of metabolically active tumor (*D*, *arrow*).

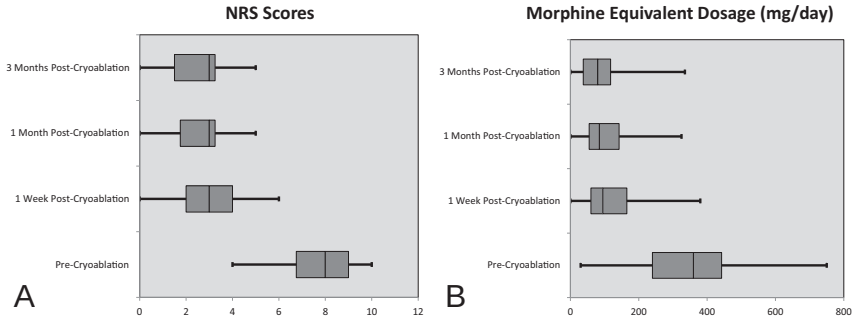

FIG 4. Distribution of NRS scores (*A*) and morphine-equivalent dosages (*B*) at study time points. There was a statistically significant decrease in postcryoablation median NRS scores and morphine-equivalent dosages ($P < .001$ for all).

3-month postprocedural time points ($P < .001$ for all). The preprocedural morphine equivalent dosage was 360 ± 105 mg/day (median ± absolute deviation). The postprocedural morphine equivalent dosages at 1-week, 1-month, and 3-month time points were 95 ± 55 mg/day (median ± absolute deviation), 85 ± 50 mg/day, and 80 ± 45 mg/day, respectively (Fig 4*B*).

DISCUSSION

Painful vertebral column metastatic disease is a substantial cause of morbidity in patients with cancer owing to its high prevalence, the weight-bearing nature of the spine, and close proximity to critical structures, including the nerve roots and spinal cord. Pain from neoplastic bone involvement in the spine is multifactorial and is a consequence of mechanical factors, including direct involvement of spinal nerve roots and mass effect on the nerve roots and spinal cord, biologic factors including osteoclast-mediated proton sensitization of the sensory fibers at the mineralized bone-tumor interface, sensitization or activation of sensory nerve fibers by products directly produced in tumor and tumor stromal cells, and distortion of mechanosensitive fibers following normal mechanical stress due to loss of tensile strength in the bone secondary to cancer.[30-32] Goblirsch et al[32] suggested that reduced tumor burden and reduced osteolysis are important for decreased pain following radiation therapy. As with the creation of pain related to osseous metastatic disease, the mechanism of action and therapeutic effects of cryoablation are likely similar and multifactorial; however, they have not been studied.[18]

While external beam radiation remains the current standard of care for the management of painful osseous metastases,[4] percutaneous cryoablation has emerged as a safe and effective treatment option for patients with musculoskeletal tumors, refractory to radiation therapy and systemic palliative therapies including chemotherapy, hormonal therapy, bisphosphonates, and analgesics.[14-23,30]

The cytotoxic effects of cryoablation are mediated through the formation of intracellular ice crystals during probe-mediated temperature manipulation. The crystals cause denaturation of proteins and shearing of intracellular structures, including cell membrane rupture. A liquid gas, commonly argon, is used to rapidly cool the tip of the cryoprobe, forming an enlarging ice-ball with time followed by a "thawing" phase, commonly achieved with helium gas, resulting in an osmotic gradient.[33] The osmotic gradient causes water to rush into, swell, and then burst the tumor cell, eventually leading to cell hypoxia via indirect ischemic injury.[34]

Investigators have reported scattered cases of spinal metastases treated with percutaneous cryoablation as part of larger series of patients ablated for extraspinal musculoskeletal metastatic disease or as case series.[14,18,20,23,26] In 2006, Callstrom et al[14] reported 3 spinal tumors (2 in the sacrum and 1 in the lamina) as part of a 14-patient study managed effectively by cryoablation. As part of a multicenter prospective single-arm clinical trial of 61 patients who underwent image-guided cryoablation for the palliation of painful osseous metastases, Callstrom et al[18] reported 6 spinal tumors (5 in the sacrum and 1 in the vertebral body), which were effectively palliated with significant decreases in pain and subjective improvement in the quality of life at 1, 4, 8, and 24 weeks following the procedure.

Kurup et al[20] reported a case series of 6 patients with sacrococ-

cygeal metastases who underwent imaging-guided cryoablation and suggested that cryoablation may be a safe and relatively effective technique for the management of recurrent sacrococcygeal neoplasms for local control or palliation of pain with short-term follow-up. In 2014, Prologo el al[23] reported 2 patients with pedicle lesions as part of larger series of 50 patients with musculoskeletal metastases managed by cryoablation for pain palliation. Subsequently, in 2014, Kurup et al[26] reported the utility of motor-evoked potential monitoring during cryoablation of musculoskeletal tumors in 52 patients. The authors reported cryoablation in 27 spine and 3 sacral tumors, which were monitored by motor-evoked potentials. However, the effectiveness of cryoablation for pain palliation and local tumor control was not discussed.[26]

In a retrospective analysis of data from patients with single vertebral metastasis, Masala et al[19] described the safety and efficacy—through reduced pain (Visual Analog Scale scores) and disability (Oswestry Disability Index)—of cryoablation combined with vertebroplasty for the palliation of painful vertebral metastases, which was at least equivalent to vertebroplasty alone. However, the safety and efficacy of cryoablation as an exclusive treatment approach could not be evaluated because vertebroplasty was performed in all cases.

To our knowledge, this is the first single-center review describing the safety and effectiveness of cryoablation as the exclusive thermal ablation technique for local tumor control and palliation of painful spinal osteoblastic and osteolytic metastatic disease. The present study data suggest that percutaneous cryoablation is safe and effective for vertebral local tumor control and palliation of painful spine metastases. There was statistically significant pain palliation reflected by a substantial decrease in postprocedural NRS scores and analgesic use. Two patients (2 lesions) had persistent but improved pain following cryoablation. Local tumor control, evidenced by no radiographic evidence of active tumor at treated sites, was achieved in 96.7% (30/31 lesions) of lesions on the basis of postprocedural cross-sectional imaging. One patient with sacral metastases did not benefit from the procedure and developed progression of disease despite technically adequate cryoablation.

The safety of the procedure was supported by a lack of major complications and only 2 minor transient complications based on the Society of Interventional Radiology guidelines.[29] Thermal protection measures should be implemented in all spine cryoablations to ascertain safety before the procedure. In the current study, these techniques included neuroforaminal thermal monitoring with epidural or neuroforaminal injection of carbon dioxide or warmed 5% dextrose water; thermal isolation of critical abdominal and pelvic soft tissues, including by intraprocedural injection of carbon dioxide; and cutaneous thermal protection by surface application of warm saline during freezing cycles. In addition, intraprocedural motor-evoked potential monitoring was performed during a single ablation performed with the patient under general anesthesia.[26,27]

The efficiency of cryoablation for the treatment of osteoblastic spine metastases has not been studied previously. Radiofrequency ablation is rendered ineffective for the treatment of sclerotic metastases due to high impedance levels in attenuated bone. Cryoablation is emerging as an attractive alternative to RFA for palliation of sclerotic metastases. In 2011, de Freitas et al[30] reported the effectiveness of cryoablation in a single patient with T9 and sacral osteoblastic metastatic disease. In the current study, 9 osteoblastic vertebral metastases were effectively palliated.

Nerve roots are more vulnerable to potential thermal injury with cryoablation compared with RFA, due to less tissue sensitivity to cold versus heat. This limitation is mitigated by implementation of thermoprotection techniques with the patient under conscious sedation and the use of sensory and motor-evoked potential monitoring with general anesthesia. In addition, posterior central vertebral body lesions are more challenging to access via a transpedicular approach by using straight cryoprobes.

The major limitation of the present study is the single-arm nature of the analysis with no control group and the lack of comparison to other treatment modalities, specifically radiation therapy. Additional limitations of the present study include its retrospective methodology, use of NRS scores for pre- and postprocedural pain assessment versus the more inclusive Brief Pain Inventory, and the relatively small number of palliated tumors.

CONCLUSIONS

Our safety and efficacy spine cryoablation results are commensurate with published studies of image-guided cryoablation in the setting of painful extraspinal musculoskeletal metastatic disease and may have contributory value in establishing the reproducibility of these procedures for pain palliation and local tumor control of vertebral metastatic disease. Additional work including prospective randomized studies of this therapy versus the historic standard of care, radiation therapy, will be valuable to further establish the efficacy of spine cryoablation for management of spine metastatic disease.

Disclosures: Adam Wallace—*UNRELATED*: *Grants/Grants Pending*: McDonnell Center for Systems Neuroscience,* *Comments*: pending $40,000 grant to study normal cerebral vasculature and blood flow across the lifespan; pending grants to be supplied with radiofrequency ablation probes (Dfine, San Jose, California), cryoablation probes (Galil Medical, St. Paul, Minnesota), and microwave ablation probes (Covidien, Irvine, California) for an animal study. Travis J. Hillen—*UNRELATED*: *Payment for Lectures (including service on Speakers Bureaus)*: Dfine, *Comments*: lectures at cadaver labs; *Other*: Dfine, *Comments*: paid for proctoring cadaver labs. Jack W. Jennings—*UNRELATED*: *Consultancy*: Dfine; *Payment for Lectures (including service on Speakers Bureaus)*: Dfine. *Money paid to the institution.

REFERENCES

1. Boland PJ, Lane JM, Sundaresan N. **Metastatic disease of the spine.** *Clin Orthop Relat Res* 1982;169:95–102 Medline
2. Harrington KD. **Metastatic disease of the spine.** *J Bone Joint Surg Am* 1986;68:1110–15 Medline
3. Wong DA, Fornasier VL, MacNab I. **Spinal metastases: the obvious, the occult, and the impostors.** *Spine (Phila Pa 1976)* 1990;15:1–4 CrossRef Medline
4. Lutz S, Berk L, Chang E, et al. **Palliative radiotherapy for bone metastases: an ASTRO evidence-based guideline.** *Int J Radiat Oncol Biol Phys* 2011;79:965–76 CrossRef Medline
5. Tong D, Gillick L, Hendrickson FR. **The palliation of symptomatic osseous metastases: final results of the study by the Radiation Therapy Oncology Group.** *Cancer* 1982;50:893–99 CrossRef Medline
6. Rosenthal D, Callstrom MR. **Critical review and state of the art in interventional oncology: benign and metastatic disease involving bone.** *Radiology* 2012;262:765–80 CrossRef Medline
7. Hara S. **Opioids for metastatic bone pain.** *Oncology* 2008;74(suppl 1):52–54 CrossRef Medline

8. Gangi A, Kastler B, Klinkert A, et al. **Injection of alcohol into bone metastases under CT guidance.** *J Comput Assist Tomogr* 1994;18: 932–35 CrossRef Medline
9. Groenemeyer DH, Schirp S, Gevargez A. **Image-guided percutaneous thermal ablation of bone tumors.** *Acad Radiol* 2002;9:467–77 CrossRef Medline
10. Callstrom MR, Charboneau JW, Goetz MP, et al. **Painful metastases involving bone: feasibility of percutaneous CT- and US-guided radio-frequency ablation.** *Radiology* 2002;224:87–97 CrossRef Medline
11. Hillen TJ, Anchala P, Friedman MV, et al. **Treatment of metastatic posterior vertebral body osseous tumors by using a targeted bipolar radiofrequency ablation device: technical note.** *Radiology* 2014;273: 261–67 CrossRef Medline
12. Goetz MP, Callstrom MR, Charboneau JW, et al. **Percutaneous image-guided radiofrequency ablation of painful metastases involving bone: a multicenter study.** *J Clin Oncol* 2004;22:300–06 CrossRef Medline
13. Dupuy DE, Liu D, Hartfeil D, et al. **Percutaneous radiofrequency ablation of painful osseous metastases: a multicenter American College of Radiology Imaging Network trial.** *Cancer* 2010;116: 989–97 CrossRef Medline
14. Callstrom MR, Atwell TD, Charboneau JW, et al. **Painful metastases involving bone: percutaneous image-guided cryoablation–prospective trial interim analysis.** *Radiology* 2006;241:572–80 CrossRef Medline
15. Gangi A, Buy X. **Percutaneous bone tumor management.** *Semin Intervent Radiol* 2010;27:124–36 CrossRef Medline
16. Thacker PG, Callstrom MR, Curry TB, et al. **Palliation of painful metastatic disease involving bone with imaging-guided treatment: comparison of patients' immediate response to radiofrequency ablation and cryoablation.** *AJR Am J Roentgenol* 2011;197:510–15 CrossRef Medline
17. Castañeda Rodriguez WR, Callstrom MR. **Effective pain palliation and prevention of fracture for axial-loading skeletal metastases using combined cryoablation and cementoplasty.** *Tech Vasc Interv Radiol* 2011;14:160–69 CrossRef Medline
18. Callstrom MR, Dupuy DE, Solomon SB, et al. **Percutaneous image-guided cryoablation of painful metastases involving bone: multicenter trial.** *Cancer* 2013;119:1033–41 CrossRef Medline
19. Masala S, Chiocchi M, Taglieri A, et al. **Combined use of percutaneous cryoablation and vertebroplasty with 3D rotational angiograph in treatment of single vertebral metastasis: comparison with vertebroplasty.** *Neuroradiology* 2013;55:193–200 CrossRef Medline
20. Kurup AN, Woodrum DA, Morris JM, et al. **Cryoablation of recurrent sacrococcygeal tumors.** *J Vasc Interv Radiol* 2012;23:1070–75 CrossRef Medline
21. McMenomy BP, Kurup AN, Johnson GB, et al. **Percutaneous cryoablation of musculoskeletal oligometastatic disease for complete remission.** *J Vasc Interv Radiol* 2013;24:207–13 CrossRef Medline
22. Masala S, Schillaci O, Bartolucci AD, et al. **Metabolic and clinical assessment of efficacy of cryoablation therapy on skeletal masses by 18F-FDG positron emission tomography/computed tomography (PET/CT) and visual analogue scale (VAS): initial experience.** *Skeletal Radiol* 2011;40:159–65 CrossRef Medline
23. Prologo JD, Passalacqua M, Patel I, et al. **Image-guided cryoablation for the treatment of painful musculoskeletal metastatic disease: a single-center experience.** *Skeletal Radiol* 2014;43:1551–59 CrossRef Medline
24. Saliken JC, McKinnon JG, Gray R. **CT for monitoring cryotherapy.** *AJR Am J Roentgenol* 1996;166:853–55 CrossRef Medline
25. Daut RL, Cleeland CS, Flanery RC. **Development of the Wisconsin Brief Pain Questionnaire to assess pain in cancer and other diseases.** *Pain* 1983;17:197–210 CrossRef Medline
26. Kurup AN, Morris JM, Boon AJ, et al. **Motor evoked potential monitoring during cryoablation of musculoskeletal tumors.** *J Vasc Interv Radiol* 2014;25:1657–64 CrossRef Medline
27. Tsoumakidou G, Garnon J, Ramamurthy N, et al. **Interest of electrostimulation of peripheral motor nerves during percutaneous thermal ablation.** *Cardiovasc Intervent Radiol* 2013;36:1624–28 CrossRef Medline
28. Gordon DB, Stevenson KK, Griffie J, et al. **Opioid equianalgesic calculations.** *J Palliat Med* 1999;2:209–18 CrossRef Medline
29. Goldberg SN, Charboneau JW, Dodd GD 3rd, et al; International Working Group on Image-Guided Tumor Ablation. **Image-guided tumor ablation: proposal for standardization of terms and reporting criteria.** *Radiology* 2003;228:335–45 CrossRef Medline
30. de Freitas RM, de Menezes MR, Cerri GG, et al. **Sclerotic vertebral metastases: pain palliation using percutaneous image-guided cryoablation.** *Cardiovasc Intervent Radiol* 2011;34(suppl 2):S294–99 CrossRef Medline
31. Mercadante S, Fulfaro F. **Management of painful bone metastases.** *Curr Opin Oncol* 2007;19:308–14 CrossRef Medline
32. Goblirsch MJ, Zwolak PP, Clohisy DR. **Biology of bone cancer pain.** *Clin Cancer Res* 2006;12(20 pt 2):6231s–35s CrossRef Medline
33. Gage AA, Baust JG. **Cryosurgery for tumors.** *J Am Coll Surg* 2007; 205:342–56 CrossRef Medline
34. Theodorescu D. **Cancer cryotherapy: evolution and biology.** *Rev Urol* 2004;6(suppl 4):S9–S19 Medline

Georges Salamon

Georges Salamon, one of neuroradiology's pioneers, early thought leaders, and international spokesmen, died on October 10, 2015, at 84 years of age. Born in Montpellier, France, to a Russian father and a Polish mother of Jewish descent, he acutely experienced the traumas of World War II but kept, throughout his life, a unique, optimistic spirit of adventure. Knowing the costs and benefits of the vicissitudes of life, Georges maintained an exceptional open-mindedness and a zest for change and new opportunities.

Receiving his Doctor of Medicine from the Faculty of Aix-Marseille in 1958, he was spurred into specialty training by his teachers, Herman Fischgold, Henri Gastaut, and Robert Naquet, graduating in radiology in 1962 and neurology in 1965. This dual experience in imaging and neuroscience provided the stimulus for Georges to enter the nascent field of neuroradiology and the basis of a prestigious career bridging these disciplines. Posttraining, Georges quickly joined the Hôpital de la Timone in that "considerable town," Marseille, first as assistant professor in 1964 and then as head of the Department of Neuroradiology from 1972 to 1996.

Although broadly curious and an eclectic thinker, Georges' first scientific love was neuroanatomy. Between 1965 and 1970, his students' numerous theses on cerebral vasculature formed the basis of and culminated in the publication of the *Atlas of Arteries of the Human Brain* in 1971 (Sandoz), of *Radiologic Anatomy of the Brain* in collaboration with Y.P. Huang in 1976 (Springer Verlag Berlin), and *Vascularisation et Circulation de L'Enceìphale* with G. Lazorthes and A. Gill (Masson) that same year. This work became the anatomic bible for a whole generation of neuroradiologists and neurosurgeons. It also served as a basis for the subsequent development of therapeutic angiography and the emergence in France of a new generation of vascular neuroradiologists under the joint stimulus of Georges Salamon and René Djindjian.

The cross-sectional microradiographs of injected brains emanating from the Institut National de la Santé et de la Recherche Médicale U6 laboratory that Georges founded in 1972 fascinated young neuroscientists everywhere. Thus, in the 1970s and 1980s, close collaborations were established between Marseille and the United States, Sweden, and Japan. Stimulated by this research and its early clinical applications, residents, fellows, and full professors traveled to and from Marseille to participate in research projects, perfect their training, and share their angiographic know-how. Such ventures with Georges often held surprises, such as one American visitor who found himself unexpectedly responsible for fresh cadaveric material. Georges' American colleagues listed in the 2006 American Society of Neuroradiology (ASNR) Honorary Member summary reads like a *Who's Who* of the ASNR, including Juan Taveras, Ernest Wood, Sadek Hilal, Gordon Potts, Norm Chase, Irv Kricheff, Norman Leeds, Paul New, Giovanni DiChiro, Hans Newton, Bill Hanafee, and Gabriel Wilson.

Neuroanatomy also underpinned the clinical applications of cross-sectional imaging, x-ray CT, and MR imaging as well as functional PET and MR imaging. In the mid-1990s, Georges brought together neuroimagers and his old Parisian friend and neurosurgical colleague, Jean Talairach, fostering the subsequent conversion of 1940s analog paper images into the now pervasive digital atlases with Talairach coordinates. The Marseille school remained in the foreground, with his pupil, Charles Raybaud, one of the pioneers of pediatric neuroradiology, succeeding him as head of the Neuroradiology Department at la Timone. Charles Raybaud is now the Chief of Pediatric Neuroradiology at the Hospital for Sick Children in Toronto.

Beginning in the 1970s, Georges Salamon encouraged formal national and international professional organizations: He was a founding member and president of the Societe Francaise de Neuroradiologie in 1970 and the European Society of Neuroradiology (ESNR) in 1972. International recognition was the fair return: In 1984, he was appointed Honorary Member of the American College of Radiology; in 1994, the Radiological Society of North America; in 1995, the ESNR; in 2000, the Japanese Society of Radiology; and in 2006, the ASNR.

Although a tireless worker, Georges could have retired to satisfy other passions such as sailing on *Chipie*, his boat on which he invited his many friends, or contemporary art and painting. He was, from 1989 to 1995, President of the Association of the Museums of Marseille. A visit with Georges to La Vieille Charite in Marseille or the Getty Foundation in Los Angeles was a delight.

Instead, in character, at 62 years of age, Georges became engaged in a wonderful new life through a "chance encounter" with Noriko Murayama, then a visiting fellow from Japan. Noriko

Salamon-Murayama has since been his most charming and deeply caring wife for the past 22 years and is now Professor of Neuroradiology at the University of California, Los Angeles (UCLA). Although always a Frenchman, Georges had long expressed a special fondness for the United States, and this unexpected winter/spring relationship sealed his cross-Atlantic destiny. Together Georges and Noriko settled in the United States. Her interests in academic neuroradiology and his reasoned enthusiasm for the new imaging techniques and expertise in neuroscience led them first to Chicago, where he was Research Professor at Northwestern University with Eric Russell from 1996 to 2002, and then to Los Angeles, where he was a Researcher at UCLA with Dieter Enzmann.

It was Georges' pleasure to return regularly to France to see his family and to participate again in the stimulating, lively annual Val d 'Isère Course on "CT, MRI, and Ultrasound," which he had created in the 1970s and of which he was particularly proud. One American speaker vividly remembers being handed a carousel of slides on the sella turcica 30 minutes before the session and being instructed by Georges to present his talk, in French, so he, Georges, could show the speaker's teenaged daughter the slopes of Val d'Isère. The young lady was, of course, enchanted by Georges and remains so to this day. Such was life around Georges, often unpredictable, but always invigorating.

A marvelous career—passionate researcher, intuitive investigator, galvanizing lecturer, with unbounded joie de vivre—that was Georges Salamon. He is survived by his wife Noriko, sisters Marguerite and Yvonne, his brother Roger, his children Christopher, Marie Hélène, and Ivan, and his 8 grandchildren. The ASNR and our sister neuroradiology societies around the world offer our most sincere condolences to his family and friends. Georges, tu vas nous manquer, mais nous ne t'oublierons pas: We will miss you, but we will not forget you.

C. Manelfe
University Paul Sabatier
Toulouse, France
R.N. Bryan
University of Pennsylvania
Philadelphia, Pennsylvania
C. Strother
University of Wisconsin
Madison, Wisconsin

http://dx.doi.org/10.3174/ajnr.A4621

Celebrating 35 Years of the AJNR

January 1981 edition

CT of Subarachnoid Hemorrhage due to Ruptured Aneurysm

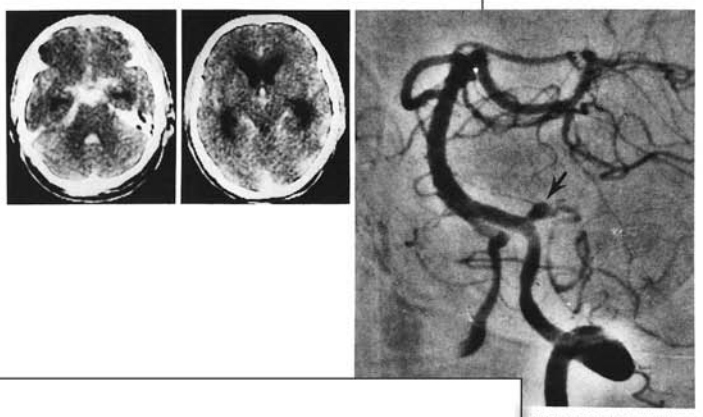

Computed tomographic scans in 81 consecutive patients with subarachnoid hemorrhage due to ruptured aneurysm were analyzed for patterns of hemorrhage and lucency and correlated with the development of spasm and hydrocephalus. The circulation time was measured angiographically in representative cases of spasm. Hemorrhage corresponded in a general way to the fossa of aneurysm origin and, when there was parenchymal or ventricular hemorrhage, in more specific ways to anterior communicating, middle cerebral, and posterior inferior cerebellar artery aneurysms. Basal ganglionic hemorrhages due to aneurysm ruptures occurred in two cases and could not be distinguished by appearance from hypertensive hemorrhage. Regions of low attenuation (lucencies) were often persistent and had lateralizing value; they showed a high correlation with arterial spasm. Conversely, spasm, particularly of a distal type, showed a significant correlation with increased circulation time and the occurrence of brain lucency. In cases of multiple aneurysms arising from different vessels in which there was hemorrhage or lucency, CT scans correctly predicted the site of aneurysm in 77% of cases. Periventricular lucency was a weak predictor of progressive hydrocephalus, while an intraventricular hemorrhage was a strong predictor of moderate to severe hydrocephalus.

To determine the localizing features of hemorrhage due to ruptured aneurysms and to evaluate the significance of associated ischemic changes and hydrocephalus, CT scans and angiograms were reviewed in 81 consecutive patients with subarachnoid hemorrhage due to aneurysm.

Materials and Methods

Subarachnoid hemorrhage was established by lumbar puncture; the presence of aneurysms was demonstrated by angiography and confirmed either by surgery or autopsy. Most CT scans were performed on a first generation head scanner with water bag; some recent scans were done on a high resolution scanner. All patients were scanned in the first 5 weeks after subarachnoid hemorrhage. The circulation time was measured in those cases of spasm in which complete serial angiography was available.

For purposes of this study, the aneurysms were divided into seven groups by location (table 1). These groups were further subdivided according to whether the aneurysms were single or multiple and whether hemorrhage was present on the CT scan (table 2). Determination of which of multiple aneurysms had bled was made by a combination of radiologic and clinical means, including surgery.

Results

Hemorrhage

The earliest scan after subarachnoid hemorrhage in each case was analyzed for intracerebral, intraventricular, and subarachnoid hemorrhage, as well as for subdural hematoma. Fifty cases showed hemorrhage on the initial scan; the median time of scan was 6 days. The hemorrhages were tabulated according to

ute of New York, Columbia-Presbyterian Medical Center, 710 W. 168th St., New York, NY 10032. Address reprint requests to A. J. Silver.

[1] Department of Neurosurgery, Neurological Institute of New York, Columbia-Presbyterian Medical Center, New York, NY 10032.

AJNR 2:13–22, January/February 1981
0195–6108/81/0021–0013 $00.00

Complete Myelography with Metrizamide

Allan J. Fox[1]
Fernando Vinuela
Gerard Debrun

Thorough myelography of the entire spinal cord including the foramen magnum region can be accomplished consistently and promptly after metrizamide injection via lumbar or lateral cervical puncture. When lumbar puncture is used the patient's torso is oblique, but the neck is prone and straight and the table is tilted 20° head-down to allow direct cervical filling with contrast material. Each region is filmed in several projections, the patient being turned gently from the prone cervical to the supine thoracic position. Of 100 cases without block studied in this way, all had adequate cervical and foramen magnum films. In only five was the contrast material too dilute to show the edges of the spinal cord well and the subarachnoid sac adequately in the thoracic region. In 29 patients, there were mild side effects not requiring medication, while 20 had side effects of a more moderate to severe nature. No seizures were encountered. Metrizamide proved a convenient, efficient, and acceptable contrast medium for myelography when a study of the entire spinal cord is indicated.

Since the introduction of metrizamide in the last decade [1–4], there have been numerous clinical reports of its use for myelography of cervical and thoracic regions [1–17]. Depending on the approach of specific authors, metrizamide has been injected in varying amounts and concentrations via lumbar puncture, lateral C1–C2 puncture, or suboccipital puncture. Films have been obtained as spot films, overhead films, or tomograms, depending both on the technique and on the equipment available in the respective radiology departments. While generally the myelographic quality in the area of interest has been good, examining more than one region of the spine as part of the same procedure has decreased the chance for success [6, 18, 19] due to the limitations of metrizamide dose and dilution produced by excessive movement [2]. We describe the use of metrizamide as the primary myelographic contrast medium for "complete myelography" in patients being studied for myelopathy or radicular symptoms referable to the cervical region.

Materials and Methods

In the first 12 months after its introduction in our area, 228 myelographic studies were performed with metrizamide in our radiology department. There were 109 myelograms for lumbar radicular or cauda equina problems and 119 for cervical radicular or myelopathy problems.

The 100 (of 119) metrizamide myelograms that showed no block and were performed for radicular cervical or spinal cord problems formed the basis of this study. We had some previous experience with metrizamide when its availability was limited. Although the technique we used was reasonably standardized, the study participants included five radiology house staff members who were introduced to metrizamide myelography for the first time. Thus, the prime operator in each case had a variable background. Myelograms that showed a complete or almost complete block were excluded because the best metrizamide films are easily obtained at an intraspinal block, making these myelograms technically different from cases without block.

Received June 2, 1980; accepted after revision August 26, 1980.

Presented at the annual meeting of the American Society of Neuroradiology, Los Angeles, CA, March 1980.

[1] All authors: Departments of Diagnostic Radiology and Clinical Neurosciences, University Hospital, University of Western Ontario, London, Ontario, Canada N6A 5A5. Address reprint requests to A. J. Fox.

AJNR 2:79–84, January/February 1981
0195–6108/81/0021–0079 $00.00

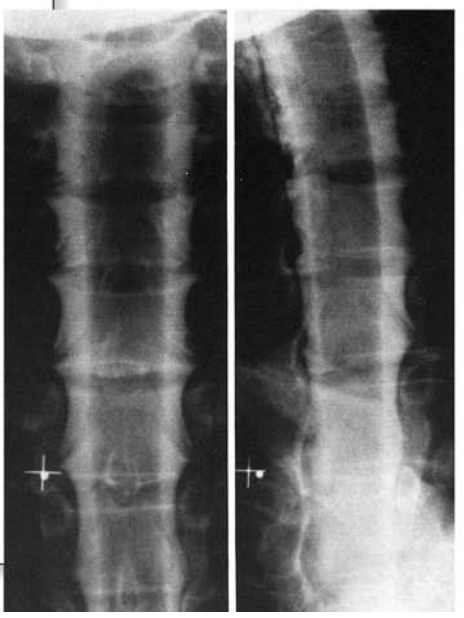

Recent Advances in Understanding Gadolinium Retention in the Brain

We wish to comment on the August 2015 article of Adin et al[1] in the *American Journal of Neuroradiology* (*AJNR*) entitled "Hyperintense Dentate Nuclei on T1-Weighted MRI: Relation to Repeat Gadolinium Administration." The authors reported the relationship between the hyperintense dentate nucleus on unenhanced T1WI and past gadolinium based–contrast agent (GBCA) administration. This relationship was first reported by our group on December 7, 2013.[2] Since then, several important reports have been published, and knowledge regarding gadolinium deposition has increased remarkably.

Our group[3] and Radbruch et al[4] evaluated the difference in the signal change between patients repeatedly administered linear GBCA and macrocyclic GBCA. A change in the signal intensity of the dentate nucleus was observed in the former, but not in the latter. McDonald et al[5] and our group[6] evaluated the brain tissue from postmortem specimens, and gadolinium deposition was verified from the brain tissue.[7] Robert et al[8] injected GBCA 20 times into rats and evaluated the signal-intensity change of the dentate nucleus on T1WI and gadolinium concentration in the brain. A hyperintense dentate nucleus was observed in rats with repeat linear GBCA administration, but not with repeat macrocyclic GBCA administration. The gadolinium concentration of the brain with repeat linear GBCA administration was 14 times greater than that with repeat macrocyclic GBCA administration.[8] The work of Adin et al[1] was confirmed in our first study. It was accepted by *AJNR* on February 19, 2015, and was published on-line on August 20, 2015. In this short period, studies on gadolinium deposition advance so rapidly, a more prompt publication schedule from *AJNR* would be desirable.

In previous studies (our study), a hyperintense dentate nucleus on T1WI was detected in subjects with >5 previous administrations of gadodiamide or gadopentetate dimeglumine. In contrast, in this study, some of the subjects with >12 previous administrations of GBCA did not show hyperintensity in the dentate nucleus. One reason may be the use of macrocyclic GBCAs in these subjects. In addition, the detectability of the hyperintense dentate nucleus on various sequences of T1WI may have influenced their results. According to our experience with several cases, the detectability of high signal intensity in the dentate nucleus differs between spin-echo T1WI and T1 FLAIR (Fig 1). Adin et al[1] evaluated the hyperintense dentate nucleus with various T1WI sequences, such as MPRAGE, spin-echo, and T1 FLAIR. The different detectabilities of hyperintense dentate nuclei on these sequences may have influenced their results.

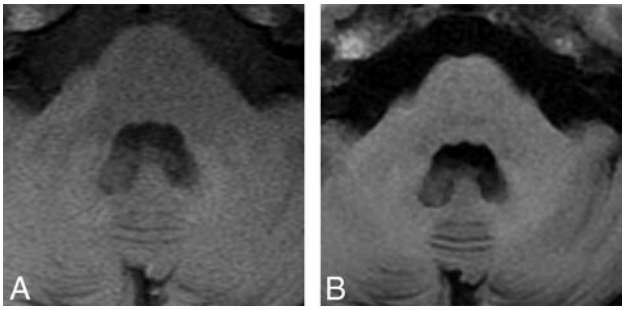

FIG 1. Images in a 41-year-old woman with a history of malignant lymphoma and 7 administrations of gadopentetate dimeglumine. The dentate nucleus is hyperintense on spin-echo T1WI (*A*), but not on T1 FLAIR (*B*).

REFERENCES

1. Adin ME, Kleinberg L, Vaidya D, et al. **Hyperintense dentate nuclei on T1-weighted MRI: relation to repeat gadolinium administration.** *AJNR Am J Neuroradiol* 2015 Aug 20. [Epub ahead of print] CrossRef Medline
2. Kanda T, Ishii K, Kawaguchi H, et al. **High signal intensity in the dentate nucleus and globus pallidus on unenhanced T1-weighted MR images: relationship with increasing cumulative dose of a gadolinium-based contrast material.** *Radiology* 2014;270:834–41 CrossRef Medline
3. Kanda T, Osawa M, Oba H, et al. **High signal intensity in dentate nucleus on unenhanced T1-weighted MR images: association with linear versus macrocyclic gadolinium chelate administration.** *Radiology* 2015;275:803–09 CrossRef Medline
4. Radbruch A, Weberling LD, Kieslich PJ, et al. **Gadolinium retention in the dentate nucleus and globus pallidus is dependent on the class of contrast agent.** *Radiology* 2015;275:783–91 CrossRef Medline
5. McDonald RJ, McDonald JS, Kallmes DF, et al. **Intracranial gadolinium deposition after contrast-enhanced MR imaging.** *Radiology* 2015;275:772–82 CrossRef Medline

Indicates open access to non-subscribers at www.ajnr.org

http://dx.doi.org/10.3174/ajnr.A4586

6. Kanda T, Fukusato T, Matsuda M, et al. **Gadolinium-based contrast agent accumulates in the brain even in subjects without severe renal dysfunction: evaluation of autopsy brain specimens with inductively coupled plasma mass spectroscopy.** *Radiology* 2015;276: 228–32 CrossRef Medline
7. Kanal E, Tweedle MF. **Residual or retained gadolinium: practical implications for radiologists and our patients.** *Radiology* 2015;275: 630–34 CrossRef Medline
8. Robert P, Lehericy S, Grand S, et al. **T1-weighted hypersignal in the deep cerebellar nuclei after repeated administrations of gadolinium-based contrast agents in healthy rats: difference between linear and macrocyclic agents.** *Invest Radiol* 2015;50: 473–80 CrossRef Medline

T. Kanda
H. Oba
K. Toyoda
S. Furui
Department of Radiology
Teikyo University School of Medicine
Itabashi-ku, Japan

REPLY:

Our study commenced in the last quarter of 2013, concluded in May 2014, and was presented at the Symposium Neuroradiologicum held in Istanbul on September 7–12, 2014. As a result of multipdisciplinary authorship and distant collaborations, the manuscript was finally submitted to the *American Journal of Neuroradiology* in December 2014. At the initial period of our study, there were 2 articles in the literature concluding that hyperintense dentate nuclei (HDN) on T1-weighted MR imaging were secondary to rapidly progressive MS and radiation therapy (RT) effect.[1,2] We, therefore, investigated this entity in a large cohort of irradiated individuals and found no apparent associations between HDN and RT. During the data gathering and after the submission of our manuscript, several studies were published on this topic, mainly arguing the possible association of HDN and repeated performance of gadolinium-enhanced MR imaging.[3,4] McDonald et al[5] were the first to show actual gadolinium deposition in the human brain by using inductively coupled plasma mass spectrometry in postmortem subjects. Although linear gadolinium-based contrast agents were reported to be associated with HDN, the exact mechanism and clinical ramifications remain unclear.[6-8]

T1-weighted FLAIR is a recently described MR imaging sequence.[9] In brain imaging, it is mainly used to better differentiate gray and white matter, owing to its improved contrast difference. In our institution, it is not a part of the standard brain MR imaging protocol and is mainly performed for epilepsy. Because our cohort was obtained from those with a history of RT for underlying tumoral lesions, only a handful of the subjects were imaged with the T1 FLAIR sequence. As far as the authors' qualitative assessment, differentiating HDN from normal dentate nuclei (NDN) on axial T1 FLAIR images was not a matter of debate in any of subjects included in our study (Fig 1). On sagittal T1 FLAIR images, given the enhanced brightness of white matter, qualitative differentiation of faint HDN and NDN could be doubtful, particularly if the reader is not familiar with appearance of HDN. Nevertheless, without specific research on this topic, we do not speculate on the superiority of one technique (T1 FSE, FLAIR, MPRAGE, and so forth) over another in differentiating faint HDN from NDN. From our study cohort, we randomly looked into 7 subjects with NDN who underwent at least 6 contrast-enhanced MR imaging examinations by using linear gadolinium agents (Table). Not a single case was imaged with T1 FLAIR, practically excluding the possibility of HDN being misinterpreted as NDN.

The mechanism of gadolinium retention in the dentate nuclei is unknown, and individual factors contributing to the normal appearance of the dentate nuclei in some patients, despite the large amount of gadolinium administered, remain unclear.

http://dx.doi.org/10.3174/ajnr.A4608

ACKNOWLEDGMENTS

We thank Kanda et al for their interest in our study and their contribution to the knowledge of gadolinium safety.

REFERENCES

1. Roccatagliata L, Vuolo L, Bonzano L, et al. **Multiple sclerosis: hyperintense dentate nucleus on unenhanced T1-weighted MR images is associated with the secondary progressive subtype.** *Radiology* 2009; 251:503–10 CrossRef Medline
2. Kasahara S, Miki Y, Kanagaki M, et al. **Hyperintense dentate nucleus on unenhanced T1-weighted MR images is associated with a history of brain irradiation.** *Radiology* 2011;258:222–28 CrossRef Medline
3. Kanda T, Ishii K, Kawaguchi H, et al. **High signal intensity in the dentate nucleus and globus pallidus on unenhanced T1-weighted MR images: relationship with increasing cumulative dose of a gadolinium-based contrast material.** *Radiology* 2014;270:834–41 CrossRef Medline
4. Errante Y, Cirimele V, Mallio CA, et al. **Progressive increase of T1 signal intensity of the dentate nucleus on unenhanced magnetic resonance images is associated with cumulative doses of intravenously administered gadodiamide in patients with normal renal function, suggesting dechelation.** *Invest Radiol* 2014;49:685–90 CrossRef Medline
5. McDonald RJ, McDonald JS, Kallmes DF, et al. **Intracranial gadolinium deposition after contrast-enhanced MR imaging.** *Radiology* 2015;275:772–82 CrossRef Medline
6. Kanda T, Osawa M, Oba H, et al. **High signal intensity in dentate nucleus on unenhanced T1-weighted MR images: association with linear versus macrocyclic gadolinium chelate administration.** *Radiology* 2015;275:803–09 CrossRef Medline
7. Quattrocchi CC, Mallio CA, Errante Y, et al. **Gadodiamide and dentate nucleus T1 hyperintensity in patients with meningioma evaluated by multiple follow-up contrast-enhanced magnetic resonance examinations with no systemic interval therapy.** *Invest Radiol* 2015; 50:470–72 CrossRef Medline
8. Robert P, Lehericy S, Grand S, et al. **T1-weighted hypersignal in the deep cerebellar nuclei after repeated administrations of gadolinium-based contrast agents in healthy rats: difference between linear and macrocyclic agents.** *Invest Radiol* 2015;50:473–80 CrossRef Medline
9. Hori M, Okubo T, Uozumi K, et al. **T1-weighted fluid attenuated inversion recovery at low-field strength: a viable alternative for T1-weighted intracranial imaging.** *AJNR Am J Neuroradiol* 2003;24: 648–51 Medline

M.E. Adin
Division of Neuroradiology
The Russell H. Morgan Department of Radiology and Radiological Science
The Johns Hopkins Medical Institutions
Baltimore, Maryland
L. Kleinberg
Department of Radiation Oncology and Radiation Molecular Sciences
The Johns Hopkins Medical Institutions
Baltimore, Maryland
D. Vaidya
Johns Hopkins Bloomberg School of Public Health
The Johns Hopkins Medical Institutions
Baltimore, Maryland
E. Zan
S. Mirbagheri
D.M. Yousem
Division of Neuroradiology
The Russell H. Morgan Department of Radiology and Radiological Science
The Johns Hopkins Medical Institutions
Baltimore, Maryland

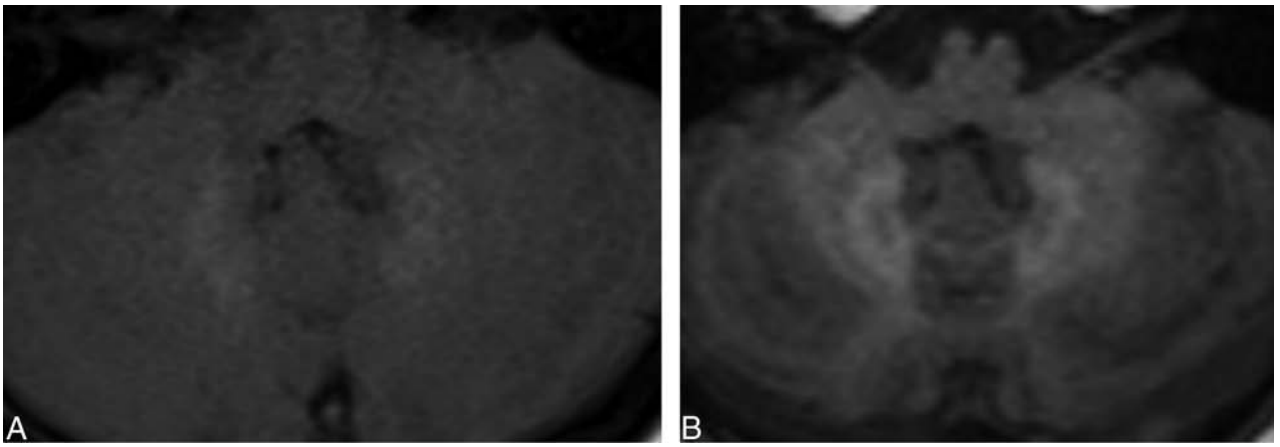

FIG 1. A 16-year-old girl who underwent periodic MR imaging after gadopentetate dimeglumine (Magnevist; Bayer HealthCare Pharmaceuticals, Wayne, New Jersey) administration for operated pilocytic astrocytoma of the optic nerve during 14 years. HDN was clearly visible on both sequences (*A*, FSE T1WI; TE, 526 ms; TE, 12 ms. *B*, T1 FLAIR; TR, 1200 ms; TE, 2.46 ms; inversion recovery, 600).

Number of contrast-enhanced MRIs and amount of gadolinium administration per scan[a]

No.	Agent Used	Subject 1	Subject 2	Subject 3	Subject 4	Subject 5	Subject 6	Subject 7
1	Magnevist	11 mL	13 mL	13 mL	17 mL	18 mL	3.6 mL	10 mL
2	Magnevist	11 mL	13 mL	13 mL	18 mL	19 mL	4 mL	10 mL
3	Magnevist	12 mL	15 mL	15 mL	20 mL	19 mL	4 mL	11 mL
4	Magnevist	13 mL	15 mL	15 mL	20 mL	19 mL	4 mL	11 mL
5	Magnevist	13 mL	15 mL	15 mL	20 mL	19 mL	4 mL	20 mL
6	Magnevist	13 mL	15 mL	17 mL	20 mL	20 mL	4 mL	
7	Magnevist	13 mL	15 mL	17 mL	20 mL	20 mL	4 mL	
8	Magnevist	15 mL	15 mL	17 mL	20 mL	20 mL		
9	Magnevist	15 mL	15 mL	20 mL	20 mL			
10	Magnevist	15 mL	15 mL	20 mL	20 mL			
11	Magnevist	20 mL	15 mL	20 mL				
12	Magnevist	20 mL	15 mL					
13	Omniscan	13 mL						17 mL
14	Omniscan	13 mL						
15	Omniscan	13 mL						

[a] T1 FLAIR was performed only in subjects 4 and 5. Although the subjects with a history of outside contrast-enhanced MRIs had been excluded, there may have been more contrast administration at outside centers because subjects had long follow-up times for underlying lesions. Therefore, the numbers illustrated in this Table should be considered as the least number of gadolinium administrations.

Carotid Web: Appearance at MR Angiography

In their article entitled "Carotid Webs and Recurrent Ischemic Strokes in the Era of CT Angiography," Choi et al[1] described the prevalence, demographics, clinical presentation, imaging features, histopathology, and stroke risk associated with carotid webs. We read this thorough review with great interest, and it has already helped us in our clinical practice.

Recently, an otherwise healthy 49-year-old woman presented to our hospital with neck pain and left-sided numbness, prompting an imaging work-up, including CTA of the head and neck. On sagittal reformatted images (Fig 1*A*), we noticed a thin intraluminal filling defect along the posterior wall of the carotid bulb, which appeared as a septum on axial images (Fig 2*A*). When we used the definition set forth by Choi et al,[1] our patient had findings consistent with a carotid web. No other abnormality was identified on her CTA. The carotid web was ipsilateral to the patient's clinically diagnosed TIA. Work by Choi et al and and Morgenlander and Goldstein[2] has demonstrated an association between TIA and ipsilateral carotid webs and has provided evidence to support the diagnosis in this patient.

Choi et al[1] mentioned that the MR imaging appearance of carotid webs has not been reported in the literature. Our patient also underwent MRA of the neck during her hospitalization, which included 2D time-of-flight and a black-blood, axial T1-weighted fat-suppressed sequence for the evaluation of vessel wall pathology. On the T1-weighted fat-saturated images, we observed a crescentic hyperintense signal (Fig 2*A*) consistent with hemorrhage.[3,4] The finding of Choi et al[1] of hemorrhage in 2 of the 4 patients for which carotid endarterectomy specimens were available is consistent with our findings on T1-weighted black-blood imaging in this patient. Axial source images from the 2D TOF image (Fig 2*B*) demonstrated abnormal flow-related enhancement in the area of the known web, possibly due to diminished or turbulent flow. The significance of abnormal flow in carotid webs in the pathogenesis of ipsilateral brain ischemia is uncertain but may be explained by the hypothesis of Choi et al[1] that "the existence of turbulence and stasis in a cul-de-sac upstream to the web…could potentially create a thrombogenic milieu."

Our case also demonstrates that when evaluated without CTA, a carotid web containing hemorrhage can be indistinguishable from hemorrhage in a nonstenosing atherosclerotic plaque. Whether carotid webs containing plaque hemorrhage confer a greater risk of ipsilateral ischemic events than webs without hemorrhage is unclear and requires future investigation.

In conclusion, we thank the authors for bringing the perhaps underdiagnosed entity of carotid web to our attention.

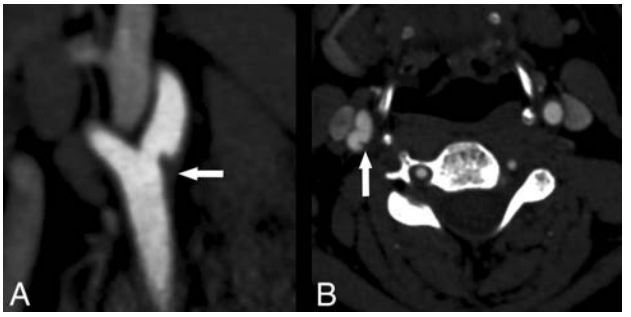

FIG 1. Sagittal reformat (*A*) from a CT angiogram demonstrates a thin intraluminal filling defect (*arrow*) along the posterior wall of the carotid bulb just beyond the carotid bifurcation. Axial source image (*B*) demonstrates a thin posterior septum (*arrow*) projecting into the lumen of the proximal right internal carotid artery. This finding is consistent with a carotid web using the definition set forth by Choi et al.[1]

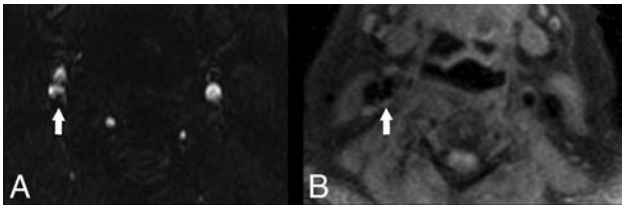

FIG 2. Axial source image from a 2D TOF MR angiogram (*A*) demonstrates some loss of flow-related enhancement (*arrow*) associated with the web, indicative of diminished or absence of flow. Axial T1-weighted fat-suppressed image (*B*) through the level of the carotid bulb demonstrates T1 shortening (*arrow*) consistent with hemorrhage associated with the carotid web seen on the CTA.

REFERENCES

1. Choi PM, Singh D, Trivedi A, et al. **Carotid webs and recurrent ischemic strokes in the era of CT angiography.** *AJNR Am J Neuroradiol* 2015 Jul 30. [Epub ahead of print] CrossRef Medline

http://dx.doi.org/10.3174/ajnr.A4598

2. Morgenlander JC, Goldstein LB. **Recurrent transient ischemic attacks and stroke in association with an internal carotid artery web.** *Stroke* 1991;22:94–98 CrossRef Medline
3. Gupta A, Baradaran H, Schweitzer AD, et al. **Carotid plaque MRI and stroke risk: a systematic review and meta-analysis.** *Stroke* 2013;44: 3071–77 CrossRef Medline
4. Gupta A, Baradaran H, Kamel H, et al. **Intraplaque high-intensity signal on 3D time-of-flight MR angiography is strongly associated with symptomatic carotid artery stenosis.** *AJNR Am J Neuroradiol* 2014;35:557–61 CrossRef Medline

J.E. Lantos
J.L. Chazen
A. Gupta
Department of Radiology
Weill Cornell Medical College
New York, New York

Risk of Malignancy in Symptomatic Nodular Goiter Treated with Radiofrequency Ablation

We read with great interest the recent article by Che et al.[1] In this article, the authors compared the efficacy, safety, and cost-effectiveness of surgery versus radiofrequency ablation (RFA) for the treatment of benign thyroid nodules. Two hundred patients were retrospectively selected for each group. The authors assessed procedure-related complications, the length of hospitalization, and cost. In addition, nodule volume, incidence of hypothyroidism, and the rate of residual nodules were assessed at 1-year follow-up. All of these outcomes uniformly favored RFA over surgery; the cost between the 2 procedures was not significantly different. Consequently, the authors advocated RFA as the first-line treatment for benign thyroid nodules.

We commend the authors for conducting the largest retrospective cohort study comparing these 2 treatment options for benign thyroid nodules. However, the result could be significantly confounded by patient-selection bias. The authors used different criterion standards to define benign thyroid nodules in the surgery-versus-RFA groups (surgery pathology and cytology from fine-needle aspiration, respectively). This patient-selection method excluded patients whose nodules were benign by cytology but malignant by surgical pathology in the surgery group. In fact, the potential of mistreating malignant nodules as benign ones is the strongest argument against RFA as the first-line treatment for symptomatic nodular goiter.[2]

Two studies in the literature compared surgery and RFA as a treatment for benign thyroid nodules. One is the current study.[1] In the other study, the authors found that 8% of their patients (6 of 74) in the surgical arm were misdiagnosed as having benign nodules.[3] Surgical pathologies in these patients later revealed malignant cells in their nodules.[3] RFA did not allow any pathologic analysis of the nodules. On the basis of these results, the authors concluded that RFA was not a safe alternative to surgery for the treatment of hyperfunctioning nodules.

In a related study, Negro et al[4] assessed the risk of undiagnosed malignancy in patients with multinodular goiter presumed to have benign thyroid disease and eligible for nonsurgical treatments. They found that 84 of 970 (8.6%) patients who underwent thyroidectomy had malignancy by histologic examination (5% incidental thyroid cancer and 3.6% false-negative fine-needle aspiration cytology).[4] Although 67 of these malignant thyroid nodules (79.8%) were stage I disease by the American Joint Committee on Cancer criteria, the authors concluded that the risk of malignancy in presumably benign thyroid disease cannot be overlooked.

In another related study of 1161 patients who underwent total thyroidectomy for diffuse multinodular goiter, 252 (21.7%) were cases of thyroid cancer.[5] In this study, the sensitivity of thyroid sonography and fine-needle aspiration cytology for cancer detection was only 30.3% and 64.1%, respectively. By preselecting patients who have benign disease on surgical pathology to compare with the RFA group, the current article effectively bypassed the most important question facing clinicians who need to discuss the pros and cons of the 2 approaches with their patients: What is the risk of a missed malignancy if I choose RFA over surgery? The consequence of such missed malignancy is currently unclear.

In conclusion, a randomized controlled trial is needed to compare the safety and efficacy of surgery versus RFA for the treatment of "benign" nodular goiter. If this is not feasible, long-term follow-up of patients treated with RFA is required before it can be recommended as first-line therapy.

ACKNOWLEDGEMENTS

This work was supported by the Natural Science Foundation of China (grant number 81301988) to Li Yang, and China Ministry of Education Doctoral Program Spot Foundation (grant number 20130162120061) to Li Yang.

REFERENCES

1. Che Y, Jin S, Shi C, et al. **Treatment of benign thyroid nodules: comparison of surgery with radiofrequency ablation.** *AJNR Am J Neuroradiol* 2015;36:1321–25 CrossRef Medline
2. Arora N, Scognamiglio T, Zhu B, et al. **Do benign thyroid nodules have malignant potential? An evidence-based review.** *World J Surg* 2008;32:1237–46 CrossRef Medline
3. Bernardi S, Dobrinja C, Fabris B, et al. **Radiofrequency ablation**

Indicates open access to non-subscribers at www.ajnr.org

http://dx.doi.org/10.3174/ajnr.A4580

compared to surgery for the treatment of benign thyroid nodules. *Int J Endocrinol* 2014;2014:934595 CrossRef Medline
4. Negro R, Piana S, Ferrari M, et al. **Assessing the risk of false-negative fine-needle aspiration cytology and of incidental cancer in nodular goiter.** *Endocr Pract* 2013;19:444–50 CrossRef Medline
5. Lasithiotakis K, Grisbolaki E, Koutsomanolis D, et al. **Indications for surgery and significance of unrecognized cancer in endemic multinodular goiter.** *World J Surg* 2012;36:1286–92 CrossRef Medline

L. Yang
Department of Neurology
The Second Xiangya Hospital of Central South University
Changsha, China
H. Tang
Department of Radiology
The First Xiangya Hospital of Central South University
Changsha, China
A.M. Lee
Department of Radiology
Hospital of the University of Pennsylvania
Philadelphia, Pennsylvania
Y. Zou
X. Huang
X. Tang
Department of Neurology
The Second Xiangya Hospital of Central South University
Changsha, China
H.X. Bai
Department of Radiology
Hospital of the University of Pennsylvania
Philadelphia, Pennsylvania

REPLY:

Radiofrequency ablation (RFA) has been used for more than 20 years as a minimally invasive treatment of tumor. It has been widely recognized by scholars.[1,2] In the past 10 years, RFA of thyroid nodules has developed rapidly because of the application of moving-shot technique, solving the problem of the important structures around the thyroid. A number of studies have shown that among the current treatment methods for benign thyroid nodules, RFA has many prominent advantages over the others, such as being minimally invasive, effective, relatively safe, cosmetically satisfactory, and having lower recurrence and so forth.[3,4]

Obviously, however, how to select the RFA cases, not only to treat but also to identify them, was a key issue that concerned Bai et al. Based on a comprehensive analysis of the literature, the results of multicenter studies, and expert consensus, an RFA recommendation was published in 2012 by Korean Society of Thyroid Radiology (KSThR).[5] In this publication, the indications for RFA of benign thyroid nodules included patients with nodule-related clinical problems: 1) symptoms of neck pain, dysphasia, foreign body sensation, discomfort, and cough; 2) cosmetic problems; and 3) autonomously functioning thyroid nodules causing problems related to thyrotoxicosis. Patients with nodules with a maximum diameter of >2 cm that continue to grow may be considered for thyroid RFA on the basis of symptoms and clinical concerns. The KSThR did not recommend thyroid RFA for follicular neoplasms or primary thyroid cancers because there is no evidence of treatment benefit. Before treatment, thyroid nodules should be confirmed as benign on at least 2 separate sonography-guided fine-needle aspirations and/or core needle biopsies.

At present, the concerning issue is the risk of malignancy in symptomatic nodular goiter. Ucler et al[6] and Lee et al[7] showed that the accuracy of fine-needle aspiration biopsy (FNAB) was 64.1%–99.6%. The diagnosis of false-negative findings was mainly due to groups of small cancer cells in the nodules and small cancers invisible under sonography. The results of the 2 punctures of the nodules in different places at different times should be benign, to avoid the risk of malignancy.[8] Furthermore, with combined elastography or contrast-enhanced sonography, the puncture point and results are more accurate. The operation for benign thyroid nodules is thyroidectomy, and the identification standard is intraoperative frozen pathology. Prades et al[9] reported that the accuracy of frozen pathology was 90% and maybe the potential malignancy was emerged in "benign" nodules. Negro et al[10] reported that postoperative pathology of symptomatic nodular goiter accidentally confirmed microcarcinoma in 5%; papillary thyroid microcarcinoma (PTMC) was 96%, and there was the possibility of recurrence. With no difference from pathology, which determined the operation mode, FNAB was used for preoperative diagnosis in all minimally invasive treatments. Ito et al[11] reported that there was no obvious growth and metastasis in the 8-year follow-up without treatment of 732 cases of PTMC. Yue et al[12] reported that during the 3-month follow-up period, ablation appears to be a safe and effective technique for solitary T1N0M0 PTMC.

Genetic testing had been used in the diagnosis of benign nodules undetermined by FNAB. Several molecular assays have been developed to detect the B-Raf proto-oncogene (*BRAF*) V600E mutation in fine-needle aspirates for the diagnosis of papillary thyroid cancer (PTC).[13] Musholt et al[14] considered that mutations of *RET/PTC*, *RAS*, and *PAX8*/peroxisome proliferator-activated receptor γ (*PPARγ*) were predominantly associated with thyroid malignancy with varying frequency and had less impact on the clinical management. However, in the study of Song et al,[15] *BRAF* mutations were the most common ones observed in PTCs, followed by *RET/PTC* rearrangements and *RAS* mutations, while follicular thyroid cancers were more likely to have *RAS* mutations or *PAX8/PPARγ* rearrangements.[15] Therefore, more extensive research is needed in genetic testing.

In conclusion, we suggested that RFA would be used as the first-line treatment of benign thyroid nodules with strict indications chosen. Elastography, contrast-enhanced sonography, and genetic testing would be used to differentiate the benign and malignant lesions.

http://dx.doi.org/10.3174/ajnr.A4612

REFERENCES

1. Rossi S, Di Stasi M, Buscarini E, et al. **Percutaneous radiofrequency interstitial thermal ablation in the treatment of small hepatocellular carcinoma.** *Cancer J Sci Am* 1995;1:73–81 Medline
2. Hefaiedh R, Sabbeh M, Ennaifer R, et al. **Percutaneous treatment versus hepatic resection for the treatment of small hepatocellular carcinoma.** *Tunis Med* 2014;92:711–16 Medline
3. Deandrea M, Sung JY, Limone P, et al. **Efficacy and safety of radiofrequency ablation versus observation for nonfunctioning benign thyroid nodules: a randomized controlled international collaborative trial.** *Thyroid* 2015;25:890–96 CrossRef Medline
4. Valcavi R, Tsamatropoulos P. **Health-related quality of life after percutaneous radiofrequency ablation of cold, solid, benign thyroid nodules: a 2-year follow-up study in 40 patients.** *Endocr Pract* 2015;21:887–96 CrossRef Medline
5. Na DG, Lee JH, Jung SL, et al; Korean Society of Thyroid Radiology (KSThR), Korean Society of Radiology. **Radiofrequency ablation of benign thyroid nodules and recurrent thyroid cancers: consensus statement and recommendations.** *Korean J Radiol* 2012;13:117–25 CrossRef Medline
6. Ucler R, Usluogulları CA, Tam AA, et al. **The diagnostic accuracy of ultrasound-guided fine-needle aspiration biopsy for thyroid nodules three centimeters or larger in size.** *Diagn Cytopathol* 2015;43:622–28 CrossRef Medline
7. Lee YJ, Kim DW, Park YM, et al. **Comparison of sonographic and cytological diagnoses of solid thyroid nodules: emphasis on the discordant cases.** *Diagn Cytopathol* 2015 Sep 21. [Epub ahead of print] CrossRef Medline
8. Singh Ospina N, Sebo TJ, Morris JC, et al. **The value of repeat thyroid fine-needle aspiration biopsy in patients with a previously benign result: how often does it alter management?** *Thyroid* 2015;25:1121–26 CrossRef Medline
9. Prades JM, Querat C, Dumollard JM, et al. **Thyroid nodule surgery: predictive diagnostic value of fine-needle aspiration cytology and frozen section.** *Eur Ann Otorhinolaryngol Head Neck Dis* 2013;130:195–99 CrossRef Medline
10. Negro R, Piana S, Ferrari M, et al. **Assessing the risk of false-negative fine-needle aspiration cytology and of incidental cancer in nodular goiter.** *Endocr Pract* 2013;19:444–50 CrossRef Medline
11. Ito Y, Uruno T, Nakano K. **An observation trial without surgical**

treatment in patients with papillary microcarcinoma of the thyroid. *Thyroid* 2003;13:381–87 CrossRef Medline
12. Yue W, Wang S, Yu S, et al. **Ultrasound-guided percutaneous microwave ablation of solitary T1N0M0 papillary thyroid microcarcinoma: initial experience.** *Int J Hyperthermia* 2014;30:150–57 CrossRef Medline
13. Choi R, Park KS, Kim JW, et al. **Evaluation of the Anyplex BRAF V600E real-time detection assay using dual-priming oligonucleotide technology in fine-needle aspirates of thyroid nodules.** *Ann Lab Med* 2015;35:624–29 CrossRef Medline
14. Musholt TJ, Musholt PB. **Molecular genetic markers for thyroid FNAB. Established assays and future perspective.** *Nuklearmedizin* 2015;54:94–100 Medline
15. Song YS, Lim JA, Park YJ. **Mutation profile of well-differentiated thyroid cancer in Asians.** *Endocrinol Metab (Seoul)* 2015;30:252–62 CrossRef Medline

Y. Che
Department of Ultrasound
First Affiliated Hospital of Dalian Medical University
Liaoning, China